

Best Available Copy

(12)

LIBRARY  
S. 1000  
1000

Best Available Copy

35 02 21 022

SECURITY CLASSIFICATION OF THIS PAGE (When Data Entered)

DD FORM 1 JAN 73 1473 EDITION OF 1 NOV 65 IS OBSOLETE  
S/N 0100-LF-014-6601

SECURITY CLASSIFICATION OF THIS PAGE (When Data Entered)

AERO-HYDROACOUSTICS FOR SHIPS

Accession For	
NTIS GRA&I	<input checked="checked" type="checkbox"/>
DTIC TAB	<input type="checkbox"/>
Unannounced	<input type="checkbox"/>
Justification	
By	
Distribution/	
Availability Codes	
Dist	Avail and/or Special
A-1	



# AERO-HYDROACOUSTICS FOR SHIPS

BY

WILLIAM K. BLAKE

Research Physicist  
Ship Acoustics Department

DAVID TAYLOR NAVAL SHIP RESEARCH  
AND DEVELOPMENT CENTER

VOLUME I

Chapters 1 to 6

JUNE 1984



## FOREWORD

This book is a comprehensive and unified treatment of the mechanisms of flow-generated sound that occurs on ships and in marine machinery. Often the control of these mechanisms involves the essentials of both fluid mechanics and structural dynamics.

Dynamical properties of various types of flow and of various structural elements that are typical of ship application are thus examined in detail beginning with the fundamentals of each physical source. Organization of the book provides for the treatment of elementary sources of flow noise and the principles of random vibration. In Volume 1, Normal mode analysis is the cornerstone of the methods used there to describe the behavior of flow induced vibration. Naval applications that involve turbulent boundary layer and lifting surface flows are discussed in Volume 2. Aerodynamic noise sources, in so far as they occur anogously in underwater acoustics, are examined in detail for low Mach number marine application.

## PREFACE

The requirements for reduced levels of shipboard sound and vibration have become increasingly demanding as each technological advancement in ship systems leads to a more sophisticated design goal. It is now clear that many traditional means of control that invoke the obstruction of transmission paths and the mechanical isolation of sound sources have now been fully exploited and in many instances are proving inadequate. This is particularly true in cases involving fluid flow. Modern technology now requires noise and vibration control that is fully integrated with the design of hydraulic machinery, propulsion equipment, and turbo machinery, to name only a few. It is often the case that the physical fundamentals of design also involve parameters which are essentially common to noise and vibration production and that very useful performance and acoustic tradeoffs may be conducted in design if only the noise-producing fundamentals are recognized by the designer. These tradeoffs may even be conducted as early as the preliminary design stage. These tradeoffs are as feasible in the private sector as they are in the Navy. In fact in almost every aspect of noise and vibration control which is important to the Navy, there is a parallel development of understanding in some other application. The purpose of this book is thus to provide an integrated description of the fundamentals of fluid-dynamically generated sound and vibration which is founded on the combined principles of acoustics, classical fluid mechanics, and vibration.

It is the aim of this book to set down the fundamentals of sound generation by different classes of fluid motions and flow-body interactions. Since the generation of sound is intimately connected with the creation of turbulence and other manifestations of flow unsteadiness, it is important to understand both acoustics and the appropriate elements of unsteady fluid mechanics. Thus a great deal of attention has been placed on the essentials of various turbulent flows, hydrodynamics of cavitation, boundary layer theory, and lifting surface theory. The purpose is to develop understanding and perspective on the part of the reader; for this reason, theoretical relationships that are derived are copiously illustrated with experimental data. This is often done through the use of dimensionless forms which give generalized presentations to support and extend the theory. In most cases that involve experimental results not collected by the author, this has required a

complete reworking of the data into a form that is consistent with the philosophy of the book. Fluid dynamic sources so treated include such classes of flows as flow tones, jet noise, cavitation, vortex shedding sounds, all forms of subsonic lifting surface noise, and sources which occur in axial flow machinery. Since in underwater acoustics, vibration often plays a dominant role, there is a chapter on the fundamentals of random vibration as it relates to flow-excited structures.

The scope of the book is broad, and all topics could not be covered completely. So, each chapter includes an extensive reference list. The lists are not exhaustive, but are reasonably complete.

The book is written for scientists and engineers who are not experts in fluid mechanics or acoustics; however, a knowledge of the fundamentals of each, particularly fluid mechanics, would be helpful. The treatment of structural vibration and structural acoustics is relatively cursory because there are already rather good monographs on those subjects that are available, as referenced. Although much of the mathematical treatment used is rather sophisticated, the analyses have been concentrated and kept identifiably separate from physical discussions whenever possible. This is so that readers desiring a more descriptive approach may also be served by the book.

The book has evolved from the author's own research experiences, as well as from the literature of both the aeroacoustics and hydroacoustics communities. The author is indebted to his colleagues at the Center and, in particular, to those in the Hydroacoustics Branch of the Ship Acoustics Department for their continuing interest in the project. Many people contributed to the preparation of the various chapters. Special thanks go to Professor Patrick Leehey of MIT whose graduate course on flow noise provided me with both instruction and inspiration, and to Drs. Alan Powell and Maurice Sevik who provided continuing understanding, stimulation, and encouragement as the work progressed. The work could not have been undertaken at all without the help of S. Blazek and A. R. Paladino of the Naval Sea Systems Command who sponsored much of the writing. Technical consultations with current and past colleagues at the Center on as many aspects of the work as possible were necessary to give the work depth and perspective; thanks are extended to G. Franz, J. T. C. Shen, G. Maidanik, M. Strasberg, F. C. DeMetz, as well as to T. Brooks of NASA, and R. Schlinker of UTRC. From time to time I imposed on a variety of experts to review selected chapters for content; gratitude is extended to

M. Casarella, D. Crighton, M. Howe, R. E. A. Arndt, R. Armstrong, F. B. Peterson, A. Kilcullen, D. Feit, M. C. Junger, F. E. Geib, R. Henderson, R. A. Cumming, W. B. Morgan, L. J. Maga, and R. E. Biancardi. Thanks are also due to D. Paladino and J. Gershfeld who read all or part of the manuscript and located many of the inconsistencies and errors.

The creation of camera-ready copy was made possible by a team of B. Devaney, B. Hay, J. Seidenstricker, and M. Gotthardt of DTNSRDC. C. Naas (also of DTNSRDC) and K. Simon (of Forte, Inc.) did the exceptionally difficult job of editing. T. Gilleland and R. Schmidt of the Center's Publications Department coordinated the typing and artwork.

Finally, the main debts are owed to my wife Donna who initially suggested the project and whose enduring gifts of love, support, and patience made possible its completion and to our daughters Kristen and Helen for their cheerfulness as they virtually grew up with the book around them.

W. K. Blake

Bethesda, MD

June 1984

# CONTENTS

	<u>Page</u>
PREFACE . . . . .	vii
LIST OF RECURRING SYMBOLS . . . . .	xvii

## VOLUME I

### CHAPTER 1 - INTRODUCTION

1.1 THE DISCIPLINES OF FLOW NOISE . . . . .	1
1.2 DIMENSIONAL ANALYSIS. . . . .	3
1.3 SIMILITUDE IN AERO-HYDROACOUSTIC MODEL TESTING. . . . .	12
1.4 REPRESENTATIONS OF SOUND LEVELS . . . . .	16
1.4.1 Sound Level Definition . . . . .	16
1.4.2 Sound Pressure Spectra . . . . .	18
1.4.3 Combination of Levels. . . . .	23
1.4.4 Use of Dimensionless Spectrum Levels . . . . .	24

### CHAPTER 2 - GENERAL THEORIES OF FLOW-INDUCED NOISE

2.1 FUNDAMENTALS OF LINEAR ACOUSTICS THEORY . . . . .	34
2.1.1 The Wave Equation. . . . .	34
2.1.2 Characteristics of Multipole Radiation . . . . .	42
2.2 SOMMERFELD'S RADIATION CONDITION. . . . .	51
2.3 Lighthill's THEORY OF AERODYNAMIC NOISE . . . . .	52
2.3.1 The Wave Equation. . . . .	52
2.3.2 Kirchhoff's Integral Equation and the Retarded Potential . . . . .	56
2.3.3 Acoustic Radiation from Free Turbulence. . . . .	61
2.4 EFFECTS OF SURFACES ON FLOW-INDUCED NOISE . . . . .	67
2.4.1 Curle's Development of Lighthill's Wave Equation . . . . .	67
2.4.2 Illustration I: Radiation from a Heaving Sphere . . . . .	71
2.4.3 Illustration II: Radiation from a Concentrated Hydrodynamic Force: The Force Dipole . . . . .	73
2.4.4 Powell's Reflection Theorem. . . . .	74
2.5 POWELL'S THEORY OF VORTEX SOUND . . . . .	80
2.5.1 General Implications. . . . .	80
2.5.2 Derivation of the Wave Equation with Vortical Sources. . . . .	81
2.5.3 The Physical Significance of the Vorticity Source. . . . .	83
2.5.4 The Effect of Solid Boundaries . . . . .	90
2.6 REPRESENTATIONS IN THE FREQUENCY DOMAIN . . . . .	91
2.6.1 Helmholtz Integral Equation. . . . .	92
2.6.2 Generalized Transforms and Stochastic Variables. . . . .	96
2.7 APPENDIX - DIPOLE RADIATION FROM THE HEAVING SPHERE: EXACT AND ASYMPTOTIC SOLUTIONS. . . . .	107
2.7.1 Asymptotic Formulas. . . . .	107
2.7.2 Exact Solutions. . . . .	111
2.8 REFERENCES. . . . .	113

## CHAPTER 3 - JETS, WHISTLES, AND OTHER SHEAR-FLOW NOISES

3.1	INTRODUCTION. . . . .	116
3.2	SHEAR FLOW INSTABILITIES AND THE GENERATION OF VORTICITY. . . . .	117
3.3	FREE SHEAR LAYER AND CAVITY RESONANCE . . . . .	125
3.4	SELF-EXCITATION OF LAMINAR JETS . . . . .	135
	3.4.1 Dimensionless Frequencies of Tonal Disturbances. . . . .	135
	3.4.2 Hole, Ring, and Edge Tones . . . . .	142
3.5	A SUMMARY OF STATISTICAL DESCRIPTIONS OF TURBULENCE . . . . .	150
	3.5.1 General Comments . . . . .	150
	3.5.2 Correlation Functions of Random Variables. . . . .	151
	3.5.3 Frequency and Wave Number Spectra. . . . .	155
3.6	FUNDAMENTALS OF NOISE FROM SUBSONIC TURBULENT JETS. . . . .	160
	3.6.1 Formal Analytical Relationships for Source Convection. . . . .	160
	3.6.2 Measured Characteristics of Jet Noise. . . . .	166
	3.6.3 Some Qualities of Jet Noise Deduced from Flow Structure. . . . .	173
3.7	NOISE FROM UNSTEADY MASS INJECTION. . . . .	197
	3.7.1 Sound From Efflux Inhomogeneities. . . . .	198
	3.7.2 Inhomogeneities in the Free Turbulent Field. . . . .	205
3.8	APPENDIX A - MEASUREMENT OF CROSS SPECTRAL DENSITIES WITH FILTERED SIGNALS. . . . .	208
3.9	REFERENCES. . . . .	219

## CHAPTER 4 - TWO-PHASE FLOW NOISE

4.1	INTRODUCTION. . . . .	229
	4.1.1 General Concepts . . . . .	229
	4.1.2 The Cavitation Index and Cavitation Similitude . . . . .	233
4.2	BASIC EQUATIONS OF BUBBLE DYNAMICS. . . . .	238
	4.2.1 Linear Bubble Motions. . . . .	238
	4.2.2 Sound Propagation in Bubbly Liquids. . . . .	248
	4.2.3 Theoretical Cavitation Thresholds; Non-Linear Oscillations Spherical Bubbles. . . . .	259
	4.2.4 Effects of Gas Content and Nuclei Distribution . . . . .	272
	4.2.5 The Collapse of Cavitation Bubbles . . . . .	283
4.3	HYDRODYNAMIC CAVITATION INCEPTION . . . . .	302
	4.3.1 General Equilibrium Theory . . . . .	302
	4.3.2 Examples of Cavitation Inception in Turbulent Flows. . . . .	316
4.4	HYDRODYNAMIC CAVITATION NOISE . . . . .	334
	4.4.1 Theoretical Spectrum of Single-Bubble Cavitation Noise . . . . .	334
	4.4.2 Simple Rules of Similitude . . . . .	344
	4.4.3 Examples of Hydrodynamically-Induced Cavitation Noise. . . . .	353
	4.4.4 Propeller Cavitation . . . . .	365
	4.4.5 Stochastic Models of Bubble Cavitation Noise . . . . .	381
4.5	SOUNDS FROM OTHER BUBBLE MOTIONS. . . . .	397
	4.5.1 Sound Pulses from Formation and Splitting. . . . .	397
	4.5.2 Bubbles Excited by a Pressure Field: Speed Dependence. . . . .	404
	4.5.3 Measurements of Bubble Noise . . . . .	407
	4.5.4 Hydromechanics of Bubble Formation . . . . .	411

4.6	APPENDIX A - DERIVATION OF APPROXIMATE SPECTRAL FUNCTIONS . . . . .	424
4.7	APPENDIX B - PHYSICAL PROPERTIES OF AIR AND WATER . . . . .	427
4.8	APPENDIX C - NOMOGRAPHS FOR COMPUTING PROPELLER PARAMETERS. . . . .	428
4.9	REFERENCES. . . . .	431

## CHAPTER 5 - GENERATION OF AEOLIAN TONES BY RIGID CYLINDERS

5.1	INTRODUCTION: GENERAL DESCRIPTION OF VORTEX FLOW, LIFT FLUCTUATION, AND SOUND . . . . .	448
5.2	MECHANICS OF VORTEX FORMATION BEHIND CIRCULAR CYLINDERS . . . . .	450
5.2.1	General Description of Wake Structure and Vortex Generation . . . . .	450
5.2.2	Wave-Mechanical Analysis of Vortex Production. . . . .	453
5.2.3	Secondary Disturbances in the Vortex Formation Zone. . . . .	462
5.3	MEASURED FLOW-INDUCED FORCES AND THEIR FREQUENCIES. . . . .	462
5.3.1	Mean Drag and Vortex Shedding Frequencies. . . . .	462
5.3.2	Oscillatory Lift and Drag on Circular Cylinders. . . . .	472
5.3.3	Representations of Axial Phase-Uniformity: Correlation Lengths. . . . .	476
5.4	ENVIRONMENTAL INFLUENCES ON VORTEX SHEDDING . . . . .	481
5.5	ESTIMATIONS OF WAKE-INDUCED FORCES IN TWO-DIMENSIONAL FLOW. . . . .	486
5.6	FORMULATION OF THE ACOUSTIC PROBLEM FOR COMPACT SURFACES. . . . .	497
5.6.1	General Equations. . . . .	497
5.6.2	Importance of Quadrupole Radiation . . . . .	500
5.6.3	Radiation from a Rigid Cylinder in a Cross-Flow. . . . .	502
5.6.4	Review of Measured Acoustic Intensities. . . . .	506
5.7	RADIATION FROM ROTATING RODS. . . . .	511
5.8	OTHER TOPICS IN VORTEX-INDUCED NOISE. . . . .	517
5.8.1	Cylinders with Non Circular Cross Sections . . . . .	519
5.8.2	Unsteadiness in Tube Bundles . . . . .	521
5.8.3	Methods of Reducing Vortex-Induced Forces. . . . .	526
5.9	REFERENCES. . . . .	529

## CHAPTER 6 - STOCHASTIC THEORY OF FLOW-INDUCED VIBRATION AND NOISE

6.1	INTRODUCTION. . . . .	537
6.2	RESPONSE OF SINGLE-DEGREE-OF-FREEDOM SYSTEMS TO TEMPORALLY RANDOM EXCITATION . . . . .	539
6.3	GENERAL FEATURES OF STRUCTURES DRIVEN BY RANDOMLY-DISTRIBUTED PRESSURE FIELDS . . . . .	545
6.3.1	Modal Velocities and Excitation Functions. . . . .	545
6.3.2	Vibration of Effectively Infinite Surfaces; The Infinite Plate . . . . .	549
6.3.3	Random Excitation of Single Mode Oscillators . . . . .	552
6.3.4	Response Estimates for Structures of Many Modes. . . . .	556
6.4	MODAL SHAPE FUNCTIONS FOR SIMPLE STRUCTURES . . . . .	565
6.5	ESSENTIAL FEATURES OF STRUCTURAL RADIATION. . . . .	571
6.5.1	Analysis of a Simply Supported Panel . . . . .	571
6.5.2	Fluid Impedance of a Simply Supported Panel. . . . .	576
6.5.3	Radiated Acoustic Power. . . . .	579
6.5.4	Radiation Efficiencies of Simple Structures. . . . .	584

	<u>Page</u>
6.5.5 Relationships for Estimating Total Acoustic Power. . . . .	587
6.5.6 Added Masses of Simple Structures. . . . .	593
6.6 RADIATION FROM STRUCTURES IN HEAVY FLUIDS . . . . .	594
6.6.1 Radiation From Essentially Infinite Point-Driven Plates. . . . .	594
6.6.2 Elements of Fluid Loading Without Modal Coupling . . . . .	596
6.7 EXAMPLE 1: RADIATION FROM A RECTANGULAR PANEL DRIVEN BY A TONAL LOCAL FORCE . . . . .	599
6.7.1 Determination of Mode Order. . . . .	600
6.7.2 Acoustic Classification of Mode Order. . . . .	602
6.7.3 Response Amplitude of the Panel. . . . .	604
6.7.4 Location in Space of the Maximum Sound Pressure Level. . . . .	604
6.7.5 Magnitude of the Far Field Pressure. . . . .	606
6.8 EXAMPLE II: RADIATION FROM A RECTANGULAR PANEL DRIVEN BY A BROADBAND FORCE . . . . .	610
6.9 REFERENCES. . . . .	619
INDEX (Repeated from Volume II) . . . . .	622a

## VOLUME II

### CHAPTER 7 - TURBULENT-BOUNDARY-LAYER STRUCTURE AND SURFACE PRESSURE

7.1 INTRODUCTION. . . . .	623
7.2 EQUILIBRIUM TURBULENT BOUNDARY LAYERS . . . . .	625
7.2.1 General Relationships and Dimensionless Representations. . . . .	625
7.2.2 Dimensionless Representations of the Mean Velocity Profile . . . . .	632
7.2.3 Prediction of the Wall-Shear Coefficient and Boundary- Layer Length Scales. . . . .	641
7.2.4 Turbulence Intensities and Statistical Correlations. . . . .	648
7.2.5 Description of Turbulence in the Frequency Domain . . . . .	660
7.2.6 Modern Views of Boundary-Layer Structure . . . . .	673
7.3 ANALYTICAL DESCRIPTIONS OF THE WALL PRESSURE FIELD. . . . .	683
7.3.1 General Relationships. . . . .	683
7.3.2 Overall Considerations of the Wave Number Spectrum . . . . .	694
7.3.3 Features of Turbulence Structure Affecting the Wave Number Spectrum of Wall Pressure . . . . .	702
7.3.4 Characteristics of the Frequency Spectrum of Wall Pressure . . . . .	708
7.3.5 Kinematic Modeling of Turbulence Using Wave Mechanics Analogies. . . . .	712
7.3.6 Low Wave Number Spectrum and Unsteady Local Convection . . . . .	717
7.3.7 Recent Modeling of $\hat{p}_p(\vec{k}, \omega)$ . . . . .	723
7.4 PRESSURE FLUCTUATIONS BENEATH EQUILIBRIUM WALL LAYERS . . . . .	729
7.4.1 Intensity and Frequency Dependence of Wall Pressures . . . . .	729
7.4.2 Spatial Characteristics and Convection of Wall Pressures . . . . .	737
7.4.3 Description in the Wave Number Domain. . . . .	747
7.4.4 Measured Pressures at Low Wave Numbers Using Spatial Filtering Techniques . . . . .	752
7.4.5 Particularities of Rough-Wall Boundary-Layer Pressures . . . . .	770
7.4.6 Effects of Transducer Size and Shape: The Response Function . . . . .	772



	<u>Page</u>
7.4.7 Transduction of Boundary-Layer Pressure Through Rubber Blankets. . . . .	779
7.4.8 Pressure Fluctuations in Turbulent Pipe Flow . . . . .	783
7.5 TURBULENT FLOW OVER CURVED SURFACES . . . . .	785
7.5.1 Transition to Turbulence . . . . .	785
7.5.2 Adverse and Favorable Static Pressure Gradients in Fully Developed Turbulence . . . . .	799
7.5.3 Pressure Fluctuations Beneath Separated Turbulent Flow . . . . .	806
7.5.4 Thick Axisymmetric Turbulent Boundary Layers: The Circular Cylinder. . . . .	807
7.6 REFERENCES. . . . .	813

## CHAPTER 8 - BOUNDARY-LAYER-INDUCED VIBRATION AND NOISE

8.1 INTRODUCTION. . . . .	832
8.2 FLOW-EXCITED STRUCTURAL VIBRATION . . . . .	833
8.2.1 General Method . . . . .	833
8.2.2 Effects of Hydrodynamic Coincidence on Single-Mode Response. . .	838
8.2.3 Empirical Confirmation . . . . .	846
8.2.4 Average Response of Many Modes . . . . .	849
8.3 SOUND FROM FLOW-INDUCED VIBRATION . . . . .	856
8.4 GENERAL RULES FOR HYDROACOUSTIC SIMILARITY AND NOISE CONTROL. . . . .	861
8.5 HISTORICAL NOTES ON MODELING $\phi_p(k, \omega)$ . . . . .	868
8.6 DIRECT RADIATION FROM TURBULENT BOUNDARY LAYERS . . . . .	870
8.6.1 Qualitative Analysis of Direct Radiation . . . . .	871
8.6.2 Recent Analyses of Direct Radiation. . . . .	875
8.7 REFERENCES. . . . .	892

## CHAPTER 9 - THE HYDROACOUSTICS OF NON CAVITATING LIFTING SURFACES

9.1 INTRODUCTION. . . . .	898
9.2 FUNDAMENTALS OF LIFTING-SURFACE NOISE . . . . .	899
9.2.1 Classifications of Flow Disturbances . . . . .	899
9.2.2 Characteristic Length and Time Scales for Acoustic and Aerodynamic Classifications. . . . .	901
9.2.3 Low and High Frequency Limits of Theory. . . . .	908
9.3 NOISE FROM INFLOW UPSTEADINESS. . . . .	924
9.3.1 Elements of Unsteady Airfoil Theory. . . . .	924
9.3.2 Oscillatory Lift Spectra from Ingested Turbulence. . . . .	936
9.3.3 Surface Pressures Resulting From Unsteady Loads. . . . .	943
9.3.4 Observations of Noise From Inflow Inhomogeneities. . . . .	946
9.4 VISCOUS EFFECTS: BOUNDARY-LAYER AND VORTEX-WAKE DEVELOPMENT. . . . .	953
9.4.1 Boundary-Layer Growth on Lifting Surfaces. . . . .	955
9.4.2 Conditions for Vortex Formation at Trailing Edges of Rigid Surfaces . . . . .	959
9.4.3 Suppression of Vortex Shedding With Changes in Edge Geometry . .	965
9.4.4 Alternative Definitions of Strouhal Numbers. . . . .	969
9.5 SELF-INDUCED SURFACE PRESSURE FLUCTUATIONS. . . . .	978
9.5.1 Tonal Surface Pressures From Vortex Shedding: Theory. . . . .	979
9.5.2 Measured Pressures From Vortex Shedding. . . . .	988

	<u>Page</u>
9.5.3 Pressures From Turbulent Separation. . . . .	993
9.5.4 Spanwise Correlation Lengths . . . . .	998
9.5.5 The Flow-Induced Forces at Trailing Edges. . . . .	1000
9.6 SOUND FROM TRAILING-EDGE FLOW . . . . .	1001
9.6.1 Summary. . . . .	1001
9.6.2 Acoustic Tones From Vortex Shedding. . . . .	1003
9.6.3 Sound From Aeroacoustic Scattering . . . . .	1011
9.7 FLOW-INDUCED VIBRATION AND SINGING. . . . .	1037
9.7.1 Linear Flow Excitation of Lifting Surfaces . . . . .	1038
9.7.2 Vibration Induced by Vortex Shedding From Cylinders and Airfoils . . . . .	1046
9.8 ILLUSTRATION: ESTIMATION OF RADIATED NOISE FROM A HYDROFOIL. . . . .	1068
9.8.1 Noise From Inflow Turbulence . . . . .	1070
9.8.2 Trailing-Edge Noise. . . . .	1071
9.8.3 Acoustic Tones from Vortex Shedding. . . . .	1072
9.8.4 Enhancement From Surface Vibration . . . . .	1073
9.8.5 Relative Sound Levels from Surface Motion and Pressures. . . . .	1076
9.9 REFERENCES. . . . .	1082
 CHAPTER 10 - NOISE FROM AXIAL FLOW MACHINERY	
10.1 INTRODUCTION. . . . .	1096
10.2 ELEMENTARY ACOUSTICS OF ROTATING MACHINERY. . . . .	1097
10.2.1 Sources of Noise. . . . .	1097
10.2.2 The Tonal Spectrum of Compressor Noise. . . . .	1100
10.2.3 Elementary Considerations for the Control of Interaction Noise . . . . .	1104
10.3 DESIGN PARAMETERS OF ROTORS AS LIFTING SURFACES . . . . .	1110
10.3.1 Similitude of Turbomachines . . . . .	1111
10.3.2 Propeller Blades as Lifting Surfaces. . . . .	1115
10.4 THEORETICAL FREE-FIELD ACOUSTICS OF ROTORS. . . . .	1124
10.4.1 Fundamental Analysis. . . . .	1124
10.4.2 Interaction Tones from Rotating Blade Forces. . . . .	1131
10.5 SELF-NOISE FROM ROTATING MACHINERY. . . . .	1142
10.5.1 Sounds From Steady Loading: Gutf Sound. . . . .	1142
10.5.2 Laminar Flow Surfaces . . . . .	1145
10.5.3 Turbulent Trailing-Edge Noise . . . . .	1149
10.5.4 Broadband Noise Related to Loading. . . . .	1152
10.5.5 Propeller Singing . . . . .	1158
10.5.6 Thickness Noise . . . . .	1159
10.6 INTERACTION NOISE IN AXIAL FLOW MACHINES. . . . .	1160
10.6.1 Deterministic Unsteady Loading. . . . .	1160
10.6.2 Turbulent Inflows . . . . .	1181
10.7 ROTATING MACHINERY IN ENCLOSURES. . . . .	1193
10.7.1 Elementary Duct Acoustics . . . . .	1193
10.7.2 Propagating Modes of a Ducted Rotor . . . . .	1196
10.8 REFERENCES. . . . .	1202
INDEX . . . . .	1213

# LIST OF RECURRING SYMBOLS

$R$	Aspect ratio
$A_p$	Area of a panel, or hydrofoil
$b$	Shear layer length scale (Chapter 3)
$B$	No. of blades in a rotor or propeller
$C$	Blade chord
$C_D, C_L, C_f, C_p$	Drag, lift, friction, and pressure coefficients, respectively
$c$	Wave speed, subscripted: $0$ - acoustic $b$ - flexural bending $m$ - membrane (Chapter 6) $m$ - mixture (Chapters 3 and 4) $l$ - longitudinal $g$ - group (Chapter 6), gas (Chapter 4)
$D$	Drag
$D$	Diameter (jet, propeller, rotor in Chapters 3, 4, 9)
$d$	Cylinder diameter, cross section
$E(x)$	Expected value of $x(=\bar{x})$
$f$	Frequency
$F_i(t)$	Force, or force per unit area, in $i$ direction
$F_r$	Froude number
$G(\vec{x}, \vec{y}), G(\vec{x}, \vec{y}, \omega)$	Green functions
$h$	Thickness of plate, hydrofoil, propeller blade
$H_n(\xi)$	Cylindrical Hankel function, $n^{th}$ order
$I$	Acoustic intensity
$J$	Propeller advance coefficient
$J_n(\xi)$	Bessel's function, first kind, $n^{th}$ order
$k, k_i$	Wave number: $i, i^{th}$ direction; $k_{13}$ , in the 1, 3 plane

$k_g$	Geometric roughness height
$k_s$	Equivalent hydrodynamic sand roughness height
$k_o$	Acoustic wave number $\omega/c_o$
$k_n, k_{mn}$	Wave numbers of n-th or m, n modes
$k_p$	Plate bending wave number, $k_p = \omega/C_b$
$k_T, k_q$	Thrust and torque coefficients for propellers and rotors, Equations (9-4), (9-5)
$K$	Cavitation index $(P_\infty - P_v)/q_\infty$
$L$	Lift or lift per unit area
$L_1, L_3$	Length across the stream, span
$L_i$	Geometric length in i-th direction
$\lambda_o$	Length scale used to denote a characteristic of fluid motion
$\lambda_c, \lambda_f$	Spanwise correlation length, eddy formation length
$M$	Mass
$m_s$	Structural plating mass per unit area
$m_m, m_{mn}$	Fluid added mass per unit area for m or mn vibration mode
$M_c, M_T, M$	Mach numbers: convection (c), tip (T)
$n_s$	Shaft speed, revolutions per second
$n(k), n(\omega)$	Mode number densities
$\vec{n}, n_j$	Unit normal vector
$n(R)$	Bubble distribution density number of bubbles per fluid volume per radius increment
$N$	Number of bubbles per unit fluid volume
$p$	Fluctuating pressure; occasionally subscripted for clarity: a or rad - acoustic, b - boundary layer, h - hydrodynamic
$P$	Average pressure
$P_\infty$	Upstream pressure

$P, P(\omega, \Delta\omega)$	Power, total and in bandwidth $\Delta\omega$ , respectively
$P_i$	Rotor pitch
$\dot{q}$	Rate of mass injection per unit volume
$q_\infty, q_T$	Dynamic pressures based on $U_\infty$ and $U_T$
$Q$	Torque
$Re_L$	Reynolds number based on any given length scale $L$ , and velocity scale, $U_\infty$ ( $U_\infty L/\nu$ )
$R$	Radius; used in Chapter 4 for general bubble radius, Chapter 10 for propeller radius coordinate
$R_b$	Bubble radius
$R_T, R_H$	Rotor Tip and Hub Radii, respectively
$R_{pp}$	Correlation function of pressure, normalized
$R_{ij}$	Correlation function of velocity fluctuations $u_i$ and $u_j$ , normalized
$r$	Acoustic range, occasionally subscripted to clarify special source point-field point identification
$\vec{r}, r_i$	Correlation point separation — the distribution from $r$ is clear in the text
$S$	Strouhal number $f_s l/U$ where $l$ and $U$ depend on the shedding body
$S_{mn}(\vec{k})$	Modal spectrum function
$S_e, S_{2D}$	One- and two-dimensional Sears functions
$S_p(r, \omega)$	Spectrum function used in Chapter 4 for cavitation noise
$t$	time
$T_{ij}$	Lighthill's stress tensor (page 54)
$U$	Average velocity, advance, $U_a$ free stream, $U_\infty$ convection, $U_c$ tip, $U_T$ hydrodynamic friction, $U_f = \sqrt{\tau_w/\rho_o}$ shedding, $U_s = U_\infty \sqrt{1 - C_{p_b}}$

$\vec{u}, u_i$	fluctuating velocities
$T$	Average time
$\bar{T}, T(t)$	Thrust, steady and unsteady
$V$	Vane number in Chapter 10
$v$	Volume fluctuation
$v(t)$	Transverse velocity of vibrating plate, beam, hydrofoil
$We$	Weber number in Chapter 4
$\vec{x}, x_i$	Acoustic field point coordinate
$\vec{y}, y_i$	Acoustic source point coordinate
$y_f$	Cross-wake shear layer thickness at point of maximum streamwise velocity fluctuation in wake

#### GREEK SYMBOLS:

$\alpha$	Complex wave number, used in stability analyses and as dummy variable
$\beta$	Volumetric concentration (Chapters 3 and 4); fluid loading factor $\rho_o c_o / \rho_p h \omega$ (Chapters 1, 6, 7, 8)
$\Gamma$	Vortex circulation
$\gamma$	Adiabatic gas constant (Chapter 4), rotor blade angle (Chapter 10)
$\delta$	Boundary layer or shear-layer thickness, also $\delta(.99)$ and $\delta(.995)$
$\delta(x)$	Dirac delta function, $\int \delta(x) dx = 1$
$\delta^*$	Boundary (shear) layer displacement thickness
$\eta_t, \eta_{rad}, \eta_m, \eta_v, \eta_h$	Loss factors: t, total; rad, radiation; m, mechanical; v, viscous; h, hydrodynamic
$\eta_i, \eta_p$	Powering efficiencies: i, ideal; p, propeller
$\theta$	Angular coordinate
$\theta_\tau$	Integral time scale of turbulence
$\phi$	Angular coordinate

$\Phi_v(\omega)$	Auto-spectral density of $V(t)$ , subscripted: p for $p(t)$ ; i for $u_i(t)$ , f for $F(t)$
$\Phi_v(\vec{y}, \omega)$	Auto-spectral density of $V(f)$ with dependence on location $y$ emphasized, other subscripts as above
$\Phi_{pp}(\vec{k}, \omega)$	Wave number, frequency spectrum of pressures
$\phi_m(\omega - \vec{U}_c \cdot \vec{k})$	moving axis spectrum
$\phi_i(k_j)$	Wave number spectrum of velocity fluctuation $u_i$
$\phi_{ij}(\vec{r}, \omega)$	Cross-spectral density between $u_i(\vec{y}, t)$ and $u_j(\vec{y} + \vec{r}, t)$
$\kappa$	von Karman constant (Chapter 7), radius of gyration of vibrating plate, beam, hydrofoil (Chapters 6, 8, 9)
$\vec{\kappa}, \kappa_{13}$	dummy wave number variables
$\lambda$	Wavelength (also turbulent microscale in Chapters 4 and 7, when subscripted with i, j, or t)
$\Lambda$	Integral correlation length; for spatial separations in i direction, $\Lambda_i$
$\mu$	Viscosity
$\nu$	Kinematic viscosity, $\nu_e$ eddy viscosity
$\nu_p$	Poisson's ratio
$\pi(\omega)$	Power spectral density
$\rho$	Density: $\rho_o$ , average fluid; $\rho_g$ , gas; $\rho_m$ , mixture; $\rho_p$ , plate material
$\sigma_{mn}$	Radiation efficiency of mn mode, also $\sigma_{rad}$
$\tau$	Time delay, correlation
$\tau_w$	Wall shear
$\tau_{ij}$	Viscous shear stress tensor, p. 53
$\phi(\vec{y}), \phi(y_i)$	Potential functions
$\Psi_{mn}(\vec{y}) \Psi_m(\vec{y})$	Mode shape functions
$\psi(\vec{y})$	Stream function
$\omega$	Circular frequency, $\omega = 2\pi f$
$\vec{\omega}, \omega_i$	Vorticity vector, component
$\Omega$	Shaft rate

# CHAPTER 1

## INTRODUCTION

### 1.1 THE DISCIPLINES OF FLOW NOISE

Sound and vibration produced by the flow of fluids has provided important limitations to various types of ships, aircraft, and fluid machinery. In many industrial and marine applications, thresholds are set for allowable levels of sound and vibration for reasons of habitability as well as the acceptable performance of onboard acoustic sensors on marine vessels. Flow-induced vibration may also generate fracture and damage in many structures that are exposed to flow; such structures include turbine blades, propellers, and buildings. Yet, in spite of this importance, the control of flow induced sound and vibration in engineering applications is a discipline that is more-or-less reserved for specialists. This is in some contrast to other more classical areas of sound and vibration for which the practicing engineer has at his disposal any number of texts. One of the purposes of this book is to fill that gap. The problems of vibration and sound that involve fluid flow are made worthy of separate and special treatment because of a three-way interaction of unsteady fluid mechanics, structural vibration, and acoustics. This book, then, presents an interdisciplinary look at a truly interdisciplinary subject area.

In a practical sense the generation of vibration and sound may be expected whenever there is a relative motion between two adjacent bodies of fluid, as in the case of jet noise, or between a fluid and a body moving through it, as in the case of noises from air frames, propeller fans, and helicopters. Thus, the sounds generated by sources such as cavitation, the formation of gas bubbles, propellers, ventilation fans, fairings over sonar systems, flow over cavities and discontinuities in surfaces, and the flow past wings, control surfaces, and rotor blades, and many more, are all determined by the nature of the flow disturbances as well as by the vibrational acceptance of the surfaces to flow excitation and the ability of those surfaces to then radiate sound. This book will deal with each aspect of this process.

Also, by tradition, hydroacoustics has often been regarded as the subject area produced by a flow-body interaction, particularly when the fluid is a single phase, and the direct result of the time-varying forces exerted at the fluid-body interface which are set up by the locally-generated flow disturbances. The interaction can be made more complicated if the motions of the body and fluid become coupled by



some feedback mechanism; such cases are referred to as "self-excited." The emitted sound is a superposition of fields created by the fluid forces as well as the induced body vibration. Noise control in all such situations may be possible by modifying the flow-induced forces, the structural response to those forces, and the efficiency by which structures radiate sound. Clearly then, effective engineering of sound and vibration requires an understanding of the many features of fluid-structure interactions in the machine under design.

Traditionally, the subject of aeroacoustics has been regarded to include those flow-induced noises that involve aerodynamic interactions of fluids and bodies. Therefore, it includes jet noise, air frame noise (which includes noises from flow over slots, gaps, and leading and trailing edges of lifting surfaces), the Aeolian tone (the singing of wires in the wind), and cabin noise due to boundary layer flow over aircraft fuselages. By accident, really, it is generally assumed that if the noise arises from a flow-body interaction, the surface is either rigid, or if it does vibrate, the noise primarily results from the distribution of aerodynamic forces on the body and only secondarily from the vibration of the body itself. Quite often practical interest will lie in high speed flow noise because of the application to modern aircraft.

Also, by tradition, hydroacoustics has often been regarded as the subject area of two-phase flow noise, e.g., sounds from cavitation, bubble formation, and splashes. Application generally lies with low speed marine vehicles and so such topics as jet noise are of little importance to marine application because the radiation efficiency of this noise is very small at low speeds. The other sounds due to interactions between bodies and single-phase flow, that are important to aeroacoustics are equally important here, but they are made complicated by the fact that the body ceases to act as a reflector, but rather as a more active contributor to the overall sound field. Quite often the structurally-generated sounds are more important because of the poor radiation efficiency of the fundamental fluid dynamic noise source. Propeller singing falls within this class of sources.

This book will take a broader look at the subject of vibration and sound. We begin with a comprehensive theoretical treatment of acoustics and sound generated by fluid motions and surface vibration in chapter 2. Following this we shall deal with three classical source types that do not necessarily involve vibration of a structure. These are monopole (cavitation, chapter 4) dipole (vortex-shedding sounds, chapter 5) and quadrupole (jets, chapter 3). General theoretical analysis

is again presented in chapter 6 when we examine the fundamentals of random vibration. The next three chapters deal with specialized topics that involve boundary layers (chapters 7 and 8) and flow around lifting surfaces (chapter 9). The broad and important subject of sound radiation from axial flow machines is examined in chapter 10.

## 1.2 DIMENSIONAL ANALYSIS

Three elements, then, must be considered in a comprehensive solution of a problem of flow induced sound and vibration: the unsteady fluid mechanics (turbulence characteristics), the response of any contiguous structure (impedance distribution, damping), the acoustic radiation field of any body vibration and turbulent flow sources. In view of this variety of interacting components of flow-noise problems, it is necessary to establish a systematic approach toward identifying the controlling parameters. This will be done now using dimensional analysis for the example of turbulent flow past a lifting surface such as is typical of turbo-machinery, aircraft, and marine components without cavitation. The analytical approach used here has wide application. As illustrated in Figure 1.1, the surface has a chord  $L$ , and thickness  $h$ ; the fluid moves past the surface at velocity  $U_\infty$  and

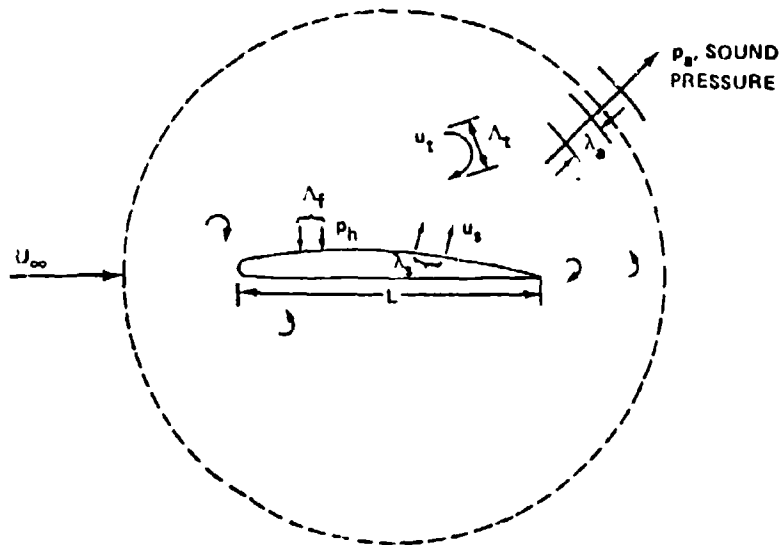


Figure 1.1 - Illustration of a Body Subjected to a Disturbed Flow; Body Vibration  $u_s$  of Wavelength  $\lambda_s$  Resulting from Surface Pressures  $p_h$  of Integral Length Scale  $\lambda_f$

surrounds it with a turbulent field of intensity  $u_t$  ( $|u_t| < 0.3 U_\infty$ , generally) and length scale  $\Lambda_t$ . Forces are exerted on the surface from a pressure distribution of magnitude  $p_h$  and length scale  $\Lambda_f$ . Just how these pressures are developed will be the subject of later chapters (5 through 10), but for now we simply say that they are only correlated over the area  $\Lambda_f^2$ . Therefore, we may think of a distribution of localized forces  $F_h$  of magnitude

$$F_h = p_h \Lambda_f^2$$

If  $A_s$  is the area of the surface, and if the pressures are evenly distributed over it, then the number of such forces is of order  $A_s / \Lambda_f^2$ . The lengths  $\Lambda_f$  and  $\Lambda_t$  may not be equal, one having to do with the ambient turbulence, the other with the bounding flow adjacent to the surface. In either case, each may be proportional to the chord  $L$  if all the turbulence is created by the subject surface. The force distribution will induce a flexural vibration level  $u_s$  on the surface, with a wavelength  $\lambda_s$ . To complete the picture, the sound pressure radiated from the surface  $p_a$  has a wavelength  $\lambda_a$ . Having introduced the vibrational wavelength, the acoustic wavelength, and the fluid length scale, we have acknowledged the existence of laws of similitude based on relationships among them. We shall identify next the circumstances under which these scales become important. The turbulent pressures are distributed over a range of frequencies  $f$  with a continuous spectrum function  $G_p(f)$  which is bounded by the upper and lower frequencies  $f_u$  and  $f_l$ . The pressure is related to its spectrum by (see section 1.4.2)

$$\overline{p_h^2} = (\rho_o U_\infty^2)^2 \int_{f_l}^{f_u} G_p(f) df$$

and similarly for the power

$$P = \int_{f_l}^{f_u} \pi(f) df$$

The sound pressure is a superposition of contributions from the free turbulence region, the force distribution over the surface which is imposed equally and in phase opposition to the force on the fluid, and the flow-induced vibration. In actuality, the superposition of radiated pressures from each source type must

regard both the amplitude and phase, but for now we are only interested in the gross relative magnitudes of sound power that are possible from each source acting separately.

First, the total radiated sound power  $P_T$  from the dynamic shearing motions in the turbulent region alone (neglecting the surface stresses and vibration due to the presence of the body) will follow the similarity law (Sections 2.3.3 and 3.6)

$$P_T \sim \rho_o \frac{U_\infty^8}{c_o^5} \frac{V_o}{\Lambda_t} \quad (1.1)$$

where  $c_o$  is the speed of sound in the liquid and  $V_o$  is the total volume occupied by the turbulent region. Equation (1.1) shows that  $P_T$  increases as Mach number to the fifth power. This shows that radiation from free turbulence at low Mach numbers is significantly less important than at high values. If we assume, for the moment, that the free turbulence is created only by the motion of the body, and accordingly that  $V_o$  is proportional to  $L^3$  and  $\Lambda_t$  is proportional to  $L$ , then the law of similitude will be

$$P_T \sim \rho_o U_\infty^3 L^2 M^5$$

where  $M = V_o/c_o$  is the Mach number of the flow. The power consumed by the surface in working against the flow will behave as

$$\bar{P} \sim \rho_o U_\infty^3 L^2$$

so that we may define an acoustic power loss factor as

$$\frac{P_T}{\bar{P}} = \eta_{acT}$$

and

$$\eta_{acT} \sim M^5 \quad (1.2)$$

Thus, the relative efficiency of sound production by the dynamics of the turbulent region increases as the fifth power of Mach number in agreement with the previous assessment of quadrupole sound power. This dependence on speed is shown in Figure 1.2.

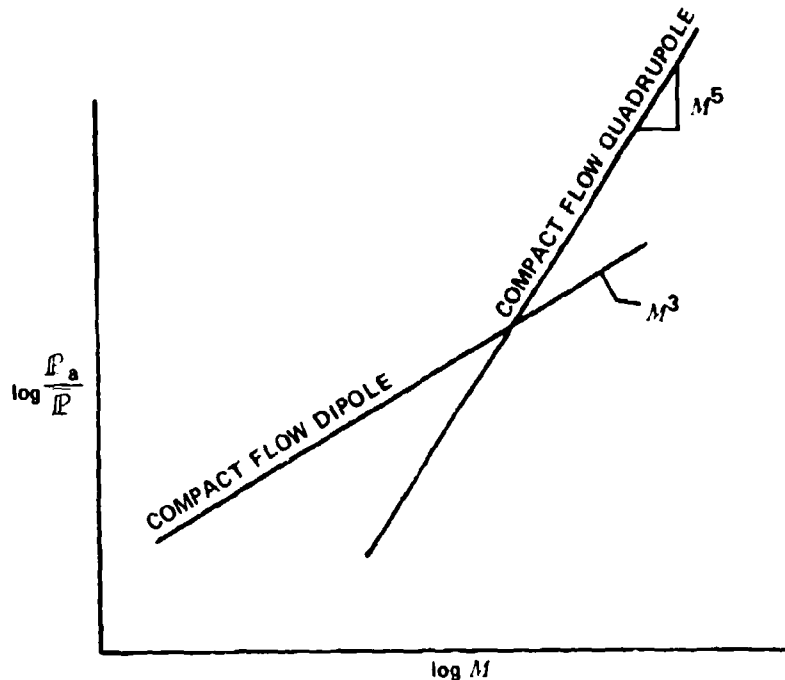


Figure 1.2 - Dependence of Radiated Acoustic Power on Mach Number for Elementary Compact Flow Dipoles and Quadrupoles. Acoustic Power is Shown in Relation to the Available Fluid Power

The radiated power spectrum from the force distribution over the surface, assuming that the surface is rigid, has a frequency spectrum (Sections 2.4.3, 5.6, and 9.2) which may be expressed as

$$\pi_D(f) \sim \left( \frac{F_h(f) f^2}{\rho_o c_o^3} \right) \cdot \left( \frac{A_s}{A_f^2} \right) \cdot D \left( \frac{fL}{c_o}, \frac{fA_f}{c_o} \right)$$

The function  $F_h(f)f^2$  represents the frequency spectrum of the rate of change of hydrodynamic forces at a point on the surface. The first term represents contribution to the total power by each of the uncorrelated force elements, the second term

represents the number of such elements on the surface, and the third term represents the various scattering effects which may occur when the chord exceeds an acoustic wavelength,  $\lambda_a = c_o/f$ , or when the correlation length  $\Lambda_f$  exceeds  $\lambda_a$ . The factor  $\mathcal{D}$  expresses the spatial matching between the pressures on the surface and the sound and it approaches one when  $L/\lambda_a$  or  $\Lambda_f/\lambda_a$  are both much less than one. These effects are discussed at length in Chapter 8. From the above it can be stated that  $\overline{F_h^2}(f)$  will depend on the parameters of the problem as

$$\overline{F_h^2}(f) \sim (\rho_o U_\infty^2)^2 \Lambda_f^4 G_p(f) \quad (1.3)$$

therefore, we may write the acoustic power spectrum as

$$\pi_D(f) \sim \left(\frac{U_\infty}{c_o}\right)^3 \rho_o U_\infty^3 L^2 \left(\frac{fL}{U_\infty}\right)^2 \left(\frac{\Lambda_f}{L}\right)^2 G_p(f) \cdot \mathcal{D}\left(\frac{fL}{c_o}, \frac{f\Lambda_f}{c_o}\right) \quad (1.4)$$

or

$$\pi_D(f) \sim M^3 \rho_o U_\infty^2 L^2 G_p(f) \left(\frac{fL}{c_o}\right)^2 \left(\frac{\Lambda_f}{L}\right)^2 \cdot \mathcal{D}\left(\frac{fL}{c_o}, \frac{f\Lambda_f}{c_o}\right)$$

The predominant frequency of the flow excitation is  $f_\lambda$  which we shall let be  $f_\lambda \sim U_\infty/\Lambda_f$ . Now, if we let  $\Lambda_f \sim L$ , as done for the noise from free turbulence, then the ratio of the total acoustic power to the mechanical power depends on Mach number as

$$\eta_{ac} \sim M^3 \quad (1.5)$$

Thus, the total sound power efficiency for the force-dipole increases with Mach number less rapidly than for the quadrupole power, as shown in Figure 1.2. This means that at low Mach numbers, dipole sound caused by acoustically compact surface forces may be more important than quadrupole sound emitted by the distribution of shear stresses in the turbulent flow around and in the wake of the body. Note the above analysis has shown the relationship between these co-existent sources to be speed dependent and that quadrupole sound may tend to become relatively more important than dipole sound at high speeds.

A third source of sound power arises from the surface vibration, the sound power spectrum from which is dependent on the vibrational surface velocity as

$$\pi_s(f) \sim \rho_o c_o A_s \sigma_r \left( \frac{f \lambda_s}{c_o}, \frac{f L}{c_o} \right) \overline{u_s^2}(f)$$

The function  $\sigma_r(f \lambda_s / c_o, f L / c_o) \leq 1$  is the radiation efficiency (see Section 6.5) of the structure. It is a function of the overall geometry of the structure, and of the ratios  $\lambda_s / \lambda_a$  and  $L / \lambda_a$ . As  $\lambda_s / \lambda_a \rightarrow 1$  and  $L / \lambda_a > 1$  then  $\sigma \rightarrow 1$ . The vibrational velocity of the surface is related to the surface impedance,  $Z(f)$  and to the local force spectrum  $\overline{F_h^2}(f)$  as (see Sections 6.3, 6.4, 7.6.1, and 8.6.1)

$$\overline{u_s^2}(f) = \frac{F_h^2(f) \frac{A_s}{(\lambda_f)^2}}{|Z(f)|^2} G\left(\frac{\lambda_f}{\lambda_s}\right)$$

where the factor  $A_s / \lambda_f^2$  accounts for the number of local force units of magnitude  $F_h$  on the surface where  $G(\lambda_f / \lambda_s)$  is a coefficient that expresses the spatial matching of the hydrodynamic force distribution with the wavelength of vibration in the structure; it is analogous to  $D(L / \lambda_a, \lambda_f / \lambda_a)$  of Equation (1.3) and it also is a function of geometry. If each vibrational mode of the structure behaves as a linear harmonic oscillator, then at a given frequency (Section 6.2) the flexural impedance of any mode will behave as

$$Z(f) = -i (\rho_p h f_r A_s) \left[ \left( \frac{f}{f_r} \right)^2 + i \eta \left( \frac{f}{f_r} \right) - 1 \right]$$

or, introducing a nondimensional impedance function  $z(f/f_r)$ ,

$$Z(f) = (\rho_p h f_r A_s) z \left( \frac{f}{f_r} \right) \cdot \left( \frac{f}{f_r} \right)^{-1}$$

where  $\eta$  is the loss factor of the structure. The resonance frequencies  $f_r$  form a discrete set which, for a given structural geometry, vary with the body length scale  $L$  and bending wave speed  $c_b$ , as

$$f_r L \sim c_b$$

and  $c_b$  varies as

$$c_b \sim (f_r h c_\ell)^{1/2}$$

where  $c_\ell$  is the bar wave speed in the structural material. If we fix the value of  $f/f_r$  and combine terms then we can write the power spectrum in the general form

$$\pi_s(f) \sim \rho_o c_o A_s \cdot \sigma_r \left( \frac{f \lambda_s}{c_o}, \frac{f L}{c_o} \right) \cdot \frac{\overline{F}_h^2(f) \left( \frac{A_s}{\lambda_f^2} \right)}{[A_s \rho_p h]^2 f_r^2} \cdot \frac{G \left( \frac{\lambda_f}{\lambda_s} \right) \left( \frac{f}{f_r} \right)^2}{\left| z \left( \frac{f}{f_r} \right) \right|^2}$$

Introducing Equation (1.3), and rearranging, we find the sound power spectral density radiated by each mode in the same form as Equation (1.4)

$$\pi_s(f) \sim \frac{U_\infty}{c_o} \cdot \rho_o U_\infty^3 L^2 \cdot \left( \frac{\lambda_f}{L} \right)^2 \left( \frac{\rho_o c_o}{\rho_p h f_r} \right)^2 \cdot \sigma_r \left( \frac{f \lambda_s}{c_o}, \frac{f L}{c_o} \right) \frac{G \left( \frac{\lambda_f}{\lambda_s} \right) \left( \frac{f}{f_r} \right)^2}{\left| z \left( \frac{f}{f_r} \right) \right|^2} G_p(f) \quad (1.6)$$

as the general similarity function for the sound power spectral density radiated from flow-induced structural vibration. Equation (1.6) contains in general fashion all the factors pertaining to the hydroacoustic coupling of the unsteady fluid motion, the structural vibration, and the acoustical properties of the fluid medium. To proceed further in our assessment of the importance of structural vibration versus radiation from flow-dipoles we must invoke certain particularities of the factors  $\sigma_r$ ,  $z(f/f_r)$  and  $\mathcal{D}(fL/c_o, f\lambda_f/c_o)$  in Equations (1.4) and (1.6).

Part of Figure 1.3 shows Equation (1.4) to arbitrary scale nondimensionalized on the mechanical power factor  $\rho_o U_\infty^3 L^2$  and normalized on the hydrodynamic pressure spectral density acting on the surface. The curve represents an "acoustic radiation efficiency" as a function of frequency of the hydrodynamic dipole forces acting on the surface as if it were completely rigid. The departure of the curve from an  $f^2$ -dependence at frequencies  $fL/c_o > 1$  is provided by the fact that  $\mathcal{D}(fL/c_o)$  decreases



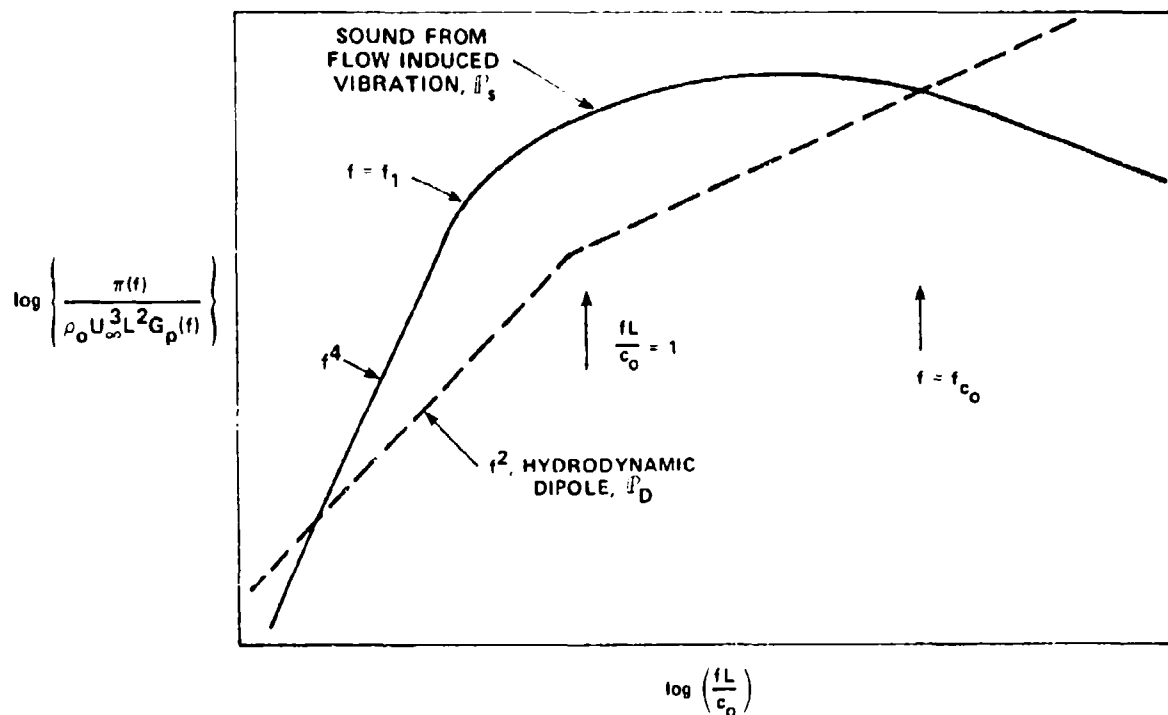


Figure 1.3 - Relative Spectra of Radiated Sound Power from Fluid Dynamically Induced Vibration and Surface Forces

inversely with frequency when the surface becomes larger than an acoustic wave length. The fundamentals of this are given in Section 9.2.

We deal now with the behavior of  $P_s(f)$  also shown in Figure 1.3. The coupling factor  $G(\lambda_f/\lambda_s)$  may be assumed to vary slowly or not at all with frequency in comparison with the other factors in Equation (1.6). Very low and very high frequency regions may be identified in which certain simplifications may be made. In the very low frequency limit, which lies below the fundamental structural resonance, i.e., for  $f < f_r$  the impedance function behaves as  $|z| = 1$ . The fundamental resonance frequency may be thought of as "scaling" on the length parameter  $L$  and the thickness parameter  $h$  as indicated above, so we may say roughly that  $f_r \sim C_\lambda h/L^2$  for a particular structural configuration. At these low frequencies, the acoustic wave lengths are larger than the extent of the body, i.e., for  $fL/c_o < 1$ , considerations of Sections 2.1.2 and 6.5.4 suggest the behavior

$$\sigma_r \sim \left( \frac{fL}{c_o} \right)^m$$

where the minimum value of  $m$  is 2 for a baffled structure, or for a volume source (Section 2.1.2). Accordingly, equation (1.6) may be rearranged into the form (with  $m=2$ )

$$P_s(f) \sim M \rho_o U_\infty^3 L^2 G_p(f) \cdot \left( \frac{\rho_o c_o}{\rho_p c_\ell} \right)^2 \left( \frac{L}{h} \right)^6 \left( \frac{c_o}{c_\ell} \right)^2 \left( \frac{fL}{c_o} \right)^4 G \left( \frac{\lambda}{\lambda_s} \right) \quad (1.7)$$

for  $f < f_{res}$  and  $fL/c_o \ll 1$ . This result differs from Equation (1.4) in two important characteristics which provide for the importance of structural vibration. First the factor  $(\rho_o c_o / \rho_p c_\ell)^2$  provides for very different radiation impedances for similar structures in dissimilar fluids. For example, two geometrically similar structures of a given structural material in air and in water will radiate acoustic power in proportion to the ratio of fluid acoustic impedances squared. Since  $\rho_o c_o$  of water is  $4.5 \times 10^3$  larger than for air, the  $(\rho_o c_o)^2$  term will account for 70 decibels greater sound output in water than in air. The second important feature in comparing Equations (1.4) to (1.7) is the presence of  $f^4$  compared to  $f^2$ . Thus, low-frequency energy conversion will increase more rapidly with frequency for flow-induced vibration than for radiation due to the forces themselves.

We now consider a high frequency limit. At frequencies above the fundamental resonance of the structure, the behavior of  $|z|^2$  is marked by a sequence of minima and maxima which are due to the many structural resonances of the structure. A simple means of conceptually avoiding this complication is to obtain an average value of  $P_s(f)$ . This is obtained by summing the responses of all resonant modes between two limiting frequencies,  $f_1$  and  $f_1 + \Delta f$ , where  $\Delta f$  increases in direct proportion to  $f_1$ . Dividing the summed power by  $\Delta f$  we find the average power spectrum

$$\bar{P}_s(f) = \frac{1}{\Delta f} \int_{f_1}^{f_1 + \Delta f} P_s(f) df$$

In Section 6.3.2 it is shown for flexural vibrations of a plate that the effective value of  $1/|z|^2$  behaves in proportion to  $f A_s (\eta h C_\ell)^{-1}$ . We take this behavior as representative of typical structural impedances. Also at high frequencies such that the acoustic wavelength is smaller than both a structural wavelength and the dimensions of the structure, i.e.,  $f \lambda_s / c_o > 1$  and  $f L / c_o > 1$ , then  $\sigma_r = 1$  (see Section 6.5.4). The average power spectrum then is of the form (assuming constant  $G \left( \frac{\lambda_f}{\lambda_s} \right)$ )

$$\bar{P}_s(f) \sim M \rho_o U_\infty^3 L^2 G_p(f) \cdot \left( \frac{\rho_o c_o}{\rho_p C_\ell} \right)^2 \left( \frac{C_\ell}{f L} \right) \left( \frac{L}{h} \right)^3 \quad (1.8)$$

which is also shown in Figure 1.3. We note that the frequency for which  $f \lambda_s / c_o = 1$  is called the acoustic coincidence frequency  $f_{co}$  of the flexural waves; equation (1.8) only applies at frequencies greater than this. Between the two frequencies  $f_1$  and  $f_{co}$  the function  $\bar{P}_s$  peaks at some maximum value as indicated. The details of the fluid-structure interaction would determine both the magnitude and the frequency of this maximum. Figure 1.3 shows that for a given structure geometry the relative importance of the two radiation contributions will increase or decrease in proportion to  $(\rho_o c_o) / (\rho_p C_\ell)$ . It is therefore often, though not exclusively, the case that in certain frequency regions  $\bar{P}_s(f) > \bar{P}_D(f)$  in hydroacoustic applications and that  $\bar{P}_D(f) > \bar{P}_s(f)$  in aeroacoustic applications. As Figure 1.3 implies, there may be frequency ranges for which the roles of the sources may be reversed.

The above remarks, therefore, are not to be taken to suggest that aeroacoustics is exclusively a rigid body phenomena. Two prominent examples of aerodynamically-induced structural radiation are cabin noise of aircraft and certain sounds of circular saw blades. Therefore, the above equations are derived to be suggestive of the parameters which control radiation from the two sources. A specific example is worked out in Chapter 9.

### 1.3 SIMILITUDE IN AERO- AND HYDROACOUSTIC MODEL TESTING

Equations (1.1), (1.3), (1.4), and (1.6) through (1.8) indicate what essential conditions of dynamic similitude must be maintained in model testing for the respective source strengths. First, regarding the fluid, Equation (1.3) reflects the fact that the fluid forces will be simulated when  $U_\infty$ ,  $\lambda_f$ , and  $\rho_o$  are maintained in appropriate relationship. This relationship is assured when the inertial forces, which

are proportional to  $\rho_o U_\infty^2 \Lambda_f^2$ , are maintained in the correct proportion to viscous forces which scale on  $\mu U_\infty \Lambda_f$ . Thus, hydrodynamic similitude requires that the ratio

$$\frac{\text{inertial forces}}{\text{viscous forces}} = \frac{\rho_o U_\infty \Lambda_f}{\mu}$$

is fixed in two scales. Now, when this ratio of forces is maintained for models of two sizes,  $\Lambda_f$  will be proportional to the body dimension, i.e.,  $\Lambda_f \sim L$ , so that we finally state that the requirement is that the ratio

$$R = \frac{\rho_o U_\infty L}{\mu}$$

is constant for both scales and that, in general,  $\Lambda_f/L$  is a function of  $R$

$$\frac{\Lambda_f}{L} = F(R)$$

The ratio  $R$  is the Reynolds number of the flow. Dimensional arguments further dictate that the frequency will scale as

$$\frac{f \Lambda_f}{U_\infty} \sim \frac{f L}{U_\infty}$$

so that a dimensionless representation of the flow-induced force field is

$$\frac{\overline{F_h^2} \left( \frac{fL}{U_\infty} \right)}{\rho_o^2 U_\infty^4 L^4} = G_p \left( \frac{fL}{U_\infty}, R \right)$$

where  $G_p(fL/U_\infty)$  is a dimensionless function of the dimensionless frequency and Reynolds number. Also required is the maintenance of the function  $\mathcal{D}(fL/c_o)$  in the

two scales; this requires acoustic similitude which implies that the ratio of the inertial to compressive stresses in the fluid is also maintained. This ratio is

$$\left( \frac{\rho_o U_\infty^2}{\rho_o c_o^2} \right) = M^2$$

which means that the Mach number  $M$  must be comparable in both scales. Reynolds number and Mach number similitude also ensure appropriate representation of both quadrupole noise (Equation (1.1)) and force dipole noise (Equation (1.4)), as can be seen by examining the terms involved.

A contradiction arises, however, when we hold model and full-scale measurements to the same fluid medium. In this case equality of both Reynolds numbers and Mach numbers can only be achieved when the model size  $L_m$  equals the full-size,  $L_f$ . Therefore, the only practical resolution is to select one of these dimensionless parameters to be maintained equal in both scales. Generally the selection is made to maintain Mach number similitude and to assume or verify by some indirect means that the dichotomy in  $R$  caused by the smaller size  $L_m < L_f$  does not seriously limit the validity of results.

Similar arguments apply when structural vibration is the dominant sound source. First, maintenance of acoustic similitude requires that

$$M_m = M_f$$

If the fluid and structural media are the same in both scales, then we also have

$$\left( \frac{\rho_o c_o^2}{\rho_p c_\ell^2} \right)_m = \left( \frac{\rho_o c_o^2}{\rho_p c_\ell^2} \right)_f$$

At the scaled frequencies,

$$f_m = f_f \left( \frac{L_f}{L_m} \right) \left( \frac{c_{\ell_m}}{c_{\ell_f}} \right)$$

$$= f_f \left( \frac{L_f}{L_m} \right) \left( \frac{U_m}{U_f} \right)$$

then, we therefore have equal coupling coefficients: in Equation (1.6)

$$\text{radiation efficiency} \quad (\sigma_r)_m = (\sigma_r)_f$$

$$\text{structural impedance} \quad (Z)_m = (Z)_f$$

$$\text{fluid structure coupling} \quad (G_a)_m = (G_a)_f$$

if and only if we can be sure that

$$\frac{(\Lambda_f)_m}{L_m} \approx \frac{(\Lambda_f)_f}{L_f}$$

and that the nondimensional hydrodynamic force spectra are similar, i.e.,

$$G_p \left( \frac{fL}{U}, R_m \right) \approx G_p \left( \frac{fL}{U}, R_f \right)$$

even though it might be stipulated that the Reynolds numbers are disproportionate by a factor

$$R_m = \frac{L_m}{L_f} R_f$$

If the integral scale and spectrum function are each weak functions of Reynolds number then the above near equalities in  $\Lambda_f/L$  and  $G_p(fL/U)$  will hold. This is what often happens in practice when the flows are fully turbulent. Exceptions occur when

the flow is transitional between laminar and turbulent, the flow is characterized by a discrete vortex formation, and flow-structure-acoustic interactions are mutually coupled through a complex feedback mechanism. In these three interaction classes the fluid mechanics will be especially sensitive to the delicate force and impedance relationships that characterize each aspect of interaction. Another variable which must be either simulated or measured is the damping in the structure  $\eta$ . This is a difficult parameter to scale when it depends on internal friction in joints of structural members. Damping is scaled when it is due to hydrodynamic or radiation losses so that similarity in the above structural and acoustic variables is maintained.

Table 1.1 summarizes the various force relationships which must be simulated in aero- and hydroacoustic modeling. The parameters Weber ( $We$ ), Froude ( $Fr$ ), and cavitation indices ( $K$ ) apply to the simulation of two-phase fluid mechanics. These variables will be discussed in Chapter 4. The table is exhaustive for all processes that do not involve heat conduction, mass transfer, or chemical reaction. It is not possible to rank the dimensionless variables in the order of importance in similitude, because such a ranking depends on the test objective and the groupings that are important in each test. About the only generalization to be made is that  $We$ ,  $Fr$ , and  $K$  are irrelevant in single-phase fluid media. The compressibility  $\rho c^2$  applies to both two-phase fluid and fluid-structure interactions. Also listed, although not previously discussed here, is a similarity in surface finish shape and size. Along with similarity in  $R$  this requirement maintains proper simulation of flows which are transitional between laminar and turbulent. The similitude in  $We$  for fluid-body interactions also implies similarity in wettability.

## 1.4 REPRESENTATIONS OF SOUND LEVELS

### 1.4.1 Sound Level Definition

In dealing with acoustic signals radiated by a source into free space, the parameter most often measured is the sound pressure at some point in the fluid. This quantity may be related very simply to the acoustic intensity radiated from the source as long as the pressure measured is entirely due to dilatational (acoustic) deformation of the fluid. Also, it is required that the measurement must be made far enough from the radiating source so that the radius of curvature of the acoustic

TABLE 1.1  
DIMENSIONLESS RATIOS APPROPRIATE TO REQUIREMENTS OF SIMILITUDE

Similitude		Parameter	Application
(Inertial forces) : (Viscous forces)		$R = \rho_o UL/\mu$	All flows
Geometry	Gross:	Body size, shape	All flows
	Surface Finish:	$(k_g/L)_1 = (k_g/L)_2$	
(Inertial stress) : (Compressive stress)		$M = \bar{u}/c_o$	All flows
Material (fluid) compressibility		$(\rho c^2)_1 \div (\rho c^2)_2$	Fluid [1] - fluid [2] and fluid [1] structure [2] interactions
(Fluid (acoustic) impedance) : (Structural mass impedance)		$\rho_o c_o / \rho_p h$	Fluid-structure interactions
(Energy dissipated) ÷ (Kinetic energy)		$\eta$	Fluid-structure interactions, hydroelastic coupling
(Pressure stresses) : (Inertial stresses)		$K = (P_\infty - P_v) / \frac{1}{2} \rho_o U^2$	Cavitation
(Inertial forces) : (Gravitational forces)		$F_r = u/(gL)^{1/2}$	Buoyancy and hydrostatic effects
(Gas inertial stresses) : (Surface tension)		$W_e = \rho_o U_g^2 L/S$	Gas jet disintegration in liquids, bubble splitting

wave fronts is much greater than an acoustic wavelength. When these conditions are met then the "far field" intensity  $I$  and acoustic pressure  $p$  are related by

$$I = \frac{p^2}{\rho_o c_o}$$

where  $\rho_o c_o$  is the specific acoustic impedance of the fluid. The time average of the intensity or of the pressure squared is the reported parameter

$$\bar{I} = \frac{1}{T} \int_{-T/2}^{T/2} I(t) dt$$

or



$$\overline{p^2} = \frac{1}{T} \int_{-T/2}^{T/2} p^2(t) dt$$

which is also called the time mean square of the pressure.

The sound pressure level is defined in decibel notation as\*

$$L_S = 10 \log \frac{\overline{p^2}}{p_{\text{ref}}^2}$$

where  $p_{\text{ref}}^2$  is  $10^{-6} \text{ n/m}^2$  (1  $\mu\text{Pa}$  or micropascal) for sound pressures measured in liquids, or  $p_{\text{ref}}$  is  $2 \times 10^{-5} \text{ n/m}^2$  (20  $\mu\text{Pa}$ ) for sound pressures measured in gases. Similarly, a sound intensity level may be defined

$$L_I = 10 \log \frac{I}{I_{\text{ref}}}$$

where  $I_{\text{ref}}$  is  $10^{-12} \text{ W/m}^2$ . A third level determinant, the sound power level, is defined as

$$L_P = 10 \log \frac{P}{P_{\text{ref}}}$$

where  $P_{\text{ref}} = 10^{-12} \text{ W}$ . The sound power is obtained by integrating the sound intensity flux across a surface circumscribing the source. The full meaning of acoustic pressure, intensity, and power will become clear in Chapter 2 when we discuss radiation from particular sources.

### 1.4.2 Sound Pressure Spectra

The sound pressure, being a temporally dynamic variable, is composed of a superposition of disturbances at different frequencies. In the traditional sense, in order to sample the acoustic pressure at specific frequencies, the signal sensed by a microphone or hydrophone is electronically filtered over a frequency band, squared,

---

\*One decibel is an increase of sound power or intensity by a factor of 1.259.

and time averaged. This quantity  $\overline{p^2}(f, \Delta f)$  is the mean square pressure measured with bandwidth  $\Delta f$  centered on  $f$ . If  $\Delta f = f_2 - f_1$ , then  $f$  is defined as the geometric mean of  $f_2, f_1$ , i.e.,  $f = (f_1 f_2)^{1/2}$ . Figure 1.4 describes the functional operation of a "frequency analyzer" that performs this operation.\* The overall mean square pressure  $\overline{p^2}$  of all frequencies and  $\overline{p^2}(f, \Delta f)$  of the filtered pressure are related (see the appendix of Chapter 3) by the spectrum function  $G(f)$ . This relationship is found as follows:

$$\overline{p^2}(f, \Delta f) = \int_0^{\infty} G(f) |H(f)|^2 df \quad (1.9)$$

where  $|H(f)|^2$  is the filter response function which ideally passes signals only between  $f_2$  and  $f_1$  and no other frequencies; accordingly, we may have

$$\overline{p^2}(f, \Delta f) = \int_{f_1}^{f_2} G(f) df$$

for a flat filter pass band. We can deduce from the above that the spectrum function is given in the limit of narrow bandwidth, i.e.,

$$\lim_{\Delta f \rightarrow 0} \frac{\overline{p^2}(f, \Delta f)}{\Delta f} = G(f)$$

Put in a more operationally significant form, if  $G(f_2) \approx G(f) \approx G(f_1)$  this says that

$$\overline{p^2}(f, \Delta f) \approx G(f) \Delta f$$

---

\*The filtering and averaging process shown is known as an analog frequency analysis and was, at one time, the only method used. The frequency analysis of time dependent signals is now accomplished with modern sophisticated digital or hybrid digital-analog instrumentation. For the purposes of the current discussion, no distinction needs to be made between them.

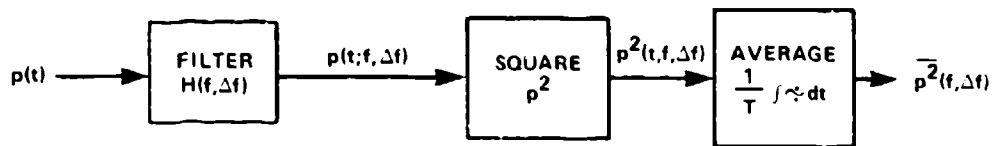
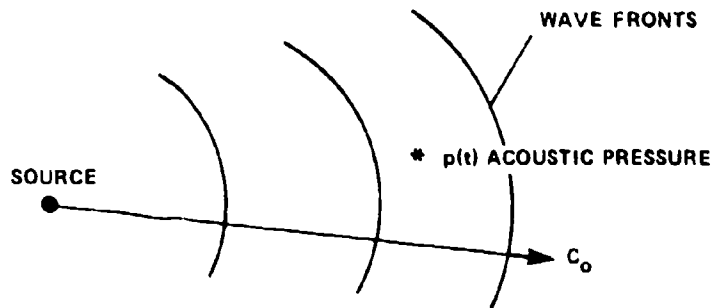


Figure 1.4 - Illustration of Acoustic Pressure Measurement and the Functional Diagram of a Frequency Analyzer

(Symbol  $p$  represents instantaneous voltages proportional to acoustic pressure. Identical notions hold for such measurements as acceleration, displacement, velocity, and force, etc.)

The overall sound pressure level is found from the spectral density function by

$$\overline{p^2} = \int_0^{\infty} G(f) df \quad (1.10)$$

Therefore, if, as illustrated in Figure 1.5, we have  $\overline{p^2}(f, \Delta f)$  in a series of adjacent bands between  $f_1$  and  $f_2$ , i.e.,  $\Delta f_1, \Delta f_2, \Delta f_3, \dots$ , etc., then

$$f_2 - f_1 = \sum_{i=1}^N \Delta f_i$$

and

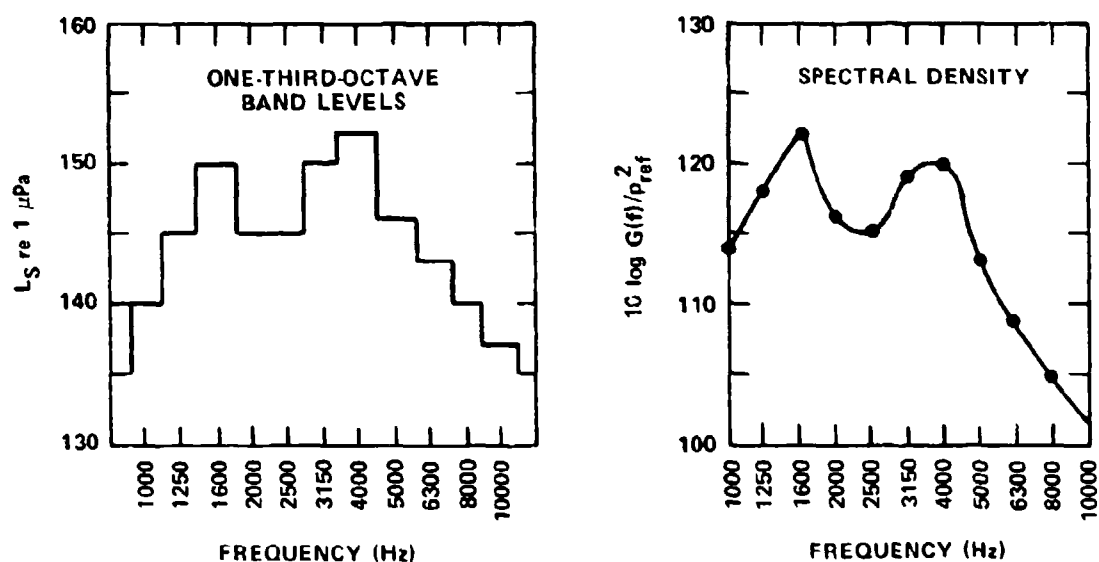


Figure 1.5 - Example of a One-Third Octave Spectrum ( $L_S$ ) and the Equivalent 1-Hertz Spectral Density  $G(f)$

$$\overline{p^2} = \sum_{i=1}^N \overline{p^2}(f_i, \Delta f_i) \quad (1.11)$$

where  $f_i$  = center frequency of the  $i^{\text{th}}$  band

$\Delta f_i$  = bandwidth

$N$  = number of bands in  $f_2 - f_1$

When the bandwidth of the pressure spectrum is narrower than the bandwidth of the filter, as illustrated in Figure 1.6, then Equation (1.9) gives

$$\begin{aligned} \overline{p^2}(f, \Delta f) &= |H(f_o)|^2 \int_0^\infty G(f) df \\ &= \overline{p^2} \quad \text{for } f_1 < f_o < f_2 \\ &= 0 \quad \text{for } f_o < f_1 \text{ or } f_o > f_2 \end{aligned}$$

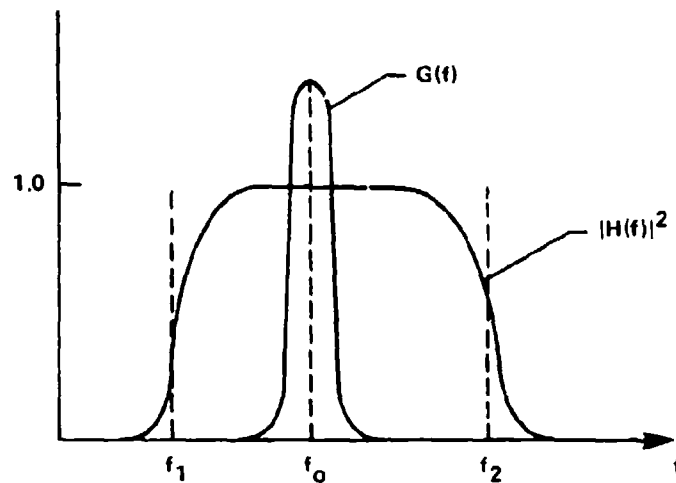


Figure 1.6 - Filtering of a Narrow Band Signal; the Filter Output Equals the Mean Square Level

This means that the filter passes the overall mean square pressure of a narrow band pressure and the increasing or decreasing of the filter bandwidth  $f_2 - f_1$  has no effect on the value of  $\overline{p^2}(f, \Delta f)$  unless  $f_2 - f_1$  is reduced to be smaller than the bandwidth of  $G(f)$ . For broadband pressure spectral densities, Equation (1.10) shows that the value  $\overline{p^2}(f, \Delta f)$  increases with increasing  $\Delta f$ .

Commonly used frequency bands are proportional bands for which  $\Delta f$  is proportional to the center frequency of the filter. An octave band is that for which  $\Delta f = f_2 - f_1$  and  $f_2 = 2f_1$ . One-third octave bands are those for which  $f_2 = 2^{1/3}f_1$ ;  $1/m$  octave bands are those for which  $f_2 = (2^{1/m})f_1$ . Accordingly, for the most commonly used proportional band, the  $1/3$  octave band,  $\Delta f = 0.232f$  where  $f$  is the center frequency  $(f_2 f_1)^{1/2}$ . In general,

$$\frac{\Delta f}{f} = \frac{2^{1/m} - 1}{2^{1/2m}}$$

where typically  $m = 1, 3, \text{ or } 10$ .

### 1.4.3 Combination of Levels

Sound pressure levels radiated from two uncorrelated sources A and B power-sum; i.e., the net contribution from the sources is

$$\overline{p^2} = \overline{p_A^2} + \overline{p_B^2}$$

the sound pressure level is

$$\begin{aligned} (L_S)_{TOT} &= 10 \log \left\{ 10^{(L_S)_A/10} + 10^{(L_S)_B/10} \right\} \\ &= L_{S_A} + 10 \log \left\{ 1 + 10^{(L_{S_B} - L_{S_A})/10} \right\} \end{aligned}$$

The rather complicated-looking term on the right is the quantity to be added to  $L_{S_A}$  to obtain  $(L_S)_{TOT}$ . For example, if the individual sound pressure levels are equal ( $L_{S_A} = L_{S_B}$ ) the net sound pressure level will be  $10 \log (2 \overline{p_A^2} / p_{ref}^2)$  or  $(L_S)_A + 3$ . Figure 1.7 shows the number of decibels to be added to  $(L_S)_A$  to obtain  $(L_S)_{TOT}$  as a function of  $L_{S_A} - L_{S_B}$ .

To find the average of two mean square sound pressures, we note that

$$\overline{p_{AV}^2} = \frac{1}{2} \overline{p_{TOT}^2}$$

accordingly,

$$(L_S)_{AV} = (L_S)_{TOT} - 3$$

These level combination formulas are useful in obtaining overall sound pressure levels from spectra of one-third octave band levels. Equation (1.11) formally describes this process. The overall sound pressure level, which we may denote as

$$L_{OA} = (L_S)_1 + 10 \log \sum_{i=2}^N \left\{ 1 + 10^{[(L_S)_i - (L_S)_1]/10} \right\}$$

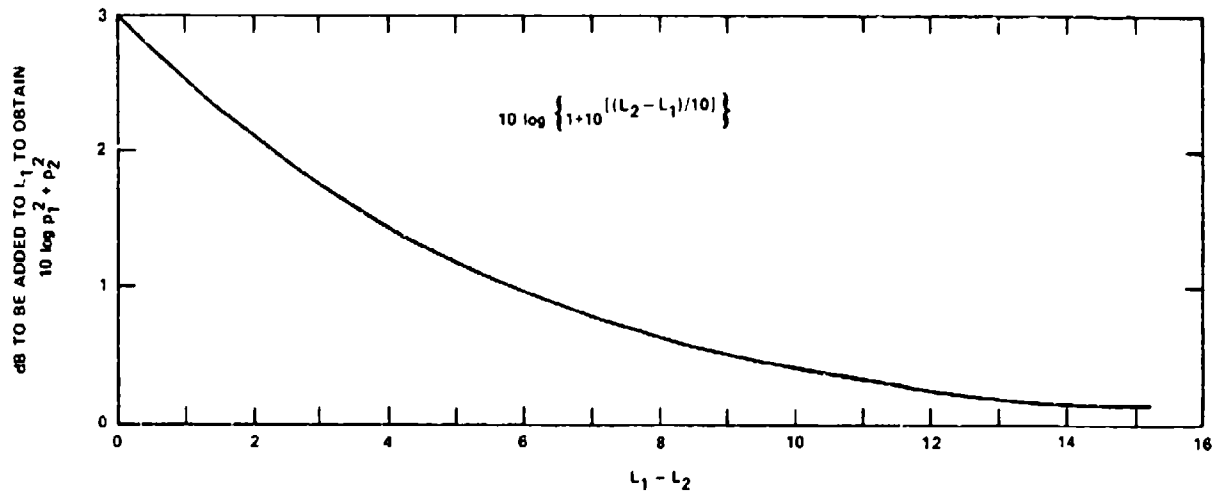


Figure 1.7 - Decibel Addition Chart for Combining Levels  $L_1$  and  $L_2$

can be evaluated by successively combining pairs of levels. Figure 1.8 illustrates this pairing process for a spectrum of band levels defined as

$$L_S(f, \Delta f) = 10 \log \left[ \overline{p^2}(f, \Delta f) / p_{\text{ref}}^2 \right]$$

#### 1.4.4 Use of Dimensionless Spectrum Levels

In this book we will be continuously relating engineering estimations of  $L_S(f, \Delta f)$  with both theoretical relationships and laboratory measurements. Analytical treatments as used in this book introduce the Fourier transform pair

$$A(\omega) = \frac{1}{2\pi} \int_{-\infty}^{\infty} a(t) e^{i\omega t} dt$$

and

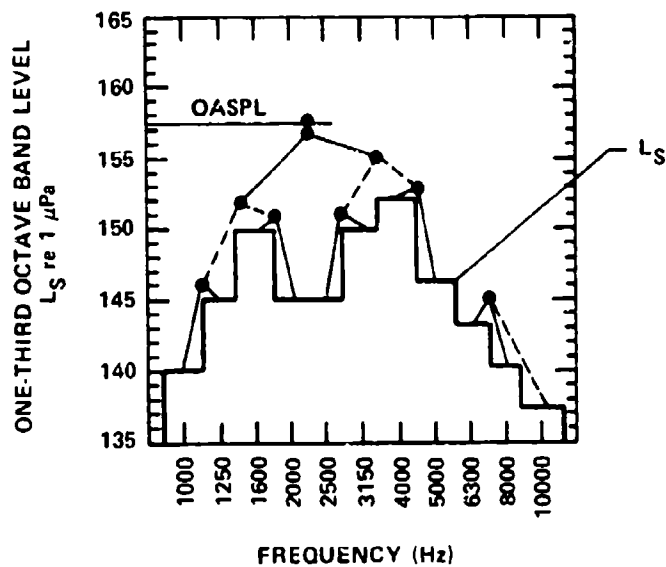


Figure 1.8 - Level Combination Scheme to Determine the Overall Sound Pressure Level (OASPL) of the Spectrum Shown in Figure 1.5.

(Note  $L_S$  levels at 6300 Hz through 10,000 Hz contribute little to the OASPL.)

$$a(t) = \int_{-\infty}^{\infty} A(\omega) e^{-i\omega t} d\omega$$

where  $\omega$  is angular frequency. As we shall see in Chapters 2 and 3, if the mean square pressure is independent of both the duration of time from averaging and the instant that the averaging is begun, then it is related to the spectral density  $\Phi(\omega)$

$$\overline{p^2} = \int_{-\infty}^{\infty} \Phi(\omega) d\omega \quad (1.12)$$

where  $\Phi(\omega)$  is symmetric about  $\omega = 0$ . This integral relationship is fully consistent with the above definition of the Fourier transform.



The angular frequency  $\omega$  is related to the frequency  $f$  by

$$\omega = 2\pi f \quad (1.13)$$

The spectrum functions  $G(f)$  and  $\Phi(\omega)$  are also proportionately related. Equations (1.10) and (1.12) give the equation

$$2 \Phi(\omega) \Delta\omega = G(f) \Delta f$$

the 2 on the left-hand side accounts for the symmetry of  $\Phi(\omega)$  on  $\omega < 0$  and  $\omega > 0$ . By virtue of Equation (1.13) we can write

$$\Phi(\omega) = \frac{G(f)}{4\pi} \quad (1.14)$$

in terms of the operation used for obtaining  $G(f)$  we can calculate  $\Phi(\omega)$  from measured band levels using the formula

$$\Phi(\omega) = \frac{1}{4\pi} \lim_{\Delta f \rightarrow 0} \frac{\overline{p^2}(f, \Delta f)}{\Delta f}$$

If we can assume that  $G(f)$  is nearly flat over  $\Delta f$  then the following may be written:

$$10 \log G(f) = 10 \log \overline{p^2}(f, \Delta f) - 10 \log \Delta f$$

or

$$10 \log \frac{G(f)}{p_{\text{ref}}^2} = L_s(f, \Delta f) - 10 \log \Delta f \quad (1.15)$$

and, therefore,

$$\begin{aligned}
 10 \log \Phi(\omega) &= L_S(f, \Delta f) + 10 \log p_{\text{ref}}^2 - 10 \log 4\pi - 10 \log \Delta f \\
 &= L_S(f, \Delta f) + 20 \log p_{\text{ref}} - 11 - 10 \log \Delta f
 \end{aligned} \tag{1.16}$$

Equations (1.15) and (1.16) may be used to determine the required spectrum quantities from measured sound pressure levels.

It is typical in flow-induced noise problems that the sound levels increase as speed to the fifth or sixth power, and for dominant frequencies to increase in direct proportion to speed.

Accordingly, if we normalized  $G(f)$  or  $\Phi(\omega)$  on the standard acoustic reference pressure, we would need a spectrum for each velocity condition. However, theoretically the spectrum function may be scaled on definite functions of speed. Using the nomenclature introduced earlier to describe similitude, we often find that the sound pressure spectral density can be expressed in dimensionless forms such as (see for example pages 515, 516 for vortex sound)

$$\frac{\Phi(\omega) \frac{U}{L}}{q^2 M^2 \left(\frac{L}{r}\right)^2} \sim \frac{\omega L}{U}$$

in which the spectrum may be also written  $\Phi(\omega)U/L = \Phi(\omega L/U)$ . The factors  $q^2$  and  $U/L$  take account of the dimensionality of  $\Phi(\omega)$  which is pressure squared times time. The factors  $M^2$  and  $(L/r)^2$  are scale factors determined by acoustical properties of the source;  $\Phi(\omega L/U)$  has dimensions of pressure squared. These parameters will vary from case to case as we shall see in various chapters. Current interest is in relating the Equation (1.16) to Equations (1.14) and (1.15). Figure 1.9 shows dimensionless and dimensional representations for spectral functions for the sound pressure as described by Equation (1.16). At a scaled frequency

$$\frac{\omega L}{U} = \frac{2\pi f L}{U}$$

with

$$\Delta\omega = 2\pi\Delta f$$

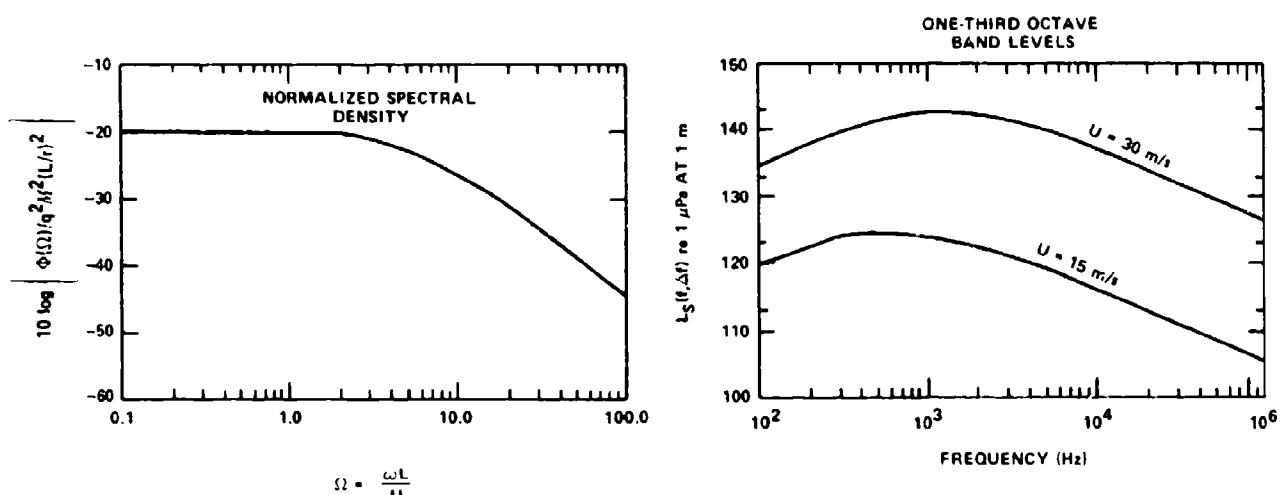


Figure 1.9 - Dimensionless and Dimensional Spectral Levels of a Flow-Induced Noise in Water

( $L = 2.5$  cm,  $r = 1$  m,  $U = 15$  m/s and  $30$  m/s)

the scaled spectrum level is

$$10 \log \Phi(\omega) = 10 \log \frac{\Phi(\omega) \frac{U}{L}}{q^2 M^2 \left(\frac{L}{r}\right)^2} + 20 \log q + 20 \log M + 20 \log \frac{L}{r} - 10 \log \frac{U}{L}$$

Accordingly, using Equation (1.15)

$$L_S(f, \Delta f) = 10 \log \frac{\Phi(\omega) \frac{U}{L}}{q^2 M^2 \left(\frac{L}{r}\right)^2} + 20 \log \frac{q}{p_{\text{ref}}} + 10 \log 4\pi \frac{\Delta f L}{U} + 20 \log M + 20 \log \frac{L}{r}$$

or combining

$$L_S(f, \Delta f) = 10 \log \left\{ \frac{2\phi\left(\frac{\omega L}{U}\right) \frac{(\Delta \omega) L}{U}}{q^2 M^2 \left(\frac{L}{r}\right)^2} \right\} + L_q + 20 \log M + 20 \log \frac{L}{r} \quad (1.17)$$

where  $L_q = 20 \log q/p_{\text{ref}}$ .

Returning momentarily to the expressions relating  $\Phi(\omega)$  and  $G(f)$ , we note that spectra of dimensionless scaled frequencies and of absolute frequencies are simply related. If  $\Omega = \omega L/U$  then

$$2\Phi(\omega)\Delta\omega = 2\Phi(\Omega)\Delta\Omega = G(f)\Delta f$$

accordingly,

$$\Phi(\omega) = \Phi(\Omega) \frac{U}{L} = \left(\frac{1}{4\pi}\right) G(f) \frac{U}{L}$$

with

$$\Omega = \frac{\omega L}{U} = \frac{2\pi f L}{U}$$

Also incremental bandwidths of scaled frequencies are simply related to incremental bandwidths of absolute frequencies; that is if true similitude exists for given  $L$  and  $U$ ,

$$\frac{\Delta\omega L}{U} = \Delta \left( \frac{\omega L}{U} \right) = (\Delta\omega) \frac{L}{U} = \Delta\Omega$$

Accordingly, we have all the simple identities

$$\begin{aligned} \overline{p^2}(f, \Delta f) &= 2\Phi \left( \frac{\omega L}{U} \right) \frac{(\Delta\omega)L}{U} = 2\Phi(\omega)\Delta\omega \\ &= G(f)\Delta f \end{aligned}$$

that allow a particularly simple interpretation of spectrum functions.

The commonly used scaling factors  $L_q = 20 \log q/p_{\text{ref}}$ ,  $10 \log M$ , and  $20 \log M$  are shown in the nomographs in Figures 1.10 and 1.11. The determination of dimensionless sound levels from absolute sound pressure measurements will be conducted using the above equations in a reverse process. When dealing with propellers and rotors, the primary variable on which sound levels must be normalized is the tip speed of the blades  $U_T$ . The forward velocity of the rotor is  $V_a$ , so that since  $\Omega$  is the angular velocity of the rotor and  $R_T = D/2$  is its radius, the tip speed is

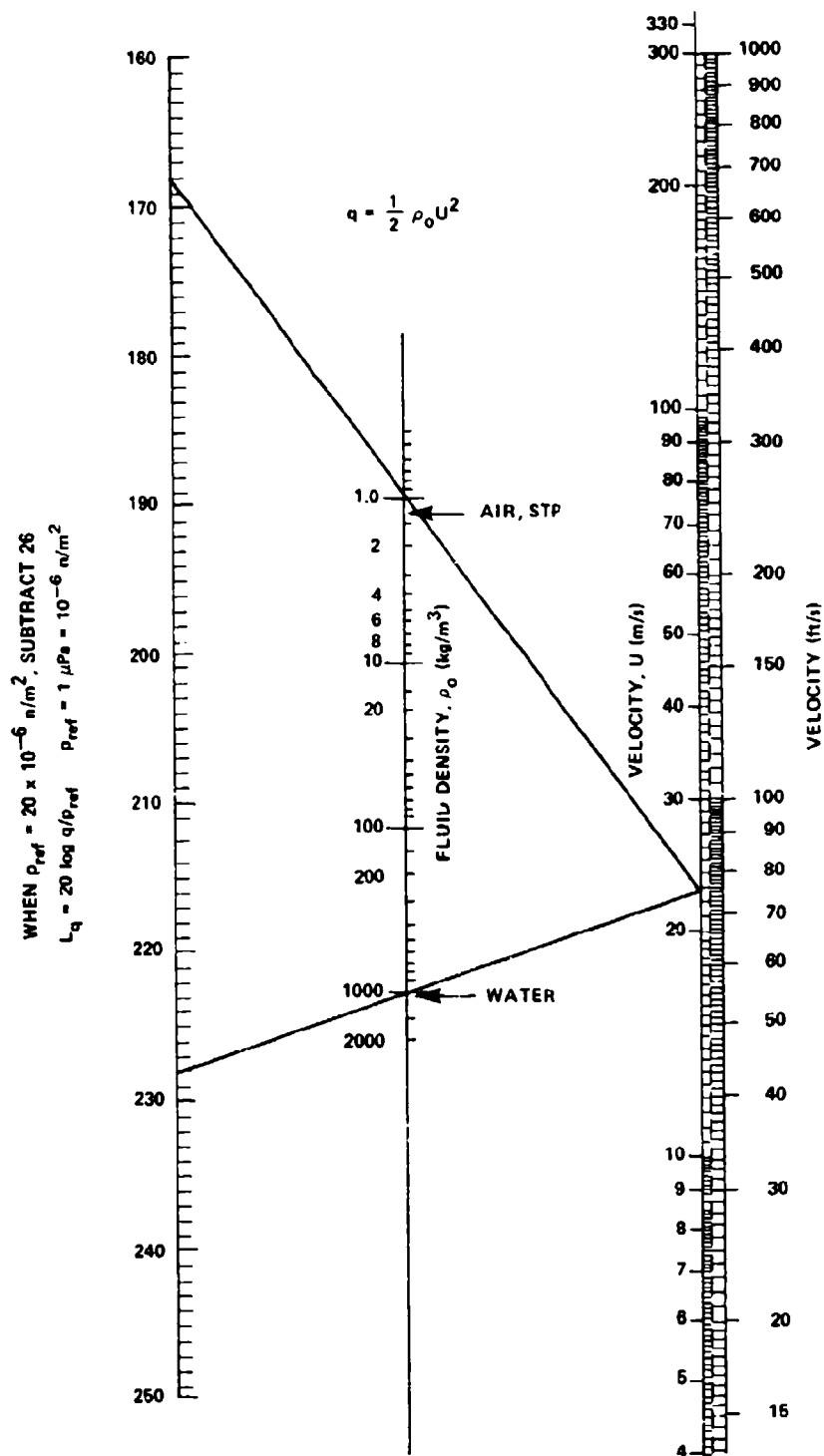


Figure 1.10 - Nomograph for Calculating  $20 \log q/p_{ref}$  for Fluids of Varying Density and Speed

( $L_q = 168$  at 23 m/s in air.)

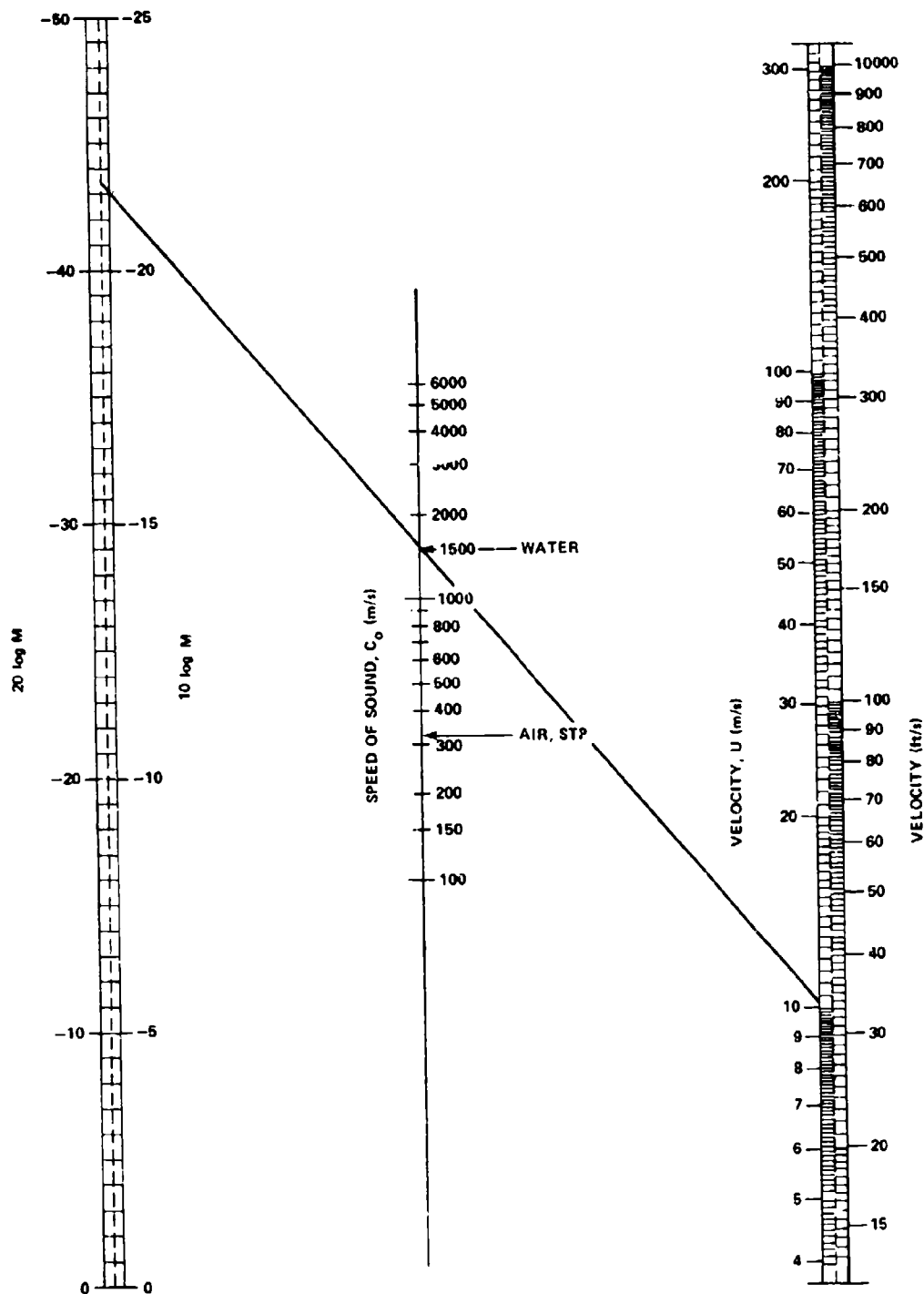


Figure 1.11 - Nomograph for Computing  $20 \log M = 20 \log U/C_o$   
for Velocities of Various Fluids

$$U_T = [(R_T \Omega)^2 + V_a^2]^{1/2}$$

the advance coefficient of the rotor J is defined as

$$J = \frac{V_a}{Dn}$$

$$= \pi \frac{V_a}{R_T \Omega}$$

where n is the shaft rotation frequency, expressed in revolutions per second when the velocity is expressed in ft/s. Therefore,

$$U_T = \pi(Dn) \left[ 1 + \left( \frac{J}{\pi} \right)^2 \right]^{1/2}$$

The tip velocity is completely determined by any three of the parameters  $\Omega$ , J,  $V_a$ , and D. The nomograph in Figure 1.12 allows computation of  $U_T$  for any such combinations of these parameters. Rather than specifying J, often the ratio  $60n/V_a = N/V_a$ , where N, in revolutions per minute, is specified for a propeller of diameter D. This ratio, in the units rpm/knots (turns per knot or TPK) is also given in the center of the nomograph.

Accordingly, if an  $L_q$  based on rotor tip velocity is desired for a given forward velocity (knots) of a rotor of known TPK and D, one finds  $U_T$  in Figure 1.12 and  $L_q$  in Figure 1.10.

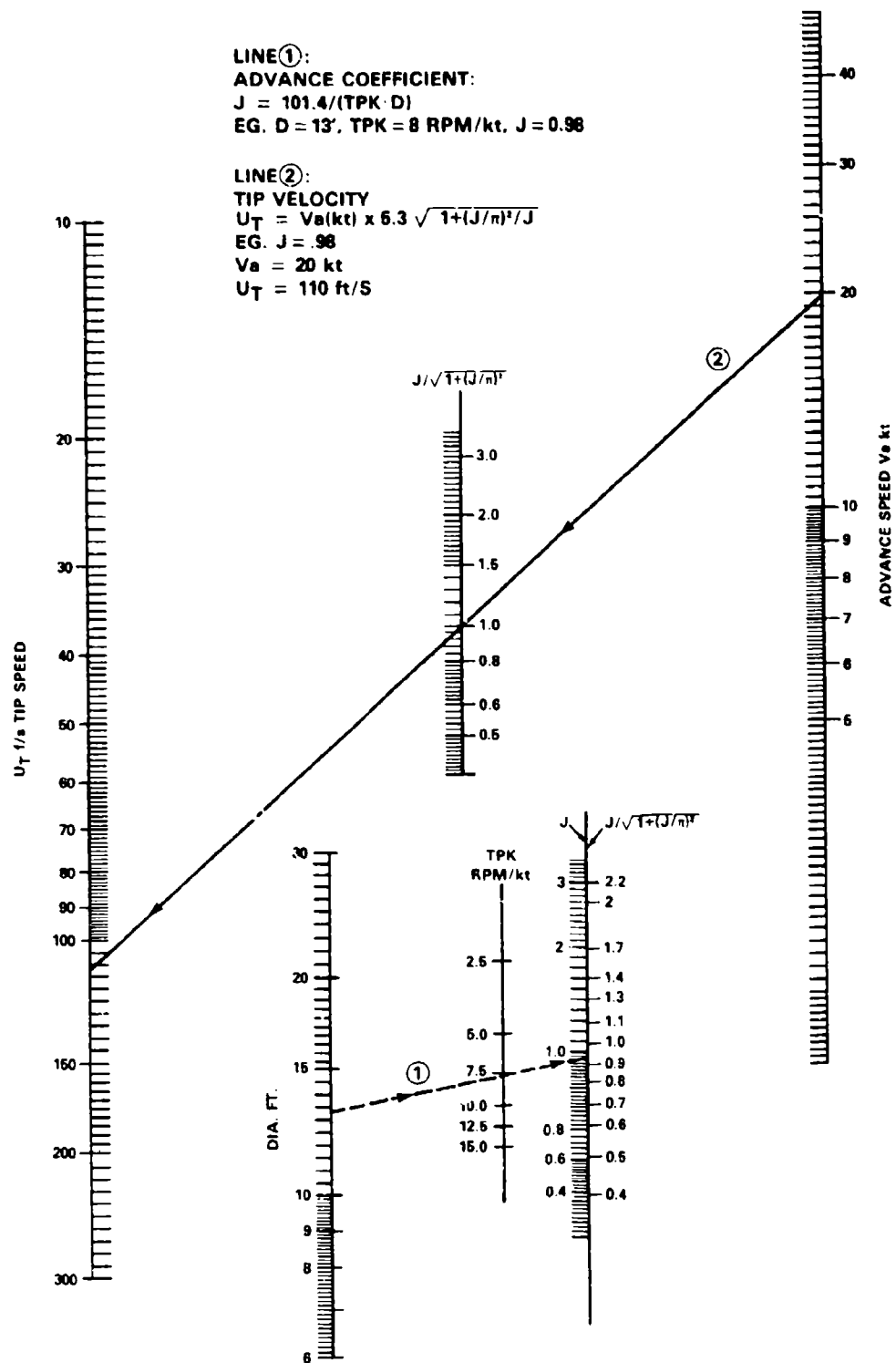


Figure 1.12 - Nomograph for Computing Tip Velocity of a Propeller



## CHAPTER 2

### GENERAL THEORIES OF FLOW-INDUCED NOISE

In this chapter we will discuss the theories and derive the equations which are the foundations of theoretical hydroacoustics. The general relationships will be specialized in later chapters for application to experimental acoustics. First, the common relationships of simple linear-acoustic theory will be explored to emphasize the fundamental qualities of single and multipole source-types. The general theory of fluid-induced noise generation will then be derived with considerable attention given to the classification of source-types and noise mechanics, as well as to the influences of solid boundaries of various types on radiated intensity.

#### 2.1 FUNDAMENTALS OF LINEAR ACOUSTICS THEORY

##### 2.1.1 The Wave Equation

We begin with the equations of continuity and momentum for inviscid, fluid motion.\* In tensor notation, these are, for a fluid free of volume sources

$$\frac{\partial \rho}{\partial t} + \frac{\partial}{\partial x_i} (\rho u_i) = 0 \quad (2.1)$$

and the momentum, or Euler's, equation is

$$\rho \frac{\partial u_i}{\partial t} + \rho u_j \frac{\partial u_i}{\partial x_j} = - \frac{\partial p}{\partial x_i} \quad (2.2)$$

respectively, where

$\rho$	= instantaneous fluid density
$p$	= instantaneous pressure
$u_i$	= three-dimensional local fluid velocity
$x_i$ and $t$	= space and time variables, respectively

---

\*The equations are derived in this form in a number of basic texts, among them are those of Milne-Thompson,<sup>1\*\*</sup> Batchelor,<sup>2</sup> and Sabersky and Acosta.<sup>3</sup>

\*\*A complete listing of references is given on page 113

We will have occasion later in this chapter, and elsewhere in the book, to manipulate these equations in vector form for which we make use of the del operator, which is

$$\nabla = \frac{\partial}{\partial x} \hat{i} + \frac{\partial}{\partial y} \hat{j} + \frac{\partial}{\partial z} \hat{k}$$

in three dimensions, where  $\hat{i}$ ,  $\hat{j}$ , and  $\hat{k}$  are the unit vectors in the x, y, and z directions, respectively. In this notation, the equations of continuity and momentum then are

$$\frac{\partial \rho}{\partial t} + \nabla \cdot (\rho \vec{u}) = 0 \quad (2.3)$$

where  $\nabla \cdot (\rho \vec{u})$  is the divergence of  $\rho \vec{u}$  and

$$\rho \frac{\partial \vec{u}}{\partial t} + \rho (\vec{u} \cdot \nabla) \vec{u} = -\nabla P \quad (2.4)$$

respectively, where  $\vec{u} = (u_x \hat{i} + u_y \hat{j} + u_z \hat{k}) = (u_i)$  and  $\nabla P$  is the gradient of the pressure. These equations apply to fluid regions which are free of local mass, momentum, and heat introduction, or of gravitational (or body) forces. For barotropic fluids we can write the pressure in terms of the density as

$$P - P_0 = \text{constant } (\rho - \rho_0)^\alpha$$

in which  $\alpha$  has special values depending on the thermodynamic equation of state of the fluid. For ideal gases undergoing isothermal expansions  $\alpha = 1$ ; conversely, for adiabatic expansions (vanishing heat transfer among adjacent fluid elements)  $\alpha = \gamma = c_p/c_v$ , where  $c_p$  and  $c_v$  are the specific heats at constant pressure and volume, respectively. For liquids, the state equation takes on a more complex form, however, the variations in pressure and density are related through the fluid compressibility.

The speed of sound in the fluid is determined by the rate of change of pressure with density at constant entropy using the relationship:

$$c_o^2 = \left( \frac{\partial P}{\partial \rho} \right)_s \quad (2.5)$$

For the present, we will restrict considerations to lossless (or inviscid) fluids so that the acoustic compression-expansion process is certainly adiabatic. The so-called linear acoustic approximation results from the assumption that local velocities  $u$  are much less than the speed of sound in the fluid. Even for real fluids, if the disturbances are of long enough wavelength then the fluid gradients are small so that nearly adiabatic expansions occur. Under these conditions small deviations of pressure and density from an equilibrium can be expressed as an acoustic pressure  $p_a$

$$p_a = P - P_o = c_o^2 (\rho - \rho_o) \quad (2.6)$$

where  $P_o$  and  $\rho_o$  are the equilibrium pressure and density, respectively.

The linear wave equation is obtained by taking the time derivative of Equation (2.1) and the gradient  $\partial/\partial x_1$  of Equation (2.2). Neglecting the resulting second-order terms we obtain (see also e.g., refs 28, 38, or 39)

$$\frac{\partial^2 \rho}{\partial t^2} = - \frac{\partial}{\partial t} \left( u_1 \frac{\partial \rho}{\partial x_1} + \rho \frac{\partial u_1}{\partial x_1} \right) \approx - \frac{\partial}{\partial t} \left( \rho_o \frac{\partial u_1}{\partial x_1} \right)$$

$$\frac{-\partial^2 p}{\partial x_1^2} = \rho \frac{\partial^2 u_1}{\partial x_1 \partial t} + \frac{\partial \rho}{\partial x_1} \frac{\partial u_1}{\partial t} + \frac{\partial}{\partial x_1} \left[ \rho u_j \frac{\partial u_1}{\partial x_j} \right] \approx \rho_o \frac{\partial^2 u_1}{\partial x_1 \partial t}$$

$$dp_a = c_o^2 d\rho$$

Combining these equations, the wave equation for density fluctuations in a homogeneous fluid is obtained

$$\frac{\partial^2 \rho}{\partial t^2} - c_o^2 \frac{\partial^2 \rho}{\partial x_1^2} = \square^2 \rho = 0 \quad (2.7)$$

or

$$\frac{\partial^2 p_a}{\partial t^2} - c_o^2 \frac{\partial^2 p_a}{\partial x_1^2} = \square^2 p_a \quad (2.8)$$

for the pressure fluctuations, where  $\partial^2/\partial x_1^2 = \nabla^2$  is the Laplacian operator.

Specific functional forms of solutions of the wave equation depend on the geometric order (one-, two-, or three-dimensions) of the fluid region. The solutions are also obviously dependent on whatever temporal and spatial character the boundary of the fluid has. In consideration of the sound field that is realized at some distance from a vibrating body, the sound pressure at a given time is the linear superposition of the acoustic contributions from each of the spatial wave harmonics that are invoked to describe the surface motion and all the frequencies that describe the time variation of each of the spatial harmonics. In a few instances, however, consideration of acoustic energetics can be simplified. These are classified into two options. Either the motion is spatially uniform over the surface, i.e., of the zero-order spatial harmonics, or the motion has a prescribed spatial variation of a given harmonic and the time behavior has a single frequency. In all other more general cases the temporal wave forms at fixed values of differences  $(r - c_o t)$  but varying  $r$  will depend on  $r$ .

Considering, now, only those cases which fall into the above options; solutions of the wave equation consist of functions

$$f(r, t) = G(r + c_o t) + g(r - c_o t)$$

where  $r$  is the magnitude of the distance to the observation point from the source. Wave functions  $g$  and  $G$  with arguments of the form  $r + c_o t = \text{constant}$  are constant valued for decreasing  $r$  as time increases. These correspond to waves travelling

toward the origin of  $r$ . Alternatively, wave functions for which  $r - c_0 t = \text{constant}$  apply to disturbances which remain constant as  $r$  increases with time; these are outward-travelling waves. The functions  $g$  and  $G$  may be the same or different depending on the boundary conditions, e.g., in the case of standing waves on a string they are the same.

We examine the general characteristics of the radiated sound at distances from a source which are large compared to a typical dimension of the source and compared to an acoustic wavelength. This point we shall call the acoustic far field. We express this sound pressure in the form

$$p_a(x_1, t) = r^{-m} S(\vec{s}) g(r - c_0 t) \quad (2.9)$$

which separates the radial and surface functions from the characteristic wave behavior. In this representation  $S(\vec{s})$  is a surface function of the surface vector coordinate  $\vec{s}$  which is independent of distance from the source and which depends only on the shape of the body and the coordinate system used, i.e., whether it is spherical, cylindrical, elliptical, etc. The surface function satisfies a requirement that the Laplacian with respect to variations in the surface plane describes node lines of wavelength  $2\pi/k_s$ , i.e.,  $\nabla_s^2 S(\vec{s}) = -k_s^2 S(\vec{s})$ . In the radial function  $r^{-m}$ ,  $m$  depends on the dimensionality of the radiation;  $m$  is greater than zero and it will be determined below. The function  $r^m p_a(x_1, t) = S(\vec{s}) g(r - c_0 t)$  clearly satisfies the wave equation

$$c_0^2 \frac{\partial^2 (r^m p_a)}{\partial r^2} - \frac{\partial^2 (r^m p_a)}{\partial t^2} = 0 \quad (2.10)$$

If  $k_s = 0$ , i.e., the surface motion is the lowest order, or breathing mode,  $S(s) = \alpha$ , where  $\alpha$  is a constant. The linear form of Equation (2.2), i.e.,

$$\rho_0 \frac{\partial u_r}{\partial t} = - \frac{\partial p_a}{\partial r} \quad (2.11)$$

gives the perturbation velocity in the  $r$ -direction  $u_r$ , as

$$\begin{aligned}\rho_o \frac{\partial u_r}{\partial t} &= + r^{-(m+1)} \alpha g(r-c_o t) - r^{-m} \alpha g'(r-c_o t) \\ &\approx - r^{-m} \alpha g'(r-c_o t)\end{aligned}\tag{2.12}$$

in the far field since, for  $r \gg 1$ , the term  $r^{-m-1}$  diminishes with respect to the term  $r^{-m}$ .

Now, by integration we find the radial velocity in the far field

$$\begin{aligned}u_r &= \frac{1}{\rho_o} \int \frac{\partial u_r}{\partial t} dt = - \frac{\alpha}{\rho_o c_o} \frac{1}{r^m} \int g'(r-c_o t) d(c_o t) \\ u_r &= \frac{\alpha}{\rho_o c_o} \frac{1}{r^m} g(r-c_o t)\end{aligned}$$

This shows that the far field radiated sound pressure and fluid velocity are related by the specific acoustic impedance of the fluid  $\rho_o c_o$ , since

$$\frac{p_a^2(\vec{x}, t)}{\rho_o c_o} = u_r(\vec{x}, t)\tag{2.13}$$

This relationship is fundamental to all far field acoustics. The radial component of the acoustic intensity  $I_r(\vec{x}, t)$ , which is the instantaneous power flux along the radially oriented acoustic ray, is

$$I_r(\vec{x}, t) = p_a(\vec{x}, t) u_r(\vec{x}, t)\tag{2.14}$$

so that, using Equation (2.13)

$$I_r(\vec{x}, t) = \frac{p_a^2(\vec{x}, t)}{\rho_o c_o}\tag{2.15}$$

These relationships permit a determination of  $m$  in Equation (2.9) by considering the acoustic power which is transmitted through a surface  $\vec{s}_r$  located a distance  $r$  from the source. At this point we must make a distinction between cylindrically (two-dimensional) and spherically (three-dimensional) radiating surfaces, for these determine the precise radial dependence. In any case, the instantaneous acoustic power transmitted across a far field surface  $S_0$  is

$$P(t) = \iint_{S_0} \frac{p_a^2(\vec{s}, t)}{\rho_0 c_0} d\vec{s}_r \quad (2.16)$$

where  $s$  is the coordinate in the plane of the surface and  $\vec{s}_r$  is the surface vector. Examples are shown in Figures 2.1a and 2.1b for cylindrical and spherical geometries. In the case of radiation from a line source oriented along the  $z$ -axis we consider the power per unit axial length which is

$$\frac{d}{dz} [P(t)] = \frac{1}{\rho_0 c_0} \int_0^{2\pi} \alpha^2 r^{-2m+1} g^2(r-c_0 t) d\theta$$

for the cylindrical coordinate system as shown in Figure 2.1a. We see that the power is conserved only if  $m = 1/2$  because only this radial dependence ensures that the total power radiated through a closed fluid surface is independent of the surface chosen. This condition must be satisfied because the fluid is assumed to be frictionless. Thus the cylindrically spreading far field acoustic pressure is given by

$$p_a(\vec{x}, t) = p_a(r, z, \theta, t) = r^{-1/2} \alpha g(r-c_0 t) \quad (2.17)$$

Similarly, for a spherically radiating source, the instantaneous power is

$$\begin{aligned} P(t) &= \int_S \frac{p_a^2(\vec{x}, t)}{\rho_0 c_0} r^2 \sin \phi d\phi d\theta \\ &= \frac{1}{\rho_0 c_0} \int_0^\pi \int_0^{2\pi} \alpha^2 r^{-2m+2} g^2(r-c_0 t) \sin \phi d\phi d\theta \end{aligned} \quad (2.18)$$

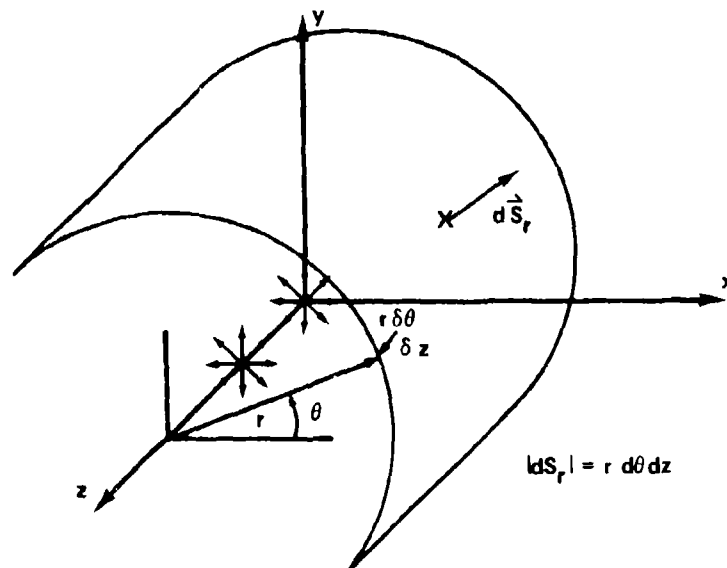


Figure 2.1a - Cylindrically Spreading Acoustic Waves for a Line Source Parallel to the z-Axis

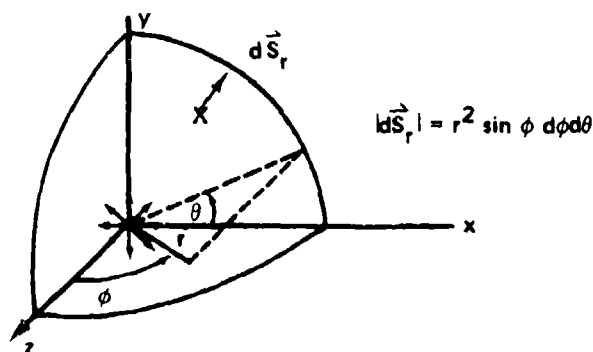


Figure 2.1b - Spherically Spreading Acoustic Waves

Figure 2.1 - Cylindrical and Spherical Coordinate Systems

Integration is over the spherical surface, as shown in Figure 2.1b. The condition  $m = 1$  ensures power conservation at all distances from the source. Thus, a spherically spreading sound wave behaves as

$$p_a(\vec{x}, t) = \frac{c_0}{r} g(r - c_0 t) \quad (2.19)$$

in the acoustic far field. On the surface of a sphere, the first term of Equation (2.12) gives the volume acceleration  $V(t)$ ,



$$\begin{aligned}\ddot{V}(t) &= \int \frac{\partial u_r(r=a)}{\partial t} ds = \frac{\alpha g(a-c_o t)}{\rho_o a^2} \iint S(\vec{s}) d\vec{s} \\ &= 4\pi \frac{\alpha g(a-c_o t) a^2}{\rho_o a^2}\end{aligned}$$

since  $S(\vec{s}) = S(\phi, \theta) = 1$ . The acoustic pressure fluctuation in the fluid is found by substituting into Equation (2.13)

$$p_a(r, t) = \frac{\rho_o \ddot{V} \left( t - \frac{r-a}{c_o} \right)}{4\pi r} \quad (2.20)$$

Analogous results for waves propagating to the far field when  $S(\vec{s})$  is not a constant on the surface may be derived for a fixed frequency by using the methods of Section 2.6. In this case, as we shall see in Chapter 6, nondecaying outward propagating waves occur only when there are surface harmonics such that  $k_s$  is less than or equal to  $k_o$ .

### 2.1.2 Characteristics of Multipole Radiation

In the later analytical treatments of this chapter, complex formulations will be interpreted in terms of combinations of simple sources. In the following analysis it will be shown that these source combinations can represent the driving of the fluid by localized time-varying volumetric (or dilatational) changes, forces, and moments.

Monopole Sources. To begin, the relationship for acoustic radiation from a volumetric pulsation is derived. Physically, this source can represent the radiated sound from an axisymmetric bubble vibration. The time-varying characteristic of the pressure at a single frequency is assumed to be given by

$$p(r, t) = \tilde{p}(r, \omega) e^{-i\omega t} \quad (2.21)$$

where  $\tilde{p}(r, \omega)$  is a complex pressure amplitude. The source motion is completely radial so that the wave equation for the radiated acoustic pressure is

$$\frac{1}{r} \frac{\partial}{\partial r} \left( r^2 \frac{\partial \tilde{p}(r, \omega)}{\partial r} \right) + \frac{\omega^2}{c_o^2} \tilde{p}(r, \omega) = 0 \quad (2.22a)$$

which is equivalent to

$$\frac{\partial^2 [r \tilde{p}(r, \omega)]}{\partial r^2} + \left( \frac{\omega}{c_o} \right)^2 [r \tilde{p}(r, \omega)] = 0 \quad (2.22b)$$

The acoustic wave number is

$$k_o = \frac{\omega}{c_o} \quad (2.23)$$

and the solution to Equation (2.22) is

$$\tilde{p}(r, \omega) = \frac{A}{r} e^{\pm i k_o r} \quad (2.24)$$

The positive root of  $\sqrt{-1} = +i$  is chosen for outward-travelling waves. The instantaneous volume of the sphere of radius  $a$  is

$$Q = \frac{4}{3} \pi a^3$$

and the (small) amplitude of the time rate of volume change, the volume velocity, is

$$\dot{Q}(\omega) = 4 \pi a^2 u_r(\omega) \quad (2.25)$$

The amplitude of radial motion of the surface must be small compared to the radius of the sphere. The boundary condition on the surface is given by Equation (2.11). Combination of Equations (2.11), (2.24), and (2.25) yields

$$A \left[ \frac{1}{a^2} - \frac{i k_o}{a} \right] e^{+i k_o a} = i \omega \rho_o u_r(\omega)$$

so that

$$A = \frac{-i \omega \rho_o \dot{Q}(\omega)}{4 \pi (1 + i k_o a)} e^{-i k_o a} \quad (2.26)$$

therefore,

$$p_a(r, t) = \frac{-i\omega\rho_0 \dot{Q}(\omega)}{4\pi r} e^{+ik_0(r-a)-i\omega t} \quad (2.27)$$

is the radiated pressure from the source when  $k_0 a \ll 1$ . This condition states that the diameter of the sphere is small compared to the acoustic wavelength,  $\lambda_0 = 2\pi/k_0$ , so that  $2a/\lambda_0 \ll 1/\pi$ . This result is identical to Equation (2.20).

Dipole Sources. The next order of source complexity is the dipole which can be represented by the case of the heaving sphere. This, and equivalent interpretations which will be described subsequently, are demonstrated in Figure 2.2. The center of the sphere oscillates along the z-axis with velocity  $U(t) = U_z e^{-i\omega t}$ ; the sphere is impervious. In this case, the motion of the sphere causes a back and forth "sloshing" of fluid without any net volume change. As the sphere moves forward, fluid moves to its rear. The motion is symmetric about the z-axis and unsymmetric about the angle  $\phi$ . The acoustic pressure amplitude satisfies the equation<sup>4,5</sup>

$$\frac{1}{r^2} \frac{\partial}{\partial r} \left( r^2 \frac{\partial \tilde{p}}{\partial r} \right) + \frac{1}{r^2} \frac{1}{\sin \phi} \frac{\partial}{\partial \phi} \left( \sin \phi \frac{\partial \tilde{p}}{\partial \phi} \right) + k_0^2 \tilde{p} = 0 \quad (2.28)$$

the boundary condition

$$-\frac{1}{\rho_0} \frac{\partial \tilde{p}(a, \phi)}{\partial r} = -i\omega u_r(\omega, \phi) = -i\omega U_z(\omega) \cos \phi \quad (2.29)$$

and the far field radiation condition

$$\lim_{r \rightarrow \infty} \tilde{p}(r, \phi) \sim r^{-1} \quad (2.30)$$

The formal solution to these equations is derived in Appendix A. On the surface of the sphere, which is assumed to be small, the amplitude of the pressure is

$$\tilde{p}(a, \phi) \approx \frac{-1}{2} \omega \rho_o \frac{a^3}{r} U_z \cos \phi \quad (2.31)$$

for  $k_o a \ll 1$ ,  $r = a$ , and in the far field

$$p_a(r, \phi, t) \approx \frac{1}{2} \rho_o c_o (k_o a)^3 \frac{U_z \cos \phi}{k_o r} e^{i(k_o r - \omega t)} \quad (2.32)$$

for  $k_o r > 1 \gg k_o a$ .

The pressure on the surface of the sphere is directly proportional to the radial acceleration  $i\omega U_z \cos \phi$  and, therefore, it represents the inertial loading of the oscillating fluid. The total force in the z-direction required to overcome the inertial loading is

$$F_z = \int_s \tilde{p}(a, \phi) n_z dS(a, \phi) \quad (2.33)$$

where the component of the outward normal in the z-direction is  $n_z = \cos \phi$ , and the incremental surface element is

$$dS(a, \phi) = a^2 \sin \phi d\theta d\phi$$

thus, the inertial force is

$$F_z = \int_{\theta=0}^{2\pi} \int_{\phi=0}^{\pi} \left[ \frac{\rho_o}{2} a i \omega U_z \cos \phi \right] [\cos \phi] [a^2 \sin \phi d\theta d\phi] \quad (2.34)$$

$$= \frac{-12\pi}{3} \rho_o a^3 \omega U_z$$

Since this force is inertial it may be regarded as an entrained fluid mass times the acceleration ( $-i\omega U_z$ ) of the surface. The added mass at low  $k_0 a$  for the heaving sphere is thus simply  $(1/2) \rho_0 V_s$ , where  $V_s$  is the displaced volume of fluid.

The radiated sound pressure is shown by Equation (2.32) to be directed along the  $z$  (or  $\phi=0$ ) axis. It is zero in the antisymmetric about the  $x$ - $y$  plane. We emphasize that Equation (2.32) applies in the cases for which  $k_0 r \gg 1$ . In the intermediate region of  $k_0 a < k_0 r < 1$  the field is given by the spherical Bessel function, as explained in Appendix A, but the angular directivity is still  $\cos \phi$ . This directivity is characteristic of dipole radiation which results from the imposition of a concentrated force to the fluid. The equivalency can be seen by substituting the axial force  $F_z$  from Equation (2.34) into Equation (2.32) to obtain

$$\tilde{p}(r, \phi) = \frac{+3}{4\pi} \cos \phi \frac{-i\omega F_z}{c_0 r} e^{+ik_0 r} \quad (2.35)$$

This shows that the radiated pressure is proportional to the time rate of change of the inertial force exerted on the fluid by the sphere. The sound has the  $\cos \phi$  directivity in the direction of the force. This result has a much more general significance as will be discussed later on, see Sections 2.5.3 and 5.6.3. The dipole-force representation is shown in Figure 2.2b.

These results can also be derived by considering the acoustic field of a pair of simple sources which are aligned with the  $z$ -axis as shown in Figure 2.2c. The vector distance between the sources is  $2d_z$ . The field point from the centroid of the system is at the coordinates  $r, \phi$ , with individual ranges  $r_1$  and  $r_2$ . The resultant sound pressure is given by the sum of individual contributions

$$\tilde{p}(r, \phi) = \frac{-i\omega \rho_0 \dot{Q}(\omega)}{4\pi} \left[ \frac{e^{+ik_0 r_1}}{r_1} + \frac{e^{+ik_0 r_2}}{r_2} \right]$$

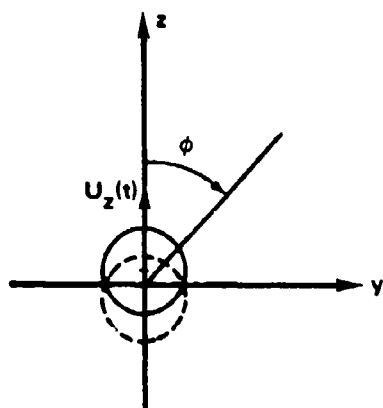


Figure 2.2a - Oscillating  
Sphere

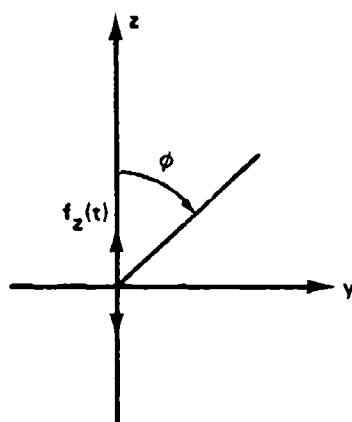


Figure 2.2b - Point  
Force

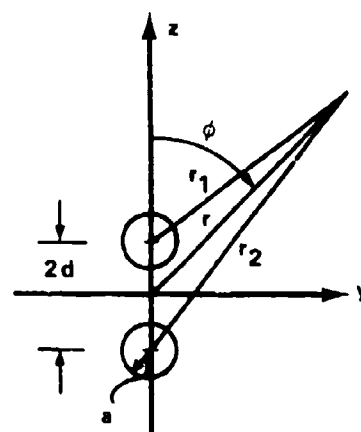


Figure 2.2c - Image System  
of Sources

Figure 2.2 - Equivalent Dipole Forms

The sign applies to the phasing of the sources. For separations  $d_z \ll r$ , we need not make a distinction between the small directivity differences for the two sources. Thus, we can write

$$r_1^2 = r^2 + d_z^2 - 2rd_z \cos \phi \approx r^2 - 2rd_z \cos \phi$$

$$r_2^2 = r^2 + d_z^2 + 2rd_z \cos \phi \approx r^2 + 2rd_z \cos \phi$$

for  $r \gg d_z$  in the far field so that the far field acoustic pressure is

$$\tilde{p}(r, \phi) = \frac{2\omega\rho_o \dot{Q}(\omega)}{4\pi r} \begin{Bmatrix} \cos(k_o d_z \cos \phi) \\ \sin(k_o d_z \cos \phi) \end{Bmatrix} e^{+ik_o r} \quad (2.36)$$

where the cosine and sine apply to sources which are either in phase or out of phase, respectively.

In the case that  $k_o d_z \ll 1$ , the  $\cos(k_o d_z \cos \phi)$  is replaced by unity at all angles because the sources simply reinforce each other. The interesting function, from our point of view, is  $\sin(k_o d_z \cos \phi)$  which becomes simply  $k_o d_z \cos \phi$  for  $k_o d_z \ll 1$ . In this case the resultant acoustic pressure is

$$\tilde{p}(r, \phi) \sim \rho_o c_o k_o^3 [2d_z \dot{Q}(\omega)] \cos \phi \frac{e^{+ik_o r}}{4\pi k_o r} \quad (2.37)$$

and  $2d_z \dot{Q}(\omega)$  is the dipole strength. So comparing Equations (2.37) and (2.32) we obtain

$$2d_z \dot{Q}(\omega) = 2\pi a^2 u_z(\omega)$$

as the effective dipole strength of the oscillating sphere. This treatment shows that, although the sound from two sources reaches a given point in space, because the disturbances were not produced in phase, they interfere. Thus, even though there is a certain degree of near field fluid motion ("sloshing") because there is no net introduction of fluid into the region, the radiated sound pressure is greatly diminished. The treatment also demonstrates that the nature of the dipole is such that it pertains to a gradient of a disturbance in the fluid. In this case the gradient, represented by the two closely placed sources in phase opposition, gives rise to an additional  $k_o$ -dependence in the radiation compared to that arising in the radiation from the simple source.

The result has other important implications regarding sound pressures radiated by sources near boundaries.<sup>5</sup> In the case depicted in Figure 2.2b, the x-y plane is a model of a rigid boundary when the sources are in phase. This can be seen by evaluating the tangential gradient  $(1/r) \partial p(r, \phi) / \partial \phi$  as  $\phi = \pi/2$  and noting that it vanishes there. Thus we see that the normal velocity vanishes everywhere in the  $z = 0$  plane as it would physically on a rigid surface. Alternatively, sources in phase opposition give a vanishing pressure and a velocity-maximum on the  $z = 0$  plane. This is as it would be on a free-surface. Thus, a compact simple source (i.e., one whose largest dimension is smaller than acoustic wavelength) in water near the surface would be expected to behave as a simple dipole as long as  $2hk_o \ll 1$  where  $h$  is the depth of the source. These boundaries can influence the acoustic power output.

The time averaged, far field acoustic power for the simple source is obtained using Equations (2.27) and (2.18);

$$\bar{P}_M = \frac{1}{2} \int_0^{2\pi} d\theta \int_0^\pi d\phi \frac{\rho_o^2 \omega^2 |\dot{Q}(\omega)|^2}{\rho_o c_o 16\pi^2} \sin \phi = \frac{\rho_o^2 \omega^2 |\dot{Q}(\omega)|^2}{8\pi \rho_o c_o}$$

where the factor 1/2 accounts for time averaging. For the dipole we use Equation (2.37) to obtain

$$\begin{aligned}\bar{P}_D &= \frac{1}{2} \int_0^{2\pi} d\theta \int_0^\pi d\phi \frac{\rho_o^2 \omega^2 |\dot{Q}(\omega)|^2 [2k_o d_z]^2}{\rho_o c_o 16\pi^2} \cos^2 \phi \sin \phi \\ &= \frac{\rho_o^2 \omega^2 |\dot{Q}(\omega)|^2}{8\pi \rho_o c_o} \cdot \frac{1}{3} [2k_o d_z]^2 \\ &= \bar{P}_M \frac{1}{3} [2k_o d]^2\end{aligned}$$

The presence of the free (pressure-release) surface reduces the power output of the monopole by the factor  $1/3(2k_o d)^2$ . In contrast, Equation (2.36) shows that the presence of a rigid surface increases the acoustic power output by  $2^2$  when  $k_o d_z \ll 1$ .

Quadrupole Sources. Compositions of quadrupoles with dipole pairs are shown in Figure 2.3. In sketch a, the quadrupole is represented as an array of four simple sources, or two dipoles in the z-y plane separated by a distance  $2d_y$ . In sketch b, the quadrupole is shown as a pair of force couples separated a distance  $2d_x$  and  $2d_y$ . This pair of force couples imposes no net moment. These two orientations of dipoles which impose a fluid moment-pair are called lateral quadrupoles. Another orientation of dipoles in which the forces are in-line is called a longitudinal quadrupole, which imposes no net moment and no net force on the fluid.

Of importance in most fluid applications is the lateral quadrupole for which the far field directivity will now be derived. The far field pressure amplitude from the dipole system of Figure 2.3a can be written in the terms of Equation (2.37) as

$$\tilde{p}(r, \phi, \theta) \approx \frac{\rho_o c_o k_o^3}{4\pi k_o r} [2d_z \dot{Q}(\omega)] \cos \phi \left[ \frac{e^{+ik_o r_1}}{r_1} - \frac{e^{+ik_o r_2}}{r_2} \right] \quad (2.38)$$



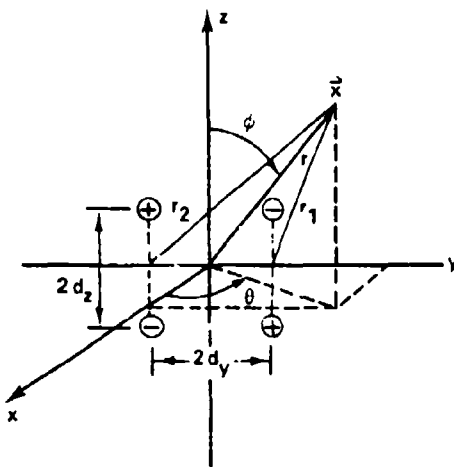


Figure 2.3a - Four Simple Sources Lateral Quadrupole

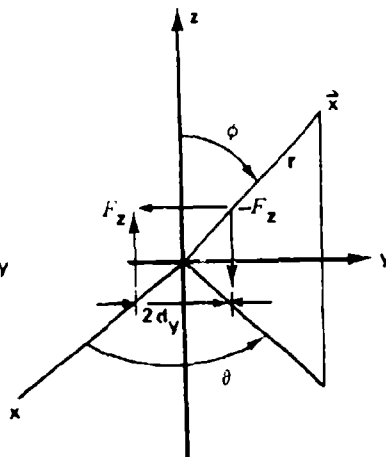


Figure 2.3b - Force Couple Lateral Quadrupole, Net Moment = 0

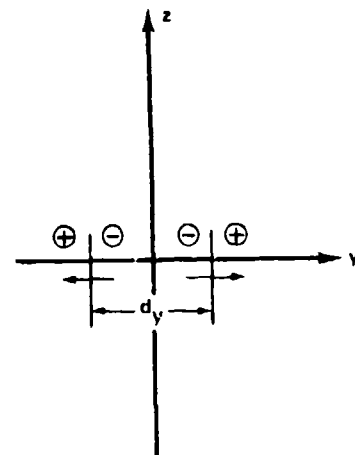


Figure 2.3c - Longitudinal Quadrupole

Figure 2.3 - Quadrupole Forms

where Equation (2.21) applies. As in the analysis of the dipole we write

$$r_1 \approx r \pm d_y \sin \phi \sin \theta$$

for  $r \gg d_y$ . Substitution into Equation (2.38) yields

$$\tilde{p}(r, \phi, \theta) \approx \frac{1}{2} \rho_0 c_0^4 [2d_z 2d_y \dot{Q}(\omega)] \sin 2\phi \sin \theta \frac{e^{+ik_0 r}}{4\pi k_0 r} \quad (2.39)$$

where we shall call  $2d_z 2d_y \dot{Q}(\omega)$  the quadrupole strength. This can be written in terms of the dipole force, Equation (2.34),

$$2d_z 2d_y \dot{Q}(\omega) = \frac{-3i}{\rho k_0 c_0} 2d_y F_z$$

so that

$$\tilde{p}(r, \phi, \theta) \approx \frac{3}{2} k_0^2 [2d_y F_z] \sin 2\phi \sin \theta \frac{e^{+ik_0 r}}{4\pi r} \quad (2.40)$$

This expression shows that the quadrupole pressure is of order  $2k_0 d_y$  less than the equivalent dipole pressure. Thus, the spatial gradient represented by two closely spaced dipoles gives rise to an additional  $k_0$ -dependence compared to dipole radiation. In other terms, the two spatial gradients represented by four monopoles gives a  $k_0^2$ -dependence compared to simple monopole radiation. The net force on the fluid is also instantaneously zero, yet since the fluid disturbances emitted from each dipole do not cancel identically; sound is still radiated. Statements which were made above for the monopole imaging apply equally well to the imaging of the dipole. The directivity of the sound from the lateral quadrupole is concentrated on four lobes which are oriented at  $\phi = (2n+1) \pi/4$ ,  $n = 1, 2, 3, 4$ . The sound pressure level is zero on the x-y and x-z planes.

## 2.2 SOMMERFELD'S RADIATION CONDITION

The far field radiation from multipole sources has been shown to be dependent on the distance from the source as  $e^{+ik_0 r}/4\pi r$ . This can be seen by reference to Equations (2.27), (2.37), and (2.39). Further reference to Equation (2.19) shows that for outward travelling waves the general spherical wave propagation is given by

$$rg(r-c_0 t) = \frac{1}{4\pi} e^{ik_0(r-c_0 t)}$$

Therefore, for these outward travelling waves we have the far field condition that

$$\lim_{r \rightarrow \infty} r \left( \frac{\partial p}{\partial r} - ik_0 p \right) = 0 \quad (2.41)$$

Alternatively, for inward travelling waves, we have

$$rg(r+c_0 t) = \frac{1}{4\pi} e^{ik_0(r+c_0 t)}$$

so that

$$\lim_{r \rightarrow \infty} r \left( \frac{\partial p}{\partial r} + ik_0 p \right) = 0 \quad (2.42)$$

This has been termed the absorption condition by Sommerfeld.<sup>6</sup>

These radiation conditions have been shown by Sommerfeld<sup>6</sup> to be necessary for the uniqueness of a solution of the wave equation for an unbounded medium surrounding the source. In two dimensions, the radiation condition is

$$\lim_{r \rightarrow \infty} \sqrt{r} \left( \frac{\partial p}{\partial r} - i k_0 r \right) = 0$$

and similarly for the absorption condition. Quite simply, the radiation condition ensures that for a single source distribution which radiates to the far field the solution of the wave equation excludes inward radiation. It amounts to a far field boundary condition. Similarly, in the case of a surface source distribution which radiates to an interior, the absorption condition rules out any internal sources which radiate outward.

## 2.3 Lighthill's Theory of Aerodynamic Noise

### 2.3.1 The Wave Equation

We will now determine the wave equation for the acoustic pressure which results from turbulent motion. For a spatially concentrated region of turbulent fluid motion, Lighthill's<sup>7,8,9</sup> formulation is unique in that it considers this region as an acoustic source which drives the surrounding fluid. The starting point of the analysis will again be the equations of continuity and momentum. However, now the velocity disturbance  $u_1$  that we are considering, includes both acoustic and, in a restricted region, hydrodynamic contributions. We will not assume inviscid motion in the region of turbulence.

In this case, the equation of continuity is, again,

$$\frac{\partial \rho}{\partial t} + \frac{\partial}{\partial y_1} (\rho u_1) = 0 \quad (2.43)$$

and Euler's equation is

$$\rho \frac{\partial u_1}{\partial t} + \rho u_j \frac{\partial u_1}{\partial y_j} = + \frac{\partial \tau_{1j}}{\partial y_j} \quad (2.44)$$

where  $\tau_{ij}$  is the Stokes stress tensor.<sup>10</sup> This stress tensor is written

$$\tau_{ij} = -P \delta_{ij} - \left(\frac{2}{3}\right) \mu \epsilon_{kk} \delta_{ij} + 2\mu \epsilon_{ij} \quad (2.45)$$

where

$$\epsilon_{ij} = \frac{1}{2} \left( \frac{\partial u_i}{\partial y_j} + \frac{\partial u_j}{\partial y_i} \right) \quad (2.46)$$

As before, the fluid pressure is  $P$  and  $\epsilon_{ij}$  are the fluid strains. The momentum equation can be written in the form

$$\frac{\partial \rho u_i}{\partial t} = \frac{\partial \tau_{ij}}{\partial y_j} - \frac{\partial}{\partial y_j} (\rho u_i u_j) \quad (2.47)$$

as long as the fluid region is free of volume sources

$$\frac{\partial \rho u_i}{\partial t} = \rho \frac{\partial u_i}{\partial t} + u_i \frac{\partial \rho}{\partial t} = \rho \frac{\partial u_i}{\partial t} - u_i \frac{\partial \rho u_j}{\partial y_j}$$

Thus, taking the divergence of Equation (2.47) and the time derivative of Equation (2.1) for a fluid medium that is free of volumetric sources, we have

$$\frac{\partial^2 \rho}{\partial t^2} = - \frac{\partial^2 \tau_{ij}}{\partial y_i \partial y_j} + \frac{\partial^2}{\partial y_j \partial y_i} (\rho u_i u_j)$$

Now, since  $c_o^2 \nabla^2 \rho = \frac{\partial^2 [\rho c_o^2 \delta_{ij}]}{\partial y_i \partial y_j}$ , we have

$$\frac{\partial^2 \rho}{\partial t^2} - c_o^2 \nabla^2 \rho = \frac{-\partial^2}{\partial y_i \partial y_j} [\tau_{ij} - \rho u_i u_j + c_o^2 \rho \delta_{ij}]$$

By rewriting the stress tensor as

$$\tau_{ij} = -p\delta_{ij} + \tau'_{ij} \quad (2.48)$$

we can separate the contributions of the viscous stresses and the pressures, or normal stresses to obtain the wave equation in the final form

$$\frac{\partial^2 \rho}{\partial t^2} - c_o^2 \nabla^2 \rho = \frac{\partial^2 T_{ij}}{\partial y_i \partial y_j} \quad (2.49)$$

where

$$T_{ij} = \rho u_i u_j + (p - c_o^2 \rho) \delta_{ij} - \tau'_{ij} \quad (2.50)$$

is Lighthill's stress tensor. The tensor  $\rho u_i u_j$  is called the Reynolds stress, and it expresses the intensity of the turbulence in the source region. In a strictly irrotational or vorticity-free flow, Phillips<sup>11</sup> has shown that  $\overline{u_i u_j} \equiv 0$ . The pressure  $p$  and density  $\rho$  are the local instantaneous pressure and density of the fluid.

The noise producing character of the fluid field is such that outside a specified region of the disturbances

$$\frac{\partial^2 T_{ij}}{\partial y_i \partial y_j} \equiv 0$$

Now, the pressure and density in the far field ambient, undisturbed fluid are  $P_o$  and  $\rho_o$ . These quantities are constant so that spatial and temporal gradients of  $P_o$  and  $\rho_o$  are both zero. Thus, we can write the wave equation for the instantaneous density fluctuation (in the absence of mass injection) as

$$\frac{\partial^2}{\partial t^2} (\rho - \rho_o) - c_o^2 \nabla^2 (\rho - \rho_o) = \frac{\partial^2}{\partial y_i \partial y_j} \left\{ \rho u_i u_j + [P - P_o - c_o^2 (\rho - \rho_o)] \delta_{ij} - \tau'_{ij} \right\} \quad (2.51)$$

where we now introduce the fluctuation of pressure  $P - P_0$  into the stress tensor. If, in the fluid region, the fluctuation in pressure is a thermodynamic variable with adiabatic fluctuations, then the pressure and density fluctuations are related by Equation (2.6). Under this circumstance the pressure and density terms cancel identically in Equation (2.51). Often the magnitudes of the Reynolds stresses dominate the viscous stresses in turbulent motion. The wave equation in the absence of mass injection is now finally reduced to the more simplified form

$$\frac{\partial^2 (\rho - \rho_0)}{\partial t^2} - c_0^2 \nabla^2 (\rho - \rho_0) = \frac{\partial^2 (\rho_0 u_i u_j)}{\partial y_i \partial y_j} \quad (2.52)$$

which shows that the acoustic field is driven by the region of fluctuating Reynolds stresses. Outside the region of the Reynolds stress fluctuations, the velocity fluctuations are acoustic. Thus, outside the region of turbulent fluid motion Lighthill's equation reduces to the wave equation of linear acoustics theory. As we shall see later in this chapter, the knowledge of the behavior of the stress tensor  $T_{ij}$ , in the source region is crucial to the analytical modeling of acoustic radiation.

It is often the case in hydroacoustic applications that sources of mass injection (simple sources) coexist with turbulent sources in the fluid medium. These sources may be represented by adding a term  $\rho q$  to the right hand side of Equation (2.43). This term represents the rate of mass injection per unit volume to the region. It is the modified continuity equation which connects the mass and dilatational variations of an elemental volume of the fluid to  $q$ . When  $q = 0$  these two variations compensate and the standard continuity equation holds. The momentum equation in the form of Equation (2.47) is unaffected by the presence of the mass source, as long as it can be stipulated that the source injects fluid with no additional momentum, say at zero velocity. This can be deduced by examining the momentum of an elemental control volume enclosing the source and fixed with the fluid. The elemental force on the volume is

$$\begin{aligned} \delta F_i &= D[(\rho u_i) \delta V] / Dt \\ &= [D(\rho u_i) / Dt + \rho u_i \nabla \cdot \mathbf{U}] \delta V \end{aligned}$$

Equation (2.47) follows directly from this equation. The new wave equation may be derived as above and includes an additional volume source  $\dot{q}$  or, nearly equivalently,  $\rho_0 \ddot{V}$  in the context of Equation (2.20). The appropriate form of the wave equation which applies to mass injection co-existent with turbulent stresses is

$$-\frac{\partial^2(\rho-\rho_0)}{\partial t^2} - c_0^2 \nabla^2(\rho-\rho_0) = \frac{\partial^2(\rho u_1 u_1)}{\partial y_1 \partial y_1} + \rho_0 \frac{\partial q}{\partial t} \quad (2.52a)$$

in which the second order term  $q(\rho-\rho_0)$  has been neglected compared with the first-order  $\rho_0 q$ .

### 2.3.2 Kirchhoff's Integral Equation and the Retarded Potential

The acoustic field radiated outward to a point in free space from a distributed region of sources is the summation the individual contributions which result from each of the sources which compose the region. In the physical summation process that occurs, contributions reinforce and interfere depending on the instantaneous phase relationships among the various sources. In a rudimentary sense, this summation process has already been demonstrated in Section 2.1.2 to determine the acoustic fields of dipole and quadrupole source distributions. In more complicated physical situations, the acoustic radiation is determined as a weighted integral of the source distribution as well as the propagation to the far field. In the mathematical integral formulation described below, this is accomplished by the use of the retarded potential.

We begin by deriving an integral equation for the density fluctuation  $\rho_a = \rho - \rho_0$ , in the manner of Reference 12, although References 13, 14, and 15 have alternative derivations. The wave equation is written

$$\nabla^2 \rho_a - \frac{1}{c_0^2} \frac{\partial^2 \rho_a}{\partial t^2} = \frac{-\sigma(\vec{y}, t)}{c_0^2} \quad (2.53)$$

where  $\sigma(\vec{y}, t)$  is the source term of Equations (2.51) or (2.52), and where  $\sigma = \frac{\partial^2 T_{1j}}{\partial y_1 \partial y_j}$  is specified over a volume  $V_0$  contained in the problem volume  $V$  as illustrated in Figure 2.4a. The field point  $\vec{x}$  is considered to be surrounded by a small surface  $S_x$ , while the point  $\vec{y}$  is located somewhere within the region  $V$  which is surrounded by

surface  $\Sigma$ . A function that is defined as  $v(\mathbf{x}, y, z, t) = \rho_a(\mathbf{x}, y, z, t - r/c_0)$  where  $r = |\mathbf{x} - \mathbf{y}|$ , can be shown<sup>12</sup> to satisfy the equation

$$\nabla^2 v + \frac{2r}{c_0} \left\{ \frac{\partial}{\partial y_1} \left( \frac{r_1}{r^2} \frac{\partial v}{\partial t} \right) \right\} + \frac{1}{2} \sigma \left( \mathbf{y}, t - \frac{r}{c_0} \right) = 0 \quad (2.54)$$

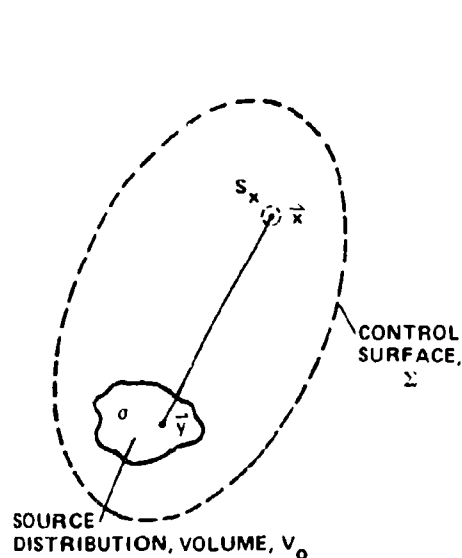


Figure 2.4a - General Radiation Geometry

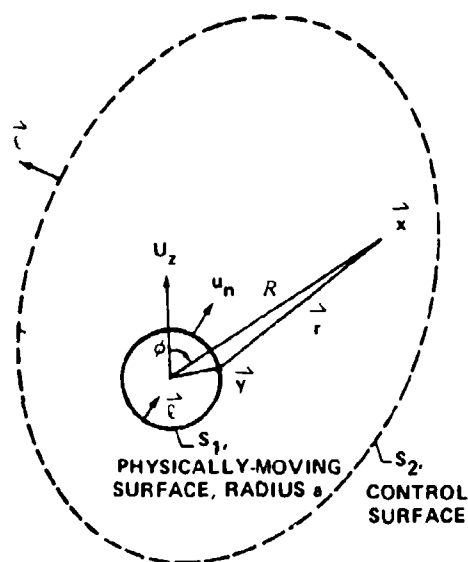


Figure 2.4b - Radiation Field for a Heaving Sphere

Figure 2.4 - Illustrations of Control Volumes Surrounding Source Regions and Fields of Interest



by substitution into Equation (2.53). Multiplication of Equation (2.54) by  $1/r$  and integration of that relationship throughout the entire volume contained within the surface  $\Sigma$  yields

$$\begin{aligned} \iiint_V \frac{1}{r} \nabla^2 v \, dV(\vec{y}) + \frac{2}{c_0} \iiint_V \frac{\partial}{\partial y_1} \left[ \frac{r_1}{r^2} \frac{\partial v}{\partial t} \right] dV(\vec{y}) \\ + \frac{1}{c_0} \iiint_V \frac{\sigma \left( \vec{y}, t - \frac{r}{c_0} \right)}{r} dV(\vec{y}) = 0 \end{aligned}$$

Green's theorem yields the relationship

$$\iiint_V \left\{ \frac{1}{r} \nabla^2 v - v \nabla^2 \left( \frac{1}{r} \right) \right\} dV(\vec{y}) = \iint_{\Sigma + S_x} \left\{ \frac{1}{r} \frac{\partial v}{\partial n} - v \frac{\partial}{\partial n} \left( \frac{1}{r} \right) \right\} dS(\vec{y})$$

Therefore, in conjunction with Equation (2.54), we obtain

$$\begin{aligned} \iiint_V \left\{ \frac{1}{r} \nabla^2 v - v \nabla^2 \left( \frac{1}{r} \right) \right\} dV(\vec{y}) &= \iint_{\Sigma + S_x} \left\{ \frac{1}{r} \frac{\partial v}{\partial n} - v \frac{\partial}{\partial n} \left( \frac{1}{r} \right) \right\} dS(\vec{y}) \\ &= \frac{-1}{c_0} \iiint_V \frac{\sigma \left( x, y, z, t - \frac{r}{c_0} \right)}{r} dV(\vec{y}) \\ &\quad - \frac{2}{c_0} \iint_{\Sigma + S_x} n_1 \frac{r_1}{r^2} \left( \frac{\partial v}{\partial t} \right) dS(\vec{y}) \end{aligned}$$

The surface integrals include all surfaces. If  $\vec{x}$  lies within the circumscribing surface  $\Sigma$  and if this point is surrounded by a surface  $S_x$  of vanishing radius then

$$\int_{S_x} \int v \frac{\partial}{\partial n} \left( \frac{1}{r} \right) dS(\vec{y}) = v(\vec{x}) \lim_{r \rightarrow 0} \iint_{\Omega} \frac{\partial}{\partial n} \left( \frac{1}{r} \right) r^2 d\Omega = 4\pi v(\vec{x})$$

However, if  $\vec{x}$  does not lie inside  $S_x$ , then

$$\int_{S_x} \int v \frac{\partial}{\partial n} \left( \frac{1}{r} \right) dS(\vec{y}) \equiv 0$$

Thus, we have

$$4\pi v(\vec{x}) = \frac{1}{c_0^2} \iiint_V \frac{\sigma \left( y, t - \frac{r}{c_0} \right)}{r} dV(\vec{y}) + \iint_{\Sigma} \left\{ \frac{2}{c_0} \frac{1}{r} \frac{\partial r}{\partial n} \left( \frac{\partial v}{\partial t} \right) + \frac{1}{r} \frac{\partial v}{\partial n} - v \frac{\partial}{\partial n} \left( \frac{1}{r} \right) \right\} dS(\vec{y})$$

for  $\vec{x}$  inside  $\Sigma$  and

$$0 = \frac{1}{c_0^2} \iiint_V \frac{\sigma \left( y, t - \frac{r}{c_0} \right)}{r} dV(\vec{y}) + \iint_{\Sigma} \left\{ \frac{2}{c_0} \frac{1}{r} \frac{\partial r}{\partial n} \left( \frac{\partial v}{\partial t} \right) + \frac{1}{r} \frac{\partial v}{\partial n} - v \frac{\partial}{\partial n} \left( \frac{1}{r} \right) \right\} dS(\vec{y})$$

for  $\vec{x}$  outside  $\Sigma$ . Now, considering only that  $\vec{x}$  lies within  $\Sigma$ , we have that  $v(\vec{x}, t) = \rho_a(\vec{x}, t)$ , and that

$$\frac{\partial v}{\partial n} = \frac{\partial}{\partial n} \left[ \rho_a \left( y, t - \frac{r}{c_0} \right) \right] = \left[ \frac{\partial \rho_a}{\partial n} \right] - \frac{1}{c_0} \frac{\partial r}{\partial n} \left[ \frac{\partial \rho_a}{\partial t} \right]$$

where the brackets denote that the function is evaluated at the retarded time  $t-r/c_0$ , i.e.,  $[f] = f(t-r/c_0)$ . Use of this function now yields the instantaneous density fluctuation as

$$4\pi\rho_a(\vec{x},t) = \frac{1}{c_o^2} \iiint \frac{[\sigma(\vec{y})]}{r} dV(\vec{y}) + \iint_{\Sigma} \left\{ \frac{1}{c_o r} \frac{\partial r}{\partial n} \left[ \frac{\partial \rho_a}{\partial t} \right] - [\rho_a] \frac{\partial \left( \frac{1}{r} \right)}{\partial n} + \frac{1}{r} \left[ \frac{\partial \rho_a}{\partial n} \right] \right\} dS(\vec{y}) \quad (2.55)$$

which is Kirchhoff's equation for the fluctuating fluid density. The surface integral is taken over all surfaces which are contiguous to the subject volume,  $V$ ; the volume  $V_o$  has been introduced since the source density is presumed to vanish outside  $V_o$ . Unless other surfaces are present, the bounding surface  $\Sigma$  may be expanded indefinitely far from both  $V_o$  and  $\vec{x}$  so that the surface integral vanishes. This can be seen by noting that if the disturbance is initiated at  $t = t_o$ , a surface  $\Sigma$  can be selected suitably far from the sources that  $\rho_a(t_o - r/c_o)$  and its derivatives vanish identically. The condition is analogous to the radiation condition. Thus, the instantaneous density fluctuation is given by volume integral

$$4\pi\rho_a(\vec{x},t) = \frac{1}{c_o^2} \iiint_{V_o} \frac{[\sigma(\vec{y})]}{r} dV(\vec{y}) \quad (2.56)$$

If  $V_o$  is finite, then this equation shows that  $\rho_a(\vec{x},t) \sim 1/r$  sufficiently far from  $V_o$ .

Now, using a comparison of Equations (2.52), (2.53), and (2.56), we find the Kirchhoff formulation from Lighthill's wave equation as

$$4\pi[\rho(\vec{x},t) - \rho_o] = \frac{1}{c_o^2} \iiint_{V_o} \frac{1}{r} \left[ \frac{\partial^2 (\rho u_i u_j)}{\partial y_i \partial y_j} \right] dV(\vec{y}) \quad (2.57)$$

where  $c_o^2(\rho(\vec{x},t) - \rho_o) = p_a(\vec{x},t)$ . As before, the bracket in the integrand denotes that the retarded time is used. This equation is the central result of this section

because the integrand includes the required retardation or phase effects which give rise to the multipole nature of complex source regions.

The source term in Equations (2.49), (2.52), and (2.57) involves two spatial gradients. Now, in Section 2.1.2 it was shown that the quadrupole radiation results from two spatial fluid gradients. Lighthill's source term is, therefore, interpreted as having a quadrupole nature. Furthermore, the source term is determined by correlated fluid velocities which give rise to the stress tensor  $T_{ij}$ . Physically, those local stresses are either in-line or lateral, as illustrated in Figure 2.3. Thus, the compressive stresses  $T_{ii}$ ,  $T_{jj}$ ,  $T_{kk}$  represent longitudinal quadrupoles, while the shearing stresses  $T_{ij}$  ( $i \neq j$ ) represent lateral quadrupoles.

### 2.3.3 Acoustic Radiation from Free Turbulence

In Chapter 3 the radiation from subsonic jets will be examined in considerable detail. However, it is instructional to examine here some of the elementary aspects of the radiation from stochastic fluid motion in order to illustrate the types of analytical manipulations that are common in applying the previous results to hydroacoustic problems. This is most easily accomplished without the reference to specific detailed applications. It is the purpose of this section only to examine some basic concepts. The first treatment of Lighthill's source term in this manner was done by Proudman.<sup>16</sup>

We will recast Equation (2.57) into a form which permits an estimate of the radiated sound intensity from a restricted region of convected turbulence when solid surfaces are not present. This estimate will depend on an appropriate statistical representation of the turbulence. We note the following relationships for the retarded function  $[F] = F(y, t-r/c_0)$ , and its derivatives:

$$\frac{\partial}{\partial x_i} \iiint \frac{F\left(y, t - \frac{r}{c_0}\right)}{r} dV(\vec{y}) = \iiint \left\{ \left[ \frac{\partial F}{\partial t} \right] \left( \frac{-1}{c_0} \right) \frac{(x_i - y_i)}{r^2} - \frac{[F]}{r^2} \frac{(x_i - y_i)}{r} \right\} dV(\vec{y})$$

and

$$\iiint \frac{\partial}{\partial y_i} \left[ \frac{F}{r} \right] dV(\vec{y}) = \iiint \left[ \frac{\partial F}{\partial y_i} \right] \frac{dV(\vec{y})}{r} + \iiint \left\{ \left[ \frac{\partial F}{\partial t} \right] \frac{1}{c_0} \frac{(x_i - y_i)}{r^2} + \frac{[F]}{r^2} \frac{(x_i - y_i)}{r} \right\} dV(\vec{y})$$

so that combining we have,

$$\iiint \frac{\partial}{\partial y_i} \left[ \frac{F}{r} \right] dV(\vec{y}) = \iiint \left[ \frac{\partial F}{\partial y_i} \right] \frac{dV(\vec{y})}{r} - \frac{\partial}{\partial x_i} \iiint \frac{[F]}{r} dV(\vec{y})$$

Now, Gauss' theorem provides that

$$\iiint \frac{\partial}{\partial y_i} \left[ \frac{F}{r} \right] dV(\vec{y}) = \iint_{\Sigma} n_i \frac{[F]}{r} dS(\vec{y})$$

where  $n_i$  is the outward normal to the surface  $\Sigma$ . Since this surface can be arbitrarily selected to be far enough from the source region that outward-travelling waves have not reached a range  $r > c_0 t$ , we can set the surface integral equal to zero. Thus we have the identity (in free space, no surfaces)

$$\iiint \left[ \frac{\partial F}{\partial y_i} \right] \frac{dV(\vec{y})}{r} = \frac{\partial}{\partial x_i} \iiint \frac{[F]}{r} dV(\vec{y}) \quad (2.58)$$

This relationship is a formal mathematical statement of the operation leading to Equation (2.37). Recall, that expression for the far field radiation from two closely spaced sources in phase opposition involved a gradient of the acoustic field pressure from the single simple source. This can be seen by comparing Equations (2.27) and (2.37). Similarly, by the repeated application of these operations, we have

$$4\pi(\rho(\vec{x}, t) - \rho_0) = \frac{1}{c_0^2} \frac{\partial^2}{\partial x_i \partial x_j} \iiint \frac{[T_{ij}]}{r} dV(\vec{y}) \quad (2.59)$$

as a free-space form of Lighthill's equation which applies only when there are no solid surfaces enclosed by the surface  $\Sigma$ . Under the assumption that the largest linear dimension of the source volume is small relative to the range  $r$ , and that the

velocity of the source relative to the receiver is small compared to  $c_o$ , the derivatives in Equation (2.59) yield

$$4\pi(\rho(\vec{x}, t) - \rho_o) = \frac{1}{c_o} \iiint \frac{(x_i - y_i)(x_j - y_j)}{r^3} \left[ \frac{\partial^2 T_{ij}}{\partial t^2} \right] dV(\vec{y})$$

$$= \frac{1}{c_o} \frac{x_i x_j}{r^3} \iiint \left[ \frac{\partial^2 T_{ij}}{\partial t^2} \right] dV(\vec{y}) \quad (2.60)$$

since  $\frac{\partial^2 T_{ij}}{\partial t^2} = 0$ . Near field terms of the order  $r^{-3}$  are neglected compared to terms of the order  $r^{-1}$ .

Our next objective will be to determine the time averaged acoustic intensity in the far field due to fluctuations in the Reynolds stresses using Equation (2.60). The intensity is (Equation (2-15))

$$\overline{I(\vec{x})} = \frac{c_o}{\rho_o} \overline{(\rho - \rho_o)^2}$$

or, using Equation (2.60) we have

$$\overline{I(\vec{x})} = \frac{1}{(4\pi)^2 \rho_o c_o^5} \left[ \frac{x_i x_j}{r^3} \right] \left( \frac{x_k x_l}{r^3} \right) \times \iiint \cdot \iiint$$

$$\times \left\{ \frac{\partial^2 T'_{ij} \left( \vec{y}_1, t - \frac{r_1}{c_o} \right)}{\partial t^2} \cdot \frac{\partial^2 T'_{kl} \left( \vec{y}_2, t - \frac{r_2}{c_o} \right)}{\partial t^2} \right\} dV(\vec{y}_1) dV(\vec{y}_2) \quad (2.61)$$

where

$$T'_{ij} = T_{ij} - \bar{T}_{ij}$$

and  $T'_{ij}$  must approach zero at least as fast as  $|y|^{-3}$  as  $|y| \rightarrow \infty$  (see also Crow<sup>17</sup>). The term in brackets is the spatial covariance of the retarded stress tensor which is a function of both position vectors  $\vec{y}_1$  and  $\vec{y}_2$ . The integration with both of these vectors extends over the source volume  $V_0$ . The covariance of the stress tensor involves products of velocity fluctuations of the form

$$\overline{\frac{\partial^2 T'_{ij}}{\partial t^2}} \cdot \overline{\frac{\partial^2 T'_{kl}}{\partial t^2}} = \overline{\frac{\partial^2}{\partial t^2} (\rho u_i u_j)_{\vec{y}=\vec{y}_1}} \cdot \overline{\frac{\partial^2}{\partial t^2} (\rho u_k u_l)_{\vec{y}=\vec{y}_2}}$$

where  $(\rho u_i u_j) = \rho u_i u_j - \overline{\rho u_i u_j}$  and where we have used the source terms introduced in Equations (2.52) and (2.57).

We shall formally consider the mathematical consequences of specific forms of covariance functions in future chapters. However, for now we will develop certain general notions as they apply to turbulent fluid flow. Let us consider that the disturbances are the result of the irregular motion of a collection of eddies of typical correlation length  $\Lambda$ . This length is interpreted as a limiting separation of two velocity sensors in the flow so that the temporal average of the product of the signals from the sensors is considered negligible compared to the temporal mean square of each signal separately. For example, letting the velocities in the  $i$  and  $k$  directions at two points in the volume  $V_0$  be  $u_i(\vec{y}_1, t)$  and  $u_k(\vec{y}_2, t)$  we can write, with  $\vec{y}_2 = \vec{y}_1 + \vec{\xi}$ ,

$$u_i^2(\vec{y}_2, t) \approx u_k^2(\vec{y}_2 + \vec{\Lambda}, t) \gg u_i(\vec{y}_1, t) u_k(\vec{y}_1 + \vec{\Lambda}, t) \quad (2.62)$$

i.e., the mean squares of the separate signals exceed the covariance of the signals for  $\vec{\xi} \geq \vec{\Lambda}$ . For small separations  $\vec{\xi} \ll \vec{\Lambda}$  the covariance approaches the product of the root-mean-squares of the separate signals; i.e.,

$$\lim_{|\vec{\xi}| \rightarrow 0} \overline{[u_i(\vec{y}, t) u_k(\vec{y}_1 + \vec{\xi}, t)]} \approx [\overline{u_i^2(\vec{y}_1, t)} \overline{u_k^2(\vec{y} + \vec{\xi}, t)}]^{1/2} \quad (2.63)$$

The covariance of  $u_i$  and  $u_k$  is a continuous function of  $\vec{\xi}$ . Now, we will assume that the turbulent patch is translated at a constant velocity  $U_c$  which is uniform throughout  $V_o$ . Under this assumption, the individual eddies are locally translated in a wavelike manner according to the formula  $x - U_c t = \text{constant}$ . Thus, a measure of the time variation is

$$\frac{\partial}{\partial t} \sim \frac{U_c}{\Lambda}$$

Now, we further assume that  $\overline{u_1^2} \sim U_c^2$  and that  $U_c \ll c_o$ . Under these simplifications Equation (2.61) can be written as

$$I(\vec{x}) \sim \frac{1}{(4\pi)^2} \frac{1}{\rho_o c_o^5} \frac{1}{r^2} \cdot \left(\frac{U_c}{\Lambda}\right)^4 (\rho_o U_c^2)^2 \cdot \Lambda^3 V_o \quad (2.64)$$

This result follows directly from Equation (2.62) which implies the representation

$$T'_{ij} \left( \vec{y}_1, t - \frac{|\vec{x} - \vec{y}_1|}{c_o} \right) T'_{kl} \left( \vec{y}_1 + \vec{\xi}, t - \frac{|\vec{x} - \vec{y}_1 - \vec{\xi}|}{c_o} \right) \sim \rho_o^2 \overline{u_k^2} \overline{u_k^2} R(\vec{y}, \vec{\xi}) \quad (2.65)$$



where  $R(\vec{y}, \vec{\xi})$  is a correlation function of the stress tensor fluctuation and where by definition  $R(\vec{y}, 0) \equiv 1$ , and  $R(\vec{y}, \vec{\Lambda}) \approx 0$ . Finally, by neglecting the retardation effects we can write

$$\begin{aligned} & \iiint \overline{\frac{\partial^2}{\partial t^2} (T_{ij})_1 \frac{\partial^2}{\partial t^2} (T_{kl})_2} dV(\vec{\xi}) \\ & \sim \rho_o^2 \left( \frac{U_c}{\Lambda} \right)^4 \overline{u_i^2} \overline{u_k^2} \iiint R(\vec{y}, \vec{\xi}) dV(\vec{\xi}) \\ & \sim \rho_o^2 \left( \frac{U_c}{\Lambda} \right)^4 \overline{u_i^2} \overline{u_k^2} \Lambda^3 \end{aligned}$$

as long as the eddy correlation length  $\Lambda$  and the characteristic length scale of  $V_o$  are much less than an acoustic wavelength and propagation velocity, respectively. Equation (2.64) is rearranged as

$$I(\vec{x}) \sim \frac{1}{(4\pi)^2} \rho_o \frac{U_c^8}{c_o^5} \frac{V_o}{\Lambda r^2} \quad (2.66)$$

in order to emphasize that the acoustic intensity from free convecting turbulence increases as the eight power of the convection velocity and is linearly proportional to the acoustically compact volume of the volume of turbulence. A review of the derivation leading to Equation (2.60) will show that the existence of the two spatial gradients in the compact source gives rise to the  $c_o^{-4}$  dependence in the acoustic intensity. The high exponent on the Mach number is, therefore, set by the double spatial gradient in the source term and is thus a characteristic of sound emitted from a distribution of subsonic flow quadrupoles in an unbounded acoustic medium.

This fundamental result gives the often quoted eighth power velocity dependence of radiated sound power from free turbulence. Equation (2.66) is a much simplified

relationship which gives some variable dependencies that apply to noise from free jets and wakes. Chapter 3 will consider some more exact theories which will account for explicit forms of the correlation function,  $R(\vec{y}, \vec{\xi})$ , effects of turbulence convection on radiation efficiency, and kinematic scaling.

## 2.4 EFFECTS OF SURFACES ON FLOW-INDUCED NOISE

It must be emphasized that the expression for the acoustic radiation from a restricted zone of fluid stress fluctuations given in the last section applies only when there are no reflecting boundaries in the field of consideration. When a boundary exists and its surface impedance is not identically equal to that of the fluid, its effect is to physically alter the sound field by causing acoustic reflections. It may also disturb the flow locally causing surface pressures which act as radiating dipoles. The mathematical fundamentals of this class of situations have been developed by Curle<sup>18</sup> and by Powell.<sup>19</sup>

### 2.4.1 Curle's Development of Lighthill's Wave Equation

Provision has already been made in our discussions for considering these effects. Equation (2.55) is a general formulation which applies as long as the observation point  $\vec{x}$  remains somewhere within the control surface fixed with respect to the acoustic medium which we have designated as  $\Sigma$ , as shown in Figure 2.4a.

Let us now let  $\Sigma$  not necessarily be so far from the source region that disturbances have not reached  $r_{\Sigma} = c_0 t$ . This is a relaxation of our former condition on  $\Sigma$  and it allows for reflections from some surfaces in the control volume. Equation (2.55) expresses the acoustic density fluctuation as a volume integral of the source region plus surface integrals over  $\Sigma$  of the density fluctuations. The surface integrals can represent the effects of reflections if the surfaces of integration coincide with physical boundaries. Equation (2.55) for density fluctuations in the fluid is now rewritten

$$\begin{aligned}
4\pi(\rho(\vec{x}, t) - \rho_o) &= \frac{1}{c_o^2} \iiint_V \frac{\partial^2 [T_{ij}]}{\partial y_i \partial y_j} \frac{dV(\vec{y})}{r} \\
&+ \iint_{\Sigma} \left\{ \frac{1}{c_o r} \frac{\partial r}{\partial n} \left[ \frac{\partial \rho}{\partial t} \right] - [\rho] \frac{\partial \left( \frac{1}{r} \right)}{\partial n} + \frac{1}{r} \left[ \frac{\partial \rho}{\partial n} \right] \right\} dS(\vec{y}) \quad (2.67)
\end{aligned}$$

to reintroduce the control volume  $V$  and to explicitly denote the source term. Since all derivatives of the ambient density  $\rho_o$  are necessarily 0, we can use  $\rho_a$  and  $\rho$  interchangeably. We have let  $\Sigma$  be any closed region which includes both  $V_o$  and the observation point  $x$ . Applying Gauss' theorem to the volume integral as in the beginning of Section 2.3.3, we obtain

$$\begin{aligned}
\iiint_V \left[ \frac{\partial}{\partial y_i} \left( \frac{\partial T_{ij}}{\partial y_j} \right) \right] \frac{dV(\vec{y})}{r} &= \frac{\partial^2}{\partial x_i \partial x_j} \iiint_{V_o} \frac{[T_{ij}]}{r} dV(\vec{y}) \\
&+ \iint_{\Sigma} \ell_i \left[ \frac{\partial T_{ij}}{\partial y_j} \right] \frac{dS(\vec{y})}{r} + \frac{\partial}{\partial x_i} \iint_{\Sigma} \ell_j [T_{ij}] \frac{dS(\vec{y})}{r} \quad (2.68)
\end{aligned}$$

where the only part of the region within  $V$  for which  $T_{ij} \neq 0$  is  $V_o$ .

Substitution of Equation (2.68) into Equation (2.67) yields

$$\begin{aligned}
4\pi(\rho(\vec{x}, t) - \rho_o) &= \frac{1}{c_o^2} \frac{\partial^2}{\partial x_i \partial x_j} \iiint_{V_o} \frac{[T_{ij}]}{r} dV(\vec{y}) \\
&+ \frac{1}{c_o^2} \iint_{\Sigma} \frac{\ell_i}{r} \left[ \frac{\partial}{\partial y_i} (T_{ij} + \rho c_o^2 \delta_{ij}) \right] dS(\vec{y}) \\
&+ \frac{1}{c_o^2} \frac{\partial}{\partial x_i} \iint_{\Sigma} \frac{\ell_j}{r} [T_{ij} + \rho c_o^2 \delta_{ij}] dS(\vec{y}) \quad (2.69)
\end{aligned}$$

since the surface integral in Equation (2.55) can be rewritten

$$\begin{aligned}
& \iint_{\Sigma} \left\{ \frac{\ell_1}{c_0 r} \frac{\partial r}{\partial y_1} \left[ \frac{\partial \rho}{\partial t} \right] - \ell_1 [\rho] \frac{\partial \left( \frac{1}{r} \right)}{\partial y_1} + \frac{\ell_1}{r} \left[ \frac{\partial \rho}{\partial y_1} \right] \right\} dS(\vec{y}) \\
&= \iint_{\Sigma} \left\{ \frac{-\ell_1}{c_0 r} \frac{\partial r}{\partial x_1} \left[ \frac{\partial \rho}{\partial t} \right] + \ell_1 [\rho] \frac{\partial \left( \frac{1}{r} \right)}{\partial x_1} + \frac{\ell_1}{r} \left[ \frac{\partial \rho}{\partial y_1} \right] \right\} dS(\vec{y}) \\
&= \iint_{\Sigma} \ell_1 \left\{ \frac{\partial}{\partial x_1} \left( \frac{1}{r} [\rho] \right) + \frac{1}{r} \left[ \frac{\partial \rho}{\partial y_1} \right] \right\} dS(\vec{y}) \\
&= \iint_{\Sigma} \ell_j \left\{ \frac{\partial}{\partial x_1} \left( \frac{1}{r} [\rho \delta_{1j}] \right) + \frac{1}{r} \left[ \frac{\partial \rho \delta_{1j}}{\partial y_1} \right] \right\} dS(\vec{y}) \quad (2.70)
\end{aligned}$$

Now, since Lighthill's stress tensor is given by Equation (2.50), Equation (2.69) becomes, by substitution

$$\begin{aligned}
4\pi c_0^2 (\rho(\vec{x}, t) - \rho_0) &= \frac{\partial^2}{\partial x_1 \partial x_j} \iiint_{V_0} \frac{[T_{1j}]}{r} dV(\vec{y}) \\
&+ \iint_{\Sigma} \frac{\ell_1}{r} \left[ \frac{\partial}{\partial y_1} (\rho u_1 u_j + \tau'_{1j} + p \delta_{1j}) \right] dS(\vec{y}) \\
&+ \frac{\partial}{\partial x_1} \iint_{\Sigma} \frac{\ell_j}{r} [\rho u_1 u_j + \tau'_{1j} + p \delta_{1j}] dS(\vec{y}) \quad (2.71)
\end{aligned}$$

which is Curle's<sup>18</sup> result. Equation (2.71) states that the acoustic pressure is directly radiated from a volume distribution of quadrupoles plus a contribution from motions and stresses existing on any surfaces present. The surface effect can be interpreted as a distribution of dipoles as can be deduced by comparing the surface

integrals to a model of the dipole in Section 2.3. Recall that the method leading to Equation (2.37) involved the calculation of radiation from two sources in phase opposition. To do this, it was necessary to determine the gradient of the free space Green function,  $\left(\frac{1}{r}\right) e^{-ik_0 r}$ , in the direction of the vector between the source centers. This is a limiting form of the operations on the surface integrals in Equation (2.71). Those integrals provide contributions which are proportional to the resultant fluid forces on the surfaces.

The momentum theorem, Equation (2.2), rewritten as

$$\ell_i \frac{\partial}{\partial y_i} [\rho u_i u_j + \tau'_{ij} + p \delta_{ij}] = -\ell_i \frac{\partial(\rho U_i)}{\partial t} \quad (2.72)$$

is used to change the integrand in the first surface integral of Equation (2.71).

Thus,

$$\begin{aligned} 4\pi c_0^2 (\rho(\vec{x}, t) - \rho_0) &= \frac{\partial^2}{\partial x_i \partial x_j} \iiint \frac{[T_{ij}]}{r} dV(\vec{y}) - \iint_{\Sigma} \frac{\ell_i}{r} \left[ \frac{\partial(\rho U_i)}{\partial t} \right] dS(\vec{y}) \\ &+ \frac{\partial}{\partial x_i} \iint_{\Sigma} \frac{\ell_j}{r} [\rho u_i u_j + \tau'_{ij} + p \delta_{ij}] dS(\vec{y}) \end{aligned} \quad (2.73)$$

The second term is, thus, a dipole contribution from the acceleration of the body in a direction normal to its surface.

Therefore, the sound pressure is the resultant of three contributions: the radiation from the turbulent domain, radiation due to the instantaneous contiguous surface motion with phase cancellations included, and radiation from a distribution of forces acting on the region. Equation (2.73) could as well have been derived from direct use of Equation (2.56), but with the source term representing a superposition of monopole, dipole, and quadrupole sources. An equivalent inhomogeneous wave equation may accordingly be written

$$\nabla^2 p_a - \frac{1}{c_o^2} \frac{\partial^2 p_a}{\partial t^2} = -\rho_o \frac{\partial q}{\partial t} + \frac{\partial F_i}{\partial y_i} - \frac{\partial^2 T_{ij}}{\partial y_i \partial y_j} \quad (2.74)$$

where  $\dot{q}$  = volume velocity of simple source

$F_i$  =  $i^{th}$  component of the force vector per unit area normal to  $i$

$T_{ij}$  = stress tensor

In using Equation (2.74)  $\rho_o \dot{q}$  denotes all the mass flux and  $F_i$  denotes all the forces acting on the region. In the context of the integral form above,  $F_i$  includes all of the  $\partial_j (\rho u_i u_j + \tau'_{ij} + p \delta_{ij})$ . As we shall see next, the efficacy of Curle's result and of Equation (2.74) in describing the nature of flow-induced noise is particularly realized when the surface in question is much smaller than an acoustic wavelength; then  $\partial F_i / \partial y_i$  represents a divergence of the concentrated force exerted on the fluid.

#### 2.4.2 Illustration 1: Radiation from a Heaving Sphere

To illustrate the dipole equivalency particularly with regard to surface acceleration we will reexamine the radiation from a heaving sphere. Figure 2.4b is a diagram of the source region as it pertains to Equation (2.71). The amplitude of heaving motions is infinitesimal compared with the radius of the sphere. The surface  $\Sigma$ , therefore, consists of a surface  $S_1$ , which encloses the moving physical surface and the far field control surface of the complete fluid region  $S_2$ . The source point  $\vec{y}$  is shown to be on the surface of the sphere of a radius  $a$  which is translating in an oscillatory fashion along the  $z$ -axis (see Figure 2.2a for the coordinate system) as

$$U_z(t) = U_z e^{-i\omega t}$$

Expansion of the  $\partial/\partial x_i$  derivative of the second surface integral, yields terms of the order  $u_y/c_o$  and  $a/r$  compared to the first integral. Far enough from the sphere and for small velocity amplitudes, this term may be neglected. The quadrupole

term is also neglected because only very weak Reynolds stresses are generated by the oscillating vortical flow setup in the hydrodynamic near field of the sphere. Therefore, Equation (2.73) gives the far field radiated pressure as

$$\begin{aligned}
 4\pi p_a(\vec{x}, t) &= \iint_{S_1} \frac{l_i}{r} \left[ \rho_o \frac{\partial u_i(\vec{y}, t)}{\partial t} \right] dS(\vec{y}) \\
 &= \iint_{S_1} \frac{1}{r} \left[ \rho_o \frac{\partial u_n(\vec{y}, t)}{\partial t} \right] dS(\vec{y}) \\
 &= \iint_{S_1} \frac{i\omega \rho_o U_Z \cos \phi(\vec{y})}{r} e^{-i\left(\omega t - \frac{r}{c_o}\right)} dS(\vec{y})
 \end{aligned}$$

since  $l_i u_i = u_n$  is the fluctuating velocity normal to the surface. The retardation effect is approximated by writing for  $R \gg a$

$$r \approx R - a \cos(\phi - \phi(\vec{y}))$$

so that the exponential becomes

$$e^{-i\omega\left(t - \frac{r}{c_o}\right)} \approx e^{-i\omega\left(t - \frac{R}{c_o}\right)} [1 - ik_o a \cos(\phi - \phi(\vec{y}))] \quad (2.75)$$

where  $\phi$  is the angle made by the position vector  $\vec{x}$  with the direction of motion and  $\phi(\vec{y})$  is that angle made with  $\vec{y}$ . This allows the acoustic pressure to be written down as

$$p_a(x, t) = \frac{\rho_o c_o k_o^2 a^3 U_Z}{4\pi R} \cos \phi e^{-i(\omega t - k_o R)} 2\pi \int_0^\pi \cos^2 \phi(\vec{y}) \cdot \sin \phi(\vec{y}) \cdot \phi(\vec{y}) \cdot d\phi(\vec{y})$$

which is functionally identical to the result obtained in Section 2.2. This can be seen by combining Equations (2.34) and (2.35).

Note that if we had carelessly ignored the retardation effect, the resulting surface integral would have been exactly zero. Thus, the dipole radiation emerges here as a second order effect of the motion of the sphere; it is a mathematical consequence of the series expansion of Equation (2.75) and a physical consequence that the excess pressure and suction at opposite poles of the sphere do not instantaneously cancel identically.

### 2.4.3 Illustration 2: Radiation from a Concentrated Hydrodynamic Force: The Force Dipole

If, instead of a surface in motion in a stagnant body of fluid, we consider a fixed surface in a moving fluid we are led to another important relationship which characterizes dipole radiation. The geometry of Figure 2.4b applies to this problem, except that now  $S_1$  is a rigid surface on which  $u_i \ell_i = u_n = 0$ . Specific instances will be considered in later chapters. The flow around the surfaces is presumed to be unsteady, generating dynamic pressures on  $S_1$ . For a closed rigid surface, Equation (2.73) reduces to

$$4\pi c_0^2 (\rho(\vec{x}, t) - \rho_0) = \frac{\partial}{\partial x_i} \iint_{S_1} \ell_i p \left( \vec{y}, t - \frac{r}{c_0} \right) \frac{dS(\vec{y})}{r} \quad (2.76)$$

if we ignore the viscous surface stresses  $\tau'_{ij}$  and the contribution of Reynold's stresses in the wake. (This latter simplification is considered in more detail in Chapter 5.)

For any surface whose dimension is substantially less than an acoustic wavelength, Equation (2.76) reduces to give the acoustic pressure fluctuation as

$$4\pi c_0^2 (\rho(\vec{x}, t) - \rho_0) = - \frac{\partial}{\partial x_i} \left[ \frac{f_i}{r} \right]$$



which expands to

$$4\pi p_a(\vec{x}, t) = + \frac{1}{c_o} \frac{x_1}{r^2} \left[ \frac{\partial f_1}{\partial t} \right] \quad (2.77)$$

as the radiated pressure resulting from the concentrated force,  $f_1$ , exerted on the fluid. Note that the pressure is greatest in the direction of the force since  $x_1 = r \cos \phi$  where  $\phi$  is the angle measured from the force direction, see Figure 2.2b and Equation (2.35).

Note that we could have derived this result by replacing  $\sigma(\vec{y}, t)$  in Equation (2.53) by the concentrated force gradient, i.e.,

$$\nabla^2 p_a - \frac{1}{c_o^2} \frac{\partial^2 p_a}{\partial t^2} = \frac{\partial f_1(t)}{\partial y_1} \delta(\vec{y} - \vec{y}_o)$$

as in Equation (2.76). Incorporating Equations (2.56) and (2.58) yields (2.77) directly. The result could also have been derived from Equation (2.74).

#### 2.4.4 Powell's Reflection Theorem

In Figure 2.5, we specify the bounding surface to come in contact with the source region. Now, we have dissected  $\Sigma$  to be

$$\Sigma = S_o + S_1 + S_2$$

where  $S_2$  = control surface of the region of interest

$S_1$  = an impedance boundary which can reflect sound and which intersects  $S_2$  far from  $V_o$

$S_o$  = adjacent to the disturbance region and it does not necessarily have the same impedance as  $S_1$

As before, we select  $S_2$  to lie far enough from  $V_o$  that disturbances have not yet reached  $S_2$ . Since  $T_{ij} = 0$  outside  $V_o$  it vanishes on  $S_1$ , but not on  $S_o$ . Therefore, using Equations (2.59) and (2.72), Equation (2.71) can be written (since  $\ell_1 u_1 = \ell_n u_n = u_n$ ):

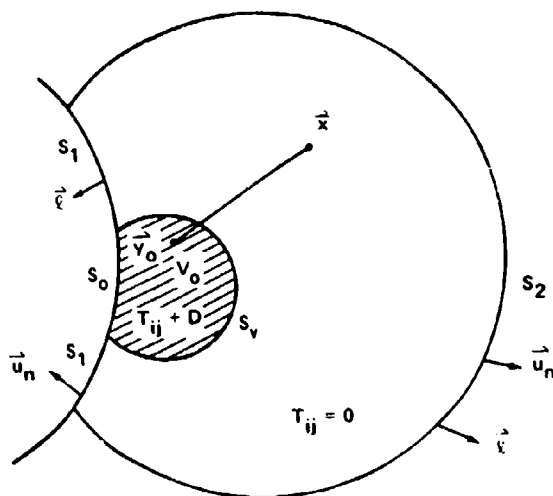


Figure 2.5a - Simple Boundaries Including Surfaces Contiguous to a Fluid Disturbance Region

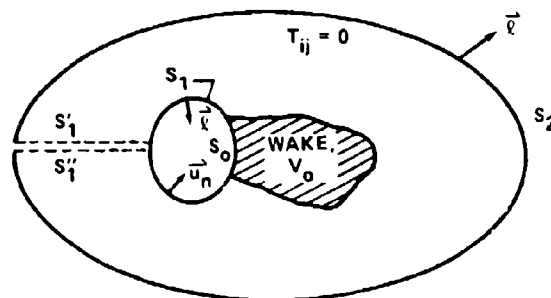


Figure 2.5b - Fluid Stress Region Adjacent to a Physically Closed Reflecting Body

Figure 2.5 - Surface Geometries Used to Illustrate Powell's Analysis of the Influences of Surfaces on Radiation

$$\begin{aligned}
 4\pi p_a(\vec{x}, t) = & \frac{\partial^2}{\partial x_i \partial x_j} \iiint_{V_0} \frac{[T_{ij}]}{r} dV(\vec{y}) \\
 & - \iint_{S_0} \frac{\hat{\ell}_n}{r} \left[ \rho \frac{\partial u_n}{\partial t} \right] dS(\vec{y}) + \frac{\partial}{\partial x_i} \iint_{S_0} \frac{1}{r} [\rho u_i u_n + \tau'_{in} + p \delta_{in}] dS(\vec{y}) \\
 & - \iint_{S_1} \frac{\hat{\ell}_n}{r} \left[ \rho \frac{\partial u_n}{\partial t} \right] dS(\vec{y}) + \frac{\partial}{\partial x_i} \iint_{S_1} \frac{\hat{\ell}_i}{r} [p_a(\vec{y}, t)] dS(\vec{y}) \quad (2.78)
 \end{aligned}$$

This expression, which is really just a restatement of Equation (2.73), emphasizes the multiple effects of the adjacent boundary. On the boundary contiguous to the source volume, a contribution is emitted by the acceleration in the direction normal to the surface,  $\partial u_n / \partial t$ . Another contribution arises from the distributed stresses on the surface which are  $\hat{\ell}_j [\rho u_i u_j + \tau'_{ij} + p \delta_{ij}] = \rho u_i u_n + \tau'_{in} + p \delta_{in}$ . The fluid pressure

fluctuations include both hydrodynamic and acoustic contributions and they account for the normal stresses on the surface. Viscous,  $\tau'_{ij}$ , and Reynolds stresses,  $\rho u_i u_j$ , which involve normal motions and gradients on the surface will also radiate. The contributions from the adjacent surface  $S_1$  involve the normal motion of that surface as well as the scattering of the acoustic pressure  $p_a$ . The integral relationship of Equation (2.78), originally derived by Powell,<sup>19</sup> is an extension of Curle's<sup>18</sup> result that emphasizes the influences of boundaries adjacent to the region of the turbulent stresses. The result is general and it includes all of the acoustic and hydrodynamic effects on the fluid region. Although the result applies for boundaries of any shape, it will be seen in later chapters\* that evaluations of Equation (2.78) are not trivial. When the turbulent region encloses a physical body, as shown in Figure 2.5b, the surface of the body consists of  $S_0$  and part of  $S_1$  is extended on both sides of a strip of vanishing thickness to connect to control surface  $S_2$ . It is clear the contributions from the connecting surfaces  $S'_1$  and  $S''_1$  must cancel. This analytical situation could apply to noise from a wake behind a body in flow.

Another situation could arise in which surfaces  $S'_1$  and  $S''_1$  coincide with the physical boundaries of a wedge. Thus, in Figure 2.5 the surface  $S_1 + S_0$  reduces to a point at the apex of the wedge and the turbulent region could be adjacent to the wedge surface. This problem includes acoustic diffraction about the sharp apex and so is difficult to solve using straightforward estimations of the integrals in Equation (2.78). The difficulty arises because a priori knowledge of the acoustic pressure on the surface is not available.

A situation which consists of  $V_0$  being adjacent to a plane boundary has application to boundary-layer induced noise. This problem was considered by Powell<sup>19</sup> and its result has important general implications for any flow region adjacent to a boundary of large radius of curvature.

An illustration of Powell's problem is given in Figure 2.6. The plane surface  $S_0 + S_1$  separates a real fluid region from its virtual image, denoted by primes. This image system is provided to account for reflections at the boundary  $S_0 + S_1$ . For the image stress system  $T'_{ij}$ , enclosed by the surface  $S'_0 + S'_1 + S'_2$ , the acoustic field outside at position  $\vec{x}$  vanishes identically. Velocity fluctuations in the plane of the surface are designated by  $u_s$ . Thus, using Equation (2.78) we have

---

\*In Chapter 8 this integral relationship will be further examined for application to turbulent boundary layer noise.

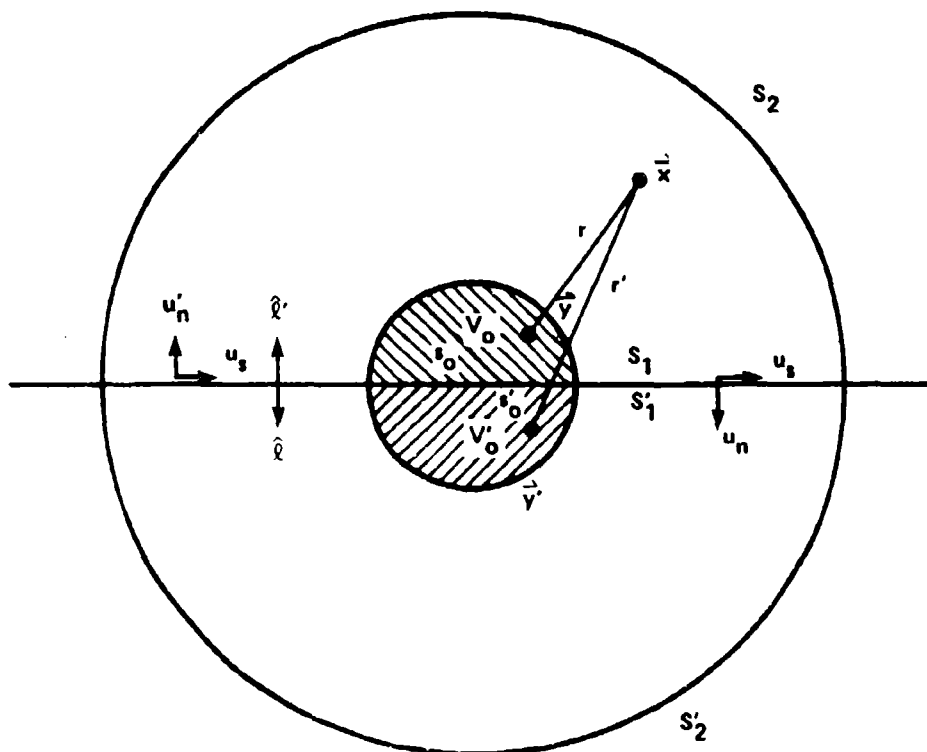


Figure 2.6 - An Illustration for Powell's Reflection Theorem

$$\begin{aligned}
 0 = & \frac{\partial^2}{\partial x_1' \partial x_1'} \iiint_{V_0'} \frac{[T_{ij}']}{r'} dV(\vec{y}') \\
 & - \iint_{S_0'} \frac{\hat{x}_n'}{r} \left[ \rho' \frac{\partial u_n'}{\partial t} \right] dS(\vec{y}') + \frac{\partial}{\partial x_1} \iint_{S_0'} \frac{1}{r'} [\rho u_1' u_n' + \tau_{1n}' + p' \delta_{1n}] dS(y') \\
 & - \iint_{S_1} \frac{\hat{x}_n'}{r} \left[ \rho' \frac{\partial u_n'}{\partial t} \right] dS(\vec{y}') + \frac{\partial}{\partial x_1} \iint_{S_1'} \frac{\hat{x}_1'}{r} [p_a'(\vec{y}', t)] dS(\vec{y}') \quad (2.79)
 \end{aligned}$$

Equation (2.79) will be added to Equation (2.78). On the boundary and in the volume  $V_0 + V_0'$

$$\hat{\ell} = -\hat{\ell}' \quad u_n = -u'_n, \quad u_s = u'_s$$

$$p = p' \quad \frac{\partial}{\partial y_n} = -\frac{\partial}{\partial y'_n}$$

but

$$\ell_n u_n = \ell'_n u'_n$$

Thus, we have

$$\frac{\partial}{\partial x_i} \int_S [\rho u_i u_n + \tau'_{in}] \frac{dS(\vec{y})}{r} = \frac{\partial}{\partial x_i} \int_{S'} [\rho u'_i u'_n + (\tau'_{in})'] \frac{dS(\vec{y}')}{r}$$

when  $i \neq j$

and

$$\frac{\partial}{\partial x_n} \int_S [\rho u_n^2 + \tau'_{nn} + p] \frac{dS(\vec{y})}{r} = -\frac{\partial}{\partial x_n} \int_{S'} [\rho u_n'^2 + \tau'_{nn}' + p] \frac{dS(\vec{y}')}{r'}$$

then

$$\begin{aligned} 4\pi p_a(\vec{x}, t) &= \frac{\partial^2}{\partial x_i \partial x_j} \iiint_{V_o + V'_o} \frac{[T_{ij}]}{r} dV_o(\vec{y}) \\ &- \iint_{S_o} \frac{2}{r} \left[ \rho \frac{\partial u_n}{\partial t} \right] dS(\vec{y}) - \iint_{S_1} \frac{2}{r} \left[ \rho \frac{\partial u_n}{\partial t} \right] dS(\vec{y}) \\ &+ \frac{\partial}{\partial x_s} \iint_{S_o} \frac{2}{r} [\rho u_s u_n + \tau'_{sn}] dS(\vec{y}) \end{aligned} \quad (2.80)$$

When the surface  $S_1 + S_0$  is rigid and the fluid is assumed inviscid,  $\tau'_{sn} = 0$ , we have the simple result that

$$4\pi p_a(\vec{x}, t) = \frac{\partial^2}{\partial x_i \partial x_j} \iiint_{V_0 + V'_0} \frac{[T_{ij}]}{r} dV_0(\vec{y}) \quad (2.81)$$

which is the statement of Powell's<sup>19</sup> reflection theorem. This theorem states that:

"The pressure dipole distribution on a plane, infinite, and rigid surface accounts for the reflection in that surface of the volume distribution of acoustic quadrupole generators of a contiguous inviscid fluid flow, and for nothing more, when these distributions are determined in accordance with Lighthill's concept of aerodynamic noise generation and its natural extension."

Powell goes on to state that the result, Equations (2.80) and (2.81), are independent of the Mach number of the mean flow as well as the wavelength of the sound. The stress tensor itself accounts for all effects of refraction and scattering by fluid inhomogeneities. The above result emphasizes the confusion that could arise from the interpretation of Curle's result, Equation (2.73), as indicating that the presence of a surface contiguous to a turbulent region results in the generation of three physically distinct acoustic sources. This is patently not the case when the contiguous surface is large compared with an acoustic wavelength whether or not the surface may react to the stresses induced on it by the turbulence.

In these more general cases, Equation (2.80) isolates the importance of dipoles oriented in the plane of the surface whose strengths become doubled by the plane. Ffowcs-Williams<sup>20</sup> considered the more general case of a flow source region over nonrigid, plane, homogeneous boundaries. To consider the simple case of a very soft boundary, the difference between Equations (2.78) and (2.79) is taken which gives

$$\begin{aligned} 4\pi p_a(\vec{x}, t) = & \frac{\partial}{\partial x_i \partial x_j} \iiint_{V_0} \frac{[T_{ij}]}{r} dV_0(\vec{y}) - \frac{\partial}{\partial x_i \partial x_j} \iiint_{V'_0} \frac{[T_{ij}]}{r} dV_0(\vec{y}) \\ & + \frac{\partial}{\partial x_n} \iint_{S_0} \frac{2}{r} [\rho u_n^2 + \tau'_{nn} + p] dS(y) + \frac{\partial}{\partial x_n} \iint_{S_1} \frac{2}{r} [p] dS(\vec{y}) \end{aligned} \quad (2.82)$$

If the surface is limp enough so that no normal stresses may be maintained, then  $p = 0$  (i.e., it is pressure release) on  $S_0$ . The surface  $S_1$  Ffowcs-Williams takes far enough from the source region that it vanishes. The sound field then consists of the interference of the primary source field with its negative image except for the addition of the term involving the induced surface motion. This term Ffowcs-Williams speculates is second order. For more complicated boundaries whose impedances are intermediate between hard and soft, Ffowcs-Williams shows that the effect is still only to modify the sound field by adding to the primary wave field given by the integral over  $V_0$ , a reflected wave, given above by the integrals over  $V'_0$ . A reflection coefficient appropriate to the surface impedance causes a phase shift, but no resonances. Thus, the sound resulting from a turbulent flow over any plane homogeneous surface is essentially quadrupole or higher order with no alteration in the physical mechanism of the radiation, barring the possible contribution of shear stress dipoles. This has broad implications since what is required for enhancement of the sound field are inhomogeneities of surface impedance (scatterers) or inhomogeneities in the surface stresses. These implications will be discussed at greater length in Section 8.5.2. The benefit of Equation (2.82) over (2.80) for the case of pressure release boundaries lies in the removal of the unknown integral of  $u_n$  over the bounding surface.

Equations (2.81) and (2.82), in the latter with  $p = 0$ , for the completely rigid or completely soft surfaces, respectively, bring out an interesting aspect of imaging multipole sources. Consider the thickness of the stress layer in a direction normal to the surface to be much smaller than an acoustic wavelength. Then, using the idealizations for the lateral and longitudinal quadrupoles shown in Figure 2.3, it is easy to see that a rigid surface causes destructive interference of lateral quadrupoles (call the result an octupole!), but a doubling of the sound for longitudinal quadrupoles. The converse holds true for quadrupole sources near a soft boundary. Similarly, one can deduce alternate reinforcements for dipoles near either hard or soft surfaces. Therefore, in Equation (2.82), the volume integrals do not cancel.

## 2.5 POWELL'S THEORY OF VORTEX SOUND

### 2.5.1 General Implications

The formulation of a region of vortex motion as an acoustic source was a major step towards a physical understanding of turbulence induced noise. However, the

consideration of the acoustic sound pressure as a volume integral of the Reynolds stress sheds little light on the details of the mechanism. Lighthill's theory does not identify the characteristics of vortex dynamics that are noise producing. It seems that Lighthill was motivated toward a description of sound intensity in terms of the statistical characteristics of the turbulent source region. It was necessary to use representations which could be substituted by measured velocity correlations and length scales. Furthermore, the identification of the acoustic character of the source field as a distribution of quadrupoles and then the subsequent establishment of the effects of eddy convection on the acoustic pressure, were directed at an understanding of the observed acoustic aspects of jet noise.

Powell,<sup>21</sup> on the other hand, was apparently interested in the aerodynamic (hydrodynamic) aspects of the flow which caused the noise. The question involves an understanding of what characteristics of the eddy motion actually produce the noise. From this perspective Powell examined the connection between vortex motion and sound generation. The identification of the formation of vortices in the flow as the fundamental noise-producing mechanism is the result of this analysis.

### 2.5.2 Derivation of the Wave Equation with Vortical Sources

In our discussion we will first derive the source term in Powell's<sup>21</sup> form and then discuss its physical implications. As before, we consider the fluid motions to be isentropic. Powell makes use of the well-known vector identities:

$$\begin{aligned} \nabla \left( \frac{1}{2} u^2 \right) &= u_j \frac{\partial u_i}{\partial x_j} - \left[ \left( \frac{\partial u_k}{\partial x_i} - \frac{\partial u_i}{\partial x_k} \right) u_k - \left( \frac{\partial u_j}{\partial x_i} - \frac{\partial u_i}{\partial x_j} \right) u_j \right] \\ &= (\vec{u} \cdot \nabla) \vec{u} - (\nabla \times \vec{u}) \times \vec{u} = (\vec{u} \cdot \nabla) \vec{u} - \vec{\omega} \times \vec{u} \end{aligned} \quad (2.83)$$

and

$$\nabla^2 u_i - \frac{\partial}{\partial x_i} \left( \frac{\partial u_j}{\partial x_j} \right) = - \frac{\partial}{\partial x_j} \left( \frac{\partial u_j}{\partial x_i} - \frac{\partial u_i}{\partial x_j} \right) - \frac{\partial}{\partial x_k} \left( \frac{\partial u_k}{\partial x_i} - \frac{\partial u_i}{\partial x_k} \right) \quad (2.84)$$

or



$$\nabla^2 \vec{u} + \nabla(\nabla \cdot \vec{u}) = + \nabla \times (\nabla \times \vec{u})$$

The curl of the velocity,  $\nabla \times \vec{u}$ , is the vorticity vector  $\vec{\omega}$ . These relationships\* are used to transform the equations of continuity and momentum to

$$\frac{\partial \rho}{\partial t} + (\vec{u} \cdot \nabla) \rho + \rho \nabla \cdot \vec{u} = 0 \quad (2.85)$$

and

$$\rho \frac{\partial \vec{u}}{\partial t} + \rho (\vec{\omega} \times \vec{u}) + \nabla \left( \frac{1}{2} \rho u^2 \right) = -\nabla p \quad (2.86)$$

The combination of Equations (2.85) and (2.86) can be performed in the same manner as in Section 2.2 to obtain the wave equation for the density as

$$\frac{\partial^2 \rho}{\partial t^2} - c_o^2 \nabla^2 \rho = +\nabla \cdot \left\{ \rho (\vec{\omega} \times \vec{u}) - \vec{u} \frac{\partial \rho}{\partial t} + \nabla \left( p + \rho \frac{u^2}{2} \right) - \left( c_o^2 + \frac{u^2}{2} \right) \nabla \rho \right\} \quad (2.87)$$

This equation is an analog to Lighthill's equation where the divergence term is identical to Lighthill's source term. The equation is exact except for the neglect of the Stokes' stress tensor  $\tau'_{ij}$ , but the above representation exposes the influence of changes in vorticity on the radiated density fluctuations. The term  $\vec{\omega} \times \vec{u}$  incorporates the sound due to the stretching of vortex filaments by an imposed velocity  $\vec{u}$ . The term  $\vec{u} \cdot \partial \rho / \partial t$  is a contribution caused by local convection of density disturbances and it is generally second order since  $|\vec{u}| \ll c_o$ . The term  $\nabla(p + \rho u^2/2)$  includes both the hydrodynamic as well as the acoustic pressure. Inside the source region if the flow is perfectly irrotational, i.e.,  $\vec{\omega} = 0$  everywhere, the Bernoulli equation for the hydrodynamic pressure is

---

\*Both the vector and the tensor notations have been shown in order to effect for the reader an easy transition from one notation to the other. In the following we shall make liberal use of vector notation in order to compress expressions dealing with the curl operation.

$$\frac{p}{\rho} + \frac{u^2}{2} + \frac{\partial \phi_h}{\partial t} = \text{constant} \quad (2.88)$$

where  $\phi_h$  is the fluid potential. Thus,

$$\nabla \left( \frac{p}{\rho} + \frac{u^2}{2} \right) = - \frac{\partial}{\partial t} \nabla \phi_h$$

and, since  $\nabla^2 \phi_h = 0$  only for irrotational flow, this term may be legitimately neglected only when  $\vec{\omega} = 0$ . Regarding the acoustic pressure, we note that when  $c_0^2 \gg u^2/2$  (as is found in most situations involving flow of low Mach number) the acoustic pressure exactly balances  $c_0^2 \rho$ . Therefore, Equation (2.87) can be now written to include only the first-order terms;

$$\nabla^2 p_a - \frac{1}{c_0^2} \frac{\partial^2 p_a}{\partial t^2} = -\nabla \cdot \left\{ \rho (\vec{\omega} \times \vec{u}) + \nabla \left( p - c_0^2 \rho + \rho \frac{u^2}{2} \right) \right\} \quad (2.89)$$

to give the wave equation for the acoustic pressure. Equation (2.89) should be compared to Equation (2.49). This equation is essentially that which was derived by Powell and, in terms of exactness, it departs from Lighthill's in the neglect of the viscous stresses,  $\tau'_{ij}$ , and of terms for which  $u \ll c_0$ .

### 2.5.3 The Physical Significance of the Vorticity Source

In order to appreciate the importance of the vorticity as a source of radiation, Powell considered the generation of fluid disturbances by the motion of an isolated ring. An equivalence is sought between changes in vorticity and changes in fluid momentum which can be interpreted as dipole and quadrupole acoustic sources.

The well-known relationship for the incompressible fluid velocity  $\vec{u}(\vec{x})$  generated by a vortex filament is

$$\vec{u}(\vec{x}) = -\frac{1}{4\pi} \oint \Gamma \frac{\vec{r} \times d\vec{\ell}(\vec{y})}{r^2} = -\frac{1}{4\pi} \oint \nabla_y \left( \frac{\Gamma}{r} \right) \times d\vec{\ell}(\vec{y}) \quad (2.90)$$

As shown in Figure 2.7 the vector from the source point to the field point is  $\vec{r} = \vec{x} - \vec{y}$ ;  $d\vec{\ell}(\vec{y})$  is an increment of the vortex filament of vorticity (note that  $\vec{\omega} \times d\vec{\ell} \equiv 0$ ). By definition the circulation is

$$\Gamma = \oint_{C'} \vec{u} \cdot d\vec{C}' \quad (2.91)$$

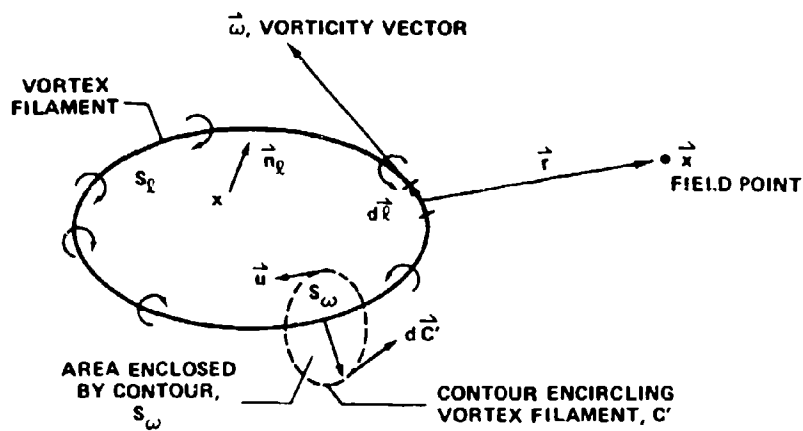


Figure 2.7 - Application of Stokes' Theorem

where  $C'$  is a closed circuit in the fluid. As long as  $C'$  encircles a vortex filament, as shown in Figure 2.7, the circulation is nonzero. Otherwise, it is identically zero. Stokes' theorem states that

$$\Gamma = \oint_{C'} \vec{u} \cdot d\vec{C}' \quad (2.92)$$

$$= \iint_{S_\omega} \vec{n}_\omega \cdot (\nabla \times \vec{u}) dS \quad (2.93)$$

$$= \iint_{S_\omega} \vec{n}_\omega \cdot \vec{\omega} dS = \int_{S_\omega} |\vec{\omega}| dS_\omega \quad (2.94)$$

where  $dS_\omega$  = an element in the surface enclosed by the circuit  $C'$

$\vec{n}_\omega$  = the component of the normal vector to this surface in the direction of  $d\vec{\ell}$  (or of  $\vec{\omega}$ )

$S_\omega$  = a component of  $S$  projected in the plane that is perpendicular to the vorticity vector  $\vec{\omega}$

We will assume that  $\Gamma$  is constant along the vortex filament  $\vec{\ell}$ . Also, by Stokes' theorem we have

$$\begin{aligned} \vec{u}(\vec{x}) &= \frac{1}{4\pi} \oint d\vec{\ell}(\vec{y}) \times \nabla_y \left( \frac{\Gamma}{r} \right) = \frac{1}{4\pi} \iint_{S_\omega} (\vec{n}_\ell \times \nabla_y) \times \nabla_y \left( \frac{\Gamma}{r} \right) dS(\vec{y}) \\ &= \frac{-1}{4\pi} \iint_{S_\ell} (\nabla_y \times \vec{n}_\ell) \times \nabla_y \left( \frac{\Gamma}{r} \right) dS(y) \end{aligned} \quad (2.95)$$

where  $S_\ell$  is circumscribed by the vortex filament and  $\vec{n}_\ell$  is the normal to the surface, see Figure 2.8. Since

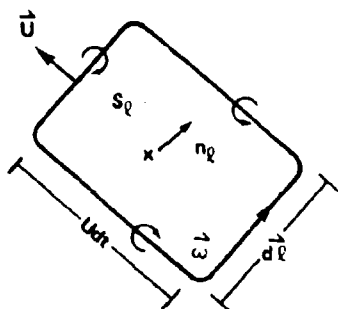


Figure 2.8a - Ideal Vortex Filament Stretching

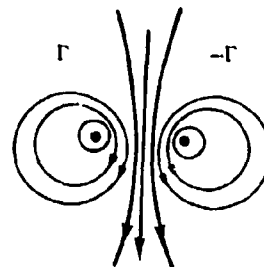


Figure 2.8b - Cross Section of Vortex Pair with Streamlines

Figure 2.8 - Geometry of Vortex Filament

$$(\vec{n}_\ell \times \vec{\nabla}_y) \times \vec{\nabla}_y \left( \frac{\Gamma}{r} \right) = \vec{\nabla}_y \cdot \vec{n}_\ell \cdot \vec{\nabla}_y \left( \frac{\Gamma}{r} \right) - \vec{n}_\ell \cdot \nabla^2 \left( \frac{\Gamma}{r} \right) = \vec{\nabla}_y \cdot \vec{n}_\ell \cdot \vec{\nabla}_y \left( \frac{\Gamma}{r} \right)$$

Equation (2.95) becomes

$$\vec{u}(\vec{x}) = \frac{1}{4\pi} \iint_{S_\ell} \vec{\nabla}_y \cdot \vec{n}_\ell \cdot \vec{\nabla}_y \left( \frac{\Gamma}{r} \right) dS(\vec{y}) = \frac{-1}{4\pi} \vec{\nabla}_x \cdot \iint_{S_\ell} \vec{n}_\ell \cdot \vec{\nabla}_x \left( \frac{\Gamma}{r} \right) dS(\vec{y}) \quad (2.96)$$

If the distance to the observation point is large compared to the dimension of the vortex ring, Equation (2.96) becomes

$$\vec{u}(\vec{x}) = \vec{\nabla}_x \cdot \left\{ \frac{1}{4\pi} [\vec{n}_\ell] \cdot \vec{\nabla}_x \left( \frac{\Gamma S_\ell}{r} \right) \right\} \quad (2.97)$$

where  $\Gamma S_\ell$  is the strength of the vortex and  $\vec{n}_\ell$  is the average normal to the surface of area  $S_\ell$ . Equation (2.97) is now of the form of a potential gradient,  $\vec{u} = \vec{\nabla}_x(\phi)$ , and so we recognize the term in brackets to be the far field potential due to a concentrated vortex filament.

The important step in the analysis was Powell's recognition that the analog of Equation (2.97) for a slightly compressible flow is

$$\vec{u}(\vec{x}, t) = \nabla_{\vec{x}} \cdot \left\{ \frac{1}{4\pi} \nabla_{\vec{x}} \cdot \frac{[\vec{n}_{\ell} \Gamma S_{\ell}]}{r} \right\} \quad (2.98)$$

where the term in brackets [ ] is now evaluated at the retarded time  $t - r/c_o$ . Equation (2.98) holds as long as the wavelength of sound is much larger than the vortex ring and it implies that the vortex streamlines in the slightly compressible flow are the same as if the fluid were incompressible. This is an important notion since it states that the flow field is established hydrodynamically and the sound is a by product of the hydrodynamic motion.

The pressure disturbance in the far field is found by carrying out the indicated operations, and noting that  $p_a = \rho_o c_o u$

$$p_a(\vec{x}, t) = \frac{\rho_o}{4\pi c_o} \frac{\vec{r}}{r^3} \cdot \left[ \frac{\partial^2 \vec{n}_{\ell} \Gamma S_{\ell}}{\partial t^2} \right] \quad (2.99)$$

The far field velocity is proportional to the time differential of the rate of change of the vortex strength. Also, since the fluid momentum  $\vec{M}$  associated with the vortex ring is

$$\vec{M} = \rho_o \Gamma \vec{n}_{\ell} S_{\ell}$$

the velocity perturbation is also seen to be proportional to the time derivative of the rate of change of fluid momentum in the direction of observation. The force applied to the fluid by the motion of the vortex ring is related to the rate of change of momentum by

$$\vec{F} = \frac{\partial \vec{M}}{\partial t}$$

Thus, Equation (2.99) can be rewritten as

$$p_a(\vec{x}, t) = \frac{1}{4\pi c_o} \left[ \frac{\vec{r}}{r^2} \cdot \frac{\partial \vec{F}}{\partial t} \right] \quad (2.100)$$

which is the same as Equation (2.77). The radiated velocity is determined by the rate of change of the force applied to the fluid by the vortex motion. This relationship will be considered extensively in Chapter 5; it is the fundamental relationship for dipole sound radiation.

If the area of the vortex ring  $S_\ell$  remains constant, the strength changes with the circulation so that the velocity perturbation is given by

$$\vec{u}(\vec{x}, t) = \frac{\vec{r}}{4\pi c_o^2} \frac{\vec{n}_\ell \cdot \vec{r} S_\ell}{r^3} \left[ \frac{\partial^2 \Gamma}{\partial t^2} \right]$$

In the alternative instance of a constant circulation  $\Gamma$  yet changing area  $S_\ell$  the velocity perturbation is proportional to  $\partial^2 S_\ell / \partial t^2$ . This change can arise from vortex-line stretching by flow as depicted in Figure 2.8. The vortex line stretches due to translation at velocity  $\vec{U}$  so that the change in the enclosed vector area  $\vec{n}_\ell \delta S_\ell$  in the time interval  $\delta t$  is  $\vec{n}_\ell \delta S_\ell = (\vec{U} \delta t) \times d\vec{\ell}$ . Thus, the Equation (2.99) becomes

$$\vec{u}(\vec{x}, t) = \frac{\vec{r}}{4\pi c_o^2} \frac{\vec{r}}{r^3} \cdot \left[ \frac{\partial}{\partial t} \oint \Gamma \vec{U} \times d\vec{\ell} \right]$$

If we consider the vortex lines to exist throughout the region of flow and introduce Equation (2.94) we find

$$\begin{aligned} \vec{u}(\vec{x}, t) &= \frac{\vec{r}}{4\pi c_o^2} \frac{\vec{r}}{r^3} \cdot \left[ \frac{\partial}{\partial t} \oint \iint (\vec{n}_\omega \cdot \omega dS_\omega) \vec{u} \times d\vec{\ell} \right] \\ &= \frac{-\vec{r}}{4\pi c_o^2} \frac{\vec{r}}{r^3} \cdot \left[ \frac{\partial}{\partial t} \iiint_V (\vec{\omega} \times \vec{u}) dv \right] \end{aligned} \quad (2.101)$$

since  $(\vec{n}_\omega \cdot \vec{\omega} dS_\omega) \vec{U} \times d\vec{\ell} = (\vec{U} \times \vec{\omega}) \cdot \vec{n}_\omega \cdot d\vec{\ell} dS_\omega$  and because the  $d\vec{\ell}$  and  $\vec{\omega}$  vectors are coincident. This shows that the velocity perturbation is proportional to the change in the rate of vortex stretching by the fluid. The intensity is maximum in the plane normal to the vector  $\vec{\omega} \times \vec{U}$ , i.e., normal to the surface enclosed by the vortex ring of vorticity  $\vec{\omega}$ . Powell gives the term "vortex sound" to the far field sound radiation from a finite region of vorticity since it emanates from changes in the net vortex strength of the region.

The integrand in Equation (2.101) is also recognized as the first of the source terms of Equations (2.87) and (2.89). This equivalence complements the interpretation, given at the end of Section 2.4.1, of the source term so that we now have a complete physical explanation. The sound radiation from a localized region of turbulent unsteadiness is caused by the stretching of vortex lines and the rate of change of fluid potential associated with the dynamics of the region.

An important physical example of the generation of vortex sound is the Aeolian tone radiated from a circular cylinder in a cross flow. In this situation diagrammed in Figure 2.9 (dealt with in detail in Chapter 5) fluid flows steadily past a cylinder so that the direction of fluid motion is perpendicular to the axis of the

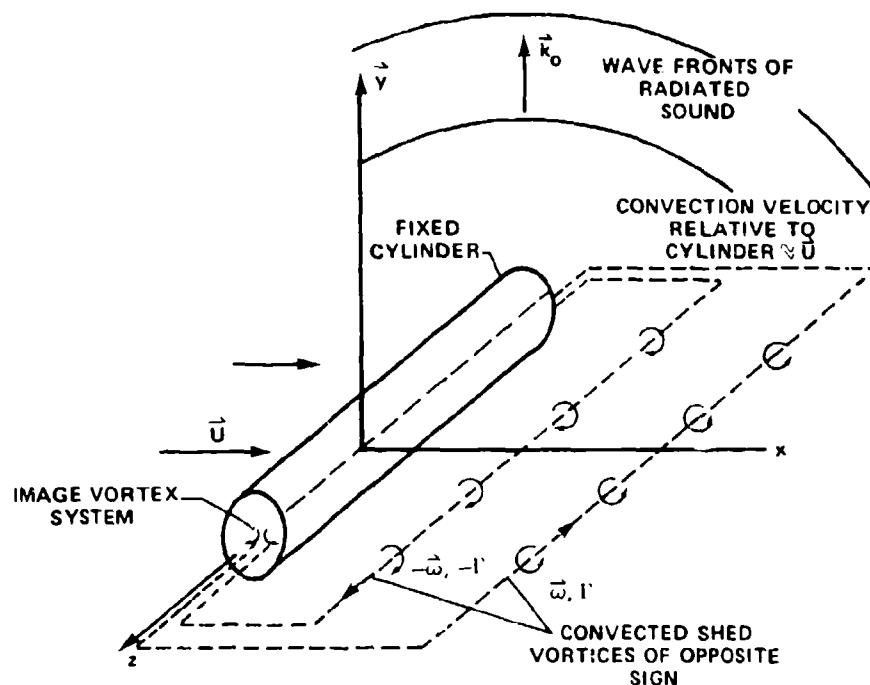


Figure 2.9 - Diagram of Cylinder and its Vortex Systems in a Cross-Wind



cylinder. Vortices are shed downstream of the cylinder with alternately varying changes in sign. Since the circulation of an element of the fluid incident on the cylinder is zero, the net circulation in the flow-cylinder system must remain zero downstream of the cylinder. This requires that for every vortex formed in the fluid an image vortex must be formed in the cylinder. The resulting vortex pair is composed of two legs of a closed ring as shown in Figures 2.9 and 2.8b. In this manner we can see that the periodic formation of vortex pairs, one bound to the cylinder and the other formed in the wake and convected downstream, results in a similarly periodic change in vortex strength and, therefore, sound radiated in a direction normal to the plane of the vortex ring. This direction is also the perpendicular to the plane formed by the flow vector and the axis of the cylinder. The magnitude of the sound in this direction is proportional to the circulation ( $\Gamma$ ) of the vortices formed and to the square of the reciprocal of the temporal period of the vortex formation. Another derivation of Equation (2.100) which pertains specifically to this problem, will be discussed in Chapter 5.

#### 2.5.4 The Effect of Solid Boundaries

We now turn our attention to the integral form of the wave equation analogous to Equations (2.71) and (2.78), yet incorporating Powell's source term. Combining Equations (2.67) and (2.89) we obtain the acoustic pressure as

$$4\pi p_a(\vec{x}, t) = \iiint_V \frac{\partial}{\partial y_1} [\rho(\vec{\omega} \times \vec{u})_1] \frac{dV(\vec{y})}{r} + \iiint_V \frac{\partial^2}{\partial y_1^2} \left[ p - \rho c_o^2 + \frac{1}{2} \rho u^2 \right] \frac{dV(\vec{y})}{r} \\ + \iint_{\Sigma} \left\{ \frac{1}{c_o r} \frac{\partial r}{\partial n} \left[ \frac{\partial \rho c_o^2}{\partial t} \right] - \frac{\partial \left( \frac{1}{r} \right)}{\partial n} [\rho c_o^2] + \frac{1}{r} \left[ \frac{\partial \rho c_o^2}{\partial n} \right] \right\} dS(\vec{y}) \quad (2.102)$$

where  $\Sigma$  is the total surface enclosing both the source volume and the observation point as in Figure 2.4a. Noting that  $\partial r / \partial n = \partial r / \partial y_n = -\partial r / \partial x_n$ , using the divergence theorem as in the beginning of Section 2.3.3 and in Equation (2.68), and using Equation (2.86), it is a simple matter to write down the acoustic pressure as

$$\begin{aligned}
4\pi p_a(\vec{x}, t) = & \frac{\partial}{\partial x_1} \iiint_V \frac{[\rho(\vec{\omega} \times \vec{u})_1]}{r} dV(\vec{y}) + \frac{1}{c_o^2} \frac{\partial^2}{\partial t^2} \iiint_V \left[ p - \rho c_o^2 + \frac{1}{2} \rho u^2 \right] \frac{dV(\vec{y})}{r} \\
& + \frac{\partial}{\partial x_n} \iint_{\Sigma} \left[ p + \frac{1}{2} \rho u^2 \right] \frac{dS(\vec{y})}{r} - \iint_{\Sigma} \left[ \rho \frac{\partial u_n}{\partial t} \right] \frac{dS(\vec{y})}{r} \quad (2.103)
\end{aligned}$$

The surface  $\Sigma$  may be interpreted to pertain to specific applications, e.g., as shown in Figure 2.5. As Powell<sup>21</sup> explains, Equation (2.103) gives the acoustic pressure as the sum of four contributions:

1. A volume distribution of dipoles proportional to  $\vec{\omega} \times \vec{u}$ .
2. A volume distribution of nondirectional sources  $\frac{\partial^2}{\partial t^2} \left( p - \rho c_o^2 + \frac{1}{2} \rho u^2 \right)$ .
3. A surface distribution of dipoles whose strength is proportional to the Bernoulli pressure on the surface,  $p + 1/2 \rho u^2$ .
4. A monopole distribution whose strength is proportional to the acceleration of the surface normal to itself,  $\partial u_n / \partial t$ .

Furthermore, the surface-integral terms are equivalent to those in Equations (2.71) and (2.78) (note being taken of the inviscid nature of the current problem), while the volume distribution has been reexpressed. The second volume integral involves quantities of order  $(u/c_o)^2$  and  $p(\rho c_o^2)^{-1}$  which can be safely ignored in favor of the other terms for low Mach number flows. The pertinent nature of the Reynolds stress distribution as involving a change in vortex strength is thus exposed.

## 2.6 REPRESENTATIONS IN THE FREQUENCY DOMAIN

When the integral relationships of this chapter are used for the solution of specific physical problems it is often convenient to invoke various types of harmonic analyses. In this text the Fourier transform, applied for both time and space variables, will be used almost exclusive of other transforms when harmonic analysis is necessary. We have already used a simplified form of Fourier analysis when we specified time dependence to be of the form  $e^{-i\omega t}$  in sections 2.1.2, 2.2, and 2.4.2.

### 2.6.1 Helmholtz Integral Equation

We begin by deriving analogous forms of Equations (2.53) and (2.67) using the time Fourier transform. The Fourier transform  $V(\omega)$  of a variable  $v(t)$  is

$$V(\omega) = \frac{1}{2\pi} \int_{-\infty}^{\infty} e^{+i\omega t} v(t) dt \quad (2.104)$$

and its inverse is

$$v(t) = \int_{-\infty}^{\infty} e^{-i\omega t} V(\omega) d\omega \quad (2.105)$$

Thus, since  $p_a(\vec{x}, t) = c_0^2 \rho_a(\vec{x}, t)$ , then the transform of the inhomogeneous wave equation, Equation (2.53), is called the inhomogeneous reduced wave equation

$$\nabla^2 p_a(\vec{y}, \omega) + k_0^2 p_a(\vec{y}, \omega) = -\tilde{\sigma}(\vec{y}, \omega) \quad (2.106)$$

where  $k_0 = \omega/c_0$  is the magnitude of the acoustic wave number and  $\tilde{\sigma}(\vec{y}, \omega)$  is the Fourier transform of  $\sigma(\vec{y}, t)$ . The solutions of the homogeneous wave equation are of the form

$$p_a(\vec{y}, \omega) = A \frac{e^{\pm i k_0 r}}{r} \quad (2.107)$$

which are appropriate for propagating waves in free space. In fact, the function

$$g(r) = \frac{e^{\pm i k_0 r}}{4\pi r} \quad (2.108)$$

is called the "Free-Space Green Function." The selection of  $+i$  and  $-i$  depends on the invoking of the radiation or absorption condition of propagating waves (Section 2.2). For outward travelling waves, we select  $-i$ . Now, the retarded potential is given by

$$v\left(t - \frac{r}{c_0}\right) = \int_{-\infty}^{\infty} e^{-i\omega t} e^{+ik_0 r} V(\omega) d\omega \quad (2.109)$$

Substituting inverse Fourier transform, Equation (2.109), into Equation (2.67) gives:

$$p_a(\vec{x}, \omega) = \iiint_{V_0} \frac{\partial^2 \tilde{T}_{1j}(\vec{y}, \omega)}{\partial y_1 \partial y_j} \frac{e^{+ik_0 r}}{4\pi r} dv(\vec{y}) \\ + \iint_{\Sigma} \left\{ \frac{e^{+ik_0 r}}{4\pi r} \frac{\partial p_a(\vec{y}, \omega)}{\partial n} - p_a(\vec{y}, \omega) \frac{\partial}{\partial n} \left( \frac{e^{+ik_0 r}}{4\pi r} \right) \right\} dS(\vec{y}) \quad (2.110)$$

Here we have let  $\tilde{T}_{1j}(\vec{y}, \omega)$  be the Fourier transform of  $T_{1j}(\vec{y}, t)$ , using the tilda and the changed independent variable to denote the transform. Equation (2.110) is the Helmholtz integral equation. It could have been derived<sup>4,5</sup> from Equation (2.106) by using the divergence theorem and the equation

$$\nabla_{\vec{y}}^2 g(|\vec{x} - \vec{y}|, \omega) + k_0^2 g(|\vec{x} - \vec{y}|, \omega) = -\delta(\vec{x} - \vec{y}) \quad (2.111)$$

for the free-space Green function when  $\nabla_{\vec{y}}^2$  denotes the Laplacian operation with respect to the variable  $\vec{y}$  only.

We see, regarding Equation (2.110) and Figure 2.4, that if  $\Sigma$  is a control surface a distance  $R$  from a compact source region of volume  $V_0$ , then

$$p_a(\vec{x}, \omega) = \iiint_{V_0} \frac{\partial^2 T_{1j}(\vec{y}, \omega)}{\partial y_1 \partial y_j} \frac{e^{+ik_0 r}}{4\pi r} dV(\vec{y}) \quad (2.112)$$

if

$$\lim_{R \rightarrow \infty} \left( +ik_0 R p_a(R, \omega) + R \frac{\partial p_a(R, \omega)}{\partial r} \right) = 0$$

Recall that this last condition is just Sommerfeld's radiation condition (Section 2.2). Equation (2.112) is the equivalent to Equation (2.57), but in the frequency domain.

A more general use of the Helmholtz integral equation lies in situations for which impedance boundaries or surfaces are present in the control volume. In these situations the free-space Green function in Equation (2.108) is replaced by  $G(\vec{x}, \vec{y}, \omega)$  which is a solution of

$$\nabla_{\vec{y}}^2 G(\vec{x}, \vec{y}, \omega) + k_0^2 G(\vec{x}, \vec{y}, \omega) = \delta(\vec{x} - \vec{y}) \quad (2.113)$$

In contrast to the free-space Green function, the function  $G(\vec{x}, \vec{y}, \omega)$  is determined for the geometry under consideration and subject to certain boundary conditions. The Helmholtz integral equation is

$$p_a(\vec{x}, \omega) = \iiint_{V_0} \frac{\partial^2 T_{1j}(\vec{y}, \omega)}{\partial y_1 \partial y_j} G(\vec{x}, \vec{y}, \omega) dV(\vec{y}) \\ + \iint_S \left\{ G(\vec{x}, \vec{y}, \omega) \frac{\partial p_a(\vec{y}, \omega)}{\partial n} - p_a(\vec{y}, \omega) \frac{\partial G(\vec{x}, \vec{y}, \omega)}{\partial n} \right\} dS(\vec{y}) \quad (2.114)$$

where  $S$  is the surface of the boundary that is present, e.g.,  $S_1 + S_0$  in Figure 2.5. The radiation condition has been invoked to eliminate the integral over the control surface,  $S_2$ . Now, if  $p_a(\vec{y}, \omega)$  is known on the surface, then the imposition of the boundary condition  $G(\vec{x}, \vec{y}, \omega) = 0$  on  $S$  will put Equation (2.114) into a form involving known functions. This boundary condition<sup>4</sup> is known as the Dirichlet boundary condition. Alternatively, if the normal gradient  $\partial p_a(\vec{y}, \omega) / \partial n$  is known on  $S$  then the boundary condition  $\partial G(\vec{x}, \vec{y}, \omega) / \partial n = 0$  on  $S$ , known<sup>4</sup> as the Newmann boundary condition, puts Equation (2.114) into a form which may be evaluated. The potency of the method is especially apparent if we consider the case of the rigid boundary. In this type problem the velocity normal to the surface  $u_n$  is zero. Thus,  $\partial p_a(\vec{y}, \omega) / \partial n = 0$  so that the imposition of a Newmann boundary condition reduces Equation (2.114) to the form

$$p_a(\vec{x}, \omega) = \iiint_{V_0} \frac{\partial^2 \hat{T}_{ij}(\vec{y}, \omega)}{\partial y_i \partial y_j} G(\vec{x}, \vec{y}, \omega) dV(\vec{y}) \quad (2.115)$$

The Green function  $G(\vec{x}, \vec{y}, \omega)$  now accounts for both the impedance and the geometry of the boundary.

The method was used to solve problems on aerodynamic noise by Ffowcs-Williams and Hall<sup>22</sup> to determine the sound field from turbulence convected past a half plane. Some other aerodynamic noise problems have been attacked in this manner by Howe,<sup>23</sup> Chase,<sup>24,25</sup> Davies and Ffowcs-Williams,<sup>26</sup> and Crighton and Ffowcs-Williams,<sup>27</sup> see Chapter 9.

A simplified example of the use of the Green function for the Newmann boundary condition can be shown for the case of the plane boundary. A solution of Equation (2.113) which is valid for the rigid plane boundary is given by

$$G(\vec{x}, \vec{y}, \omega) = e^{\frac{+ik_0 r_1}{4\pi r_1}} + e^{\frac{+ik_0 r_2}{4\pi r_2}} \quad (2.116)$$

where  $r_1^2 = (x_1 - x_2)^2 + (y_1 - y_2)^2 + (z_1 - z_2)^2$  and  $r_2^2 = (x_1 - x_2)^2 + (y_1 - y_2)^2 + (z_1 + z_2)^2$ . The ranges  $r_1, r_2$  are the same as those shown for the primary and image source

system in Figure 2.2c and they correspond to the  $\vec{r}, \vec{r}'$  in Figure 2.6. The field point is  $\vec{x} = (x_1, y_1, z_1)$  and the source point is  $\vec{y} = (x_2, y_2, z_2)$ . Also it can be easily shown that on the surface  $z_2 = 0$

$$\left. \frac{\partial G(\vec{x}, \vec{y}, \omega)}{\partial z_2} \right|_{z_2=0} = \left. \frac{\partial G(\vec{x}, \vec{y}, \omega)}{\partial z_2} \right|_{z_2=0} = 0$$

and for  $k_0 z_2 \ll 1$ , Equation (2.116) reduces to the functional form of Equation (2.36). Substitution of Equation (2.116) into Equation (2.115) yields

$$p_a(\vec{x}, \omega) = \iiint_{V_{o_1} + V_{o_2}} \frac{\partial^2 T_{ij}(\vec{y}, \omega)}{\partial y_i \partial y_j} \frac{e^{-ik_0 |\vec{x}-\vec{y}|}}{4\pi |\vec{x}-\vec{y}|} dV(\vec{y}) \quad (2.117)$$

where integration now extends over both the physical source distribution and its image distribution. The mechanics of such an integration would have to account for the symmetric and nonsymmetric reflections of the  $T_{ij}$  about  $y_2 = 0$ , as discussed in Section 2.4.4. Equation (2.117) is identical to Equation (2.81).

Other known functions  $G(\vec{x}, \vec{y}, \omega)$  for a wide variety of geometries have been given in books by Morse and Feshbach,<sup>28</sup> by Morse and Ingard,<sup>4</sup> and Junger and Feit.<sup>5</sup> Generally simple closed-form functions exist for circular cylinders, spheres, infinite planes. Analytically more complicated functions also exist for slits, half planes, and spheroidal bodies.

## 2.6.2 Generalized Transforms and Stochastic Variables

In Section 2.3.3 we utilized the correlation function of the stress tensor to determine the time averaged acoustic intensity, Equation (2.61), far from a turbulent region. The introduction of the correlation function was necessary because the temporal and spatial variations of the velocity fluctuations are uncertain, yet occurring within certain limits of probability. For example, the velocity at any instant and location can be given by

$$u_1'(\vec{x}, t) = U(\vec{x}) + u_1(\vec{x}, t)$$

where  $U$  is the time averaged velocity and  $u_1$  is the stochastic velocity fluctuation with zero mean value, i.e.,

$$\overline{u_1(\vec{x}, t)} = \lim_{T \rightarrow \infty} \frac{1}{T} \int_{-T/2}^{T/2} u_1(\vec{x}, t) dt = \lim_{V \rightarrow \infty} \frac{1}{V} \iiint_V u_1(\vec{x}, t) d\vec{x} \equiv 0 \quad (2.118)$$

where  $T$  is the time of averaging and  $V$  is the volume over which the velocity is instantaneously sampled. Fluid fields for which the equivalency of Equation (2.118) holds are said to be homogeneous. The time mean square velocity fluctuation is

$$\begin{aligned} \overline{u_1'^2(\vec{x}, t)} &= \overline{(\bar{U}(\vec{x}) + u_1(\vec{x}, t))^2} \\ &= \lim_{T \rightarrow \infty} \frac{1}{T} \int_{-T/2}^{T/2} (\bar{U}(\vec{x}) + u_1(\vec{x}, t))^2 dt \\ &= \bar{U}^2 + \overline{u_1^2(\vec{x}, t)} \end{aligned} \quad (2.119)$$

If the fluid region is truly homogeneous, then

$$\overline{u_1'^2(\vec{x}, t)} = \overline{u_1'^2(\vec{x}, t)}_{\vec{x}} = \overline{u_1'^2}$$

also, note that the average over space of the fluctuating velocity at any instant in time will also be zero in the homogeneous turbulent field. Notice now that we have introduced the vincula  $\overline{\quad}_t$  and  $\overline{\quad}_{\vec{x}}$  to distinguish between time and space averaging, respectively.



We now consider some general representations of the turbulent field and its resulting sound. More extensive analyses will be given in Chapter 3. Equation (2.118) constitutes a boundedness on the integral of  $u_1(\vec{x}, t)$  and it permits a definition of a generalized Fourier transform<sup>29,30</sup> which we will write as

$$\tilde{u}_1(\vec{x}, \omega) = \frac{1}{2\pi} \int_{-\infty}^{\infty} e^{+i\omega t} u_1(\vec{x}, t) dt \quad (2.120a)$$

and

$$u_1(\vec{x}, t) = \int_{-\infty}^{\infty} e^{-i\omega t} \tilde{u}_1(\vec{x}, \omega) d\omega \quad (2.120b)$$

The space-time covariance of the velocity fluctuations is given by (see also Batchelor,<sup>30</sup> Lin,<sup>31</sup> and Kinsman<sup>32</sup>)

$$\begin{aligned} & \overline{[u_1^2(\vec{y}, t) u_1^2(\vec{x}, t)]^{1/2}} R_{u_1 u_1}(\vec{y}, \vec{x}, \tau) \\ &= \lim_{T \rightarrow \infty} \frac{1}{2T} \int_{-T}^T u_1(\vec{x}, t) u(\vec{y}, t+\tau) dt \\ &= \lim_{T \rightarrow \infty} \frac{1}{2T} \int_{-T}^T dt \int_{-\infty}^{\infty} e^{+i\omega t} \tilde{u}_1^*(\vec{x}, \omega') d\omega' \int_{-\infty}^{\infty} e^{-i\omega(t+\tau)} \tilde{u}_1(\vec{y}, \omega) d\omega \quad (2.121) \end{aligned}$$

where  $R_{u_1 u_1}(\vec{x}, \vec{x}, 0) = R_{u_1 u_1}(\vec{y}, \vec{y}, 0) = 1 > R_{u_1 u_1}(\vec{x}, \vec{y}, 0) > R_{u_1 u_1}(\vec{x}, \vec{y}, \tau)$ . We have replaced the physical velocity fluctuation by inverse transform of  $\tilde{u}_1(\vec{x}, \omega)$  using Equation (2.120b).

The complicated integral can be cleared up by examining the behavior of

$$\frac{1}{T} \int_{-T/2}^{T/2} e^{i(\omega-\omega')t} dt = \frac{1}{T} \frac{e^{i(\omega-\omega')T/2} - e^{-i(\omega-\omega')T/2}}{2i(\omega-\omega')} = \frac{\sin(\omega-\omega') \frac{T}{2}}{\frac{T}{2} (\omega-\omega')}$$

As  $T$  increases, this function becomes more and more peaked near  $\omega = \omega'$  so that if their integrals over all frequency are to be equal we can write

$$\lim_{T \rightarrow \infty} \frac{\sin(\omega-\omega') \frac{T}{2}}{(\omega-\omega') \frac{T}{2}} = \frac{2\pi}{T} \delta(\omega-\omega') \quad (2.122)$$

The equivalence

$$\delta(\omega-\omega') = \frac{1}{2\pi} \int_{-\infty}^{\infty} e^{+i(\omega-\omega')t} dt \quad (2.123)$$

where  $\delta(0) = 1$  and  $\delta(\Omega \neq 0) = 0$  is the delta function. Formally, it has the integral definition

$$f(\Omega_0) = \int_{-\infty}^{\infty} f(\Omega) \delta(\Omega - \Omega_0) d\Omega$$

This relationship can also be established by virtue of the definition of the Fourier transform and its inverse.

This equivalence converts Equation (2.121) to the form

$$\begin{aligned} & \overline{u_1^2(\vec{x}, t)} \overline{u_1^2(\vec{y}, t)} R_{u_1 u_1}(\vec{y}, \vec{x}, \tau) \\ &= 2\pi \int_{-\infty}^{\infty} \int_{-\infty}^{\infty} \frac{\delta(\omega-\omega')}{T} e^{-i\omega\tau} \tilde{u}_1^*(\vec{x}, \omega') \tilde{u}_1(\vec{y}, \omega) d\omega d\omega' \\ &= \int_{-\infty}^{\infty} e^{-i\omega\tau} \left\{ \frac{2\pi}{T} \tilde{u}_1^*(\vec{x}, \omega) \tilde{u}_1(\vec{y}, \omega) \right\} d\omega \end{aligned}$$

This defines<sup>30-33</sup> the covariance function as an inverse Fourier transform of a function which we will call the two-point cross spectral density of the velocity fluctuation. We will write this function as

$$\left\{ \frac{2\pi}{T} \tilde{u}_1^*(\vec{x}, \omega) \tilde{u}_1(\vec{y}, \omega) \right\} = \overline{u_1^2(\vec{x}, t)} \overline{u_1^2(\vec{y}, t)} \phi_{u_1 u_1}(\vec{y}, \vec{x}, \omega) \quad (2.124a)$$

in the limit as  $T \rightarrow \infty$ , so that the space-time covariance  $R(\vec{y}, \vec{x}, \tau)$  and the two-point cross spectral density are Fourier transform pairs:

$$R(\vec{y}, \vec{x}, \tau) = \int_{-\infty}^{\infty} e^{-i\omega\tau} \phi(\vec{y}, \vec{x}, \omega) d\omega \quad (2.124b)$$

In Section 3.5 we will see how to accomplish these analytical manipulations without having to constantly carry the formal  $T \rightarrow \infty$  limit.

The acoustic pressure from a region of turbulence will be a stochastic variable that is related to the turbulence through a Green function for the geometry involved. Thus, the Fourier transform for the acoustic pressure in Equation (2.115) must be considered in the same generalized sense as we have also done for the velocity. Therefore, the acoustic pressure spectral density at the field point  $\vec{x}$  is given by

$$\overline{p_a^2} \phi_{pp}(\vec{x}, \omega) = \frac{2\pi}{T} \{ p_a(\vec{x}, \omega) p_a^*(\vec{x}, \omega) \} .$$

where  $\overline{p_a^2}$  is the total mean square pressure and the integral of the spectral density over all frequency is normalized according to

$$\int_{-\infty}^{\infty} \phi_{pp}(\vec{x}, \omega) d\omega = 1$$

In the specific instance of radiated sound from a turbulent region, the pressure spectral density is related to the cross spectral density of the source term,

$$\Phi_{TT}(\vec{y}_1, \vec{y}_2, \omega) = \lim_{T \rightarrow \infty} \frac{2\pi}{T} \left\{ \frac{\partial^2 \vec{T}_{1j}(\vec{y}_1, \omega)}{\partial y_1 \partial y_j} \cdot \frac{\partial^2 \vec{T}_{1j}^*(\vec{y}_2, \omega)}{\partial y_1 \partial y_j} \right\}$$

by an integral relationship that is analogous to the one for deterministic processes, Equation (2.115),

$$\overline{p_a^2} \phi_{pp}(\vec{x}, \omega) = \iiint_V \cdot \iiint_V \Phi_{TT}(\vec{y}_1, \vec{y}_2, \omega) G^*(\vec{x}, \vec{y}_1, \omega) G(\vec{x}, \vec{y}_2, \omega) d\vec{y}_1 d\vec{y}_2 \quad (2.125)$$

Equation (2.125) is perfectly general, it is essentially the spectral representation of the acoustic pressure and it is the spectral analog of Equation (2.61), in which the Green function is the one for free space. (The formal equivalence can be appreciated by the reader by making the necessary substitutions into either of Equations (2.61) or (2.125).) The importance of Equation (2.125) lies in the fact that the covariance or the cross spectral density of the turbulence are physically identifiable and measurable quantities, while the instantaneous quantity  $\partial^2 u_1 u_j / \partial y_1 \partial y_j$  is not a practical physical quantity to work with because it is a random variable of time and space. The value of the spectral representation is found in the fact that it is often the acoustic intensities of specific frequencies, rather than the overall intensity, that is of importance in many applications. There are many other forms of Equation (2.125) that will be used in subsequent chapters, which involve some of the alternative source functions. For example, rather than a cross spectrum of the stress tensor as above, it may be more suitable to invoke cross spectra of any of the other source terms appearing in Equation (2.74) whenever there are localized surface forces induced on a body placed in the flow. Extensive use of Equation (2.125), or of the methods to obtain it will be the underlying feature of the remainder of the chapters, excepting perhaps Chapter 4.

We will, in fact, make liberal use of the stochastic representations of this section in the remainder of this monograph. Most fluid dynamic processes which are

unsteady are also turbulent. Their stochastic nature makes these or similar time- (or space-) averaged quantities the only useful means of representing the properties of the flow. Yet, as can be seen from a study of this chapter, the acoustic propagation characteristics are often deterministic. In these cases, far field acoustic power is just a convolution integral involving a measurable covariance or cross spectral function and a geometrically influenced deterministic Green function. In the case of acoustic reflection and refraction by local turbulent density and velocity fluctuations even the propagation characteristics must be considered in a stochastic sense.

Generalization of the stochastic representations to include both space and time is simple especially when we are concerned with the far field acoustic spectrum. Restricting our attention to one frequency, the Green function  $G(\vec{x}, \vec{y}, \omega)$  can be separated into a product of separate functions of the source coordinate and the field coordinate, i.e.,

$$G(\vec{x}, \vec{y}, \omega) = G_x(\vec{x}, \omega) G_y(\vec{y}, \omega) \quad (2.126)$$

as long as the field point is in the far field  $|\vec{x}| \gg |\vec{y}|$  and  $k_0 |\vec{x}| \rightarrow \infty$ . We introduce the spatial Fourier transform pair of the source Green function

$$\tilde{G}_y(\vec{k}, \omega) = \iiint_{-\infty}^{\infty} G_y(\vec{y}, \omega) e^{i\vec{k} \cdot \vec{y}} d\vec{y}$$

and

$$G_y(\vec{y}, \omega) = \frac{1}{(2\pi)^3} \iiint_{-\infty}^{\infty} \tilde{G}_y(\vec{k}, \omega) e^{-i\vec{k} \cdot \vec{y}} d\vec{k} \quad (2.127a)$$

with a complex conjugate

$$G_y^*(\vec{y}, \omega) = \frac{1}{(2\pi)^3} \iiint_{-\infty}^{\infty} \tilde{G}_y^*(\vec{k}, \omega) e^{i\vec{k} \cdot \vec{y}} d\vec{k} \quad (2.127b)$$

Substitution of Equations (2.126) and (2.127) into Equation (2.125) yields

$$\begin{aligned} p_a^2 \phi_{pp}(\vec{x}, \omega) &= |G_x(\vec{x}, \omega)|^2 \int_{-\infty}^{\infty} d\vec{k} \int_{-\infty}^{\infty} d\vec{\kappa} \\ &\times \left[ \int_V d\vec{y}_1 \int_V d\vec{y}_2 \phi_{TT}(\vec{y}_1, \vec{y}_2, \omega) e^{-i(\vec{k} \cdot \vec{y}_1 - \vec{\kappa} \cdot \vec{y}_2)} \right] \times \tilde{G}_y(\vec{k}, \omega) \tilde{G}_y^*(\vec{\kappa}, \omega) \end{aligned} \quad (2.128)$$

This integral expression for the far field sound spectrum can be simplified considerably if the statistics of the turbulent source field are spatially homogeneous, i.e., that

$$\phi_{TT}(\vec{y}_1, \vec{y}_2, \omega) = \phi_{TT}(\vec{y}_2, \vec{y}_1, \omega) = \phi_{TT}(\vec{y}_2 - \vec{y}_1, \omega) \quad (2.129)$$

The cross spectral density of the source function is, in this case, a function only of the difference in the separation variables. Then, letting

$$\vec{y}_2 = \vec{y}_1 + \vec{r}$$

and

$$d\vec{y}_2 = d\vec{r}$$

Equation (2.128) may be rewritten

$$\begin{aligned}
\overline{p^2} \phi_{pp}(\vec{x}, \omega) &= |G_x(\vec{x}, \omega)|^2 \int_{-\infty}^{\infty} d\vec{k} \int_{-\infty}^{\infty} d\vec{\kappa} \cdot \tilde{G}_y(\vec{k}, \omega) \tilde{G}_y^*(\vec{\kappa}, \omega) \\
&\times \frac{1}{(2\pi)^3} \int_{-\infty}^{\infty} \phi_{TT}(\vec{r}, \omega) e^{i\vec{k} \cdot \vec{r}} d\vec{r} \cdot \frac{1}{(2\pi)^3} \int_{-\infty}^{\infty} e^{i(\vec{k}-\vec{\kappa}) \cdot \vec{y}_1} d\vec{y}_1 \quad (2.130)
\end{aligned}$$

The integrals over  $\vec{y}_1$  and  $\vec{\kappa}$  are analogous to Equation (2.123) and give

$$\int_{-\infty}^{\infty} e^{i(\vec{k}-\vec{\kappa}) \cdot \vec{y}_1} d^3\vec{y}_1 = \iiint_{-\infty}^{\infty} e^{i(\vec{k}-\vec{\kappa}) \cdot \vec{y}_1} d\vec{y}_1 = \delta(\vec{k}-\vec{\kappa}) \quad (2.131)$$

where

$$\delta(\vec{k}-\vec{\kappa}) = \prod_{i=1}^3 \delta(k_i - \kappa_i)$$

It is to be noted that occasionally one is interested in the approximation of a bounded source zone with characteristics of a much larger, effectively unbounded one. In such cases note that

$$\lim_{L_1 \rightarrow \infty} \left[ \frac{\sin(k-\kappa)_1 \left( \frac{L_1}{2} \right)}{\pi(k-\kappa)_1} \right] = \delta(k_1 - \kappa_1) \quad (2.132)$$

for all values of  $(k-\kappa)_1 > L_1^{-1}$ . Thus we see that wave number overlap caused by a finite spatial region always diminishes as the extent of the zone increases.

Now, returning to the mainstream of the analysis, the spatial Fourier transform of the cross spectral density of the sources is called the "wave number spectral density"

$$\phi_{TT}(\vec{k}, \omega) = \frac{1}{(2\pi)^3} \iiint_{-\infty}^{\infty} \phi_{TT}(\vec{r}, \omega) e^{i\vec{k} \cdot \vec{r}} d\vec{r} \quad (2.133)$$

Equation (2.130) now reduces to the simple form

$$\overline{p^2} \phi_{pp}(\vec{x}, \omega) = |G_x(\vec{x}, \omega)|^2 \iiint_{-\infty}^{\infty} \phi_{TT}(\vec{k}, \omega) |\tilde{G}_y(\vec{k}, \omega)|^2 d\vec{k} \quad (2.134)$$

Since the integrals are shown to extend over the infinite domain of wave number and physical it must be stipulated that all effects on the wave number spectrum of spatial finiteness of the sources are included in the definition of  $\phi_{TT}(\vec{k}, \omega)$ .

Equation (2.134) shows that an acoustic field can be regarded as a linear system driven by a spatially and temporally random input. In this case, however, the filtering is spatial rather than temporal and what Equation (2.134) gives is the acoustical response to a spatially steady state (homogeneous) input field. Equations (2.125) and (2.134) are therefore equivalent alternative expressions for the radiated sound pressure, except that Equation (2.134) presupposes spatial homogeneity of the source field. If the homogeneity assumption, Equation (2.129), were to be introduced, then Equation (2.125) would give the autospectrum of the acoustic pressure as a spatial convolution integral which is analogous to the initial value temporal response of a linear filter. Although the integrals over infinite wave number domains given in Equations (2.128), (2.130), and (2.134) are formally correct, it must be understood that the far field acoustic pressure is determined by the wave number range  $|k| < k_0$ . In most applications the Green function  $G_y(\vec{k}, \omega)$  is strongly peaked as the magnitude  $|k|$  approaches  $k_0$  in the region  $0 \leq |k| \leq k_0$ . Therefore, the integrals such as in Equation (2.139) are frequently dominated by a region  $|k| \sim k_0$  as shall be illustrated in some detail in the later Chapters 3 and 6 through 10. Contributions from sources at wave numbers which are outside  $|k| < k_0$  do not radiate sound. Rather these disturbances result in so-called near field pressures which decay exponentially with distance away from the source. Such near field motion is inertial, and in the case of a source comprised of an oscillating body, accounts for the added mass.

Equations (2.125) and (2.134) will be used in various forms throughout this book. Equation (2.125) is, in general, the less restrictive of the two because its application is not limited by the condition of spatial homogeneity. These relations



have direct application to jet noise (Chapter 3), Aeolian tone (Chapter 5), and lifting surface noise (Chapters 9 and 10). They have two-dimensional analogies in flow-induced sound from shell-like structures (Chapters 6 and 8).

## 2.7 APPENDIX A — DIPOLE RADIATION FROM THE HEAVING SPHERE: EXACT AND ASYMPTOTIC SOLUTIONS

The radiation from the heaving sphere in free-space will be reexamined from two aspects. First, we shall determine alternative expressions for the pressure field which are valid either far from or near to the sphere. Second, we shall write down a formal expression which is valid for all field points. In the first approach, our analysis will formalize the notions of the near and the far fields of radiating bodies. Liberal use of these concepts will be made in later chapters.

### 2.7.1 Asymptotic Formulas

Equation (2.28) can be rewritten in the form

$$\frac{1}{\sin \phi} \frac{1}{(k_0 r)^2} \frac{\partial}{\partial \phi} \left( \sin \phi \frac{\partial(r\tilde{p})}{\partial \phi} \right) + \frac{\partial^2(r\tilde{p})}{\partial (k_0 r)^2} + (r\tilde{p}) = 0 \quad (2.A135)$$

Using this equation we clarify the limits

1.  $k_0 r \gg 1$  with  $a/r \ll 1$  applying to the far field and
2.  $k_0 a \ll 1$  with  $a/r \sim 1$  applying to the near field,

where  $a$  is the radius of the sphere, Figure 2.2. For the far field solution, if we let

$$r\tilde{p} \sim [A_0 + A_1(k_0 r)^{-1} + A_2(k_0 r)^{-2} + \text{-----}] \cos \phi e^{-ik_0 r} \quad (2.A136)$$

we rule out the existence of acoustical singularities at large values of  $k_0 r$ .<sup>\*</sup> In limit of  $k_0 r$  approaching infinity, both Equation (2.A136) and its solution, Equation (2.A135), approach the  $k_0 r$  dependence for the monopole shown by Equations (2.22b) and (2.24). We determine the coefficients  $A_n$  by the substitution of Equation (2.A136) into (2.A135) which yields a relationship of the form

---

<sup>\*</sup>The specialization of  $\cos \phi$  directivity provides a slight loss of generality, but as we shall see in Section 2.7.2 of the appendix it is an unavoidable consequence of the normal velocity being  $U_n = U_z \cos \phi$  on the surface of the sphere.

$$\frac{\partial^2 g(\kappa)}{\partial \kappa^2} + g(\kappa) = \frac{2g(\kappa)}{\kappa^2}$$

where  $g(\kappa) = g(k_0 r)$  is the term in brackets in Equation (2.A136). The function on the right vanishes in the far field for  $\kappa = k_0 r \gg 1$ , leaving only the simple reduced wave equation which has a solution characteristic of spherical spreading. Carrying out the substitution and matching of the real and imaginary parts which are combinations of the coefficients  $A_n$  we find for the first three terms,

$$A_1 = 1 (A_2 - A_0) \quad (2.A137)$$

The near field expansion can be examined by rewriting Equation (2A.135) in the form

$$\frac{\partial^2(r\tilde{p})}{\partial x^2} + (k_0 a)^2 (r\tilde{p}) + \frac{1}{\sin \phi} \frac{1}{x^2} \frac{\partial}{\partial \phi} \left( \sin \phi \frac{\partial(r\tilde{p})}{\partial \phi} \right) = 0 \quad (2.A138)$$

where  $x = r/a$  is a stretched radial coordinate which allows for a separate examination of variations of distances on the order of the radius of the sphere and of changes in acoustic wavelength relative to the radius of the sphere. In the long wavelength limit,  $k_0 a$  approaching zero, the term which is quadratic in  $(k_0 a)$  may be neglected. The general solution to the remaining differential equation is

$$r\tilde{p} = \sum_m \{a_m x^m + b_m x^{-m}\} \cos \phi \quad (2.A139)$$

which reduces to

$$r\tilde{p} = \{a_{-1} x^{-2} + a_2 x^2\} \cos \phi$$

as can be seen by substitution into Equation (2.A138). This solution must be bounded for distances large compared to  $a$ , i.e., for  $x \gg 1$ , so that we must have  $a_2 = 0$ . Also the boundary condition on the sphere,

$$-\frac{1}{\rho_0} \frac{\partial \tilde{p}}{\partial r} = -i\omega U_z(\omega) \cos \phi$$

yields

$$a_{-1} = \frac{-i\omega \rho_0 a^2 U_z}{2}$$

Thus, our near field pressure becomes

$$\begin{aligned} r\tilde{p}(r, \phi) &= a_{-1} x^{-1} \cos \phi \\ r\tilde{p}(r, \phi) &\approx \frac{-i\omega \rho_0 a^2 U_z \cos \phi}{x} \end{aligned} \quad (2.A140)$$

and the far field pressure (combining Equations (2.A136) and (2.A137)) is

$$r\tilde{p}(r, \phi) \approx \{A_0 + i(A_2 + A_0) \kappa^{-1} + A_2 \kappa^{-2} + \dots\} \cos \phi e^{-i\kappa} \quad (2.A141)$$

To complete the solution we match the near field and far field solutions by using a rudimentary and greatly simplified matching procedure. We do this (see Reference 34 for a complete general examination of matching procedures and Reference 35 for application of those methods to acoustics) by expanding the far field solution in terms of the variables which are characteristic of the near field solution. Reexpressing Equation (2.A141) in terms of the stretched variable  $x = r/a$  so that  $k_0 r = k_0 a x$ , we have

$$r\tilde{p} \sim \left\{ \left( \frac{A_2 - 4A_0}{6} \right) (k_0 a x)^2 + i \left( \frac{4A_2}{6} + \frac{A_0}{2} \right) (k_0 a x) + \frac{A_2}{2} + iA_0 (k_0 a x)^{-1} + A_2 (k_0 a x)^{-2} + \dots \right\} \cos \phi \quad (2.A142)$$

which is valid for  $k_0 a x \ll 1$ . We have used the small argument expansion for  $e^{+ix} = 1 + ix - 1/2x^2 + i/6x^3 + \dots$ . For  $k_0 a x \ll 1$ , the leading terms in the expression for pressure amplitude are

$$r\tilde{p} \sim \{-iA_0 (k_0 a x)^{-1} + A_2 (k_0 a x)^{-2} + \dots\} \cos \phi$$

However, comparison with Equation (2.A139) yields the first and second terms

$$-iA_0 (k_0 a)^{-1} = a_{-1} \quad (2.A143)$$

and

$$A_2 = 0$$

Thus, the far field expression for the pressure amplitude is

$$r\tilde{p}(r, \phi) \sim + \frac{1}{2} \rho_0 c_0 (k_0 a)^2 a U_z \cos \phi [1 - i(k_0 r)^{-1}] \quad (2.A144)$$

for  $k_0 a \ll 1$ .

This expression becomes equal to Equation (2.A140) for small values of  $k_0 r$ . It is also equal to results that were obtained in Section 2.2. Note that taking the limit of small  $k_0 a$ , with a finite value of  $x$ , permitted the truncation of the wave equation to emphasize the inertial loading on the sphere. The second-order terms, those involving higher powers in  $k_0 r$  in Equation (2.A136), would be required for

situations in which  $k_o a \geq 1$  and  $k_o r > 1$ . This simplified matching technique could be extended to higher-order terms to accomplish this calculation. It could also be expanded to include other angular functions and to verify the  $\cos \phi$  dependence. For methods of pursuing such elaborations and extensions the reader is referred to Reference 34.

## 2.7.2 Exact Solutions

An exact solution to Equation (2.28), or for that matter Equation (2.A135), has been given by a number of authors, e.g., References 4, 5, and 13. We will, therefore, only outline the analysis. The pressure amplitude is written as

$$\tilde{p}(r, \phi) = \sum_{m=0}^{\infty} A_m h_m^{(1)}(k_o r) P_m(\cos \phi) \quad (2.A145)$$

where  $P_m(\cos \phi)$  is the  $m^{\text{th}}$  degree, order zero, Legendre polynomial,<sup>36,37</sup>  $h_m^{(1)}(k_o r)$  is the spherical Hankel function of the third kind<sup>37</sup> and the coefficient  $A_m$  is to be determined from the boundary condition. For our purposes, we need only to consider the first three degrees of the infinite set of Legendre functions,

$$P_0(\cos \phi) = 1$$

$$P_1(\cos \phi) = \cos \phi$$

$$P_2(\cos \phi) = \frac{1}{2} (3 \cos^2 \phi - 1)$$

because all others contain higher powers of the cosine. Matching Equation (2.A145) to the boundary condition results in all the coefficients  $A_m$  being equal to zero except  $A_1$ . This is because only  $P_1(\cos \phi)$  contains a  $(\cos \phi)$  function. Thus, Equation (2.A145) becomes

$$\tilde{p}(r, \phi) = i \rho_o c_o U_z(\omega) \cos \phi \frac{h_1^{(1)}(k_o r)}{\frac{\partial}{\partial k_o} [h_1^{(1)}(k_o a)]} \quad (2.A146)$$

The function  $h_1^{(1)}(k_0 r)$  and its first derivative have been tabulated by Abramowitz and Stegun.<sup>37</sup> That Equation (2.A146) reduces to the functions already derived is seen by noting that<sup>5</sup>

$$\lim_{k_0 r \rightarrow \infty} h_1^{(1)}(k_0 r) = \frac{ik_0 r}{k_0 r}$$

and that

$$\lim_{k_0 r \rightarrow 0} h_1^{(1)}(k_0 r) = -i \frac{1}{(k_0 r)^2}$$

and substituting these equations into Equation (2.A146).

We have only touched on the mathematical techniques of determining this formal solution of the wave equation, because an emphasis on the physical aspects is desired. For a more complete study of these mathematical aspects, the reader is referred to the references quoted in this Appendix.

## 2.8 REFERENCES

1. Milne-Thompson, L.M., "Theoretical Hydrodynamics," The Macmillian Co., 4th Ed. (1960).
2. Batchelor, G.K., "An Introduction to Fluid Dynamics," Cambridge Univ. Press (1967).
3. Sabersky, R.H. and A.J. Acosta, "Fluid Flow," the Macmillan Co. (1964).
4. Morse, P.M. and K.U. Ingard, "Linear Acoustic Theory," Handbuck Der Physik, S. Flugge, Ed., Springer-Verlag, Berlin (1961).
5. Junger, M.C. and D. Feit, "Sound Structures and their Interaction," MIT Press (1972).
6. Sommerfeld, A., "Partial Differential Equations in Physics, Lectures in Theoretical Physics," Vol. VI, Academic Press (1964).
7. Lighthill, M.J., "On Sound Generated Aerodynamically I, General Theory," Proc. Roy. Soc., London, Vol. 211A, pp. 564-587 (1952).
8. Lighthill, M.J., "On Sound Generated Aerodynamically II, Turbulence as a Source of Sound," Proc. Roy. Soc., London, Vol. 222A, pp. 1-32 (1954).
9. Lighthill, M.J., "Sound Generated Aerodynamically," Proc. Roy. Soc., London, Vol. 267A, pp. 147-182 (1962).
10. Schlichting, H., "Boundary Layer Theory," McGraw Hill (1979).
11. Phillips, O.M., "The Irrotational Motion Outside a Free Turbulent Boundary," Proc. Camb. Phil. Soc., Vol. 51, pp. 220-229 (1955).
12. Bateman, H., "Partial Differential Equations of Mathematical Physics," Camb. Univ. Press (1959).
13. Stratton, J.A., "Electromagnetic Theory," McGraw-Hill (1941).
14. Jackson, J.D., "Classical Electrodynamics," J. Wiley and Sons, Inc. (1967).
15. Jones, D.S., "The Theory of Electromagnetism," Pergamon Press (1964).
16. Proudman, I., "The Generation of Noise by Isotropic Turbulence," Proc. Roy. Soc., London, Ser. A214, pp. 119-132 (1952).



17. Crow, S.C., "Aerodynamic Sound Emission as a Singular Perturbation Problem," *Studies in Applied Mathematics*, Vol. 49, pp. 21-44 (1970).
18. Curle, N., "The Influence of Solid Boundaries upon Aerodynamic Sound," *Proc. Roy. Soc. London, Ser A231*, pp. 505-514 (1955).
19. Powell, A., "Aerodynamic Noise and the Plane Boundary," *J. Acoust. Soc. Am.*, Vol. 32, pp. 982-990 (1960).
20. Ffowcs Williams, J.E., "Sound Radiation from Turbulent Boundary Layers Formed on Compliant Surfaces," *J. Fluid Mech.*, Vol. 22, pp. 347-358 (1965).
21. Powell, A., "Theory of Vortex Sound," *J. Acoust. Soc. Am.*, Vol. 36, pp. 177-195 (1964).
22. Ffowcs Williams, J.E. and Hall, "Aerodynamic Sound Generation by Turbulent Flow in the Vicinity of a Scattering Half Plane," *J. Fluid Mech.*, Vol. 40, pp. 657-670 (1970).
23. Howe, M.S., "Contributions to the Theory of Aerodynamic Sound, with Application to Excess Jet Noise and the Theory of the Flute," *J. Fluid Mech.*, Vol. 71, pp. 625-673 (1975).
24. Chase, D.M., "Sound Radiated by Turbulent Flow Off a Rigid Half-Plane as Obtained from a Wave-Vector Spectrum of Hydrodynamic Pressure," *J. Acoust. Soc. Am.*, Vol. 52, pp. 1011-1023 (1971).
25. Chase, D.M., "Noise Radiated from an Edge in Turbulent Flow," *AIAA Journal*, Vol. 13, pp. 1041-1047 (1975).
26. Davies, H.G. and J.E. Ffowcs Williams, "Aerodynamic Sound Generation in a Pipe," *J. Fluid Mech.*, Vol. 32, pp. 765-778 (1968).
27. Crighton, D.G. and J.E. Ffowcs Williams, "Real Space-Time Green's Functions Applied to Plate Vibration Induced by Turbulent Flow," *J. Fluid Mech.*, Vol. 38, pp. 305-313 (1969).
28. Morse, P.M. and H. Feshbach, "Methods of Theoretical Physics," McGraw-Hill (1953).
29. Titchmarsh, E.C., "Introduction to the Theory of Fourier Integrals," 2 ed., Oxford (1948).

30. Batchelor, G.K., "The Theory of Homogeneous Turbulence," Cambridge Univ. Press (1969).
31. Lin, Y.K., "Probabilistic Theory of Structural Dynamics," McGraw-Hill (1967).
32. Kinsman, B., "Wind Waves," Prentice Hall (1965).
33. Lee, Y.W., "Statistical Theory of Communication," J. Wiley and Sons (1960).
34. Van Dyke, M., "Perturbation Methods in Fluid Mechanics," Parabolic Press (1975).
35. Crighton, D.G., "Application of Matched Expansion Methods to Problems in Acoustics," DTNSRDC Report 77-0105 (1977).
36. Hildebrand, F., "Advanced Calculus for Applications," Prentice-Hall (1962).
37. Abramowitz, M. and L.A. Stegun, "Handbook of Mathematical Functions," National Bureau of Standards, Applied Mathematics Series 55 (1964).
38. Pierce, A.D., "Acoustics: An Introduction to Its Physical Principles and Applications," McGraw-Hill (1981).
39. Kinsler, L.E. and A.R. Frey, "Fundamentals of Acoustics," J. Wiley and Sons, Inc. (1962).

## CHAPTER 3

### JETS, WHISTLES, AND OTHER SHEAR-FLOW NOISES

#### 3.1 INTRODUCTION

Whether or not a moving fluid is stable or unstable to some applied stimulation, for example an incident sound field, adjacent surface vibration, or buffeting from upstream turbulence, has largely to do with the spatial gradient and curvature of the mean velocity profile in the flow. A wide range of flow types are not stable to applied disturbances; such as jets, wakes, and flow over cavities. Often the time dependence of fluid motions in these types of flow is characterized by a predominant frequency that is dependent on a characteristic average velocity and a characteristic linear dimension of the flow region. As shown in the preceding chapter (e.g., Equations (2.49) and (2.89)), sound is potentially produced whenever there is a disturbance-filled fluid region. Furthermore, as shown in Chapter 2, the presence of surfaces complicates the sound field by providing not only acoustic reflections but also modifications in the primary hydrodynamic flow field that is responsible for the disturbance region. Therefore, in this chapter, we will consider in a basic fashion the unstable characteristics of flow which are required to create fluid disturbances, and relate those characteristics to the eventual breakdown into both regular and random vortex structures. We will also introduce many of the analytical and experimental techniques that are used when the flow disturbances become irregular or turbulent.

As practical applications of the general theory of shear-layer disturbances, we will develop rules for predicting the occurrence of various types of vortex induced tones in holes, cavities, and obstructed jets. The part played by ambient turbulence in the basic flow and the influence of Reynolds number on the vortex structures will be shown. Finally, some fundamental concepts in the similarity principles that govern noise from turbulent jets and some experimental approaches to validate those concepts will be introduced as a foundation to other flow types to be discussed in the body of this monograph.

The disturbances in wakes behind cylinders and hydrofoils are, by themselves, so important that they will be dealt with separately in later chapters.

### 3.2 SHEAR-FLOW INSTABILITIES AND THE GENERATION OF VORTICITY

Unstable flows are generally those which have gradients of mean velocity; the classical types which have been extensively examined analytically and experimentally are illustrated in Figure 3.1. Profile (a) was the first one to be theoretically

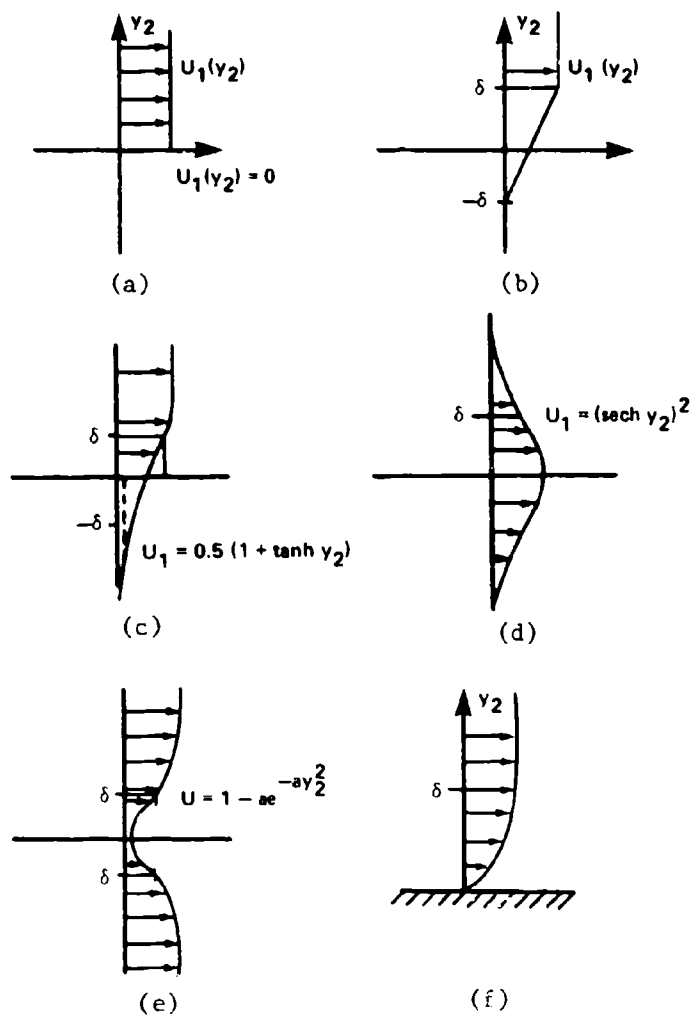


Figure 3.1 - Classical Types of Shear Flow: (a) Discontinuous; (b) Linear; (c) Hyperbolic Tangent; (d) Jet,  $\text{sech}^2 y_2$ ; (e) Gaussian Wake; and (f) Blasius Laminar Boundary Layer

examined by Helmholtz in 1868 (see Rayleigh<sup>1\*</sup> or Lamb<sup>2</sup>) who showed that the arrangement is unstable to disturbances of any frequency or wavelength. In this instance, the gradient of the velocity in  $y_2$  is singular at the interface  $y_2 = 0$  and the interface is therefore said to constitute a vortex sheet, i.e.,

$$\frac{\partial u_1(y_2)}{\partial y_2} = \lim_{\epsilon \rightarrow 0} \frac{U_1(y_2=\epsilon) - U_1(y_2=-\epsilon)}{2\epsilon} = \omega_3 \delta(y_2)$$

showing that the vorticity,  $\omega_3 = \partial u_1 / \partial y_2$ , is zero everywhere, but on the surface  $y_2 = 0$ . In more realistic circumstances the interface between the two moving fluids is less well defined as in illustrations (b) and (c). The former case of a linear velocity profile provides a constant region of vorticity  $\omega_3 = U_1/\delta$  inside the region of  $|y_2| < \delta$ . This case has been examined by Rayleigh<sup>1</sup> and Esch<sup>3</sup> while the latter has been extensively examined by, e.g., Michalke,<sup>4-6</sup> Browand,<sup>7</sup> Esch,<sup>3</sup> Sato,<sup>8</sup> Schade,<sup>9</sup> and Tatsumi and Gotoh;<sup>10</sup> the hyperbolic tangent profile has been experimentally examined by Browand<sup>7</sup> and it has practical application in the production of cavity tones.\*\* The jet profile (d) approximated by a hyperbolic secant squared, has been examined by Sato and Sakas<sup>11</sup> and Sato,<sup>12</sup> the wake (e), approximated by a gaussian velocity profile has been examined by Sato and Kuriki<sup>13</sup> both analytically and experimentally. Finally, the Blasius form of the boundary-layer mean velocity profile has been exhaustively examined analytically and experimentally; extensive surveys include those of Lin,<sup>14</sup> Betchov and Criminale,<sup>15</sup> and Schlichting.<sup>16</sup> We shall reserve further comments on boundary-layer waves and stability for Chapter 7.

The traditional analyses of flow stability begin with an assumption that a small-magnitude disturbance is present in the flow and we are interested in the growth of that disturbance in time or space as it moves along with the remainder of the fluid. Thus, the total fluid velocity (mean plus fluctuating) is written in a two-dimensional mean flow field as\*\*\*

---

\*A complete listing of references is given on page 219.

\*\*The definition of  $\delta$  is such that  $d^3 U_1(\delta) / dy_2^3 = 0$ , i.e., that the curvature is a maximum.

\*\*\*These problems are generally set in two-dimensional mean flow. Then, according to Squires' theorem, the most unstable disturbance waves are those whose wave propagation directions are aligned with the flow direction.

$$\vec{u} = \vec{u}_1(y_2) + \vec{u}(y_1, y_2, t) \quad (3.1)$$

where the disturbance velocity  $\vec{u}(y_2, t)$  vanishes as  $y_2 \rightarrow \pm \infty$  in an unbounded medium and simply as  $y_2 \rightarrow \infty$  in a boundary layer. Now it is generally assumed further\* that the disturbances may be written as

$$\vec{u}(y_1, y_2, t) = \hat{u}(y_2) e^{i\alpha(y_1 - Ct)} \quad (3.2)$$

where the real wave number  $\alpha$  is related to the frequency at which waves travel passed a fixed point of observation at the wave speed  $C_r$ ,

$$\frac{\omega}{\alpha} = C_r \quad (3.3)$$

where  $C_r$  is the real part of the complex velocity

$$C = C_r + iC_i$$

Thus described, the disturbance amplitude is modeled to grow exponentially in time at a rate

$$\frac{|\vec{u}(y_2, y_1)|}{|\hat{u}(y_2)|} \approx e^{\alpha C_i t} \approx e^{\alpha \frac{C_i}{C_r} y_1}$$

so that the least stable disturbances are those with the largest positive value of  $C_i$ .

In an alternate formulation, the wave is assumed to grow exponentially in space, i.e., instead of Equation (3.2) we have

$$\vec{u}(y_2, y_1, t) = \hat{u}(y_2) e^{i(\alpha y_1 - \omega t)}$$

---

\*See also Chapters 5 and 7.

where  $\alpha$  is complex ( $\alpha = \alpha_r + i\alpha_i$ ) and  $\omega$  is real. The two points of view are not identical, as pointed out by Gaster,<sup>17</sup> but only roughly equivalent as long as  $C_i \ll C_r$  or  $\alpha_i \ll \alpha_r$ . Then the near equivalencies hold:

$$[\alpha_i]_{\text{spatial}} \approx - \left[ \alpha \frac{C_i}{C_r} \right]_{\text{temporal}}$$

$$[\alpha_r]_{\text{spatial}} \approx [\alpha]_{\text{temporal}}$$

In this text we shall generally refer to temporal growth rates, although for shear flows the equivalency may break down due to similar values of  $C_R$  and  $C_I$ .

When Equations (3.1) and (3.2) are substituted into Equations (2.1) (with  $q=0$ ) and (2.44), and all terms that include products of disturbance amplitudes are ignored in relation to others, the resulting equations retain only the linear first order terms. It is called the Orr-Sommerfeld equation:

$$\begin{aligned} [U(y_2) - c] [\phi'' - \alpha^2 \phi] - U'' \phi \\ + \frac{1}{\alpha R_\delta} (\phi^{1v} - 2\alpha^2 \phi'' + \alpha^4 \phi) = 0 \end{aligned} \quad (3.4)$$

for small disturbances in an incompressible shear flow of a mean velocity distribution  $U_1(y_2)$ . In this equation we have expressed the fluctuating vertical velocity  $u_2(y_1, y_2, t)$  in terms of a fluctuating potential  $\phi(y_2)$  of the linearized disturbance; i.e., from Equation (3.2)

$$u_2(y_1, y_2, t) = \hat{u}_2(y_2) e^{i\alpha(y_1 - ct)}$$

which may be used to introduce the potential function

$$u_2(y_1, y_2, t) = -i\alpha\phi(y_2) e^{i\alpha(y_1 - ct)} \quad (3.5)$$

The wave speed  $C$  and the wave number  $\alpha$  are assumed to be independent of both  $y_1$  and  $y_2$ . However, the relationship between  $C_r$  and  $C_i$  will depend on the shape of  $U_1(y_2)$  and on the Reynolds number

$$R_\delta = \frac{U_o \delta}{\nu}$$

For a given type of flow, there is a critical value of  $R_\delta$  above which  $C_i$  is positive and the disturbances grow. For the free shear flow types (c) through (e) this critical value can be as low as 30 (see also Figure 3.15), while for the Blasius layer bounded by the rigid wall it is of order 2500. Thus in relation to the wall layer, the free shear layer is less stable. Furthermore, when  $R_\delta \gg (R_\delta)_{crit}$ , then the dependence of  $C_i$  on Reynolds number diminishes while the dependence of  $C_i$  on wave number  $\alpha$  remains dominant. This independence of  $C_i$  on Reynolds number generally pertains to the growth rates shown in Figure 3.2 for all the free shear layers

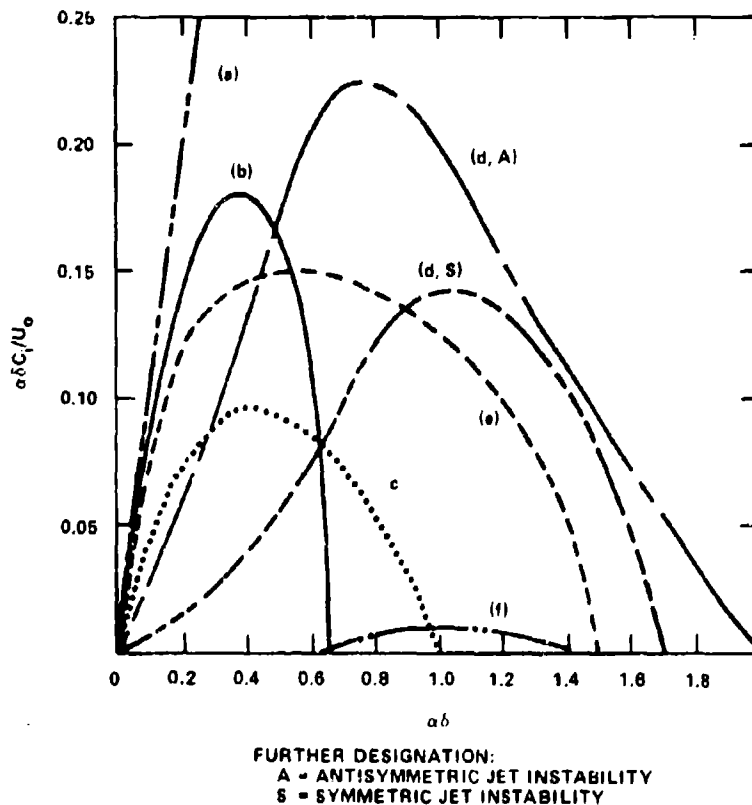


Figure 3.2 - Theoretical Growth Rates Based on Temporal Instabilities in the Shear Layers of Figure 3.1



illustrated in Figure 3.1. The relative instabilities of disturbances in the various shear layers at Reynolds numbers well above the critical value is thus quantified. Profile (a) is unstable to waves of all wavelengths, while the remainder of profiles are unstable to restricted ranges of wave number, generally greater than zero and less than  $2\delta^{-1}$ .

The large instability associated with the jets and wakes is caused by the pair of inflection points on either half of the shear layer which makes these flow types very sensitive to acoustic and hydrodynamic stimulus. Furthermore, the characteristic length scale of the wavy motion is dependent on the shape of the velocity profile, as illustrated and as discussed later in Section 3.4.1.

The jet is capable of two degrees of freedom, both of which have been observed in experimental environments. The least stable mode is the wavy pattern diagrammed in Figure 3.3a, while the more stable (symmetric) mode is diagrammed in Figure 3.3b;

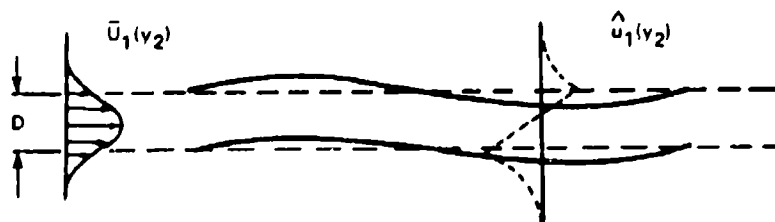


Figure 3.3a - Antisymmetric Jet Mode, Early Stage for Laminar Jets,  $\delta = D$

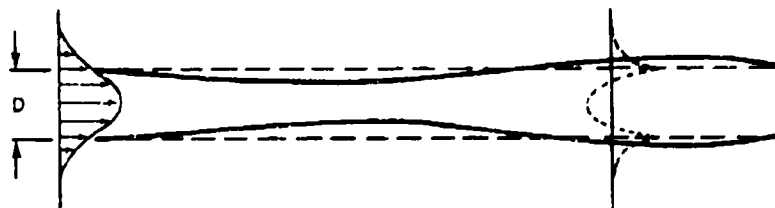


Figure 3.3b - Symmetric Jet Mode, Early Stage for Laminar Jets,  $\delta = D$

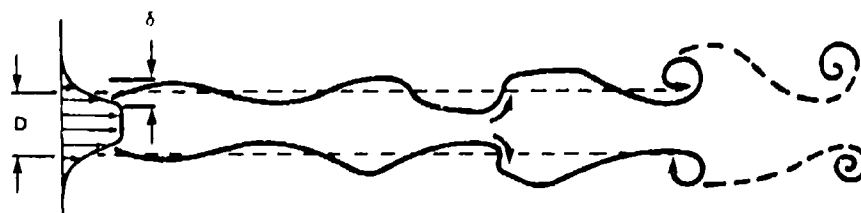


Figure 3.3c - Symmetric Jet Mode with Plug Flow,  $\delta < D$ , Later Stage for Laminar Jets

Figure 3.3 - Illustrations of Jet Modes

both modes can often be reinforced by sound.<sup>12</sup> Jet instabilities can also involve dynamics of thin annular shear layers when the efflux contains a central region for which the mean velocity is constant, Figure 3.3c. In these cases, an annular shear layer of thickness  $\delta$  undergoes instabilities, much like those of single free shear layers. The waves are of shorter length relative to the diameter of the jet than the waves shown in Figures 3.3a and 3.3b however, and the characteristic length scale of the waves is  $\delta$  rather than  $D$ . In all cases of axisymmetric jets, the growing waves, as shown in the excellent photographs of Brown<sup>18</sup> and later by Becker and Massaro,<sup>19</sup> begin to "crest" as sketched in Figure 3.3c causing a necking-down. In subsequent stages of development the necked-down regions separate the successive ballooned-out portions forming a street of rings or "puffs." Each of these puffs is a ring vortex. In the asymmetric mode, the later development results in a spiral vortex. The mode of instability determines the initial spatial scale for the vortices formed in later disturbances. This shall be seen more clearly below.

The development of a vortex structure from a particular mode of instability is an important concept in the generation of flow noise. It implies that a relationship ultimately exists between a flow type and the amount of noise produced. This relationship is made possible by the dependence of the sound pressure on unsteady vorticity as expressed in Equation (2.89). The less stable a type of flow, the more likely it is that the generation of vortices is possible. However, a formal mathematical connection between the mode of linear first-order instability of the type expressed in Figure 3.2 and a vortex structure has been limited to only idealized shear-layer types. These shear layers consist of one or more parallel vortex sheets of the type (a) in Figure 3.1. In this idealization, the physical shear layer is concentrated into sheets. Rosenhead's<sup>20</sup> calculation for the single layer, Figure 3.4, shows the gradual transition from a wave-like motion that involves a sheet of vorticity that is initially independent of  $x_1$  into a discrete set of point vortices as time increases. Each wave steepens at the downstream side of a crest to ultimately form a single vortex. The character of flow changes from a crested sinusoid at  $tU/\lambda = 0.30$  to a vortex at  $tU/\lambda = 0.35$ . The far field disturbance caused by the redistribution of vorticity is given by Equations (2.99) or (2.101) and it is maximum when the local acceleration of momentum due to the redistribution of vorticity with time maximizes; this occurs in the interval between  $tU/\lambda = 0.30$  to

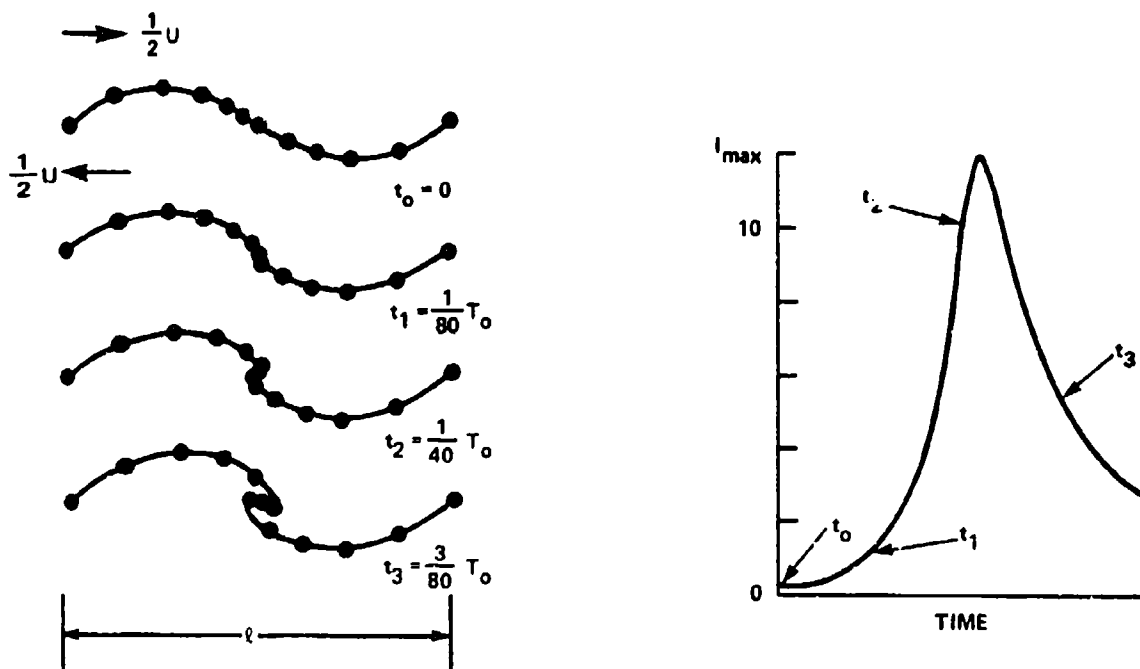


Figure 3.4 - Shear Layer Represented by a Set of Point Vortices<sup>21</sup>  
 (The time  $T_0$  is the periodic time  $U/2\ell$ . The maximum intensity of the rotating sound field is also shown, corresponding points in the two diagrams being indicated.)

0.35. The dependence of the sound on time is also illustrated in Figure 3.4, taken from Reference 21. To quantify the illustration somewhat we combine Equations (2.92) and (2.99) to find the acoustic particle velocity in the radial direction (per unit length normal to the page) as

$$p_a(\vec{x}, t) = \frac{\rho_o}{4\pi c_o r} \frac{\partial^2}{\partial t^2} \int \omega(y_1, 0, t - \frac{|\vec{x} - y_1|}{c_o}) dy_1$$

where  $\theta$  is the angle between the  $y_1$  direction and the field location. When the flow lines begin to roll back on one another, the instantaneous spatial distribution of vorticity changes rapidly even though the total vorticity and circulation in the fluid remains constant. Therefore, the phases of the induced motion of the fluid

particles change with the development of the vortices so that the above integral is not instantaneously zero, but is time-varying giving the double derivative shown in Figure 3.4. The most noise is generated at the moment when the change of this circulation distribution with time is greatest as illustrated. Other shear-layer motions have been calculated by Michalke<sup>4-6</sup> for the hyperbolic tangent profile and they show similar circulation regions, although far-field acoustic disturbances have not been calculated for such motions.

Deflections of streamlines, similar to those calculated by Rosenhead, have been calculated on a computer for a pair of parallel vortex sheets by Abernathy and Kronauer<sup>22</sup> and by Boldman, Brinich and Goldstein.<sup>23</sup> In the case of two vortex sheets each wavelength results in the formation of two concentrations of vorticity of opposite sign, see Chapter 9.

### 3.3 FREE SHEAR LAYER AND CAVITY RESONANCE

An important application of the concept of flow instability occurs with the passage of flow past a slot in a wall and the occurrence of separation-induced vibration in gate valves.<sup>24</sup> In these situations (Figure 3.5) the flow external to the slot may consist of a thin laminar boundary layer or a possibly thicker (relative to the opening dimension) turbulent boundary layer. Each of these situations, it turns out,<sup>21</sup> has a somewhat different relationship governing the disturbance frequency, speed, and cavity dimension.

In the case of a laminar boundary layer, in which the thickness of the layer  $\delta$  is less than the streamwise dimension of the opening  $b$ , the passage of the fluid beyond the upstream edge into the opening resembles the development of the classical free-shear layer.<sup>25</sup> This layer is well described by the hyperbolic tangent profile<sup>4,6,7</sup> (Figure 3.1c) and it is theoretically least stable to disturbance wave numbers (Figure 3.2) of magnitude

$$\alpha \delta = 0.42 \quad (3.6)$$

where  $\alpha$  is given by Equation (3.3). For the hyperbolic tangent velocity profile, the momentum thickness, given by

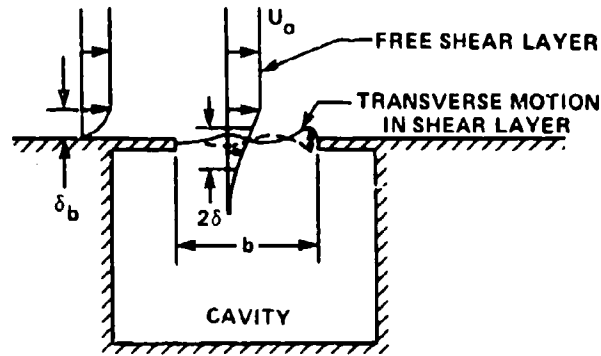


Figure 3.5a - Laminar Boundary Layer

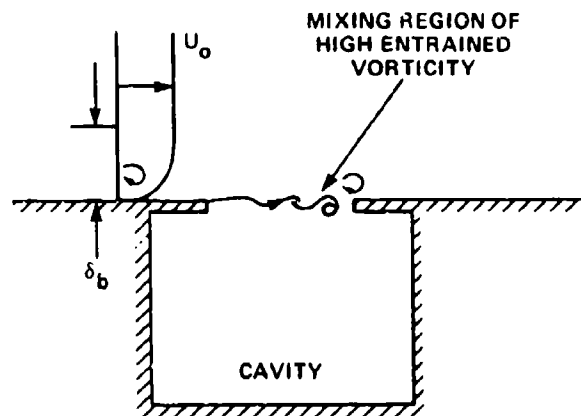


Figure 3.5b - Turbulent Boundary Layer

Figure 3.5 - Idealizations of Flow Past Cavities which are Coupled to External Boundary Layers by Slots or Orifices

$$\theta = \int_{-\infty}^{\infty} \frac{U_1}{U_o} \left( 1 - \frac{U_1}{U_o} \right) dy_2 \quad (3.7)$$

where  $U_o$  is the local freestream velocity, is identically equal to  $\delta/2$ . Theoretically, the wave speed is equal to the mean velocity at the inflection in the velocity profile, i.e. where  $d^2U(y_2)/dy_2^2$  is maximum,

$$C_r = \frac{1}{2} U_o \quad (3.8)$$

so that Equation (3.6) gives the dimensionless frequency, or Strouhal number\* at which the disturbances are propagated or convected downstream from the upstream edge as

$$\frac{f\theta}{U_o} = 0.017 \quad (3.9)$$

This is also the frequency at which the disturbances encounter the downstream edge.

Now, the motion of this shear layer has associated with it a transverse velocity which is, in the approximation of linear disturbances, nearly sinuous across the opening. At the upstream edge, the velocity transverse to the flat surface is zero so that separation is avoided. At the downstream edge of the aperture the transverse velocity magnitude in the shear layer will be approximated by

$$u_2(y_1=b, y_2) = \hat{u}_2(y_2) e^{C_1 \alpha b / C_r} \sin(\alpha b + \phi)$$

where  $C_r$  and  $C_1$  are based on the average mean velocity profile found in the opening. The mean streamwise velocity in the opening  $\bar{U}$  will combine with this transverse velocity to give a local small angle of attack to the edge of approximately  $\gamma = u_2(y_1=b, y_2)/\bar{U}$ . If the edge is sharp, separation of flow can occur leading to the formation of additional unsteady vorticity at the edge at a frequency given by Equation (3.8). For more blunt edges, the alternate influx and efflux of fluid from the cavity at this location will set up synchronous motions within and these will, in turn, influence the initial conditions at the upstream origin of the shear layer. In either case a condition for maximum transverse velocity at the downstream edge of the cavity is that  $\sin(\alpha b + \phi)$  is unity. This requires that

$$\alpha b + \phi = 2\pi \left( n + \frac{1}{4} \right) \quad \text{for } n = 1, 2, \dots \quad (3.10)$$

---

\*A Strouhal number is a dimensionless frequency of a fluid perturbation which is formed with a length scale of the flow and the flow velocity. It is so named in honor of V. Strouhal who first studied the vortex shedding from cylinders, as discussed in Chapter 5.

where  $\phi$  is an arbitrary phase angle that accounts for the possibility of a phase lag between the encounter of the disturbance with the edge and the response of the shear to this encounter, and where the plus or minus sign allows for motions either into or out of the orifice. Since  $\alpha = 2\pi/\lambda$ , where  $\lambda$  is a representative wavelength of the instability mode across the opening, we have alternatively

$$\frac{b}{\lambda} = n \pm \frac{1}{4} - \frac{\phi}{2\pi} \quad (3.11)$$

The possible relationships between the wavelength and the phase that can be deduced from Equation (3.3) are

$$\frac{fb}{U_o} = \frac{C_r}{U_o} \left( n + \frac{1}{4} - \frac{\phi}{2\pi} \right) \quad \text{for } n = 1, 2, \dots \quad (3.12a)$$

or

$$= \frac{C_r}{U_o} \left( n - \frac{1}{4} - \frac{\phi}{2\pi} \right) \quad \text{for } n = 1, 2, \dots \quad (3.12b)$$

where, now,  $C_r$  is a hydrodynamic phase velocity averaged across the opening. Equation (3.12b) with  $\phi = 0$  most generally applies to a shear layer at the mouth of an enclosure.

The representation of the disturbance frequencies in this manner has been suggested on similar grounds by Dunham<sup>26</sup> who proposed the existence of selected modes corresponding to integer numbers of vortices entrapped within the orifice. It was Rossiter<sup>27</sup> who proposed a relationship similar to Equation (3.12b) with  $\phi = 0$  and with  $n = \pi/4$ . A velocity at the downstream edge into the cavity will provide an increased pressure in the cavity that will exert an upward stimulus on the leading edge. This upward disturbance will be exerted instantaneously when the cavity is small.\*

Another rationalization proposed by King, Doyle, and Ogle<sup>29</sup> and later extended by Martin, Naudascher, and Padmanabhan<sup>30</sup> and by Rockwell<sup>31</sup> concerns the integrated

---

\*A similar condition of reinforcement was found to apply to a round jet passing through a sealed enclosure.<sup>28</sup> It was found that  $fL/U_j \approx (n - 0.25 - fL/C_o) U_c/U_j$  where  $U_c \sim 0.6 U_j$ ,  $n = 1, 2, \dots$ , and  $L$  is the length of the enclosure.

disturbance across the opening. Following Bilanin and Covert<sup>32</sup> the vertical displacement of the shear layer across the cavity  $\delta_2$  is given by the proportionality

$$\delta_2(y_1, t) = \delta_0 e^{C_1 \alpha y_1 / C_r} \cos(\alpha y_1 - \omega t) \quad (3.13)$$

so that the instantaneous volume change per unit width imposed on the interior is

$$\delta V = \int_0^b \delta_2(y_1, t) dy_1 \quad (3.14)$$

This volume must be absorbed in the elasticity of either the fluid or the cavity structure, but the important point is that a negative volume change will cause a positive pressure. This positive pressure reinforces a positive value of deflection at the origin of the shear layer,  $\delta_2(0, t)$ . Integration of Equation (3.14) using Equation (3.13) gives the volume change explicitly in terms of the parameters  $C_1$ ,  $C_r$ , and  $\alpha$ . Further, the condition that  $(\alpha b C_1 / C_r) > 1$  provides a simple relationship just as Equation (3.12) with  $\phi = 0$  and  $n = \pi/4$ . Rockwell<sup>31</sup> has treated the relationships more exactly, replacing  $\alpha y_1$  by integrated values across the opening. This procedure accounts for the fact that, for long cavities, particularly, the shear layer changes with  $y_1$ . For example, in Equation (3.12), the wave speed  $C_r$  is a function of distance from the leading edge of the opening.

Equations (3.9) and (3.12) provide alternate nondimensionalizations of the frequencies of disturbances in the opening in terms of the size of the opening and the velocity of the external fluid. The first definition, Equation (3.9), is based on stability conditions, while the second, Equation (3.12), is required by geometric constraints. In reality, the disturbances are neither exclusively propagating nor always representative of standing modes.

Measurements of the frequencies of cavity tones have been made for a variety of external turbulent boundary layers. The measurements in Figure 3.6a show a general decrease in Strouhal number as the boundary layer thickness increases in relation to the streamwise dimension of the opening. The values reported by DeMetz



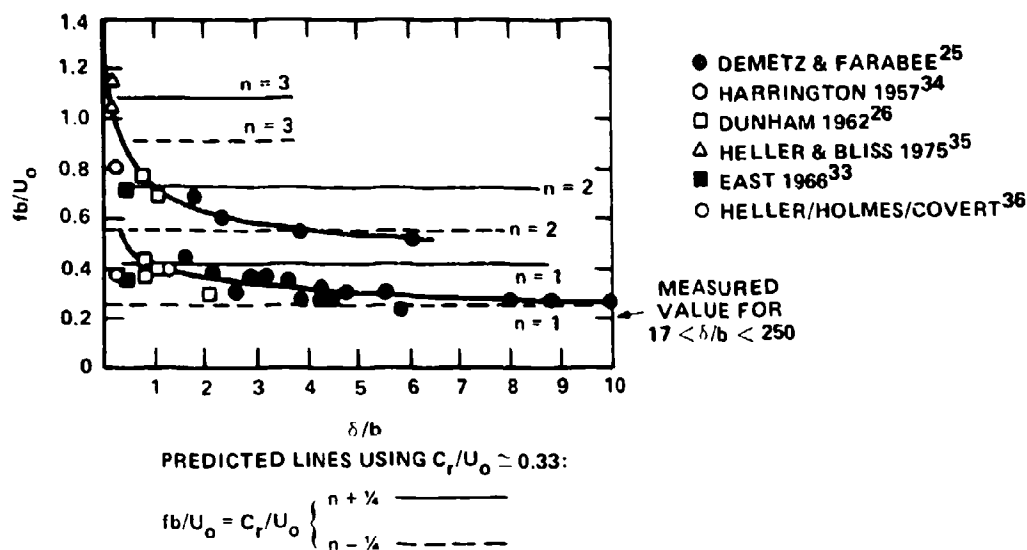


Figure 3.6a - Cavity Resonance Frequency Scaling for Turbulent Boundary Layer Excitation  
(From DeMetz and Farabee<sup>25</sup>)

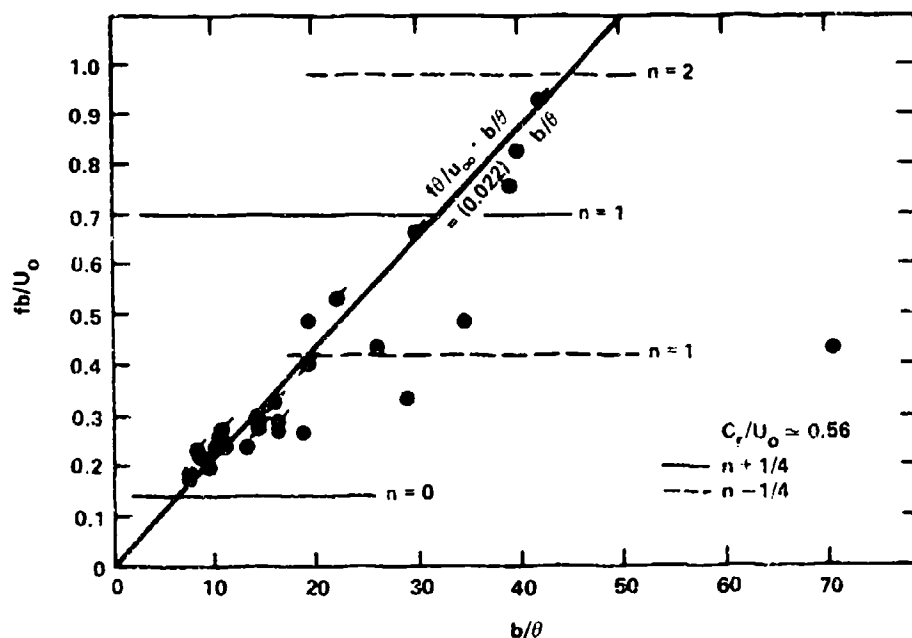


Figure 3.6b - Frequencies of Cavity Tones Driven by Laminar Boundary Layers  
(Data courtesy of DeMetz and Farabee)

Figure 3.6 - Representations of Cavity Tone Frequencies

and Farabee<sup>25</sup> were obtained on both circular openings and rectangular slots in air; Dunham's<sup>26</sup> results were obtained in air and water media with slotted openings. The two tones shown by DeMetz and Farabee,<sup>25</sup> Dunham,<sup>26</sup> East,<sup>33</sup> and Harrington<sup>34</sup> can be explained from the flow-visualizations of Dunham. These frequencies correspond to the entrainment into the cavity mouth of either one or two vortices in the cavity; the vortices originating from the rapid breakdown of the shear-layer instabilities downstream of the upstream lip. The convection velocity of these vortices across the mouth as reported by DeMetz and Farabee was approximately  $0.33 U_o$ . Each of the modes of oscillation, then can be predicted from Equation (3.12) with  $C_r/U_o = 0.33$  and  $\phi = 0$ . The horizontal lines in Figure 3.6a show the various modes for  $n \pm 1/4$  which generally bracket the observed Strouhal frequencies and which represent either one or two standing waves or vortices in the opening. The measured results of Heller and Bliss<sup>35</sup> and of Heller, Holmes, and Covert<sup>36</sup> were obtained with very long cavities and appear to correspond to a higher mode of oscillation. The uncertainty in selection of  $\pm 1/4$  that is apparent in Figure 3.6a is additionally caused by the fact that the actual value of  $C_r$  and its variation with  $\delta/b$  is unknown. Recent discussion of this question may be found in ref. 143.

When the external boundary layer was laminar, DeMetz and Farabee reported Strouhal numbers that take on a more continuous rather than the discrete behavior observed with external turbulent flow. In the laminar flow case the tone frequency increased continuously with velocity according to a form that is similar to Equation (3.9), i.e., with

$$\frac{fb}{U_o} = 0.022$$

which is determined by the observed value of  $C_r = 0.56 U_o$ . The limited reinforcement that could be observed was evident only at the  $n=1$  mode of Equation (3.12b).

Thus far, we have been concerned only with the shear-layer dynamics in the opening without considering the influence of the cavity volume behind the aperture. The general agreement among investigators in the reported values of Strouhal number attest to the first-order independence of  $fb/U_o$  on the cavity shape. For rectangular U-shaped slots, Ethembabaoglu (reported by Rockwell<sup>31</sup>) reports a slight increase in  $fb/U_o$  as the width exceeds the depth of the slot. Hardin and Martin<sup>37</sup> have examined theoretically the radiation properties of these type cavities in terms of their entrained vortices. Measurements of DeMetz and Farabee<sup>25</sup> were made with the

openings of cylindrically-shaped Helmholtz resonators with the center of the hole at the axis of the cavity. Relatively large pressure amplitudes were measured in the cavity at coincidence of an aperture resonance and a volume resonance of the cavity or any of its harmonics. The limiting maximum amplitude of pressure at the bottom of the cylindrical cavity occurring at the cavity resonance frequencies appears to be limited by

$$\frac{p_{cav}^2}{q_0}^{1/2} < 1$$

where

$$q_0 = \frac{1}{2} \rho_0 U_0^2$$

At disturbance frequencies unequal to the cavity resonance frequency, the cavity pressures can be as low as  $10^{-3} q_0$ .

The pressure in the cavity can be related to the far field acoustic pressure. When the dimension of the cavity is smaller than an acoustic wavelength then, using the notation of Figure 3.7, the piston-like motion in the opening causes a sound pressure

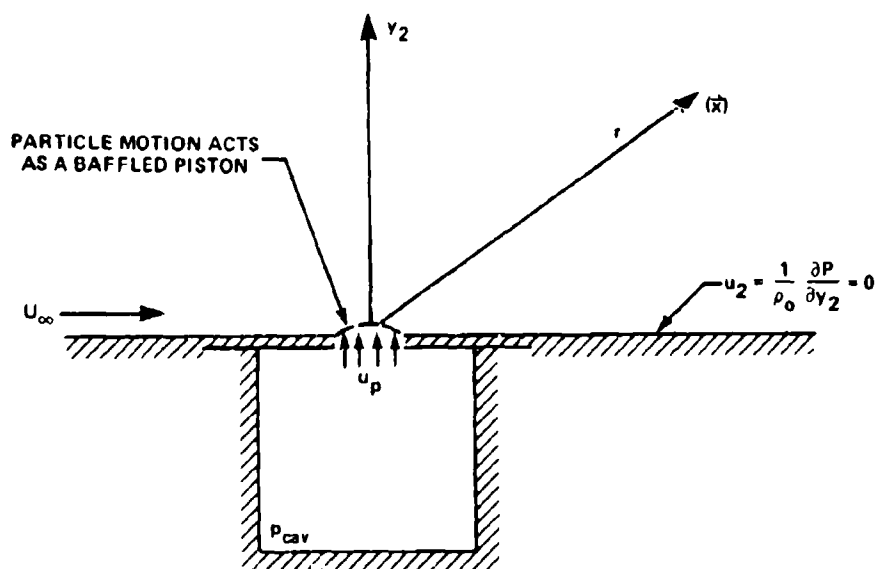


Figure 3.7 - Geometry of Radiation Problem Involving a Resonating Cavity Coupled to an Unbounded Acoustic Fluid Medium

$$p_{\text{rad}} \approx \frac{i \rho_o c k_o a^2 u_p}{2r} e^{i k_o r} \quad (3.15)$$

when  $k_o a \ll 1$  and the wall is essentially an infinite plane. This result is easily derivable from Equations (2.114) and (2.116) for the otherwise source-free region ( $T_{ij}=0$ ) external to the rigid plane. For this classical situation the Green function is (Equation (2.116))

$$G(\vec{x}, \vec{y}, \omega) = \frac{e^{i k_o r}}{2\pi r}$$

since  $r_1 = r_2 = r$ , and

$$\lim_{y_2 \rightarrow 0} \frac{\partial G}{\partial y_2} = 0$$

Therefore, when  $y_2 = 0$ ,

$$\frac{\partial p_a}{\partial y_2} = i \omega \rho_o u_p$$

only in the small opening and is zero on the surface otherwise. Then Equation (2.114) gives the result, Equation (3.15), directly.

Depending on the size of the cavity, the pressure in the cavity is related to  $u_p$  by either of two asymptotic forms. In either case, if the medium is an ideal gas, the pressure change for a fractional change in a unit volume is given by

$$\delta p = - \rho_o c_o^2 \frac{\delta V}{V} \quad (3.15)$$

If the cavity is small compared to a wavelength, the  $\delta \dot{V} = \pi a^2 u_p$  and  $V = V_{\text{cav}}$  so Equation (3.15) gives ( $\delta \dot{V} = \omega \delta V$  where  $\omega$  is the resonance frequency of the cavity),

$$\frac{|p_{\text{rad}}|}{|p_{\text{cav}}|} \approx \frac{1}{2\pi} \frac{a}{r} \quad \lambda_o \gg \text{cavity dimensions.} \quad (3.17)$$

Use is made of the Helmholtz frequency (given below) and we assume that the hole radius is much larger than the length (depth) of the hole that connects the inner and outer fluid. The alternative expression can be written for a cavity whose dimension exceeds an acoustic wavelength. Then the unit volume, for example, for an organ pipe of radius  $a_p$ ,

$$V = \lambda_o \pi a_p$$

where  $\lambda_o$  is the wavelength of sound. The pressure fluctuation in the cavity is

$$\delta p_{\text{cav}} \approx \rho_o c_o u_p$$

and we find

$$\frac{|p_{\text{rad}}|}{|p_{\text{cav}}|} = \frac{\omega A_c}{c_o r} \quad (3.18)$$

where  $A_c$  is the area of the cavity. This relationship, previously derived by Elder<sup>38</sup> for organ pipe excitation, shows an omnidirectional sound field with a sound pressure level which is inversely proportional to the sound speed. Thus, the sound pressure has a monopole-like directivity, but a dipole-like wave number dependence. The factor  $(p_{\text{cav}} A)$  represents the time rate of change of the force exerted on the external fluid by the pressure in the cavity. Equation (3.18), therefore, includes the same parameters as Equation (2.77) for the true dipole with the exception of the directivity factor. Howe<sup>39</sup> and Elder<sup>40</sup> have given more extensive treatments to the flow excited Helmholtz resonator and other resonators.

The elastic character of the cavity structure has received little attention, however, in the case of rigid walled cavities with fluid compressibility governing

the cavity stiffness. Relationships for the frequency have been given by Raleigh.<sup>1</sup> The classical Helmholtz resonance frequency can be found in numerous texts.<sup>1,41</sup> For circular openings

$$f = \frac{c_o}{2\pi} \sqrt{\left(\frac{\pi}{V} \cdot \frac{a^2}{L + \Delta R}\right)^{1/2}} \quad (3.19)$$

where  $a$  = radius of the opening

$V$  = volume of the cavity

$L$  = length of the opening

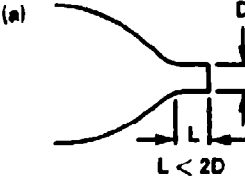
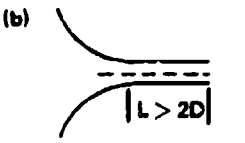
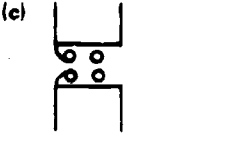
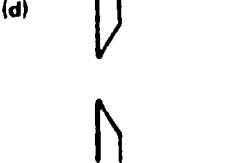
$\Delta R$  = end correction approximately equal to  $1.64a$

This can be generalized to openings of other dimensions by replacing  $\pi a^2$  by the area of the opening  $S$ , and  $\Delta R$  by  $(\pi S)^{1/2}/2$ . Dunham<sup>26</sup> and later Covert,<sup>42</sup> Ingard and Dean,<sup>43</sup> and Elder,<sup>38,40</sup> have considered some general impedance characteristics of cavities and how these characteristics influence coupling of the cavity and shear-layer dynamics. Miles and Watson<sup>44</sup> measured the flow-excited pressures of acoustic modes in a nearly cylindrical cavity with its axis set perpendicular to the flow direction and slotted along its length.

### 3.4 SELF-EXCITATION OF LAMINAR JETS

#### 3.4.1 Dimensionless Frequencies of Tonal Disturbances

The disturbances that occur in circular jets are dependent on the character of the mean velocity profile of the efflux, and, therefore, somewhat on the type of nozzle used. It should be emphasized that the dependence of the jet tone frequency on efflux velocity will depend on the shape of the velocity profile at efflux. For short, potential-flow nozzles (a) in Figure 3.8, the efflux contains a modestly-sized potential core with an annular shear layer so that  $2\delta/D \ll 1$ , where  $\delta$  is the shear-layer thickness illustrated in Figure 3.3c. When the nozzle is made many diameters longer, the flow in the tube is fully sheared so that velocity profiles with shapes generally similar to those shown in Figure 3.1d occur (in these profiles the shear layer incorporates most of a half-diameter). These two extremes,  $\delta < D$  and  $\delta = D$  provide alternative dependence of Strouhal number on Reynolds number as shall be described below. The efflux will be laminar for Reynolds numbers ( $U_o D/\nu$ ) less than 1400 when the inlet to the nozzle is well formed to avoid separation of flow inside the nozzle. For jets ensuing from long square-edged orifices such as (c),

NOZZLE TYPE	$(R_D)_{CRIT}$	REFERENCE
(a)  SHORT RADIUS $L < 2D$	1400	BECKER AND MASSARO <sup>45</sup> CROW AND CHAMPAGNE <sup>48</sup> BROWAND AND LAUFER <sup>47</sup>
(b)  LONG NOZZLE $L > 2D$	$\sim 1000$	SATO AND SAKAO <sup>11</sup> SATO <sup>12</sup> CHANAUD AND POWELL <sup>51</sup>
(c)  SQUARE- EDGED ORIFICE	600	ANDERSON <sup>54-60</sup> KURZWEG <sup>72</sup>
(d)  KNIFE- EDGED ORIFICE	500	BEAVERS AND WILSON <sup>50</sup> JOHANSEN <sup>49</sup>

$(R_D)_{CRIT}$  - REYNOLDS NUMBER FOR WHICH VORTICES BEGIN TO FORM IN THE JET FLOW. AMPLIFIED SINUOUS DISTURBANCES OCCUR AT LOWER REYNOLDS NUMBERS

Figure 3.8 - Illustrations of Nozzles and Orifices that Produce Jet Tones

the efflux is laminar only for  $R_D < 600$  because vortices caused by separation of flow are generated at the inlet for larger Reynolds numbers. Finally, in the case of knife-edged orifices, the jets are disturbance-sensitive at Reynolds numbers greater than 500 because of the rather thin shear layer in the efflux. The references cited in Figure 3.8 are those for which extensive flow visualizations and quantitative measurements were obtained over a wide range of Reynolds number. The critical Reynolds numbers cited are the minimum values for which growing sinuous disturbances give way to clearly-defined vortex structures. This critical value of Reynolds number is not well defined since it is often influenced by the presence of extraneous disturbances and its identification also depends on experimental detail and on the manner of observation. Jets are disturbance-sensitive at Reynolds numbers that are as low as 100.

Visualizations of large-scale vortical structures in circular jets have been made by numerous experimenters for the last 40 years or so, see ref 143. The photographs of Becker and Massaro<sup>45</sup> which cover a wide range of Reynolds numbers are shown in Figure 3.9. Their efflux was laminar at least until moderate values of  $R_D$  and the vortex structures are clearly evident.

The frequencies of disturbances in this case are determined by the thickness of the annular shear layer and are typical of cases for which  $\delta < D/2$ . The shear-layer, therefore, is thought of as two parallel hyperbolic tangent profiles so that the unstable wave numbers of the jet correspond to

$$\alpha \delta = \text{constant}$$

Now for an initially laminar jet, resulting from a laminar boundary-layer on the wall of the nozzle, the shear-layer thickness will depend on Reynolds number approximately\* as

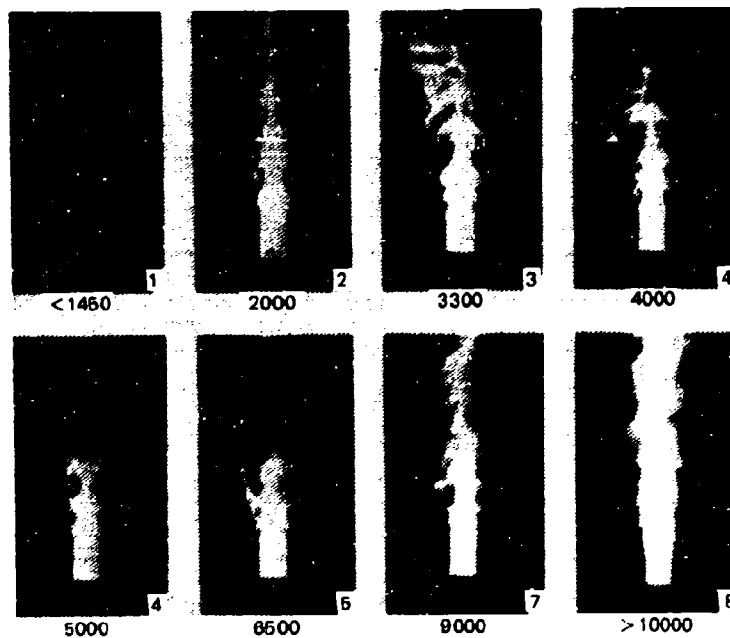


Figure 3.9 - Smoke Jets from Laminar Flow Exiting an ASME Short-Radius Circular Nozzle (By Becker and Massaro<sup>45</sup>)  
(Numbers refer to approximate Reynolds numbers)

\*See Chapter 7.



$$\frac{\delta}{D} = \alpha (R_D)^{-1/2}$$

Since we can write

$$\alpha = \frac{2\pi}{\lambda} = \frac{2\pi f}{C_r} \approx \frac{2\pi f}{U_J}$$

where  $U_J$  is the efflux velocity of the jet, the Strouhal number for these naturally-growing jet instabilities can be written as

$$\frac{fD}{U_J} = a_1 (R_D)^{1/2} \quad (3.20)$$

The constant of proportionality appears to range from 0.012 to 0.0195 (Michalke and Schade)<sup>46</sup> as shown in Figure 3.10. Trends are shown as well as the isolated observations of Browand and Laufer<sup>47</sup> and of Crow and Champagne.<sup>48</sup> This behavior with Reynolds number is apparently not reported at  $R_D$  greater than 20,000 or 30,000.

Strouhal numbers observed for other types of round jets are also shown in Figure 3.10. Values of  $S_D$  for tones of knife edge orifices are constant with  $R_D$ . Flow visualizations of Johansen<sup>49</sup> ( $\delta \approx D/2$ ) and of Beavers and Wilson<sup>50</sup> show that the responsible jet modes are axisymmetric. See also ref 143.

For two-dimensional jets with shear layers that include most of the width  $w$ , measurements of Sato and Sakao<sup>11</sup> show frequencies of antisymmetric modes given by  $S_w \approx 0.14$  for  $2000 < R_w < 10,000$ , while for low Reynolds number\* they found

$$\frac{fw}{U_J} = S_w \approx (7.7 \times 10^{-5}) R_w$$

Frequencies of axisymmetric modes<sup>12</sup> followed  $S_w \approx 0.23$  for  $1500 < R_w < 8000$ ; while at values of  $R_w$  on the order of  $3 \times 10^4$ ,  $S_w$  on the order of 1.25 was reported. In the range of Reynolds numbers less than  $10^4$ , the oscillations of both jet modes were accurately described by the theory of hydrodynamic stability based on profile (d) of Figure 3.1.

---

\*Based on the mean centerline velocity at the jet-exit.

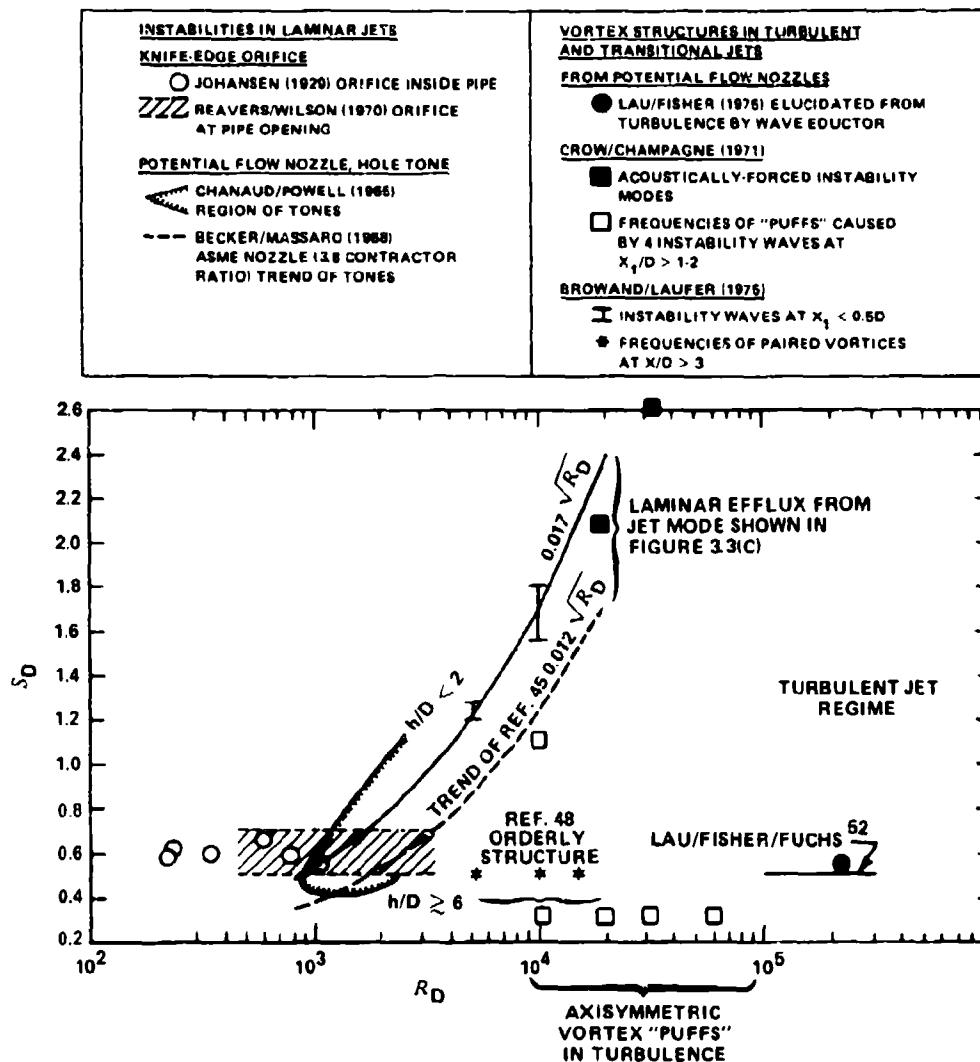


Figure 3.10 - Strouhal Numbers for Vortex Formation in Circular Jets with Axisymmetric Disturbances

The hole tones observed by Chanaud and Powell<sup>51</sup> are bounded between the Strouhal numbers being either constant or proportional to  $R_D^{1/2}$ . These tones are reinforced by placing a second orifice opposite the efflux, as shown in Figure 3.11a. Separation of flow and the subsequent formation of vortices at the downstream knife edge cause disturbances which feed back and reinforce the axisymmetric-mode instabilities of the primary efflux. Although the frequencies of tones will depend on the ratio of orifice spacing to diameter  $h/D_j$ , in a manner to be examined subsequently,

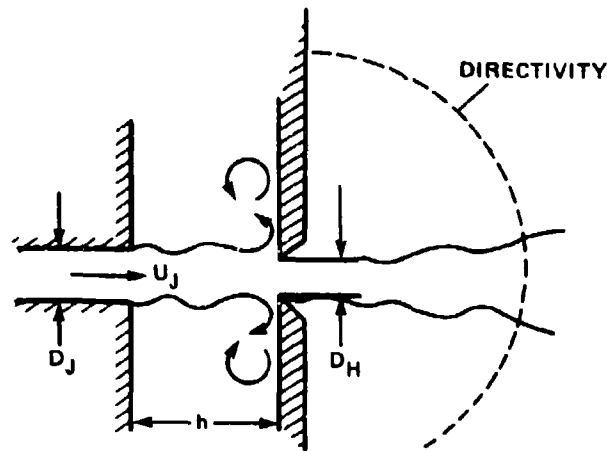


Figure 3.11a - Hole-Tone, Involving Axisymmetric Modes and Causing Omnidirectional Radiation Observed<sup>62</sup> for  $h/D_J = 2.0, 2.5, \text{ and } 3.0$

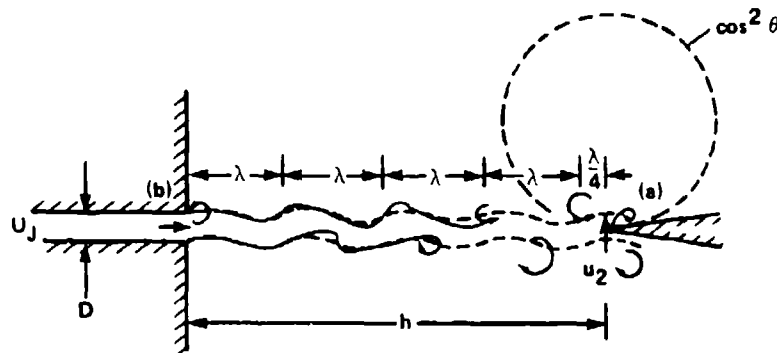


Figure 3.11b - Edge-Tone, Involving Antisymmetric Modes and Causing Dipole Directionality, Observed<sup>70</sup> for  $3 < h/D < 30$  (See Section 3.4.2)

Figure 3.11 - Hole-Tone and Edge-Tone Geometries

the tones are possible only because of the available range of wavelengths for jet instabilities to occur (Figure 3.2). Thus, the region enclosed within the branches in Figure 3.10 describes the available Strouhal numbers of amplification.

As Reynolds numbers exceed  $10^4$ , larger, clearly defined growing waves are less apparent and axisymmetric vortex structures begin to dominate the jet dynamics. In the measurements of Crow and Champagne,<sup>48</sup> wave-like disturbances initiated at the lip of the jet coalesce as they propagate downstream forming longer waves. After

two stages of coalescence, the wave-like disturbances breakdown to vortices (or "puffs"). Strouhal numbers for the formation of waves and of vortices downstream of the nozzle ( $y_1 > (1-2)D_j$ ) are both shown. The Strouhal number for vortex formation was on the order of 0.3; at this frequency the jet could be acoustically driven to larger-magnitude axisymmetric disturbances. Observations of Browand and Laufer<sup>47</sup> disclosed a similar breakdown of wave-like dynamics into vortex-pairing. In both cases, the observed Strouhal number of vortex formation was 0.5. At still larger values of  $R_D$  measurements by Lau, Fisher, and Fuchs<sup>52</sup> of the frequency spectra of velocity and pressure fluctuations in the potential core were peaked about  $fD/U_j \sim 0.5$  to 0.6. This frequency was later confirmed as related to a regular pattern of large vortices by the use of signal-conditioning techniques by Lau and Fisher.<sup>35</sup> The fluctuations sensed in the potential core are impressed by these axisymmetric vortices in the annular mixing layer. In a recent review<sup>143</sup> of some early sound measurements of Powell, it is shown that high Reynolds number tones may be generated by separating flow nozzles. Strouhal frequencies of these tones are roughly 0.45 at Reynolds numbers ranging from  $5 \times 10^5$  to  $9 \times 10^6$ . Also some measurements by Quick<sup>144</sup> and Ho<sup>145</sup> disclose tones emanated by subsonic wall jets at high Reynolds numbers with Strouhal numbers of order 0.38. These tones are clearly seen in photographs to be related to the motion of large vortices of the same form as reported by Crow and Champagne.

Tonal disturbances have also been observed emanating from square-edged orifice plates, (c) of Figure 3.8 by Anderson.<sup>54-60</sup> Strouhal numbers based on the orifice diameter and efflux velocity are shown in Figure 3.12 together with a schematic of the experimental arrangement used. The sloped lines show that the numbers are functions of the ratio of thickness to diameter. For each parameter

$$S_t = \frac{ft}{U_j}$$

the values of  $S_D$  generally range from 0.4 to 1.0. This range corresponds roughly to the observed range of numbers observed for free laminar jets in Figure 3.10. The limit of  $t/D_j = 0$  corresponds to the knife edge orifices used by Beavers and Wilson and Johansen. Parametric dependence of  $S_D$  on  $t/D$  will be discussed at the end of the next subsection.

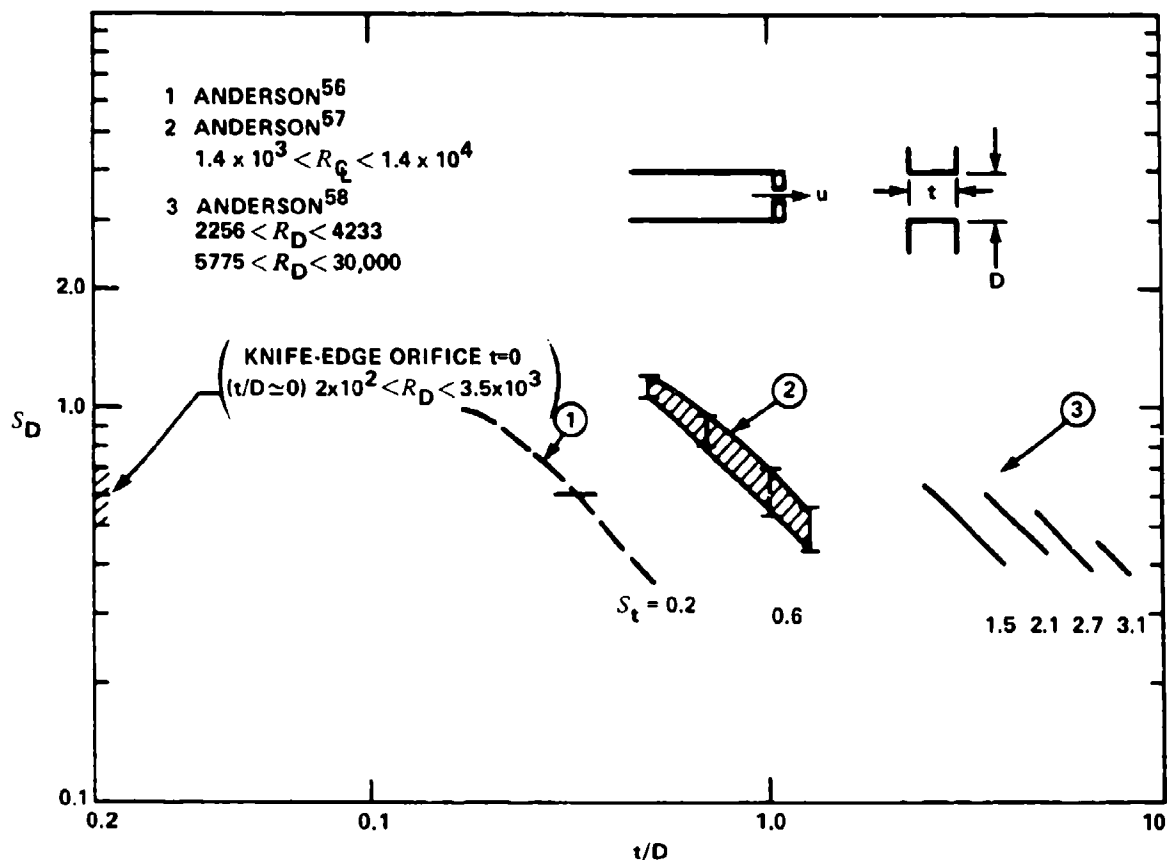


Figure 3.12 - Tone Frequencies for Square-Edge Orifice Plates Terminating a Pipe, from Anderson, Compared with  $S_D$  for Knife-Edged Orifices from Johansen<sup>49</sup> and Beavers and Wilson<sup>63</sup>

### 3.4.2 Hole, Ring, and Edge Tones

The general sensitivity of jets to external stimulation by sound, vibration, and by reflected hydrodynamic and acoustic disturbances is recognized as the primary cause of the many varieties of musical tones observed over the years. It is interesting to note the variety of commonplace observations of such instabilities afforded by acoustically excited flames (Tyndall<sup>61</sup> and Rayleigh<sup>1</sup>), bird calls and whistling tea kettles (Rayleigh<sup>1</sup> and Chanaud and Powell<sup>62</sup>), human whistles (Wilson, Beavers, DeCosler, Holger, and Regenfuss<sup>63</sup>), Pfeifentone (pipe tone),<sup>54-60</sup> and a variety of musical instruments<sup>1</sup> (also, e.g., References 64-67 are some of the more

recent and include interesting bibliographies). The fundamental feature of all these tones is that the jet is an oscillating system, with its available continuum of "resonance" frequencies, becomes dynamically coupled to another mechanical system. Figure 3.11 shows two of the most important generic jet oscillators.

The hole tone, previously discussed, is generated when a plate with a sharp-edged orifice is placed coaxially with a circular jet. Rayleigh<sup>1</sup> discusses in great detail the aspects of construction of this oscillator which is the source of bird calls, tea kettle whistles, and human whistling. Axisymmetric disturbances are caused at the hole which reinforce the initiating disturbances at the efflux. Sound radiation results from the pulsating efflux at the second plate. In the experiments of Chanaud and Powell,<sup>51</sup> the second plate was larger than the wavelength of the sound emanated so that the radiation was omnidirectional. The ring tone<sup>51</sup> works on the same principle, however, the hole is replaced by a coaxial ring. Toroidal vortices shed from the ring cause alternating forces on the ring. These dipoles radiate in the direction of the jet axis. The edge tone, (b) of Figure 3.11 involves the interaction of the asymmetric modes of a jet with a rigid edge. The to and fro oscillation of the jet causes an alternating force on the edge. It generally occurs with two dimensional jets, but it can occur with square circular jets. This force has a reaction at the jet efflux.

The edge tone, which is typical of self-excited jet tones, has been given considerable attention in recent years because of its clear manifestation of the relationship between jet stability and geometric constraint. The relationship between the frequency of the tone and geometry that is generally accepted today has been given by Curle<sup>68</sup> and by Powell.<sup>69</sup> The accepted mechanism of edge tones as given below was first elucidated by Powell.<sup>69,70</sup> The coupling between the edge and the efflux comes about at the generation of a vortex at the edge. This generation occurs when there is a disturbance velocity perpendicular to the edge causing separation and a vortex. As the jet undulates, the transverse velocity (and, therefore, the vortex strength) changes sign. At separation, as a vortex (a) is formed at the edge, a disturbance at the nozzle occurs at (b) which reinforces the direction of deflection. The example of the edge tone carries with it many aspects which are common to all self-sustained tonal fluid-structure interactions. As depicted in Figure 3.13, the shear layer undergoes a spatial amplification of disturbances which are subsequently incident on the edge. The interaction of the edge with the incident flow results in the generation of another disturbance,

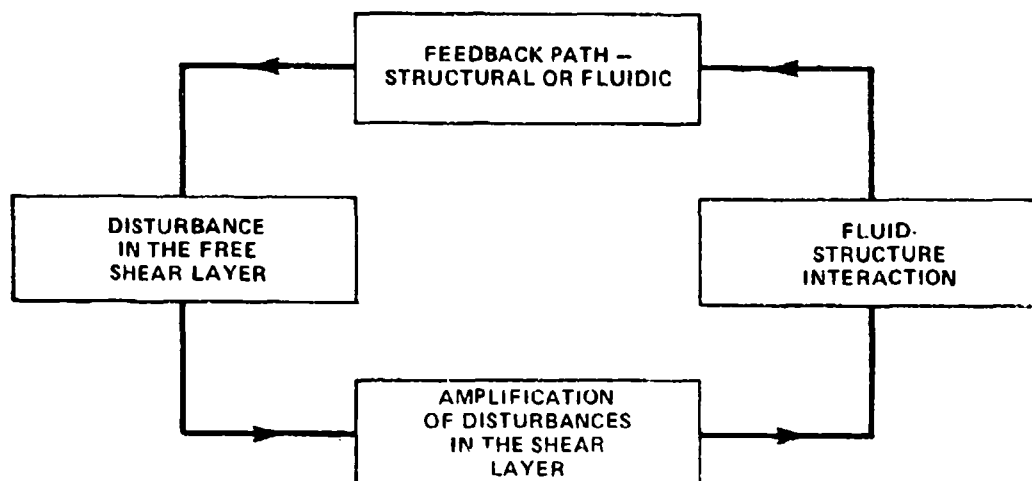


Figure 3.13 - Necessary Ingredients in the Feedback Loop Common to all Self-Sustained Tonal Vibration or Sound Radiation; Characteristic of Many Fluid-Resonator Interactions

often manifested in the production of vorticity. These secondary disturbances occur only because of the presence of the surface in the flow stream and they must be transmitted back to the origin of the initial flow-instability. Reinforcement of this instability is essential for the self-sustained tone and it, therefore, requires the establishment of a distinct phase relationship between the initiating disturbance and the interaction disturbance. The mechanics of transmission of this feedback is varied, depending on the structure geometry and the type of flow. In the case of the edge tone, the feedback was fluid-borne resulting in the formation of lip vorticity at the jet efflux, while in the case of the cavity it was a mode of recirculation of flow entrained beneath the shear flow. The feedback of hole and ring tones is similar to that of the edge tone, but involving symmetric jet modes. Flow over cylinders and hydrofoils, Chapters 5 and 9, results in the formation of a vortex street in the wake. The induced forces on the shedding body can cause that body to vibrate resulting in a structural transmission of a disturbance back to the point of flow separation on the body. Thus, all these self-excitation phenomena must have the elements of a shear layer which is unstable to stimulation, a fluid-structure interaction, and a feedback path. Disruption of any one of these elements will break the loop and reduce the intensity of the tone. Insofar as the disturbances in the jet are sinusoidal, the transverse velocity at the edge will be such as to reinforce the initial direction of efflux disturbance every

1/4 wavelength into a cycle. The geometric constraint on reinforcement is, therefore, deduced from Figure 3.11b as

$$h = n\lambda + \frac{\lambda}{4} \quad \text{for } h = 1, 2, \dots \quad (3.21)$$

where  $\lambda$  is the wavelength of hydrodynamic jet disturbances, which is similar to the relationship derived for cavity-shear-layer interaction (Equation (3.11)). In the event that  $h$  is not small compared to an acoustic wavelength, a phase angle must be included in Equation (3.21). A Strouhal number can then be defined as

$$\frac{fh}{U_J} \sim \frac{C_r}{U_J} \left( n + \frac{1}{4} \right) \quad (3.22)$$

where  $C_r/U_J$  is the average disturbance wave speed from the jet exit to the wedge. This wave speed will depend on the details of the jet efflux and the ratio  $h/D$ ; it is roughly limited by<sup>70</sup>  $0.3 < C_r/U_J < 0.5$ .

To determine the frequency-speed relationships for a given type of jet, the geometric requirements for the tone given by Equation (3.22) must match the conditions for stability. As an example, Figure 3.2 shows that the range of wave numbers of unstable modes is  $0 < \alpha_m \delta < 2$  with the least stable being  $\alpha_m \delta \approx 0.8$ . The length scale  $\delta$  is approximately  $D/3$ , as indicated by the two-dimensional experiments of Sato,<sup>12</sup> so the wavelengths of the unstable modes are crudely determined by the condition

$$\lambda \gtrsim D$$

when  $D$  is the slit height shown in Figure 3-11b. The least stable mode occurs at

$$(\lambda)_{\text{least stable}} \approx 2.5D$$

although the numerical values will vary somewhat from case-to-case. Since



$$\lambda = \frac{C_r}{f} \approx \frac{0.5U_J}{f}$$

these stability requirements will restrict the allowable tones to within the approximate limit

$$0 < \frac{fD}{U_J} < 0.5 \quad (3.23)$$

and

$$\frac{fD}{U_J} = \left( \frac{C_r}{U_J} \right) \left( n + \frac{1}{4} \right) \left( \frac{D}{h} \right) \quad (3.24)$$

although in specific instances these limits will be somewhat governed by Reynolds number, nozzle geometry, and the spacing  $L/D$ .<sup>68-70</sup> Figure 3.14 shows the Strouhal numbers observed by Brown<sup>71</sup> for a two-dimensional jet of width  $D$ . These results are generally in agreement with values reported by Powell<sup>70</sup> at a Reynolds number of 300,

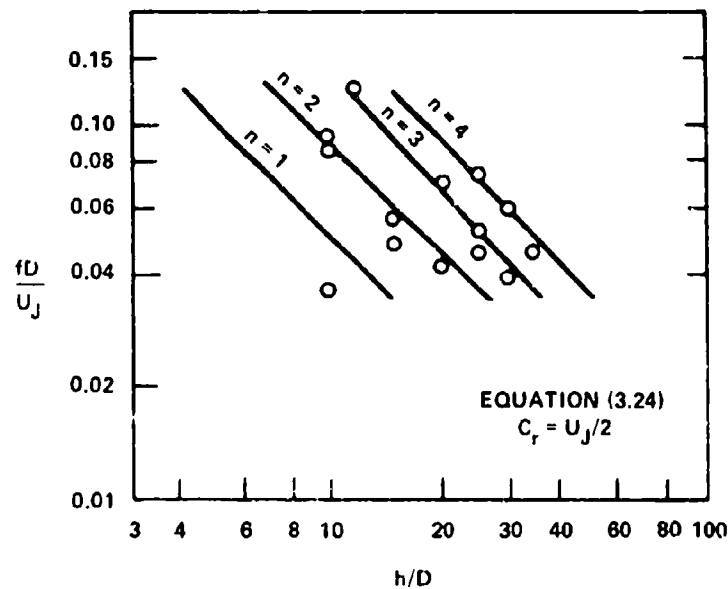


Figure 3.14 - Strouhal Numbers for the First Four Stages of Brown's<sup>72</sup> Edge Tone

although Powell's results disclose a significant dependence on Reynolds number. The important aspect of Figure 3.14, aside from the range of absolute values of  $S_D$  quoted, is the confirmation of the  $n + 1/4$  relationship among various edge tone stages that depend on the Reynolds number and  $h/D$ . Powell quotes Strouhal numbers anywhere from 0.01 to 0.3 for  $100 < R_D < 2400$ ; this dependence on Reynolds number is illustrated in Figure 3.15 with the curve of neutral stability of the two-dimensional jet. The cross-hatched region corresponds to the upper and lower limits of validity of Equation (3.24) which replace the limits in Equation (3.23). There is apparently

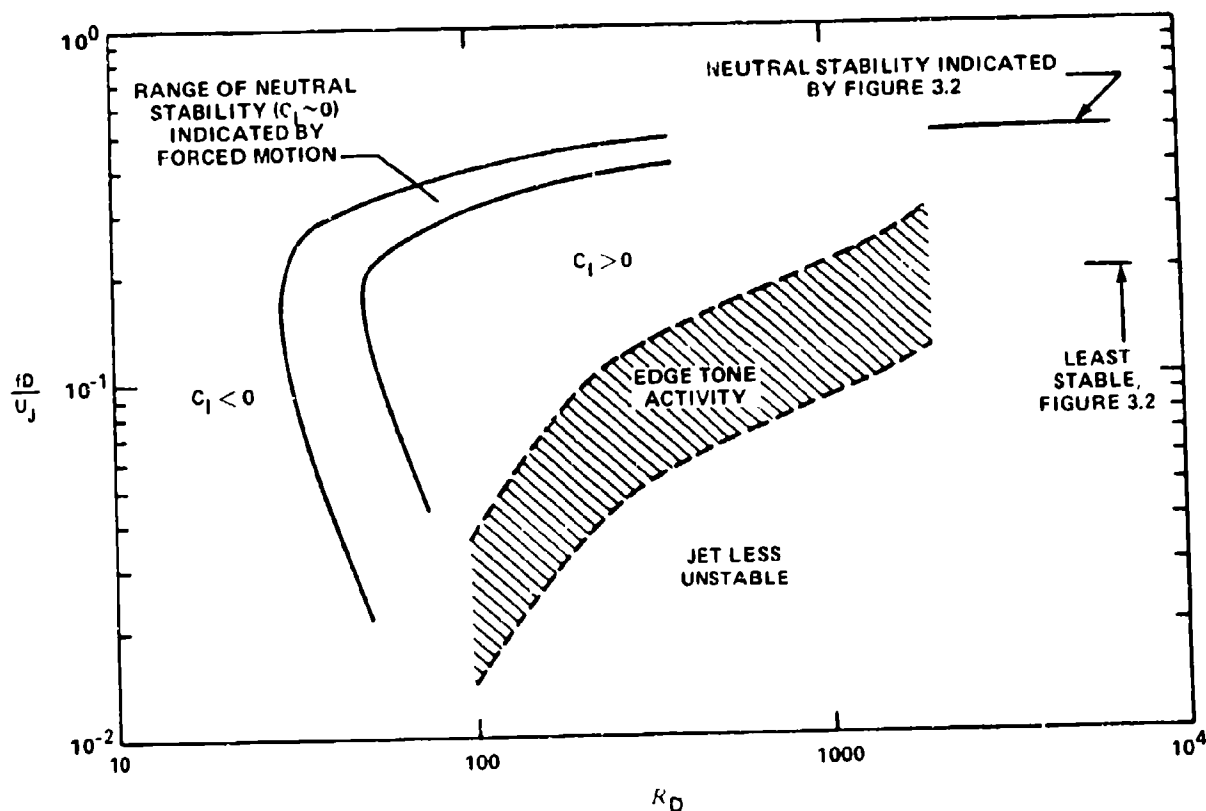


Figure 3.15 - Stability Diagram of the Antisymmetric Mode,  
for Two-Dimensional Laminar Jets (see Fig. 3.3a)  
Showing the Region of Edge Tone Activity  
Observed by Powell<sup>70</sup>

a region  $R_D < \sim 30$  for which no tones exist because the jet is stable, and an upper region  $R_D > 2500$  beyond which the jet is turbulent. There is also apparently a minimum value<sup>62</sup> of  $L/D$  between 2.5 and 4.5 (with the larger value required at low values of  $R_D$ ) for which edge tones will exist.

The unsteady force exerted on the edge by the jet has been shown by Powell<sup>70</sup> to have an amplitude bounded by

$$|F| \lesssim \frac{20}{9} \rho_o U_J^2 L_3 D = \frac{40}{9} q_{J,3} D \quad (3.25)$$

where  $L_3$  is the width and  $D$  is the thickness of the jet. This upper limit was deduced from measurements in air of the sound pressure radiated from laboratory edge tones which showed that the force is actually a function of both  $L/D$  and  $R_D$ . The relationship between the force and the sound pressure is deduced from Equation (2.77), as long as  $L_3$ ,  $D$ , and  $h$  are all less than the wavelength of sound. Letting

$$f_i(t) = |F| e^{-i\omega t}$$

Equation (2.77) gives

$$p_a(r, \omega) = \frac{-i\omega \cos \theta}{4\pi C_o r} |F| e^{ik_o r} \quad (3.26)$$

where  $\omega = 2\pi f$ , and  $\theta = \pi/2$  coincides with the vectorial direction of jet flow. This limit given by Equation (3.25) has been supported<sup>70</sup> by kinematic considerations which take into account the strengths of vortices formed at the edge and their influence on the unsteady transverse momentum of the jet. Therefore, this upper bound is expected to be generally applicable. Both the sound pressure and the force were simultaneously measured by Powell<sup>70</sup> and found to obey Equation (3.26) in magnitude and directivity. This represents one of the earliest unambiguous confirmations of Curle's theory.

The hole tone of Chanaud and Powell<sup>62</sup> (Figures 3.10 and 3.11a) can now be interpreted. For  $h/D > (h/D)_{crit}$ , the tone was emitted at one or more Strouhal numbers contained within the cross-hatched zone of Figure 3.10 in the region  $900 < R_D < 2500$ . For a given value  $h/D$ , the Strouhal number was constant over a

range of  $R_D$  and it would change to a second stage at some critical value of  $R_D$ . For example, at  $h/D = 3$ ,  $S_D \approx 0.5$  for  $1350 < R_D < 1900$ , changing to  $S_D \approx 0.65$  at  $R_D = 1900$  and continuing at this value until  $R_D = 2500$ . When the Reynolds number is reduced by reducing speed, this value of  $S_D$  was maintained down to  $R_D = 1400$  when  $S_D$  reverted to  $\sim 0.5$ . This type of hysteretic behavior is commonly observed in self-sustained fluid oscillations.

The behavior of the Strouhal numbers observed by Anderson, shown in Figure 3.12, may also be interpreted in the above terms. Flow in sharp-edged orifices observed by Kurzweg<sup>72</sup> disclosed a train of axisymmetric ring vortices. Parallel to Equations (3.11) and (3.20), we write this condition as

$$t = n\Lambda$$

where  $\Lambda$  = vortex spacing

$t$  = thickness of the orifice plate

$n$  = integral number of vortices in the orifice

Letting

$$\frac{f\Lambda}{U_J} = \Omega = \text{constant}$$

where  $U_J$  is the velocity of the orificial flow, so that

$$S_t = \frac{ft}{U_J} = n\Omega \quad \text{for } n \geq 1$$

describes the Strouhal numbers for the various stages of tones. If we let the allowable range of  $S_D$  for the jet to be between  $0.2 < S_D < 1$  (as suggested by Figure 3.10) at the appropriate value of  $R_D$ , then the dependence of stages on  $d/t$  is given by

$$0.2 < S_D = \left(\frac{d}{t}\right) (S_t) < 1$$

which corresponds to the diagonal lines shown in Figure 3.12 with the indicated values of  $S_t$ .

### 3.5 A SUMMARY OF STATISTICAL DESCRIPTIONS OF TURBULENCE

#### 3.5.1 General Comments

We have seen that in the case of jets and all other flows, the disturbances become disordered, or random, at large values of Reynolds number. In order to conveniently deal with such disordered flows, it has been necessary to look toward statistical representations which usefully characterize the average, or expected, behavior of certain properties of the flow. These properties generally include fluctuating velocities in the turbulent region, fluctuating pressures, and density fluctuations. When radiated sound is the result of a random, or turbulent, process, then the far field sound pressure will be a temporary random variable. Therefore, in order to apply the deterministic relationships derived in Chapter 2 to realistic noise-producing flows, techniques have been developed for relating the statistics of flow fields to statistics of radiated sound. An example of the use of a deterministic Green function for sound production from a field of random (in time and spatial distribution) sources has already been given in Equations (2.125) and (2.133). In this section we will extend our analysis to cover alternative statistical formulations and apply them, in an elementary way, to the production of sound from turbulent jets.

The foundations of the modern statistical approaches to turbulence measurement are probably found in Taylor's series of papers on the statistics of isotropic turbulence<sup>73</sup> and on the spectrum of turbulence.<sup>74</sup> In these, the interrelationships between time and space through eddy convection were first realized, and methods of extracting measures of the largest and smallest eddies through correlation were outlined. In the forty years since, the importance of these statistical measures has become well-recognized. Electronic instrumentation has also become more sophisticated allowing observations of identifiable turbulence events through the merits of signal conditioning; interpretations of correlations have, therefore, recently matured, leading to more elaborate hypotheses of turbulence structure which relate to the production and maintenance of turbulence in virtually all forms of turbulent shear layers; jets, wakes, and boundary layers. The most extensive treatments of stochastic representations of many types of flows are those of Batchelor,<sup>75</sup> Hinze,<sup>76</sup> Townsend,<sup>77</sup> and Lumley.<sup>78</sup> The reader is referred to these sources for rigorous derivations and theorems of mathematical validity. Our discussions will deal with review and applications.

Noise and vibration are caused by fluidic and structural reactions to the contiguous turbulent field. In Chapter 2 linear cause and effect deterministic relationships were derived for the radiation process and in Chapter 6 similar relationships will be derived for structural response as well. In either case the input is stochastic, the transfer function is postulated as linear, so that the output of the linear system is also stochastic. The fundamentals in the treatment of these systems have been developed in communication theory (see for example Reference 79), with subsequent development<sup>80</sup> of sampling criteria, frequency-time relationships, and nonstationarity. Treatises on the application of these techniques to physical systems have been developed for the generation of water waves<sup>81</sup> and the vibration of structures by random disturbances.<sup>82-84</sup>

### 3.5.2 Correlation Functions of Random Variables

In the formal treatment of random phenomena, the variable in question, for example, a vector component of velocity or a pressure, has a certain probability of attaining a value. Giving the symbol  $u'$  to the random property and the symbol  $P(u')$  to its probability of occurrence, then if the disturbance is to occur at all we have

$$\int_{-\infty}^{\infty} P(u') du \equiv 1 \quad (3.27)$$

i.e., there is certainty that  $u$  will have some value between plus infinity and minus infinity. The average of  $u'$ , or the expectation of  $u$ , is defined as

$$\begin{aligned} E(u') &= \int_{-\infty}^{\infty} u' P(u') du' \\ &= \bar{u} \end{aligned} \quad (3.28)$$

Equation (3.28) is also called the first moment of  $P(u)$ . In the hydroacoustic sense, Equation (3.28) just defines the mean velocity, or in the case of pressures, the

static pressure of the random quantity. A third property of the probability is the mean square,

$$\begin{aligned} E(u'^2) &= \int_{-\infty}^{\infty} u'^2 P(u') du' \\ &= \overline{u'^2} \end{aligned} \quad (3.29)$$

and the variance is defined as

$$\text{Var}(u') = E(u'^2) - (E(u'))^2 \quad (3.30)$$

In fluid mechanical applications, the manipulations of relationships are simplified by treating the random variable as a variation about the mean. This permits us to decouple the mean and turbulent motions, finding first the mean, or steady, component of velocity or pressure and then deduce the behavior of the random component to varying degrees of precision. In this way, the random motion is viewed as superimposed on the mean flow. Thus, if we have been defining our random variable as

$$u' = \bar{U} + u$$

with a probability density of  $u$  given by  $P(u)$ , then it is easy to apply Equations (3.27) through (3.30) to see that

$$E(u) = 0$$

and

$$\begin{aligned} E(u^2) &= \overline{u^2} \\ &= \text{Var}(u^2) \end{aligned}$$

which are simpler relationships to deal with.

To apply these notions to the problem of describing real turbulence quantities which are random in time and space, let

$$u = u(\vec{y}, t)$$

where  $\vec{y}$  is the space variable and  $t$  is time. The joint expectation of  $u$  at locations  $\vec{y}_1$  and  $\vec{y}_2$  and times  $t_1$  and  $t_2$  is a generalization<sup>75,82</sup> of Equation (3.29)

$$\begin{aligned} E[u(\vec{y}_1, t_1) u(\vec{y}_2, t_2)] &= \langle u(\vec{y}_1, t_1) u(\vec{y}_2, t_2) \rangle \\ &= \int_{-\infty}^{\infty} u(\vec{y}_1, t_1) u(\vec{y}_2, t_2) P(u(\vec{y}_1, t_1)) \\ &\quad \times P(u(\vec{y}_2, t_2)) du(\vec{y}_1, t_1) du(\vec{y}_2, t_2) \end{aligned} \quad (3.31)$$

The brackets  $\langle \rangle$  will henceforth denote the taking of an ensemble average in the formal sense. If the functions  $P(u(\vec{y}, t))$  are independent of spatial position, then Batchelor calls  $u(\vec{y}, t)$  a spatially homogeneous random variable. The ensemble average  $\langle u(\vec{y}_1, t) u(\vec{y}_2, t) \rangle$  is called a covariance or a correlation function. It is independent of the origin of  $\vec{y}_1$ , but it is dependent on the relative separation of  $\vec{y}_1$  and  $\vec{y}_2$ . Alternatively, when  $P(u)$  and, therefore, the ensemble average, is independent of the time, but dependent on time difference,  $\tau = t_2 - t_1$ , then  $u$  is temporally homogeneous or temporally stationary.

To carry out the integration in Equation (3.31) in practice,  $u(y_1, t_1)$  and  $u(y_2, t_2)$  would have to be sampled in a large number of experiments and then the integration performed over the complete ensemble of all possible values. This being impractical we seek simpler alternative approaches in which the formal operation of Equation (3.31) is replaced by a time or a space average. That is, we define the temporal average



$$\overline{u(y_1, t_1) u(y_2, t_2)}^t = \overline{u(y_1, t) u(y_2, t+\tau)}^t$$

$$= \lim_{T \rightarrow \infty} \frac{1}{T} \int_{-T/2}^{T/2} u(y_1, t) u(y_2, t+\tau) dt \quad (3.32)$$

and the spatial average

$$\overline{u(\vec{y}_1, t_1) u(\vec{y}_2, t_2)}^{\vec{y}} = \overline{u(\vec{y}_1, t_1) u(\vec{y}_1 + \vec{r}, t_2)}^{\vec{y}}$$

$$= \lim_{V \rightarrow \infty} \frac{1}{V} \int_V u(\vec{y}, t_1) u(\vec{y}_1 + \vec{r}, t_2) d\vec{y} \quad (3.33)$$

In order to carry out this procedure. When

$$\langle u_1 u_2 \rangle \equiv \overline{u_1 u_2}^t \quad (3.34)$$

$$\langle u_1 u_2 \rangle \equiv \overline{u_1 u_2}^y \quad (3.35)$$

the process is said to be ergodic; there are certain formal requirements for ergodicity that are described in References 79 through 82.

It will be assumed in this monograph that Equation (3.34) holds, unless it is stipulated otherwise. This assumption is typical of the fluid dynamics of turbulence. The relationship of Equation (3.35), however, does not generally hold for all types of flow. Specifically, the disturbances in developing jets, wakes, and transitional boundary layers do not satisfy spatial homogeneity. Fully developed turbulent boundary layers also do not strictly satisfy Equation (3.34), however, they are generally assumed to do so. This assumption is required in order to develop theorems for the description of the response of contiguous structures, Chapters 6 and 7, in terms of boundary layer properties. Even though many flows do

not formally satisfy Equation (3.35), their correlation volumes are often small compared to the extent of the developing flow so that making the assumption leads to accurate predictions.

### 3.5.3 Frequency and Wave Number Spectra

In this section we will generalize the stochastic representations of Section 2.6.2 into time and thus space dimensions. In the case of the time variable we have already dealt with the frequency auto- and cross-spectral densities. Since  $u(\vec{y}, t)$  is a stationary random variable, then the Fourier transform of Equation (2.105)

$$u(\vec{y}, \omega) = \frac{1}{2\pi} \int_{-\infty}^{\infty} e^{+i\omega t} u(\vec{y}, t) dt$$

is also a stationary random variable. Using this definition, we have derived the cross-spectral density of  $u$  at  $\vec{y}_1$  and  $\vec{y}_2$  in Section 2.6.2 to be

$$\overline{u(\vec{y}_1, t) u(\vec{y}_2, t+\tau)} = \int_{-\infty}^{\infty} \lim_{T \rightarrow \infty} \left[ \frac{2\pi u(\vec{y}_1, \omega) u^*(\vec{y}_2, \omega)}{T} \right] e^{-i\omega\tau} d\omega \quad (3.36)$$

The cross spectral density is defined as the Fourier transform of  $\overline{u(\vec{y}_1, t) u(\vec{y}_2, t+\tau)}$ , i.e., define

$$\phi_{uu}(\vec{y}_1, \vec{y}_2, \omega) = \frac{1}{2\pi} \int_{-\infty}^{\infty} \overline{u(\vec{y}_1, t) u(\vec{y}_2, t-\tau)} e^{i\omega\tau} d\tau \quad (3.37)$$

where  $u_1 = u(\vec{y}_1, t)$  etc., with an inverse

$$\overline{u(\vec{y}_1, t) u(\vec{y}_2, t+\tau)} = \int_{-\infty}^{\infty} \phi_{uu}(\vec{y}_1, \vec{y}_2, \omega) e^{-i\omega\tau} d\omega \quad (3.38)$$

therefore, by identity

$$\Phi_{uu}(\vec{y}_1, \vec{y}_2, \omega) \delta(\omega - \omega') \equiv \lim_{T \rightarrow \infty} \frac{2\pi u(\vec{y}_1, \omega) u^*(\vec{y}_2, \omega')}{T} \quad (3.39)$$

which is independent of  $T$ .

This derivation could have proceeded along simpler lines if we had just taken the ensemble average:<sup>75,81</sup>

$$\begin{aligned} \langle u(\vec{y}_1, t) u(\vec{y}_2, t+\tau) \rangle = \\ \int_{-\infty}^{\infty} \int_{-\infty}^{\infty} \langle e^{i(\omega - \omega')t} \rangle \langle u(\vec{y}_1, \omega) u^*(\vec{y}_2, \omega') \rangle d\omega' \cdot e^{-i\omega\tau} d\omega \end{aligned} \quad (3.40)$$

where

$$\langle \exp(i(\omega - \omega')t) \rangle = \int_{-\infty}^{\infty} e^{i(\omega - \omega')t} dt = 2\pi \delta(\omega - \omega') \quad (3.41)$$

The equivalence of Equations (3.38) and (3.40) requires the cross-spectral density to be given by

$$\Phi_{uu}(\vec{y}_1, \vec{y}_2, \omega) = \int_{-\infty}^{\infty} e^{i(\omega - \omega')t} \langle u(\vec{y}_1, \omega) \cdot u(\vec{y}_2, \omega') \rangle d\omega' \quad (3.42)$$

If the cross spectral density is to be independent of time  $t$ , then this requires the equivalence,

$$\langle u(\vec{y}_1, \omega) u^*(\vec{y}_2, \omega') \rangle \equiv \Phi_{uu}(\vec{y}_1, \vec{y}_2, \omega) \delta(\omega - \omega') \quad (3.43)$$

Equations (3.39) and (3.43) are equivalent ways of formally relating the generalized Fourier transform of a random variable to the cross-spectral density.

For spatially homogeneous flow fields, the correlation functions for positions  $\vec{y}_1$  and  $\vec{y}_2$  may be considered independent of reference location. Accordingly, just as in the case of Equation (2.129),  $\phi_{uu}(\vec{y}_1, \vec{y}_2, \omega)$  depends only on the separation vector, i.e.,

$$\phi_{uu}(\vec{y}_1, \vec{y}_2, \omega) = \phi_{uu}(\vec{y}_2 - \vec{y}_1, \omega)$$

In the following chapters the multidimensional space-time Fourier transform will be used. This is defined as

$$u(k_1 \dots k_n, \omega) =$$

$$\frac{1}{(2\pi)} \frac{1}{(2\pi)^n} \int_{-\infty}^{\infty} dy_1 \dots \int_{-\infty}^{\infty} dy_n \int_{-\infty}^{\infty} dt u(\vec{y}, t) e^{-i[(k_1 y_1 + \dots k_n y_n) - \omega t]}$$

where  $n$  varies from 1 to 3 space dimensions. The relationship equivalent to Equation (3.39) for spatially-homogeneous fields requiring both space and time averaging is (for  $k_i L_i \rightarrow \infty$ )

$$\begin{aligned} \phi_{uu}(k_1 \dots k_n, \omega) \delta(\omega - \omega') \delta(k_1 - k'_1) \dots \delta(k_n - k'_n) \equiv \\ \frac{(2\pi)^n}{L_1 \dots L_n} \frac{2\pi}{T} u_1(k_1 \dots k_n, \omega) u_2^*(k_1 \dots k_n, \omega) \end{aligned} \quad (3.44)$$

or

$$\begin{aligned} \phi_{uu}(k_1 \dots k_n, \omega) \delta(\omega - \omega') \delta(k_1 - k'_1) \dots \delta(k_n - k'_n) \equiv \\ \langle u_1(k_1 \dots k_n, \omega) u_2^*(k'_1 \dots k'_n, \omega') \rangle \end{aligned} \quad (3.45)$$

rather than Equation (3.43). The function  $\phi_{uu}(k_1 \dots k_n, \omega)$  has already been called the wave number frequency spectral density of the disturbance  $u$ .

For spatially and temporally stationary variables

$$\overline{u_1^2} \equiv \overline{u_2^2} = \overline{u^2}$$

The autospectrum  $\Phi(\omega)$ , the cross-spectrum  $\Phi(\vec{r}, \omega)$  and the wave number frequency spectrum  $\Phi(\vec{k}, \omega)$  are related to correlation functions. These relationships which form the cornerstone of hydroacoustics will be used extensively throughout this monograph. The temporal autocorrelation is

$$\langle u(\vec{y}, t) u(\vec{y}, t+\tau) \rangle = \langle u^2 \rangle R_{uu}(\tau) \quad (3.46)$$

so that the autospectrum function is

$$\frac{\Phi_{uu}(\omega)}{\langle u^2 \rangle} = \frac{1}{2\pi} \int_{-\infty}^{\infty} e^{i\omega\tau} R_{uu}(\tau) d\tau \quad (3.47)$$

The variable  $u$  could represent any combination of physical variables, pressure, velocity, acceleration, displacement, etc.

The cross-spectral density and the wave number spectrum are related to the space-time correlation of two variables  $a$  and  $b$

$$\langle a(\vec{y}, t) b(\vec{y}+\vec{r}, t+\tau) \rangle = [\langle a^2(\vec{y}) \rangle \langle b^2(\vec{y}+\vec{r}) \rangle]^{1/2} R_{ab}(\vec{r}, \tau) \quad (3.48)$$

If the field is spatially homogeneous the

$$\langle a^2(\vec{y}+\vec{r}, t) \rangle = \langle a^2(\vec{y}, t) \rangle \quad (3.49)$$

and the cross-spectral density is, by Equation (3.37)

$$\frac{\Phi_{ab}(\vec{r}, \omega)}{[\langle a^2 \rangle \langle b^2 \rangle]^{1/2}} = \frac{1}{2\pi} \int_{-\infty}^{\infty} e^{i\omega\tau} R_{ab}(\vec{r}, \tau) d\tau \quad (3.50)$$

For a nonhomogeneous field, Equation (3.49) does not hold and accordingly the cross correlation is not a function of the separation only, rather it is, in general, a function of the  $\vec{y}$  and  $\vec{y} + \vec{r}$  variables separately. Occasionally, for simplicity, the nonhomogeneity is handled by retaining separate dependence on  $\vec{y}$  and  $\vec{y} + \vec{r}$  in the mean square variables and retaining  $R_{ab}(\vec{y}, \vec{y} + \vec{r}, \tau)$  as a function only of  $\vec{r}$  and  $\tau$ , i.e.,  $R_{ab}(\vec{r}, \tau)$ .

The n-dimensional wave number spectrum is

$$\begin{aligned} \phi_{ab}(k_1, \dots, k_n, \omega) &= \frac{1}{(2\pi)^{n+1}} \int_{-\infty}^{\infty} \cdot \int e^{i\omega\tau - (k_1 r_1 + \dots + k_n r_n)} \\ &\times [\langle a^2(\vec{y}) \rangle \langle b^2(\vec{y} + \vec{r}) \rangle]^{1/2} R_{ab}(\vec{r}, \tau) \\ &\times dr_1 \dots dr_n d\tau \end{aligned} \quad (3.51)$$

where  $n = 1, 2$ , or  $3$  for n-dimensional  $\vec{r}$  and where, again, we have dropped the mean-square values for simplicity. The convention used in this monograph places the mean flow vector along the (1) axis with the lateral direction along the (3) axis or in the tangential direction for cylindrical flows,  $dU/dy_3 = 0$  generally. The cross stream, where usually  $U_1$  varies to produce shear (i.e.,  $dU_1/dy_2 \neq 0$ ), is given either the (2) axis or the radial direction. It is especially in the  $y_2$  or  $r$  direction that statistical homogeneity does not hold in a shear flow. Then Equation (3.51) becomes

$$\begin{aligned} \phi_{ab}(k_1, k_3, \omega, y_2, y_2') &= \frac{1}{(2\pi)^3} \iiint_{-\infty}^{\infty} e^{i(\omega\tau - k_1 r_1 - k_3 r_3)} [\langle a^2(\vec{y}) \rangle \langle b^2(\vec{y} + \vec{r}) \rangle]^{1/2} \\ &R_{ab}(r_1, r_3, \tau; y_2, y_2') \times dr_1 dr_3 d\tau \end{aligned}$$

This convention denotes the correlation function as homogeneous in  $y_1$ ,  $y_3$ , and nonhomogeneous as  $(y_2, y_2') = (y_2, y_2 + r_2)$ .

The correlation functions used in this monograph will always have the normalizations implied by Equations (3.46) or (3.48). Therefore, by definition

$$\lim_{\vec{r} \rightarrow 0} R_{ab}(\vec{r}, \tau) = R_{ab}(0, \tau) = R_{ab}(\tau) \quad (3.52)$$

and

$$\lim_{\tau \rightarrow 0} R(\tau) = R(0) = 1.0 \quad (3.53)$$

In general they shall have the property

$$R_{ab}(0, 0) \geq R_{ab}(\vec{r}, \tau)$$

Spectral density functions will be normalized as above so that

$$[\langle a^2 \rangle \langle b^2 \rangle]^{1/2} = \int_{-\infty}^{\infty} d\omega \int_{\text{all } \vec{k}} d\vec{k} \phi_{ab}(\vec{k}, \omega) \quad (3.54)$$

and

$$\phi_{ab}^{(in)} = \int_{\text{all } \vec{k}} d\vec{k} \phi_{ab}(\vec{k}, \omega) \quad (3.55)$$

Occasionally, throughout the text normalized spectrum functions will be used so that the integral Equation (3.54) will be unity instead of the product of root mean squares. In such cases, the lower case symbol  $\phi$  rather than  $\Phi$  will be used.

## 3.6 FUNDAMENTALS OF NOISE FROM SUBSONIC TURBULENT JETS

### 3.6.1 Formal Analytical Relationships for Source Convection

In this section we will discuss some of the well-known characteristics of noise from cold subsonic turbulent jets. Explanations of those properties in terms of the statistical parameters of the turbulence structure will also be given. Noise from developing jets, being quadrupole in nature, is not generally a dominant source at the very low Mach numbers that are typical of hydroacoustic problems. We will consider this type of noise because of its historical importance, it being a

prime-mover for Lighthill's work, and because it provides an excellent example of the marriage of general hydroacoustic theory and the classical problems of describing the stochastic properties of turbulent flow. The problems of theoretically describing jet noise, even of subsonic jets, go far beyond the simple dimensional analysis that was offered in Section 2.3.3. The reader will find more extensive discussions of jet noise given by Goldstein<sup>85</sup> as well as a recent review of the subject by Powell.<sup>21</sup> As a practical circumstance, jet noise can be an hydroacoustic problem when the efflux is turbulent or when it contains density gradients (as with two-phase fluids). In these cases, the noise may be monopole or dipole rather than quadrupole.

The treatment of Section 2.3.3 considered only the most rudimentary aspects of shear-flow noise, overlooking the real problems of source-convection, developing flow, and the correlation volume of physical eddies. That analysis also overlooked the essential spatial matching of the sound field with the disturbance field and the effect of source convection on the sound power radiated.\* To examine the effects of mean convection of the sources in a medium at rest; begin by considering again Equation (2.60) in light of the preceding descriptors of random variables. Define the generalized four-dimensional Fourier transform of the stress tensor  $T_{ij}(\vec{y}, t)$ , as

$$T_{ij}(\vec{y}, t) = \iiint_{-\infty}^{\infty} T_{ij}(\vec{k}, \omega) e^{+i(\vec{k} \cdot \vec{y} - \omega t)} d^3\vec{k} d\omega$$

where the transformed variable is distinguished from the real variable by noting its independent variables. Therefore, we have

$$\frac{\partial^2 T_{ij}(\vec{y}, t)}{\partial t^2} = - \iiint_{-\infty}^{\infty} \omega^2 T_{ij}(\vec{k}, \omega) e^{i(\vec{k} \cdot \vec{y} - \omega t)} d^3\vec{k} d\omega \quad (3.56)$$

---

\*An additional modification to the theory that will not be considered here is the refraction of the emitted sound by the enshrouding shear layer. This convection of the sound by the mean flow, distinct from the convection of the sources, affects the directivity of the sound at angles that are not perpendicular to the jets axis.<sup>86,87</sup> Generally, the results obtained in this section will be valid near broad-side radiation at low Mach number.



and the value of this variable at the retarded time is written as

$$\left[ \frac{\partial^2 T_{ij}(\vec{y}, t)}{\partial t^2} \right] = - \iiint_{-\infty}^{\infty} \omega^2 T_{ij}(\vec{k}, \omega) e^{i(\vec{k} \cdot \vec{y} - \omega t)} e^{i\omega r/c_0} d\vec{k} d\omega \quad (3.57)$$

The radiated far field sound pressure is given by substituting Equation (3.57) into Equation (2.60) to obtain (with  $p_a(\vec{x}, t) \equiv c_0^2(\rho(\vec{x}, t) - \rho_0)$ )

$$p_a(\vec{x}, t) = - \frac{1}{4\pi} \frac{1}{c_0^2 r} \frac{x_i x_j}{r^2} \iiint_{-\infty}^{\infty} \cdot \iiint_{-\infty}^{\infty} \omega^2 T_{ij}(\vec{k}, \omega) e^{i(\vec{k} \cdot \vec{y} - \omega t)} e^{i\omega r/c_0} d\vec{k} d\omega d\vec{y} \quad (3.58)$$

summation over all combinations of  $i, j$  is assumed. Integration over  $\vec{y}$  extends over the turbulence volume. Equation (3.58) expresses the sound pressure in terms of the spatial transform of the sources and it can be used to identify the manner in which the sources cause the sound. A similar methodology has been used by Ffowcs Williams<sup>88</sup> and by Crighton.<sup>89</sup> Equation (3.58) can be further manipulated when the source location vector  $\vec{y}_0$  is decomposed into a component  $y_r$  along the range vector  $\vec{r}$  and components in the plane normal to  $\vec{r}$ , see Figure 3.16. Therefore,

$$\vec{r} = \vec{r}_0 - \vec{y}_r$$

where  $\vec{r}_0$  is some reference range. The phases of exponentials in Equation (3.57) can then be rearranged to be  $(k_0 = \omega/c_0)$

$$\vec{k} \cdot \vec{y} + k_0 r_0 =$$

$$k_n \cdot \vec{y}_n + k_0 r_0 + (k_r - k_0) y_r$$

where

$$k^2 = k_n^2 + k_r^2$$



$$\phi_{ijk\ell}(\vec{k}, \omega) = \frac{1}{(2\pi)^4} \iiint_{-\infty}^{\infty} e^{-i(\vec{k} \cdot \vec{r} - \omega \tau)} \overline{T_{ij}(\vec{y}, t) T_{ij}(\vec{y} + \vec{r}, t + \tau)} d\vec{r} d\tau \quad (3.60)$$

it is only approximately independent of  $\vec{y}_1$  and since  $T_{ij}$  is unequal to zero only inside the region of turbulence,  $V_J$ , so the integral only formally extends to  $\pm\infty$ . Equation (3.59) is in the same form as Equation (2.133) and represents one of those circumstances where the wave number spectrum must be evaluated in approximate forms. The integration over  $\vec{y}$  is carried out in the same fashion as in Equation (3.41) and yields a product of delta functions, i.e.

$$\iiint_{-\infty}^{\infty} e^{-i(k_r - k_o)y_r} e^{-i(\vec{k}_n \cdot \vec{y}_n)} d^3\vec{y} = \iiint_{-\infty}^{\infty} e^{i(k - k_o \cos \phi)|y|} d^3\vec{y}$$

$$= (2\pi)^3 \delta(k - k_o \cos \phi)$$

or

$$= (2\pi)^3 \delta(k_r - k_o) \delta(\vec{k}_n) \quad (3.61)$$

which is equivalent to  $|G_y(\vec{k}, \omega)|^2$  in Equation (2.133), where  $k^2 = k_r^2 + k_n^2$  and  $k_r = k/\cos \phi$  is the trace wave number in the direction of the observer. If the wave number spectrum is replaced by a value averaged over the source region, then Equations (3.59) and (3.61) give an autospectrum of the sound pressure

$$\phi_p(\vec{x}, \omega) = \frac{1}{16\pi^2} \frac{1}{c_o^4 r^2} \left( \frac{x_1 x_j x_k x_\ell}{r^4} \right) \omega^4 [V_J \overline{\phi_{ijk\ell}(k_r = k_o, \omega)}] \quad (3.62)$$

where  $\langle p^2(\vec{x}) \rangle = \int_{-\infty}^{\infty} \phi_p(\vec{x}, \omega) d\omega$  defines the autospectrum, and the vinculum over the

spectrum function symbolizes the volume average. We shall see that the wave number spectrum  $\phi_{ijk\ell}(\vec{k} \rightarrow 0, \omega)$  is interpreted (e.g., Equations (3.107) and (3.109)) as a correlation volume of the turbulence. Summation still extends over all combinations  $i, j, k, \ell$ .

To include the influence of rectilinear mean convection of the sources on the radiated sound, we note that the Fourier transform introduced in Equation (3.56) is relative to a fixed frame of reference. To compensate for the mean motion of the sources, the fixed coordinate  $\vec{y}$  moving with eddy field,

$$\vec{y}_0 = \vec{y} - \vec{U}_c t$$

and the source term in the moving frame is denoted by  $\tilde{T}_{ij}(\vec{y}_0, t)$ . Therefore,

$$T_{ij}(\vec{y}, t) = \tilde{T}_{ij}(\vec{y} - \vec{U}_c t)$$

and the generalized Fourier transform is

$$\begin{aligned} T_{ij}(\vec{k}, \omega) &= \frac{1}{(2\pi)^4} \iiint_{-\infty}^{\infty} T_{ij}(\vec{y}, t) e^{-i(\vec{k} \cdot \vec{y} - \omega t)} d\vec{y} dt \\ &= \frac{1}{(2\pi)^4} \iiint_{-\infty}^{\infty} \tilde{T}_{ij}(\vec{y} - \vec{U}_c t, t) e^{-i(\vec{k} \cdot \vec{y} - \omega t)} d\vec{y} dt \\ &= \frac{1}{(2\pi)^4} \iiint_{-\infty}^{\infty} \tilde{T}_{ij}(\vec{y}_0, t) e^{-i(k_0 y_0 - [\omega - (\vec{k} \cdot \vec{U}_c)] t)} d\vec{y}_0 dt \\ &= \tilde{T}_{ij}(\vec{k}, \omega - \vec{U}_c \cdot \vec{k}) \end{aligned}$$

The wave number frequency spectrum is then given by

$$\Phi_{ijkl}(\vec{k}, \omega) = \tilde{\Phi}_{ijkl}(\vec{k}, \omega - \vec{U}_c \cdot \vec{k})$$

where  $\tilde{\Phi}_{ijkl}(\vec{k}, \omega)$  is the spectrum determined in the frame moving with the eddy. The spectrum of radiated sound then becomes (with  $\vec{U}_c \cdot \vec{k} = U_c k_r = U_c k_r \cos \theta$  and  $M_c = U_c / c_0$ )

$$\phi_p(\vec{x}, \omega) \sim \frac{1}{16\pi^2} \frac{1}{c_o^4 r^2} \left( \frac{x_i x_j x_k x_\ell}{r^4} \right) \frac{\Omega^4}{(1-M_c \cos \theta)^4} \left[ v_J \overline{\tilde{\phi}_{ijkl}(k_r=k_o, \Omega)} \right] \quad (3.63)$$

where  $\Omega = \omega(1-M_c \cos \theta)$  accounts for a frequency shift due to source convection in the direction of the observer, and the time-averaged acoustic intensity is

$$I(x) = \frac{1}{16\pi^2} \frac{1}{c_o^5 r^2} \left( \frac{x_i x_j x_k x_\ell}{r^4} \right) (1-M_c \cos \theta)^{-5} \times \left[ v_J \int_{-\infty}^{\infty} \overline{\Omega^4 \tilde{\phi}_{ijkl}(k_r=k_o, \Omega)} d\Omega \right] \quad (3.64)$$

### 3.6.2 Measured Characteristics of Jet Noise

These formulas show that the radiated sound will be caused by the stress tensor at all wave numbers whose component in the radial direction equals  $k_o$ . The mean-square sound intensity in a frequency band  $\Delta\omega$  which is proportional to the center frequency of the band, i.e.,  $\Delta\omega \propto \omega$  will depend on the jet parameters as

$$I(x, \omega, \Delta\omega) = \frac{\rho_o U_1^8 D^2}{c_o^5 (1-M_c \cos \theta)^5 r^2} \cdot D(\Omega, \theta) \quad (3.65)$$

where

$$D\left(\frac{\Omega D}{U_J}, \theta\right) = \sum_{ijkl} \left\{ \frac{\pi}{2} \cdot \frac{x_i x_j x_k x_\ell}{r^4} \cdot \frac{v_J}{D^3} \int_{\Delta\Omega} \left( \frac{\Omega D}{U_J} \right)^4 \frac{\tilde{\phi}_{ijkl}(k_o, \Omega) d\Omega}{\rho_o^2 U_J^4 D^3} \right\}$$

where the term in brackets has been summed over all combinations of  $ijkl$  and it depends only on frequency and angle  $\theta$ . Equation (3.65) is the fundamental similarity formula of jet noise which was first derived by Lighthill<sup>90,91</sup> although re-derivations of the relationships can be found in a number of other places. The presence of the

factor  $(1-M_c \cos \theta)^{-5}$  was derived by Ffowcs Williams,<sup>88</sup> but a similar type dependence had been derived earlier by Lighthill.<sup>92</sup> In the summation for  $D(\Omega D/U_j, \theta)$  each of the products of the various velocity disturbances will give somewhat different directivities through the different direction cosines,  $x_1/r$ . We shall touch on some of these aspects later, but for the present we will assume that the combined directivity of the composite turbulent structure is omnidirectional, so that  $D(\Omega, \theta)$  is just influenced by the Doppler shift, i.e.,  $D(\omega(1-M_c \cos \theta) D/U_j)$ . Therefore, the primary angular dependence of the overall far field sound intensity is brought on by  $(1-M_c \cos \theta)^{-5}$  which shows an augmentation for  $\theta < \pi/2$  relative to the intensity at  $\theta > \pi/2$ . This behavior of enhanced sound in the direction of eddy convection has been confirmed by a number of experimenters, e.g., References 93 through 99 using subsonic jets. At large values of Mach number, the sound near the jet axis,  $\theta < \pi/4$ , is reduced relative to the theory. This behavior is now believed to be due in part to refraction.<sup>21,96,100</sup> It is interesting to note that in some of the earlier measurements<sup>91,93</sup> some high-frequency backward-directed sound was measured and this was attributed to the existence of preferred quadrupole radiation from the highly sheared mixing region. The subsequent measurements, Reference 94 and later references, indicate that this backward radiation was an artifact of experimental arrangement. Figure 3.17 shows, in confirmation with Equation (3.64) that the

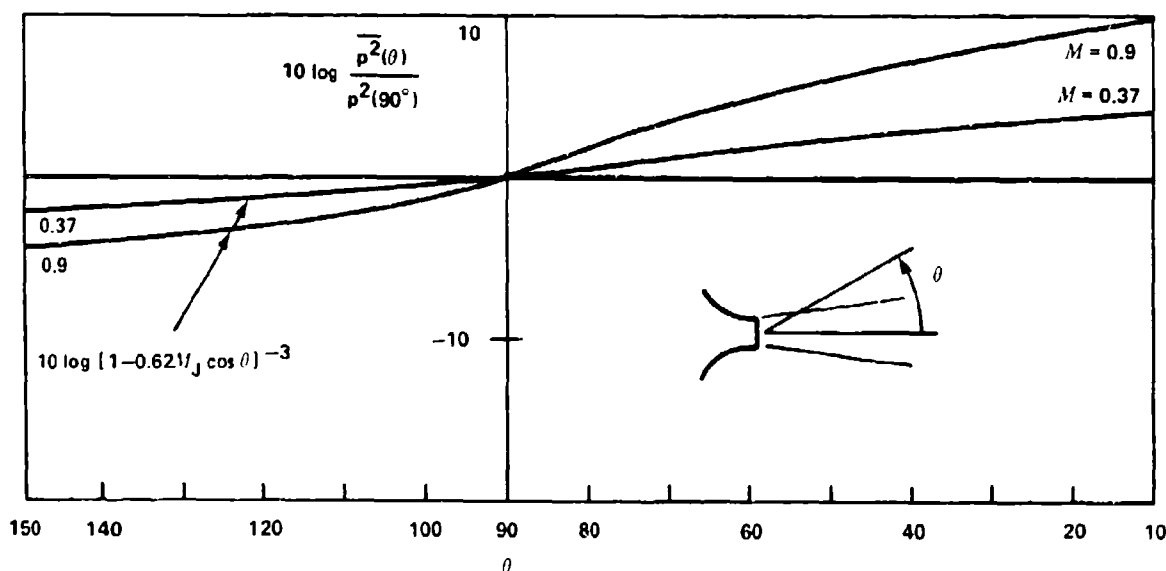


Figure 3.17 - Angular Dependence of Far Field Sound Pressure Level at Various Jet Mach Numbers  
(From Reference 97)

angular dependence is a function of Mach number. Furthermore, Equation (3.64) yields,<sup>92</sup> for the total radiated acoustic power,

$$\begin{aligned} P &= \int_0^{2\pi} \int_0^\pi I(x, \theta) (r \sin \theta d\phi) r d\theta \\ &\approx \frac{1}{c_o^5 \rho_o} \left\{ \int_0^\pi (1 - M_c \cos \theta)^{-5} \sin \theta d\theta \right\} \\ &\quad \times \rho_o^2 U_J^8 D^2 \cdot F(R_D, M_c) \end{aligned}$$

so that the radiated power is

$$P = \frac{\rho_o^2 U_J^8 D^2}{\rho_o c_o^5} \cdot \frac{1 + M_c^2}{(1 - M_c^2)^4} \cdot F(R_D, M_c) \quad (3.66)$$

where the function  $F(R_D, M_c)$  includes the dependence on Reynolds number and Mach number of the summed and integrated wave number spectrum in Equation (3.64). Figure 3.18 shows the total power nondimensionalized on  $\rho_o U_J^3 D^2$ , as a function of the exit Mach number,

$$M_J = \frac{U_J}{c_o}$$

This presentation represents the relative increase of acoustic power compared to jet power as the Mach number increases, and it is a classical result. Furthermore, the data indicate that  $F(R_D, M_c)$  is a nearly constant value between  $0.3 \times 10^{-4}$  and  $1.2 \times 10^{-4}$ .

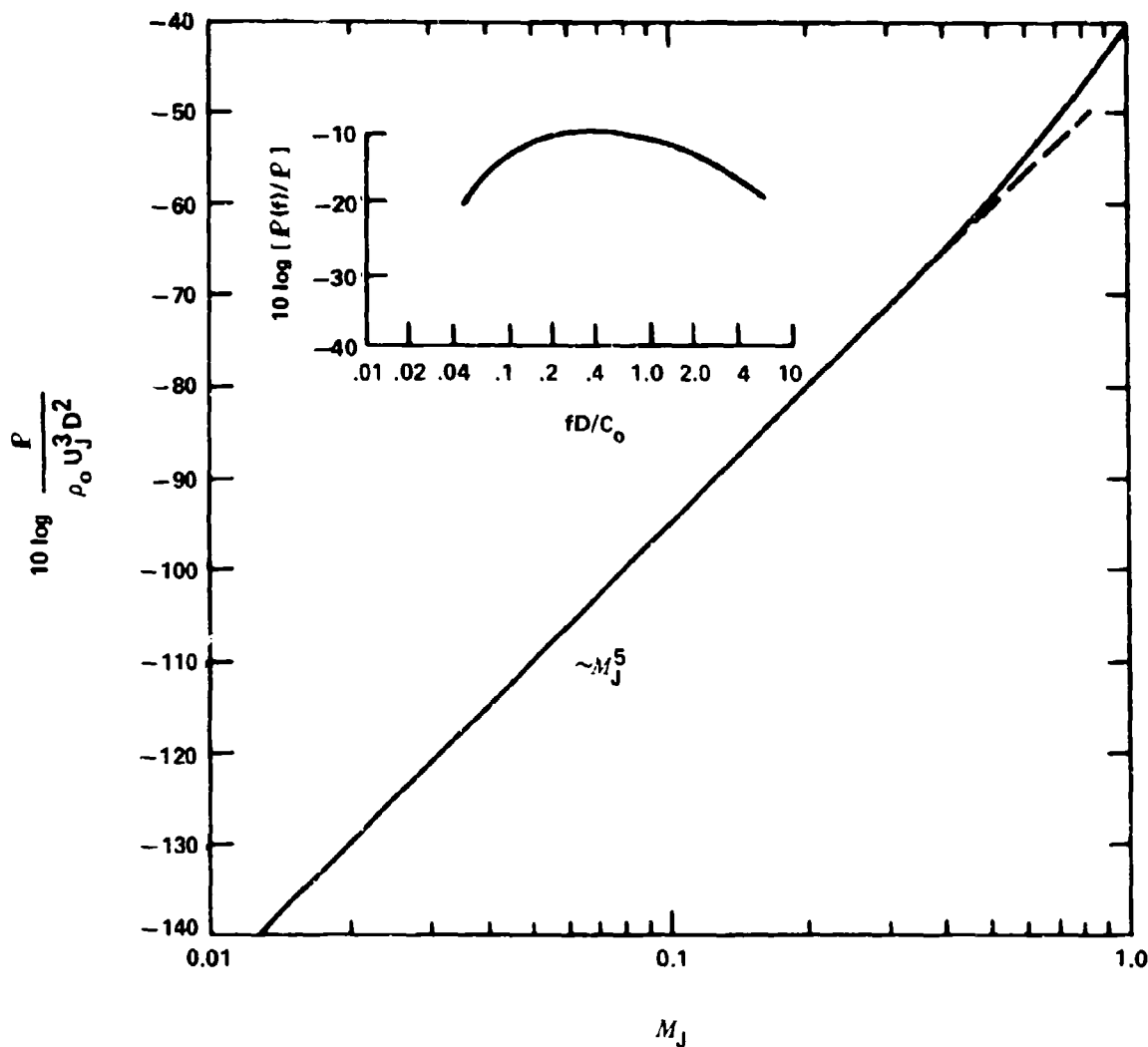


Figure 3.18 - Sound Power and Its Spectrum for Jet Noise Using  
Laminar-Flow Nozzles  $\sim 10^5 < R_D < \sim 10^6$   
(From data in Reference 97)

The inset of Figure 3.18 shows the one-third-octave power spectrum nondimensionalized on the overall power as a function of reduced frequency  $fD/C_0$ . The peak in the far field intensity spectrum at any angle will change in frequency such that the peak will occur at constant values of  $(fD/U)(1-M_c \cos \theta)$  when  $\theta > \pi/4$ , however,



at angles near the jet axis Lush<sup>96</sup> shows anomalously low values of noise at frequencies large enough that refraction is important. The noise power spectrum, therefore, has a peak frequency that depends on  $D/c_0$ ; the constancy of the dimensionless frequency of the peak in the power spectrum, first observed by Fitzpatrick and Lee,<sup>101</sup> is now well known. At  $\theta = \pi/2$ , the dependence of the sound pressure or intensity spectrum, Equations (3.63) and (3.65), on  $M_c$  decreases and the spectrum becomes a function of  $fD/U_j$  as shown in Figure 3.19.

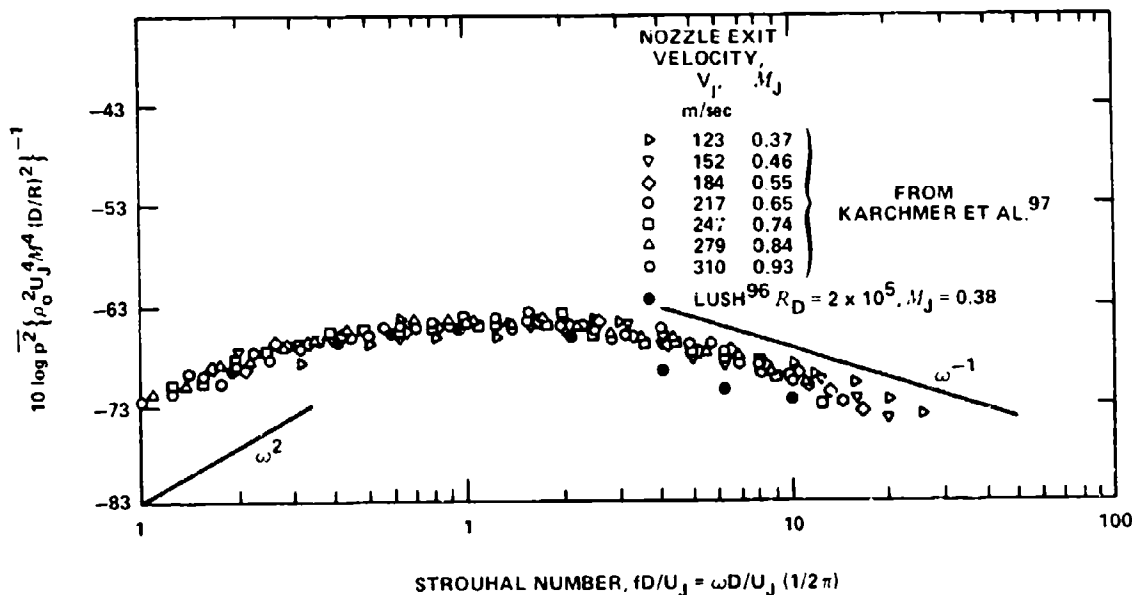


Figure 3.19 - Normalized Sound Pressure Level Spectra at Microphone Angle of 90 Degrees for 15.2-Centimeter-Diameter Potential Flow Nozzle (Adapted from Reference 97)

Measurements of the spatial correlation of far field sound pressure were made by Maestrello.<sup>102,103</sup> Around a circle in the azimuthal plane (normal to the jet axis) the spatial correlation depends on angle  $\theta$  (see Figure 3.17 for  $\theta$ ) and for microphones on opposite sides of the jet ( $\phi=\pi$ ) the correlation coefficient is small and negative for  $\theta > \pi/4$ . This behavior was interpreted by Maestrello as indicating radiation from a distribution of sources which are uncorrelated around the axis of the jet. For smaller angles to the jet axis,  $\theta < \pi/4$ , the correlations on opposite sides were of positive values and larger than 0.3, suggesting the existence of effective sources with considerable axisymmetry.

One attempt to predict both the speed-dependence and the directional characteristics (that were neglected above) has been undertaken by Ribner<sup>100,104,105</sup> incorporating many of the ideas initially used by Proudman,<sup>106</sup> and Jones.<sup>107</sup> The approach has also found wide spread use in predicting boundary layer pressure, see Chapter 7. The sound field is determined by integrating the fourth derivative, with respect to time delay, of the space-time correlation of  $T_{ij}$  over the entire source volume. This operation is completely analogous to the integration performed in Equation (3.59), giving as in Equation (2.61)

$$\langle p^2(\vec{x}) \rangle = \frac{1}{16\pi^2} \frac{1}{c_o^4 r^2} \left( \frac{x_i x_j x_k x_l}{r^4} \right) \iiint_{-\infty}^{\infty} \frac{\partial^4}{\partial \tau^4} \langle T'_{ij}(\vec{y}, t) T'_{kl}(\vec{y} + \vec{r}, t + \tau) \rangle d^3 \vec{r} \quad (3.67)$$

In Ribner's analysis, the various terms of the stress tensor are approximated by assuming that the turbulence is locally isotropic. Then, writing the instantaneous Reynolds stress

$$T'_{ij}(\vec{y}, t) = T_{ij}(\vec{y}, t) - \overline{T_{ij}(\vec{y}, t)}$$

for cold, low velocity jets,

$$T'_{ij}(\vec{y}, t) = \rho_o u_i u_j - \rho_o \overline{u_i u_j}$$

Ribner has

$$\langle T'_{ij}(\vec{y}, t) T'_{kl}(\vec{y} + \vec{r}, t + \tau) \rangle = \rho_o^2 \langle u_i(\vec{y}, t) u_j(\vec{y}, t) u_k(\vec{y} + \vec{r}, t + \tau) u_l(\vec{y} + \vec{r}, t + \tau) \rangle$$

which is a fourth-order correlation function of the velocities. Since the velocity consists of a mean plus fluctuating component, the correlation tensor contains a set of terms involving the mean velocity and second-order correlations; e.g.,

$$\langle T'_{12}(\vec{y}, t) T'_{12}(\vec{y}+\vec{r}, t+\tau) \rangle \approx u_1(\vec{y}) u_1(\vec{y}+\vec{r}) \langle u_2(\vec{y}, t) u_2(\vec{y}+\vec{r}, t+\tau) \rangle$$

$$+ \langle u_1(\vec{y}, t) u_2(\vec{y}, t) u_1(\vec{y}+\vec{r}, t+\tau) u_2(\vec{y}+\vec{r}, t+\tau) \rangle - \langle u_1(\vec{y}, t) u_2(\vec{y}, t) \rangle \langle u_1(\vec{y}+\vec{r}, t) u_2(\vec{y}+\vec{r}, t) \rangle$$

$$u_2(\vec{y}+\vec{r}, t) \rangle$$

The first term\* Ribner calls the "shear noise," while the second two he calls "self-noise." The shear noise he finds to be directional in the direction of the jet, while the self-noise he found to be nearly omnidirectional. Specifically, ignoring the multiplicative convective amplification  $(1-M_c \cos \theta)$ ,

$$\langle p^2(x, t) \rangle \sim A + \frac{B(\cos^4 \theta + \cos^2 \theta)}{2}$$

where A represents the self-noise for which elemental contributions combine to yield omnidirectional sound, and the B-term represents the shear noise which results from the combination of two quadrupoles. Ribner reduces fourth order correlations to the second order correlations by assuming that the statistical variations of the turbulence are describable as Gaussian probability density functions. Thus, the relative orders of magnitude of A and B are established as being nearly equal. This approximation had been previously used by Proudman (see Chapter 2), and it is common in similar analyses of boundary layer pressure (see Section 7.3.6).

Another approach used by Michalke and Fuchs<sup>108</sup> modifies the Lighthill source term, Equations (2.49) and (2.50) so that it contains terms that involve only the local temporal variations of fluctuating pressure and spatial gradients of the mean velocity. The relationship is linearized and predicts only what Ribner called the shear noise. The pressure fluctuations in the jet are then expanded in terms of circumferential harmonics with stochastic coefficients which could be evaluated statistically using pressure correlations in the jet. Results so far show that only low orders of circumferential variation, including axisymmetric, are indicated by the correlations.<sup>108,109</sup> A full application of the correlation measurements to the theory has not yet been made.

---

\*The alternative names turbulence-mean shear interaction and turbulence-turbulence interaction have also been used. See page 693.

### 3.6.3 Some Qualities of Jet Noise Deduced from Flow Structure

**3.6.3.1 Properties of the Mean Shear Term.** As a basis for discussing some of the more fundamental features of the coupling of turbulence and sound we adopt Ribner's<sup>104</sup> simplification that the magnitude of shear noise is qualitatively representative of the total noise level as described in the last section, and so take the contribution due to the  $\langle T'_{11}(\vec{y}, t) T'_{11}(\vec{y} + \vec{r}, t + \tau) \rangle$  correlation as showing typical behavior of the jet noise sources. The source can be written

$$\langle T'_{11}(\vec{y}, t) T'_{11}(\vec{y} + \vec{r}, t + \tau) \rangle \approx 4\rho_0^2 U_1^2 \langle u_1(\vec{y}, t) u_1(\vec{y} + \vec{r}, t + \tau) \rangle \quad (3.68)$$

where  $U_1(\vec{y})$  and  $U_1(\vec{y} + \vec{r})$  are taken as equal to  $U_1$ . Therefore, the wave number spectrum is

$$\Phi_{1111}(\vec{k}, \omega) = 4\rho_0^2 U_1^2 \frac{1}{(2\pi)^4} \iiint e^{-i(\vec{k} \cdot \vec{r} - \omega \tau)} \langle u_1(\vec{y}, t) u_1(\vec{y} + \vec{r}, t + \tau) \rangle d\vec{r} d\tau \quad (3.69a)$$

$$= 4\rho_0^2 U_1^2 \Phi_{11}(\vec{k}, \omega; \vec{y}) \quad (3.69b)$$

The correlation  $\langle u_1 u_1' \rangle$  is a two-point space-time covariance of the axial component of velocity fluctuations. We will define a correlation function as

$$R_{11}(\vec{r}, \tau) = \frac{\overline{u_1(\vec{y}, t) u_1(\vec{y} + \vec{r}, t + \tau)}}{\left[ \overline{u_1^2(\vec{y}, t)} \overline{u_1^2(\vec{y} + \vec{r}, t)} \right]^{1/2}} \quad (3.70)$$

$$= R_{11}(r_1, r_r, r_\theta, \tau)$$

which could depend on the datum  $\vec{y}$ . Below, we relate the correlation function and its transform to measured properties of jet turbulence.

Extensive measurements of the correlation function  $R_{11}(r_1, \tau)$ , with the sensors displaced in the streamwise direction, were made by Fisher and Davies,<sup>110</sup> Bradshaw, Ferris, and Johnson,<sup>111</sup> Davies, Fisher and Barratt,<sup>112</sup> and Kolpin.<sup>113</sup> The measurements of Bradshaw, Ferris, and Johnson include autospectra of velocity fluctuations, and Fisher and Davies and Kolpin provide narrowband correlations from which cross spectral densities can be deduced.

3.6.3.2 Measured Characteristics of Jet Noise and Taylor Hypothesis. Some of the important properties of jets at  $R_D$  greater than  $10^5$  are shown in Figure 3.20. Within four to six diameters, the jet develops in an annular shear flow that surrounds the so-called potential core. The core region has a mean velocity that is independent of radius and is, therefore, relatively disturbance free except for an unsteadiness that is imposed by a large-scale vortex structure in the annular mixing zone, as shown by Lau, Fisher, and Fuchs,<sup>52</sup> and by Ko and Davies.<sup>114</sup> The maximum turbulence intensities in the mixing zone measured by Davies, Fisher, and Barratt<sup>112</sup> are shown in the lower part of Figure 3.20. The radial distribution of the turbulence in this region satisfies the similarity rule,

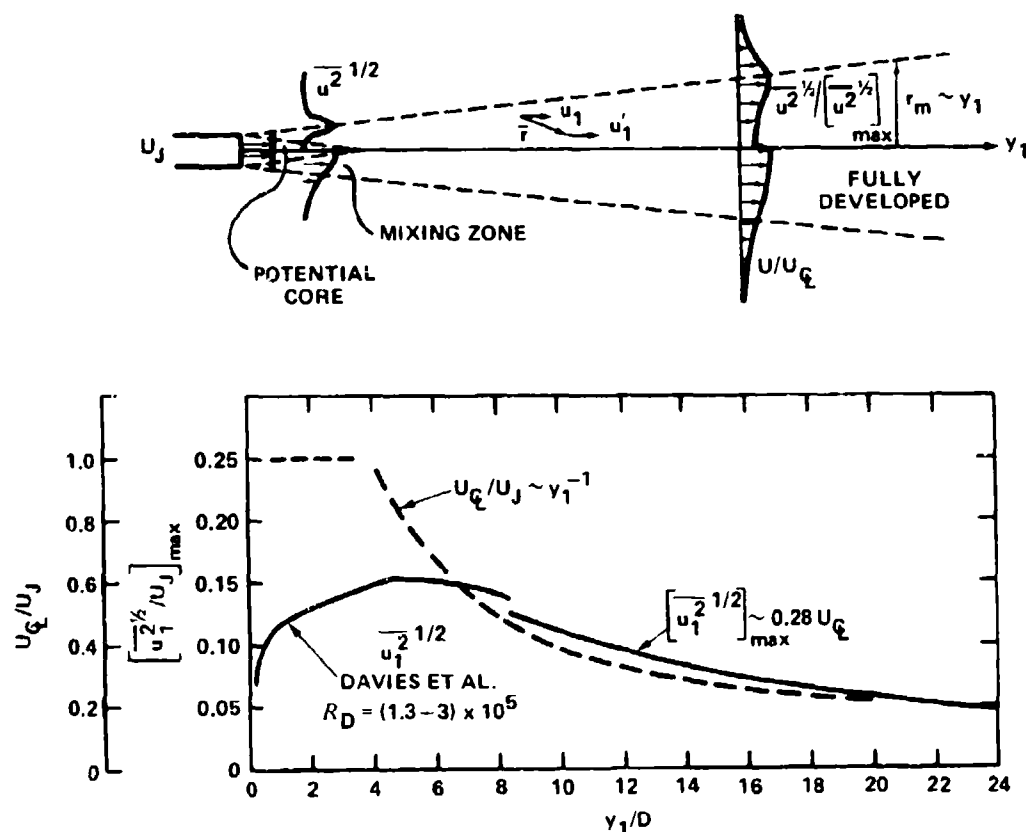


Figure 3.20 - Development of Jet Turbulence and Mean Velocity of Free Jets

$$\frac{u_1^{1/2}}{(u_1^{1/2})_{\max}} = f_1 \left( \frac{r - \frac{D}{2}}{y_1} \right) \quad (3.71)$$

where  $f(0) = 1$ , and the mean velocity in the mixing region  $U_1(r, y_1)$  behaves according to<sup>112,113</sup>

$$\frac{U_1(r, y_1)}{U_J} = g_1 \left( \frac{r - \frac{D}{2}}{y_1} \right) \quad (3.72)$$

These similarity functions reflect the fact that the length scale of the shear layer increases linearly with distance from the nozzle exit. This linear increase continues into the fully developed region downstream of  $y_1/D = 4$  to 5. In the fully developed region the inner extremity of the annular shear layer has merged and, although the mean velocity is still maximum on  $r = 0$ , it decreases linearly with  $y_1$ . According to Forstall and Shapiro,<sup>115,116</sup> the center line velocity is given by

$$\frac{U_c}{U_J} = \frac{(y_1)_c}{y_1} \quad (3.73)$$

where

$$\frac{(y_1)_c}{D} \approx (4 \text{ to } 5) \quad (3.74)$$

Replacing the two similarity forms, Equations (3.71) and (3.72), in the fully developed region, Hinze<sup>76</sup> and Townsend<sup>77</sup> give, for the mean velocity,

$$\frac{U_1(r, y_1)}{U_c} = f_2 \left( \frac{r}{y_1 + (y_1)_c} \right) \quad (3.75)$$

where  $(y_1)_c$  is a constant measure of the effective datum of the jet and for the turbulent velocity

$$\frac{u_1}{u_c} = g_2 \left( \frac{r}{y_1 + (y_1)_c} \right) \quad (3.76)$$

where  $g_2$  is maximum near to or just off the center line of the jet. Forstall and Shapiro<sup>115,116</sup> give an alternative functional dependence in terms of a variable jet radius  $r_j(y_1)$

$$\frac{u_1(r, y_1)}{u_c} = f_3 \left( \frac{r}{r_j(y_1)} \right) \quad (3.77)$$

where  $r_j(y_1)$  is determined by

$$\frac{u(r_j, y_1)}{u_c} = f_3(1) = \frac{1}{2} \quad (3.78)$$

and it depends on  $y_1$  as

$$\frac{2r_j(y_1)}{D} = \left( \frac{y_1}{(y_1)_c} \right) \quad (3.79)$$

$(y_1)_c$  being the length of the potential core given by Equation (3.73). These geometric factors are all illustrated in Figure 3.20.

As shown by Equations (3.59) and (3.68) the mean-square sound pressure will depend on the space-time covariance of the source tensor, which, by Equations (3.68) and (3.69b), can be crudely represented in terms of the two-point space-time statistics of the velocity fluctuations.

Space-time correlations of the axial velocity fluctuations in the mixing zone obtained by Fisher and Davies<sup>110</sup> are shown in Figure 3.21. These correlations, obtained as a function of time delay for fixed anemometer probe separations, show maxima at a combination of  $r_1$  and  $\tau$  that are shown in the lower part of the figure. An envelope can be drawn through the correlation values at these points that can be described in terms of the original correlation

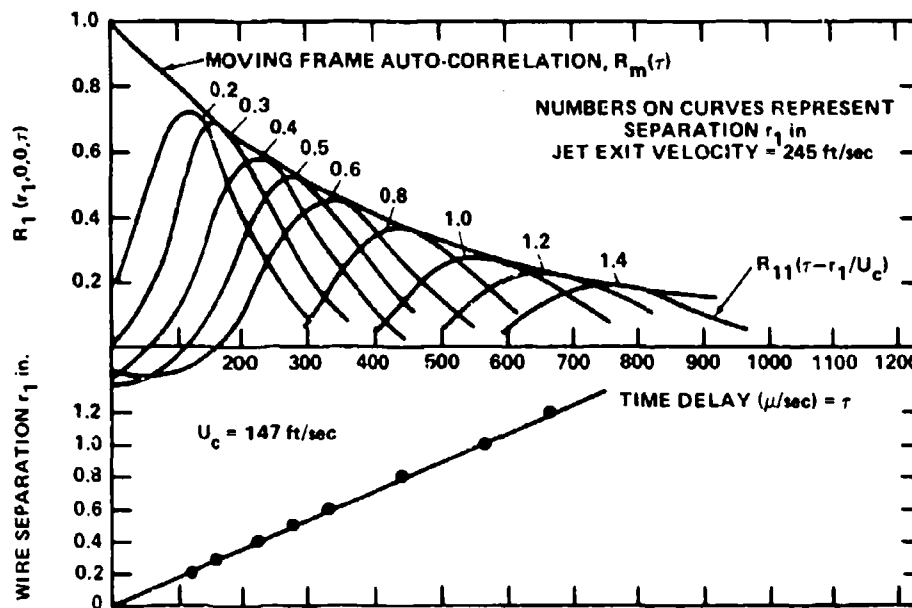


Figure 3.21 - Space-Time Correlation of Axial Velocity Fluctuations (Downstream Separation). Fixed Probe at  $y_1/D = 1.5$ ,  $y_2/D = 0.5$ .

$R_D = 1.2 \times 10^5$ ,  $D = 1$  inch.  
(From Fisher and Davies<sup>110</sup>)

$$R_{11}(r_1, \tau) = R_{11}(r_1 - U_c \tau, \tau) \quad (3.80)$$

to give the maximum correlation as

$$R_m(\tau) = R_{11}(r_1 = U_c \tau, \tau) \quad (3.81)$$

This relationship between  $r_1$  and  $\tau$ , therefore, defines a convection velocity  $U_c \approx 0.6 U_j$  of the disturbances as they move downstream from the nozzle.  $R_m(\tau)$  is called a moving axis correlation<sup>112</sup> because the covariance is interpreted as a correlation in a frame of reference moving with the average speed of the eddy field. The deviation of  $R_m(\tau)$  from unity is caused by combination of turbulent mixing, in which eddies stretch and entrain fluid from the outer undisturbed environment, and by viscous decay of smaller eddies as they are convected by the mean flow.

The autospectrum,  $\Phi_{11}(\omega; \vec{y})$ , can be interpreted in terms of the energy spectrum of various sized convected eddies. Thus, starting with the temporal autocorrelation



$$\Phi_{11}(\omega, \vec{y}) = \frac{1}{2\pi} \int_{-\infty}^{\infty} e^{i\omega\tau} \overline{u_1^2} R_{11}(r_1=0, \tau) d\tau \quad (3.82)$$

if we assume that the turbulence is convected without any loss of correlation, i.e., that  $R_m(\tau) = 1$ , then the correlation coefficient is written in the special form

$$R_{11}(r_1, \tau) \approx R_{11}(r_1 - U_c \tau) \quad (3.83)$$

where  $R_{11}(r_1 - U_c \tau)$  is unity for all  $r_1$  satisfying  $r = U_c t$ . This condition of convection is called "Taylors' Hypothesis" of frozen convection.<sup>73,74</sup> Then we can write the autospectrum (with  $r=0$ ) as

$$\Phi_{11}(\omega, \vec{y}) \approx \frac{1}{2\pi} \frac{\overline{u_1^2}}{U_c} \int_{-\infty}^{\infty} e^{i(\omega/U_c)(U_c \tau)} R_{11}(U_c \tau) d(U_c \tau) \quad (3.84)$$

If, now, a wave number spectrum is defined as

$$\phi_{11}(k_1, \vec{y}) = \frac{1}{2\pi} \int_{-\infty}^{\infty} e^{-ik_1 r_1} \overline{u_1^2} R_{11}(r_1, \tau=0) dr_1 \quad (3.85)$$

$$\approx \frac{1}{2\pi} \int_{-\infty}^{\infty} e^{-ik_1 r_1} \overline{u_1^2} R_{11}(r_1) dr_1 \quad (3.86)$$

the approximation given by Equation (3.83) allows us to write

$$U_c \phi_{11}(\omega, \vec{y}) \approx \phi_{11}(k_1, \vec{y}) \quad (3.87)$$

and the wave number is dependent on frequency as

$$k_1 = \frac{\omega}{U_c} \quad (3.88)$$

The autospectrum in Figure 3.22 represents an approximate spectrum of disturbances of varying wavelength as can be seen by the equivalence

$$\begin{aligned} \frac{f y_1}{U_J} &= \frac{\omega y_1}{2\pi U_c} \frac{U_c}{U_J} \\ &= \frac{1}{2\pi} (k_1 y_1) \frac{U_c}{U_J} \sim \left( \frac{y_1}{\lambda_1} \right) \frac{U_c}{U_J} \end{aligned}$$

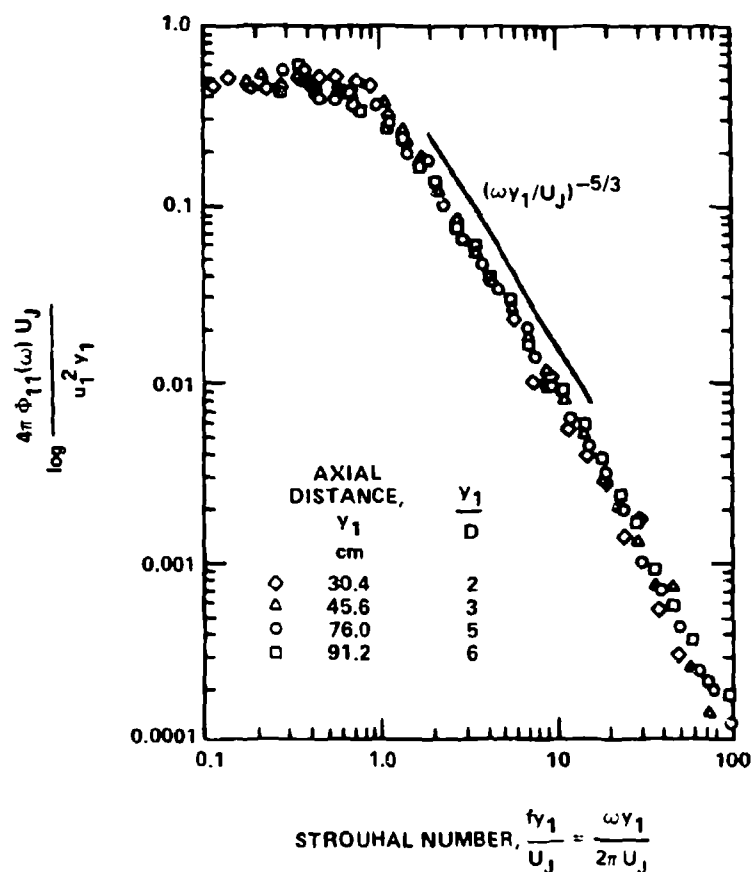


Figure 3.22 - Turbulent Axial Velocity Spectral Density at Lip Axis.  
Mean Nozzle Exit Velocity, 122 Meters per Second; Radial Position,  
7.6 Centimeters,  $R_D = 1.2 \times 10^6$   
(From Karchmer et al.<sup>98</sup>)

where  $U_c \sim 0.6 U_J$  and  $\lambda_1$  is an effective eddy wavelength so that

$$\frac{ry_1}{U_J} \sim \frac{0.6 y_1}{\lambda_1}$$

The autospectrum discloses then, that most of the mean-square turbulence intensity, given by the integral

$$\overline{u_1^2}(\vec{y}) = \int_{-\infty}^{\infty} \phi_{11}(\omega; \vec{y}) d\omega \quad (3.89)$$

is determined by eddies with effective wavelengths that are less than the axial distance  $y_1$ . An integral length scale, or macroscale, of the convected eddies, defined by an integral of the broadband spatial correlation,

$$\Lambda_1 = \int_0^{\infty} R_{11}(r_1, \tau=0) dr_1 \quad (3.90a)$$

has been related to the autospectrum in the case of the streamwise,  $r_1$ , direction as

$$\frac{\Lambda_1}{\pi} = \lim_{k_1 \rightarrow 0} \frac{\phi_{11}(k_1)}{\overline{u_1^2}} \quad (3.90b)$$

or nearly equivalently

$$\frac{\Lambda_1}{\pi} \approx \lim_{\omega \rightarrow 0} U_c \frac{\phi_{11}(\omega, \vec{y})}{\overline{u_1^2}} \quad (3.90c)$$

only to the extent that  $R_m(\tau)$  can be considered as near unity. We shall see below that this equivalence is not generally valid. The nondimensionalized spectra in Figure 3.22 show that the integral scale is approximated by

$$\Lambda_1 \sim \pi \left[ U_c \cdot \frac{y_1}{4\pi U_J} \cdot (0.5) \right]$$

$$\Lambda_1 \sim 0.1 y_1$$

Measurements of  $\Lambda_1$  at Reynolds numbers near  $10^5$  by Davies, Fisher, and Barratt<sup>112</sup> and by Laurence<sup>117</sup> also give

$$\Lambda_1 \sim 0.13 y_1$$

for  $D < y_1 < 6D$ , independently of radial location from the centerline.

A radial integral scale, given by Laurence,<sup>117</sup> is

$$\Lambda_r \sim 0.05 y_1$$

where

$$\Lambda_r = \int_0^\infty R(0, r_r, 0, 0; \vec{y}) dr_r$$

Integral scales were measured by Jones<sup>107</sup> in a rectangular jet using frequency-filtered signals. With the 1,2,3 directions pertaining to the flow, vertical, and width directions respectively, he found for broadband (unfiltered) velocities  $\Lambda_2 \approx \Lambda_3 \approx 0.014 (y_1 + h)$  and  $\Lambda_1 \approx 0.04 (y_1 + h)$  where  $h$  is the height of the exit. For filtered signals he again found  $\Lambda_2(\omega) \approx \Lambda_3(\omega)$ , but that all  $\Lambda_i/y_1$  decreased as  $\omega y_1/U_J$  increased, although the decrease was not as rapid as  $(\omega y_1/U_J)^{-1}$ .

3.6.3.3 Methods of Approximating the Wave Number Spectrum. Referring to Equation (3.62) it is seen that the required quantity is an integral over the volume of the jet of the wave number spectrum that is evaluated at  $\vec{k} = \vec{k}_r = \vec{k}_0$ , where  $\vec{k}_r$  is in the direction of the field point. To realize the implications of this particular value of  $\Phi_{ijkl}(\vec{k}, \omega)$  in light of the above discussion, we shall write down the complete expression of the wave number spectrum, Equation (3.60), using the representative mean-shear term, Equations (3.68) and (3.69b), and employing the alternate functional definition of correlation variables, Equation (3.80) to give

$$\begin{aligned} \Phi_{1111}(\vec{k}, \omega; \vec{y}) &= 4\rho_0^2 U_1^2(\vec{y}) \overline{u_1^2(\vec{y})} \frac{1}{(2\pi)^4} \iiint_{-\infty}^{\infty} e^{-i(\vec{k} \cdot \vec{r} - \omega\tau)} \\ &\quad \times R_{11}(r_1 - U_c \tau, r_r, r_\theta; \tau) d\vec{r}_1 d\tau \\ &= 4\rho_0^2 U_1^2(\vec{y}) \overline{u_1^2(\vec{y})} \left[ \frac{1}{(2\pi)^4} \iiint_{-\infty}^{\infty} e^{-i(k_1 \eta_1 + \vec{k}_n \cdot \vec{r}_n)} e^{i(\omega - k_1 U_c)\tau} \right. \\ &\quad \left. \times R_{11}(\eta_1, \vec{r}_n, \tau) d\vec{r}_n d\tau \right] \end{aligned} \quad (3.91)$$

where  $\vec{r}_n = r_r, r_\theta$  and where  $\eta_1 = r_1 - U_c \tau$ . If we approximate the correlation function as the product of a spatial correlation moving with the eddy field ( $R_{11}^S(\eta_1, \vec{r}_n)$ ) and a correlation as the eddy field is convected  $R_m(\tau)$ , then

$$R_{11}(\eta_1, \vec{r}_n, \tau) = R_{11}^S(\eta_1, \vec{r}_n) R_m(\tau) \quad (3.92)$$

which still satisfies the condition stated by Equation (3.74) and reduces to Equation (3.83) when  $R_m(\tau) = 1$  and  $\vec{r}_n = 0$ . This gives a wave number frequency spectrum that is also separable

$$\Phi_{11}(\vec{k}, \omega; \vec{y}) = 4\rho_0^2 U_1^2(\vec{y}) \Phi_{11}(\vec{k}) \Phi_m(\omega - k_1 U_c) \quad (3.93)$$

where

$$\frac{\phi_{11}(\vec{k})}{u_1^2} \equiv \frac{1}{(2\pi)^3} \iiint e^{-i\vec{k} \cdot \vec{r}} R_{11}^S(\eta_1, \vec{r}_n) d\eta_1 d^2\vec{r}_n \quad (3.94)$$

and  $R_{11}^S(\vec{r}) = R_{11}^S(r_1, \vec{r}_n)$  is a spatial correlation function defined as

$$R_{11}^S(\vec{r}) = R_{11}(\vec{r}, \tau=0)$$

The function  $\phi_m(\omega - U_c k_1)$  is just the Fourier transform of  $R_m(\tau)$  where the transform variable is  $\omega - U_c k_1$ . It shall be called the moving axis spectrum, and it may be determined from data such as the envelope shown in Figure 3.21. When the eddy field is convected in a frozen pattern as with Taylors' hypothesis i.e., when  $R_m(\tau) \equiv 1$ , then  $\phi_m(\omega - U_c k_1)$  is nonzero only at  $\omega = U_c k_1$ , i.e.,

$$\phi_m(\omega - U_c k_1) = \delta(\omega - U_c k_1) \quad (3.95)$$

where  $\delta(\omega)$  is the delta function. However, if, as illustrated,  $R_m(\tau)$  has the shape of an exponential decay,

$$R_m(\tau) = e^{-|\tau|/\theta_\tau} \quad (3.96)$$

then the Fourier transform of  $R_m(\tau)$  in Equation (3.91) yields a moving axis spectrum

$$\begin{aligned} \phi_m(\omega) &= \frac{1}{2\pi} \int_{-\infty}^{\infty} e^{i(\omega - U_c k_1)\tau} R_m(\tau) d\tau \\ \phi_m(\omega) &= \frac{\theta_\tau}{\pi} \frac{1}{1 + (\omega - U_c k_1)^2 \theta_\tau^2} \end{aligned} \quad (3.97)$$

This function is peaked at frequencies  $\omega = U_c k_1$ , but at wave numbers which are very much less than  $\omega/U_c$  it is finite-valued; at high frequencies  $\omega \theta_\tau > 1$  the spectrum

will depend on time scale as  $(\theta_\tau)^{-1}$ . This means that high-frequency, low wave number fluctuations increase as the eddy decay time in the moving axis coordinate system decreases.

The additional wave number spectrum appearing in Equation (3.93) is

$$\phi_{11}(k) = \frac{1}{(2\pi)^3} \iiint_{-\infty}^{\infty} e^{-i(k_1 \eta_1 + \vec{k}_n \cdot \vec{r}_n)} R_{11}^s(\eta_1, \vec{r}_n) d\eta_1 d\vec{r}_n \quad (3.98)$$

If the correlation function is also presumed to be separable as the product of the separate spatial correlation in each of the axial, radial, and tangential directions then (with  $\eta_1 = r_1 - U_c \tau$ )

$$R_{11}^s(\eta_1, \vec{r}_n) = R_{11}(\eta_1) R_{11}(\vec{r}_n) \quad (3.99)$$

or further,

$$R_{11}^s(\eta_1, \vec{r}_n) = R_{11}(\eta_1) R_{11}(r_r) R_{11}(r_\theta) \quad (3.100)$$

Note that when  $\tau = 0$ ,  $R_{11}(\eta_1)$  reduces to the spatial correlation function  $R_{11}(r_1)$  introduced above, see Equation (3.85). Various forms of these correlation functions have been used for various needs. A typical functional form that is used is simply, e.g.,

$$R_{11}(r_r) = e^{-|r_r|/\Lambda_i}$$

where  $\Lambda_i$  is the integral correlation length, Equation (3.90a), for separation distances in the  $i$  direction so that the wave number spectrum is

$$\phi_{11}(k_i) = \frac{\Lambda_i}{\pi} \frac{1}{1 + (k_i \Lambda_i)^2} \quad (3.101)$$

The separable representation, Equation (3.92), does not imply the same separability of the cross spectrum. The cross-spectral density  $\phi_{11}(\vec{r}, \omega; \vec{y})$  is related to the correlation by

$$\phi_{11}(\vec{r}, \omega; \vec{y}) = \frac{1}{2\pi} \int_{-\infty}^{\infty} e^{i\omega\tau} \overline{u_1^2} R_{11}(r_1 - U_c \tau, \vec{r}_n, \tau, \vec{y}) d\tau$$

which is rewritten in a separable form

$$\phi_{11}(\vec{r}, \omega; \vec{y}) = \frac{1}{2\pi} \int_{-\infty}^{\infty} e^{i\omega\tau} \overline{u_1^2} R_{11}^s(r_1 - U_c \tau, \vec{r}_n) R_m(\tau) d\tau$$

letting  $\tau' = \tau - r_1/U_c$ ,

$$\phi_{11}(\vec{r}, \omega; \vec{y}) = \frac{\overline{u_1^2}}{2\pi} \int_{-\infty}^{\infty} e^{i\omega(r_1/U_c + \tau')} R_{11}^s(U_c \tau', \vec{r}_n) R_m\left(\tau' + \frac{r_1}{U_c}\right) d\tau' \quad (3.102)$$

The moving axis correlation is the same as the one above, and the correlation  $R_{11}^s(U_c \tau', \vec{r}_n)$  is a spatial correlation in a frame of reference moving with the eddy field. It too is the same as the one introduced in Equation (3.92), but now the  $r_1$  variation is expressed as a time delay. Using the separation of variables shown in Equation (3.100), the cross-spectral density of Equation (3.102) can be written in the form

$$\begin{aligned} \phi_{11}(\vec{r}, \omega; \vec{y}) &= e^{i\omega r_1/U_c} R_n(\vec{r}_n) \\ &\times \frac{\overline{u_1^2}}{2\pi} \frac{1}{U_c} \int_{-\infty}^{\infty} e^{i(\omega/U_c)U_c \tau'} R_{11}(U_c \tau') R_m\left(\tau' + \frac{r_1}{U_c}\right) d(U_c \tau') \end{aligned}$$



which does not have the exact form of Equation (3.99). Note, however, that except for  $R_m(\tau' + r_1/U_c)$ , the integral in this equation is the same as that in Equation (3.85), therefore, to the extent that  $R_m(\tau' + r_1/U_c)$  varies slowly with its argument compared to the variation of  $R_{11}(U_c \tau')$  with  $U_c \tau'$ , the influence of the two correlation functions in the integral can be approximated as multiplicative. So, if the time-scales of the two correlations are very different as can be deduced by comparing their shapes in Figure 3.21, the cross spectrum can be written in the separable form

$$\phi_{11}(\vec{r}, \omega; \vec{y}) \approx e^{i\omega r_1/U_c} \phi_{11}(\omega) R_n(\vec{r}_n) \phi_m(r_1, \omega) \quad (3.103)$$

where

$$\alpha = \omega r_1/U_c$$

is the phase of the cross spectrum expressed in terms of a convection velocity  $U_c$ . Recalling Equation (3.80),  $\phi_{11}(\omega)$  has replaced the wave number spectrum  $\phi_{11}(\omega/U_c) U_c^{-1}$ . The function  $\phi_m(r_1, \omega)$  shows the decorrelation of the component of frequency  $\omega$  of the eddy field as it moves past the fixed reference frame over a distance  $r_1$  and the phase factor  $\omega r_1/U_c$  expresses the propagation of the component as a wave. At  $r_1 = 0$ ,  $\phi_m(0, \omega) = 1$ . Measurements of  $\phi_{11}(r, \omega; y)$  from which  $\phi_m(r_1, \omega)$  may be deduced in jets are sparse, although there are a restricted number of measurements of  $\phi_{11}(r_1, \omega; \vec{y})$  which are shown in Figure 3.23. The magnitude of the cross spectrum has been normalized on the autospectrum,

$$\frac{|\phi_{11}(r_1, \omega; \vec{y})|}{\phi_{11}(\omega, \vec{y})} = \phi_m(r_1, \omega)$$

The measurements have been made by Jones<sup>107</sup> in a rectangular jet. Those measurements by Kolpin<sup>113</sup> and by Fisher and Davies<sup>110</sup> in a round jet cover a range of frequencies and streamwise separations in the mixing zone, and they show clearly that the cross-spectral density with streamwise separation is a function of the variable  $\omega r_1/U_j$ . Furthermore, the convection velocities, determined from the filtered velocity signals over a range of frequencies, vary from  $0.45 U_j$  to  $0.7 U_j$  for the respective frequency range of  $fD/U_j$  from 2.08 to 0.52. The measurements shown in Figure 3.23 are the only ones known, and they hardly give a complete picture of the structure of the jet turbulence as a function of frequency. What is shown is that the components lose their identity when  $\omega r_1/U_j \approx 9$ , i.e., for  $\phi_m(r_1, \omega) = 0.1$ , this number corresponds to

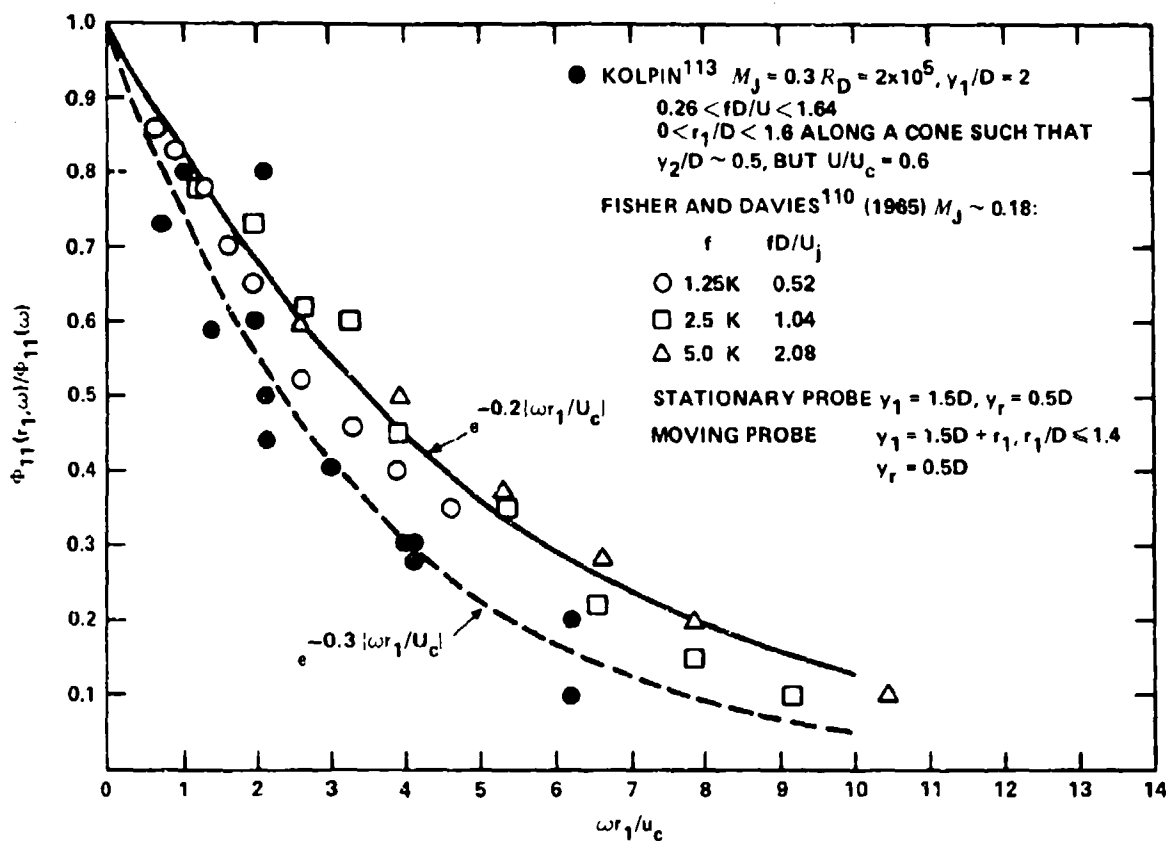


Figure 3.23 - Normalized Cross Spectral Densities of Jet Turbulence at Low Mach Numbers;  $0.45 < U_c(\omega)/U_j < 0.7$

$$\frac{r_1}{\lambda_1} \sim 2.5$$

when  $U_c \sim 0.6 U_j$ . This result has the alternate interpretation that eddies lose their identities after they are convected distances comparable with 2.5 times the eddy size.

The wave number spectrum included in Equation (5.69) now can be written with Equation (3.103) as

$$\Phi_{11}(\vec{k}, \omega; \vec{y}) = \Phi_{11}(\omega) \frac{1}{(2\pi)^3} \iiint_{-\infty}^{\infty} e^{-i(\vec{k} \cdot \vec{r} - \omega r_1 / U_c)} R_n(\vec{r}_n) \phi_m(r_1, \omega) d^3\vec{r} \quad (3.104)$$

which can be written as the product of three spectra

$$\phi_{11}(\vec{k}, \omega; \vec{y}) = \phi_{11}(\omega) \phi_n(\vec{k}_n) \phi_m\left(k_1 - \frac{\omega}{U_c}\right) \quad (3.105)$$

where the subscripts match the wave number spectra with the respective correlation functions. Equations (3.93) and (3.105) show equivalent representations for nearly frozen convection and near  $k_1 = \omega/U_c$ . Since  $\phi_{11}(\vec{k})$  can be written in the separable form  $\phi_{11}(k_1) \phi_n(\vec{k}_n)$ , then

$$\phi_{11}(k_1) \phi_m(\omega - k_1 U_c) \approx \phi_{11}(\omega) \phi_m\left(k_1 - \frac{\omega}{U_c}\right)$$

The wave number spectrum as a function of  $k_1$  has its maximum near  $k_1 = \omega/U_c$  and it falls to a lower limit that is equivalent to the product of integral scales at low wave numbers. If the eddies were convected without change, then  $\phi_{11}(\vec{k}=0, \omega; \vec{y})$  would be identically zero by virtue of the delta function approximation on  $\phi_m(k_1 - \omega/U_c)$ . Figure 3.24 shows contours of  $\phi_{11}(\vec{k}, \omega)$  in the  $k_1, \omega$  plane for  $\vec{k}_n = 0$ , the relative spectrum levels shown here are intended only to show the relationship of  $\phi_{11}(\vec{k}, \omega)$  to the wave number  $k_1 = k_o$  of acoustic propagation and the importance of the integral length scales. For approximating Equations (3.63) through (3.65) in terms of turbulence dynamics, it is necessary to evaluate  $\phi_{11}(k=k_r=k_o, \omega; \vec{y})$ , where  $k_r$  is the trace wave number in the direction of the observer and, for subsonic jets  $k_o \ll \omega/U_c$ . Regardless of what the orientation of the observer is relative to the jet, if  $k_o \ll 2\pi/\Lambda_1$ , where  $\Lambda_1$  is any of the turbulence integral scales, then the integration becomes quite simple. In fact, from Equation (3.104)

$$\begin{aligned} \phi_{11}\left(k_1=k_o \ll \frac{\omega}{U_c}, \vec{k}_n \ll \frac{2\pi}{\Lambda_1}, \omega; \vec{y}\right) &\sim \frac{\phi_{11}(\omega)}{(2\pi)^3} \cdot \iint_{-\infty}^{\infty} R_n(\vec{r}_n) d^2 r_n \\ &\times \int_{-\infty}^{\infty} e^{i\omega r_1/U_c} \phi_m(r_1, \omega) dr_1 \end{aligned} \quad (3.106)$$

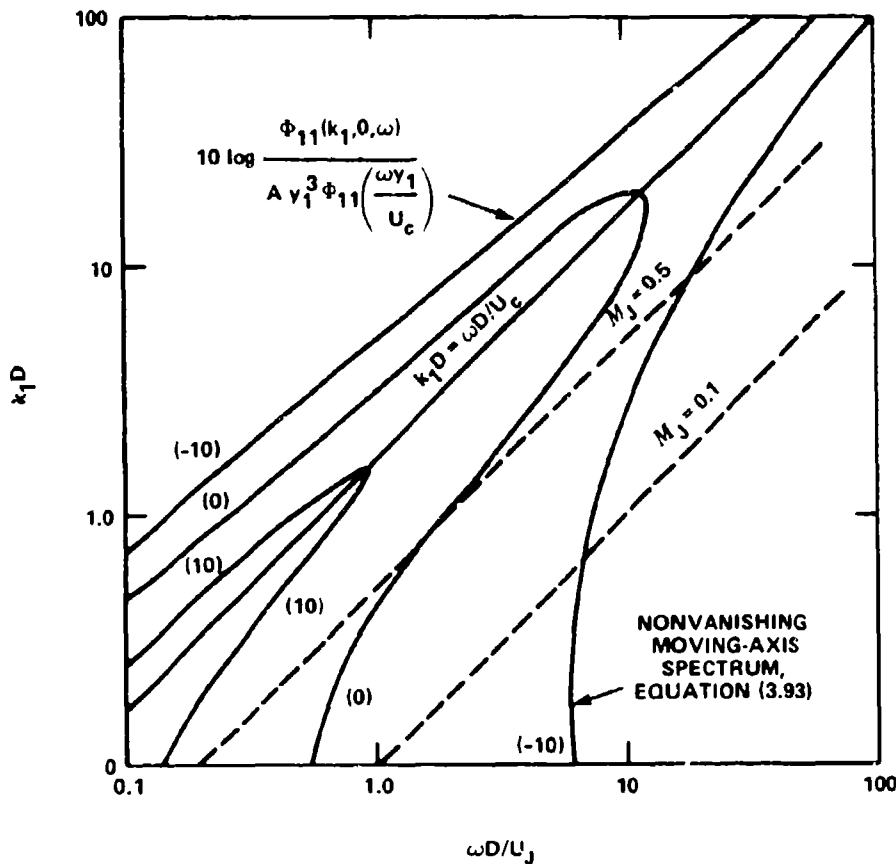


Figure 3.24 - Wave Number-Frequency Contours for Constant Source Spectrum Levels of Typical Subsonic Jets. The Normalizer "A" is Arbitrary.

$$\sim \Phi_{11}(\omega) \frac{\Lambda_r \Lambda_\theta}{(\pi)^3} \Lambda_{1m}(\omega) \quad (3.107)$$

or incorporating the limit at small  $k_1$  of the moving axis spectrum

$$\sim \Phi_{11}(\omega) \frac{\Lambda_r \Lambda_\theta}{\pi^2} \lim_{k_1 = k_0 \rightarrow 0} \phi_m \left( k_1 - \frac{\omega}{U_c} \right) \quad (3.108)$$

The quantity  $8 \Lambda_r \Lambda_\theta \Lambda_{1m}(\omega)$  is a frequency-dependent correlation volume\* of the turbulence.

\*In the same vein, an area integral of a correlation function  $R(\vec{r})$  yields a correlation area, say  $\Lambda_{1m}(\omega) \Lambda_j$  where  $\Lambda_j$  is perpendicular to  $\Lambda_{1m}$ .

Equation (3.106) shows that the value of  $\phi_{11}(\vec{k}, \omega)$  at low wave numbers depends not only on the radial and tangential integral scales of the eddies, but also on the rate of decorrelation of the eddy field as it moves with the jet exhaust. This means that for subsonic jets, noise can only be produced when the eddies experience a change. Eddies convected in a frozen pattern at speeds  $U_c \ll C_0$  cannot radiate sound regardless of how large they are. The most typically considered modes of change are vortex pairing and spatial growth as the vorticity propagates away from the nozzle; such modes and their acoustical implications have been examined by Ffowcs Williams and Kempton.<sup>118</sup> See also Section 3.6.3.5.

The  $\Lambda_{1m}(\omega)$  in Equation (3.107) is a frequency dependent correlation length in the streamwise direction that is determined from the cross-spectral density. This is determined approximately by integrating

$$\Lambda_m(\omega) = \pi \lim_{k_1 \rightarrow 0} \phi_m \left( k_{11} - \frac{\omega}{U_c} \right) \approx \frac{1}{2} \int_{-\infty}^{\infty} e^{i\omega r_1 / U_c} e^{-\alpha_1 |\omega r_1 / U_c|} dr_1$$

where the exponential function is shown in Figure 3.23 with  $0.2 < \alpha_1 < 0.3$ . Evaluation gives

$$\Lambda_m(\omega) \approx \frac{\alpha_1 \left( \frac{U_c}{\omega} \right)}{\alpha_1^2 + 1}$$

which shows a trend of decreasing integral scales at high frequencies. The wave number spectrum becomes of the dimensionless form

$$\frac{\phi_{11}(\vec{k} \approx 0, \omega; \vec{y})}{\phi_{11} \left( \frac{\omega y_1}{U_J} \right) y_1^3} \approx \frac{1}{\pi^3} \left( \frac{\omega y_1}{U_J} \right)^{-1} \frac{U_c}{U_J} \left( \frac{\Lambda_r}{y_1} \right) \left( \frac{\Lambda_\theta}{y_1} \right) \frac{\alpha_1}{\alpha_1^2 + 1} \quad (3.109)$$

This equation gives the asymptotic limit to the low wave number spectrum. Jones' measurements of  $\phi_m(\omega r_1 / U_c)$  in the potential core of a rectangular jet showed that

at a given frequency,  $\alpha_1$  decreases as  $y_1$  increases, i.e., that the correlation length at a given frequency increases with  $y_1$ . His measurements can be approximated as

$$\frac{\Lambda_m(\omega)}{y_1} \sim 0.63 \left( \frac{\omega y_1}{U_J} \right)^{-1/2}, \quad 2 < \frac{\omega y_1}{U_J} < 20$$

from which, we approximate

$$\alpha_1 \sim 1.6 \left( \frac{\omega y_1}{U_J} \right)^{-1/2}$$

In the orthogonal direction, using the collective results of Jones,<sup>107</sup> Kolpin,<sup>113</sup> and Fisher and Davis,<sup>110</sup> we set

$$\Lambda_r \approx \Lambda_\theta \sim y_1$$

and if  $\alpha > 1$  the variation of spectral density with distance from the jet becomes,

$$\frac{\phi_{11}(\vec{k} \approx 0, \omega; \vec{y})}{\phi_{11} \left( \frac{\omega y_1}{U_J} \right) D^3} \sim \left( \frac{\omega D}{U_J} \right)^{-1/2} \left( \frac{y_1}{D} \right)^{2.5} \quad (3.110)$$

which if  $\alpha < 1$

$$\sim \left( \frac{\omega D}{U_J} \right)^{-3/2} \left( \frac{y_1}{D} \right)^{1.5} \quad (3.111)$$

The function shows that as the flow develops, the correlation volume of the eddies increases, but there is some latitude indicated in the rate of increase. Jones made use of this frequency-dependent correlation volume in Equation (3.62) to

correctly predict the shape of the autospectrum of noise measured by Mollo-Christensen, Kolpin, and Martuccelli<sup>94</sup> over the frequency range of approximately  $0.4 < \omega D/U_J < 13$ .

3.6.3.4 The General Frequency Dependence of the Noise. The method of estimating the characteristics of the noise from these statistical qualities of the turbulence will now be illustrated for a simple case. Simple laws of similitude of jet noise that are based on a hypothesis that the sources of noise are due to local motions of the eddies in the jet have been given by Powell.<sup>119</sup> The analysis can be easily reproduced from the above relationships by invoking certain of the measured characteristics of the jet flow. Equations (3.63) and (3.69b), and a modification of Equation (3.109) which implies simply that\*  $\Lambda_m(\omega) \sim y_1$ , gives the dependence of the autospectrum of the sound on fluid parameters as

$$\Phi_p(r, \omega) \sim \frac{1}{c_o^4 r^2} \cdot \rho_o^2 U_J^2 \iiint_{vol} \omega^4 y_1^3 \left[ \frac{y_1}{U_J} \phi_{11} \left( \frac{\omega y_1}{U_J} \right) \right] dA_J dy_1 \quad (3.112)$$

where  $dA_J$  is the elemental cross-sectional area of the jet and where the integral length scales  $\Lambda_r$ ,  $\Lambda_\theta$ ,  $\Lambda_m(\omega)$  are each assumed to be proportional to  $y_1$ , (i.e., replace the 2.5 power in Equation (3.110) by 3). Now, from Figure 3.22 most of the turbulent energy is confined to the dimensionless frequency range

$$\Delta \left( \frac{\omega y_1}{U_J} \right) < 2\pi \quad (3.113)$$

The jet mechanics fall into two classifications depending on  $y_1$  being either less than or greater than  $4D$ , as shown in Figure 3.20. Therefore, in integrating over  $y_1$ , these separate regions must be considered. Also at a given frequency  $\omega$ , the region  $\Delta y_1$  over which the turbulence energy density is large, is defined by Equation (3.113), and this region is located at

---

\*This analysis, however, is insensitive to the dependence of  $\Lambda_m(\omega)$  on  $y_1$  selected because of the simple dimensional similitude that is established among  $\omega$ ,  $y_1$ ,  $U_J$ , and the intensity of the turbulence.

$$y_{1_0} \sim \frac{U_J}{\omega} \quad (3.114)$$

Consider, too, the sound pressure level measured in a frequency band  $\Delta\omega$  which is proportional to  $\omega$  so that the mean-square pressure  $\overline{p_1^2}$  is proportional to  $\omega \phi_p(r, \omega)$ . From Equation (3.114) the contribution from the mixing region ( $y_{1_0} < 4D$ ) will be generally high frequency while that from the fully developed region ( $y_{1_0} > 4D$ ) will control the low frequency sound. Therefore,

1. For  $y_{1_0} < 4D$ , the following situation arises.

The shear flow occupies an annular region of area,

$$A_J \sim Dr_m \sim y_{1_0} D$$

the intensity goes as,

$$\overline{u^2} \sim U_J^2$$

and the dimensionless spectrum as

$$\Delta \left( \frac{\omega y_{1_0}}{U_J} \right) \cdot \phi_{11} \left( \frac{\omega y_{1_0}}{U_J} \right) \sim \overline{u^2}$$

then the radiated sound pressure behaves as

$$\begin{aligned} \overline{p^2}(r, \omega) &\sim \frac{\rho_o^2 U_J^2}{c_o^4 r^2} \cdot \omega^4 \phi_{11} \left( \frac{\omega y_{1_0}}{U_J} \right) \frac{\omega y_{1_0}}{U_J} y_{1_0}^3 \cdot Dy_{1_0} \cdot \Delta y_{1_0} \\ &\sim \frac{\rho_o^2 U_J^7}{c_o^4 r^2} \frac{D}{\omega} \left( \frac{\omega y_{1_0}}{U_J} \right) \overline{u^2} \\ \overline{p^2}(r, \omega) &\sim \frac{\rho_o^2 U_J^8}{c_o^4 r^2} \frac{D^2}{\omega^2} \left( \frac{\omega D}{U_J} \right)^{-1}, \quad \frac{\omega D}{U_J} > 1 \end{aligned} \quad (3.115a)$$



since  $\frac{\omega y_{1o}}{U_J} = \left(\frac{\omega D}{U_J}\right) \left(\frac{y_{1o}}{D}\right) \sim \text{constant}$

2. For  $y_{1o} > 4D$ , the following situation arises.

The jet spreads with its characteristic velocity being  $U_c$ . Now

$$U_c \sim y_1^{-1}$$

$$A_J \sim r_m^2 \sim y_1^2$$

$$\overline{u^2} \sim U_{cL}^2 \sim U_J^2 \left(\frac{y_1}{D}\right)^{-2}$$

$$\Delta \left(\frac{\omega y_1}{U_\xi}\right) \phi_{11} \left(\frac{\omega y_1}{U_\xi}\right) \sim \overline{u^2}$$

but for a bandwidth dependent on  $U_\xi$

$$\Delta \left(\frac{\omega y_1}{U_\xi}\right) < 2\pi$$

so that the source location is

$$y_{1o} \sim \frac{U_\xi}{\omega}$$

Then the integral becomes

$$\begin{aligned} \overline{p^2}(r, \omega) &\sim \frac{\rho_o^2 U_J^2}{c_o^4 r^2} \omega^4 y_{1o}^3 \frac{\omega y_1}{U_\xi} \phi_{11} \left(\frac{\omega y_1}{U_\xi}\right) \cdot y_{1o}^2 \Delta y_1 \\ &\sim \frac{\rho_o^2 U_J^2}{c_o^4 r^2} \cdot \omega^4 \overline{u^2} y_{1o} y_{1o}^3 y_{1o}^2 \end{aligned}$$

which, upon regrouping, becomes

$$\overline{p^2}(r, \omega) \sim \frac{\rho_o^2 U_J^8 D^2}{c_o^4 r^2} \left( \frac{\omega D}{U_J} \right)^2, \quad \frac{\omega D}{U_J} < \frac{1}{2} \quad (3.115b)$$

since

$$\frac{\omega y_{1o}}{U_J} \sim \frac{\omega D}{U_J} \left( \frac{y_{1o}}{D} \right)^2 \sim \text{constant}$$

Equations (3.115) are the two classical similarity formulae, and they are shown in Figure 3.19 to roughly correspond to the extreme frequency ranges of the measured sound pressure levels. The analysis suggested<sup>21,119</sup> that the low and high frequency pressures are strongly dependent on the turbulence in the developed jet and mixing-layer regions, respectively, and that the midrange frequencies are determined by the flow at the end of the potential core region. The Equations (3.115) also show the simple  $U_J^8$  dependence of the noise that had emerged earlier in this section (Equation (3.65)) from the requirement of simple similarity of the sources being dependent on  $\omega D/U_J$  and  $\rho_o^2 U_J^4 D^3$ . Other similar simple arguments concerning the effective source-location had been given by Dyer.<sup>120</sup> In ignoring refraction across the moving-quiescent fluid interface, the above analysis applies only to broadside radiation,  $\theta = 90^\circ$ .

Although we have set the frame work for a more elaborate synthesis of the noise in terms of the statistics of the Reynolds stresses, we have stopped short of that analysis because of the labor required to accomplish it. Reference to the work of Ribner<sup>100,104</sup> (summarized by Goldstein)<sup>85</sup> and the more recent work, e.g., of Moon and Zelanzy<sup>121</sup> by the interested reader will give the details of such analyses.

The similarity arguments given above have shown the importance of the mixing region in determining the intensity spectrum levels at high frequencies, and, therefore, the dominance of the mixing region dynamics of the overall power. Recent measurements of sound using a directional microphone in the far field by Grosche, Jones, and Wilhold<sup>122</sup> indicated that the effective source distribution lies near the end of the mixing region. The problem in interpreting such intensity measurements with directional receivers is that one first assumes that a simple localized

convected source model truly describes the physical process then he deduces the distribution of average source strength. The noise is actually an integrated resultant of the effects of a distribution of sources, and there may be many possible distributions giving rise to a given far field intensity.<sup>123</sup> However, it has been found useful to deduce the distribution of apparent sources and additional schemes<sup>124-126</sup> have been developed to do so.

A different approach by Maestrello<sup>127,128</sup> for deducing sound source locations utilizes the correlations of pressure gradients near, but outside, the jet. The sound pressure, at a distant point in space, is uniquely given by an integral, over a surface surrounding the jet, of the normal gradient of the pressure on that surface multiplied by the Neumann-Green function for that surface. Since the ambient fluid is isolated from the jet by this surface, and since the ambient fluid is source-free, the correlation between far field and (directional) near field pressure gradients signifies a cause-effect relationship between an effective source and resulting noise. Maestrello<sup>127</sup> reports that the maximum source density results from a region at  $y_1 \sim 9D$ , which is downstream of the mixing zone.

3.6.3.5 The Role of Axisymmetric Disturbances in Jet Noise. A major shortcoming exists in full reliance of turbulence measurements such as shown in Figures 3.21 and 3.23 to evaluate Equation (3.64) particularly for subsonic jets. That is, behavior of the wave number spectrum for  $k \sim k_0 \ll \omega/U_c$  cannot be elucidated from the measurements of turbulence. More contemporary research has therefore taken a different tack, that is, to interconnect the various events which take place in the development of subsonic jet structure and noise. The visualization of axisymmetric eddies in jets by Crow and Champagne<sup>48</sup> and Browand and Laufer<sup>47</sup> allows the clear qualitative identification of the responsibility of these eddies in the development of disturbances. Furthermore, these eddies can be ultimately traced to the modes of axisymmetric instability, as can be deduced from the early studies of shear layers<sup>20,22,23</sup> previously discussed in Section 3.2 (Figures 3.3 and 3.9). The existence of instability waves at high Reynolds number, although deduced by Crow and Champagne, has been analytically confirmed by Crighton and Gaster<sup>129</sup> using stability theory. Furthermore, a connection between the existence of forced shear layer instability and radiated sound was identified in the experiments of Moore<sup>130</sup> and Bechert and Pfizenmaier<sup>131</sup> although it had been earlier suggested by Mollo-Christensen.<sup>95</sup> In Moore's experiment, the circular jet shear layer was driven by a

loud speaker inside the plenum chamber of the nozzle. Pressure and velocity waves propagating along the centerline from the nozzle were seen to amplify when the frequencies of those waves were confined to a restricted range that coincided with the range of unstable axisymmetric mode frequencies of the undisturbed jet. These waves were determined by visualization to modulate the vortex formation and pairing in the mixing region. With high-level excitation of the jet, the magnitude of induced disturbances at the driving frequencies did not increase in proportion to the excitation level, but rather the broadband centerline pressure and velocity levels were increased somewhat by the excitation. The broadband far field sound pressure was also increased when driving the jet with a root mean square pressure of only 0.08 percent of the dynamic pressure of the centerline ( $1/2 \rho_o u_J^2$ ). The results were interpreted to show that in the formation of ordered vorticity from the spatially growing shear layer vibration, undisturbed fluid entrainment by the large eddies lead to increased turbulence that apparently increases the magnitude of the  $\rho_o u_1 u_J$  acoustic sources. As shown in Equation (3.108), the wave motion of the shear layer itself cannot radiate sound unless the value of  $\partial^2 / \partial t^2 (\rho_o u_1 u_J)$  is large enough in the wave number range of  $|\vec{k}| = k_o$ ; i.e., unless this second time derivative is correlated over regions which are comparable to  $2\pi k_o$ . It remains to be seen whether, under conditions of vortex pairing,<sup>46,47,132,133</sup> the time and space scales in subsonic jets match the acoustic wave number. That these motions may be plausibly considered as<sup>134-136</sup> radiators in supersonic jets is well-founded since their wave speeds  $U_c$  exceed the speed of sound, but this is a class of flow which is well-beyond the scope of hydroacoustics.

### 3.7 NOISE FROM UNSTEADY MASS INJECTION

This section will deal with certain general characteristics of noise that result from a jet efflux that is either turbulent or bubbly. The latter case has to do with unsteady two-phase motions (liquid and gas) although the complete subject will be examined in Chapter 4. Unsteadiness of exiting flow brings about a  $U_J^4$  or  $U_J^6$  speed dependence depending on the mechanism and this dependence contrasts sharply with the classical  $U_J^8$  dependence that is known for the developing free-jet. Furthermore, in the case of two-phase turbulent jets, one would also expect a  $U_J^8$  speed dependence, but amplified by a factor which is the fourth power of the ratio of the speed of sound in the acoustic medium to the speed of sound in the two-phase jet.

### 3.7.1 Sound from Efflux Inhomogeneities

When an inhomogeneous fluid is exhausted into a homogeneous medium, as illustrated in Figure 3.25, sound can be created as a result of volume velocity fluctuations induced at the orifice and turbulence in the ensuing two-phase jet. The topic of the unsteady orifice flow was given attention by Ffowcs Williams and Gordon<sup>137</sup> and Ffowcs Williams<sup>138</sup> who examined the noise from low speed turbulence exhaust. Ffowcs Williams<sup>138</sup> deduced a  $U^4$  speed dependence for this noise, but the result is now superseded by a later paper (Ffowcs Williams and Howe)<sup>139</sup> which treats the matter in more detail. Apparently, in the earlier paper, the compressibility of the fluid in the nozzle was overlooked.

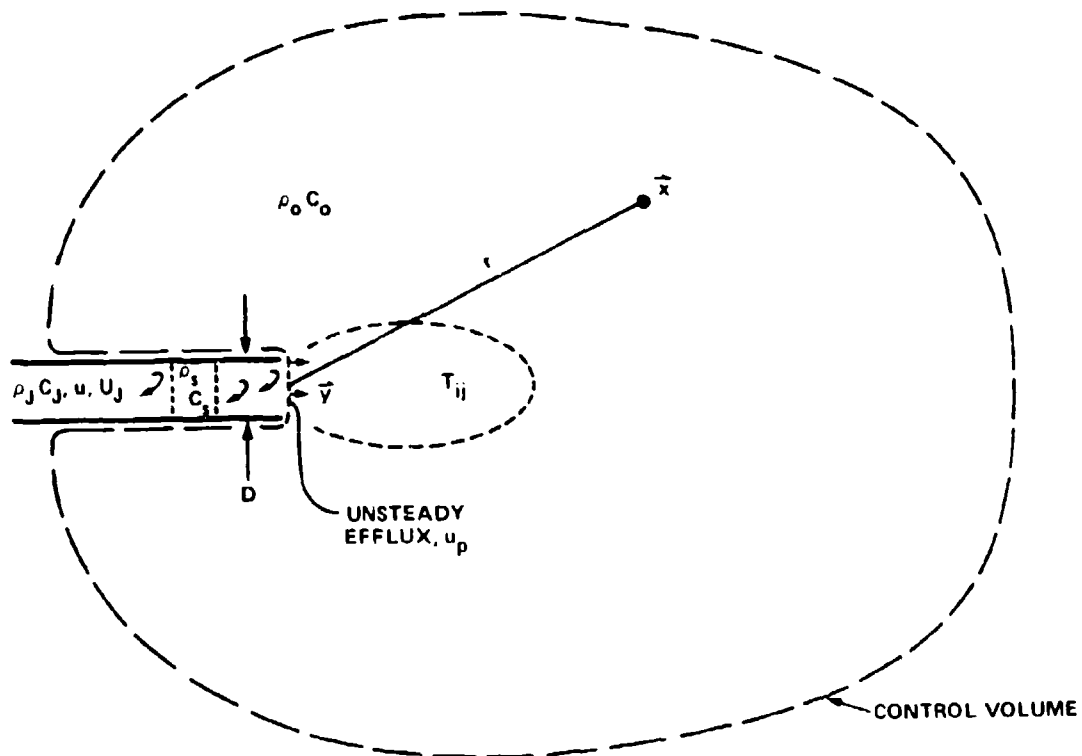


Figure 3.25 - Geometry of the Problem of Unsteady Efflux into an Unbounded Medium,  $D \ll \lambda_o$

That result applies to the case of the unsteady pumping of an incompressible fluid from an enclosed plenum into a free space. In this case the pipe length from the pump to the exit must be shorter than an acoustic wavelength. There is then a time varying rate of volume injection  $q$ , so that the far field sound pressure from the (unbuffed nozzle) is (Equation (2.27))

$$p(r,t) = \frac{\rho_o [\dot{q}]_{t-r/c_o}}{4\pi r}$$

Now,  $[\dot{q}] = \omega_v u A_n$

where  $\omega_v$  = pulsation frequency of the pump

$u$  = amplitude of the velocity fluctuation at the nozzle

$A_n$  = nozzle area

The pulsation frequency  $\omega_v$  will be proportional to the shaft speed  $\Omega$ ; the velocity fluctuation will also increase in proportion to  $\Omega D$  (where  $D$  is pump diameter) with the proportionality dependent on the pump type. Accordingly, for a given pump the mean-square sound pressure should increase as

$$\overline{p^2} \sim \rho_o^2 \frac{\Omega^4}{r^2} A_n^2 D^2$$

which is the fourth power of shaft speed.

We shall now consider cases in which compressibility enters the solution. The noise produced due to  $T_{ij}$  in the jet will be discussed in the next subsection. In the first case, consider the noise produced by a density inhomogeneity in the efflux. This will be modeled as a slug, shown generally in Figure 3.25 and in detail in Figure 3.26, which passes through a nozzle into the outer fluid. The length of the fluid slug, the length of the nozzle, and the diameter of the discharge nozzle will be considered small compared to an acoustic wavelength. This problem was treated in general fashion by Ffowcs Williams and Howe,<sup>139</sup> but here we will offer a few physical arguments (retrospectively) in order to illustrate the fundamentals.

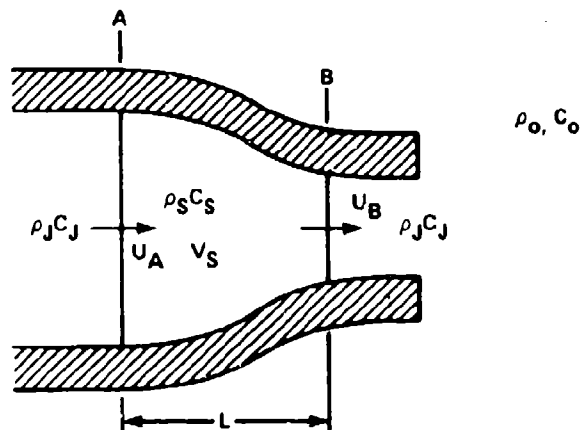


Figure 3.26 - Slug Passing through a Nozzle

The average flow through the nozzle is essentially one-dimensional and  $\omega L/c_s < 1$ . The noise comes from two sources. The first occurs as each of the slug interfaces A and E are ejected; a pressure surge occurs in the nozzle that is equal to the change in dynamic pressure (due to the different densities). This pressure surge induces a piston-like particle motion across the orifice. The second is due to a volume change in the slug as it passes through the pressure field of the contraction. The sound from the first source is derived from the one-dimensional momentum Equation (2.2) integrated across each interface:

$$\rho \frac{\partial u_1}{\partial t} + \frac{\partial}{\partial x_1} \left( P + \rho \frac{u_1^2}{2} \right) = 0$$

so the integral across interface A is

$$\int \rho \dot{u}_A dx_1 = - \frac{\rho_s - \rho_J}{2} U_A^2$$

and across interface B it is

$$\int \rho \dot{u}_B dx_1 = - \frac{\rho_J - \rho_s}{2} U_B^2$$

That result applies to the case of the unsteady pumping of an incompressible fluid from an enclosed plenum into a free space. In this case the pipe length from the pump to the exit must be shorter than an acoustic wavelength. There is then a time varying rate of volume injection  $q$ , so that the far field sound pressure from the (unbaffled nozzle) is (Equation (2.27))

$$p(r,t) = \frac{\rho_o [\dot{q}]_{t-r/c_o}}{4\pi r}$$

Now,  $\left[ \dot{q} \right] = \omega_v u A_n$

where  $\omega_v$  = pulsation frequency of the pump

$u$  = amplitude of the velocity fluctuation at the nozzle

$A_n$  = nozzle area

The pulsation frequency  $\omega_v$  will be proportional to the shaft speed  $\Omega$ ; the velocity fluctuation will also increase in proportion to  $\Omega D$  (where  $D$  is pump diameter) with the proportionality dependent on the pump type. Accordingly, for a given pump the mean-square sound pressure should increase as

$$\overline{p^2} \sim \rho_o^2 \frac{\Omega^4}{r^2} A_n^2 D^2$$

which is the fourth power of shaft speed.

We shall now consider cases in which compressibility enters the solution. The noise produced due to  $T_{ij}$  in the jet will be discussed in the next subsection. In the first case, consider the noise produced by a density inhomogeneity in the efflux. This will be modeled as a slug, shown generally in Figure 3.25 and in detail in Figure 3.26, which passes through a nozzle into the outer fluid. The length of the fluid slug, the length of the nozzle, and the diameter of the discharge nozzle will be considered small compared to an acoustic wavelength. This problem was treated in general fashion by Ffowcs Williams and Howe,<sup>139</sup> but here we will offer a few physical arguments (retrospectively) in order to illustrate the fundamentals.



$$P_{\text{rad}_m}(\vec{x}, t) \approx - \frac{V_s}{4\pi r L} \frac{\rho_o}{\rho_s} \left( \frac{U}{C_s} \right)^2 \frac{1}{U} \left[ \frac{\partial}{\partial t} (P_A - P_B) \right] \quad (3.119)$$

where the brackets denote evaluation at the retarded time. This radiation is monopole-like owing to its direct dependence on the pulsation of the volume  $V_s$ .

The two components  $P_{\text{rad}_m}$  and  $P_{\text{rad}_d}$ , however, depend on speeds of sound in such a way that the dipole component overwhelms the monopole component whenever

$$\frac{U}{C_J} \left( \frac{C_s}{U} \right)^2 \gg 1$$

or, when

$$\left( \frac{C_s}{C_J} \right)^2 \gg \frac{U}{C_J} \quad (3.120)$$

This is generally the case unless speed of sound in the slug is very low and the discharge velocity is very large.

One such instance could occur if the slug is a bubbly slurry in an otherwise homogeneous jet liquid. In this case (see Chapter 4) the speed of sound in the slug could be quite small relative to  $C_J$ .

Note that the two contributions to the radiation have different dependences on speed. Letting

$$\frac{\partial P}{\partial t} = - U \frac{\partial P}{\partial x} - \frac{U}{L} \left( \frac{1}{2} \rho_s U^2 \right) \frac{\partial C_P}{\partial \left( \frac{x}{L} \right)}$$

where the change in pressure coefficient is nondimensional, we find

$$P_{\text{rad}_d} \sim \frac{-A_o}{8\pi r L} \frac{\rho_o}{\rho_J} \left( \frac{\rho_s - \rho_J}{\rho_J} \right) \left( \frac{U}{C_J} \right)^3 \rho_J C_J^2 \quad (3.121)$$

while

$$p_{\text{rad}_m} \sim \frac{V_s}{8\pi r L^2} \frac{\rho_o}{\rho_s} \left( \frac{U}{C_J} \right)^4 \rho_J C_J^2 \quad (3.122)$$

Therefore, the dipole sound power increases as  $U^6$  while the monopole sound power increases as  $U^8$ , reflecting the inequality of Equation (3.120) that the monopole source is essentially a high-speed source.

Referring again to radiation caused by a bubbly slurry, and considering now the dipole component only, we write the density of the slug in terms of the jet liquid density  $\rho_J$ , the gas density  $\rho_g$ , and the volume fraction of gas  $\beta$ . The density is

$$\rho_s = \beta \rho_g + (1-\beta) \rho_J$$

Therefore, in Equation (3.108)

$$\frac{\rho_s - \rho_J}{\rho_J} = \frac{\beta(\rho_g - \rho_J)}{\rho_J} \approx \beta$$

if  $\rho_g \ll \rho_J$ . The radiated sound pressure can now be written

$$p_{\text{rad}_d} \sim \frac{-A_o}{8\pi r L} \beta \frac{\rho_o}{\rho_J} \left( \frac{U}{C_J} \right)^3 \rho_J C_J^2 \quad (3.123)$$

The sound pressure will increase linearly with the volume fraction and as velocity cubed. Lengthening the nozzle (increasing  $L$ ) reduces the noise. For a given volumetric flow rate ( $A_o U$ ) the sound pressure increases as the orifice area is decreased as  $A_o^{-2}$ .

Proceeding as above we can also examine the turbulent efflux of a single-phase compressible fluid. The average velocity-induced pressure fluctuation across the orifice,  $\rho_J u_o U$ , drives the fluid in the free field. This causes an acoustic particle velocity in the pipe orifice given by Equation (3.117),

$$u_p \sim \frac{\rho_J u_o U}{\rho_J C_J} \sim u_o \frac{U}{C_J}$$

so that the radiated sound pressure in the free space is

$$P_{\text{rad}} \sim \frac{\rho_o A_o}{4\pi r} [\dot{u}_p]$$

$$\sim \frac{\rho_o A_o}{4\pi r} \frac{U}{C_J} \cdot \frac{U}{\Lambda_1} u_o$$

where we have replaced  $\partial/\partial t$  by  $U/\Lambda_1$ ,  $\Lambda_1$  being the integral scale of the turbulence in the axial direction. Since  $u_o \sim U$  we can write

$$P_{\text{rad}} \sim \frac{A_o}{4\pi r \Lambda_1} \rho_o C_J^2 \left( \frac{U}{C_J} \right)^3 \quad (3.124)$$

which shows the sound power increasing as  $U^6$ .

Other problems of this sort have been examined by Ffowcs Williams and Howe<sup>139</sup> who treated the effluxes consisting of occasional slugs of fluid with density varying from the main fluid, Whitfield and Howe<sup>140</sup> who considered noises from volumetric pulsations of bubbles passing from the nozzle into an ambient pressure field (see also Chapter 4), and Plett and Summerfeld<sup>141</sup> who considered the density and velocity inhomogeneities analogous to the above.

### 3.7.2 Inhomogeneities in the Free Turbulent Field

Another problem related to two-phase jets has been treated by Crighton and Ffowcs Williams<sup>142</sup> and by Crighton.<sup>89</sup> Basically, the analysis considers a bubbly turbulent region of gas concentration  $\beta$  which is surrounded by the ambient fluid with properties  $\rho_o, C_o$ . In the absence of any net mass injection or forces on the fluid, the appropriate form of the stress tensor becomes<sup>142</sup>

$$T_{ij} = (1-\beta) \rho_o u_i u_j + (p - C_o^2 \rho) \delta_{ij} + \tau_{ij} \quad (3.125)$$

Instead of Equation (2.50) where  $p$  is the dilatational pressure fluctuation in the turbulent two-phase medium. Equation (2.59) is written as

$$\begin{aligned}
p_a(\vec{x}, t) &= \frac{1}{4\pi} \frac{\partial^2}{\partial x_i \partial x_j} \iiint \frac{[T_{ij}]}{r} dV(\vec{y}) \\
&= \frac{1}{4\pi} \frac{x_i x_j}{r^2} \frac{\partial^2}{\partial t^2} \iiint \frac{[T_{ij}]}{r} dV(\vec{y})
\end{aligned} \tag{3.126}$$

which becomes<sup>80</sup>

$$p_a(\vec{x}, t) \approx \frac{1}{4\pi C_o^2} \frac{1}{r} \frac{\partial^2}{\partial t^2} \iiint [p - \rho C_o^2] dV(\vec{y}) \tag{3.127}$$

Adiabatic pressure fluctuations in the two-phase region are related to density fluctuations in that region by  $\delta p = C_m^2 \delta \rho$  so that the time-varying part of the integrand then Equation (3.127) becomes  $\delta p - C_o^2 (\delta p / C_m^2)$ . When the external fluid is water and the bubbly region contains gas,  $C_m < C_o$  then becomes

$$p(\vec{x}, t) \approx \frac{-1}{4\pi C_o^2 r} \iiint \frac{C_o^2}{C_m^2} \frac{\partial^2 p}{\partial t^2} dV(\vec{y}) \tag{3.128}$$

Now if disturbances in the region are characterized by velocity  $u$ , then the pressure is given by  $p \sim \rho u^2 \sim \rho_o u^2$  and  $\partial/\partial t \sim u/\ell$ , where  $\ell$  is the macroscale of the disturbance. Therefore, with the elemental volume of the disturbance  $\delta V \sim \ell^3$ , Equation (3.127) gives

$$p(\vec{x}, t) \sim \left( \frac{\rho_o \ell}{C_o^2 r} \right) \left( \frac{C_o^2}{C_m^2} \right) u^4 \tag{3.129}$$

which dominates the usual quadrupole radiation,

$$p(\vec{x}, t) \sim \left( \frac{\rho_o \ell}{C_o^2 r} \right) u^4$$

by the factor  $C_o^2/C_m^2 > 1$ . Also, the field has an omnidirectional radiation rather than being of a typical quadrupole nature, as seen in comparing Equations (3.126) and (3.127).

Finally, it should be noted that the speed of sound in a mixture is given by

$$C_m = \frac{R_b \omega_b}{(3\beta)^{1/2}}$$

where  $\omega_b$  is the resonance frequency of the bubbles of radius  $R_b$  (see Equation (4.20)).

The enhancement of radiated noise intensity brought about by the factor  $(C_o/C_m)^4$ , as pointed out by Crighton<sup>89</sup> will be as much as 50 dB over that of single-phase jets for concentrations  $\beta$  on the order of 1 percent. This and the previous analysis of unsteady mass flux suggest important hydroacoustical sources for which experimental confirmation is totally lacking.

### 3.8 APPENDIX A — MEASUREMENT OF CROSS SPECTRAL DENSITIES WITH FILTERED SIGNALS

In Section 3.5.3 we examined the theoretical properties of the cross spectral density as a Fourier transform of the space-time correlation. Now we examine the operational requirements for obtaining this function in experiments. Extensive discussions of this subject are given by Lee<sup>79</sup> and Bendat and Piersol.<sup>80</sup>

Consider two sensors giving electric signals in response to velocity, pressure, or acceleration fluctuations. The physical and electronic arrangements are shown in Figure 3.A27, for the case of disturbances convected past two probes as would be the

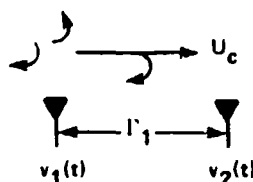


Figure 3.A27a - Physical Arrangement

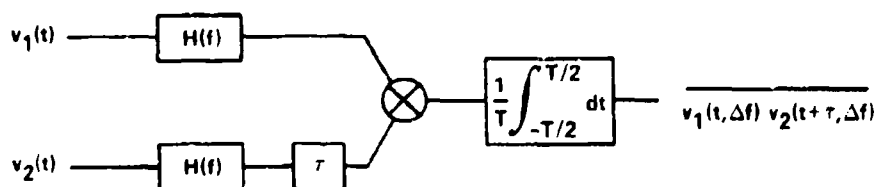


Figure 3.A27b - Electronic Arrangement

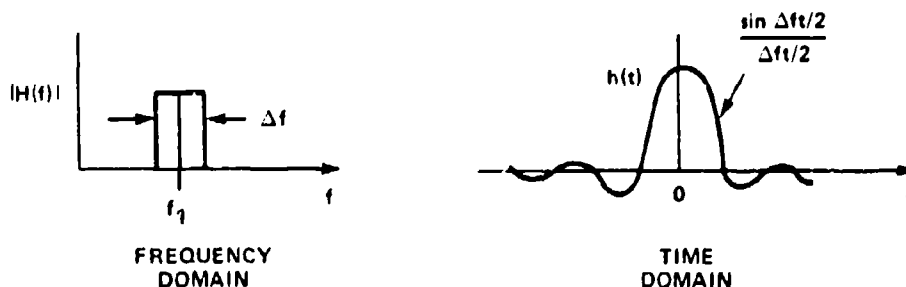


Figure 3.A27c - Idealized Filter Function

Figure 3.A27 - Diagram of Physical Arrangement and Electronic Components and Functions which are Used in Measurements of Cross Spectral Densities

case in a turbulence measurement. The electrical signals are passed through matched electronic filters, which pass energy only within the frequency range  $f_1 \pm \Delta f/2$ . For simplicity, the filter function  $H(f)$  is assumed to be rectangular in shape so that the temporal response of the filter is given to the right of Figure 3.A27c. One filtered signal is delayed a time  $\tau$  after it is filtered.

The steady-state voltage leaving the filter is given as

$$v(t, \Delta f) = \int_{-\infty}^t V(t_1) h(t-t_1) dt_1 \quad (3.A128)$$

i.e., the output of the filter at  $t$  depends on the information entering the filter for all time preceeding  $t$ . Rearranging Equation (3.A128),

$$v(t, \Delta f) = \int_0^{\infty} h(t_2) v(t_2+t) dt_2$$

or we can write

$$v(t, \Delta f) = \int_{-\infty}^{\infty} g(t_2) h(t_2) v(t_2+t) dt_2 \quad (3.A129)$$

where  $g(t_2) = 0$  for  $t_2 < 0$ . Now, introducing the generalized Fourier transforms of  $h(t)$  and  $v(t)$  we can write

$$g(t_2) h(t_2) = \frac{1}{2\pi} \int_{-\infty}^{\infty} H(\omega'') e^{-i\omega'' t_2} d\omega''$$

$$v(t_2+t) = \int_{-\infty}^{\infty} V(\omega') e^{-i\omega'(t_2+t)} d\omega'$$

so that (by Equation (2.123))

$$\begin{aligned}
 v(t, \Delta f) &= \int_{-\infty}^{\infty} dt_2 \int_{-\infty}^{\infty} d\omega'' \int_{-\infty}^{\infty} d\omega' e^{-i(\omega'' + \omega') t_2} e^{-i\omega' t} \left( \frac{1}{2\pi} \right) V(\omega') H(\omega'') \\
 &= \int_{-\infty}^{\infty} d\omega'' \int_{-\infty}^{\infty} d\omega \delta(\omega'' + \omega') e^{-i\omega' t} V(\omega') H(\omega'') \\
 &= \int_{-\infty}^{\infty} e^{i\omega t} H(\omega) V(\omega) d(\omega)
 \end{aligned} \tag{3.A130}$$

The frequency  $f$  is related to  $\omega$  by  $\omega = 2\pi f$ .

Now, the delayed filtered voltage can be written

$$v(t+\tau, \Delta f) = \int_{-\infty}^{\infty} e^{i\omega'(t+\tau)} H(\omega') V(\omega') d\omega' \tag{3.A131}$$

and the time-averaged product of the voltages becomes

$$\begin{aligned}
 \overline{v_1(t, \Delta f) v_2(t+\tau, \Delta f)} &= \frac{1}{T} \int_{-T/2}^{T/2} v_1(t, \Delta f) v_2(t+\tau, \Delta f) dt \\
 &= \int_{-\infty}^{\infty} d\omega \int_{-\infty}^{\infty} d\omega' H^*(\omega) H(\omega') V^*(\omega) V(\omega') e^{i\omega'\tau} \dots \\
 &\quad \times \frac{1}{T} \int_{-T/2}^{T/2} e^{-i(\omega - \omega')t} dt
 \end{aligned}$$



In limit as  $T \rightarrow \infty$  we invoke Equation (2.122) so that

$$\overline{v_1(t, \Delta f) v_2(t+\tau, \Delta f)} = \int_{-\infty}^{\infty} |H(\omega)|^2 \left\{ \lim_{T \rightarrow \infty} \frac{2\pi}{T} v_1^*(\omega) v_2(\omega) \right\} e^{i\omega\tau} d\omega \quad (3.A132)$$

Recalling, now, Equation (3.42), we can rewrite this result in the form of the cross spectral density of the voltages, i.e., we now have

$$\overline{v_1(t, \Delta f) v_2(t+\tau, \Delta f)} = \int_{-\infty}^{\infty} e^{i\omega\tau} \phi_{v_1 v_2}(\omega) |H(\omega)|^2 d\omega \quad (3.A133)$$

where  $\phi_{v_1 v_2}(\omega)$  has both amplitude and phase.

To complete the analysis we show the relationship between the analytical filter function  $H(\omega)$ , that is defined over  $-\infty < \omega < \infty$ , and the physical function  $H(f)$ , that is defined over  $0 < f < \infty$ . Returning to Equation (3.A129), we note that

$$\begin{aligned} H(\omega) &= \int_{-\infty}^{\infty} g(t_2) h(t_2) e^{i\omega t_2} dt_2 \\ &= \int_0^{\infty} h(t_2) e^{i\omega t_2} dt_2 \end{aligned}$$

However, since

$$H(-\omega) = \int_0^{\infty} h(t_2) e^{-i\omega t_2} dt_2$$

and since  $h(t_2) = h(-t_2)$ , we have the two-sided transform pair

$$H(\omega) + H(-\omega) = \int_{-\infty}^{\infty} h(t_2) e^{i\omega t_2} dt_2$$

and

$$h(t_2) = \frac{1}{2\pi} \int_{-\infty}^{\infty} [H(\omega) + H(-\omega)] e^{-i\omega t_2} d\omega$$

Note that  $H(-\omega) = H^*(\omega)$ , i.e., is the complex conjugate of  $H(\omega)$ . Now, we define the one-sided filter function

$$\begin{aligned} H(f) &= \int_0^{\infty} h(t_2) \cos 2\pi f t_2 dt_2 \\ &\equiv \frac{1}{2} \int_0^{\infty} h(t_2) \left( e^{i\omega t_2} + e^{-i\omega t_2} \right) dt_2 \\ &= \frac{1}{2} \int_{-\infty}^{\infty} h(t_2) e^{i\omega t_2} dt_2 \end{aligned}$$

which is the one-half of the complete transform of  $h(t)$ ; and so

$$H(f) = \frac{1}{2} [H(\omega=2\pi f) + H(-\omega=-2\pi f)]$$

is a real function, having no imaginary part, and, therefore,

$$|H(f)|^2 = |\mathcal{R}_e(H(\omega=2\pi f))|^2$$

for  $0 < f < \infty$

$$= |H(\omega=2\pi f)|^2 \quad (3.A134)$$

Using Equation (3.A133) we can determine the autospectrum of the voltage as

$$\overline{v_1(t, \Delta f) v_1(t, \Delta f)} = \int_{-\infty}^{\infty} \phi_w(\omega) |H(\omega)|^2 d\omega \quad (3.A135)$$

If we assume that the width of the filter,  $\Delta\omega = 2\pi\Delta f$ , is narrow compared to the order of variation of  $\phi_{vv}(\omega)$ , then Equation (3.A135) gives (since  $\phi(\omega) = \phi(-\omega)$ )

$$\begin{aligned} \overline{v_1^2(t, \Delta f)} &= \phi_{vv}(\omega) [|H(\omega)|^2 + |H(-\omega)|^2] \Delta\omega \\ &\equiv 2 \phi_{vv}(\omega=2\pi f) |H(f)|^2 (2\pi\Delta f) \end{aligned}$$

Therefore, the autospectral density is found by

$$\phi_{vv}(\omega=2\pi f) = \lim_{\Delta f \rightarrow 0} \frac{\overline{v_1^2(t, \Delta f)}}{4\pi \Delta f} \quad (3.A136)$$

where we have let  $|H(f)|^2 = 1$  inside the pass band of the filter. The physical spectrum, say  $G_{vv}(f)$  can be written as

$$\overline{v_1^2(t, \Delta f)} = G_{vv}(f) |H(f)|^2 \Delta f \quad \text{for } 0 < f < \infty$$

so that measured spectrum is related to the autospectral density by

$$G_{vv}(f) = 4\pi \phi_{vv}(\omega=2\pi f) \quad (3.A137)$$

The cross spectral density of  $v_1(t)$  and  $v_2(t)$  can be obtained from Equation (3.A133) as

$$\overline{v_1(t, \Delta f) v_2(t+\tau, \Delta f)} = \left[ \phi_{v_1 v_2}(\omega_o) e^{i\omega_o \tau} + \phi_{v_1 v_2}(-\omega_o) e^{-i\omega_o \tau} \right] \\ \times |H(\omega_o)|^2 \Delta\omega_o$$

Letting

$$\phi_{v_1 v_2}(\omega) = |\phi_{v_1 v_2}(\omega)| e^{i\alpha(\omega)}$$

with

$$\alpha(\omega) = -\alpha(\omega) \quad (3.A138a)$$

and

$$|\phi_{v_1 v_2}(\omega)| = |\phi_{v_1 v_2}(-\omega)| \quad (3.A138b)$$

then

$$\overline{v_1(t, \Delta f) v_2(t+\tau, \Delta f)} = |\phi_{v_1 v_2}(\omega_o = 2\pi f_o)| \cos(2\pi f_o \tau + \alpha) \quad (3.A139) \\ = C(\tau, \Delta f)$$

is the narrowband cross correlation in terms of the cross spectral density. The various components of the cross spectral density can be found from this function as

$$C\left(\tau = \frac{-1}{2f_o}\right) = + |\phi_{v_1 v_2}(\omega_o = 2\pi f_o)| \sin \alpha \quad (3.A140a)$$

and

$$C(\tau=0) = |\phi_{v_1 v_2}(\omega_0 = 2\pi f_0)| \cos \alpha \quad (3.A140b)$$

from which the amplitude and phase may be determined.

Modern laboratory instrumentation allows a direct measure of the cross spectral density in which a Fourier transform is obtained over a limited interval in which  $h(t)$  is replaced by a window in which the signal is sampled. The transform, Equation (3.A130), is then obtained directly and the spectrum functions are obtained from  $V_1(\omega)$  and  $V_2(\omega)$ .

Two symmetry properties for the cross spectral density and the filter response function were cited above, Equations (3.A134), (3.A138a), and (3.A138b). These properties arise from the behavior of the cross correlation, as illustrated in Figure 3.A28. Letting the cross correlation of the signals be  $R_{12}(\tau)$ , then the cross spectral density is

$$\phi_{12}(\omega) = \frac{1}{2\pi} \int_{-\infty}^{\infty} e^{i\omega\tau} R_{12}(\tau) d\tau$$

If  $R_{12}$  is symmetric about  $\tau = 0$ , i.e.,

$$R_{12}(\tau) = R_{12}(-\tau)$$

then

$$\phi_{12}(\omega) = \frac{1}{\pi} \int_0^{\infty} R_{12}(\tau) \cos \omega\tau d\tau$$

which is a real function. However, if the correlation function is symmetric about a time delay  $\tau = \bar{\tau}$ , for example,

$$R(\tau) = R(\tau - \bar{\tau}) \quad (3.A141)$$

then, letting  $\tau' = \tau - \bar{\tau}$

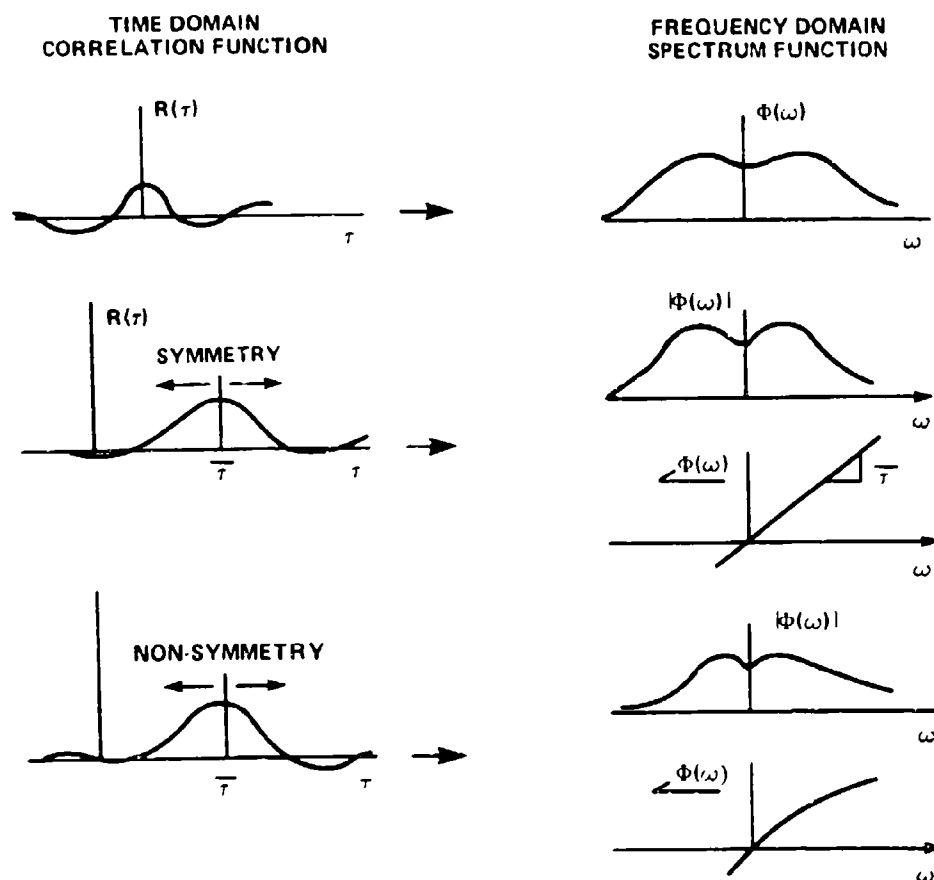


Figure 3.A28 - Illustrations of Correlations and Their Spectral Transformations

$$\begin{aligned}\phi_{12}(\omega) &= \frac{e^{i\omega\bar{\tau}}}{2\pi} \int_{-\infty}^{\infty} e^{i\omega\tau'} R(\tau') d\tau' \\ &= \frac{e^{i\omega\bar{\tau}}}{\pi} \int_0^{\infty} R(\tau') \cos \omega\tau' d\tau'\end{aligned}$$

A temporally symmetric signal, then, has a real spectrum function and conversely a nonsymmetric (about  $\tau=0$ ) signal correlation has a complex spectrum function. There

are many general cases in which the symmetry condition may not hold, in which case the phase versus frequency line will be curved, and the amplitude will not necessarily be symmetric about  $\pm \omega$ .

We have seen in Section 3.6 (as we shall see further) that space-time correlations of turbulence generally appear as in Figure 3.A28b. Therefore, a time delay  $\bar{t} = r/U_c$  (see the top of Figure 3.A27) occurs. The phase of the resulting cross spectral density is, then, of the form  $\omega r/U_c$ .

Extension of the definitions introduced in section 1.4.2 is now appropriate. Just as the pressure spectral density  $G(f)$  is defined by equation 1.101 so a power spectral density  $\pi(f)$  may be defined as

$$P = \int_0^{\infty} \pi(f) df \quad (3.A142)$$

for  $\pi(f)$  defined as a one-sided function ( $f \geq 0$ ) or as

$$P = \int_{-\infty}^{\infty} \pi(\omega) d\omega \quad (3.A143)$$

when defined as a two-sided function. The one-third octave band power spectrum used in Figure 3.18 is defined as

$$\begin{aligned} P(f) &= \int_0^{\infty} \pi(f) |H(f)|^2 df \\ &\approx \pi(f) \Delta f \\ &\approx \pi(f) [0.233] f \end{aligned} \quad (3.A144)$$

Finally a two-sided intensity spectral density is defined as

$$I = \int_{-\infty}^{\infty} I(\omega) d\omega \quad (3.A144)$$

and similarly as a one-sided spectral density.



### 3.9 REFERENCES

1. Rayleigh, J.W.S., "The Theory of Sound," Vol. II, Dover (1945).
2. Lamb, H., "Hydrodynamics," Dover (1945).
3. Esch, R.H., "The Instability of a Shear Layer Between Two Parallel Streams," J. Fluid Mech., Vol. 3, pp. 289-303 (1957).
4. Michalke, A., "On the Inviscid Instability of the Hyperbolic Tangent Velocity Profile," J. Fluid Mech., Vol. 19, pp. 543-556 (1964).
5. Michalke, A., "Vortex Formation in a Free Boundary Layer According to Stability Theory," J. Fluid Mech., Vol. 22, pp. 371-383 (1965).
6. Michalke, A., "On Spatially Growing Disturbances in an Inviscid Shear Layer," J. Fluid Mech., Vol. 23, pp. 521-544 (1965).
7. Browand, F.K., "An Experimental Investigation of the Instability of an Incompressible, Separated Shear Layer," J. Fluid Mech., Vol. 26, pp. 281-307 (1966).
8. Sato, H., "Experimental Investigation on the Transition of Laminar Separated Layer," J. Phys. Soc. Japan, Vol. II, pp. 702-709 (1956).
9. Schade, H., "Contribution to the Non-Linear Stability Theory of Inviscid Shear Layers," The Physics of Fluids, Vol. 7, pp. 623-628 (1964).
10. Tatsumi, T. and K. Gotoh, "The Stability of Free Boundary Layers Between Two Uniform Streams," J. Fluid Mech., Vol. 2, pp. 433-441 (1960).
11. Sato, H. and F. Sakao, "An Experimental Investigation of the Instability of a Two-Dimensional Jet at Low Reynolds Numbers," J. Fluid Mech., Vol. 20, pp. 337-352 (1964).
12. Sato, H., "The Stability and Transition of a Two-Dimensional Jet," J. Fluid Mech., Vol. 7, pp. 53-80 (1960).
13. Sato, H. and K. Kuriki, "The Mechanism of Transition in the Wake of a Thin Flat Plate Placed Parallel to a Uniform Flow," J. Fluid Mech., Vol. 11, pp. 321-352 (1961).
14. Lin, C.C., "The Theory of Hydrodynamic Stability," Cambridge University Press (1966).

15. Betchov, R. and W.O. Criminale, "Stability of Parallel Shear Flows," Academic Press, Inc. (1967).
16. Schlichting, H., "Boundary-Layer Theory," McGraw-Hill Book Co. (1979).
17. Gaster, M., "A Note on the Relation Between Temporally-Increasing and Spatially-Increasing Disturbances in Hydrodynamic Stability," J. Fluid Mech., Vol. 14, pp. 222-224 (1964).
18. Brown, G.B., "On Vortex Motion in Gaseous Jets and the Origin of Their Sensitivity to Sound," Proc. Phys. Soc. London, Vol. 47, pp. 703-732 (1935).
19. Becker, H.A. and T.A. Massaro, "Vortex Evolution in a Round Jets," J. Fluid Mech., Vol. 31, pp. 435-448 (1968).
20. Rosenhead, L., "The Formation of Vortices from a Surface of Discontinuity," Proc. Roy. Soc. London, Ser. A134, pp. 170-193 (1931).
21. Powell, A., "Jet Noise-Age 25," Proc. Noise-Con 75, Noise Control Foundation, N.Y.
22. Abernathy, F.H. and R.E. Kronauer, "The Formation of Vortex Streets," J. Fluid Mech., Vol. 13, pp. 1-20 (1962).
23. Boldman, D.R. et al., "Vortex Shedding from a Blunt Trailing Edge with Equal and Unequal External Mean Velocities," J. Fluid Mech., Vol. 75, pp. 721-735 (1976).
24. Naudascher, E., "From Flow-Instability to Flow-Induced Excitation," Proc. A.S.C.E., J. the Hydraulics Div., Vol. 93, pp. 15-40 (1967).
25. DeMetz, F.C. and T.M. Farabee, "Laminar and Turbulent Shear Flow Induced Cavity Resonances," Paper 77-1293 AIAA 4th Aeroacoustic Conference, Atlanta, Ga., (3-5 October 1977).
26. Dunham, W.H., "Flow-Induced Cavity Resonance in Viscous Compressible and Incompressible Fluids," 4th Symposium on Naval Hydromechanics, Washington, D.C. (1962).
27. Rossiter, J.E., "Wind Tunnel Experiments in the Flow over Rectangular Cavities at Subsonic and Transonic Speeds," R and M 3438, Aeronautical Research Council, Britain (1966).

28. Morel, T., "Experimental Study of a Jet-Driven Helmholtz Oscillator," ASME Paper 78-WA/FE-16, 1978.
29. King, J.L. et al., "Instability in Slotted Wall Tunnels," J. Fluid Mech., Vol. 4, pp. 283-305 (1958).
30. Martin, W.W. et al., "Fluid-Dynamic Excitation Involving Flow Instability," Proc. A.S.C.E., J. Hydraulics Div., Vol. 101, No. HY6, pp. 681-698 (1975).
31. Rockwell, D., "Prediction of Oscillation Frequencies for Unstable Flow Past Cavities," Trans. ASME, J. Fluids Eng., Vol. 99, pp. 294-300 (1977).
32. Bilanin, A.J. and E.E. Covert, "Estimation of Possible Excitation Frequencies for Shallow Rectangular Cavities," AIAA Journal, Vol. 11, pp. 347-351 (1973).
33. East, L.F., "Aerodynamically Induced Resonance in Rectangular Cavities," J. Sound Vib., Vol. 3, pp. 277-287 (1966).
34. Harrington, M.C., "Excitation of Cavity Resonance by Air Flow," American Physical Society, Fluid Dynamics Division Meeting (1957).
35. Heller, H.H. and D.B. Bliss, "Aerodynamically Induced Pressure Oscillations in Cavities-Physical Mechanisms and Suppression Concepts," Tech. Report AFFDL-TR-74-133, AF Flight Dynamics Laboratory, Wright Patterson Air Force Base (1975).
36. Heller, H.H. et al., "Flow-Induced Pressure Oscillations in Shallow Cavities," J. Sound Vib., Vol. 18, pp. 545-553 (1971).
37. Hardin, J.C. and J.P. Martin, "Broadband Noise Generation by a Vortex Model of Cavity Flow," AIAA Journal, Vol. 15, pp. 632-637 (1977).
38. Elder, S.A., "A Root Locus Solution of the Cavity Resonator Problem," Michelson Lab., U.S. Naval Academy Report E7801 (Feb 1978).
39. Howe, M.S., "On the Helmholtz Resonator," J. Sound Vib., Vol. 45, pp. 427-440 (1976).
40. Elder, S.A., "Self-Excited Depth-Mode Resonance for a Wall-Mounted Cavity in Turbulent Flow," J. Acoust. Soc. Am., Vol. 64, pp. 877-890 (1978).
41. Kinsler, L.E. and A.R. Frey, "Fundamentals of Acoustics," 2nd Ed. Wiley and Sons (1962).

42. Covert, E.E., "An Approximate Calculation of the Onset Velocity of Cavity Oscillations," AIAA Journal, Vol. 8, pp. 2189-2194 (1970).
43. Ingard, V. and L.W. Dean, III, "Excitation of Acoustic Resonators by Flow," 4th Symposium on Naval Hydrodynamics, Washington, D.C. (1962).
44. Miles, J.B. and G.H. Watson, "Pressure Waves for Flow-Induced Acoustic Resonance in Cavities," AIAA Journal, Vol. 9, pp. 1402-1404 (1971).
45. Becker, H.A. and T.A. Massaro, "Vortex Evolution in a Round Jet," J. Fluid Mech., Vol. 31, pp. 435-448 (1968).
46. Schade, H. and A. Michalke, "Zur Entstehung von Wirbeln in einer freien Grenzschicht," Z. Flugwiss, Vol. 10, pp. 147-154 (1962).
47. Browand, F.K. and J. Laufer, "The Role of Large Scale Structures in the Initial Development of Circular Jets," Proc. 4th Symposium on Turbulence in Liquids, Univ. of Missouri, Rolla, Mo. (1975).
48. Crow, S.C. and F.H. Champagne, "Orderly Structure in Jet Turbulence," J. Fluid Mech., Vol. 48, pp. 547-591 (1971).
49. Johansen, F.C., "Flow through Pipe Orifices at Low Reynolds Numbers," Proc. Roy. Soc. London, Ser A216, pp. 231-245 (1929).
50. Beavers, G.S. and T.A. Wilson, "Vortex Growth in Jets," J. Fluid Mech., Vol. 44, pp. 97-112 (1970).
51. Chanaud, R.C. and A. Powell, "Experiments Concerning the Sound-Sensitive Jet," J. Acoust. Soc. Am., Vol. 34, pp. 907-915 (1962).
52. Lau, J.C. et al., "The Intrinsic Structure of Turbulent Jets," J. Sound Vib., Vol. 22, pp. 379-406 (1972).
53. Lau, J.C. and M.J. Fisher, "The Vortex-Street Structure of Turbulent Jets," Part I, J. Fluid Mech., Vol. 67, pp. 299-337 (1975).
54. Anderson, A.B.C., "Dependence of Pfeifenton (Pipe Tone) Frequency on Pipe Length, Orifice Diameter, and Gas Discharge Pressure," J. Acoust. Soc. Am., Vol. 24, pp. 675-681 (1952).
55. Anderson, A.B.C., "Dependence of the Primary Pfeifenton (Pipe Tone) Frequency on Pipe-Orifice Geometry," J. Acoust. Soc. Am., Vol. 25, pp. 541-545 (1953).

56. Anderson, A.B.C., "A Circular-Orifice Number Describing Dependency of Primary Pfeifton Frequency on Differential Pressure, Gas Density, and Orifice Geometry," J. Acoust. Soc. Am., Vol. 25, pp. 626-631 (1953).
57. Anderson, A.B.C., "A Jet-Tone Orifice Number for Orifices of Small Thickness-Diameter Ratio," J. Acoust. Soc. Am., Vol. 26, pp. 21-25 (1954).
58. Anderson, A.B.C., "Metastable Jet-Tone States of Jets from Sharp-Edged, Circular, Pipe-Like Orifices," J. Acoust. Soc. Am., Vol. 27, pp. 13-21 (1955).
59. Anderson, A.B.C., "Structure and Velocity of the Periodic Vortex-Ring Flow Pattern of a Primary Pfeifton (Pipe Tone) Jet," J. Acoust. Soc. Am., Vol. 27, pp. 1048-1053 (1955).
60. Anderson, A.B.C., "Vortex Ring Structure-Transition in a Jet Emitting Discrete Acoustic Frequencies," J. Acoust. Soc. Am., Vol. 28, pp. 914-921 (1956).
61. Tyndall, J., "The Science of Sound," 1875, reprinted by the Citadel Press (1964).
62. Chanaud, P.C. and A. Powell, "Some Experiments Concerning the Hole and Ring Tone," J. Acoust. Soc. Am., Vol. 37, pp. 902-911 (1965).
63. Wilson, T.A. et al., "Experiments on the Fluid Mechanics of Whistling," J. Acoust. Soc. Am., Vol. 50, pp. 366-372 (1971).
64. Nyborg, W.L. et al., "Characteristics of Jet-Edge-Resonator Whistles," J. Acoust. Soc. Am., Vol. 25, pp. 138-146 (1953).
65. St. Helaire, A. et al., "Aerodynamic Excitation of the Harmonium Reed," J. Fluid Mech., Vol. 49, pp. 803-816 (1971).
66. Elder, S.A., "On the Mechanism of Sound Production in Organ Pipes," J. Acoust. Soc. Am., Vol. 54, pp. 1554-1564 (1973).
67. Smith, R.A. and D.M.A. Mercer, "Possible Causes of Wood Wind Tone Colour," J. Sound Vib., Vol. 32, pp. 347-358 (1974).
68. Curle, N., "The Mechanics of Edge-Tones," Proc. Roy. Soc. London, Ser. A216, pp. 412-424 (1953).
69. Powell, A., "On Edge-Tones and Associated Phenomena," Acustica, Vol. 3, pp. 233-243 (1953).

70. Powell, A., "On the Edge Tone," J. Acoust. Soc. Am., Vol. 33, pp. 395-409 (1961).
71. Brown, G.B., "Vortex Motion Causing Edge Tones," Proc. Phys. Soc., Vol 49, pp. 493-507, 520 (1937).
72. Kurzweg, H., "Neue Untersuchungen über die Entstehung der turbulenten Rohrströmung," Ann der Physik, Vol. 18, pp. 193-216 (1933).
73. Taylor, G.I., "Statistical Theory of Turbulence, Parts I-IV," Proc. Roy. Soc. London, Ser. A151, pp. 421-478 (1935).
74. Taylor, G.I., "The Spectrum of Turbulence," Proc. Roy. Soc. London, Ser. A164, pp. 476-490 (1938).
75. Batchelor, G.K., "Homogeneous Turbulence," Cambridge University Press (1960).
76. Hinze, J.O., "Turbulence," 2nd Ed. McGraw-Hill (1975).
77. Townsend, A.A., "Structure of Turbulent Shear Flow," Cambridge University Press (1976).
78. Lumley, J.L., "Stochastic Tools in Turbulence," Academic Press, N.Y. (1970).
79. Lee, Y.W., "Statistical Theory of Communication," J. Wiley and Sons (1964).
80. Bendat, J.S. and A.G. Piersol, "Measurement and Analysis of Random Data," J. Wiley and Sons (1966).
81. Kinsman, B., "Wind Waves Their Generation and Propagation on the Ocean Surface," Prentice-Hall (1965).
82. Lin, Y.K., "Probabilistic Theory of Structural Dynamics," McGraw-Hill (1967).
83. Crandall, S., "Random Vibration," Vol. 1, M.I.T. Press (1958).
84. Crandall, S., "Random Vibration," Vol. 11, M.I.T. Press (1963).
85. Goldstein, M.E., "Aeroacoustics," McGraw-Hill Book Co. (1976).
86. Mani, R., "The Influence of Jet Flow on Jet Noise, Part I - The Noise of Unheated Jets," J. Fluid Mech., Vol. 73, pp. 753-778 (1976).

87. Amiet, R.K., "Refraction of Sound by a Shear Layer," J. Sound Vib., Vol. 58, pp. 467-482 (1978).
88. Ffowcs Williams, J.E., "The Noise from Turbulence Convected at High Speed," Phil. Trans. Roy. Soc., Ser. A255, pp. 469-503 (1963).
89. Crighton, D.G., "Basic Principles of Aerodynamic Noise Generation," Prog. Aerospace Sci., Vol. 16, pp. 31-96 (1975).
90. Lighthill, M.J., "On Sound Generated Aerodynamically, I General Theory," Proc. Roy. Soc., Ser. A211, pp. 564-587 (1952).
91. Lighthill, M.J., "On Sound Generated Aerodynamically, II Turbulence as a Source of Sound," Proc. Roy. Soc., Ser. A222, pp. 1-32 (1954).
92. Lighthill, M.J., The Bakerian Lecture, "Sound Generated Aerodynamically," Proc. Roy. Soc. London, Ser. A267, pp. 147-171 (1961).
93. Gerrard, J.H., "An Investigation of Noise Produced by a Subsonic Air Jet," J. Aero. Sci., Vol. 23, pp. 855-866 (1956).
94. Mollo-Christensen, E. et al., "Experiments on Jet Flows and Jet Noise Far-Field Spectra and Directivity Patterns," J. Fluid Mech., Vol. 18, pp. 285-301 (1964).
95. Mollo-Christensen, E., "Jet Noise and Shear Flow Instability Seen from an Experimenter's Viewpoint," Trans. ASME, J. Appl. Mech., Vol. 34, pp. 1-7 (1967).
96. Lush, P.A., "Measurements of Subsonic Jet Noise and Comparison with Theory," J. Fluid Mech., Vol. 46, pp. 477-500 (1971).
97. Olsen, W.A. et al., "The Effect of Nozzle Inlet Shape; Lip Thickness, and Exit Shape and Size on Subsonic Jet Noise," NASA TM X-68182 (1973).
98. Karchmer, A.M. et al., "Acoustic Tests of a 15.2-Centimeter-Diameter Potential Flow Convergent Nozzle," NASA TM X-2980 (1974).
99. Olsen, W.A. and R. Friedman, "Jet Noise from Co-Axial Nozzles over a Wide Range of Geometric and Flow Parameters," NASA TM X-71503 (1974), also AIAA Paper 74-43 (Jan 1974).
100. Ribner, H.S., "The Generation of Sound by Turbulent Jets," Adv. Appl. Mech., Vol. 8, pp. 103-182 (1964).

101. Fitzpatrick, H. and R. Lee, "Measurements of Noise Radiated by Subsonic Air Jets," DTMB Report 835 (1952).
102. Maestrello, L., "Two-Point Correlations of Sound Pressure in the Far-Field of a Jet Experiment," NASA TM X-72835 (1976).
103. Maestrello, L., "Statistical Properties of the Sound and Source Fields of an Axisymmetric Jet," 4th AIAA Aeroacoustic Conference, Atlanta, Ga. (3-5 Oct 1977).
104. Ribner, H.S., "Quadrupole Correlations Governing the Pattern of Jet Noise," J. Fluid Mech., Vol. 38, pp. 1-24 (1969).
105. Ribner, H.S., "Theory of Two-Point Correlations of Jet Noise," NASA TN D-8330 (1976).
106. Proudman, I., "The Generation of Noise by Isotropic Turbulence," Proc. Roy. Soc. London, Ser. A214, pp. 119-132 (1952).
107. Jones, I.S., "Fluctuating Turbulent Stresses in the Noise-Producing Region of a Jet," J. Fluid Mech., Vol. 36, pp. 529-543 (1969).
108. Michalke, A. and H.V. Fuchs, "On Turbulence and Noise of an Axisymmetric Shear Flow," J. Fluid Mech., Vol. 70, pp. 179-205 (1975).
109. Armstrong, R.R., "Einfluss Der Machzahl Auf Die Kohärente Turbulenzstruktur Eines Runden Freistrahls," Dr. Ing Thesis University of Berlin (1977).
110. Fisher, M.J. and P.O.A.L. Davies, "Correlation Measurements in a Non-Frozen Pattern of Turbulence," J. Fluid Mech., Vol. 18, pp. 97-116 (1965).
111. Bradshaw, P. et al., "Turbulence in the Noise-Producing Region of a Circular Jet," J. Fluid Mech., Vol. 19, pp. 591-624 (1964).
112. Davies, P.O.A.L. et al., "The Characteristics in the Mixing Region of a Round Jet," J. Fluid Mech., Vol. 15, pp. 337-367 (1963).
113. Kolpin, M.A., "Flow in the Mixing Region of a Jet," M.I.T. Dept. of Aeronautics and Astronautics, Aeroelastic and Structures Research Laboratory Report ASRL TR 92-3 (1962).
114. Ko, N.W.M. and P.O.A.L. Davies, "Some Covariance Measurements in a Subsonic Jet," J. Sound Vib., Vol. 41, pp. 347-358 (1975).
115. Forstall, W., Jr. and A.J. Shapiro, "Momentum and Mass Transfer in Co-Axial Gas Jets," A.S.M.E. J. Appl. Mech. Tran., Vol. 72, pp. 399-408 (1950).



116. Forstall, W., Jr. and A.H. Shapiro, "Momentum and Mass Transfer in Co-Axial Gas Jets, Discussion," A.S.M.E. J. Appl. Mech. Trans., Vol. 73, pp. 219-220 (1951).
117. Laurence, J.C., "Intensity, Scale, and Spectra of Turbulence in Mixing Region of Free Subsonic Jet," NACA Report 1292 (1956).
118. Ffowcs Williams, J.E. and A.J. Kempton, "The Noise from Large-Scale Structure of a Jet," J. Fluid Mech., Vol. 84, pp. 673-694 (1978).
119. Powell, A., "Similarly and Turbulent Jet Noise," J. Acoust. Soc. Am., Vol. 31, pp. 812-813 (1959).
120. Dyer, I., "Distribution of Sound Sources in a Jet Stream," J. Acoust. Soc. Am., Vol. 31, pp. 1016-1022 (1959).
121. Moon, L.F. and S.W. Zelanzy, "Experimental and Analytical Study of Jet Noise Modeling," AIAA Journal, Vol. 13, pp. 337-393 (1975).
122. Grosche, F.R. et al., "Measurements of the Distribution of Sound Source Intensities in Turbulent Jets," AIAA Paper 73-989 (1973).
123. Ffowcs Williams, J.E., "Noise Mechanisms," AGARD Technical Evaluation Report AR-66 (1974).
124. Parthasarathy, S.P., "Evaluation of Jet Noise Sources by Cross-Correlation of Far Field Microphone Signals," AIAA Journal, Vol. 12, pp. 583-590 (1974).
125. Billingsley, J. and R. Kinns, "The Acoustic Telescope," J. Sound Vib., Vol. 48, pp. 485-510 (1976).
126. Fisher, M.J. et al., "Jet Engine Noise Source Localization: The Polar Correlation Technique," J. Sound Vib., Vol. 51, pp. 23-54 (1977).
127. Maestrello, L., "On the Relationship Between Acoustic Energy Density Flux Near the Jet Axis and Far-Field Acoustic Intensity," NASA TN-D-7269 (1973).
128. Maestrello, L. and S.P. Pao, "New Evidence of the Mechanisms of Noise Generation and Radiation of a Subsonic Jet," J. Acoust. Soc. Am., Vol. 57, pp. 959-960 (1975).
129. Crighton, D.G. and M. Gaster, "Stability of Slowly Diverging Jet Flow," J. Fluid Mech., Vol. 77, pp. 397-413 (1976).

130. Moore, C.J., "The Role of Shear-Layer Instability Waves in Jet Exhaust Noise," J. Fluid Mech., Vol. 80, pp. 321-367 (1977).
131. Bechert, D. and E. Pfizenmaier, "On the Amplification of Broadband Jet Noise by a Pure Tone Excitation," J. Sound Vib., Vol. 43, pp. 581-587 (1975).
132. Winant, C.D. and F.K. Browand, "Vortex Pairing-The Mechanism of Turbulent Mixing-Layer Growth at Moderate Reynolds Number," J. Fluid Mech., Vol. 63, pp. 237-255 (1974).
133. Acton, E., "The Modeling of Large Eddies in a Two-Dimensional Shear Layer," J. Fluid Mech., Vol. 76, pp. 561-592 (1976).
134. Merktine, L. and J.T.C. Liu, "On the Development of Noise Producing Large-Scale Wave Like Eddies in a Plane Turbulent Jet," J. Fluid Mech., Vol. 70, pp. 353-368 (1975).
135. McLaughlin, D.K. et al., "Experiments in the Instability Waves in a Supersonic Jet and Their Acoustic Radiation," J. Fluid Mech., Vol. 69, pp. 73-95 (1975).
136. McLaughlin, D.K. et al., "Reynolds Number Dependence in Supersonic Jet Noise," AIAA Paper 76-491, AIAA Aeroacoustics Conference (1976).
137. Ffowcs Williams, J.E. and C.G. Gordon, "Noise of Highly Turbulent Jets at Low Exhaust Speeds," AIAA Journal, Vol. 3, pp. 791-792 (1965).
138. Ffowcs Williams, J.E., "Jet Noise at Very Low and Very High Speed," Proc. AFOSR-UTIAS Symposium on Aerodynamic Noise. University of Toronto (1968).
139. Ffowcs Williams, J.E. and M.S. Howe, "The Generation of Sound by Density Inhomogeneities in Low Mach Number Nozzle Flows," J. Fluid Mech., Vol. 70, pp. 605-622 (1975).
140. Whitfield, O.J. and M.S. Howe, "The Generation of Sound by Two-Phase Nozzle Flows and Its Relevance to Excess Noise of Jet Engines," J. Fluid Mech., Vol. 75, pp. 553-576 (1976).
141. Plett, E.G. and M. Summerfeld, "Jet Engine Exhaust Noise due to Rough Combustion and Nonsteady Aerodynamic Sources," J. Acoust. Soc. Am., Vol. 56, pp. 516-522 (1974).

142. Crighton, D.G. and J.E. Ffowcs Williams, "Sound Generation by Turbulent Two-Phase Flow," J. Fluid Mech., Vol. 36, pp. 585-603 (1969).

143. Blake, W.K. and A. Powell, "The Development of Contemporary Views of Flow-Tone Generation," International Symposium on Recent Advances in Aerodynamics and Aeroacoustics, Stanford Univ. 1983. To be published by Springer Verlag in 1984.

144. Quick, A.W., "Zum Schall-und Stromungsfeld eines axial symmetrischen Freistrahls beim Auftreffen auf eine Wand," Zeitschrift für Flugwissenschaften, Vol. 19, pp. 30-44 (1971).

145. Ho, C.M. and N.S. Nosseir, "Dynamics of an Impinging Jet. Part 1. The Feedback Phenomenon," J. Fluid Mech., Vol. 105, pp. 119-142 (1981).

## CHAPTER 4

### TWO-PHASE FLOW NOISE

#### 4.1 INTRODUCTION

##### 4.1.1 General Concepts

This chapter will be concerned with the acoustics of bubbly mixtures, cavitation noise, and noise associated with the formation and splitting of bubbles. It will, therefore, be concerned with the wide range of monopole noise sources often occurring in hydroacoustic applications as well as with the problems of noise propagation in fluid media in which there may be considerable concentrations of suspended gas bubbles. Another class of two-phase flow-noise that will not be addressed and which occurs in solid-gas suspensions (e.g., dusty gas) is dipole-like and due to the interactions between the particles and the gas. This noise production is inefficient compared to that in liquid-gas mixtures but still potentially greater than the noise of free jets of single phase. A general theory of noise from unbounded multiple-phase fluid media, in which there are no bubble or particulate formations or injection, has been given by Crighton and Ffowcs-Williams,<sup>1\*</sup> as previously described in Section 3.7. In cases of free bubbly mixtures not adjacent to a solid body, noise is considerably augmented over single-phase shear flow noise when the bubbles split or coalesce, or when cavitation occurs.

A common feature of all the phenomena discussed in this chapter is that motions and subsequent sound production of a bubble (or a population of bubbles) are produced when the bubbles are subjected to a pressure field. The motions of the suspended bubbles which are initially spherical in shape are essentially volume pulsations, accounting for the monopole nature of the noise. Essentially, fluctuations in pressure on the liquid side of the bubble wall about an initial equilibrium value account for the motions. It shall be shown (Section 4.2.1) that suitably small pressure fluctuations initiate volumetric fluctuations which resemble a linear single-degree-of-freedom oscillator. It is this linear motion which controls classical behavior of sound propagation in bubbly media (Section 4.2.2). At larger amplitudes of pressure fluctuation which persist for a sufficiently long time, exceeding a natural period of oscillation, nonlinear behavior of the bubble dominates the motion and the bubbles may grow and collapse explosively (Section 4.2.3), thus producing cavitation.

---

\*A complete listing of references is given on page 431.

Diffusion of gas either into or out of the bubble also may account for bubble growth or disappearance, but the extent of growth by this means will depend on the concentration of dissolved gas in the liquid, the type and amount of gas in the bubble and the time scale of the pressure fluctuations. The volume accelerations that are associated with this motion are so small that no appreciable noise is produced by them. The significance of diffusion for our purposes, therefore, is that bubbles are permitted to grow to a large enough size that under subsequent undulations of environmental pressure, nonlinear explosive behavior may occur.

A study of the explosive behavior of bubbles, or cavitation, its onset, and the noise produced, will occupy the core of this chapter (Sections 4.3 and 4.4). In a crude sense, cavitation will occur when the pressure in the liquid surrounding a nucleus becomes equal to (or less than) the vapor pressure of the liquid for an appropriate length of time. A cavitation site, or nucleus, is really a small gas or vapor-filled bubble or interstice in a solid particle that is convected with the moving liquid into and through a low pressure zone. Cavitation occurs as the smaller bubble grows to many times its initial size. When the pressure surrounding the cavitation bubble subsequently increases, the conditions will favor the collapse of the large bubble implisively. This event causes most of the noise that is produced in the cavitation process. Therefore, there are four important subjects which must be understood in order to explain the onset and behavior of hydrodynamic cavitation: conditions favoring explosive growth (Sections 4.2.3 and 4.2.4), the parameters which control the maximum sizes of cavitation bubbles and their subsequent collapse (Section 4.2.5), a portrayal of bubble dynamics in terms of hydrodynamic variables (Section 4.3), and a relationship between the stages of bubble motion and the spectrum of cavitation noise (Section 4.4).

One may think of cavitation as the production of a "hole" in the liquid which collapses once the conditions favoring its creation are released. The energy released during collapse is considerable,\* and most of the energy is stored in whatever compressible gas is in the bubble and in the elastic deformations of the adjacent liquid and any contiguous solid surfaces; only a small fraction, on the order of 1 percent or 0.1 percent, is converted into sound. The cavitation is, therefore, not only capable of producing noise, but also it causes damage to

---

\*As a numerical illustration of this point, a bubble, 1 cm in radius filled with water vapor and collapsing in an ambient pressure of 1 atm will generate an average of approximately 460 watts over the 1 ms time interval of its collapse.

hydraulic structures; this damage has been termed "erosion." It is, in fact, this latter problem of cavitation erosion that has dominated the literature on applied cavitation research with comparatively little attention given to cavitation noise. However, in recent years, attention has also been given to the acoustics of cavitation as applied, for example, to the detection of potentially-damaging cavitation in pumps and reactor components as well as to the problem of improving habitability in crewspaces over propellers in merchant ships. Cavitation can also occur near high-powered acoustic sources, with a consequent reduction in the radiation efficiency of the source as well as possible damage to the active surface of the transducer.

In the case of cavitation which arises near acoustic sources, called "acoustic" or "ultrasonic" cavitation, when the local rarefaction pressure becomes less than a critical pressure, the incipient cavitation will consist of small bubbles that grow in the liquid, gradually becoming visible without microscopic aid. This critical pressure, as we will see in Section 4.2, is often comparable to, although not necessarily equal to, the liquid vapor pressure and it will depend on the nature of the impurities which may exist in the liquid. It is now generally recognized that in order for cavitation to occur, these impurities, or nuclei must exist. They consist of small suspended bubbles in some combination with particulate matter which has not been fully wetted by the water. These latter impurities contain entrapped gas and are often called "hydrophobic" particles. When the liquid has a large concentration of dissolved gas that is in equilibrium with suspended bubbles, the gas will slowly diffuse into the bubbles from the liquid phase under the influence of an undulating pressure field. This cavitation is called "gaseous cavitation."

Because incipient ultrasonic cavitation involves the response of a nucleation site to a prescribed and deterministic pressure field, the prediction of its occurrence comes down to assessing the population of nuclei or, alternatively, the tensile strength of a given sample of liquid. Consequently, a large body of literature in the area of ultrasonic cavitation deals with the assessment of liquid tensile strengths and other aspects of nucleation. Pure water, without suspended or dissolved gas or suspended particulate matter, will not cavitate until the rarefaction or tensile pressure is large; the maximum tensile strength observed for pure water is on the order of  $-280 \text{ atm.}^{2,3}$  This pressure is far below that which is achievable with hydrodynamic pressure fluctuations.

Since cavitation is an undesirable hydroacoustic phenomenon, a major portion of published work has dealt with the prediction of the onset of its occurrence or its "inception." The conditions which favor incipient hydrodynamic cavitation are more difficult to define because of the complexities which exist in both the unsteady liquid motions as well as in the distribution of cavitation nuclei. In the laminar flow around bodies at low values of Reynolds number, the incipient cavitation in liquid, which has a large number of suspended bubble nuclei, has a rather straightforward and classical behavior (see Section 4.3). When the hydrodynamics becomes turbulent, so that random hydrodynamically-induced rarefaction pressures may occur, then the inception can become more controlled by the viscous flow properties than by the population of nucleation sites. In these cases it is difficult both to scale-up prototype model performance as well as to repeat cavitation inception measurements on the same model in different laboratory facilities. Viscous effects in the boundary or shear flow may depend on such scale effects as free-stream turbulence, surface smoothness, and Reynolds number, etc. It is, therefore, frequently difficult to achieve exact dynamical similitude in all details of cavitation model testing in so far as the evaluation of incipient conditions is concerned. The acoustical problem is similarly difficult to quantify, because the motions, both of individual bubbles and of the aggregate, depend on the conditions which favor inception. Therefore, the problem of noise generation cannot be considered separately from the hydromechanics of inception.

In this chapter we shall be concerned, therefore, with the dynamical properties of single bubbles in liquids (Section 4.2), as well as with the propagation of sound in fluids with suspended bubble populations. From the dynamical behavior of single bubbles, a set of rules will emerge which may then be used to develop a format in which conditions for inception may be quantified in terms of hydrodynamic variables (Section 4.3). The dynamics of the single bubble will also be used to formulate an idealized frequency spectrum of acoustic energy, and this will be compared to measured noise from jets, hydrofoils, and propellers (Section 4.4). Finally, the noise from bubble splitting will be discussed (Section 4.5). Related texts which cover, in depth, the subjects of cavitation inception, dynamics, and damage include the review article by Flynn<sup>2</sup> and the monographs by Knapp, Daily, and Hammitt,<sup>4</sup> Rohn,<sup>5</sup> Beyer,<sup>6</sup> and Pernik.<sup>7</sup>

### 4.1.2 The Cavitation Index and Cavitation Similitude

The general elementary cavitation problem is illustrated in Figure 4.1, which shows a hydrofoil shape and its surface pressure distribution,  $P_s$ . The surface pressure is related to the tangential velocity in the flow near the surface,  $U_s$  by Bernoulli's equation for steady flow

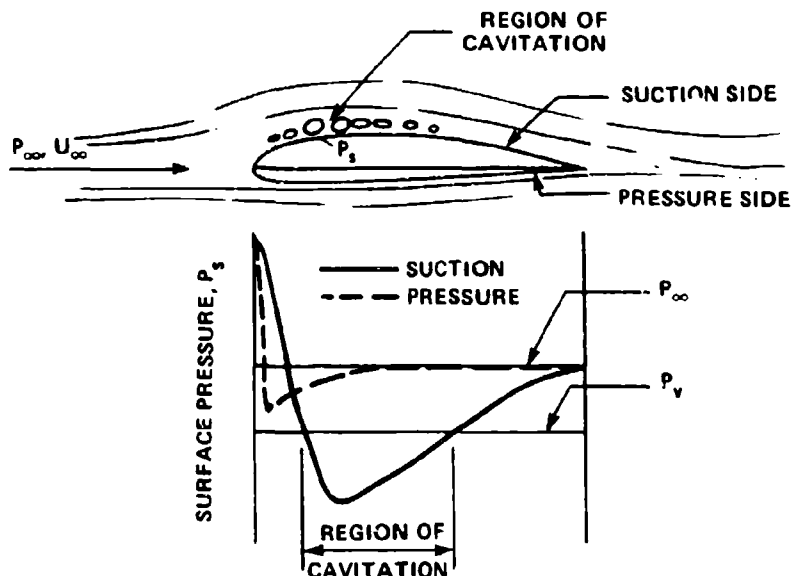


Figure 4.1 - A Cavitating Hydrofoil, its Surface Pressure Distribution, and its Region of Cavitation

$$P_{\infty} + \frac{1}{2} \rho_o U_{\infty}^2 = P_s + \frac{1}{2} \rho_o U_s^2 \quad (4.1)$$

so that a pressure coefficient  $C_p$  may be defined

$$\frac{P_s - P_{\infty}}{\frac{1}{2} \rho_o U_{\infty}^2} = C_p = 1 - \left( \frac{U_s}{U_{\infty}} \right)^2 \quad (4.2)$$

where  $P_{\infty}$  and  $U_{\infty}$  are the upstream ambient pressure and velocity, respectively. The increased velocity on the curved part of the hydrofoil causes the surface pressure to be less than the ambient pressure. Cavitation will occur when the pressure in



the liquid, which will be lowest near the surface, is rarefied down to some critical pressure, for example to the vapor pressure  $P_v$ .<sup>\*</sup> Thus, when the minimum pressure on the hydrofoil is less than  $P_v$ , cavitation will occur

$$(P_s)_{\min} \leq P_v$$

or

$$P_v \geq (C_p)_{\min} \left( \frac{1}{2} \rho_o U_\infty^2 \right) + P_\infty \quad (4.3)$$

An incipient condition will occur when the equality exists because this condition will mark the cavitation threshold. Therefore, the cavitation index is introduced as

$$K = \frac{P_\infty - P_v}{\frac{1}{2} \rho_o U_\infty^2} \quad (4.4)$$

to express the relationship between pressure and velocity that determines similarity. According to our inequality, Equation (4.3), cavitation will occur when

$$\frac{P_\infty - P_v}{\frac{1}{2} \rho_o U_\infty^2} \leq -C_{p_{\min}}$$

or, using our definition of the cavitation index, it will occur whenever

$$K \leq -C_{p_{\min}}$$

---

<sup>\*</sup>The critical pressure will be equal to  $P_v$  when the free-stream contains cavitation nuclei of  $10^{-3}$  cm radius or larger, and the flow over the hydrofoil is laminar.

The threshold or incipient condition will exist when

$$K_i = -C_{p_{min}} \quad (4.5)$$

In more complicated geometries, e.g., a pump or a propeller, the parameters of the undisturbed flow into the cavitating surface may not be known or they may not be of engineering interest. In these cases steady flow exists but there may be a velocity-dependent pressure difference, the reference pressure,  $P_{ref}$  and  $P_\infty$  for the surface; i.e.,

$$P_{ref} = P_\infty + \Delta P$$

Furthermore, rather than the resultant velocity (resultant tip velocity in the case of the propeller) a reference velocity  $U_{ref}$  is often used so that a parameter

$$K' = \frac{P_{ref} - P_v}{\frac{1}{2} \rho_o U_{ref}^2} \quad (4.6)$$

is appropriate. This parameter is related to the previously defined index by

$$K' = K \left( \frac{U_\infty}{U_{ref}} \right)^2 + \frac{\Delta P}{\frac{1}{2} \rho_o U_{ref}^2}$$

As long as dynamical similitude exists between one scale size and the next, so that fixed proportionalities between  $U_\infty$  and  $U_{ref}$  and between  $\Delta P$  and  $\frac{1}{2} \rho_o U^2$  are maintained, then  $K'$  is a dimensionless cavitation number which will describe relative cavitation performance. As previously discussed, when  $K'$  is less than some threshold value, e.g.,  $K'_1$ , then cavitation will occur in the system. In this latter usage,  $K'$  is a parameter which is a measure of the relative cavitation performance of one machine to the next. Nomographs are given in Appendix 4.C for computing cavitation indices for propellers.

Complications occur when it is desired to satisfy simultaneously viscous and cavitation similitude. In this instance it is ideally necessary to maintain equal Reynolds and cavitation numbers, i.e.,

$$R_L = \left( \frac{UL}{\nu} \right)_M = \left( \frac{UL}{\nu} \right)_S \quad (4.7)$$

and

$$K = \left( \frac{P - P_v}{\frac{1}{2} \rho_o U^2} \right)_M = \left( \frac{P - P_v}{\frac{1}{2} \rho_o U^2} \right)_S \quad (4.8)$$

If the ratio of full-size to model size is  $S > 1$ , then Equation (4.7) requires that the velocity of the model test must be in proportion to the full-scale as

$$\frac{U_M}{U_S} = S \frac{\nu_M}{\nu_S}$$

if both phenomena are examined in water at nearly equal temperatures then  $\nu_M = \nu_S$ . The pressure required in the model test is, therefore,

$$\frac{(P - P_v)_M}{(P - P_v)_S} = \left( \frac{U_M}{U_S} \right)^2 = S^2$$

If the scale factor is  $S = 10$ , then  $U_M = 10 U_S$  and  $(P - P_v)_M = 100 (P - P_v)_S$ . This high pressure may be well outside the operating range of the facility. A common practice is to forego viscous similarity and let  $U_M = U_S$  so that the model test is conducted at a low Reynolds number,

$$R_M = \frac{1}{S} R_S$$

This procedure allows the hydrostatic pressures in both scales to be equal and, therefore, within the limits of facilities.

An additional complication arises in propeller testing when it is desired to operate the propulsor in the wake of a surface ship.<sup>8-10</sup> In this case one may wish to simulate the change in hydrostatic head exerted on the propeller blades as they rotate. This requires that the ratio

$$\frac{\rho_o U^2}{\rho_o g H}$$

be held constant, where H is the depth of submergence and U is proportional to the propeller tip speed ( $\pi n D$ ). This scaling, known as Froude scaling, is represented by the constant number (called the Froude number)

$$F_r = \frac{U}{(Hg)^{1/2}} \quad (4.9)$$

so that it is required to have

$$\frac{U_M}{U_s} = \frac{1}{S^{1/2}}$$

as well as the condition of Equation (4.8). This gives, for the hydrostatic pressure,

$$\frac{(P-P_v)_M}{(P-P_v)_s} = \frac{1}{S}$$

but now the Reynolds number is even further reduced

$$R_M = \frac{1}{S^{3/2}} R_s$$

Unfortunately, the dynamics of the boundary layers (and other aspects of viscous flow) on the body in its noncavitating state are, as we shall see in

Section 4.3, intimately connected with the inception and type of cavitation. Therefore, the differences in scale size and Reynolds number bring to bear certain "scale effects" which relate to deviations in exact viscous flow simulation and which are only now being understood. Some of the early discrepancies in model testing have been reviewed in this regard by Holl and Wislicenus<sup>11</sup> and Holl<sup>12</sup> unfortunately at the time of those reviews few good explanations could be offered for the discrepancies.

## 4.2 BASIC EQUATIONS OF BUBBLE DYNAMICS

In this section we consider the conditions that are necessary for the maintenance of small-amplitude bubble vibrations, quasi-static bubble equilibrium, necessary conditions for nonlinear bubble motions leading to cavitation, and the effects of bubble gas and liquid compressibility in the collapse of cavities.

### 4.2.1 Linear Bubble Motions

The dynamics of bubbles in a liquid responding to an imposed pressure have been considered with varying degrees of complexity. The first and simplest analysis is that of Rayleigh,<sup>13</sup> later elaborated by Plesset<sup>14</sup> and by Neppiras and Noltingk,<sup>15,16</sup> in which the liquid surrounding a spherical bubble is incompressible. In Rayleigh's analysis, the medium inside the bubble is liquid vapor so that the internal pressure is constant. Plesset<sup>14</sup> and Neppiras and Noltingk<sup>15,16</sup> allowed the internal pressure to be also determined by insoluble gas as well as by surface tension. Later Houghton<sup>17</sup> introduced viscosity, Blue<sup>18</sup> calculated and Howkins<sup>19</sup> measured resonance frequencies of a bubble attached to a wall, Shima<sup>20</sup> examined effects of liquid-phase compressibility finding them small for periodic oscillations in water, and Strasberg<sup>21</sup> examined the resonance of nonspherical bubbles. Figure 4.2 shows the relevant geometry. The pressure difference across a segment of the bubble wall, is balanced by the surface tension forces. Using the notation of Figure 4.2b, this instantaneous force balance is

$$(P_i - P(R_b, t)) R_2 R_1 \Delta\phi \Delta\theta = [SR_1 \Delta\phi] \Delta\theta + [SR_2 \Delta\theta] \Delta\phi$$

where S is the surface tension for which the units are force per unit length and

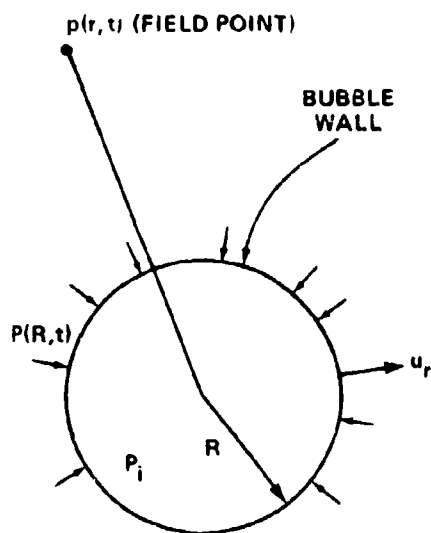


Figure 4.2a - Spherical Bubble in an Unbounded Liquid

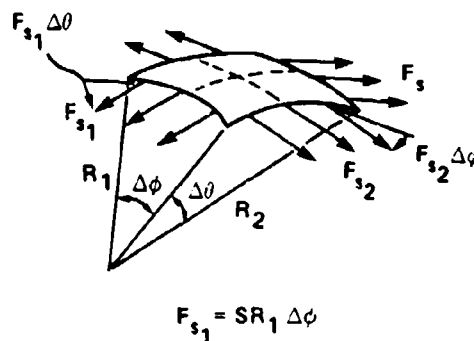


Figure 4.2b - Thin Film Segment

Figure 4.2 - Force Diagrams for a Spherical Bubble

where  $R_1$  and  $R_2$  are the (possibly different) radii of curvature in the orthogonal directions. For the spherical bubble,  $R_1 = R_2 = R$  so that the condition necessary for equilibrium is ( $R$  is the instantaneous radius and  $R_0$  is the equilibrium, or rest, radius of the bubble)

$$P_i - P(R,t) = \frac{2S}{R} \quad (4.10)$$

In the general case, the internal pressure in the bubble is the sum of partial pressures of the vapor pressure  $P_v$  and the total equilibrium partial pressure of dissolved gas  $P_g$  in the liquid. During the bubble motion, this gas is compressed or expanded so that the partial pressure varies with the bubble radius. Typically, the ideal gas law is assumed in order to simplify the thermodynamic properties of the enclosed gas and so to provide a simple equation of state. The dependence of pressure on volume is then given by the simple relationship

$$P_g = P_{g_0} \left( \frac{R_0}{R} \right)^{3\gamma}$$

where the variables subscripted "o" apply to the initial state. For adiabatic motions (no heat transfer from the gas to the liquid),  $\gamma$  is the ratio of the specific heat at constant pressure to that at constant volume ( $\gamma \approx 1.4$ ), for isothermal contraction  $\gamma = 1$ . Plesset and Hsieh<sup>22</sup> have subsequently analyzed periodic forced linear oscillations of bubbles finding that the motions are isothermal for oscillation frequencies which are less than the resonance frequency and adiabatic for oscillation frequencies which are above resonance.

The equilibrium pressure at the bubble wall when the radius is  $R$  is then given by

$$P(R, t) = P_v + P_{g_0} \left( \frac{R_0}{R} \right)^{3\gamma} - \frac{2S}{R} \quad (4.11)$$

Spherically-symmetric motions in the liquid are governed by Equation (2.2),

$$\rho_0 \frac{\partial u_r}{\partial t} + \rho_0 u_r \frac{\partial u_r}{\partial r} = - \frac{\partial P}{\partial r}$$

For the incompressible motion we let the radial velocity be the gradient of a potential,

$$u_r = \nabla_r \phi$$

so that

$$\nabla_r \left[ \frac{\partial \phi}{\partial t} + \frac{1}{2} (\nabla_r \phi)^2 \right] = - \frac{1}{\rho_0} \nabla_r P$$

and integrating along a stream tube from  $r = R$  to a distant point  $r$ , for  $r > R$

$$\frac{\partial[\phi(r)-\phi(R)]}{\partial t} + \frac{1}{2} ([\nabla_r \phi(r)]^2 - [\nabla_r \phi(R)]^2) = \frac{1}{\rho_0} [P(R)-P(r,t)]$$

For incompressible motions, Chapter 2 gives the spherically-symmetric potential

$$\phi(r) = - \frac{\dot{R}R^2}{r}$$

so that an equation for the bubble wall velocity is

$$\ddot{R}R + \frac{3}{2} (\dot{R})^2 = \frac{P(R) - P(r,t)}{\rho_0} \quad (4.12)$$

where  $r$  is now selected so that  $r \gg R$ . Equations (4.11) and (4.12) may be combined because the pressure balance of Equation (4.11) across the wall may be taken to apply for any value of  $R$ . The pressure  $P(r)$  may be considered as a time-varying hydrodynamic driving pressure.

Equation (4.12) is the basic equation for incompressible liquid motion adjacent to a bubble and it is accurate to within an order of  $\dot{R}/C_0$ , where  $C_0$  is the speed of sound in the liquid. When the local hydrodynamic pressure  $P(r)$  decreases, the bubble wall accelerates outward. For small oscillations, the term quadratic in  $\dot{R}$  is small, but for a critically small value of  $P(r,t)$  this term, which is always positive, controls the bubble growth and will dominate the linear acceleration term.

Several useful alternate forms of Equation (4.12) may be derived which cast the oscillations of bubble volume in terms of an applied perturbation pressure that is superimposed on a static equilibrium pressure. The response of the bubble volume can be found by substitution of

$$\dot{R}R^2 = \frac{\dot{V}}{4\pi}$$

where  $\dot{V}$  is the volume velocity of the bubble, into Equation (4.12) which gives the alternative relationship



$$\frac{\rho_o}{4\pi R} \ddot{V} - \frac{\rho_o}{2} \left( \frac{\dot{V}}{4\pi R^2} \right)^2 = P(R) - P(r,t) \quad (4.13)$$

The instantaneous volume will oscillate about its equilibrium value  $V_o$  under the influence of the driving pressure  $P(r,t)$  which oscillates about a static value that determines the equilibrium state of the bubble. Thus, let this static pressure be  $P_o$  so that

$$P(r,t) = P_o + p(r,t) \quad (4.14)$$

Replacing the pressure on the liquid side of the bubble wall by Equation (4.11) and noting that the equilibrium pressure of gas in the bubble of equilibrium radius  $R_o$  is, by Equation (4.10),

$$P_{g_o} = P_o(R_o) + \frac{2S}{R_o} - P_v$$

Introducing the local static ambient pressure,

$$P_{g_o} = P_o + \frac{2S}{R_o} - P_v \quad (4.15)$$

we find

$$\begin{aligned} \frac{\rho_o}{4\pi R_o} \ddot{V} - \frac{\rho_o}{2} \left( \frac{\dot{V}}{4\pi R_o^2} \right)^2 + \left[ P_v - P_o - \frac{2S}{R_o} \right] \left( \frac{V_o}{V} \right)^\gamma \\ - \left( P_v - \frac{2S}{R_o} - P_o \right) = P_o - P(r,t) \\ = -p(r,t) \end{aligned} \quad (4.16)$$

which is an alternative form to both Equations (4.12) and (4.14). For small oscillations, we use the first term of a Taylor's series

$$P_{g_0} \left( \frac{V}{V_0} \right)^\gamma - P_{g_0} \approx - \frac{\gamma}{V_0} P_{g_0} (V - V_0) \quad (4.17)$$

and assume that the bubbles are large enough that the changes in surface-tension contribution can be ignored. Equation (4.12) reduces to the linearized form derived by Strasberg<sup>23</sup>

$$\frac{\rho_0}{4\pi R_0} \ddot{V} + \frac{\gamma P_{g_0}}{V_0} (V - V_0) = -p(r, t) \quad (4.18)$$

To determine the resonance frequency assume free simple harmonic motion at a frequency  $\omega_0$  such that the volume fluctuations are given by

$$V - V_0 = v e^{-i\omega_0 t}$$

The frequency of free motion satisfies

$$-\omega_0^2 \left( \frac{\rho_0}{4\pi R_0} \right) + \left( \frac{\gamma P_{g_0}}{V_0} \right) = 0 \quad (4.19)$$

Using Equation (4.15), the equilibrium gas pressure can be replaced by the components involving the equilibrium static pressure and the surface tension so that the resonance frequency is

$$\omega_0 R_0 = \left[ \frac{3\gamma}{\rho_0} (P_0 + 2S/R_0 - P_v) \right]^{1/2} \quad (4.20)$$

At atmospheric pressure, large-enough bubbles, and  $\gamma = 1.4$ , Equation (4.20) yields

$$f_o R_o = 330 \text{ cm/sec} \quad (4.21)$$

This result was first derived by Minnaert;<sup>24</sup> it can also be found in the subsequent analyses by Neppiras and Noltingk.<sup>15,16</sup> Resonance frequencies of the fundamental breathing modes of nonspherical bubbles also closely follow Equation (4.20), as shown by Strasberg.<sup>21</sup> Figure 4.3 is a graph of Equation (4.22).

In Equation (4.18) the term multiplying the volumetric acceleration represents the added mass of the contiguous liquid so that the first term is the inertially-controlled motion. The second term represents the compressibility of gas inside the bubble which dominates the motion for pressure oscillations that have a frequency much less than the resonance frequency. At resonance, the bubble motions are controlled by dissipation which may be included by introducing a loss factor into Equation (4.18) so that the linear oscillations are given by

$$\left( \frac{\rho_o}{4\pi R_o} \right) [\ddot{v} + (1 + \omega_o^2) \dot{v} + \omega_o^2 v] = -p(r, t) \quad (4.22)$$

where  $v = V - V_o$ . This equation has been derived by Devin,<sup>25</sup> and used by Strasberg<sup>23</sup> and more recently by Whitfield and Howe.<sup>26</sup> The damping of bubbles at high frequencies (10 kHz or greater) has been given substantial attention; an extensive review of that work has been given by Flynn.<sup>2</sup> In the hydroacoustic range, Devin<sup>25</sup> has found that thermal and radiation damping control the damping over appropriate frequency ranges. Figure 4.4 shows some measured loss factors together with the individual damping contributions. The radiation and thermal losses control the total damping as summarized next.

The thermal loss factor is given by the approximate formula (valid for  $2S/RP_o < 1$ )

$$\eta_{th} = \left\{ \left[ \frac{3(\gamma-1)^2}{2\gamma} \right] \left( \frac{\rho_o}{\rho_g} \right) \frac{K_g \omega_o}{P_o C_p} \right\}^{1/2} \quad (4.23)$$

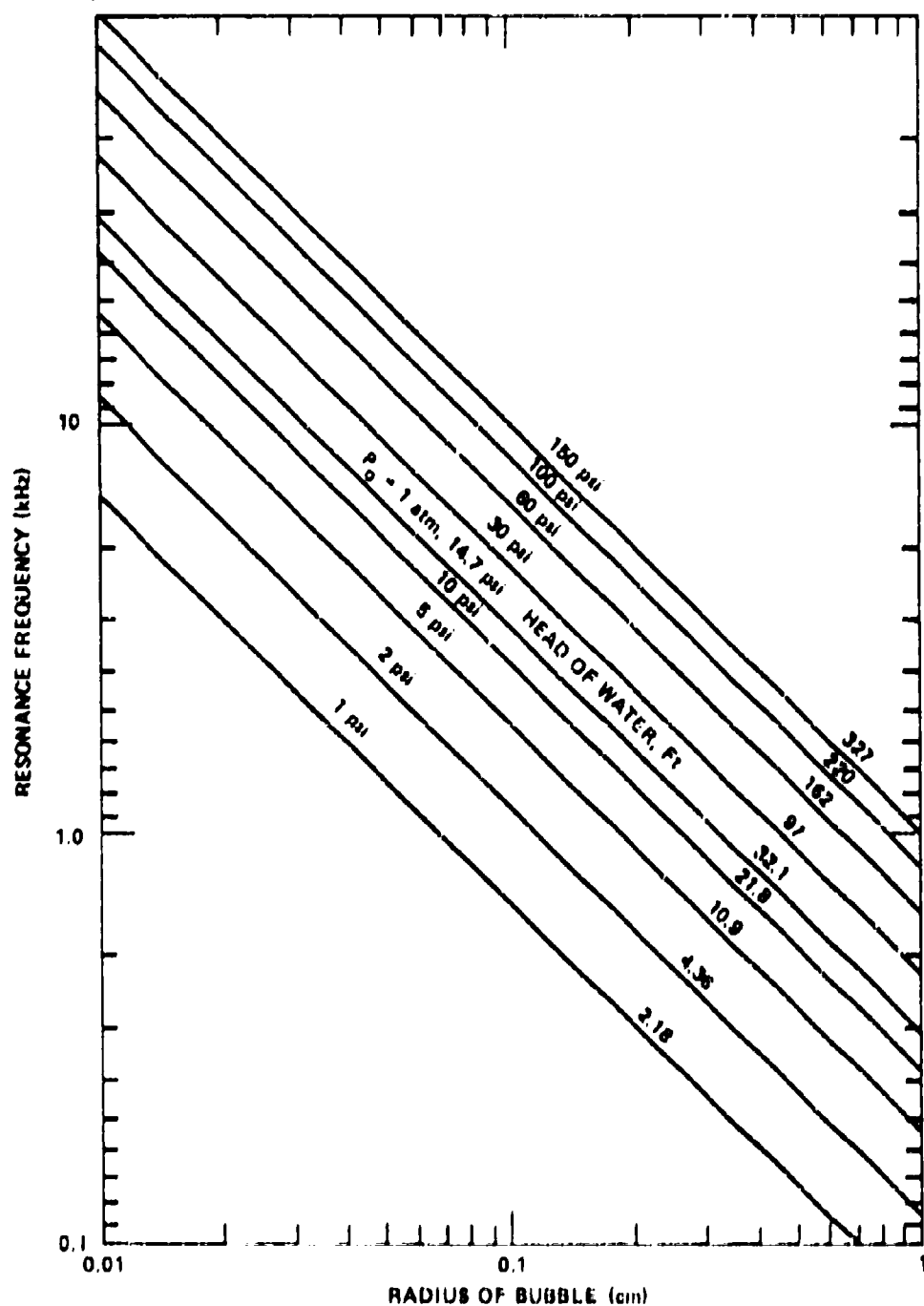


Figure 4.3 - Plot of Resonance Frequencies of Bubbles at Various Ambient Pressures. Pressures Given by  $P_0 = P_{atm} + \rho_0 g h = [32.1 + H(ft)] \rho_0 g$ ; Equation (4.20) Used for Adiabatic Oscillations,  $\gamma = 1.4$ .

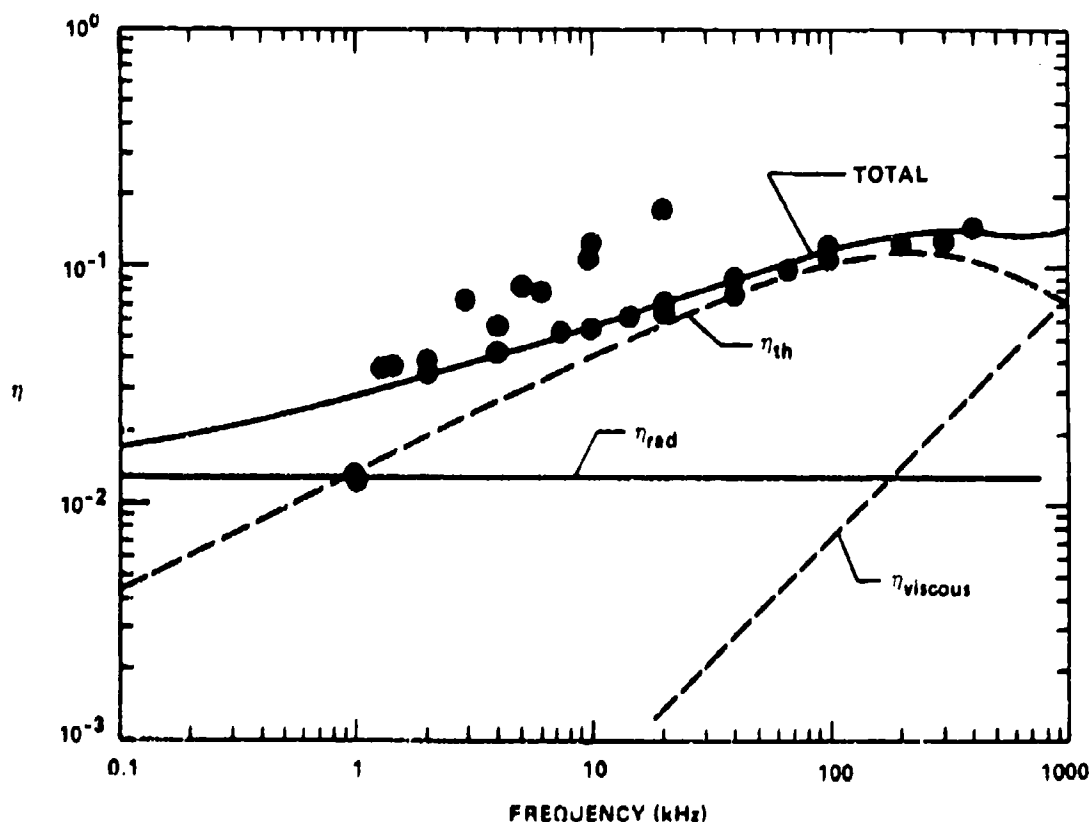


Figure 4.4 - Loss Factors of Air Bubbles in Water at One Atmosphere  
(From Devin,<sup>25</sup> points represent measurements from various sources)

where the undefined symbols are  $\gamma = 1.4$

$K_g$  = thermal conductivity of the gas  
 $= 5.6 \times 10^{-5}$  cal/cm-sec-deg C

$C_{p_g}$  = specific heat at constant pressure of the gas  
 $= 0.24$  cal/g-deg C

At atmospheric pressure, Devin finds

$$\eta_{th} = 4.4 \times 10^{-4} \left( \frac{\omega}{2\pi} \right)^{1/2} \quad (4.24)$$

The radiation loss factor can be found by expanding Equations (2.24) and (2.26) to find the pressure on the bubble surface for small  $k_o R_o$  (for small amplitude oscillations  $R$  is imperceptibly different from  $R_o$ )

$$p(R_o, t) \approx \frac{-i\omega\rho_o \dot{v}}{4\pi R_o} (1 - ik_o R_o) e^{-i\omega t} \quad (4.25)$$

The first term is the familiar inertial pressure; the second term is dissipative and it represents an acoustic resistance to the bubble wall motion by the liquid. Now the pressure given by Equation (4.12) may be compared with Equation (4.22) to disclose a radiation loss factor which is

$$\begin{aligned} \eta_{\text{rad}} &= k_o R_o \\ &= \frac{\omega_o R_o}{c_o} \end{aligned} \quad (4.26)$$

Equation (4.20) can be written in alternate forms\*

$$\eta_{\text{rad}} = \left( \frac{3\gamma P_o}{\rho_o c_o^2} \right)^{1/2} \quad (4.27)$$

$$= \left( \frac{3\rho_g c_g^2}{\rho_o c_o^2} \right)^{1/2} \quad (4.28)$$

showing that the radiation loss factor is independent of frequency.

The total loss factor is found from the sum of the contributions,

$$\eta = \eta_{\text{rad}} + \eta_{\text{th}}$$

---

\*Using the ideal gas law for adiabatic volume changes  $P_g$ , i.e.,  $P_g \propto (\rho_g)^\gamma$  (constant), which leads to  $dP_g/d\rho_g = c_g^2 = \gamma P_g/\rho_g$ .

The frequency spectrum of linear bubble motions can be determined from Equation (4.22), by Fourier transformation as

$$\frac{\rho_o V(\omega)}{4\pi R_o} (\omega_o^2 - \omega^2 - i\eta\omega\omega_o) = -p(r, \omega) \quad (4.29)$$

where  $V(\omega)$  is the Fourier transform of the volume pulsation. The spectral density of volume fluctuation can be found from methods of Section 3.5.3 as

$$\begin{aligned} \phi_{vv}(\omega) &= \frac{2\pi}{T_b} (V(\omega) V^*(\omega)) \\ &= \phi_{pp}(\omega) \left\{ \frac{16 \pi^2 R_o^2}{\rho_o^2} \left[ (\omega_o^2 - \omega^2)^2 + \eta^2 \omega^2 \omega_o^2 \right]^{-1} \right\} \end{aligned}$$

where  $T_b$  is the lifetime of the bubble oscillation which is on the order  $(\eta\omega_o)^{-1}$  and  $\phi_{pp}(\omega)$  is the spectral density of pressure fluctuations that drive the bubble.

#### 4.2.2 Sound Propagation in Bubbly Liquids

The theory of linear bubble motions has been used to describe the steady state propagation and absorption of sound waves in bubbly mixtures. The bubbles increase both the compressibility and the absorption of the two-phase fluid. We shall assume that the sizes of the bubbles are much smaller than an acoustic wavelength and that the bubbles are homogeneously dispersed throughout the liquid phase. The concentration of gas, in terms of the volume of gas per volume of liquid, shall be designated as  $\beta$  so that the density of the mixture is given by

$$\rho_m = \rho_g \beta + \rho_o (1 - \beta) \quad (4.30)$$

where  $\rho_g$  is the density of the gas phase and  $\rho_o$  is the density of the liquid phase. Because, for air and water mixtures,  $\rho_o/\rho_g \approx 800$  (at standard temperature and pressure), the density of the mixture is nearly identically  $\rho_o$ .

The speed of sound in the mixture at an angular frequency  $\omega$  is related to a complex wave number  $k_m$  through a complex wave speed  $C_m$

$$\begin{aligned}
 k_m &= \frac{\omega}{c_m} \\
 &= (k_m)_r + i(k_m)_i
 \end{aligned}
 \tag{4.31}$$

The propagation characteristics are given by

$$\begin{aligned}
 p &= p_o e^{i(k_m)_r r - \omega t} \\
 &= p_o e^{i \left[ (k_m)_r r - \omega t \right] - (k_m)_i r}
 \end{aligned}
 \tag{4.32}$$

where  $r$  is a distance referred to some origin inside the mixture and  $k_{m_i}$  gives rise to attenuation of the sound pressure. In order to determine the wave speed in the mixture, we calculate a resultant compressibility of the liquid-gas mixture. To this end note that the total volume reduction  $\delta V$  to a region of the mixture\* resulting from a pressure disturbance  $\delta p$  is the sum of the individual compressions of the liquid and gas phases,  $\delta V_\ell$  and  $\delta V_g$ , respectively,

$$\delta V = \delta V_\ell + \delta V_g
 \tag{4.33}$$

In turn,  $\delta V_g$  is the total gas compression, which for the  $i^{\text{th}}$  component bubble can be written down by using Equation (4.29),

$$(\delta V_g)_i = \frac{\frac{4\pi R_i}{\rho_o} (\delta P)}{\omega^2 + i\eta \omega \omega_o - \omega_o^2}$$

where  $\omega_o$  is the resonance frequency of the bubble of radius  $R_i$  so that the fractional volume change is an integral over the entire distribution of bubble radii,

---

\*The size of this mixture needs only to include a uniform distribution of bubbles.



$$\frac{\delta v_g}{v} = - \frac{1}{\rho_o} \frac{\delta P}{\omega^2} \int_0^\infty \frac{4\pi R n(R) dR}{\left[ \left( \frac{\omega_o}{\omega} \right)^2 - 1 - i\eta \frac{\omega_o}{\omega} \right]} \quad (4.34)$$

The integrand contains the distribution of radii in the form of the number of the bubbles of radius  $R$  per unit volume of liquid in an incremental range of radii. The total volumetric concentration of gas suspended (not dissolved) in the liquid is just

$$\begin{aligned} \beta &= \int_0^\infty \frac{4\pi}{3} R^3 n(R) dR \\ &= \int_0^\infty \frac{d\beta}{dR} dR \end{aligned} \quad (4.35)$$

The compressibility of the mixture is given by

$$\frac{\delta V}{V} = - \frac{\delta P}{\rho_m c_m^2} \quad (4.36)$$

where  $1/\rho_m c_m^2$  is the "compressibility," and  $C_m$  is the associated speed of sound in the mixture. A combination of Equations (4.33) through (4.36) gives

$$k_m = \left( \frac{\rho_m}{\rho_o} \right)^{1/2} \left\{ k_o^2 (1-\beta) + \int_0^\infty \frac{4\pi R n(R) dR}{\left( \frac{\omega_o^2}{\omega^2} - 1 \right) - i\eta \frac{\omega_o}{\omega}} \right\}^{1/2} \quad (4.37)$$

as the complex acoustic wave number in the mixture.

This relationship has been derived by Carstensen and Foldy<sup>27</sup> (who also derived reflection and transmission coefficients for bubble screens), by Meyer and

Skudrzyk,<sup>28</sup> and more recently by Hsieh and Plesset<sup>29</sup> who showed that  $C_m$  is an isothermal sound speed for values of  $\beta$  of practical interest. Experimental confirmation of Equation (4.37) has been provided by Meyer and Skudrzyk,<sup>28</sup> and by Fox, Curley, and Larson<sup>30</sup> using measurements of acoustic transmission through bubble screens, and by Silberman<sup>31</sup> using acoustic transmissions down a wave tube. The measurements are difficult to interpret in terms of the theory because of uncertainties in the screen thickness, bubble size distribution, and bubble damping as the early measurements of Carstensen and Foldy will attest. Figure 4.5, from the

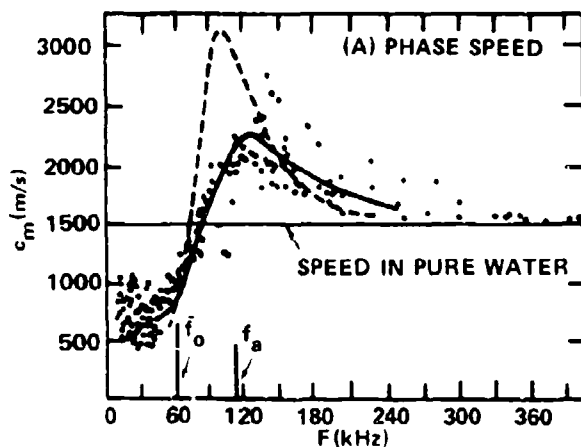


Figure 4.5a - Phase Speed

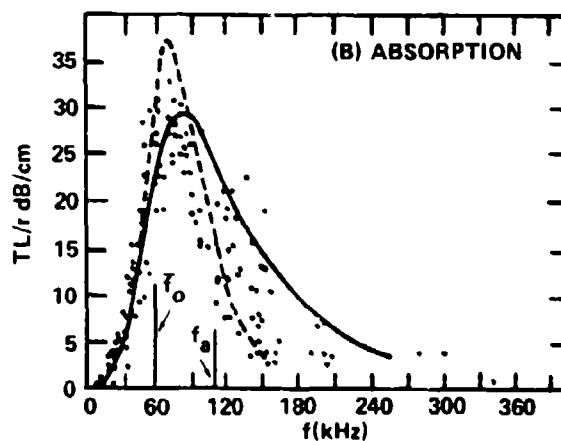


Figure 4.5b - Absorption

Figure 4.5 - Phase Speed and Absorption in a Bubbly Liquid Containing Radii 0.06 to 0.24 Millimeter Diameter ( $\bar{R} \approx 0.12$  mm,  $\sigma_R/\bar{R} \approx 1/3$ )

(Points are results of measurements; lines computed from Equation (4.40) using measured distribution (—) and idealized distribution (---) with

$\bar{R} = 0.12$  millimeters,  $\eta = 0.5$ , and  $\beta = 2 \times 10^{-4}$  cubic centimeter per cubic centimeter. From Fox et al.<sup>30</sup>) For the definitions of  $\bar{f}_0$  and  $f_a$

see the discussion following Equation (4.43).  $c_m = \omega / (k_m)_r$

measurement program of Fox, Curley, and Larson,<sup>30</sup> shows phase velocity and attenuation measurements in a bubble cloud-field that was narrowly distributed between radii of 0.06 and 0.24 mm with an average of 0.12 mm. The transmission loss (TL) over a distance  $r$  is determined from the ratio of pressures at distances  $x$  and  $x + r$  using Equation (4.32), i.e.,

$$\begin{aligned} \text{TL} &= 20 \log \frac{|p(x+r)|}{|p(x)|} \\ &= 8.69 (k_m)_i r \end{aligned} \quad (4.38)$$

The lines of Figure 4.5 represent alternative theoretical estimates derived from Equation (4.37) for a narrow distribution of bubble sizes and for a large distribution of bubble radii. For a narrow radius distribution, such that the range of radii  $\Delta R$  satisfies  $\Delta R/R < \eta$ , Equation (4.37) becomes

$$\frac{\rho_o}{\rho_m} k_m^2 = k_o^2 \left\{ 1 - \beta + \left( \frac{c_o^2 \rho_o}{c_g^2 \rho_g} \right) \beta \frac{\left( \frac{\omega_o}{\omega} \right)^2}{\left[ \left( \frac{\omega_o}{\omega} \right)^2 - 1 - i\eta \left( \frac{\omega_o}{\omega} \right) \right]} \right\} \quad (4.39)$$

using the equivalence between  $\omega R_o$  and  $\gamma P_o / \rho_o$  given by Equation (4.20) in the case of negligible effects of surface tension. For such a distribution, all bubbles are resonant at frequency  $\omega_o$  and so all participate equally in the dynamics of the medium.

An alternate relationship may be derived when the bubble radii extend over a broad range  $\Delta R$ . There is, at any frequency of excitation, a broad population of vibrating bubbles of which only some motions are resonant but others are stiffness or mass-controlled. If we let the bubble sizes be distributed about an average radius  $\bar{R}$  with an associated resonance frequency  $\bar{\omega}_o$ , we can denote the bubble distribution as a function of the differential radius

$$n(R) = n(r - \bar{R})$$

In Equation (4.37) the integration over  $R$  includes the variable resonance frequency that is a function of radius through

$$\omega_o R = \left( \frac{3\rho_o c_o^2}{\rho_g c_g} \right)^{1/2} \equiv C$$

For convenience, therefore, we normalize the radius on the fixed frequency  $\omega$  and the factor  $C$  so that we may write (with  $x=\omega R/C$  and  $\bar{x}=\omega \bar{R}/C=\omega/\bar{\omega}_o$ )

$$\begin{aligned} n(R) &= n \left( \frac{\omega \bar{R}}{C} - \frac{\omega R}{C} \right) \frac{\omega}{C} \\ &= n(x-\bar{x}) \frac{\omega}{C} \end{aligned}$$

Equation (4.37) becomes, accordingly

$$\frac{1}{1-\beta} \frac{\rho_o}{\rho_m} \frac{k_m^2}{k_o^2} = 1 + \left\{ \frac{\rho_o c_o^2}{(1-\beta) \rho_g c_g^2} \cdot \frac{4}{3} \pi \bar{R}^3 \cdot \left( \frac{\bar{\omega}_o}{\omega} \right)^3 \int_0^\infty \frac{x^3 n(x-\bar{x}) dx}{(1-x^2) - i\eta x} \right\} \quad (4.40)$$

The integrand contains the  $n(x-\bar{x})$  which we assume to be strongly peaked around  $x-\bar{x}$  with a bandwidth equal to twice the standard deviation of bubble sizes  $\sigma_R/\bar{R}$ , and the bubble admittance which is strongly peaked around  $x=1$  with a bandwidth equal to  $\eta$ . As long as  $\bar{x}$  is sufficiently removed from unity, i.e., as long as the peak of  $n(x-\bar{x})$  is sufficiently removed from the peak in the admittance, there are a negligible number of bubbles that are resonant at the excitation frequency. Equation (4.40) takes the form of Equation (4.39), but with the resonance frequency and loss factor replaced by average values, i.e.,

$$\frac{1}{1-\beta} \frac{\rho_o}{\rho_m} \frac{k_m^2}{k_o^2} = 1 + \frac{\rho_o c_o^2}{\rho_g c_g^2} \frac{\beta}{1-\beta} \frac{1 - \left( \frac{\omega}{\bar{\omega}_o} \right) + i\bar{\eta} \left( \frac{\omega}{\bar{\omega}_o} \right)}{\left[ 1 - \left( \frac{\omega}{\bar{\omega}_o} \right)^2 \right]^2 + \bar{\eta}^2 \left( \frac{\omega}{\bar{\omega}_o} \right)^2} \quad (4.41)$$

This equation is valid for, e.g.,  $|\omega/\bar{\omega}_0 - 1| > 2\sigma_R/\bar{R}$  where  $\sigma_R$  is the standard deviation of bubble radii about the average  $\bar{R}$ . This equation also holds for all frequencies when the bubble radii are narrowly distributed, i.e., when  $\sigma_R/\bar{R} < \eta$ .

When the bubble radii are widely distributed so that the range of available sizes is larger than  $\bar{\eta} \cdot \bar{R}$ , yet still concentrated about a mean, it is still possible to "decouple" the function  $n(R)$  from the admittance function when motion is near resonance. We do this in the context of a crude assumption that the radii are normally distributed\* about a radius  $\bar{R}$  with a variance  $\sigma_R^2$ , i.e.,

$$n(R) = \frac{N}{(2\pi)^{1/2} \sigma_R} \exp \left\{ -\frac{(R-\bar{R})^2}{2 \sigma_R^2} \right\}, \quad R > 0 \quad (4.42)$$

where  $N$  is the total number of bubbles. The real part of the admittance function, involving  $1 - (\omega/\bar{\omega}_0)$ , passes through zero at  $\omega = \bar{\omega}_0$ , but it also has peaks slightly above and below  $\bar{\omega}_0$ . These peaks occur at  $\omega = \bar{\omega}_0 (1 \pm \eta/2 \times 2^{1/2})$  with magnitudes on the order of  $\pm [2^{1/2}/3\eta]$ , respectively. Below  $\omega = \bar{\omega}_0$  the real admittance rapidly approaches unity, while above resonance it approaches zero. Therefore, as long as  $\eta \ll \sigma_R/\bar{R}$  the real part of the integral in Equation (4.40) is approximated simply by an integral over  $0 < x < 1$  of  $n(x-\bar{x})$ . The contributions from the oppositely-signed peaks at  $\bar{\omega}_0 (1 \pm \eta/2 (2^{1/2}))$  contribute only

$$\frac{4}{9} \eta \cdot \left. \frac{dn}{dx} \right|_{x=\bar{x}}$$

which is negligible. The imaginary part of the integral is strongly peaked at  $\omega = \bar{\omega}_0$  and only those bubbles that are resonant at the driving frequency contribute to the dissipation. The integral then becomes, close to resonance, ( $\omega \approx \bar{\omega}_0$ )

---

\*A more legitimate assumption would have been a Rayleigh distribution for which  $\sigma_R = 0.52 \bar{R}$ . See also Section 4.2.4.3, paragraph b. Equation (4.42) approximates the distribution generated in Reference 30 with  $\sigma_R \sim 0.3 \bar{R}$ .

$$\frac{c_o}{c_m} (1-\beta)^{-1} \left( \frac{k_m}{k_o} \right)^2 \approx 1 + \frac{1}{2} \left( \frac{\beta}{1-\beta} \right) \frac{\rho_o c_o^2}{\rho_g c_g^2} \left\{ 1 + \left( \frac{2}{\pi} \right)^{1/2} \left( \frac{\bar{R}}{\sigma_R} \right) \left( \frac{\bar{\omega}_o}{\omega} - 1 \right) \right. \\ \left. + i \left( \frac{\pi}{2} \right)^{1/2} \left( \frac{\bar{\omega}_o}{\omega} \right) \left( \frac{\bar{R}}{\sigma_R} \right) \exp \left[ - \left| \left( \frac{\bar{R}}{2^{1/2} \sigma_R} \right) \left( \frac{\bar{\omega}_o}{\omega} - 1 \right) \right|^2 \right] \right\} \quad (4.43)$$

for  $|\bar{\omega}_o/\omega - 1| < \sigma_R/(2R^2/\pi)^{1/2}$ ,  $\eta \ll \sigma_R/\bar{R}$ , and  $R^2/(2\sigma_R^2) \gg 1$ . The second term in Equation (4.43), involving  $(\bar{\omega}_o/\omega - 1)$ , arises from an approximation to the error function,  $\text{erf}(x) \sim x$ .

Equations (4.41) and (4.43) have many general features in common. As  $\omega$  passes through  $\bar{\omega}_R$  from below, the real admittance first adds, then subtracts from the liquid admittance. There is a frequency in each case,  $\omega = \omega_a$ , at which the real part of the admittance of the bubbles cancels the compressibility of the water so that  $k_m^2$  is identically imaginary. Both at this frequency and at resonance, the average admittance of the bubbles is such that the sound is greatly absorbed, i.e., the transmission loss is high. The behavior of the mixtures at these and other frequencies is summarized in Table 4.1 for both narrow and broad distributions of bubble radii and without any reference to a particular bubble distribution. Below the critical frequencies  $\bar{\omega}_o$  and  $\omega_a$ , all mixtures behave similarly and the transmission loss is reduced. The medium is controlled by the total stiffness of the suspended gas, while at very high frequencies the bubbles are dynamically stiff and oscillate as small rigid spheres in response to the sound. Since their radii are much less than an acoustic wavelength, the propagation approaches that of the liquid medium. At the resonance frequency, absorption is large, the propagation velocity is relatively low and in bubble distributions the standard deviation of radius replaces the damping. At the frequency,  $\omega_a$  (called "anti-resonance" by Junger<sup>32</sup>) the wave speed increases. For narrowly-distributed radii, the speed of sound increases as damping decreases, but the increase would be somewhat reduced as the distribution is made broader. The relationships in Table 4.1 closely agree with measured propagation characteristics. Figure 4.5 illustrates measurements and calculations made by Fox, Curley, and Larson.<sup>30</sup> Calculated wave parameters used a value for the

TABLE 4.1  
ASYMPTOTIC RANGES FOR PROPAGATION IN BUBBLY MIXTURES

Frequency	Speed of Sound, $\frac{C_m}{C_o} = \frac{k_o}{(k_m)^{1/2}}$	Transmission Loss $\frac{TL}{8.69 k_o r} = \frac{(k_m)^{1/2}}{k_o}$
	$\beta \ll \alpha R/R$	$\beta \ll \alpha R/R$
	$\left[ 1 + \left( \frac{\beta_o C_o^2}{\beta_g C_g^2} \right)^2 \right]^{-1/2}$	$\frac{\beta_o}{2 C_o} \left( \frac{\beta_o C_o^2}{\beta_g C_g^2} \right)^{1/2}$
	$\left[ \frac{\beta_o}{\beta_g} \left( \frac{\beta_o C_o^2}{\beta_g C_g^2} \right)^{1/2} \right]^{1/2}$	$\frac{(k_m)^{1/2}}{k_o} = \frac{C_o}{C_m}$
	$\left[ \frac{\beta_o}{\beta_g} \left( \frac{\beta_o C_o^2}{\beta_g C_g^2} \right)^{1/2} \right]^{1/2}$	$\frac{(k_m)^{1/2}}{k_o} = \frac{C_o}{C_m}$
	$\left[ 1 - \frac{\beta_o C_o^2}{\beta_g C_g^2} \left( \frac{\beta_o}{\beta_g} \right)^2 \right]^{-1/2}$	$\left[ \frac{\beta_o}{\beta_g} \left( \frac{\beta_o C_o^2}{\beta_g C_g^2} \right)^2 \right]^{1/2}$

$\beta_s$  = standard deviation of radius population  
 $\bar{R}$  = average radius  
 $\frac{\beta_o}{\beta_g} = \left( \frac{\beta_o C_o^2}{\beta_g C_g^2} \right)^{1/2}$ ,  $\beta_o > \alpha R/R$   
 $\beta$  = volumetric concentration of gas

loss factor of 0.5, which is now considered excessive in light of the more recent measurements shown in Figure 4.4. Equation (4.43) cannot be used to calculate the propagation at  $\omega_a/\omega_o$  because, at this frequency, the approximations leading to Equation (4.43) are not valid. Note also that near  $\omega_r$  and  $\omega_a$  the analog of the loss factor in the distributed medium replaces  $(1/\eta)$  by  $(\pi/2) (\bar{R}/\beta) (d\beta/dR)$ , from which comes the expression for  $c_m$  at  $\omega = \omega_a$  in the second column of Table 4.1.

Transmission losses in bubbly media have been used to determine bubble populations (Section 4.2.4.3). In those cases either of two expressions may be used. For a narrow range of bubble sizes, such that  $\sigma_{R/\bar{R}} < \eta$  the transmission loss depends on the value of the bubble damping

$$\frac{TL}{r} = 8.69 \frac{\frac{1}{2} \frac{\omega \rho_o c_o}{\eta \rho_g c_g^2}}{2} \quad (4.44)$$

with  $\eta \approx 0.1$ . For a broad bubble distribution, the transmission only depends on concentration gradient  $d\beta/dR$  rather than the loss factor explicitly so that

$$\frac{TL}{r} = 8.69 \frac{(3\pi)^{1/2}}{4} \frac{d\beta}{dR} \left( \frac{\rho_o c_o^2}{\rho_g c_g^2} \right)^{1/2} \quad (4.45)$$

for  $\sigma_{R/\bar{R}} > \eta$ . Both the wave speeds and the transmission losses are shown for selected bubble media in Figure 4.6; they serve as examples of the limits given in Table 4.1.

The acoustics of bubbly mixtures is important in modifying sound propagation near the ocean surface, especially for underwater acoustic testing and experimentation. In water tunnels without resonators, for example, after continued operation with a cavitating body, the free gas content can increase appreciably. At lower frequencies than the bubble resonance, relatively small volumetric concentrations of gas can appreciably reduce the sound speed in the fluid. The consequence of this reduction will be increased Mach numbers of moving bodies that are immersed in the two-phase fluid. It is quite possible that surface motions that are subsonic in pure water could become supersonic so that the wave-bearing qualities of the fluid will be altered relative to the characteristic length and velocity of



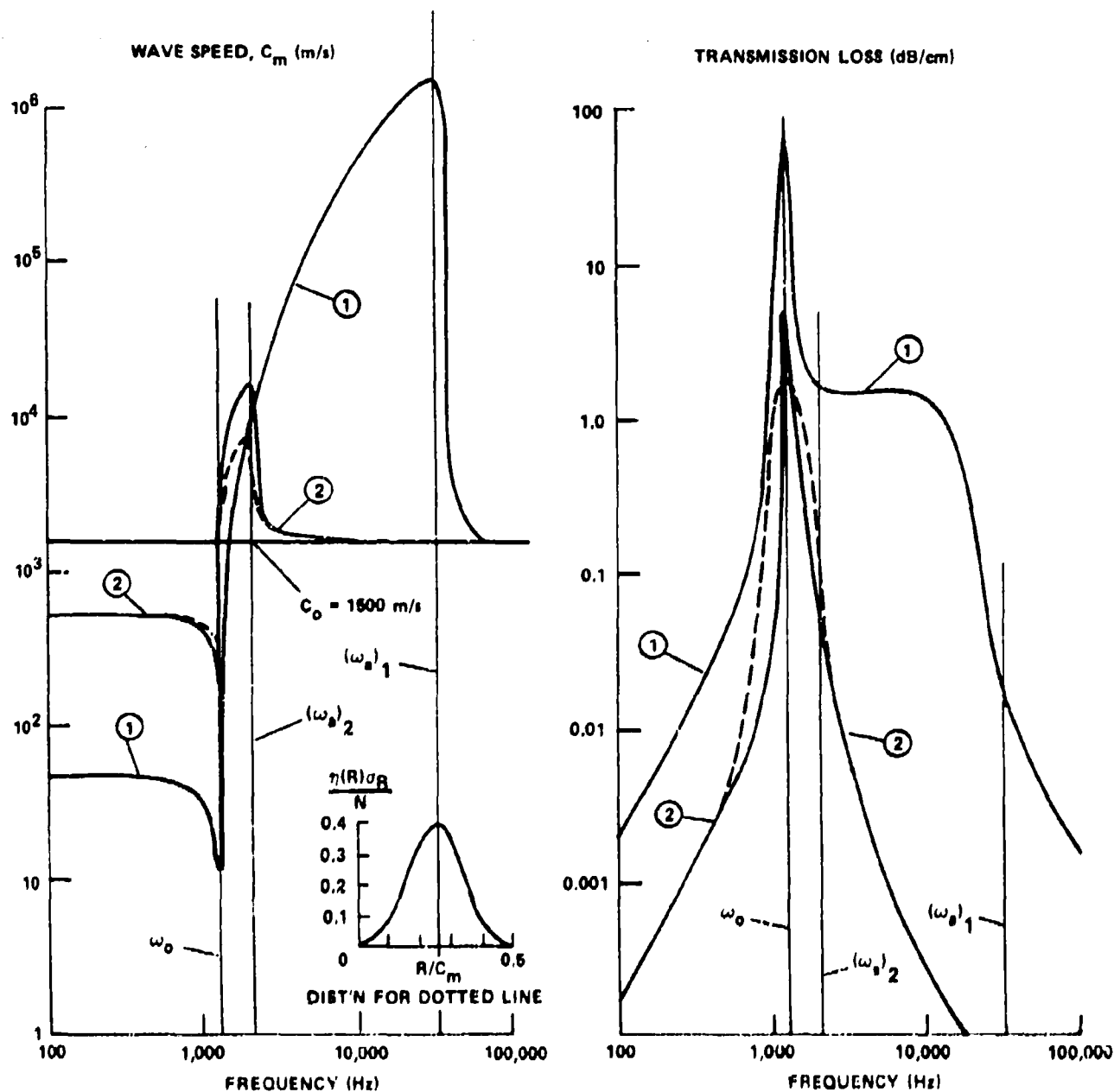


Figure 4.6 - Propagation Characteristics of Bubbly Mixtures of Air in Water  
 $(\omega_a)_1$  and  $(\omega_a)_2$  denote  $\omega_a$  for Lines (1) and (2). Line (1):

$\beta = 0.06$ ,  $R = 0.25$  cm,  $\eta = 0.03$  all bubbles the same size.

Line (2):  $\beta = 2 \times 10^{-4}$ , solid line -  $R = 0.25$  cm,  
 $\eta = 0.03$  all bubbles the same size, Dashed line -  
 bubble distribution Equation (4.42)

$R = 0.25$  cm,  $\sigma_R/R = 1/3$

the test body. Shock waves could also be formed which would make it necessary to bring into analysis thermodynamic properties of the two-phase fluid.

Some more extensive treatments of two-phase media along these lines have been given by Plesset<sup>33</sup> in connection with the stability and thermodynamics of single spherical bubbles, some further general acoustic characteristics have been examined by Crighton and Pflowce-Williams,<sup>1</sup> and propagation of shock waves in such liquids has been considered by van Wijngaarden,<sup>34</sup> Whitam,<sup>35</sup> and Benjamin.<sup>36</sup> Extensive analytical treatments of the continuum mechanics of bubbly fluids have been given by Zwick,<sup>37-39</sup> Isay and Roental<sup>40,41</sup> (who consider the effects of the compressibility on the lifting characteristics of hydrofoils), and Wallis<sup>42</sup> (who studied wave motions in bubbly mixtures).

### 4.2.3 Theoretical Cavitation Thresholds, Nonlinear Oscillations of Spherical Bubbles

4.2.3.1 The Onset of Nonlinear Oscillations. When an harmonic perturbation pressure is of such a magnitude that the velocity-squared term in the bubble equation (Equations (4.12) and (4.15)) is important, the bubble motions cease to be sinusoidal and take on a more complicated time history. Figure 4.7 illustrates this behavior

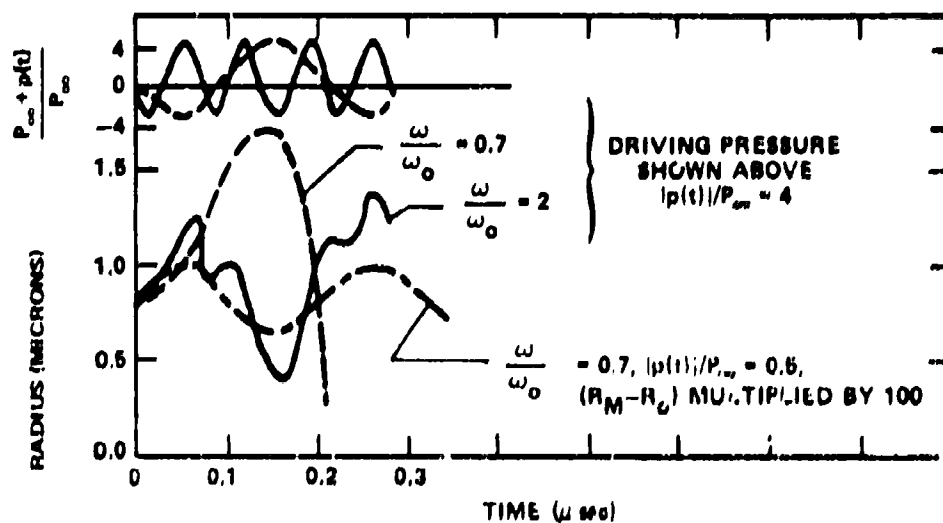


Figure 4.7 - Radius-Time Curve for Forced Oscillations of a Gas Bubble

(Note:  $R_0 = 0.8 \times 10^{-4}$  centimeters,  $\omega_0 = 4.3 \times 10^{-1}$  sec<sup>-1</sup> ( $0.8 \times 10^6$  Hz).

Curves (---) and (---) from Neppiras and Noltingk,<sup>15</sup>

Curve (-) from Solomon and Plesset<sup>33</sup> ( $\eta=0$ .)

for a variety of amplitudes of driving pressure and a variety of resonance frequencies of the bubbles. The figure illustrates the theoretical behavior that the linear or nonlinear motions of a bubble depend both on the amplitude of the pressure oscillation and on its frequency relative to the linear resonance frequency of the bubble. For rather large pressure oscillations, e.g., four times the ambient equilibrium pressure  $P_0$ , simple harmonic motion of the bubble will not exist. If the frequency of oscillation is below the resonance frequency, the bubble will grow and then rapidly collapse, this behavior is characteristic of cavitation. For larger frequencies the motion will consist of a superposition of two harmonics, one at the resonance frequency and the other at the driving frequency. For small pressure amplitudes the motion is nearly simple harmonic, as shown. The amplitude of the pressure fluctuations responsible for the cavitation is such that the pressure applied to the bubble actually becomes negative so that a tension is placed on the bubble causing the large rate of expansion necessary for cavitation. There is, in fact, a critical value of  $P_\infty$  (e.g.,  $P_{cr}$  that will be determined later) for which cavitation is to be expected. The implication made by the heavy and dashed lines in the lower portion of Figure 4.7 is that the excitation pressure must be applied for a time long enough to permit the necessary bubble growth and that this time must be measured in terms of the characteristic period of resonant oscillation. At frequencies which are small enough relative to the resonance frequency, an adequate criterion for determining the critical pressure can be determined by considering the static equilibrium of the bubble.

4.2.3.2 The Critical Pressure for Vaporous Cavitation. The critical pressure for cavitation, based on a theory of static equilibrium was first determined by Blake,<sup>44</sup> and recently extended by Akulichev.<sup>45</sup> This condition can be written in terms of the difference in static pressure at the bubble wall  $P(R)$  and the field pressure  $P(r)$ , see Figure 4.2. Then, using Equations (4.10) and (4.11),

$$P(R) - P(r) = P_v - \frac{2S}{R} - P(r) + P_0 \left( \frac{R_0}{R} \right)^3 = \Delta P \quad (4.46)$$

Note that because static conditions ( $\omega \ll \omega_0$ ) are being examined, the volume velocity ( $\dot{V}$ ) and volume acceleration ( $\ddot{V}$ ) are neglected. The static equilibrium will exist at a critical radius when, for a further increase in radius, the pressure difference will decrease. This condition for equilibrium is (see also van der Walle)<sup>46</sup>

$$\left. \frac{d(\Delta P)}{dR} \right|_{R=R_c} = 0$$

or

$$-\frac{3\gamma p_{gc}}{R_c} \left( \frac{R_0}{R_c} \right)^{3\gamma} = \frac{2S}{R_c^2} \quad (4.47)$$

where  $R_c$  is the critical bubble radius. To relate this condition to a corresponding critical pressure, we combine Equations (4.10) and (4.47) to find the partial pressure of gas in the bubble when it reaches its critical radius

$$p_{gc} = p_c(r) + \frac{2S}{R_c} - p_v = \frac{2S}{3\gamma R_c} \quad (4.48a)$$

so the critical value of the hydrodynamic pressure at  $r > R$  is

$$p_c(r) - p_v = - \left( \frac{3\gamma-1}{2\gamma} \right) \frac{4S}{3R_c} \quad (4.48b)$$

Substituting Equation (4.48) into Equation (4.46) to eliminate  $R_c$  yields the critical pressure required for the cavitation of a bubble with radius  $R_0$  in an initial ambient pressure of  $p_0(r)$

$$\begin{aligned} p_c(r) - p_v &= \frac{2S}{R_c} \left[ \frac{1}{3\gamma} - 1 \right] \\ &= - \left( \frac{2S}{R_0} \right)^{3\gamma/(3\gamma-1)} \left[ \frac{3\gamma-1}{3\gamma} \right] \frac{1}{(3\gamma)} \left[ p_0(r) - p_v + \frac{2S}{R_0} \right]^{1/(3\gamma-1)} \end{aligned} \quad (4.49)$$

Equation (4.49) shows that for cavitation to occur, i.e., for instability to exist, the critical pressure outside the bubble must become less than the vapor pressure. The relationship also shows that as  $R_0$  decreases, this critical pressure must be more negative. In other words, the tensile strength of the liquid increases as the size of suspended bubbles decreases. The limiting tensile strength so far observed<sup>2,45</sup> is  $P_c = -280$  atm. Furthermore when cavitation occurs, as in the example shown by the dashed line in the lower part of Figure 4.7, any gas in the original bubble will be expanded into a volume many times larger than in the original bubble. In such cases, because the partial pressure of gas is then greatly exceeded by the vapor pressure of liquid, the cavitation is called vaporous. Equation (4.49) is shown in Figure 4.8 (taken from Strasberg)<sup>47</sup> for the case of isothermal expansions ( $\gamma=1$ ) at an initial pressure of  $P_0(r) = 1$  atm; the expression becomes\*

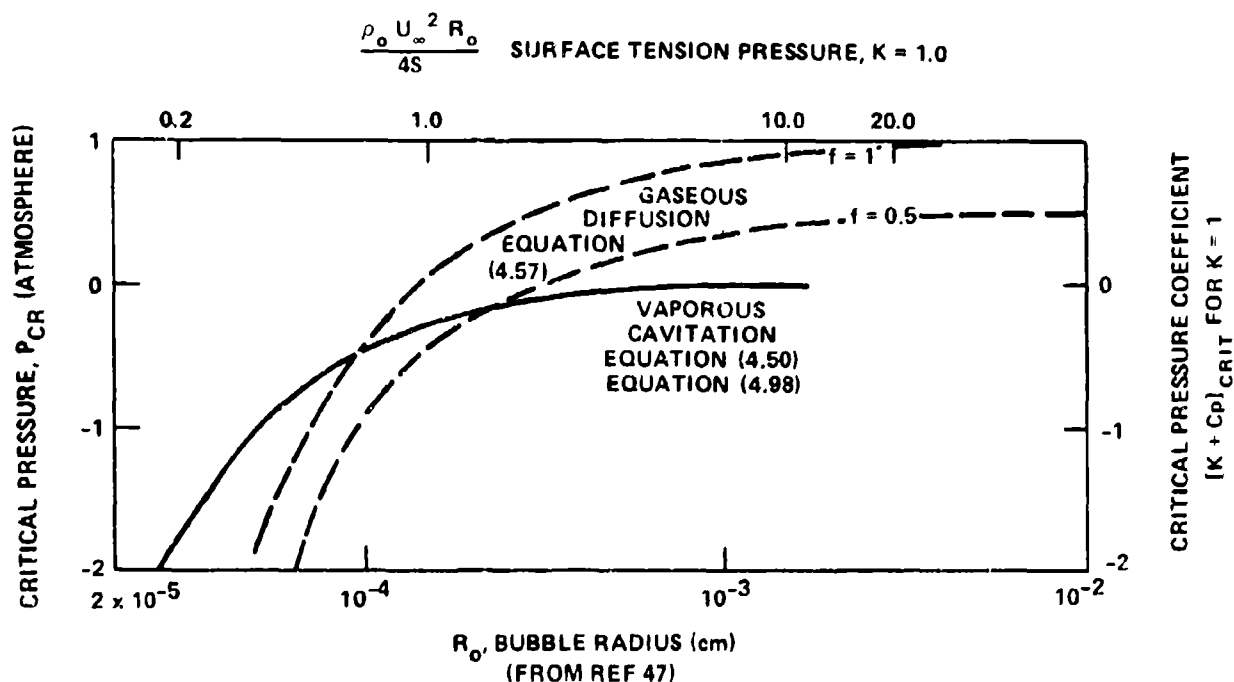


Figure 4.8 - Critical Pressure at  $P_0 = 1$  Atmosphere and Critical Pressure Coefficient at  $K = 1$  for Vaporous Cavitation, Solid Line (—). Critical Pressure for Gaseous Diffusion at  $P_0 = 1$  Atmosphere,  $P_{sat} = 1$  Atmosphere, Broken Line (---).

\*A dimensionless representation of Equation (4.50) is also shown; this representation will be discussed in Section 4.3.1.2.

$$P_c(r) - P_v = - \left( \frac{2S}{R_o} \right)^{3/2} \frac{2}{3^{1/2}} \left[ P_o(r) - P_v + \frac{2S}{R_o} \right]^{-1/2} \quad (4.50)$$

For bubble radii of  $10^{-3}$  cm and smaller, the cavitation threshold will be at increasingly negative pressures. Although Equation (4.50) shows a formal dependence of  $P_c(r)$  on  $P_o(r)$ , the dependence is effectively negligible because of the dominance by the surface tension.

The thresholds of nonlinear motions and cavitation for periodic excitation pressures were evaluated numerically by Solomon and Plesset<sup>43</sup> through a reworking of Equations (4.12) and (4.16) using the normalization

$$\underline{R} = \frac{R}{R_o}$$

They found, using Equation (4.15) that

$$\begin{aligned} \ddot{\underline{R}} + \frac{3}{2} (\dot{\underline{R}})^2 &= \frac{P_o}{\rho_o R_o^2} \underline{R}^{-3\gamma} - \frac{P_v}{\rho_o R_o^2} \underline{R}^{-3\gamma} + \frac{2S}{\rho_o R_o^2} (\underline{R}^{-3\gamma} - \underline{R}^{-1}) \\ &+ \frac{P_v}{\rho_o R_o} - \frac{P(\underline{R}, t)}{\rho_o R_o^2} \end{aligned}$$

Following Equation (4.14) and letting

$$p(\underline{R}, t) = P_o + p_o \sin(\omega t + \pi)$$

the equations of motion become

$$\ddot{\underline{R}} + \frac{3}{2} (\dot{\underline{R}})^2 = \frac{P_o - P_v}{\rho_o R_o^2} (\underline{R}^{-3\gamma} - 1) + \frac{2S}{\rho_o R_o^3} (\underline{R}^{-3\gamma} - \underline{R}^{-1}) = \frac{P_o}{\rho_o R_o} \sin(\omega t + \pi) \quad (4.51)$$

Radius-time curves, similar to those in Figure 4.7, were calculated for  $\omega/\omega_r = 0.011$ , 0.04, and 0.069. The first-order transient behavior of the bubbles was also deduced in a linearized sense by letting

$$\underline{R}(t) = 1 + \epsilon(t)$$

so that Equation (4.51) can be linearized by neglecting  $(\dot{\epsilon})^2$  relative to  $\ddot{\epsilon}$ , to give an approximate formula for the forced oscillation subject to the conditions  $\epsilon(0) = 0$  and  $\dot{\epsilon}(0) = 0$ ; i.e.,

$$\frac{R-R_o}{R_o} \approx \frac{P_o C_1}{P_o (\omega_o^2 - \omega^2)} \left\{ \frac{\omega}{\omega_o} e^{-\frac{1}{2} \eta \omega_o t} \sin \omega_o t - \sin \omega t \right\} \quad (4.52)$$

where  $|\omega/\omega_o| > \eta \omega_o$ ,  $\eta$  is the loss factor of the bubble, and

$$C_1 = \frac{P_o - P_v}{\rho_o R_o^2}$$

The forced oscillations will persist after the initial resonant disturbance decays. The curve in Figure 4.7 for  $\omega = 2\omega_o$  is misleading in this regard because bubble damping had not been included in either Neppiras and Noltingk's or Solomon and Plesset's analyses. If bubble damping had been included, the resonant motion would have persisted over roughly  $1/\pi\eta$  natural periods. As the amplitude of the excitation pressure increases so that the critical pressure is reached, the damped transient motion is replaced by the unstable transient of cavitation.

In this region of large-amplitude motion such that the  $\ddot{r}$  term dominates the  $\dot{r}$  term, the bubble radius linearly increases with time, as shown by the dashed line in Figure 4.7 for  $t$  less than 0.1  $\mu$ sec. In this case, Equation (4.51) (and Equation (4.12) as well) suggests that,

$$R \sim t \left( \frac{2}{3} \right)^{1/2} \left( \frac{P_v - (P_o - P_o)}{\rho_o} \right)^{1/2} \quad \text{for } \omega t < \pi \quad (4.53)$$

i.e., the bubble radius will be proportional to the square root of the difference between the vapor and external pressure when the latter is smaller. The limit  $\omega t < \pi$  determines the length of time that the pressure fluctuation is negative, i.e., that the pressure difference  $P_v - P_o - p_o \sin(\omega t + \pi)$  is positive. The maximum radius will then be determined by the time  $t = \pi\omega^{-1}$ , so that

$$R_M \approx 2.6 \omega^{-1} \left( \frac{P_v - (P_o - p_o)}{\rho_o} \right)^{1/2} \quad (4.54)$$

Equation (4.54) demonstrates that the maximum bubble radius is independent of the initial radius, a result first determined analytically by Neppiras and Noltingk.<sup>16</sup> Linear dependence of the bubble radius with time has been observed for motions in hydrodynamic cavitation, see, e.g., Arndt and Ippen.<sup>48</sup>

Figure 4.9 summarizes the results of calculations using the complete bubble Equation (4.51) made by Neppiras and Noltingk<sup>16</sup> (designated N&N) and by Solomon and Plesset<sup>43</sup> (designated S&P) in a form that is consistent with the above analyses. The solid lines represent the steady-state first-order linear bubble amplitude given by Equation (4.29), rewritten as

$$\frac{(R_M - R_o)}{\left(\frac{p_o}{\rho_o}\right)^{1/2}} = \frac{\omega}{\omega_o} \left[ \frac{\left(\frac{p_o}{3P_o}\right)^{1/2}}{1 - \left(\frac{\omega}{\omega_o}\right)^2 - i\eta \frac{\omega}{\omega_o}} \right] \quad (4.55)$$

and the contrasting transient nonlinear cavitation amplitude which is (see Equation (4.54))

$$\frac{\omega(R_M - R_o)}{\left(\frac{p_o}{\rho_o}\right)^{1/2}} \approx 2.6 \left( \frac{P_o - P_o}{P_o} \right)^{1/2} \quad (4.56)$$



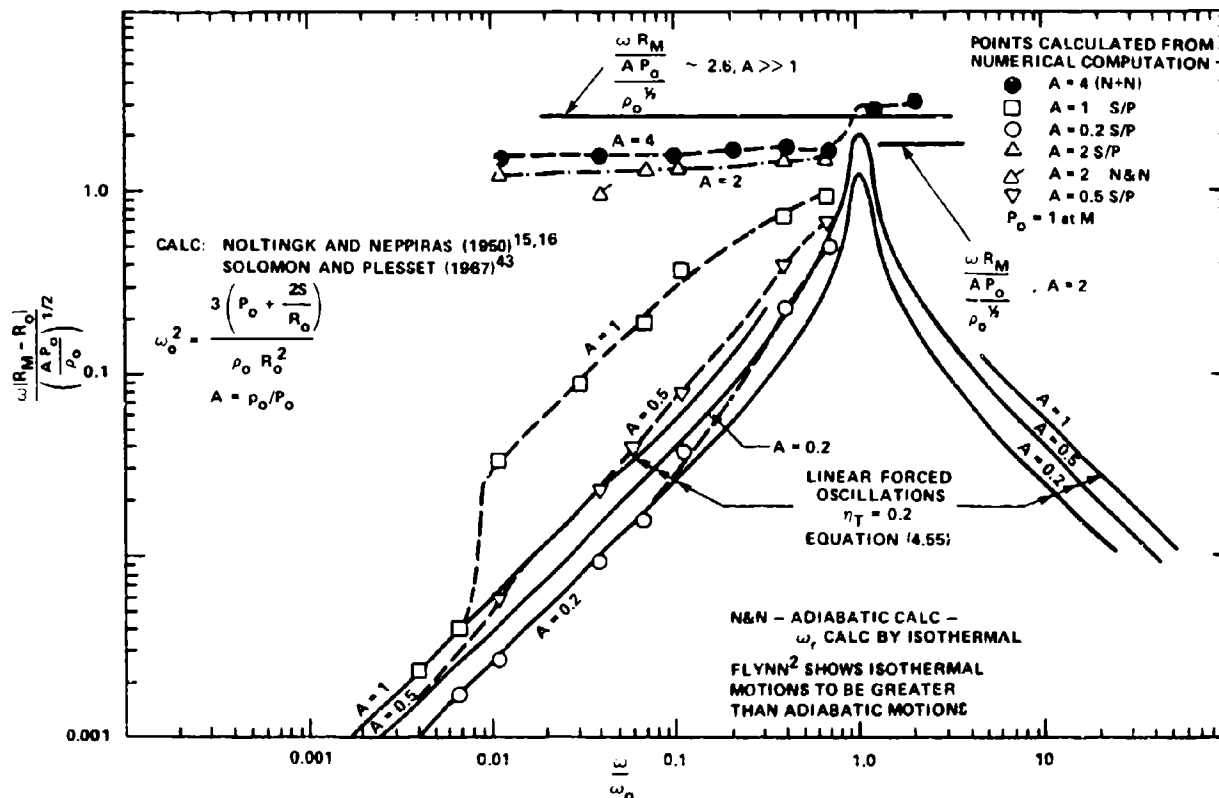


Figure 4.9 - Amplification Factor for Sinusoidally Excited Bubbles Shown as a Function of Frequency,  $\omega/\omega_0$ , for Different Pressure Amplitudes,  $A P_0 = |p| = p_0$

The calculated points, connected by dashed lines, are normalized on the ambient  $P_0$ ; for fractional values of  $p_0/P_0$ , e.g., at  $P_0 = 1$  atm, the minimum pressure is greater than the vapor pressure of water at any instant in the pressure cycle. For pressure amplitudes such that  $P_v - P_0 + p_0 > 0$  the limiting value of Equation (4.56) roughly applies. On the other hand, for small ratios of  $p_0/P_0$ , so that  $P_v - P_0 + p_0 < 0$  the admittance Equation (4.55) closely agrees with the more exact numerical calculations. For  $p_0/P_0 = 1$  it is seen that the threshold between linear and nonlinear motions depends on frequency, with the cutoff for linear oscillation being  $\omega \sim 0.01 \omega_0$ . For oscillations above the resonance frequency, only one point has

been calculated, and though the motion appears not to be cavitation-like (Figure 4.7), the computed amplitude exceeds that which would be estimated using the linear theory by about a factor of three. Cavitation thresholds in oscillating pressure fields will be independent of frequency and given by Equations (4.49) and (4.50) as long as the frequency of oscillation is much less than the bubble resonance.<sup>49</sup> At high frequencies,  $\omega > \omega_0$ , the inertial terms of Equations (4.12) and (4.16) become dominant, then the threshold pressure is given by the requirement that the pressure around the bubble must be less than the vapor pressure. However, as shown by Equation (4.54), as the frequency increases the pressure difference that is necessary to generate a bubble of a given size will also increase.\*<sup>50</sup>

4.2.3.3 The Importance of Diffusion. Diffusion can be important in both ultra-sonically and hydrodynamically induced cavitation. When the growth of a bubble is determined by the diffusion of dissolved gas into the bubble from the surrounding liquid, then the cavitation is called "gaseous cavitation" and is not explosive as in the case of the vaporous cavitation discussed in the preceding section. The time scales of bubble growth by diffusion exceed by orders of magnitude the time scales for vaporous cavitation. Diffusion can play a part in vaporous cavitation; a bubble nucleus which is too small to grow explosively may slowly grow because of diffusion of gas into the bubble until the radius increases to the critical radius given by Equation (4.48b) for the ambient pressure in question. Once having grown to the critical radius, it will explosively cavitate. Also, quite often some types of hydrodynamic cavitation, for example, sheets which are bound to the surface, leave a cloud of microbubbles that disappear downstream slowly because of the amount of gas captured in the collapsed bubbles. In this cavitation the maintenance of a steady sheet cavity provides a continuous liquid-gas interface across which vapor may continuously pass and downstream of which (the end of the cavity) the gas-vapor-filled bubbles may be continuously ejected.

Theoretical studies of diffusion in cavitation have dealt with four phenomena: a bubble in a quiescent liquid which is either supersaturated (so the bubble will grow) or undersaturated (so the bubble will dissolve),<sup>46,51</sup> a bubble that is fixed (as bonded to a surface) while being scrubbed by a moving liquid in which case it

---

\*An analysis by Guth<sup>50</sup> has indicated that large-amplitude nonlinear growth does not occur for negative relative pressures,  $A > 1$  when  $\omega > 1.6 \omega_0$ .

grows by "convective diffusion,"<sup>52,53</sup> a bubble in an otherwise quiescent liquid that is excited with an oscillating pressure (as for example generated by an acoustic transponder) in which case it grows by a process called "rectified diffusion,"<sup>44,47,54-60</sup> and finally a bubble that expands in a liquid as by vaporous cavitation during which a small quantity of gas is diffused into the bubble.<sup>61</sup> These processes all rely on the fact that gas will come out of solution whenever the partial pressure of gas in the bubble,  $P_g$ , is less than the equilibrium pressure of dissolved gas in the solution, i.e., whenever

$$P_g < P_{sat}$$

and by Henry's law the partial pressure of the gas in equilibrium with the dissolved gas concentration is

$$P_g = H\alpha$$

where  $H$  is Henry's law constant (at 25 C,  $H = 5.4 \times 10^7$  mm Hg/mole fraction for air and water) and  $\alpha_s$  is the mole fraction of dissolved gas.\* A condition for static equilibrium in which the bubble neither grows nor dissolves is

$$P_e - P_v = fP_{sat} - \frac{2S}{R} \quad (4.57)$$

where  $fP_{sat}$  replaces the partial pressure of gas in the bubble,  $P_g$ , and  $f$  is the percent of the saturation concentration  $\alpha/\alpha_s$ , or  $C/C_s$ , at the bubble wall represented by  $P_g$ , i.e.,  $P_g/P_{sat} = \alpha/\alpha_s = f$ . A liquid-gas solution may locally become either under- or oversaturated when the ambient pressure is either increased or decreased relative to the equilibrium (saturation) pressure.

Theory and computation by Epstein and Plesset<sup>51</sup> and van der Walle,<sup>46</sup> for the diffusion of gas into a small bubble in a quiescent liquid that is supersaturated with air at atmospheric pressure, show that the process is slow. For example, a bubble of  $10^{-3}$  cm in water which is 25 percent supersaturated ( $f=1.25$ ) takes 466

---

\*When the pressure of air above water is one atm,  $\alpha_s = 1.5 \times 10^{-5}$  mole/mole. This equilibrium, or saturation concentration on a volume basis is  $C = 0.019$  cm<sup>3</sup>/cm<sup>3</sup>.

seconds to grow to 10 times its initial radius. Conversely, in water that is only 50 percent of saturation ( $f=0.5$ ), a bubble of the same size should take 5 seconds to dissolve. The equation for the dissolving radius of a bubble in an undersaturated ( $f<1$ ) or oversaturated ( $f>1$ ) solution is

$$\frac{R}{R_0} = \left[ 1 + \left( \frac{2D_s c_s (f-1)}{\rho_g R_0^2} \right) \right]^{1/2} \cdot t \quad (4.58)$$

where  $c_s$  = equilibrium mass concentration of gas dissolved in the liquid at saturation (mass of dissolved gas per unit volume of liquid)

$D_s$  = diffusion coefficient ( $2 \times 10^{-5}$  cm<sup>2</sup>/sec)

$f$  = fraction of saturation, and

$\rho_g$  = density of gas in the bubble

For the supersaturated solution,  $f > 1$  and the bubble will grow. Conversely, a practical effect of diffusion is that bubbles in suspension in an undersaturated liquid ( $f<1$ ) will naturally dissolve. The implication of this theoretical observation is that cavitation nuclei can only be present in settled liquid if they are somehow stabilized. Speculations on the subject of nucleus stabilization are discussed in Section 4.2.4.2.

In the Epstein-Plesset theory, only the first term on the left hand side of the general dimensionless diffusion equation

$$\frac{\partial c}{\partial t'} + \frac{UR_0}{D_s} \cdot \{v' \cdot \nabla c\} = \nabla^2 c$$

is retained. In this equation the  $t'$  and gradient operators have been non-dimensionalized on the time scale  $R_0^2/D_s$ , where  $R_0$  is the initial radius of the bubble, and of the space scale  $R_0$ . The velocity  $v'$  is nondimensionalized on a liquid translation velocity  $U$ . Then  $U = 0$  only in a quiescent liquid or in one in which the bubble nucleus convects with the liquid. When liquid passes by a bubble with relative velocity  $U$ , the convective effects are important. When the

dimensionless number  $UR_0/D_s$ , called the Peclet number, is substantially larger than unity, then convective diffusion is important. Approximate solutions of the diffusion equation with  $\partial C/\partial t$  ignored in preference to the convection term have been provided by Parkin and Kermeen<sup>52</sup> and by van Wijngaarden.<sup>53</sup> The radius-time relationship for convective diffusion growth of a bubble in liquid of gas concentration  $c$  given by van Wijngaarden<sup>53</sup> may be approximated by the formula

$$\left(\frac{R}{R_0}\right)^{3/2} - 1 = t \frac{UR_0}{D_s} \frac{D_s C_s (f-1)}{\left(\frac{2}{3}\right)^{1/2} \pi \frac{1}{2} \rho_g R_0^2} \quad (4.59)$$

The ratio of times required for a bubble growth to the ratio  $R/R_0$  by means of convective diffusion, versus the time required to grow to the same size ratio by quiescent diffusion is given by Equations (4.58) and (4.59). This ratio is given by

$$\frac{t_{\text{convection}}}{t_{\text{no convection}}} = 1.7 \left(\frac{R_0}{R}\right)^{1/2} \left(\frac{D_s}{UR_0}\right)^{+1/2}$$

it decreases with an increase in velocity, and it increases as the radius increases. For bubble radii  $R_0$  on the order of  $10^{-4}$  cm in water and  $R = 10R_0$  with  $U = 10$  m/sec, this ratio of times is only 0.0076. By Equation (4.58) 36 seconds are required for a bubble to grow from  $10^{-4}$  cm to  $10^{-3}$  cm; by convective diffusion this time would be reduced to only 0.27 sec. This reduction in time is sufficient to make convective diffusion important in hydrodynamic problems.

Bubbles will also come out of solution under the influence of an applied pressure oscillation (as applied by an underwater transducer) when the liquid phase contains dissolved air in either saturated or undersaturated concentrations by a process of rectified diffusion. Hsieh and Plesset<sup>54</sup> and Eller and Flynn<sup>55</sup> and Eller<sup>59</sup> have provided theoretical analyses of this process. The times that are required for significant bubble growth are much longer (minutes) than those required by convective diffusion so that this mechanism of growth is less important in hydroacoustics than in ultrasonics. In undersaturated solutions, where bubbles have a natural tendency to dissolve when undisturbed, the amplitude of pressure

fluctuation must exceed some threshold value which depends on the dissolved gas content and the frequency. Threshold pressure fluctuation amplitudes that are required for the onset of rectified diffusion have been measured by Strasberg,<sup>47,56,57</sup> with calculations given by Strasberg<sup>57</sup> based on the diffusion theory of Hsieh and Plesset which give excellent agreement with measurement. Earlier calculations by Blake<sup>44</sup> and by Pode<sup>58</sup> are based on a more approximate theory than Hsieh and Plesset's and underestimate the diffusion threshold pressure by a factor of 10. Reviews of the subject have been given by Flynn<sup>2</sup> and by Beyer.<sup>6</sup> Rates of bubble growth calculated from the theory of static diffusion seem to underestimate observed rates. Here exact theory which includes self-induced convective effects (called acoustic streaming) seems to account for the observed greater rates.<sup>59,60</sup>

In general, as the size of the bubble radius decreases below  $10^{-4}$  cm, the tensile strength in the liquid at room temperature increases, so that vaporous cavitation can occur only at very low pressures, unless the liquid has a large population of stabilized hydrophobic solids. In settled water which may have a large content of dissolved gas, but still a population of bubble nuclei which are smaller than  $10^{-4}$  cm bubbles, microbubbles can be made larger by diffusion. Such growth occurs for a time until bubble radii are large enough that vaporous cavitation can occur. This sequence of events was suggested by Strasberg<sup>47</sup> as an explanation of the part which could be played by diffusion in the cavitation process. The bubble of radius  $R_1$  may be subjected to a local pressure which is greater than the critical pressure  $P_c$  that is required for vaporous cavitation. The bubble will then grow from  $R_1$  to  $R_c$  (Equation (4.48b)) in a time which is dependent upon the degree of local saturation of gas in the liquid and the type of diffusion (static, convective, rectified) that takes place. As the bubbles enter the rarified region of a lifting surface the local degree of saturation may be relatively high and the time required for moderate growth by diffusion may be shorter than the hydrodynamic time scales of the flow. With such growth, the larger bubbles may be readied for vaporous cavitation as they are convected further into rarefaction zones that are below the critical pressure. This behavior is more likely on large bodies than small.

Gas can also be diffused into bubbles undergoing vaporous cavitation in liquids with high content dissolved gas. Relationships for estimating the mass of gas diffused into nonlinearly expanding cavities in vaporous-type cavitation have been derived by Boguslavskii.<sup>61</sup> The mass introduced into the bubble expanding for a time  $t$  under a rarefaction  $P_v - P$  is

$$m \approx \frac{16}{15} (5\pi)^{1/2} \left( \frac{P_v - P}{\rho_o} \right) D_s^{1/2} C_g t^{5/2} + 1.9\pi \left( \frac{2}{3} \frac{(P_v - P)}{\rho_o} \right)^{1/2} D_s C_g t^2$$

where  $C_g$  is the concentration of dissolved gas in the liquid (mass/volume) and  $D_s$  is the diffusion coefficient. Using Equation (4.53), the first and dominant term reverts to

$$m = \frac{8}{5} (5\pi)^{1/2} t^{1/2} D_s^{1/2} C_g R_m^2$$

where  $t$  is the length of time that the bubble resides in the rarefaction region. To find the partial pressure of the gas in the expanded bubble, the ideal gas law gives

$$p_g = \frac{m}{\text{M.W.}} \frac{RT_e}{\frac{4}{3} R_M}$$

where  $T_e$  is the absolute temperature and M.W. is the molecular weight of the gas. The partial pressure of the gas diffused into the bubble during its expansion is then

$$\frac{p_g}{p_{STD}} = \frac{6}{(5\pi)^{1/2}} \frac{(tD)^{1/2}}{R_M} C_s f \quad (4.60)$$

where  $C_s$  is the equilibrium volume concentration of dissolved gas at the standard pressure  $p_{STD}$ .

## 4.2.4 Effects of Gas Content and Nuclei Distribution

4.2.4.1 Cavitation Thresholds in Real Fluids, Influence of Gas Content. A useful, yet somewhat artificial, distinction to be made regarding the experimental evaluation of cavitation thresholds is between measurements made ultrasonically in still water and hydroacoustically in moving water. Physically, of course, there should be

no real distinction, for the dynamical equations for the bubbles are common to both measurement types. The distinction lies in the circumstances which determine the mode of bubble excitation and, therefore, the mode of measurement. Ultrasonic measurements in still water (reviewed in some detail by Flynn<sup>2</sup> and Knapp, Daily, and Hammitt)<sup>4</sup> generally are conducted with liquids in which only the smallest bubbles will remain after standing.<sup>62</sup> These bubbles, being small, will permit the water to have a rather high tensile strength. In contrast, during hydroacoustic measurements, tests are conducted in moving water passing over a body,<sup>62</sup> a venturi tube,<sup>61</sup> or an optical viewing region. In these facilities there may be a greater concentration of available nucleation sites due to continual agitation and possible replenishment from the water supply. Furthermore, hydrodynamic thresholds are very much dependent on the hydrodynamic specifics of the noncavitating flow as will be discussed in Section 4.3.

An example of one of the early measurements of cavitation thresholds in a moving liquid was made by Crump<sup>63</sup> with natural sea and fresh water, the results of which are shown in Figure 4.10. The thresholds were determined by lowering the pressure in the throat of a venturi and observing visually the initial occurrence of cavitation on the wall as water was drawn from either a water tunnel or the sea. When the total gas content (expressed as a fraction of the value at saturation) increases, the critical pressure increases to approximately the vapor pressure as shown by the bands in the figure. For comparison, horizontal lines denote expected critical pressures to be expected from the vaporous cavitation of bubbles with selected radii. The curved dotted line and the point from Strasberg apply to rectified diffusion and they are included to contrast the results for vaporous cavitation. A general increase in the threshold  $P_c - P_v$  is shown as the gas content (free plus dissolved) was increased; furthermore, the threshold pressures for cavitation in sea water were observed to be somewhat larger than those observed in the laboratory at the corresponding gas content. In the laboratory, however, the water could have been degassed somewhat while the seawater could not be similarly processed thus admitting the possibility of some larger bubbles being present to provide sites of gaseous cavitation. It is now appreciated that certain particulate matter as well as small bubbles can serve as nucleation sites for cavitation.



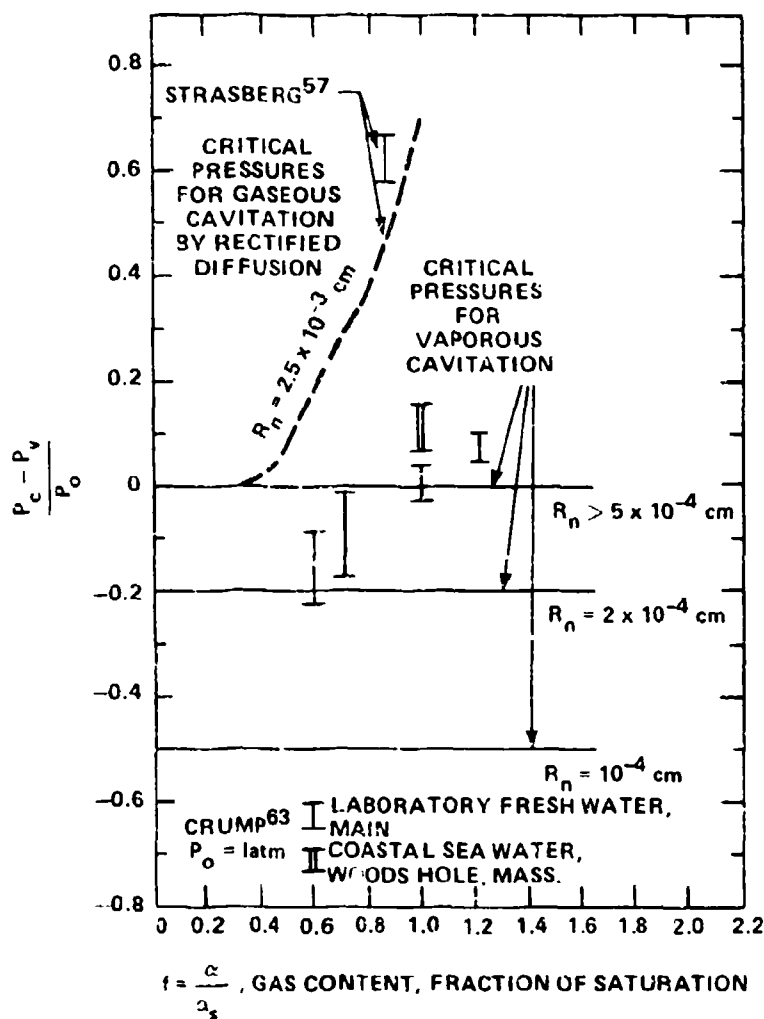


Figure 4.10 - Measured Thresholds for Vaporous and Gaseous Cavitation as a Function of Total Gas Content

The most widely used device for measuring total gas content is the van Slyke blood gas apparatus. This instrument measures the total volume of gas extracted from a volume of liquid. The gas content is then reported as the volume of gas dissolved (as well as suspended as undissolved microbubbles) in the sample.

4.2.4.2 Stabilized Cavitation Nuclei. Modern theories of nucleation have been reviewed extensively by Flynn,<sup>2</sup> Knapp, Daily, and Hammitt,<sup>4</sup> and Pernik,<sup>7</sup> therefore, a comprehensive review of these theories will not be given.

In addition to nucleation sites provided by suspended microbubbles, other nucleus-types are hypothesized to exist. One type, suggested by Fox and Herzfeld,<sup>64</sup> consists of a microbubble whose interface is stabilized by an organic skin. This type was suspected to remain in the liquid for some time after settling, thus accounting for the stabilization of cavitation thresholds with time following the preparation of a water sample. The idea, however, was later criticized by Herzfeld<sup>65</sup> who speculated that these nuclei should dissolve when the static pressure is increased beyond some limit thus crushing the skin. The measurements by Strasberg<sup>47</sup> indicated, however, a continued increase in tensile strength with increased pressurization. Recently, renewed interest in the existence of stabilization by surface films has been shown by van der Meulen.<sup>66</sup>

The second type of nucleation site consists of solid particles or of pores in the surfaces of bodies which are not completely wetted (called hydrophobic particles) and, therefore, contain amounts of trapped air. The importance of these nuclei was postulated originally by Harvey<sup>67,68</sup> and they have been given closer attention by Strasberg<sup>56</sup> and more recently by Apfel<sup>69</sup> and Yilmaz, Hammitt, and Keller.<sup>70</sup> The suggested importance of particulate matter followed the experimental observation that the critical pressures of degassed water never reached the values comparable with the expected tensile strength of water. In the case of Galloway's (ultrasonic) experiment,<sup>71</sup> for example, the expected reduction of cavitation threshold with a decrease in gas content occurred only until the liquid was 5 percent saturated. For further degassing, the threshold pressure did not become more negative. Furthermore, there was observed a dependence of an ultrasonic threshold on static pressure history by Strasberg<sup>47</sup> as earlier by Harvey et al.<sup>67</sup> The threshold became more negative as the static pressure was increased and then reduced to its original value. Finally, the addition of wetting agents has been observed to increase the ultrasonic cavitation threshold markedly. An extensive review article on the subjects of surface films and wetting has been prepared by Bernd.<sup>72</sup> This behavior, i.e., a relative independence of cavitation threshold on aging at rest and a modest dependence on history of the static pressure, is not as clearly documented in the hydrodynamics literature.

Theoretically, the solid particles may act as nuclei because of trapped gas in the pores which is not accessible for solution, but remains available as a cavitation site. Apfel<sup>69</sup> has examined interfacial stability of such trapped gas using the idealized models illustrated in Figure 4.11. In case (a) the wetting angle  $\alpha_a$  is

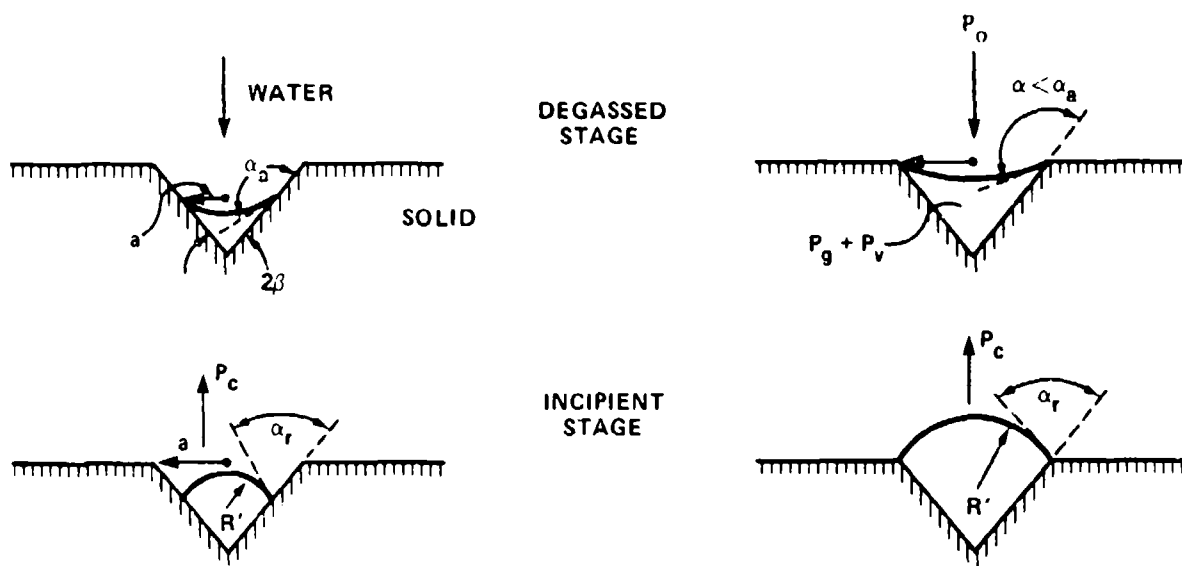


Figure 4.11a - Large Crevice

Figure 4.11b - Small Crevice

Figure 4.11 - Nucleation from Gas Trapped in a Crevice, Showing Interfacial Geometries in Crevices Larger and Smaller Than a Critical Value

such that the interface is deep enough in the well so that when placed under tension  $P_c$ , the arc remains inside. In this case the radius of curvature of the bubble segment is not dependent on the size of the well, but rather on the surface chemistry of the liquid-solid-gas system. Alternatively, in case (b), the well is small enough so that the size of the bubble in tension is controlled by the radius of the opening  $a_0$ , before the bubble breaks away. The condition for equilibrium derived by Apfel is of the form

$$P_c = P_0 + P_v - \frac{2S}{R'}$$

where  $R'$  is the radius of curvature of the convex bubble. The factor  $\gamma_0 \leq 1$  (not the adiabatic constant) accounts for the fact that when the cavitating pressure is pulsating, the gas pressure in the bubble cannot reach the equilibrium pressure if diffusion of gas into the bubble lags the bubble growth. For static equilibrium  $\gamma_0 = 1$ . The distinction between large and small crevices lies in the position of the interface. A critical size of the crevice that distinguishes demarking between "large" and "small" wells is one in which the equilibrium position in the degassed state is at the corner with a wetting angle  $\alpha_a$ . In illustration (a), as the size of the bubble increases, moving the interface outward,  $\alpha_a$  remains constant until the corner is reached. With further increase in the size of the bubble, the interface remains engaged with the corner, as in (b), but the contact angle  $\alpha$  becomes less than  $\alpha_a$  because the opening of the crevice will not permit further rise of the interface level. In the large crevice,  $R'$  is a function of both the geometry of the crevice and the surface tension, while in the case of small crevices  $R'$  is proportional to the radius of the crevice  $a$ . The condition for equilibrium then becomes

$$P_c = -AP_o + (A+\gamma_0) P_s + P_v \quad (\text{large crevice}) \quad (4.61)$$

where  $A$  depends on the angles  $\alpha_r$ ,  $\alpha_a$ , and the included angle of the opening  $2\beta$ , and

$$P_c = -P_o + \gamma_0 P_s + P_v - \frac{2S}{R'} \quad (\text{small crevice}) \quad (4.62)$$

where  $R'$  is proportional to  $a$ , to perhaps one-fifth of the actual radius of the nucleus. The distinction between the crevice sizes leads to rather different dependence of the critical pressure on the gas content ( $P_s$ ). The threshold of large crevices is controlled by  $A$  (which can be<sup>70</sup> as large as four or five) and it depends upon surface tension only indirectly whereas for small crevices  $P_c$  will be dominated by the surface tension pressure. Keeping in mind the possibility<sup>69,70</sup> that  $R' \sim a_o \sim 1/5 \times$  nucleus radius, the surface tension term could involve microscale radii so that the tension of water containing suspended particles could be rather large.

4.2.4.3 Measurements of Nucleus Distributions. The preceeding discussions have shown the importance of establishing the sizes of available cavitation nuclei in determining cavitation thresholds above and beyond the necessity of quantifying gas content. In recent years various direct and indirect methods have been developed to determine what range of nucleus radii exists in water from various sources. Morgan<sup>73</sup> has reviewed the various methods of assessing air contents and nuclei distributions with regard to instrumentation and tolerances. Before examining the specific methods we will consider the representations used in reporting nucleus distributions.

The total population of nuclei is regarded as a random variable which is distributed over a range of radii. As in Section 4.2.2 let  $n(R)$  be the number of nuclei per unit volume of liquid per unit radius so that the total number  $N$  of nuclei (bubbles, particles, etc.) is

$$N = \int_0^{\infty} n(R) dR \quad (4.63)$$

We further define the number of particles in the size range  $\Delta R$  with an average radius  $R$  as

$$N(R, \Delta R) \approx n(R) \Delta R \quad (4.64)$$

This variable has been reported by Strasberg,<sup>47</sup> Medwin,<sup>74,75</sup> Peterson,<sup>76,77</sup> Gates and Acosta,<sup>78</sup> Keller,<sup>79</sup> and Arndt and Keller.<sup>80</sup> It has been indirectly deduced from cavitation threshold pressures by Messino, Sette, and Wanderligh,<sup>71</sup> and by Ill'n, Levkovskii, and Chalov.<sup>81</sup> The probability of finding a nucleus of radius  $R$  in the size range  $\Delta R$  is then

$$P_N(R, \Delta R) = \frac{n(R)}{N} \Delta R \quad (4.65)$$

The probability has been reported by Schiebe.<sup>82,83</sup>

Figure 4.12 modified from Gates and Acosta,<sup>76</sup> summarizes the observed values of  $n(R)$  from a number of sources. Generally there is a quantitative increase in

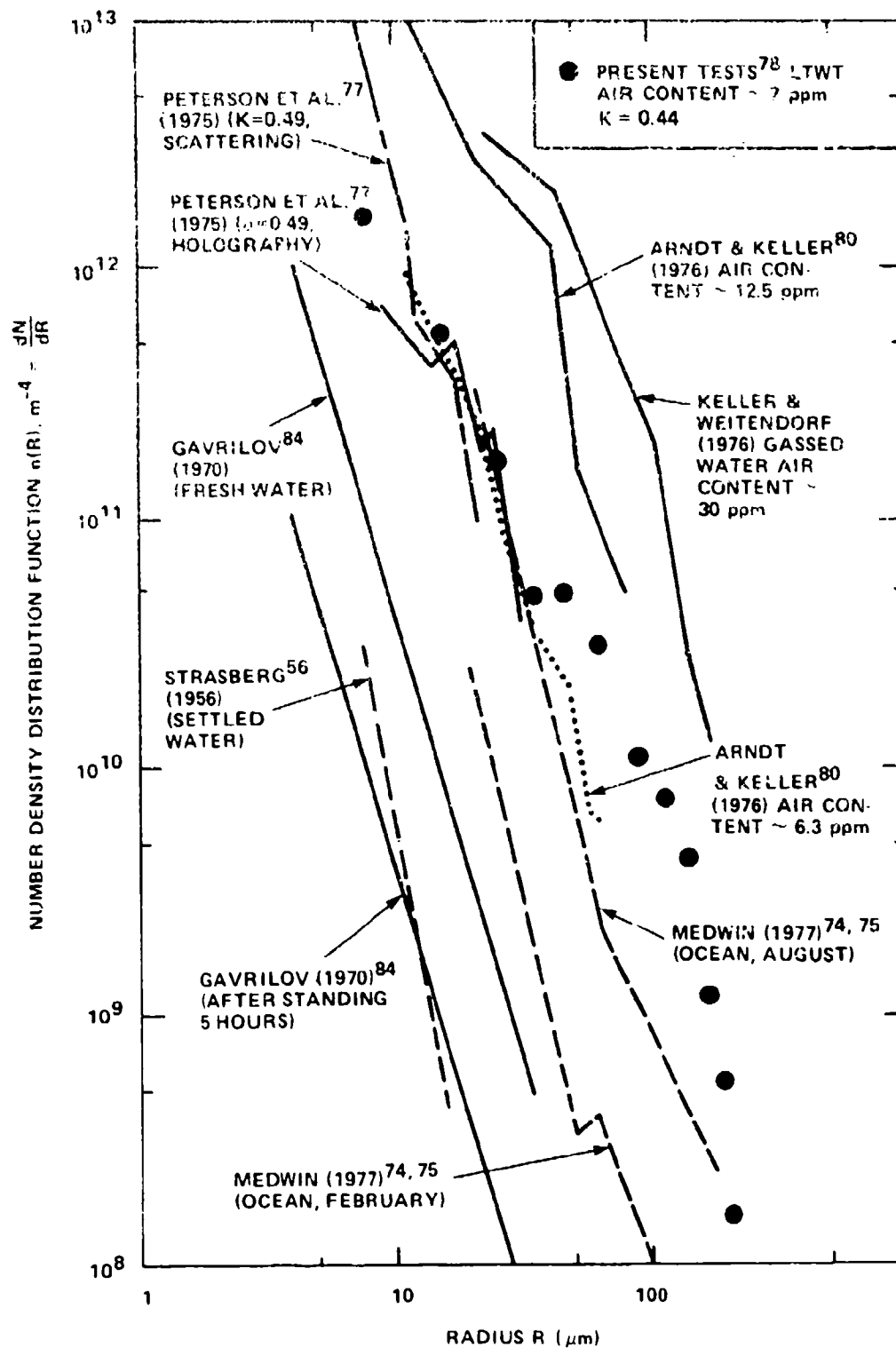


Figure 4.12 - Nuclei Distributions from Various Sources (Compiled by Gates<sup>80</sup>)

$n(r)$  with an increase in the total air content. For example, the water left standing by Saville and by Strasberg should have been relatively degassed, while super-saturated and saturated water (Arndt and Keller and Keller and Weitendorf) probably had large nucleus distributions. The slope of  $n(R)$  with  $R$  is remarkably similar for all sources. Measurements by Yilmaz, Hammitt, and Keller<sup>70</sup> have measured contaminant distributions by the light-scattering method. A dependence of the contaminant distributions in tap water as a function of settling time is shown in Figure 4.13. Other variables included gas content and the use of degassing by heating.

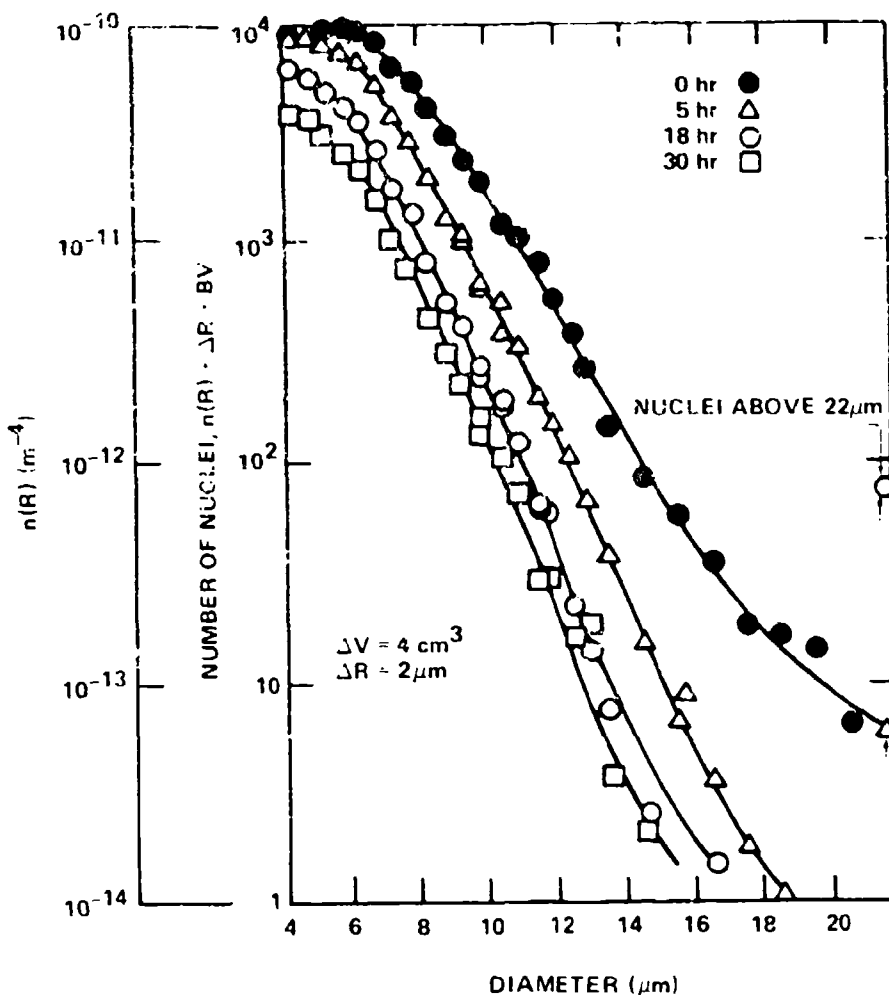


Figure 4.13 - Effect of Waiting Time on Nucleus Spectrum of Tap Water.<sup>41</sup>  
Measured by Light-Scattering Method.  
(From Yilmaz<sup>70</sup>)

In addition to using the distribution function  $n(R)$  in some cavitation noise modeling (see Section 4.3), it has been used also in analytical descriptions of the dynamics of bubble clouds under the influence of ultrasonic agitation.<sup>85-87</sup>

There are fundamentally three means of evaluating the number distribution of nuclei.

4.2.4.3.1 Event Counting. One means of assessing nucleus concentrations is to determine cavitation thresholds directly by applying gradually reduced pressures to a sample of water and noting the number of cavitation events that occur. As the test-section pressure is reduced, the initial event is caused by the largest nucleus,  $R_m$ , for example, cavitated by a threshold pressure  $P_t$ . As  $P$  is reduced below  $P_t$ , the number of cavitation events will be increased as nuclei smaller than  $R_m$  become destabilized. In this way one can quantify the number of events  $N(p)$  which occur at a pressure  $p$  less than  $P_t$ . The method first was used by Messino, Sette, and Wanderligh<sup>71</sup> using an ultrasonic source in quiescent distilled water. Subsequently, the method was adopted by Ill'in, Levkovskii, and Chalov,<sup>81</sup> and Crump<sup>63</sup> (Figure 4.10), however, they used a venturi to generate the low pressure, the water being tap water supplied from a settling tank. Using the relationship between the critical radius and critical pressure (Equation (4.48b) with  $\gamma=1$ ), they then deduced the radius distribution, between  $10^{-7}$  and  $10^{-4}$  m, that accounted for the observed variation of  $N(P)$ . Although the method directly determines pressure thresholds for cavitation sites, it only indirectly relates the pressure information to nucleus size distribution. It gives no information about the physical nature of the cavitation sites, whether they are free bubbles or hydrophobic particulate matter. Brockett<sup>88</sup> has also used event counting to set a criterion for incipient hydrodynamic cavitation.

4.2.4.3.2 Acoustic Absorption of Resonant Gas Bubbles. This method uses the theory of linear bubble motions, Section 4.2.2, to relate the absorption of acoustic tone bursts to bubble population. A fairly comprehensive review of this technique has been given by Gavrilov.<sup>84</sup> The first use of the method was by Strasberg<sup>47</sup> who related the absorption of noise (in the frequency range 15- to 550-kHz) in a reverberant chamber to the volumetric concentration of bubbles using the second of the absorption equations in Table 4.1. He reported volumetric concentrations (STP) on the



order of  $10^{-10}$  with the bubble range  $0.6 \times 10^{-3}$  cm to  $2.4 \times 10^{-3}$  cm. Equation (4.20) was used to determine the resonance frequencies of the bubble radii. Absorption techniques were later used by the St. Anthony Falls group<sup>82,83</sup> in their water-tunnel facility. They used the imaginary part of the full Equation (4.37) to relate absorption in a narrow frequency band (with frequencies in the range 10 to 60 kHz) to the bubble population. The method amounts to the use of the first of the absorption relations in Table 4.1. Bubble diameters from  $10^{-5}$  m to  $10^{-4}$  m were detected in this manner in volumetric concentrations greater than  $3 \times 10^{-8}$ . The numerical results were then reduced to form a probability distribution function  $p_r(r, \Delta r)$  which gave the fraction of bubbles of radius  $r$  in a size range  $\Delta r$ . The distribution roughly followed a Rayleigh distribution with a mean radius of about  $2 \times 10^{-5}$  m. Their program also included measurements of hydrodynamic cavitation in which the cavitation appeared as a sequence of identifiable bubbles traveling through the minimum pressure point of the nose of a body of revolution. Moderately good agreement was found between the observed rate of cavitation events, and the rate that was predicted from the measured bubble distributions and Equation (4.50) for the critical pressure. Schiebe and Killen<sup>83</sup> conclude, however, that their method was too insensitive to detect commonly-occurring bubble distributions ( $\beta < 3 \times 10^{-8}$ ) in water-tunnel facilities, furthermore, they report difficulty in resolving bubble sizes. Recently, however, Medwin,<sup>74,75</sup> with improved apparatus, used the measured acoustic absorption Equation (4.44) at sea to determine the seasonal variations and depth dependence bubble distributions in coastal waters. Essentially he used absorption formulas in Table 4.1 with  $\eta = 0.1$ ; the method gives concentrations as low as  $\beta \sim 10^{-11}$  and bubble radii as small as 20  $\mu$ m.

The use of acoustic absorption (it is also possible to measure the reduction of sound speed in bubbly mixtures) to deduce nucleus populations is direct because it defines the radii of the available bubbles and gas filled interstices. Regarding the latter it probably does not give reliable measurements of the sizes of hydrophobic particulate nuclei since the resonance frequencies of those bubbles may not necessarily follow the exact form of Equation (4.20). The method has the distinct advantage of requiring only a modest instrumentation complexity.

4.2.4.3.3 Optical Measurements. This technique has recently become popular and acceptable as the laser optics technology has been developed. The methods use both holography, which permits a discrimination between solid particulate matter and bubbles, and light scattering (which does not permit such discrimination). Optical holography has been used by Peterson<sup>76,77</sup> and by Gates and Acosta,<sup>78</sup> while light scattering has been used by Yilmaz, Hammitt, and Keller,<sup>70</sup> Keller,<sup>79</sup> and Arndt and Keller.<sup>80</sup> This technique gives an accurate distribution of foreign matter in liquids from which cavitation thresholds could be deduced. However, Peterson<sup>76</sup> has published the only simultaneous observations of nuclei and cavitation inception, but correspondences between observed light scatterers and cavitation have yet to be made. Indeed there appears to be a contrasting view which discounts particulate matter as being of only occasional importance in favor of suspended microbubbles as primary hydrodynamic nucleation sites.

## 4.2.5 The Collapse of Cavitation Bubbles

4.2.5.1 Spherical Bubbles. The time histories of bubble radii shown in Figure 4.7 show that when nonlinear bubble growth occurs (dashed line), a second of stage motion, the collapse, occurs when the rarefaction is replaced by compression. This latter stage is of short duration. Because the wall acceleration is large during collapse, it is reasonable to conclude (and it is indeed so) that the collapsing motion will contribute heavily to sound production. Therefore, we shall examine this aspect of the dynamics closely to establish what the important controlling variables are at various frequency ranges in the cavitation-noise spectrum. We shall see that at the termination of the collapse phase, the motion will be influenced by the presence of any gas in the bubble and the properties of that gas. This gas becomes important when the radius of the bubble becomes very small because the compressed gas fills the bubble. Also, the compressibility of the liquid (or two phase fluid) surrounding the bubble will become important if the wall velocity of the bubble wall becomes comparable to the speed of sound in that fluid.

The dynamics of collapse was first examined by Besant in 1859,<sup>89</sup> but the first theoretical treatment of the problem, upon which much modern thinking is fundamentally based, is due to Rayleigh.<sup>13</sup> The pressure inside the bubble was considered to be constant, therefore, Rayleigh's problem would apply to the physical circumstances of vapor-filled bubbles only. The pressure difference in Equation (4.12),

neglecting the surface tension pressure, is  $P_v - P(r)$  where now  $P(r)$  is supposed to be much larger than the vapor pressure so that the bubble will collapse. Rewriting the left-hand side of Equation (4.12), we find, equivalently

$$\frac{1}{2\dot{R} R^2} \frac{d}{dt} (R^3 \dot{R}^2) = \frac{P_v - P(r)}{\rho_o} \quad (4.66)$$

which may be rearranged to

$$\frac{d}{dt} (R^3 \dot{R}^2) = [P_v - P(r)] \frac{d}{dt} \left( \frac{2}{3} R^3 \right) \quad (4.67)$$

under the assumption that  $P_v - P(r)$  is invariant over the time scale of collapse. Further, assume the initial condition

$$\dot{R} = 0 \text{ and } R = R_M \text{ at } t = 0$$

to find

$$(\dot{R})^2 = \frac{2}{3} \frac{\Delta P}{\rho_o} \left[ 1 - \frac{R_M^3}{R^3} \right] \quad (4.68)$$

where  $\Delta P = P_v - P(r)$ , is the wall velocity of the bubble. Note that as the bubble radius becomes small, in Equation (4.68) the magnitude of  $\dot{R}$  will become infinite. The velocity, however, becomes limited by the compression of any small amount of gas trapped in the collapsing cavity, the presence of which was ignored in this simple analysis.

Even though the wall velocity becomes infinite in the Rayleigh model of constant pressure difference, the time it takes for the bubble to collapse can be determined. The reciprocal of Equation (4.68) gives the radius-time relationship

$$t = \left( \frac{3\rho_o}{2(-\Delta P)} \right)^{1/2} \int_R^{R_M} \frac{R^{3/2} dR}{(R_M^3 - R^3)^{1/2}} \quad (4.69)$$

which is integrated over the interval  $0 \leq R \leq R_M$  giving the time for complete collapse as

$$t_c = 0.915 R_M \left( \frac{\rho_o}{P(r) - P_v} \right)^{1/2} \quad (4.70)$$

In spite of its simplicity, Rayleigh's equation gives an excellent representation of the gross characteristics of single bubble cavitation dynamics. Plesset<sup>14</sup> has measured the cavitation characteristics at the nose of a body of revolution in a high-speed water tunnel. Using high-speed motion pictures (more than 20 thousand frames per second) he was able to trace the trajectory of a cavitation bubble as it passed through the region of minimum pressure on the body. Figure 4.14 shows representative bubble histories together with the matching local hydrodynamic pressure. The solid lines represent the bubble history computed from the simple Equation (4.66). To do this,  $P(r)$  is considered to be the local hydrodynamic pressure in the reference frame of the bubble. Thus, if  $P_h(s)$  is the local pressure on the body where  $s$  denotes distance from the leading edge stagnation point, and the bubble was convected at a speed  $U_c$ , then

$$P(r, t) = P_h(U_c t)$$

A similar investigation had been conducted earlier by Knapp and Hollander,<sup>90</sup> who measured five rebounds of the bubble following the initial collapse, as illustrated in Figure 4.15. Alternate rebounds are shown above and below the datum. The multiple rebounds are suspected to be strongly influenced by the stored energy in the bubble as a result of the compression of gas in the collapse phases. The collapse radius versus time was well approximated by the Rayleigh bubble equation which can be seen in the figure.

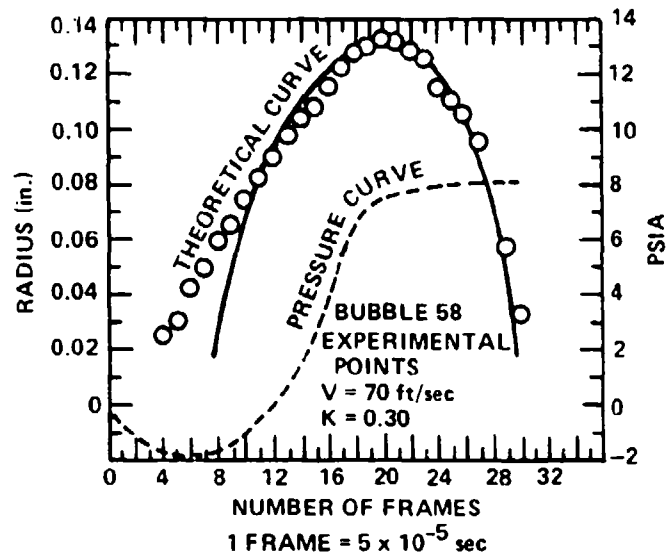


Fig .14a =  $K_1 = 0.30$ ,  $U_\infty = 70$  Feet per Second

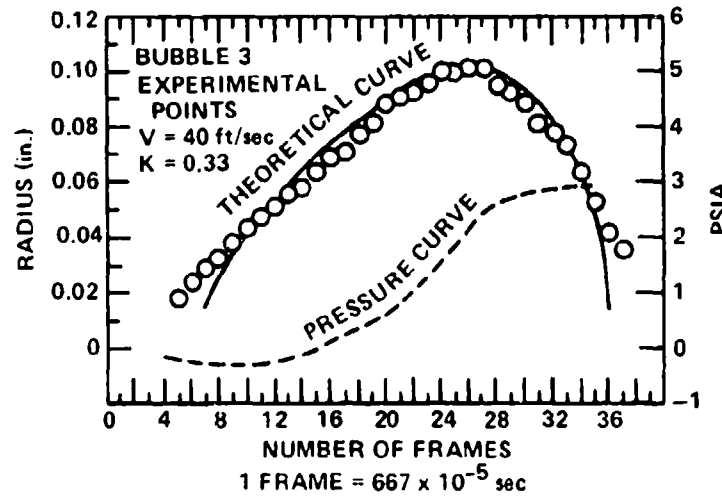


Figure 4.14b =  $K_1 = 0.33$ ,  $U_\infty = 70$  Feet per Second

Figure 4.14 - Measured and Theoretical Bubble Histories for the Indicated Pressure Distributions on a Headform  
(From Plesset<sup>14</sup>)

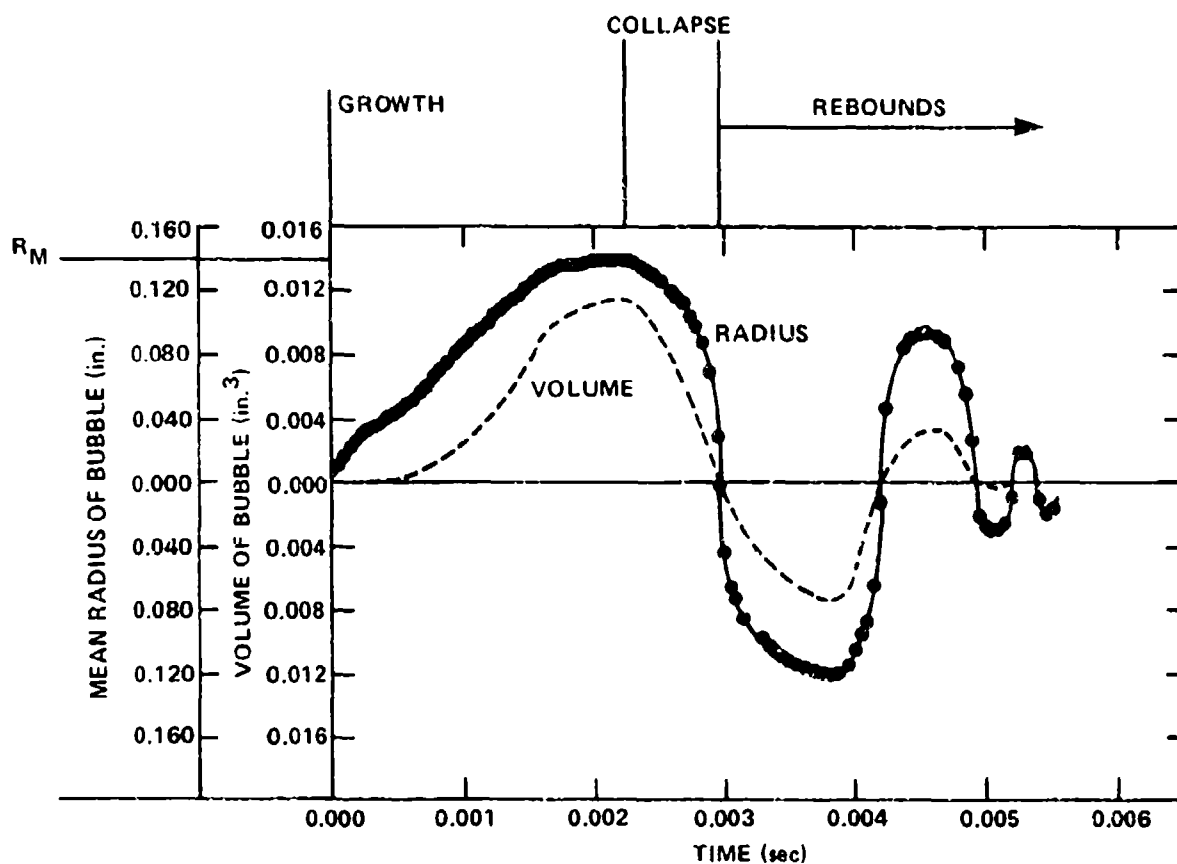


Figure 4.15 - Observed Radius History for a Cavitation Bubble on a 1.5 Caliber Ogive Nose

(Note rapid collapse compared to slower growth, the multiple rebounds due to compressible gas in the bubble. Also shown is the corresponding volume history; from Knapp and Hollander.<sup>90</sup>)

Rayleigh determined that associated with the large values of  $\dot{R}$  in the final collapse, the induced pressures in the adjacent liquid at a distance from the center of the bubble of about  $1.59R$  could match the compressibility of the liquid itself. Furthermore, he considered the possible limiting effects of the entrained gas using a calculation of the compression work on the gas; by considering, i.e., that the change in potential energy from the initiation of collapse to radius  $R$  is converted into the total kinetic energy of the entrained water plus the work done in compressing the gas in the bubble. Accordingly, he found that a limiting radius did exist for which the velocity of the bubble wall could be retarded to  $\dot{R} = 0$ .

Subsequent refinements of the theory have accounted for the compressibility of the liquid<sup>91-102</sup> to various degrees of approximation; these efforts have been surveyed elsewhere.<sup>4,6,7</sup> The most complete calculations of bubble collapse and rebound for cases involving gas-filled and empty bubbles in compressible and incompressible liquids are probably those of Hickling,<sup>99-100</sup> samples of which are shown in Figures 4.16 and 4.17. The effect of compressibility is to reduce the wall

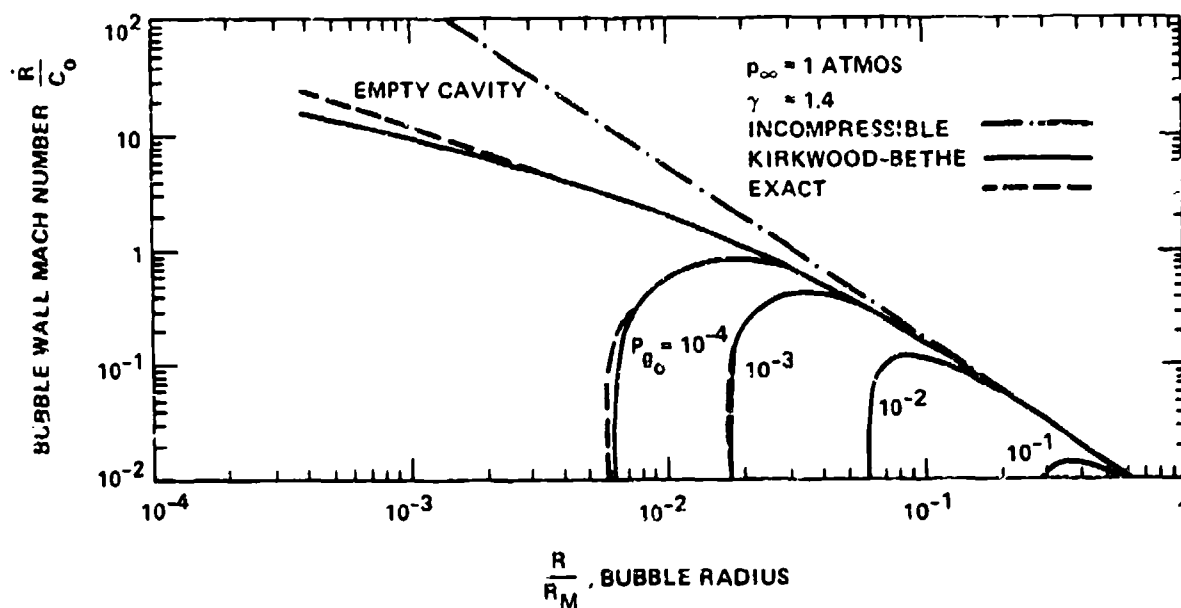


Figure 4.16 - The Bubble Wall Mach Number as a Function of the Bubble Radius for Decreasing Gas Content

(The gas content is determined by its initial pressure  $P_{g0}$  in atmospheres. The index  $\gamma$  has the value 1.4 and the ambient pressure  $P_{\infty} = P(r)$  is one atmosphere. From Hickling and Plesset.<sup>99</sup>)

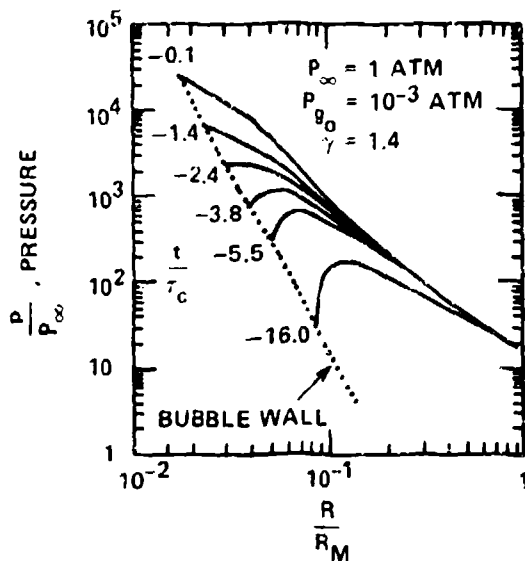


Figure 4.17a - Collapse

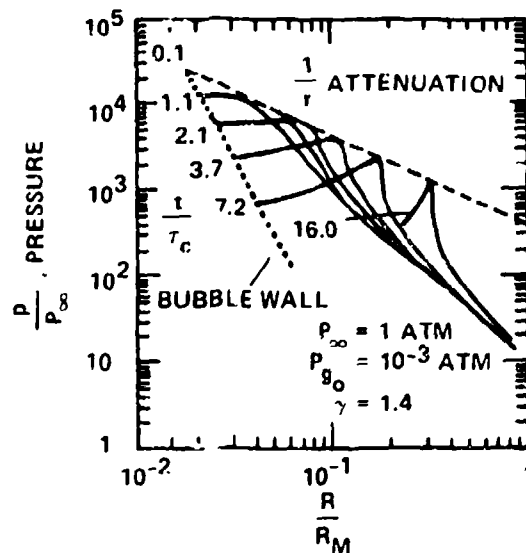


Figure 4.17b - Rebound

Figure 4.17 - Computed Pressure Histories for Gas and Vapor Bubbles in Compressible Water ( $P_\infty = P(r)$ )

(Time  $t$  is measured from the instant of collapse  $\dot{R}=0$ ; the time scale  $\tau_c$  is the collapse time, the pressures are relative to the hydrostatic pressure. From Hickling and Plesset.<sup>99</sup>)



Mach number, but all empty bubbles, i.e., those for which the internal pressure is constant, have unlimited  $\dot{R}$  at zero radius. The introduction of gas, even in small quantities, limits the collapse and the thermodynamic characteristic of the gas and influences the final limiting radius more than does the hydrostatic pressure. In Figure 4.17 is shown, in sequence, the radial variation of pressures at various instants shortly before and after collapse. The positive values denote times after the minimum radius occurs. In the collapse phase, maximum pressures occur at a distance  $r \sim R$  from the bubble wall, in the rebound phase, a compression wave develops and propagates outward with  $1/r$  attenuation.

The effect of gas in bubbles collapsing in an incompressible liquid was first determined by Neppiras and Noltingk<sup>15</sup> whose result can be derived by modifying Equation (4.66) to include adiabatic gas behavior of the type in Equation (4.46)

$$\frac{d}{dt} (R^3 \dot{R}^2) = [P_v - P(r)] \frac{d}{dt} \left( \frac{2}{3} R^3 \right) + \frac{P_{g_0}}{2\pi} \left( \frac{V_0}{V} \right)^\gamma \frac{dV}{dt}$$

where the radius function on the right has been replaced by the bubble volume to simplify notation. Now since

$$V^{-\gamma} \frac{dV}{dt} = \frac{d}{dt} \left\{ \frac{V^{-\gamma+1}}{-\gamma+1} \right\}$$

and introducing the initial conditions as before, we find for the wall velocity

$$(\dot{R})^2 = \left( \frac{2}{3} \right) \left( \frac{P(r) - P_v}{\rho_0} \right) \left\{ \left[ \left( \frac{R_M}{R} \right)^3 - 1 \right] + \frac{P_{g_0} \left( \frac{R_M}{R} \right)^3}{(P(r) - P_v) (\gamma - 1)} \left[ 1 - \left( \frac{R_M}{R} \right)^{3(\gamma-1)} \right] \right\} \quad (4.71)$$

Equation (4.71) has also been derived by Guth,<sup>103</sup> and used in this form by Khoroshev<sup>104</sup> to calculate the limiting minimum radius  $R_m/R_M$ , which is determined by the condition  $\dot{R} = 0$ . In the limit as  $R_m/R_M$  also approaches zero, Equation (4.71) reduces to the asymptotic result for the minimum radius in an incompressible liquid,

$$\frac{R_m}{R_M} \sim \left[ \frac{1}{\gamma-1} \frac{P_{g_0}}{P(r)} \right]^{1/3(\gamma-1)} \quad (4.72)$$

Finally, in the contrasting limit of isothermal gas compression,  $\gamma = 1$ , the equivalent form of Equation (4.71) is identical to that of Rayleigh

$$(\dot{R})^2 \sim \left( \frac{2}{3} \right) \frac{(P(r)-P_v)}{\rho_0} \left\{ \left[ \left( \frac{R_M}{R} \right)^3 - 1 \right] - \frac{3P_{g_0}}{P(r)-P_v} \left[ \left( \frac{R_M}{R} \right)^3 \ln \left( \frac{R_M}{R} \right) \right] \right\} \quad (4.73)$$

The minimum radius corresponding to  $\dot{R} = 0$  is, for small  $R_m/R_M$ ,

$$\frac{R_m}{R_M} \sim \exp \left[ -(P(r)-P_v)/3P_{g_0} \right] \quad (4.74)$$

Figure 4.18 summarizes the variation of the minimum radius with the gas pressure  $P_{g_0}$ , using these equations as well as the general trends given by Hickling's analysis. Pairs of curves (1 and 2) and (3 and 4) from Figure 4.18 illustrate the difference between the assumption of incompressible and compressible fluids for either the adiabatic or the isothermal gas compressions. The asymptotic dependence shown by curve 4, given by Equation (4.74), is not physically realizable since because, from Equation (4.73),  $(\dot{R})^2$  is singular in limit as  $R$  approaches zero. This singularity is removed by allowing less heat transfer ( $\gamma \neq 1$ ) in which case Equation (4.71) applies. It is to be noted that at large values of hydrostatic pressure, fluid compressibility influences collapse only slightly more than at 1 atm. Although the minimum bubble radius is dramatically influenced, the presence of gas, Khoroshev<sup>104</sup> has shown less than 10 percent increase in the collapse time

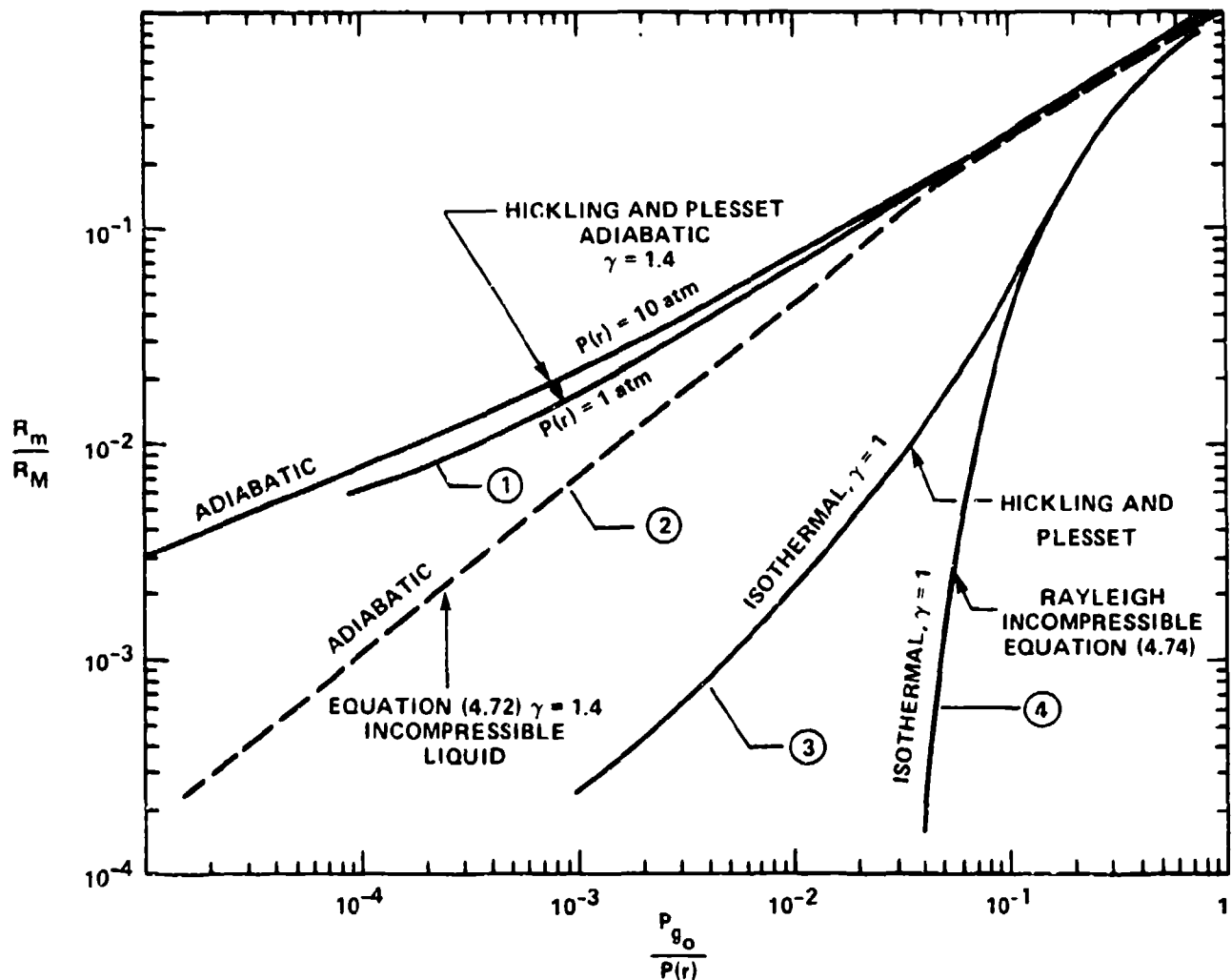


Figure 4.18 - Minimum Bubble Radius for Collapsing Bubbles for which  $R = 0$

(Rayleigh model assumes incompressible liquid, Hickling and Plesset assume compressible liquid.)

compared with the incompressible value of Equation (4.70) for values of  $P_g/P(r)$  less than 0.1. The minimum bubble radius is furthermore dependent upon both the presence of gas and the liquid compressibility, especially for small gas pressures.

In Section 4.4 we will see that the details of the bubble collapse determine much of the sound radiated by cavitation bubbles. Therefore, we shall determine approximate analytical expressions for the time dependence of the bubble motion near collapse. Near  $R = R_m \ll R_{R1}$  the equation of motion (Equations (4.12) and (4.46)) reduced to

$$\ddot{R} \sim \frac{1}{\rho_o R_m} P_{g_o} \left( \frac{R_M}{R_m} \right)^{3\gamma}$$

as long as  $\dot{R} \approx 0$  and  $(P_{g_o}) (R_M/R_m)^{3\gamma} \gg P_\infty$  and  $S/R_m$ . This is the differential equation of a parabola with a minimum at  $R = R_m$  at  $t = \tau_c$ . Thus, near  $\tau_c$

$$\frac{R - R_m}{R_M} = \frac{1}{2} \left[ \frac{P_{g_o}}{1.2 P(r)} \left( \frac{R_M}{R_m} \right)^{3\gamma+1} \right] \left( \frac{\tau_c - t}{\tau_c} \right)^2 \quad (4.75)$$

Equation (4.75) is expected to hold only in the immediate vicinity of the collapse. Figure 4.19 shows Equation (4.75) compared to points calculated by Hickling and

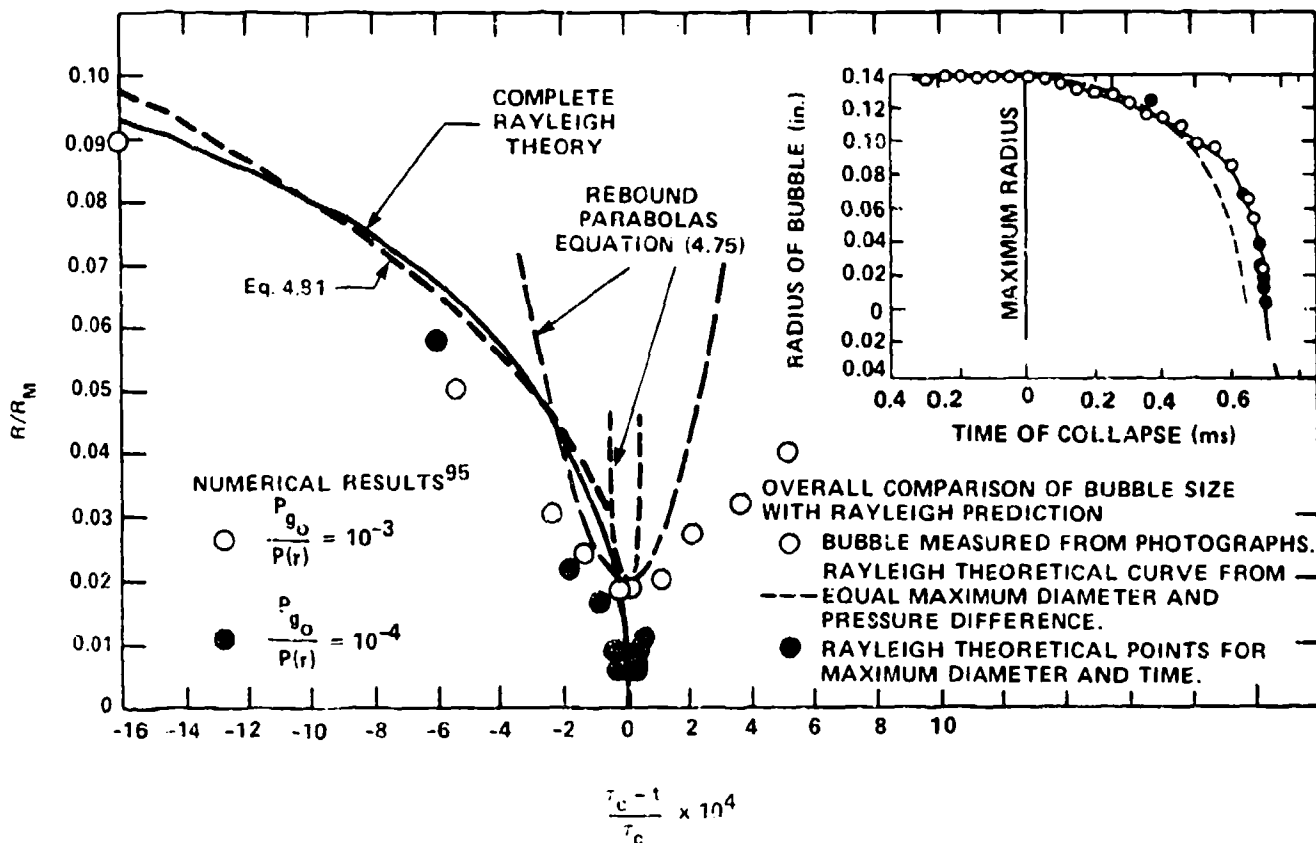


Figure 4.19 - Details of Bubble Collapse Computed by Hickling and Plesset<sup>99</sup>  
Compared with Approximate Collapse<sup>79</sup> and Rebound Parabolas<sup>83</sup>  
for Two Gas Pressures

Plesset.<sup>99</sup> Also shown in Rayleigh's result obtained by Knapp and Hollander<sup>90</sup> by integrating Equation (4.69), numerically. Now, the radius in this region is related to a time constant  $(\delta\tau)_{R=0}^*$ ,

$$\frac{R-R_m}{R_m} \approx \left( \frac{\tau_c - t}{(\delta\tau)_{R=0}^*} \right)^2 \quad (4.76)$$

which determines a rebound parabola at the final stage of collapse, and which will be seen to determine the very high-frequency noise. This time constant is

$$(\delta\tau)_{R=0}^* = \tau_c \left\{ \frac{2.4}{\rho_0} \frac{P(r)}{R_m} \left( \frac{R_m}{R_M} \right)^{3\gamma+2} \right\}^{1/2} \quad (4.77)$$

In Figure 4.19 it is apparent that Rayleigh's equation gives a reasonably accurate result for the radius for times that are less than  $\tau_c - (\delta\tau)_{R=0}^*$ .

A radius-time relationship can be derived for empty ( $P_{g_0} = 0$ ) bubbles for times somewhat earlier than  $t = \tau_c$ , but still for which  $R_M/R \gg 1$ , yet  $(\dot{R})^2 \gg \ddot{R}R$ , using Equation (4.68) which reduces to

$$(\dot{R})^2 \approx - \frac{2}{3} \frac{\Delta P}{\rho_0} \left( \frac{R_M}{R} \right)^3 \quad (4.78)$$

This equation is integrated from some  $R$  and  $t$  to  $R = 0$  at  $t = \tau_c$  to give

$$\frac{R}{R_M} \sim a^{2/5} (\tau_c - t)^{0.4} \quad (4.79)$$

where

$$\begin{aligned}
 a &= \frac{5}{2} \left( \frac{2}{3} \frac{P(r)}{\rho_o R_M^2} \right)^{1/2} \\
 &= \frac{5}{2} \left[ \frac{2}{3} \left( \frac{0.915}{t_c} \right)^2 \right]^{1/2}
 \end{aligned}
 \tag{4.80}$$

therefore,

$$\frac{R}{R_M} = 1.3 \left( \frac{t_c - t}{t_c} \right)^{0.4}
 \tag{4.81}$$

This relationship closely approximates the complete Rayleigh solution near collapse due to the neglected acceleration terms. The inset of Figure 4.19 shows the measured bubble collapse by Knapp<sup>105</sup> and Knapp and Hollander<sup>90</sup> with both the numerically-calculated radius and Equation (4.81). Unfortunately, the details of collapse are not easily observed because of the short time scales involved and because of the small value of  $t_c - t$  for which Equation (4.75) can hold. The radial velocity must decrease from nearly sonic (Figure 4.16) to zero at the final stage of collapse. Therefore, these results yield only rough approximations with which estimations of the effect of gas on the sound will be estimated in Section 4.4.

Although the large velocities of the bubble wall relative to the acoustic sound velocity occurring at the final stage of collapse had been recognized by Rayleigh, it was not until the early 1950's that numerical calculations of the compressibility effects were undertaken.

When the bubble wall velocity approaches the speed of sound in the liquid, shock waves are formed which modify the time history of the pressure wave formed in the liquid near the bubble. To get an idea of when this occurs, relative to the expected time for complete collapse, we resort again to the incompressible liquid model.

To find the acceleration of the bubble wall, at any time for a gas-filled bubble in an incompressible liquid substitute Equations (4.11) and (4.71) into Equation (4.12) to give

$$\ddot{R} = \frac{-P(r) + P_v}{\rho_o} \frac{R_M^3}{R^4} \left\{ 1 + \frac{P_{g_o}}{(P(r) - P_v)(\gamma - 1)} \left( 1 - \gamma \left( \frac{R_M}{R} \right)^{3(\gamma - 1)} \right) \right\} \quad (4.82)$$

The maximum velocity occurs when  $\dot{R} = 0$  at which time the radius is

$$\left( \frac{R_M}{R} \right)_{\dot{R}=0} = \left\{ \frac{\gamma - 1}{\gamma} \frac{P(r) - P_v}{P_{g_o}} \right\}^{1/3(\gamma - 1)} \quad (4.83)$$

where the term  $P_{g_o}/P(r)$  has been neglected compared to unity. Thus, Equation (4.82) shows that the limiting radius at which  $\dot{R}$  is maximum is zero for  $P_{g_o} = 0$  and for isothermal compression,  $\gamma = 1$ . Now, to determine what the maximum wall velocity is, we just substitute Equation (4.83) into Equation (4.71)

$$\left[ \frac{\dot{R}}{c_o} \right]_{\max} = \left( \frac{P(r) - P_v}{\rho_o c_o^2} \right)^{1/2} \left\{ \frac{2}{3} \left( \frac{\gamma - 1}{\gamma} \right) \left[ \left( \frac{\gamma - 1}{\gamma} \right) \left( \frac{P(r) - P_v}{P_{g_o}} \right) \right]^{1/(\gamma - 1)} \right\}^{1/2} \quad (4.84)$$

Equation (4.84), illustrated in Figure 4.20 for two values of hydrostatic pressure, poorly predicts wall velocity for the small gas pressures which should exist in vaporous cavitation. As the gas pressure is reduced to zero, the incompressible theory predicts an infinite radial velocity and there is a square-root dependence on the static pressure which is only given in the complete theory at moderately large gas pressures. Nonetheless, continuing to use the simple theory, the maximum wall velocity occurs at the radius given by Equation (4.84) for which the corresponding time interval prior to collapse,

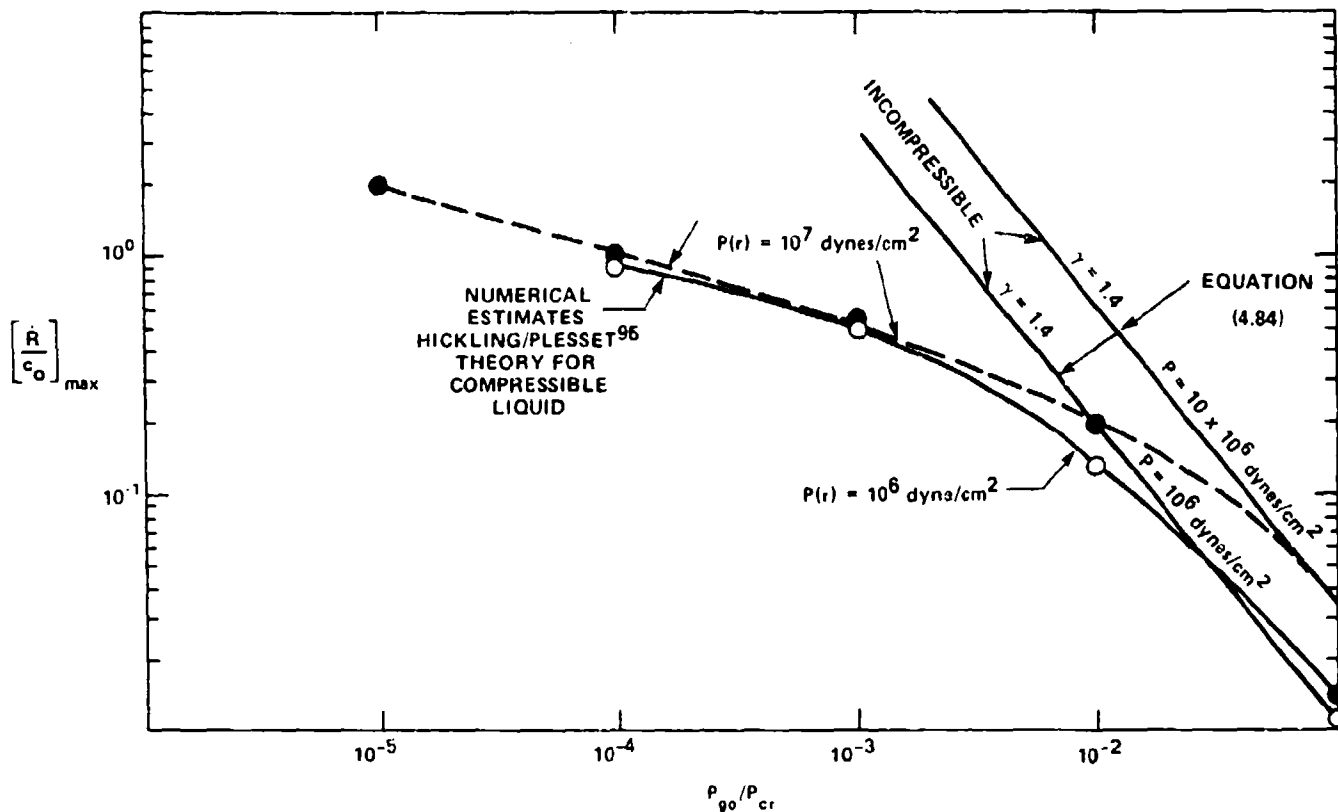


Figure 4.20 - Maximum Bubble-Wall Mach Number as a Function of Initial Inside Gas Pressure and Hydrostatic Pressure; Adiabatic Collapse

$$(\dot{\tau}_c)_{R=0} = \tau_c - \tau_{R=0}''$$

is given from Equation (4.81),

$$\frac{(\dot{\tau}_c)_{R=0}}{\tau_c} = \left[ 1.2 \left( \frac{\gamma}{\gamma-1} \frac{P_{g0}}{P(r)} \right)^{1/3(\gamma-1)} \right]^{5/2} \quad (4.85)$$

This time interval is longer than the previous one  $(\dot{\tau})_{R=0}'$  given by Equation (4.77) by the ratio



$$\frac{(\delta\tau)''_{R=0}}{(\delta\tau)'_{R=0}} \sim 1.7 \gamma^{[5/6(\gamma-1)]} (\gamma-1)^{1/2} \geq 1 \quad (4.86)$$

$$\sim 2 \text{ for } \gamma = 4/3 \text{ to } 1.4$$

$$= 0 \text{ for } \gamma = 1$$

simply because  $\ddot{R} = 0$  occurs before  $\dot{R} = 0$ , i.e., the time of maximum wall velocity occurs just before or at the time of minimum radius. Note that the ratio of these times is not dependent upon the gas pressure, rather only on the ratio of specific heats  $\gamma$ . Referring again to Figure 4.20, we see, however, that Hickling and Plesset's analyses for the gas-filled bubble in a compressible liquid suggest that the incompressible theory is not valid for gas pressures that are less than one-hundredth of the static ambient pressure. Furthermore, for rarified bubbles, the maximum radial velocity in a compressible liquid is apparently independent of the hydrostatic pressure, but still becomes virtually unbounded as the bubble becomes emptied of compressible gas, as Gilmore's<sup>92</sup> and Mellon's<sup>94,95</sup> theories (shown in Figure 4.16) will also attest. Therefore, for this time interval, for which  $\dot{R} \sim c_o$  on bubbles with little compressible gas, the compressibility of the liquid must dominate the collapse dynamics.

The pressure pulse that is formed in the liquid in this time segment has been determined by Fitzpatrick and Strasberg<sup>106</sup> using results of calculations by Mellon.<sup>95</sup> Discussion of these points will be taken up in Section 4.4.1.2.

A rough estimate of the time interval before collapse for which the liquid-compressibility should influence the wall velocity can be made by using the results of the preceeding section. Following Fitzpatrick<sup>107</sup> we postulate that liquid compressibility should become important when  $\dot{R}/c_o$  is finite, for example, greater than 0.1. For empty bubbles, using Equations (4.78) and (4.81), this criterion can be shown to correspond to a bubble radius

$$\frac{R}{R_M} \sim \left\{ \left[ \frac{2}{3} \frac{P(r) - P_v}{\rho_o c_o^2} \right]^{1/3} \right\}^{-2/3} \quad (4.87)$$

$$\sim 4 \left( \frac{P(r)}{\rho_o c_o^2} \right)^{1/2}$$

which agrees with Fitzpatrick's<sup>103</sup> result. The corresponding time before collapse is

$$\begin{aligned} \frac{\delta\tau_s}{\tau_c} &\sim 0.9 \left( \frac{P(r)}{\rho_o c_o^2} \right)^{5/6} M^{-5/3} \\ &\sim 40 \left( \frac{P(r)}{\rho_o c_o^2} \right)^{5/6} \end{aligned} \quad (4.88)$$

where  $M = \dot{R}/c_o$ . This time interval is a factor of three earlier than that derived by Fitzpatrick<sup>107</sup> partly because of the tendency of Equation (4.81) to underestimate the bubble radius. Fitzpatrick<sup>107</sup> used a different analytical function for  $R(t)$  than that used here. The radii which are indicated by Equation (4.87) for  $P(r) = 10^6$  dynes/cm<sup>2</sup> and  $10^7$  dynes/cm<sup>2</sup> are  $0.15 R_M$  and  $0.31 R_M$ , respectively. Figure 4.18, emphasizes the effect of compressibility, showing that the deviation of the compressible and incompressible theories for the minimum bubble radii occurs for minimum sizes that are less than  $(0.1)R_M$ , and Figure 4.20 shows that the maximum wall velocity is considerably below that predicted by the incompressible theory when  $\dot{R} > 0.1c_o$ .

We shall see in Section 4.4 that the peak value of an acoustic pulse will be proportional to the peak value of  $\ddot{V}$ . At the times close to complete collapse the volume acceleration is controlled by the wall velocity, i.e.,  $\ddot{V} \approx 2 R (\dot{R})^2$ . Accordingly, for  $p_{g_o}/P(r) < 10^{-2}$  as shown in Figure 4.20, the peak value of the sound pulse will be controlled by the compressibility of the liquid. Thus, as we shall see, the formation of weak shock waves are expected to occur in the vicinity of the collapsing bubble. These waves will be controlled, first, by liquid compressibility and, second by static pressure. The maximum velocity of the bubble wall will be reached at  $t = \tau_c - (\delta\tau)''_{R=0}$ , and this time will mark a cessation of shock formation. Later, but immediately before collapse at  $t \geq \tau_c - (\delta\tau)'_{R=0}$ , the bubble motion will be limited by the enclosed gas pressure and it will be a time of relatively large values of wall deceleration.

#### 4.2.5.2 Other Influences on Bubble Collapse.

4.2.5.2.1 Liquid Viscosity. Recent theoretical analysis by Kuznetsov and Shchekin,<sup>108</sup> Levkovskii,<sup>109</sup> and by Avenesov and Kuznetsov<sup>110</sup> have shown liquid viscosity to have a relatively unimportant influence on bubble collapse. Only when the bulk viscosity of the liquid becomes many thousands of times larger than that of water does the rebound of small collapsing bubbles become influenced.<sup>110</sup> For values of a Reynolds number

$$R_b = \frac{R_M \left( \frac{P(r)}{\rho_0} \right)^{1/2}}{4\eta} < 2 \sqrt{6} \left( 1 - \frac{3}{2} w_e \right)^{-1}$$

where

$$w_e = \frac{2S}{R_M P(r)}$$

Levkovskii<sup>109</sup> deduces that

$$\frac{\dot{R}}{R_M} \rightarrow w_e \cdot R_b \text{ as } R \rightarrow 0$$

in an incompressible liquid. For larger values of  $R_b$  than the critical, the classical results of the last subsection apply.

4.2.5.2.2 Nonspherical Bubbles. Measurements of collapsing spark-induced bubbles in a virtually unbounded liquid show a maintenance of sphericity, e.g., see Harrison,<sup>111</sup> and Lauterborn.<sup>112,113</sup> However, bubbles collapsing in an hydrodynamic pressure gradient, e.g., in a venturi<sup>114,115</sup> on a hydrofoil,<sup>116-118</sup> on or near a solid wall,<sup>112,119,120</sup> or within a radius of another bubble,<sup>112,113,121,122</sup> show a marked departure from spherical symmetry. Spark bubbles collapsing near boundaries can form a small jet toward the boundary (widely considered as responsible for cavitation damage), while bubbles collapsing in the streamwise gradient of a hydrofoil

assume the shape of a prolate spheroid<sup>116-118</sup> whose axis is perpendicular to the direction of the pressure gradient. These bubbles can collapse asymmetrically<sup>116-118</sup> or be disintegrated by the liquid flow separating over them.<sup>117,118</sup> In a venturi, bubbles have been observed to take the shape of an oblate spheroid with minor axis in the direction of the gradient. In the final stage of collapse,<sup>109</sup> these bubbles can form toroidal shapes. Rebounding bubbles may also appear as clouds of micro-bubbles rather than single bubbles, e.g., References 116-118.

Theoretical analyses by Plesset and Mitchell<sup>123</sup> have shown that expanding cavities will remain essentially spherical as long as the initial deformation is small compared to the initial radius. Collapsing cavities are less stable, the instability growing as  $R^{-1/4}$  whether or not surface tension is included in the analyses. Later analyses by Shima and Nakajima,<sup>124</sup> for nonhemispherical bubbles attached to a wall, showed that collapse times are closely approximated by Rayleigh's formula using a mean bubble radius. This similarity had been demonstrated earlier, however, by Plesset.<sup>33</sup> The analysis of Shima and Nakajima<sup>124</sup> showed that when the attached bubble is initially a prolate hemispheroid (with major axis perpendicular to the wall) it deforms into an oblate hemispheroid and subsequently forms a jet impinging on the wall. The numerical analysis by Shima<sup>125</sup> for initially-spherical bubbles collapsing near a solid surface, showed that when the bubble center is initially within three radii from the surface, the center of the bubble moves toward the surface in such a way that the bubble wall nearest the surface moves only slightly. The analysis of Levkovskii<sup>126</sup> has shown that when the distance from the surface to the bubble center is only one initial radius, i.e., the bubble nearly touches the wall, the collapse time differs from Equation (4.70) by no more than 20 percent. This result is important from the aspect of noise production, because it suggests that the frequency content of noise ( $f \sim 1/\tau_c$ ) for a given bubble volume will not be too sensitive to the geometry of the collapsing bubble. We shall see in Section 4.4.1.1 that for frequencies that are less than  $1/\tau_c$ , the cavitation noise spectrum depends on the overall growth of the bubbles. At higher frequencies the noise is controlled by the details of collapse. Therefore, this noise may be influenced by departures of the collapsing and rebounding bubbles from spherical symmetry, and by the formation of bubble clouds in the collapse and rebound phases.

### 4.3 HYDRODYNAMIC CAVITATION INCEPTION

The inception of cavitation is important from the point of view of acoustics because once cavitation begins, the noise level increases rapidly as the cavitation develops. Therefore, it is important to predict with fair precision the occurrence of cavitation as pressure decreases or as velocity increases. The level of cavitation noise shall be shown in the next section to depend upon the value of the cavitation inception index.

#### 4.3.1 General Equilibrium Theory

4.3.1.1 Outline of Scale Effects. The use of Equation (4.5) to predict cavitation inception, and the direct application of the classical theory of bubble dynamics to predict hydrodynamically induced bubble motions has only been successful in certain types of flows. Often real flows deviate from the ideal because of viscous and boundary influences as well as the population of free-stream versus surface nuclei. Two conditions favoring the classical cavitation inception occurring when  $K = (-C_p)_{\min}$  together with the growth and collapse of spherical bubbles, as in Sections 4.2.3 and 4.2.5, are: nonseparated boundary layer flow over the body, and an abundance of free-stream bubble nuclei (occurring generally at moderate-to-large gas contents). Such conditions have existed in the traveling-bubble observations of Plesset,<sup>14</sup> Figure 4.14, and others by Knapp and Hollander<sup>90</sup> (see Figure 4.15), Parkin,<sup>116</sup> and Blake et al.<sup>117,118</sup> Departures of cavitating flows from this ideal behavior have been termed "scale" effects.<sup>11,116</sup>

An example of measured indices for the inception of cavitation on an effectively two-dimensional hydrofoil, that does not apparently display scale effects, is found in the work of Daily,<sup>127</sup> shown in Figure 4.21. The observed values of  $K_1$  are shown to be only slightly less than the  $(-C_p)_{\min}$  determined in a wind tunnel, with the discrepancy less at small angles of attack than at large angles. Large scale effects were apparent for the indices measured on 12 percent Joukowski hydrofoils by Parkin<sup>116</sup> and shown in Figure 4.22. The indices increase markedly with an increase in Reynolds number and a decrease in size. In all cases the index increases from substantially less than  $(-C_p)_{\min}$  to approximately that value. In both cases the nucleus population was densely composed of small spherical bubbles.

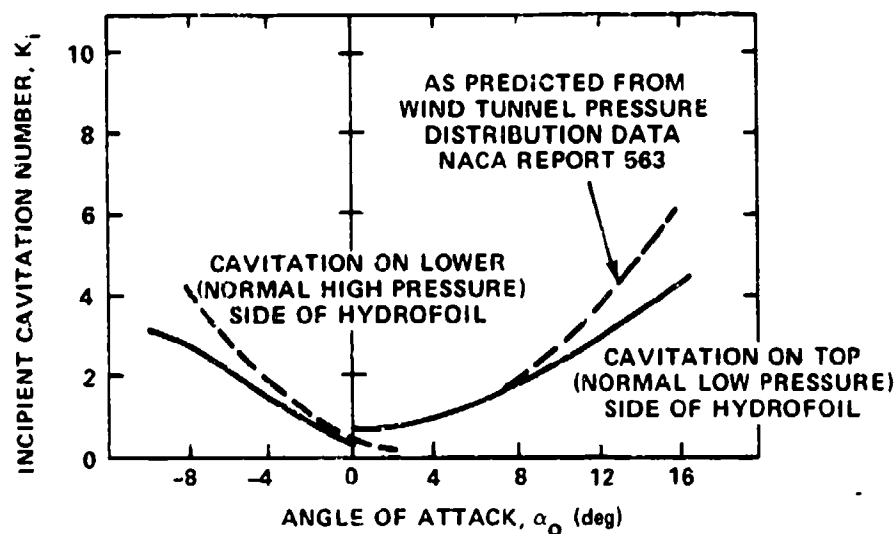


Figure 4.21 - Values of  $K_i$  at which Cavitation Begins versus Angle of Attack, NACA 4412, Camber: 0.04C (From Daily<sup>127</sup>)

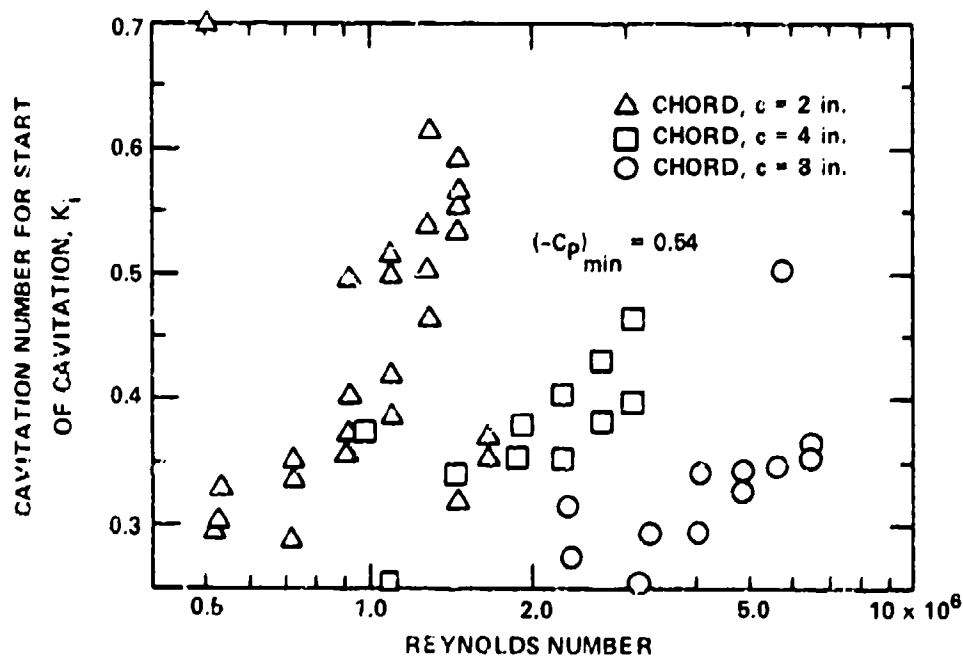


Figure 4.22 - Cavitation Number  $K_i$  for Incipient Cavitation versus the Reynolds Number  $R_c$  for the Joukowski Hydrofoils, Visual Inception (From Parkin<sup>116</sup>)

Behavior of cavitation on hydrofoils is now generally thought to be related to some combination of viscous scale effects (through influences of both laminar separation and surface roughness) and local differences in nucleus distribution (which influence the location of possible initial cavitation). Laminar boundary layer separation, which occurred at all values of  $R_c$  in Figure 4.22, is often associated with a reduction in  $K_1$ , while surface roughness increases  $K_1$ . Local nucleus concentration, which also influences inception, may depend on nucleus size relative to a flow length scale (see Figures 4.51 and 4.52) as well as on the nature of turbulent mixing in the flow. Although the interrelationships of these scale effects are not well understood, only recently has attention been given to systematically recording the condition of noncavitating flow on the body, the background turbulence in the facility, the water quality, and the surface condition and material.

Scale effects, which lead to various types of surface cavitation, have been observed on the same body in different facilities, as shown in Figure 4.23. These classical photographs were published first by Lindgren and Johnson<sup>128</sup> and show the results of a "round robin" series of experiments that was sponsored by the International Towing Tank Conference. It is now believed (see Section 4.3.2.7) that these differences in cavitation-type are due to a combination of differences in facility turbulence (which influences laminar boundary layers) and bubble nuclei. The appearances of cavitation fall into three classes: traveling bubble which is favored by large concentrations of bubble nuclei and high turbulence levels in the facility; sheet cavitation which is favored by low turbulence levels and moderate to low concentrations of gas nuclei; and bound bubble cavitation which is favored by low turbulence levels and moderate to low concentrations of gas nuclei bound but poorly wetted or hydrophobic surfaces (large concentration of surface nuclei). The location of these bubbles is stabilized by an equilibrium between surface tension and the local steady pressure gradient.<sup>48</sup> Even though there exists a large body of literature published prior to 1965, it is difficult to use many of those experimental findings in current compilations of measured cavitation inception, because one or more of the experimental conditions that are now regarded as important may not have been reported in the previous work.

Three-dimensional hydrofoils and propeller blades have tip vortex cavitation, in addition to these various forms of surface cavitation. This cavitation is caused

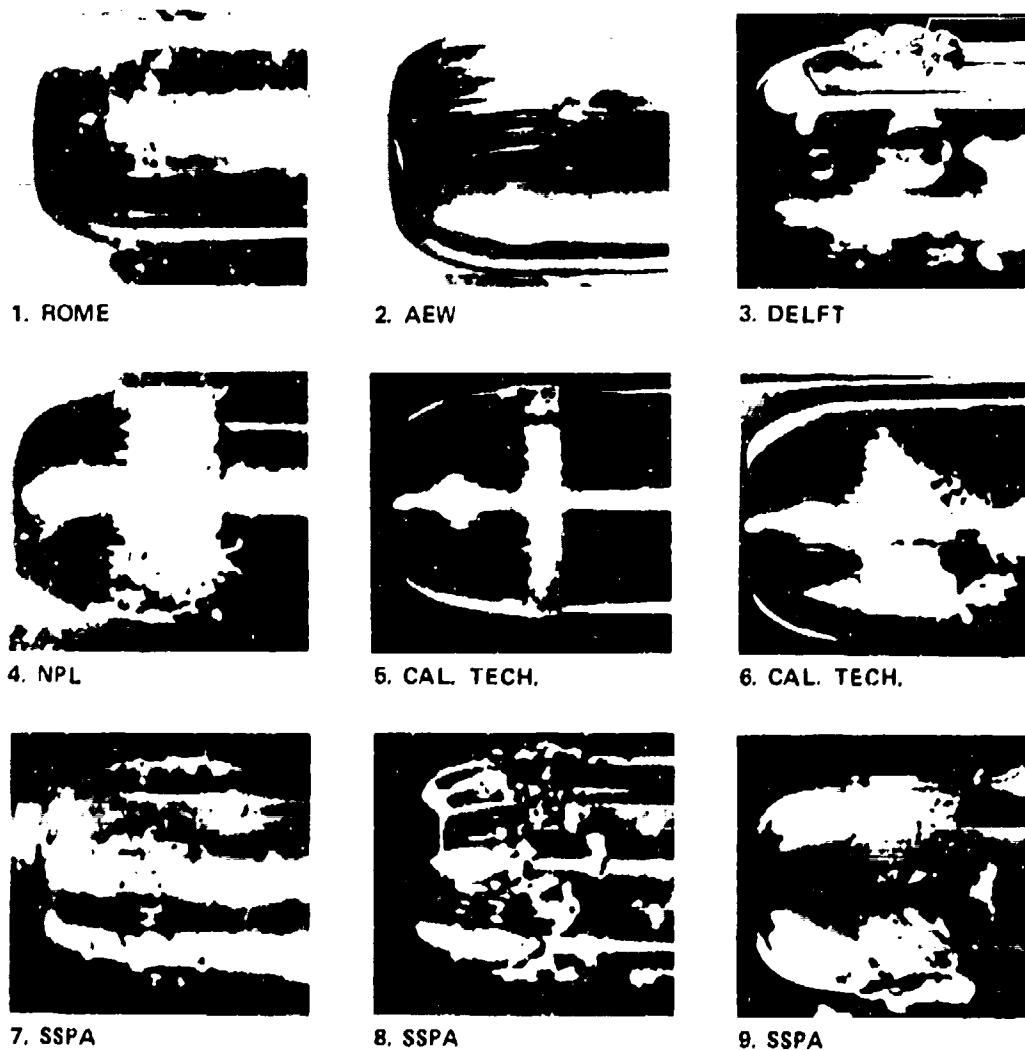


Figure 4.23 - Photographs of Cavitation on Head Forms in Different Water Tunnels

(From Lindgren and Johnson<sup>128</sup>)

by the relatively low pressures that exist in the vortex cores and its inception will depend on both the lift produced and the Reynolds number (boundary layer) of the surface flow on the hydrofoil. Free shear layers, wakes, and jets, will also cavitate, while the incipient index depends upon the circulation of eddies entrained in the flow.



4.3.1.2 Hydrodynamical Excitation of Bubble Nuclei. Compared to ultrasonic cavitation, hydrodynamic cavitation has the additional complication that the pressures surrounding the cavitation nuclei are a function of the flow Reynolds number and of the details of the flow. Therefore, it is, in general, necessary to have a priori understanding of these details prior to a reliable prediction of inception. Although some type of relationship between inception and viscous flow has been recognized for many years, a full comprehension of it is only now being realized.

Mathematically, the relationship between the turbulent field and the dynamics of the bubble nuclei entrained by it is set by the equations of bubble dynamics (Equations (4.11) and (4.12)) simultaneously with the momentum Equation (2.44). Because our interest in this section lies with incipient cavitation, the fluid mechanics that excite the bubbles may be considered as single phase and virtually incompressible (unless, of course, the concentration of free gas is rather large). We proceed now to give a general idea of the magnitudes of these pressure fluctuations in various types of flow. Superimposed on the mean flow are turbulent velocities so that the velocity and pressure in the momentum and continuity equations may be replaced by

$$\vec{u}'(\vec{y}, t) = \vec{U}(\vec{y}) + \vec{u}(\vec{y}, t) \quad (4.89)$$

and the pressure driving the bubble, replacing  $P(r)$  in Equation (4.12), is

$$p'(\vec{y}, t) = P(\vec{y}) + p(\vec{y}, t) \quad (4.90)$$

The fluctuating variables  $\vec{u}(\vec{y}, t)$  and  $p(\vec{y}, t)$  have zero mean because they are perturbations about the time-averaged local mean velocity  $\vec{U}(\vec{y})$  and local static pressure,  $P(\vec{y})$ . The fluctuating velocity and pressure possess the statistical properties outlined in Section 3.5. The various qualities of pressure fluctuations on the wall beneath the turbulent boundary layer are examined in Chapter 7. For use in the next section, we will summarize the known magnitudes of pressure fluctuations in some shear flows.

Batchelor,<sup>129</sup> essentially following the procedures of Section 7.3, has theoretically determined that the root-mean-square pressure in an isotropic turbulent field is given by

$$\overline{p^2}^{1/2} \sim 0.58 \rho_0 \overline{u^2} \quad (4.91)$$

where  $u = u_1$  is the turbulence intensity. Measurements of  $\overline{p^2}$  have been made in a turbulent jet, the most recent being those of Armstrong<sup>130</sup> which showed

$$\overline{p^2}^{1/2} \approx 1.5 \rho_0 \overline{u_1^2} \quad (4.92)$$

where  $u_1$  is the velocity fluctuation in the mixing zone of the shear layer, which is a value that is comparable to that found by others.<sup>131</sup> Because the maximum

$\overline{u_1^2} \approx 0.026 U_J^2$ , Armstrong's result gives

$$\frac{\overline{p^2}^{1/2}}{\frac{1}{2} \rho_0 U_J^2} \sim 0.08 \quad (4.93)$$

Measurements of  $p(y_1, t)$  in turbulent boundary layers are not available, but on the wall (see Chapter 7) the root-mean-square pressures are bounded by

$$\overline{p^2}^{1/2} \approx (2 \text{ to } 4) \tau_w \quad (4.94)$$

where  $\tau_w$  is the wall shear coefficient. That these pressures are of the same order of magnitude as those observed in the jet, can be seen by noting that typically near

smooth or rough walls  $\overline{u_1^2}^{1/2}$  have a range (see Chapter 7) from two to three times  $(\tau_w / \rho_0)^{1/2}$ . Therefore, at the wall, the root-mean-pressure is

$$\overline{p^2}^{1/2} \approx (0.5 \text{ to } 4) \rho_o \overline{u_1^2} \quad (4.95)$$

Recent calculations by Meechan and Tavis<sup>132</sup> have shown that pressures in the boundary layer may be 40 percent greater than those at the wall making the coefficient on  $\tau_w$  as large as 5.6.

The relationships of Equations (4.91), (4.92), and (4.94) apply to the root-mean-square pressure, however, locally the pressure may be made smaller than this value and a bubble nucleus entrained by a low-pressure region in the flow is expected to reside in it for times that are at least as long as the life-time of the eddy. Thus, in a general way, the local pressure may be written as a coefficient which includes the local mean  $P_s(\vec{y})$ , and fluctuating pressure, and the free-stream reference velocity  $U_\infty$ , i.e.,

$$\frac{P_s(\vec{y}) + p(\vec{y}, t)}{\frac{1}{2} \rho_o U_\infty^2} = C_p(\vec{y}) + (1 - C_p) \tilde{C}_p(\vec{y}, t) \quad (4.96)$$

where  $\tilde{C}_p(\vec{y}, t)$  is a local time-varying pressure coefficient defined in terms of local velocity  $U_s$  as

$$\tilde{C}_p(\vec{y}, t) = \frac{p(\vec{y}, t)}{\frac{1}{2} \rho_o U_s^2}$$

This pressure coefficient will have a probability of occurrence with positive or negative values about a zero mean. Negative values will cause earlier cavitation because of the resulting lower pressures.

The pressure excitation,  $P(\vec{y}) + p(\vec{y}, t)$  in Equation (4.12) for the bubble motion can now be replaced by Equation (4.96), and the bubble radius can be nondimensionalized on a length scale of the body  $L$ , to give a normalized equation of motion for a bubble in a hydrodynamic pressure field; using Equation (4.96)

$$\left(\frac{R}{L}\right) \left(\frac{R}{L}\right)'' - \frac{3}{2} \left[\left(\frac{R}{L}\right)'\right]^2 = -K - C_p - \frac{4S}{\rho_o R U_\infty^2} + \frac{P_{g0}}{\frac{1}{2} \rho_o U_\infty^2} \left(\frac{R_o}{R}\right)^{3\gamma} - (1 - C_p) \tilde{C}_p(t) \quad (4.97)$$

The representation  $(R/L)'$  denotes a derivative with respect to the reduced time variable

$$\frac{tU_{\infty}}{L}$$

The bubble motion must be viewed in the Lagrangian frame, i.e., moving with the fluid, so that the coordinate  $\vec{y}$  must be replaced by the time varying variable  $\vec{U} \cdot t$  and the time dependence of the pressure is determined both by the translation of bubbles through the low static pressure zone and the superimposed random pressure moving with the bubbles. Equation (4.97) is therefore analogous to the Equation (4.16) with the quantity

$$\frac{1}{2} \rho U_{\infty}^2 \left[ C_p(\vec{U} \cdot t) + (1 - C_p(\vec{U} \cdot t)) \hat{C}_p(\vec{U} \cdot t, t) \right]$$

replacing the excitation pressure. The combination of terms on the right-hand side of the equation determines a critical radius and pressure which are analogous to those of ultrasonics. A critical pressure coefficient for static divergence of an empty nucleus ( $P_{g_0} = 0$ ) is, from Equation (4.50), therefore,

$$[K + (C_p)]_{\text{crit}} = - \left( \frac{4S}{\rho_o R_o U_{\infty}^2} \right)^{3/2} \frac{2}{27^{1/2}} \left[ K + \frac{4S}{\rho_o R_o U_{\infty}^2} \right]^{-1/2} \quad (4.98)$$

where  $R_o$  is the radius of the bubble nucleus upstream of the body where  $P_s = P_{\infty}$  and  $U_s = U_{\infty}$ . The critical radius at the pressure coefficient  $C_p$  is given by

$$\frac{8S}{3R_o \rho_o U_{\infty}^2} = -K - (C_p) \quad (4.99)$$

Equation (4.98) has the same graphical representation as shown in Figure 4.8, however,  $K$ ,  $C_p$ , and  $\rho_o R_o U_{\infty}^2 / 4S$  replace the dimensional variables used earlier. Although the above relationships apply to bubble nuclei, one may further envision alternative relationships which pertain to trapped gas in crevices of hydrophobic and surface nuclei which are analogous to those developed by Harvey (or Apfel, see Equation (4.62)).

Equation (4.98) may be used to state a general static equilibrium theorem that has been used extensively in cavitation research over the years. Static equilibrium requires that  $k = \dot{R} = 0$ , therefore, Equations (4.98) and (4.99) give the inception index for the flow as being equal to the minimum value of the sum of pressure coefficients, i.e.,

$$K_i = \left\{ -(C_p) - \frac{4S}{\rho_o R U_\infty^2} + \frac{P_{g_o}}{\frac{1}{2} \rho U_\infty^2} - (1-C_p) \tilde{C}_p(t) \right\}_{\min} \quad (4.100)$$

This simple relationship superimposes the collective effects of surface tension and dissolved gas that determine bubble response as well as deviations from the ideal potential flow which are represented by instantaneously nonzero values of  $\tilde{C}_p(t)$ .

4.3.1.3 The Influence of Dissolved Air on Cavitation Inception. Just as in ultrasonically-induced cavitation, the presence of dissolved gas in hydrodynamic facilities can diffuse out of solution causing gaseous cavitation if the local pressure is low enough to cause local supersaturation. The process could also include the rectified diffusion if an undulating pressure field remains in progress for a suitable length of time. Holl<sup>133,134</sup> has considered the gaseous cavitation from this point of view. The equilibrium Equation (4.57), applies directly to this case, which Holl rewrote as

$$P_e = P_v - \frac{2S}{R} + \alpha H$$

where  $P_e$  = equilibrium pressure

$H$  = Henry's law constant

$\alpha$  = dissolved air content

$\alpha H = P_{g_o} = f P_{sat}$  in Equation (4.57)

The static equilibrium condition for the onset of gaseous diffusion may be written in dimensionless form as

$$K \leq (-C_p)_{\min} - \frac{4S}{\rho_o U_\infty^2 R_o} + \frac{\alpha H}{\frac{1}{2} \rho_o U_\infty^2} \quad (4.101)$$

These equations express the fact that when the local hydrodynamic pressure  $P(\vec{y})$  falls below  $P_e$ , the bubble will begin to expand and the partial pressure of gas in the bubble will be less than the equilibrium pressure of the dissolved gas in the ambient liquid and the bubble will continue to grow. This is because the liquid is locally supersaturated. The process will be slow, unless it is accelerated by convective diffusion, Section 4.2.3.3, with  $f$  in the equations determined by the local rarefaction pressure  $P(y)$ , the (larger) upstream ambient pressure  $P_\infty$ , and the upstream concentration  $f_\infty$  such that the local concentration is

$$f \approx \frac{f_\infty P_\infty}{P(y)}$$

For large enough bubbles that the surface tension pressure may be neglected, the limiting cavitation index for gaseous cavitation will occur when

$$K < K_i = -(C_p)_{\min} + \frac{\alpha H}{\frac{1}{2} \rho_o U_\infty^2} \quad (4.102)$$

Holl<sup>133</sup> has compared this equation to measured desinence indices on small hydrofoils with the result\* shown in Figure 4.24. The upper curve applies to stable spots of cavitation which remained as small attached, clear bubbles on the surface, while the lower curve appeared as a less stable steady state of cavitation along the span of the hydrofoil. The spots were apparently located at small nonuniformities in the surface, and that they were due to gaseous cavitation is confirmed by the agreement of Equation (4.102) with measured indices. The spots were also apparent on the NACA section, only at angles of attack above a critical value beyond which leading-edge laminar separation would be expected. The implication of these experiments is

---

\*Desinent cavitation indices  $K_d$  are obtained by increasing ambient pressure and noting the cessation of cavitation, while incipient cavitation indices  $K_i$  are noted by reducing pressure and noting the onset of cavitation. For  $K_i \leq K$ , see Reference 135, the difference diminishes as Reynolds number increases.

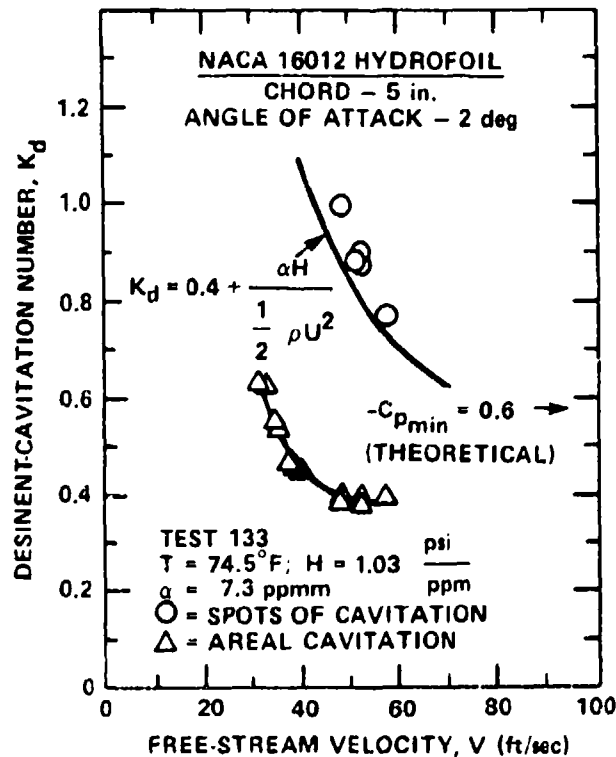


Figure 4.24 - Two Types of Cavitation on a 5-Inch NACA 16012 Hydrofoil  
 (From Holl<sup>133</sup>)

three-fold: it confirms the validity of Equation (4.102) for gaseous cavitation, it demonstrates the possible importance of viscous flow (especially flow separation which provides necessary time for diffusion to occur) as influenced by angle of attack, and it demonstrates the importance of surface condition in determining certain types of inception.

**4.3.1.4 Bubble Growth in Turbulent Flow.** As shown by Equation (4.96) unsteadiness superimposed on the mean flow causes a locally fluctuating pressure coefficient. This effect is illustrated in Figure 4.25 which shows the static pressure on or immediately above the surface and a superimposed fluctuating pressure field. The vapor pressure is shown to be less than the minimum static pressure so that without turbulence vaporous cavitation would not occur, but because of the fluctuating pressures microbubbles entrained by the boundary layer on the hydrofoil will cavitate. As illustrated, the pressure is represented as spatially varying over the surface,

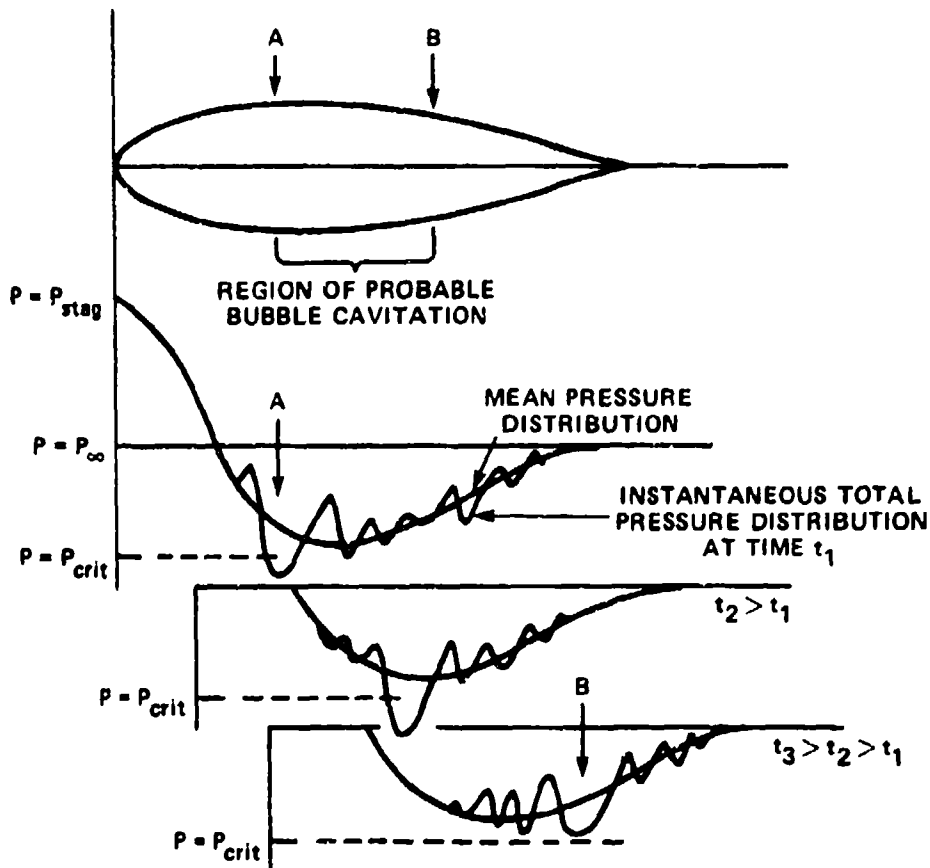


Figure 4.25 - Total (Mean Plus Fluctuating) Pressure on the Surface of a Hydrofoil. In the Situation Shown, Minimum Static Pressure,  $P_{min}$ , is Greater than

$P_{crit}$  so that  $(-C_p)_{min} < K_1$ . Instantaneous Pressures are Shown

for Three Successive Times for which the Local Instantaneous Pressure First Drops Below then Increases Above  $P_{crit}$ .

however, to a bubble convected by the mean flow, this pressure may be regarded as imposed on the bubble as it passes over the surface. Let us suppose that a nucleus happens to be attached to a fluid element at an instant at which the pressure drops beneath  $P_{crit}$ , for example, at location A. This region of low pressure is convected downstream through the varying static pressure region, so that the bubble will grow until roughly at position B, when the static pressure will be great enough that the underpressure caused by the eddy will no longer be sufficient to maintain local



rarefaction and the bubble will collapse. Alternatively, because the eddy lifetime is finite as it is convected and buffeted by the surrounding flow, the local pressure will rise as the eddy decays and, accordingly, the bubble will collapse. In parallel with the case of ultrasonically induced cavitation it can be said that there must be a certain amplification factor and time scale appropriate to the bubbles and that is analogous to Figure 4.9. This function for the radius of the cavitating bubble,  $R_M$  may be of the form

$$\frac{\omega |R_M - R_0|}{\left( \frac{q_\infty |\tilde{C}_p|}{\rho_0} \right)^{1/2}} \sim f \left( \frac{\omega}{\omega_0}, \frac{|\tilde{C}_p|}{C_p} \right) \quad (4.103)$$

where  $\omega_0$  is the resonance frequency of the nucleus  $R_0$ , and  $\omega$  is the frequency of the fluctuating pressure  $q\tilde{C}_p(t)$  in a frame of reference moving with the eddy. The specific theories of unsteady local convection in turbulent shear flows have been developed in Chapter 3 with more extensive development in Chapter 7, but for now let us say simply that the unsteady convection causes a buffetting of the bubble by the neighboring flow giving rise to the fluctuating part of Equation (4.96). The predominant frequency of such a buffetting will be roughly

$$\omega \sim \frac{u_c^2}{\Lambda} \sim \frac{u^2}{\Lambda} \quad (4.104)$$

where  $\Lambda$  is a macroscale of the turbulent flow, and  $u_c^2$  is the root-mean-square of the fluctuating convection velocity which is on the same order of magnitude as the turbulence intensity. Almost always

$$\frac{\omega}{\omega_0} \sim \frac{u_c^2}{(\Lambda \omega_0)} \ll 1$$

therefore, for a large-enough pressure fluctuation, cavitation is certain to occur with a growth time which is on the order of

$$T \sim \frac{2\pi\Lambda}{u^{1/2}}$$

Combination with the foregoing Equation (4.103) and the recollection that (Equations 4.91-4.95)  $q_\infty |\tilde{C}_p| \sim \rho_o \overline{u^2}$  suggests that the size of turbulence-induced cavitation bubbles will be limited by the turbulence scale, i.e., using Equation 4.53

$$R_M \sim \Lambda$$

Another related point of view, that is suggested by observations of incipient cavitation in turbulent boundary layers by Arndt and Ippen<sup>48</sup> (Section 4.3.2.6), is that bubbles cavitate in the cores of eddies convected in the boundary layer. The life time of such eddies  $\tau_e$  is on the order of  $\delta/U_\infty$ , where  $\delta$  is the boundary layer thickness so that by Equation 4.53

$$R_M \sim \tau_e \left( q_\infty \left( \frac{2}{3} \right) \frac{|\tilde{C}_p(t)|}{\rho_o} \right)^{1/2} \quad (4.105)$$

In the case of the bubble nuclei, the incipient index, based on the condition of static stability for the threshold of vaporous cavitation, will be

$$K + C_p - (1 - C_p) |\tilde{C}_p(t)| < [K + C_p]_{crit} \quad (4.106)$$

where  $[K + C_p]_{crit}$  is given by Equation (4.98); see Figure 4.8. Note that for large enough bubbles for which  $K \gg 2S/q_\infty R_o$  and for negligible dissolved gas, Equations (4.106) and (4.100) are equivalent because  $[K + C_p]_{crit} = 0$ .

In Section 4.3.2, the use of Equation (4.106) will be illustrated for various types of turbulent flows. The effect of the turbulence will be to increase the

incipient index above the value that would be predicted simply on the basis of potential flow theory. Equation (4.106) implies that dynamical similarity between two geometrically similar, yet differently sized, test bodies must be established in terms of the turbulent flow before cavitation similarity can be established. In the context of the above, this means that  $|C_p|/C_p$  must be similar as well as  $C_p$ ,  $\Delta$  normalized on some geometric scale of the body, and available cavitation nuclei with sizes greater than the critical radius for growth.

#### 4.3.2 Examples of Cavitation Inception of Turbulent Flows

In this section we will summarize the characteristics of some practical turbulent and vortical flows for which the cavitation inception index will differ markedly from the classical equivalence between  $K_i$  and  $(-C_p)_{\min}$ , Equation (4.5). A rationale will be presented for each flow-type that will give a specification of an effective value of  $C_p(t)$ , for example,  $C_{p_{\text{eff}}}$  for use in either Equation (4.100) (or (4.101)) or (4.106). Therefore, a general stability criterion for vaporous cavitation inception will be

$$K_i = [-C_p - (1-C_p) [C_p(t)_{\text{eff}}]_{\min} + [K+C_p]_{\text{crit}} \quad (4.107)$$

where  $[K+C_p]_{\text{crit}}$ , shown in Figure 4.8, is zero for large enough values of nucleus radius. For gaseous cavitation, the equilibrium condition is of the general form

$$K_i = \left\{ (-C_p) + (1-C_p) [C_p(t)]_{\text{eff}} + \frac{\alpha H}{2 \rho_o U_\infty^2} - \frac{4S}{\rho_o U_\infty^2 R_o} \right\}_{\min} \quad (4.108)$$

In the above equation  $\{ \}_{\min}$  indicates that inception will occur on the body at any point at which the total pressure coefficient is minimum, not necessarily at which  $(-C_p)_{\min}$  occurs.

**4.3.2.1 Vortex Cavitation.** The pressure in the core of a vortex of strength  $\Gamma$  is less than the ambient pressure, therefore, a flow that has some vorticity may provide earlier cavitation than nonvortical flows. The simplest way to represent a

vortex is to postulate a "solid" rotating core of radius  $r_c$  and angular frequency  $\Omega$ , as illustrated in Figure 4.26. This is the so-called Rankine vortex. The circulation and  $\Omega$  are related through

$$\Gamma = \int_0^{2\pi} v_\theta r d\theta \quad r \geq r_c$$

$$= 2\pi\Omega r_c^2$$

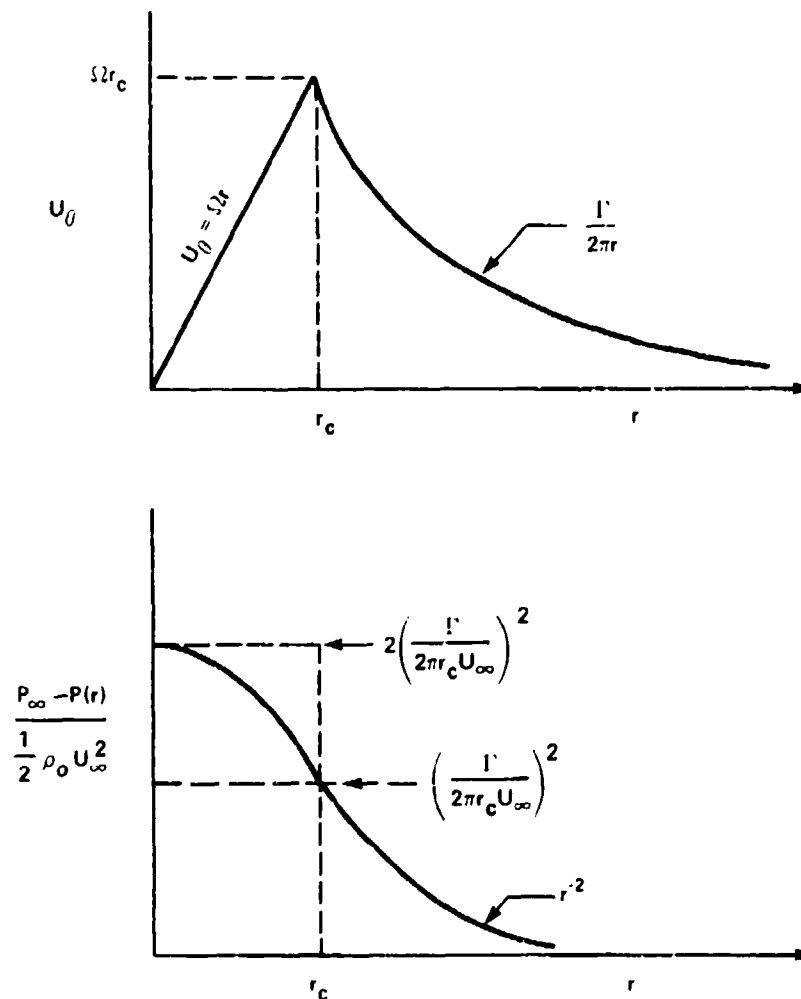


Figure 4.26 - Schematic of the Velocity and Pressure Field of a Rankine Vortex

Equation (4.71) gives the radial pressure gradient in terms of  $U_\theta$ ,

$$+ \frac{1}{\rho_o} \frac{\partial P}{\partial r} = \frac{U_\theta^2}{r}$$

where  $P \rightarrow P_\infty$  as  $r \rightarrow \infty$ . The integration gives the pressure coefficient at the center of the vortex as

$$\frac{P_\infty - P(r)}{\frac{1}{2} \rho_o U_\infty^2} = (-C_p)_{\min} = 2 \left( \frac{\Gamma}{2\pi r_c U_\infty} \right)^2 \quad (4.109)$$

where the normalizing velocity  $U_\infty$  represents the mean velocity of potential field that is superimposed on the vortex. The inception index appropriate to this class of flow is from Equation (4.101)

$$K_1 = 2 \left( \frac{\Gamma}{2\pi r_c U_\infty} \right)^2 + \frac{\alpha_H}{\frac{1}{2} \rho_o U_\infty^2} \quad (4.110)$$

The probability of gaseous cavitation occurring in this type of flow is comparatively large because of the persistence of the vortex downstream and the large volume of liquid entrained in its pressure field. Dissolved gas will diffuse out of solution and gradually fill the vortex.

McCormick<sup>136</sup> has systematically examined the cavitation of a tip vortex for the case of low enough dissolved gas content that the second term of Equation (4.110) was negligible. Using cantilever hydrofoils, the observed inception indices, Figure 4.27, were found to increase with angle of attack; the increase of load with angle of attack caused an associated increase in  $\Gamma$ . The core radius  $r_o$  was postulated as  $\delta/2$ , where  $\delta$  is the thickness of the boundary layer on the hydrofoil;  $\delta$  increases with load (lift) and decreases with Reynolds number. For a given lift coefficient, McCormick's result has been interpreted, e.g., Noordzij<sup>137</sup> and Arndt,<sup>131,138</sup> as showing a scaling relationship

$$K_1 = a R^{0.4} \quad (4.111)$$

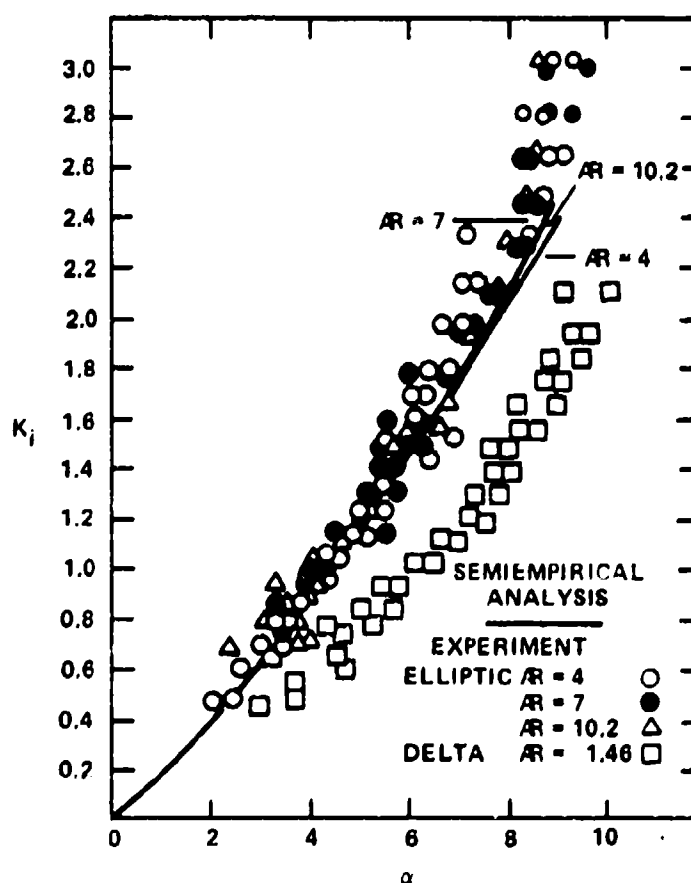


Figure 4.27 - Critical Cavitation Index versus Angle of Attack for Elliptic and Delta Wings for Tip Vortex Cavitation

(From McCormick<sup>136</sup>)

the power on  $R$  partly resulting from the dependence of the boundary layer thickness on  $R$ , i.e.,  $\delta \sim R^{-1/5}$ . In Figure 4.27 the smaller values of  $K_i$  for the delta wing compared to those for the elliptical section are due to the smaller tip loading on the delta wing. Correspondingly, the more highly loaded rectangular wing tips used by McCormick had higher values of  $K_i$  than did the elliptical wings at the same angle of attack. Noordzij<sup>137</sup> has recently applied McCormick's results to propellers approximating the dependence on angle of attack  $\alpha$  and  $R$  as

$$K_i = \alpha^{1/5} R^{0.35} \quad (4.112)$$

Subsequent work by Billet<sup>139,140</sup> has applied Equation (4.110) to the prediction of cavitation inception of a vortex trailing from the hub of a rotor. The measurements,<sup>139</sup> show an increase of  $K_1$  with additional vorticity induced by upstream turning vanes as well as the influence of gas content as indicated by Equation (4.108).

**4.3.2.2 Periodic Vortex Streets.** The vortex street shed from the trailing edges of lifting surfaces and bluff bodies (see also Chapters 5 and 9) have been observed to cavitate, e.g., References 116 and 141; but the only systematic study of the phenomenon is that of Young and Holl.<sup>142</sup> The experiments of Young and Holl, however, were mostly of well-developed cavitation such that  $K/K_1 < 0.3$ . Incipient cavitation indices were observed to be between 3 for a wedge angle of 15 deg and 6 with a wedge angle of 6 deg. In the observation made by Parkin,<sup>116</sup> the vortex street was observed to cavitate at indices  $K < 0.8$ , and Reynolds number based on chord of about  $10^6$ , although a specific value of inception was not reported. The order of magnitude of  $K_1$  to that expected in various instances may be estimated from data on wake circulations summarized in Chapter 9. For example, a 0.5 caliber section\* with a squared-off blunt trailing edge sheds a street of vortices whose individual peak strengths scale as

$$\frac{\Gamma_{\text{peak}}}{2\pi U_{\infty} r_c} \sim 0.6$$

(for a vortex core radius equal to about one-fourth the base height). Using Equation (4.110), this suggests  $K_1 \sim 0.7 + (-C_p)_v$ , where  $(C_p)_v$  is the static pressure at the vortex formation zone. The  $C_{p_v}$  is probably of the same order as the base pressure coefficient  $\sim -1.5$ , making  $K_1 \sim 2$ . The larger indices observed by Young and Holl for large wedge angles were perhaps caused by combined influences of stronger vortices in the wake plus a low static base pressure which would cause a greater relative rarefaction zone at the point of vortex formation. Therefore, we approximate

$$K_1 \approx (-C_p)_b + 2 \left( \frac{\Gamma_{\text{peak}}}{2\pi U_{\infty} r_c} \right)^2$$

---

\*A flat plate with circular leading edge.

4.3.2.3 Sharp-Edged Disk. Arndt<sup>131,138</sup> has shown

$$K_i \approx 0.44 + 0.0036 R_D^{1/2} \quad (4.113)$$

where  $R_D$  is the Reynolds number based on the diameter of the disk  $D$ . This formula was derived using Equation (4.107), appropriately adjusted to account for a vortex structure superimposed on the mean flow:

$$K_i = -(C_p)_{\min} + 2 \left( \frac{\Gamma}{2\pi r_0 U_\infty} \right)^2$$

The minimum pressure coefficient occurs at the "leeward" side of the disk. According to Kermeen, McGraw, and Parkin<sup>143</sup>  $-(C_p)_{\min} = 0.44$ . Arndt<sup>131,144</sup> assumed laminar flow on the "windward" side of the disk to determine a rate of steady shedding of circulation,  $d\Gamma/dt$ , from the edge. The shed vorticity was assumed to roll into toroidal vortices in the wake, at a frequency  $f_s$   $D/U_\infty \sim 10$ . The amplitude of the circulation in each vortex is then given by

$$\Gamma = \frac{d\Gamma}{dt} \frac{1}{f_s}$$

The vortex radius  $r_0$  Arndt related to the thickness of the laminar boundary layer on the face of the disk. Arndt's semiempirical Equation (4.113) agreed closely with experimental data of Kermeen, McGraw, and Parkin.<sup>143</sup> For  $R_D > 2 \times 10^5$ ,  $K_i \approx 2$ .

4.3.2.4 Orifice Plates. Numachi, Yamabe, and Oba<sup>145</sup> have conducted a comprehensive series of measurements which were directed at establishing the effect of cavitation on orifice coefficients. Results have shown  $K_i \approx 2.5$  based on the pressure at the downstream (corner) tap and the average velocity through the orifice. The orifice diameter to pipe diameter ratio was between 0.224 and 0.633 with  $R_D \sim 4 - 25 \times 10^4$ . In the case of flow-nozzles and sharp orifice plates with flange taps, Bell (discussor to Numachi et al.<sup>145</sup>) reported  $K_i \sim 1$  to 1.6.



4.3.2.5 Free Jets. Cavitation in turbulent jets occurs in the free shear layer, which, as discussed in Chapter 3, has turbulence intensities on the order of  $0.16 U_J$  at distances  $y_1 < 8D$ . Measurements of Rouse, quoted by Knapp et al.,<sup>4</sup> show  $K_i \sim 0.55$  to  $0.70$ .

Using Equation (4.99) the expected cavitation inception index would be on the order of

$$K_i \approx \{-C_p(\tau)\}_{\min}$$

under a hypothesis that  $p_{g_0} \sim 0$ . The minimum value of the unsteady pressure coefficient that is required to induce cavitation would be some multiple, for example,  $m$ , of the root-mean-square value. Thus, from Equation (7.70) we may write

$$K_i \approx 3m \frac{\overline{u_i^2}}{U_J^2} \\ \approx 0.08m$$

Assuming that the turbulent pressures have a Gaussian distribution about the mean, there will be a small probability (actually 0.0013) that there are pressure fluctuations less than  $-\overline{3p}^{1/2}$  and for  $m \approx 3$

$$K_i \approx 0.3$$

This value is approximately 1/2 the measured value just cited, but it is nearly equal to the value that is inferred from noise measurements of Jorgensen.<sup>146</sup> This suggests that pressure fluctuations are as much or more than three times the root-mean-square value and occurring infrequently.

Recently Arndt<sup>131</sup> has found an empirical relationship between  $K_i$  and the Reynolds stress,  $\overline{u_1 u_2}$ , in the shear layer. Hypothesing the proportionality

$$\overline{u_1^2} \sim \overline{u_s u_n} = \overline{u_1 u_2}$$

for free shear flows, he found that measured indices collapse on the curve

$$K_i \approx 16 \frac{\overline{u_1 u_2}}{U_J^2}$$

$$\approx 16 \frac{\overline{u_1^2}}{U_J^2}$$

for jets<sup>4</sup> and wakes<sup>143</sup> (in which the free-stream velocity  $U_\infty$  replaces the jet efflux velocity  $U_J$ ), as shown in Figure 4.28.

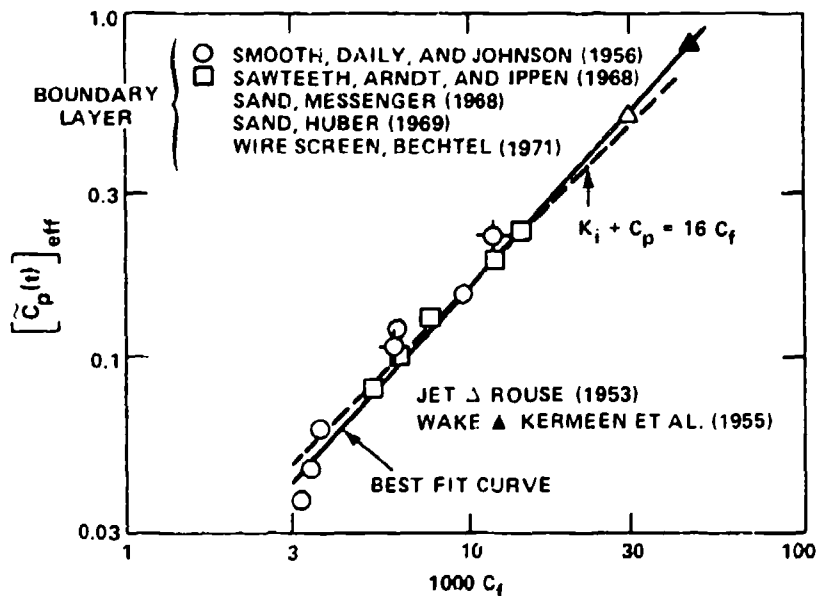


Figure 4.28 - Compilation<sup>138</sup> of Incipient Cavitation Indices for a Variety of Turbulent Shear Flows. Indices are a Function of an Effective Shear Coefficient:

$$C_f = \tau_w / \frac{1}{2} \rho_o U_\infty^2 \quad \text{- Boundary Layers}$$

$$= \frac{\overline{u_1 u_2}}{U_J^2} \quad \text{- Jets, Wakes, } C_p \approx 0$$

4.3.2.6 Cavitation in a Turbulent Boundary Layer. Incipient bubble cavitation was observed in the boundary layers of flat surfaces by Daily and Johnson<sup>147</sup> and later by Arndt and Ippen<sup>48,148</sup> on rough walls. On smooth walls Daily and Johnson observed that bubble nuclei were distributed throughout the boundary layer, with most at about  $y/\delta \approx 0.6$ , where  $\delta$  is the boundary layer thickness. The location of incipient cavitation, however, appeared to be distributed about  $y/\delta \approx 0.25$ , with none occurring at the wall where the rms turbulence intensity is largest. This led to the hypothesis that the inception was related to the presence of large vortical eddies into the cores of which bubbles become trapped. A similar observation was made later in rough wall boundary layers in the same, or similar, facility by Arndt and Ippen<sup>48,148</sup> who also observed incipient cavitation at  $y/\delta \approx 0.6$ , but the largest density of nuclei was near the wall  $y \ll \delta$ . In both sets of experiments the total gas content in the water was high; supersaturated in the case of Daily and Johnson<sup>147</sup> (so that both vaporous and gaseous cavitation were observed depending on the initial bubble size) and 80 percent saturated in the case of Arndt and Ippen.<sup>48,148</sup> Arndt<sup>131</sup> has subsequently found the cavitation inception can be displayed as in Figure 4.28 which summarizes the results within the context of the definition of Equation (4.100) or (4.107). If the boundary layer is turbulent at the minimum pressure point, and there is an ample concentration of free bubble nuclei, then

$$K_i = \left( -C_{p_{\min}} \right) + \left| \tilde{C}_p(t) \right|$$

where the  $\tilde{C}_p(t)$  is the local deviation of pressure from the static value at the wall  $\left( -C_{p_{\min}} \right)$  caused by the turbulence. As in Equation (4.94), this fluctuating coefficient has a maximum value,

$$\left[ \tilde{C}_p(t) \right]_{\text{eff}} \propto \tilde{C}_{p_{\text{rms}}} \sim 5.6 C_f$$

where

$$C_f = \frac{l_w}{2 \rho_c U_w^2}$$

which is a general proportionality to  $C_f$ . Therefore, adopting

$$\left[ \tilde{C}_p(t) \right]_{\text{eff}} \propto \tilde{C}_{p_{\text{rms}}} \approx \propto C_f$$

the inception condition determined by Arndt for smooth and rough-wall boundary layers becomes, therefore,

$$K_i \sim -C_{p_{\text{min}}} + 16 C_f \quad (4.114)$$

indicating that  $[\tilde{C}_p(t)]_{\text{eff}} \sim 2$  to  $3 [C_p]_{\text{rms}}$ . Figure 4.28 shows that bubble cavitation in shear layers appears to behave in a nearly universal way where either  $C_f$  or  $-\overline{u_1 u_2} / U_J^2$  expresses the effective strengths of the pressure fluctuations. Note that for Gaussian pressure statistics there is a probability of 0.0013 that pressures occur less than  $3 p_{\text{rms}}$ .

Other observations made by Arndt and Ippen were the cavitation bubble histories two of which are shown in Figure 4.29. The linear increase of radius with time suggests that during this portion of the life time, the bubble behaves in the appropriate form of Equation (4.97),

$$\left( \frac{\dot{R}}{U_\infty} \right) \sim \left( \frac{2}{3} \right)^{1/2} \left( \frac{-\tilde{C}_p(t) - K_i}{2} \right)^{1/2} \quad (4.115)$$

where  $-\tilde{C}_p(t)$  is nearly constant for a length of time  $t_g$ . The value of  $t_g$ , shown in Figure 4.29 corresponds roughly to a dimensionless time, using parameters of the flow, of

$$\frac{t_g \delta}{U_\infty} \sim 1$$

It is shown later in Section 7.2 (Figure 7.12) that the time  $\tau_e$  it takes for an eddy to decay to  $1/e$  of its initial value (as measured by velocity fluctuations normal

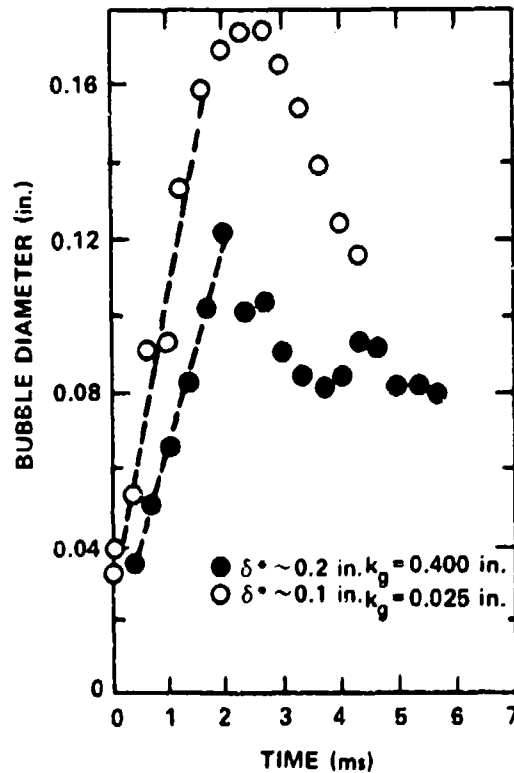


Figure 4.29 - Typical Bubble Growth Observation in a Turbulent Boundary Layer,<sup>48</sup>  $k_g$  = Roughness Height,  $\delta^*$  = Displacement Thickness

to the wall) is approximately  $\tau_e \delta / U_\infty \sim 1$ . Thus, the hypothesis leading to Equation (4.105) that incipient cavitation in shear-flow turbulence is due to bubble nuclei swept into strong vortices convected with the mean flow appears to be somewhat supported.

An alternative earlier relationship for cavitation inception scaling in boundary layers has been given by Oshima,<sup>149</sup> which is based on the hypothesis that the maximum size to which a bubble grows is proportional to the displacement thickness (see Section 7.2) of the boundary layer. Thus  $L$  in Equation (4.97) becomes, instead, a boundary-layer thickness. This yields a condition of similitude of static equilibrium that requires

$$\left\{ -K - C_P - \frac{4S}{\rho_o R U_\infty^2} + \frac{P_{g_o}}{\frac{1}{2} \rho_o U_\infty^2} \left( \frac{R_o}{R} \right)^{3\gamma} \right\} R^{2m} = \text{constant}$$

The exponent on Reynolds number is determined by the properties of the boundary layer displacement thickness,  $\delta^*$ , which behaves as

$$\frac{\delta^*}{L} \sim R_L^{-m}$$

For turbulent boundary layers  $m \sim 0.2$ , therefore, Oshima's rule reduces to

$$[-K-C_p]^{0.4} = \text{constant} \quad (4.116)$$

in cases of small gas concentration and small surface tension pressures, Oshima's hypothesis is based on the observation of Daily and Johnson<sup>147</sup> that nucleating bubbles near the wall grow to a size about equal to a boundary layer displacement thickness. However, contradictory evidence now seems prevalent in the literature. In other cases<sup>14,116</sup> it is known that Equation (4.53) applies (with the pressures being determined from the static pressure distribution) for bubbles growing near the point of minimum pressure where the growth time is determined by convection velocity of bubble and the chordwise length of the rarefied zone. Also, we have already cited Arndt's later observations of bubble growth in turbulent boundary layers which suggest that the maximum bubble size is not proportional to the displacement thickness. Figure 4.29 shows, for example, that the larger bubble radius was observed on the less rough wall with the smaller value of  $\delta^*$ . Although this evidence is not conclusive, it does indicate that Oshima's relationship may not be universally applicable. Finally, agreement between Equation (4.116) and the measurement of Kermeen et al.<sup>143</sup> was shown to be reasonably good by Oshima. However, it is now believed that those measurements were influenced by laminar separation rather than turbulent flow. Nevertheless for that flow type, the thickness of the separation zone controls the bubble size and that thickness also decreases as  $R^{-m}$ . Therefore, an analytical model analogous to Equation (4.115) may well apply to those cases involving separation.

4.3.2.7 Separating Laminar Boundary Layers. The preceeding examples of incipient cavitation have all dealt with the types that are frequently described as "traveling

bubble" cavitation. We now address sheet cavitation that occurs on surfaces beneath boundary layers which are laminar or that are transitional between laminar and turbulent. The boundary layers of this type occur at thin leading edges of lifting surfaces and generally occur at low-to-moderate Reynolds number. They are sensitive to Reynolds number,<sup>150</sup> wettability and roughness of the surface of the body,<sup>66,151-154</sup> free-stream turbulence,<sup>78,155</sup> vibration of the surface, and possibly acoustic noise in the environment. On the other hand, fully turbulent boundary layers occurring at generally larger Reynolds number for the same body shape are not nearly so sensitive to these stimuli. Historically, it has often been observed, in scale-model testing, that discrepancies exist between measurements of cavitation inception and the appearance of cavitation on the same model in various facilities and between geometrically similar bodies of different size, (recall Figure 4.23). However, a recognition of any relationship between the condition of noncavitating viscous flow and cavitation inception did not really come about until relatively recently. This is in spite of one of the most well known of the early observations by Kermeeen et al.,<sup>143</sup> that the dynamics of incipient cavities was influenced by the noncavitating fluid dynamics. The incipient cavitation observed, was then reckoned to have been caused in a laminar-to-turbulent transition zone, and the maximum bubble size was believed to have been determined by the displacement thickness of the boundary layer. More recently, observations have been made of the separated flow on the same shape of body as well as of the corresponding incipient cavitation by Arakeri and Acosta,<sup>156</sup> Gates,<sup>78,155</sup> and van der Meulen.<sup>66,151,152</sup> The situation that occurs beneath a limited region of separated flow ("short-bubble") at a leading edge is as schematically illustrated in Figure 4.30, drawn with the aid of van der Meulen's photographs. Downstream of the point of minimum pressure, Figure 4.30a, the laminar flow separates if the flow Reynolds number is less than the critical value for which the boundary layer becomes turbulent upstream of  $(-C_p)_{min}$ . The separation bubble that would occur is illustrated as a dividing streamline intersecting the body at "s." The free shear layer is laminar for a distance  $L_s$ , but becomes unsteady due to hydrodynamic instabilities (see Chapter 3). In this region of transition, the flow is irregular and the fluctuating surface pressures in the region have been observed to be as much as three times more intense than those that would be measured downstream in the fully developed boundary layer.<sup>157,158</sup> Also, the incipient bubble

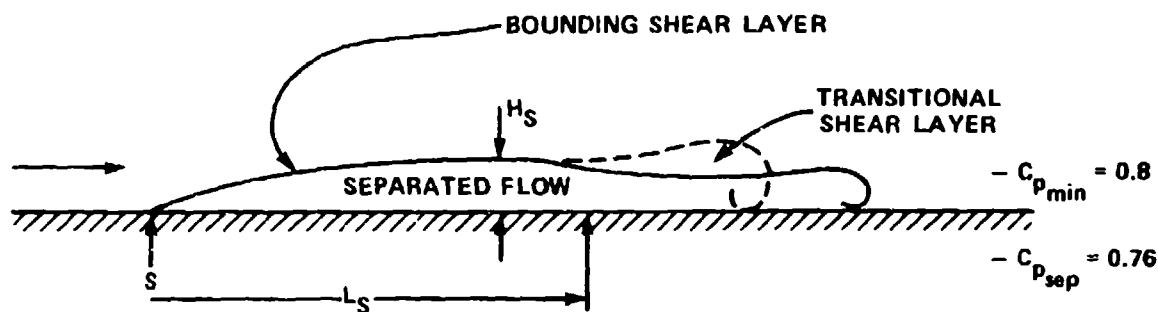


Figure 4.30a - Separated Flow Pattern, Noncavitating Flow

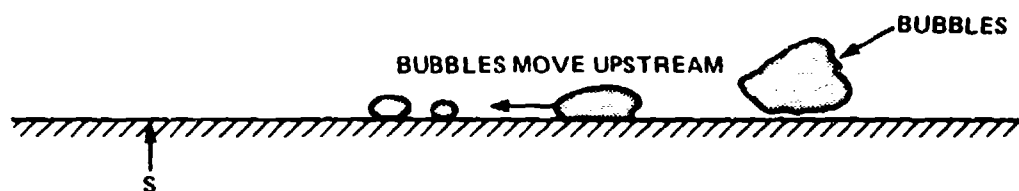


Figure 4.30b - Incipient Cavitation,  $K = K_1 = 0.6$

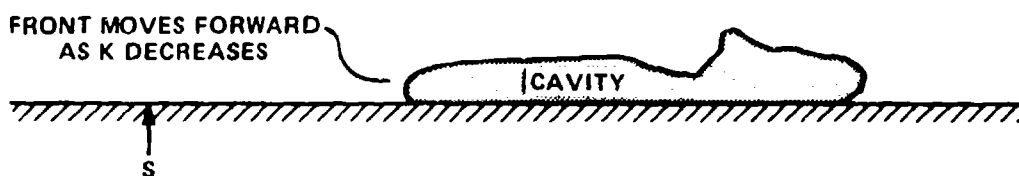


Figure 4.30c - Advancing Cavitation,  $K = 0.59$

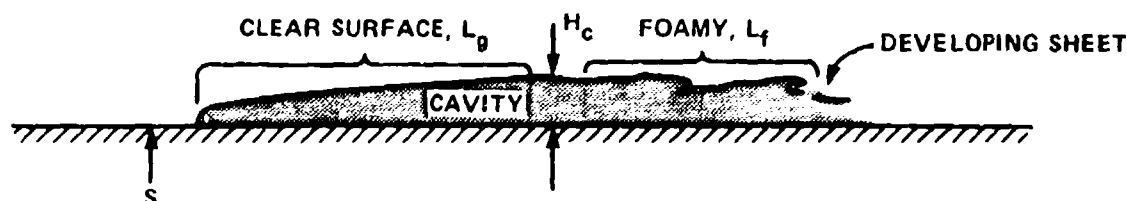


Figure 4.30d - Advancing Cavitation,  $K = 0.56$

Figure 4.30 - Progression of Cavitation from Incipient Bubbles to Sheet

observed near the wall<sup>66,143,152,156</sup> not in the stream, which suggests that the fluctuating pressures are locally most intense at the wall rather than in the than in the stream. (Recall that this is in contrast to the observations made by turbulent boundary layers where the incipient bubbles appear away from the wall.)



Once the bubbles form in the transitional zone, they grow to a critical size, of approximately the height of the shear layer then they migrate slowly upstream<sup>159</sup> against the flow, Figure 4.30b. Some become entrained by the free shear layer and are subsequently expelled into the free-stream. With further reduction of  $K$  from the incipient value, the smaller bubbles coalesce as they move upstream forming a distinct leading edge of a larger cavity with a clear-surface leading edge and a "foamy" irregular trailing edge, Figures 4.30c and 4.30d. This cavity extends laterally along, or around, the body like a strip, e.g., Figure 4.23, numbers 5 and 9. The cavitation develops further as the cavitation index is reduced so that the leading "edge" of the cavity moves as far forward as point S, while the trailing "edge" continues to progress downstream. This type of cavitation was also observed on an oscillating hydrofoil by Shen and Peterson;<sup>158</sup> the oscillations in angle of attack bringing about a temporal variation in the extent of the disordered region of the cavitation zone.

The hydrodynamic conditions favoring cavitation inception downstream rather than at the minimum pressure point will include both low static pressure and low dynamic pressure so that

$$\left[ -C_{p_t} + |\tilde{C}_p(t)| \right]_{\min} \leq -C_{p_{\min}}$$

where  $C_{p_t}$  is the static pressure coefficient downstream of separation and near the point of breakdown of the laminar shear layer. For a more extensive separation zone, the recirculating flow of separation occupies a major fraction of the body length (or chord), the outer streamlines adjust to the presence of the separation zone and the minimum pressure coefficient becomes larger than that occurring in fully attached (or potential) flow. An example of this can be seen in the next chapter, in Figure 5.11. In this case, as shown by Alexander<sup>160</sup> and Casey,<sup>161</sup> the cavitation is delayed, i.e.,

$$\left( -C_{p_{\min}} \right)_{\text{non-sep}} > K_i \approx - \left( C_{p_{\min}} \right)_{\text{sep}}$$

Returning to the case of "short-bubble" separation, Equation (4.106) gives the incipient index as, approximately,

$$K_i \approx -C_{p_t} + \frac{|p(t)|_{\text{eff}}}{q} \geq [-C_p]_{\text{min}} \quad (4.117)$$

for large-enough bubble nuclei.

A quantitative correspondence between  $[p(t)]_{\text{eff}}$  in Equation (4.117) and the large amplitude hydrodynamic pressures in the reattachment zone has, so far, not been obtained in spite of a systematic series of wind and water-tunnel measurements by Huang and Santelli.<sup>162</sup> Their work led to a near equality between  $K_i$  and  $C_{p_t}$  in spite of a relatively large value of  $p^2 / q$  in their experiment. It is quite possible that the delicate sensitivity of laminar flow to the many environmental influences listed at the beginning of this section prevented the existence of strict flow similarity in the wind- and water-tunnel experiments used. Gates and Acosta have examined these types of flow sensitivities in a systematic way.<sup>78,155</sup>

**4.3.2.8 Isolated Roughness Elements.** Isolated elements which protrude into the boundary layer cause local flow separation and attendant low pressures. These protrusions serve as cavitation sites especially if they occur at locations near the point of minimum pressure on the body, the locally-low pressures they induce may be regarded as perturbations on the potential flow static pressure distribution. The effect has been extensively evaluated by Holl,<sup>163</sup> Bohn,<sup>164</sup> and Arndt et al.<sup>165</sup>

The local perturbation pressure will depend upon the local velocity incident on the protrusion which is a function of the height of the protrusion  $k_g$ , relative to the local height of the boundary layer  $\delta$ . The velocity  $U$  will also depend on the local free-stream velocity just outside the boundary layer  $U_s$ , that also determines the local static pressure. The absolute low pressure, which occurs on the leeward side of the protrusion, will then be of the form

$$p \sim P - \frac{1}{2} \rho_o U_s^2 C_p \left( \frac{U_s \delta}{v}, \frac{k_g}{\delta} \right) \quad (4.118)$$

where  $U_s$  is the mean velocity at the outer edge of the boundary layer and  $c_p$  is a function of both the local Reynolds number  $U\delta/\nu$  and the ratio  $k_g/\delta$ . These factors account for the fact that the perturbation pressure will depend upon the relationship between velocity profile in the boundary layer and the size of the roughness. Bohn,<sup>164</sup> however, has also included the shape factor of the boundary layer as an additional parameter, but with little improvement in the resulting correlation. The local pressure coefficient is, from Equation (4.118),

$$\frac{p - p_\infty}{\frac{1}{2} \rho_o U_\infty^2} = \frac{p - p_\infty}{\frac{1}{2} \rho_o U_\infty^2} - \frac{U_s^2}{U_\infty^2} \bar{c}_p \left( \frac{U_s \delta}{\nu}, \frac{k_g}{\delta} \right)$$

Introducing the definition of the static pressure coefficient, we find

$$\frac{p - p_\infty}{\frac{1}{2} \rho_o U_\infty^2} = C_p - (1 - C_p) \bar{c}_p \left( \frac{U_s \delta}{\nu}, \frac{k_g}{\delta} \right)$$

which is equivalent to our


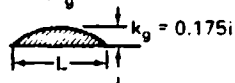
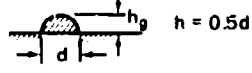
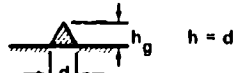
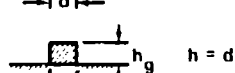
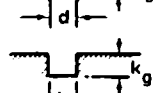
$$= C_p - (1 - C_p) \left[ \bar{C}_p(t) \right]_{\text{eff}}$$

Therefore, the condition for vaporous cavitation inception will be from Equation (4.48)

$$K_i = \left\{ -C_p + (1 - C_p) \left[ \bar{C}_p(t) \right]_{\text{eff}} \right\}_{\min} \quad (4.119)$$

where  $U_s = U_\infty (1 - C_p)$  and where  $[K + C_p]_{\text{crit}}$  is taken as zero for simplicity. Equation (4.119) for isolated elements, contrasts with Equation (4.113) for distributed roughness.

Values for  $\bar{C}_p$  shown in Figure 4.31 were empirically determined. It is seen that the points fall into classes which depend upon the shape of the body.

SYMBOL	IRREGULARITY	FLOW DIMENSIONS	DATA SOURCE	a	b	c	
△	TRIANGLES	TWO	HOLL. 1960	0.361	0.196	0.152	
○	CIRCULAR ARCS	TWO	HOLL. 1960	0.344	0.267	0.041	
▲	HEMISPHERES	THREE	BENSON 1966	0.439	0.298	0.0108	
●	CONES	THREE	BENSON 1966	0.632	0.451	0.00328	
□	CYLINDERS	THREE	BENSON 1966	0.737	0.550	0.00117	
└	SLOTS	TWO	BOHN 1972	0.041	0.510	0.000314	

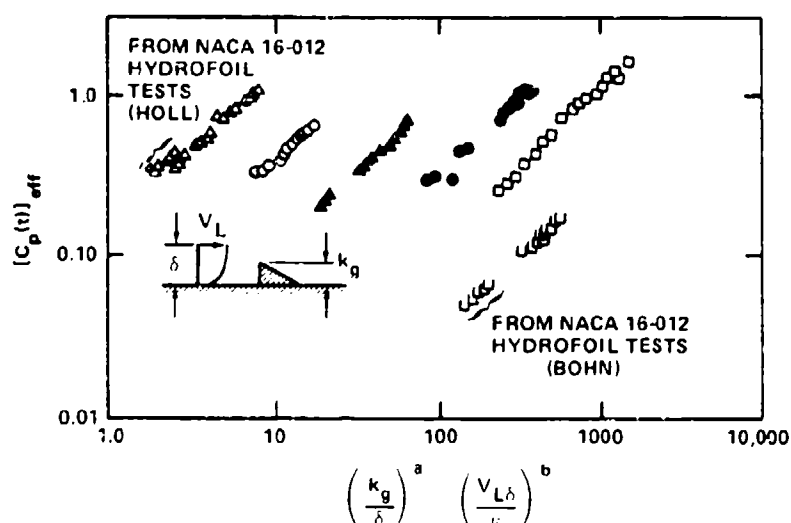


Figure 4.31 - Limited Cavitation Number for Isolated Irregularities<sup>165</sup>

Comparison of Figures 4.28 and 4.31 will show that the incipient index will be more greatly increased for isolated three-dimensional protrusions than for continuous roughnesses of either a random or geometric pattern.

## 4.4 HYDRODYNAMIC CAVITATION NOISE

### 4.4.1 Theoretical Spectrum of Single-Bubble Cavitation Noise

4.4.1.1 General Dependence on Stages of Bubble History. In dealing with cavitation noise, we are really concerned with noise resulting from the time variation of voids in the liquid. Since there are volume changes, the noise resulting is monopole governed by Equation (2.20) which is rewritten here for the sound pressure far from the bubble  $r \gg R$ , where  $R$  is the radius of the bubble,\*

$$p_a(r, t) = \frac{\rho_o \ddot{V}\left(t - \frac{r}{c_o}\right)}{4\pi r} \quad (4.120)$$

Figure 4.15 illustrates the volume history of a hydrodynamically induced cavitation bubble and it can be deduced from this that the volume acceleration will be largest at times when the radial velocity changes direction, i.e., at the times of the minimum radius. Figure 4.32 illustrates this dependence, using the volume history of the type observed by Knapp and Hollander.<sup>90</sup> The maximum sound pressure is attained in a time interval of less than  $\tau_c/2$  that is centered on the instant of collapse. The peak sound pressure would be expected to depend on the time scale  $\tau_c$  which, by Equation (4.70), depends upon the relative hydrostatic pressure  $P(r) - P_v$  and the maximum bubble radius. Equation (4.120) can then be made dimensionless on

$$\frac{p_a\left(\frac{r}{R_M}, \frac{t}{\tau_c}\right)}{P(r)} \frac{r}{R_M} = \left\{ \frac{\partial^2 \left( \frac{v}{R_M^3} \right)}{\partial \left( \frac{t}{\tau_c} \right)^2} \right\}$$

or

$$\frac{p_a\left(\frac{r}{R_M}, \frac{t}{R_M} \left( \frac{\rho_o}{P(r)} \right)^{1/2} \right) r}{P(r) R_M} = \left\{ \frac{v\left(\frac{t}{R_M} \left( \frac{\rho_o}{P(r)} \right)^{1/2} \right)}{R_M^3} \right\}'' \quad (4.121)$$

---

\*Equation (4.120) could also be written directly from Equation (4.13) by letting  $r$  replace  $R \ll r$ , then  $P(R) - P(r, t)$  represents the acoustic fluctuating pressure far from the bubble wall.

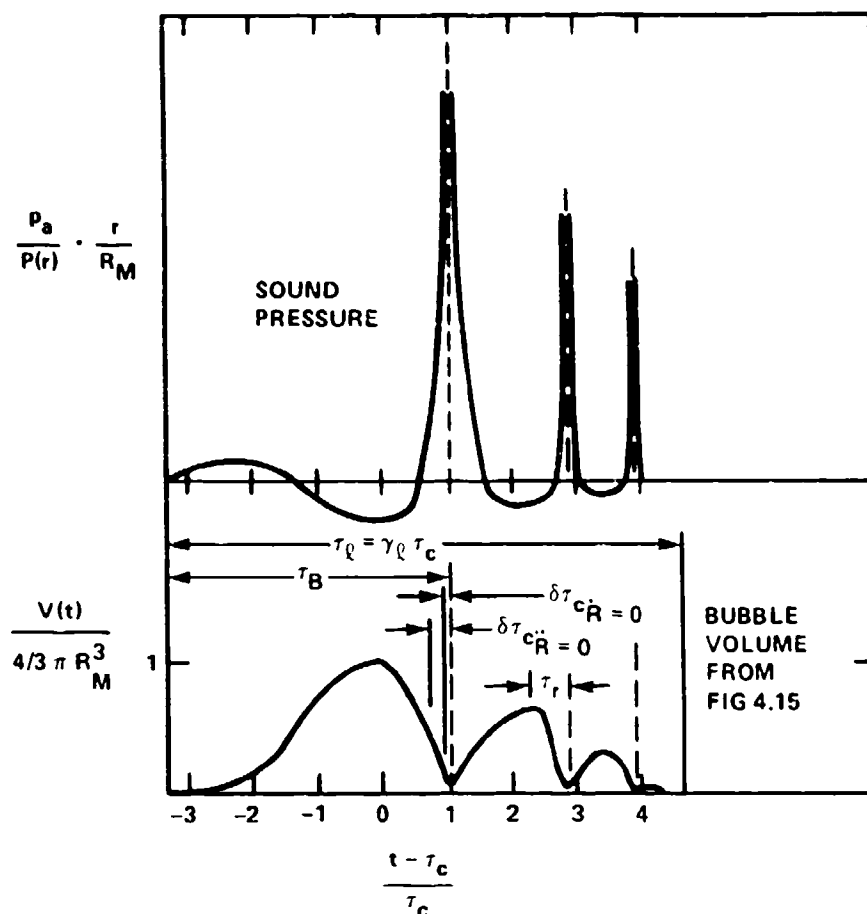


Figure 4.32 - Sound Pressure and Volume of a Single Cavitating Bubble with Two Rebounds. Also Shown are Characteristic Times Appropriate for Equations (4.70), (4.77), and (4.85).

where the notation  $f''$  indicates differentiation with respect to the reduced time

$$\frac{t}{R_M} \left( \frac{\rho_0}{P(r)} \right)^{1/2}$$

It is assumed that  $P_v \ll P(r)$ . In the following,  $P(r) = P_0$  is taken as a constant local static pressure where the bubble collapses.

In the frequency domain, the Fourier transform (Equation (2.27)) of the acoustic pressure is given by

$$p_a(r, \omega) = \frac{\rho_o}{4\pi r} \ddot{v}(\omega) e^{ik_o(r-a)} \quad (4.122)$$

where (Equation (2.105)),

$$\begin{aligned} \ddot{v}(\omega) &= \frac{1}{2\pi} \int_{-\infty}^{\infty} e^{i\omega t} \frac{d^2 v(t)}{dt^2} dt \\ &= -\frac{\omega^2}{2\pi} \int_{-\infty}^{\infty} e^{i\omega t} v(t) dt \end{aligned} \quad (4.123)$$

The auto spectrum of the sound pressure is quadratically related to  $p_a(r, \omega)$  by Equation (3.39), and

$$\tau_c \dot{\Phi}_{pa}(r, \omega) = S_p(r, \omega) \quad (4.124)$$

where  $\tau_c$  is the duration of the pulse shown in Figure 4.32.

Following Equation (4.120) these spectrum functions can be rewritten in a pair of dimensionless forms that will be used interchangeably. Letting

$$\tau_c \approx R_M \left( \frac{\rho_o}{P_o} \right)^{1/2} \quad (4.125)$$

the alternative nondimensional spectrum functions are

$$\frac{S_p(r, \omega) r^2}{P_o \rho_o R_M^4} = \tilde{S}_p \left( \frac{r}{R_M}, \omega \tau_c \right) \quad (4.126)$$

and

$$\frac{\dot{\Phi}_{pa}(r, \omega) r^2}{P_o^{3/2} \rho_o^{1/2} R_M^3} = \tilde{\Phi}_{pa} \left( \frac{r}{R_M}, \omega \tau_c \right) \quad (4.127)$$

and these are related by

$$\tilde{S}_p \left( \frac{r}{R_M}, \omega \tau_c \right) = \tau_c R_M \left( \frac{\rho_o}{P_o} \right)^{1/2} \tilde{\phi}_{pa} \left( \frac{r}{R_M}, \omega \tau_c \right)$$

Fitzpatrick and Strasberg<sup>106</sup> were the first to determine the frequency spectrum of the radiated sound from a cavitating bubble. Using an illustrative pressure-time history very much like that shown in Figure 4.32, but with peak pressure pulses taken equally for all three collapses, they were able to perform the necessary Fourier transforms. The resulting sound spectrum is shown in Figure 4.33. We will, in the following discussion, identify certain portions of the bubble history which contribute to corresponding frequency ranges.

To perform the calculation, some elements of the time history of the bubble volume may be segmented into a sequence of time intervals of duration  $\Delta t_n$ , i.e.,

$$v(t) = \sum_{n=0}^N v_n(t) u(t, \Delta t_n) \quad (4.128)$$

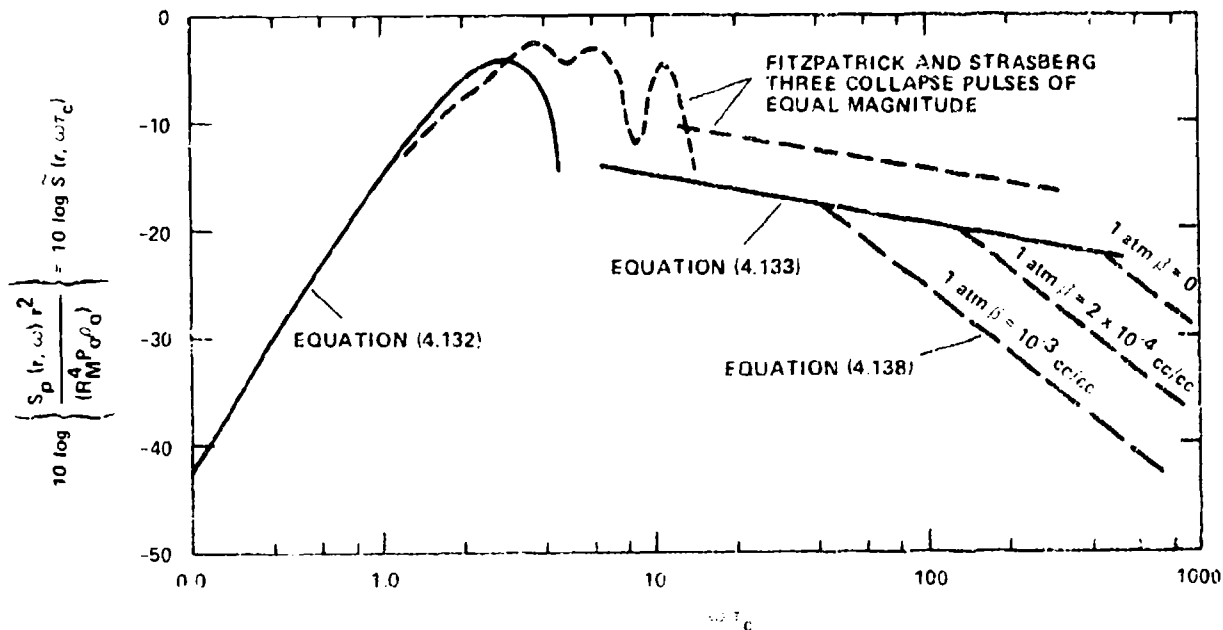


Figure 4.33 - Ideal Spectrum Function for the Sound Pressure Generated by a Single Cavitation Bubble with a Volume History such as Shown in Figure 4.32



where the unit function  $u(t, \Delta\tau_n)$  is unity only within the interval  $|t - t_n| < \Delta\tau_n$  and zero otherwise. The function  $v_n(t)$  is a power-law expression used to approximate the bubble motion in the interval  $\Delta\tau_n$ . Appendix A illustrates this calculation. Basically, if  $v_n(t)$  is of the form

$$\begin{aligned} v_n(t) &= a_n (t - t_n)^m & t > t_n \\ &= 0 & t < t_n \end{aligned} \quad (4.129)$$

Then, as long as  $\omega \Delta\tau_n > 1$ , as derived in the appendix,

$$V_n(\omega) \approx - \frac{a_n \Gamma(m+1)}{2\pi (1\omega)^{m+1}}, \quad \frac{\Delta\tau_n \omega}{2} > 1 \quad (4.130)$$

We will now consider the specific frequency ranges in Figure 4.31 that are commensurate with the various events in the bubble history highlighted in Figures 4.15, 4.19 and 4.32 and derived in Section 4.2.5.

1. low frequencies:  $\omega\tau_c < 1$ ,  $\omega\tau_\lambda < 1$

In this case, Equation (4.123) gives only

$$\begin{aligned} \ddot{V}(\omega) &\approx - \frac{\omega^2}{2\pi} \int_0^\infty V(t) dt \\ &= \frac{-\omega^2 \tau_\lambda^2}{2\pi} \bar{V}(t) \end{aligned}$$

Therefore,

$$S_p(r, \omega) \approx \frac{\omega^4 \tau_\lambda^2 \bar{V}^2}{32\pi^3 r^2} \quad (4.131)$$

where  $\bar{V} = \int_0^\infty V(t) dt \approx 1.3 V_i \tau_c$  and  $V_M$  is the volume of the bubble before collapse.

The factor 1.3 is indicated by the  $V(t)$  shown in Figure 4.32.

2. Frequency of maximum intensity,  $\omega(\delta\tau_c)''_{R=0} \ll \omega\tau_c < \omega\tau_l$

In this case, the details of collapse are unimportant and the initial bubble life can be approximated by

$$V(t) = V_m \cos \left[ \left( \frac{t-\tau_c}{\tau_c} \right) \frac{\pi}{2} \right]$$

for  $-\tau_c < t - \tau_c < \tau_c$ .

Thus,

$$V(\omega) \approx \frac{V_m \tau_c}{2} \frac{\cos \omega\tau_c}{\left( \frac{\pi}{2} \right)^2 - (\omega\tau_c)^2}$$

so that,

$$\frac{S_p(r, \omega) r^2}{R_{MOP}^4} \approx \frac{\pi}{18} (\omega\tau_c)^4 \left[ \frac{\cos \omega\tau_c}{\left( \frac{\pi}{2} \right)^2 - (\omega\tau_c)^2} \right]^2 \quad (4.132)$$

There is also a contribution from rebounds, which add to  $V(\omega)$ , of the form

$$V_{r_n} \tau_{r_n} \frac{\cos \frac{\omega\tau_{r_n}}{2}}{\left( \frac{\pi}{2} \right)^2 - \left( \frac{\omega\tau_{r_n}}{2} \right)^2} e^{-i\omega[2\tau_c - (n-1)\tau_{n-1}]}$$

where  $\tau_{r_n}$  are collapse times of successive rebounds. Because of the phase factor in the rebound contribution, there can be certain interferences at some frequencies in the vicinity of the maximum spectrum level at  $\tau_c \omega \sim \pi$ . Figure 4.33 shows an example of the influence of three equal rebounds on the spectrum, as calculated by Fitzpatrick and Strasberg.<sup>106</sup>

3. Moderate frequencies:  $\omega\tau_c > \omega(\delta\tau_c)_{R=0} > \omega\tau_c > 1$

This frequency range is limited by the segment of the collapse phase which is controlled by the constant bubble wall velocity as considered in Section 4.2.5. In this range we combine the approximate function Equation (4.130) with Equation (4.81), multiplied by 1.25 so that it would agree numerically with Rayleigh's result, to yield

$$|V(\omega)| = \frac{2V_m \tau_c}{(2\pi) (\omega\tau_c)^{1/5}}$$

and, in the form of Equation (4.127)

$$\frac{S_p(r, \omega) r^2}{R_M^4 \rho_o p_o} = \frac{2}{9\pi} (\omega\tau_c)^{-2/5} \quad (4.133)$$

4. High frequencies controlled by noncondensible gas:

$$\omega\tau_c > \omega(\delta\tau_c)_{R=0} > 1, \quad \omega\tau_c \gg 1$$

In this case, Equations (4.75) and (4.130) yield

$$|V_n(\omega)| = \frac{V_M \tau_c}{16\pi} \cdot \left(\frac{R_m}{R_M}\right)^3 \left(\frac{\tau_c}{(\delta\tau_c)_{R=0}}\right)^2 \frac{720}{(\omega\tau_c)^7}$$

and

$$\frac{S_p(r, \omega) r^2}{R_M^4 \rho_o p_o} = 3.6 \times 10^5 \left(\frac{R_m}{R_M}\right)^6 \left(\frac{\tau_c}{(\delta\tau_c)_{R=0}}\right)^4 (\omega\tau_c)^{-10} \quad (4.134)$$

$$\text{for } \omega(\delta\tau_c)_{R=0} \gg 1$$

This time constant is given by Equation (4.77). Equation (4.134) shows a rapid decrease of the spectrum level with frequency and represents the existence of an upper frequency limit on the spectrum. This band-limiting is an indicator that an upper frequency limit ensures that the spectrum represents an acoustic pulse of finite energy. A rough numerical estimate of  $(\delta\tau_c)_{R=0}$  for a partial pressure of gas in the bubble at maximum radius of  $P_g/P(r) \sim 10^{-3}$ , using the values of  $R_m/R_M$  from Figure 4.18 ( $\gamma=1.4$ ), is

$$\frac{\tau_c}{(\delta\tau_c)_{R=0}} \approx 6 \times 10^3$$

This means that when  $\omega\tau_c > 6000$ , the sound spectrum will be band-limited.

4.4.1.2 Influence of Compressibility of the Liquid. Equation (4.120) for the sound pressure is valid only as long as the linear acoustic approximation applies (see Chapter 2). This requires that the acoustic particle velocity  $u_r$  is less than the speed of sound in the liquid. However, as Figure 4.20 shows, the maximum wall velocity will be comparable to the sonic velocity for relatively modest partial pressures of gas in the cavity. In the linear acoustic theory of Chapter 2, the acoustic pressure function  $r \cdot p_a$  was propagated at speed  $C_0$ . Following upon the discussion in Section 4.2.5, recall that when the particle velocities become nearly sonic, the acoustic pressure is propagated at speed  $C_0 + u_r$ . As the collapse progresses and the wall velocity increases, the resultant velocity  $C_0 + u_r$ , accordingly increases. This means that higher-velocity later waves propagate faster than the earlier ones. As the waves propagate, the wave front steepens with the result illustrated in Figure 4.34. The time derivative of the acoustic potential  $\dot{\phi}$  is shown for an empty bubble as a function of retarded time for three field points as well as at the wall of the bubble. If the wall velocity were entirely subsonic, the  $\dot{\phi}$  would be identical to  $p_a/C_0$  and pressure pulses at each field point would coincide with the pulse at  $r = R$ . As the wave develops, the motions induced at the final instant of collapse overtake those radiated just earlier resulting in a truncated saw-tooth pulse. The dotted lines illustrate how the original pulse would have been curled back on itself, if that were physically possible, because of the advanced

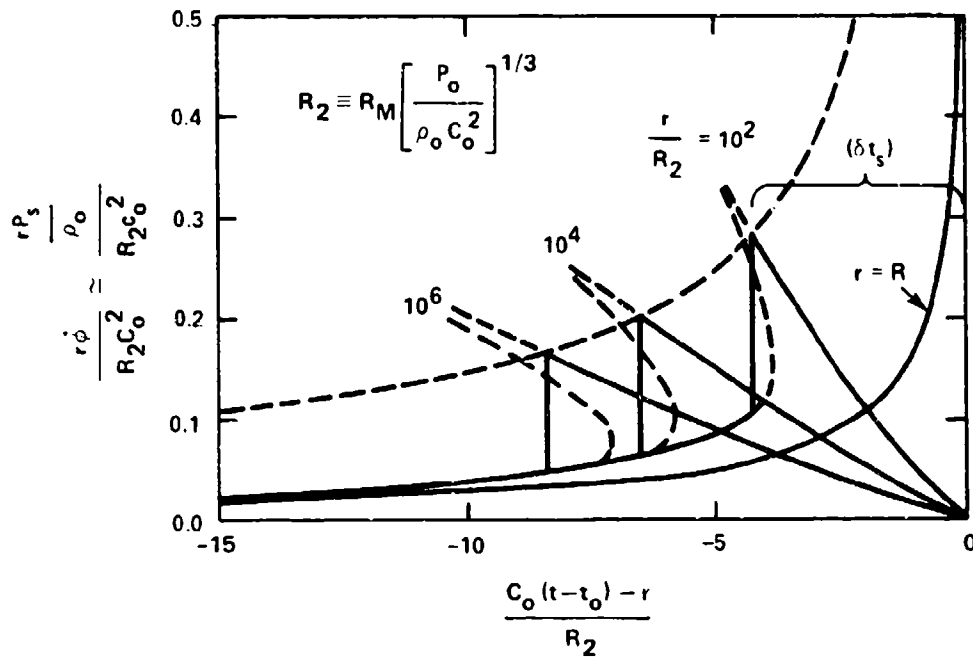


Figure 4.34 - Pressure and Shocks Radiated by a Vapor Cavity Collapsing in a Compressible Liquid

(Values according to Mellen,<sup>95</sup> curves from Fitzpatrick and Strasberg<sup>106</sup>)

arrival times of the faster pulse peak. The reduction in the pulse height continues as the pulse propagates. To construct this diagram Fitzpatrick and Strasberg<sup>106</sup> used calculations by Mellen<sup>95</sup> in which the particle paths were determined as a function of time and distance from the bubble.

The effect that this truncation of the pulse has on the noise spectrum can be deduced from the transform of a ramp function of amplitude  $p_0$  and temporal width  $(\delta t_s)$ . Thus

$$\begin{aligned}
 P(\omega) &= \frac{p_0}{2\pi} \int_0^{(\delta t_s)} e^{i\omega t} \frac{t}{(\delta t_s)} dt \\
 &= \frac{-p_0(\delta t_s)}{2\pi(\omega\delta t_s)^2} \left[ 1 - e^{i\omega(\delta t_s)} (i\omega(\delta t_s) - 1) \right]
 \end{aligned}$$

The corresponding spectrum function at high frequencies will behave as

$$S(r, \tau) \approx \frac{p_o^2}{(\omega \delta \tau_s)^2} \quad \omega(\delta \tau_s) > 1 \quad (4.135)$$

According to Figure 4.34,  $\delta \tau_s$  depends upon the distance from the bubble; at large distances it appears that

$$\frac{(\delta t)_s c_o}{R_M \left[ \frac{P(r)}{\rho_o c_o^2} \right]^{1/3}} \approx 9$$

which corresponds, approximately, to

$$\frac{(\delta t)_s}{\tau_c} \approx \left[ \frac{P(r)}{\rho_o c_o^2} \right]^{5/6} \quad (4.136)$$

Recall an alternative result had been discussed previously in Section 4.2, Equation (4.88), which suggests that the numerical coefficient (9 or 40) is really just a "ball-park" value. Adopting the value in Equation (4.136), the spectral form given by Equation (4.135) is expected to occur at frequencies

$$\omega \tau_c > \frac{1}{9} \left[ \frac{\rho_o c_o^2}{P(r)} \right]^{5/6}$$

In Figure 4.33 several lines are drawn which correspond to  $\rho_o c_o^2 = 20,000$  atmospheres for pure water and to other values of speeds of sound corresponding to bubbly mixtures of the indicated volumetric concentrations  $\beta$ . Equations (4.31) and (4.39) (Table 4.1) were used to calculate the speed of sound. It can be seen that moderate concentrations of free bubbles can influence dramatically the high frequency spectrum

levels. In water-tunnel facilities<sup>82,83</sup> volumetric concentrations of  $\beta < 10^{-7}$  may be expected in undersaturated water. As far as the cavitation noise spectrum is concerned, the liquid is essentially pure water.

Experimental evidence of the existence of shock waves has been reviewed by both Fitzpatrick and Strasberg<sup>106</sup> and by Ellis.<sup>120</sup> Generally the shocks had been observed and associated with spherical collapses of spark-induced bubbles, however, Ellis has also observed shock formation from nonsymmetrical bubbles collapsing on a surface, and from groups of bubbles. Such observations have not been made in hydrodynamically-induced cavitation, however. Evidence of the  $\omega^{-2}$  behavior in the acoustic spectrum has been deduced by Harrison<sup>111</sup> who observed on an oscilloscope wave traces of the time history of pressure pulses from hydrodynamically-induced cavitation in a venturi. Wave forms with the shape

$$p(t) = p_0 e^{-|t|/\alpha}$$

were observed and these have the temporal correlation

$$\overline{p(t)p(t+\tau)} = p_0^2 e^{-|\tau|/\alpha} \quad (4.137)$$

which gives the autospectral density

$$\phi_{pa}(\omega) = \frac{1}{2\pi} \frac{p_0^2 \alpha}{1+(\omega\alpha)^2} \quad (4.138)$$

where  $\alpha = \beta t_s$  is given by Equation (4.136).

#### 4.4.2 Simple Rules of Similitude

The spectral character of real cavitation noise is only crudely approximated by the theoretical spectrum of single-bubble noise. One of the earliest measurements to show this is that of Mellen,<sup>166</sup> whose result is reproduced in Figure 4.35. The cavitation was generated with a cylindrical rod rotated transversely to its axis;

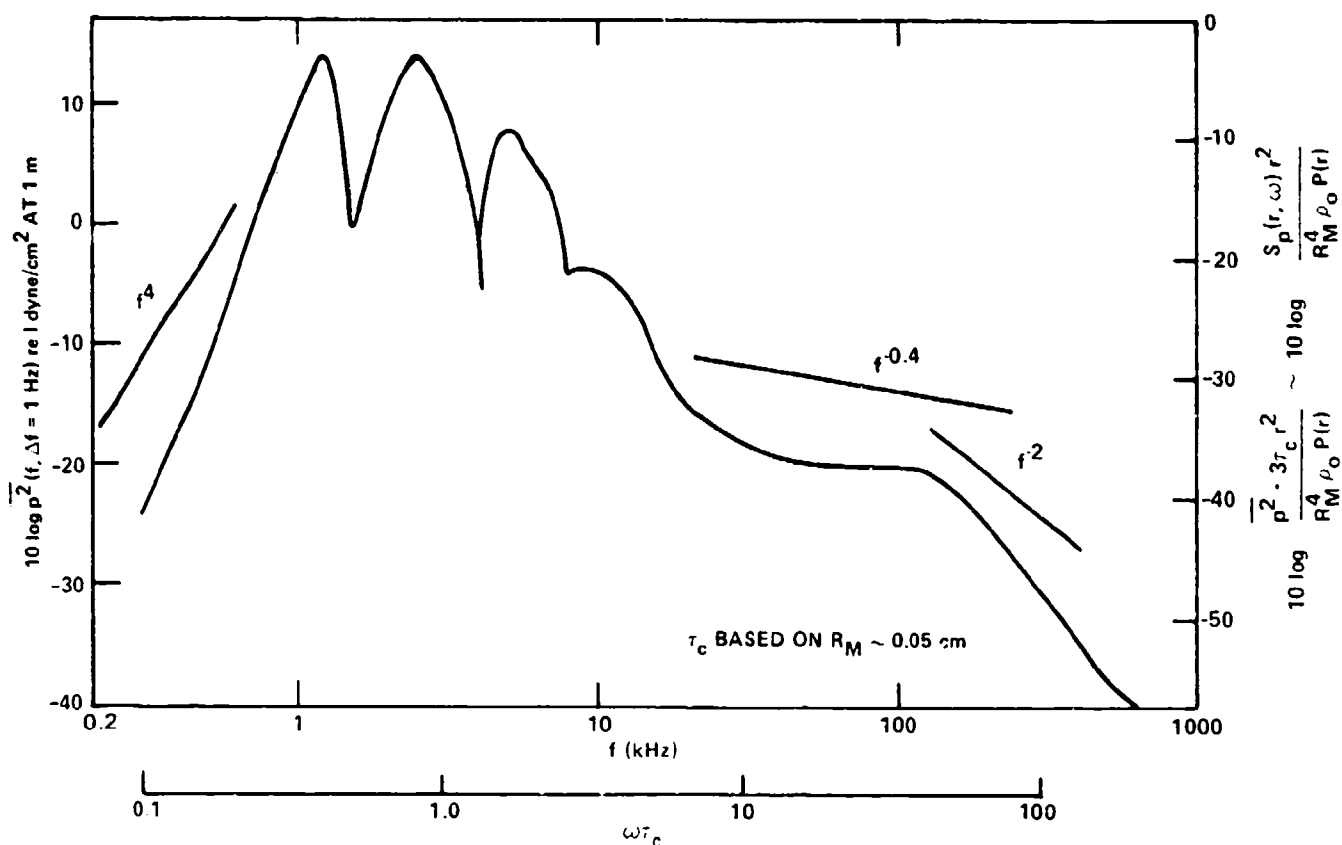


Figure 4.35 - Sound Spectrum of Cavitation Noise Generated by a Rotating Rod 2 Inches Long, 1/16-Inch Diameter Rotated at 4300 Revolutions per Minute  
(From Mellen<sup>166</sup>)

cavitation was generated at the tips of the rod. The important characteristics of the ideal noise model are borne out; maximum level at moderate frequencies with nearly the  $f^4$  on the low-frequency side. The multiple peaks are probably due to reflections. At high frequencies the spectrum falls off roughly as  $f^{-2}$ . An attempt has been made to reduce the measured 1 Hz band levels to the form of the spectrum function. The band level is converted to spectrum level by

$$\overline{p^2}(f, \Delta f) \approx 2 \Phi_{p_a}(r, \omega) \Delta \omega$$

$$\approx \frac{2 S_p(r, \omega) \Delta \omega}{\tau_f}$$



and  $\Delta\omega = 2\pi\Delta f$ . The bubble life-time  $\tau_b$  is unknown, but assumed to be equal to  $3\tau_c$ . The maximum bubble radius was observed to roughly 0.05 cm. Comparison of the dimensionless spectral density with the ideal function in Figure 4.33 will show that the measurement is only roughly represented by the ideal function. Perhaps the discrepancy is partly due to the extensive distribution of bubble sizes that probably exist instead of a single bubble as assumed for the ideal noise spectrum. Also, the real bubbles collapse in an environment that is subject to a variation in the local static pressure field of the tips of the rod.

The important fact to be recognized from the shape of the spectrum measured by Mellen is that although the acoustic energy spectrum is broadband, as predicted by the theory, the exact shape is only roughly approximated by the ideal spectrum. This discrepancy is not quantifiably understood, but it is probably partly due to the many hydrodynamic influences that can bear on bubble formation and collapse. It is nonetheless useful to examine physical noise spectra within the format of the nondimensionalization, because such a format will give a rationale for scaling noise measured on models up to prototype. It will also give a means of estimating changes in noise to be associated with design changes from one generally-similar flow system to another.

The most simple format for scaling is that recently proposed by Strasberg<sup>167</sup> (although also used by Khoroshev<sup>168</sup>) which is predicated on the assumption that the size of the cavitation region scales linearly with the dimension of the body  $L$ , at the same ratio of the cavitation index to the cavitation inception index. Then a characteristic time scale, analogous to the collapse time of a cavitation bubble, is

$$\tau = L \left( \frac{\rho_o}{P_\infty} \right)^{1/2} \quad (4.139)$$

where  $P_\infty$  is a conveniently described ambient static pressure. The size scale of the cavitation zone is a function of  $K/K_i$  and probably of Reynolds number, i.e.,

$$L_c = L f \left( \frac{K}{K_i}, R_L \right) \quad (4.140)$$

Returning attention to the equation for the linear acoustic sound field, we can write the sound pressure, Equation (4.120), in terms of scaled variables:

$$\frac{p_a \left( \frac{r}{L}, \frac{t}{\tau} \right)}{p_\infty} = \left( \frac{L}{r} \right) v'' \left( \frac{K}{K_i}, \frac{t}{\tau}, R_L \right) \quad (4.141)$$

In the frequency domain this representation has a corresponding spectral density of the general form similar to Equation (4.127):

$$\phi_{p_a} \left( \frac{r}{L}, \omega \right) \left( L \left( \frac{\rho_o}{p_\infty} \right)^{1/2} \right)^{-1} = p_\infty^2 \left( \frac{L}{r} \right)^2 \phi \left( \omega L \left( \frac{\rho_o}{p_\infty} \right)^{1/2}, K, K_i, R_L \right) \quad (4.142)$$

The sound pressure level measured in a frequency band  $\Delta\omega$ ,  $\overline{p^2}(\omega, \Delta\omega)$  will then be

$$\overline{p^2}(\omega, \Delta\omega) = p_\infty^2 \left( \frac{L}{r} \right)^2 \left[ (\Delta\omega) L \left( \frac{\rho_o}{p_\infty} \right)^{1/2} \right] \phi \left( \omega L \left( \frac{\rho_o}{p_\infty} \right)^{1/2}, K, K_i, R_L \right) \quad (4.143)$$

where  $\phi(\omega L(\rho_o/p_\infty)^{1/2}, K/K_i, R_L)$  is a dimensionless function that is dependent on the type of cavitation and it implies similarity based on equal values of  $K/K_i$  as well as equal values of  $K$  and  $K_i$ .

The scaling implied by Equations (4.141), (4.142), and (4.143) does not provide for differences in cavitation inception indices, indeed it assumes that they are the same in both model and full scale. It is understood, however, that the types of cavitation must be the same in both scales. It also does not account for different liquid compressibilities in the two scales, compressibility differences may influence the high frequency part of the spectrum, and the peak is the sound pressure pulse. These relationships were successfully used by Strasberg to scale the noise from tip vortex cavitation of propellers<sup>167</sup> (see Figures 4.47 and 4.48).

An alternative approach which has a relatively large acceptance<sup>169,170</sup> and which has been effectively used to scale propeller noise,<sup>163,164</sup> replaces Equations (4.139) and (4.140) by

$$\tau = LK^{1/2} \left( \frac{\rho_o}{P_\infty} \right)^{1/2} \quad (4.144)$$

$$= \left( \frac{L}{U} \right) \sqrt{2}$$

and

$$L_c = L f(K, R_L) \quad (4.145)$$

This leads to the scaling relationship for the pressure level in narrowbands

$$\overline{p_a^2}(\omega, \Delta\omega) = \frac{P_\infty^2}{(K)^{1/2}} \left( \frac{L}{r} \right)^2 \left[ (\Delta\omega) L \left( \frac{\rho_o}{P_\infty} \right)^{1/2} \right] \phi \left( \omega L K^{1/2} \left( \frac{\rho_o}{P_\infty} \right)^{1/2}, K, R_L \right) \quad (4.146)$$

Equation (4.145) was first used by Levkovskii<sup>121</sup> to apply to the case of equal hydrostatic pressures  $P_\infty$ , in model and full-scale. If, in addition, the model measurements are made at the same index as exist in full-scale, then Equation (4.146) reduces to Equation (4.143). The point is, however, that it is implicitly understood that the cavitation inception index  $K_i$  will be the same for both scales. Equations (4.143) and (4.146), although functionally similar in the coefficients of  $\phi$ , differ in fundamentals as expressed in the different functional dependence of  $\phi$  in each case. The difference between Equation (4.143) and Equation (4.146) is in the distinction between  $(K/K_i)$ -similarity in the former case and  $K_i$ -similarity in the latter case.

A means of introducing both the cavitation inception index and the cavitation index and, therefore, possibly adjusting for dissimilarity in  $K_i$ , borrows from the theory of single bubble dynamics. The characteristic size of the cavitating region will depend upon a length scale of the body and the difference between the local static pressure in the cavitating region and the vapor pressure. Analogous to Equation (4.53), the cavitation length scale will be

$$L_c = L (K_i - K)^{1/2}$$

the time scale will increase with the size of the bubbles and the static pressure, so that

$$\tau = L (K_1 - K)^{1/2} \left( \frac{\rho_o}{P_\infty} \right)^{1/2}$$

The mean-square pressure in a frequency band will behave as

$$\overline{p^2}(\omega, \Delta\omega) = P_\infty^2 \left( \frac{L}{r} \right)^2 \left[ \frac{(\Delta\omega) L (K_1 - K)^{1/2}}{\left( \frac{P_\infty}{\rho_o} \right)^{1/2}} \right] (K_1 - K) \quad (4.147)$$

$$\phi \left( \frac{\omega L (K_1 - K)^{1/2}}{\left( \frac{P_\infty}{\rho_o} \right)^{1/2}}, K_1, R_L \right)$$

This is essentially the representation used by Blake et al.<sup>117,118</sup> and it has been seen to effectively describe noise radiated by cavitating hydrofoils. If cavitation similarity exists then

$$(K)_{\text{model}} = (K)_{\text{full}}$$

and

$$(K_1)_{\text{model}} = (K_1)_{\text{full}}$$

in which case Equation (4.147) will reduce to Equation (4.143). The spectrum function  $\phi(\omega L (K_1 - K)^{1/2} / (P_\infty / \rho_o)^{1/2}, R_L)$  will be a function of the geometry of the body, the Reynolds number, and the reduced frequency as indicated.<sup>218</sup> It could, therefore, be possible for  $\phi$  to be additionally dependent on  $K_1$  since  $K_1$  depends on  $R_L$ .

A very different approach to cavitation noise scaling was suggested by DeBruyn and TenWolde.<sup>9</sup> They hypothesized that similarity is maintained by a fixed proportionality between the total acoustic energy radiated and the potential energy contained in the bubble-liquid system when the bubbles have their maximum radii. Accordingly, they hypothesize that the acoustic power is proportional to the time rate of change of the potential energy P.E.

$$P_a \propto \frac{d}{dt} (\text{P.E.})$$

This converts to

$$\frac{\overline{p_a^2} r^2 (4\pi)}{\rho_o c_o} \propto \frac{1}{\tau} \left( \frac{4}{3} \pi R_M^2 \right) P_\infty$$

where  $\tau$  is a time constant of the bubbly system so that they hypothesize

$$\frac{\overline{p_a^2} r^2 \tau}{\rho_o c_o R_M^3 P_\infty} = \text{constant} \quad (4.148)$$

The time constant was taken as the rotation rate of a propeller, but in the same way it could just as well be taken as a length scale of the cavitating body  $L$  divided by a velocity scale  $(P_\infty/\rho_o)^{1/2}$ . Further, they assume that

$$R_M \propto L$$

so that,

$$\frac{\overline{p_a^2}}{\left( \frac{\rho_o c_o^2}{P_\infty} \right)^2 P_\infty^2} \left( \frac{r}{L} \right)^2 \left( \frac{\rho_o c_o^2}{P_\infty} \right)^{1/2} = \text{constant} \quad (4.149)$$

The form of Equation (4.149) brings in the requirement, additional to  $K =$  constant, that the Mach number and compressibility are the same in both scales in order that complete similarity is maintained. Although the analysis circumvents explicit consideration of the details of collapse, this added similarity will necessarily ensure that the shock wave formation in the final stage will be similar as long as the partial pressure of noncondensable gas is also similar. As we have seen, the maximum wall velocity is controlled by liquid compressibility as well as by the bubble gas pressure. Even more fundamentally, the statement of an equal ratio of acoustic to potential energy also implies an equal ratio of far-field to near field particle velocity. The near field motion controls the potential energy-kinetic energy balance which, in turn, governs overall collapse. The acoustic energy, a by-product, really, of the near field motion, depends upon the speed of sound in the liquid and, therefore, the compressibility. To maintain complete similarity in the energy balance will require equal compressibilities in the manner of

$$\left( \frac{\rho_o c_o^2}{P_\infty} \right)_1 = \left( \frac{\rho_o c_o^2}{P_\infty} \right)_2$$

A variation of the similarity hypothesis expressed by Equations (4.148) and (4.149) depends also on the assumption that the sound is shock-wave controlled. Levkovskii<sup>169</sup> and Baiter<sup>170</sup> reasoned that because shock-related noise has the form of Equation (4.138), then the sound pressure level at frequencies very much less than  $(\delta t_s)^{-1}$  must behave as

$$\psi_{pp}(\omega \ll (\delta t_s)^{-1}) \sim \int p_a^2(t) dt$$

$$\sim \overline{p_a^2} \cdot (\delta t_s)$$

Therefore, Equation (4.147), with  $\tau$  replaced by  $(\delta t_s)$  implies that

$$\psi_{pp}(\omega \ll (\delta t_s)^{-1}) \sim \rho_o c_o \frac{R_M^3}{r^2} P_\infty$$

and letting

$$R_M \sim L$$

the spectral density function is written in the form

$$\frac{\overline{p^2}(\omega, \Delta\omega)}{\Delta\omega} = P_\omega \frac{L^3}{r^2} \rho_o c_o \quad (4.150)$$

and the frequency still scales as

$$\omega L \left( \frac{\rho_o}{P_\omega} \right)^{1/2} = \text{constant}$$

Equation (4.150) has been used for scaling propeller cavitation noise by Bark,<sup>171</sup> Lovik and Vannenden,<sup>172</sup> and Björheden and Aström;<sup>173</sup> their implementation of this relationship will be discussed in Section 4.4.3.3. In using Equation (4.150), complete similarity is maintained by maintaining

$$\overline{p^2}(\omega, \Delta\omega) = P_\omega^2 \left( \frac{L^2}{r^2} \right) \left( \frac{\rho_o c_o^2}{P_\omega} \right) \frac{\Delta\omega L}{c_o}$$

which is recognized as Equation (4.149), if  $\Delta\omega = \omega$  and offers the requirement of similarity in liquid compressibility as discussed above.

To the extent that one desires to simulate gaseous diffusion in a model environment, then Levkovskii<sup>174</sup> has indicated that one should scale the concentration of dissolved gas in proportion to  $L^{1/2}$  under the provision that the maximum bubble radius is proportional to  $L$ . This dependence can be deduced from Equation (4.66) by noting that

$$R_M \propto 1 + L$$

As indicated by the calculations in Section 4.4.1.1, this behavior will only be important at relatively large frequencies.

When model testing is done in water at the same value of  $P_{\infty}$  as in full-scale, Equation (4.150) gives the same scale factor as the preceeding equations.

#### 4.4.3 Examples of Hydrodynamically-Induced Cavitation Noise

We now examine two shear flows and the cavitation noise produced by each within the framework of the relationships of bubble dynamics. Measured noise spectra, made dimensionless on parameters that are deduced from these relationships, show a similarity to the theoretical bubble noise spectrum. This similarity provides evidence that certain general expressions for cavitation noise may exist and it provides a framework for developing general laws of similarity for other flow types.

**4.4.3.1 Cavitating Free Jets.** Sound pressure levels from cavitating jets were made by Jorgensen<sup>146</sup> at Reynolds numbers in the vicinity of  $6 \times 10^5$  which is well within the turbulent regime (see Chapter 3, Figure 3.10). The total air content of the water was within 10 percent of the value for saturation so that a possibility of the influence of noncondensable gases exists, but it will not be addressed here. Figure 4.36 shows some of the measured sound pressures in one-half octave bands at a

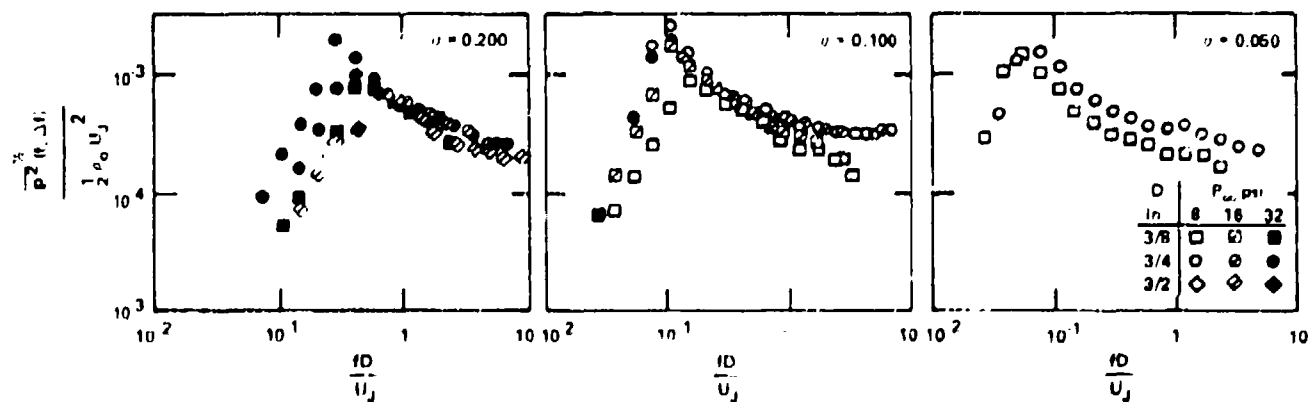


Figure 4.36 - Measured Spectra of Jet Cavitation Noise, in Half-Octave Bands  
(From Jorgensen<sup>146</sup>)



range  $r/D \approx 5.7$ . The prominent noise frequency nondimensionalized on the efflux velocity and diameter decreases as  $K$  decreases, but the maximum sound pressure level remains nearly equal to  $10^{-3}$  times the dynamic pressure for all cases.

An alternative form of nondimensionalization can be used which is based on the notions of bubble dynamics in turbulent flow. The maximum bubble size will be on the order of

$$R_M \approx \theta_t \cdot \left[ \frac{1}{2} U_J^2 (K_1 - K) \right]^{1/2} \quad (4.151)$$

where we have applied Equations (4.53) and (4.115). The time scale  $\theta_t$  is the moving axis correlation time scale for an eddy to decay to  $1/e$  of its strength, equivalent to  $\Lambda_m/U_c$  in Section 3.6.3.3, see Figure 3.21, which is

$$\frac{\theta_t U_J}{D} \approx 1.4 \quad (4.152)$$

The time constant for collapse of these bubbles is the same as given by the theoretical collapse time from bubble dynamics, from Equation (4.70),

$$\tau_c \approx \frac{0.9 R_M}{\left( \frac{P_\infty}{\rho_o} \right)^{1/2}}$$

or

$$\tau_c \approx 1.26 \frac{D}{U_J} \left( \frac{K_1 - K}{K} \right)^{1/2} \quad (4.153)$$

Adopting the dimensionless form of Equations (4.97) and (4.98), from Section 4.4.1, we find a nondimensional spectrum function\*

\*The band level is approximately related to the (two-sided) autospectrum level by

$$p^2 \approx 2\pi(r, \omega) \ln \approx \frac{2}{\tau_c \tau_c} S(r, \omega) \ln$$

$$\tilde{S}(\omega\tau_c) = \left[ \frac{\overline{p^2}}{2\tau_c \Delta\omega} \right] \frac{\gamma \tau_c^2 r^2}{\rho_o p_\infty R_M^4} \quad (4.154)$$

$$\equiv \gamma_{\tilde{\chi}} \tilde{\phi}(\omega\tau_c)$$

where  $\gamma_{\tilde{\chi}} \approx 3$  is taken as the approximate bubble life time, relative to  $\tau_c$ , and  $\omega = 2\pi f$ . The proportional bandwidth is

$$\Delta\omega \approx 0.4 \omega$$

Therefore, Equation (4.154) gives the dimensionless level:

$$\begin{aligned} (0.8 \omega\tau_c) \tilde{S}(r, \omega\tau_c) &= 0.9\gamma \left(\frac{r}{D}\right)^2 \frac{\overline{p^2}}{q_J^2 (K_1 - K) K^2} \\ &= 0.9\gamma \left(\frac{r}{D}\right)^2 \frac{\overline{p^2}}{P_o^2 (K_1 - K)} \end{aligned} \quad (4.155)$$

and

$$\begin{aligned} \omega\tau_c &= 2\pi f \cdot (1.26) \frac{D}{U_J} \left(\frac{K_1 - K}{K}\right)^{1/2} \\ &= 2\pi f D (K_1 - K)^{1/2} \left(\frac{P_o}{U_J}\right)^{-1/2} \end{aligned} \quad (4.156)$$

where  $q_J = 1/2 P_o^2 U_J^2$ . Figure 4.37 shows the resulting nondimensional spectral function for selected samples of Jorgensen's results. These levels bear a close

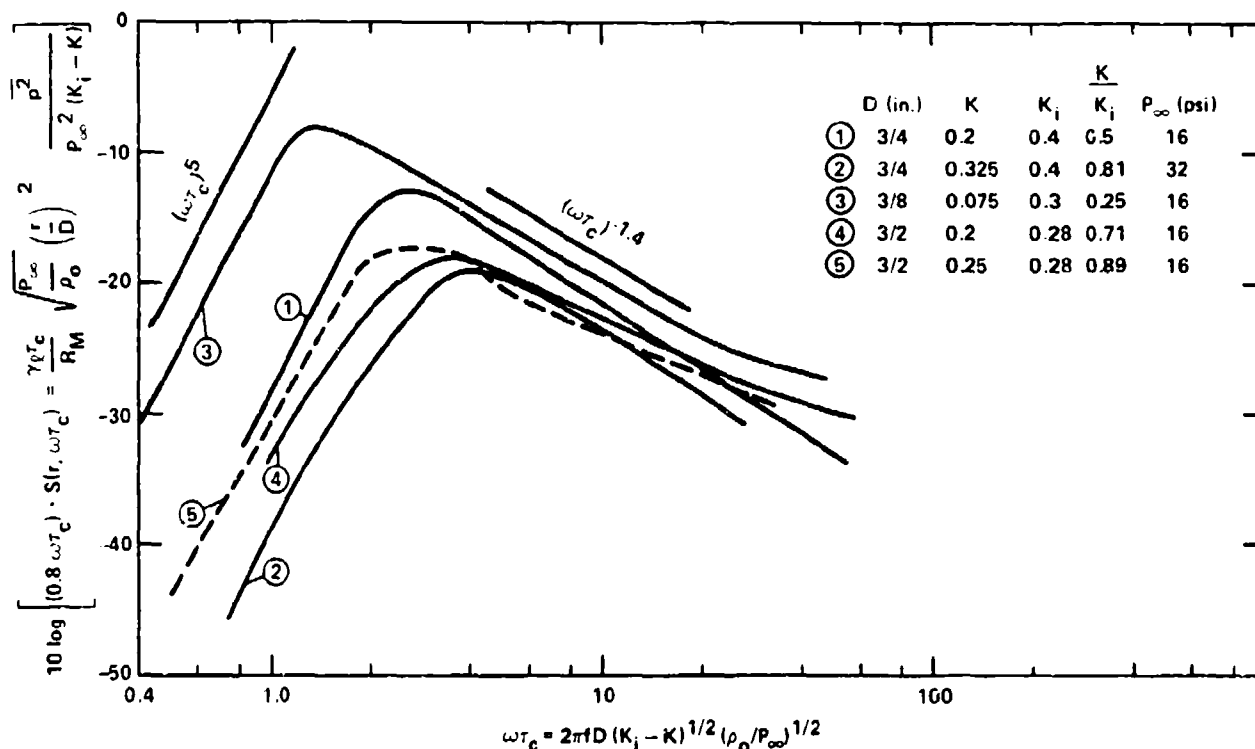


Figure 4.37 - Jorgensen's Spectra of Noise from Cavitating Jets Made Dimensionless on Estimated Bubble Sizes and the Constants;  $0.4 \omega \tau_o$  is the Dimensionless Filter Bandwidth;  $\gamma_g \approx 3$ ;

$$R_D \approx 6 \times 10^5$$

resemblance to the ideal spectrum (multiplied by  $\omega \tau_c$ ) of Figure 4.33 at low frequencies, but show a more pronounced roll-off at high frequencies. This roll-off occurs at a frequency that is much too low to be caused by effects of the compressibility of the liquid.

The nondimensionalization defined by Equations (4.155) and (4.156) does not completely reduce the noise spectra; there appears to be a residual dependence on  $K/K_1$  of both the level and the frequency of the maximum value of the spectrum that is not explained with the above theory. This residual appears as the lowest value of  $K/K_1$  and possibly is a result of the large bubbles altering the turbulence structure in the jet.

4.4.3.2 Cavitating Hydrofoils. Noise from cavitating hydrofoils has been measured in water tunnels by Barker,<sup>175,176</sup> Erdmann et al.,<sup>177</sup> by Blake et al.,<sup>112,113</sup> and by Thompson and Billet.<sup>178,179</sup> In the measurements of Blake et al., and of Erdman et al., an attempt was made to correct the sound pressure measurements made in the water tunnel for the effects of reverberation, in order to report absolute values of equivalent free-field sound pressures. The other measurements gave sound levels relative to an arbitrary reference and the magnitudes were influenced by facility reverberation and in some cases perhaps absorption from free bubbles in the facility.

The acoustic level depends upon the type of cavitation that occurs on the hydrofoil. Barker's results disclosed that a form of surface cavitation produced more noise than cavitation in a trailing vortex beginning at the tip of the hydrofoil. It was concluded by Barker that the vortex noise was mainly due to gaseous cavitation while surface cavitation noise was due to vaporous cavitation. The vortex cavity had the visual appearance of a glassy rope which extended well downstream of the diffuser section of the tunnel. This experimental characteristic may be important, for, as Morozov<sup>180</sup> has shown theoretically, the noise from a cavitating line vortex is emitted from the ends of the vortex where incomplete cancellation of the pressures caused by vibrations of the cavity-water interface will not be cancelled. Therefore, although the vortex cavitation noise may be less than that from surface cavitation, it is possible that the noisiest part of the vortex cavity was outside the test section.

Noise from specific forms of surface cavitation has been reported by Blake et al.<sup>117,118</sup> Using a hydrofoil that was designed for the generation of an extensive region of low static pressure, it was possible to develop either traveling bubble or a form of sheet cavitation depending on whether the noncavitating boundary layer on the hydrofoil was turbulent (causing traveling bubbles) or separated-laminar. Figure 4.38 illustrates both the pressure distributions and the types of cavitation that were produced on side one of the hydrofoil which is the suction side. The traveling bubble cavitation appeared as a continuum of non-spherical bubbles, some of which became disintegrated by the turbulent flow around them. The static pressure distribution downstream of the point of minimum pressure was adverse so that although the turbulent boundary layer was attached it was thick. The sheet cavitation that was generated because of laminar separation had all of the

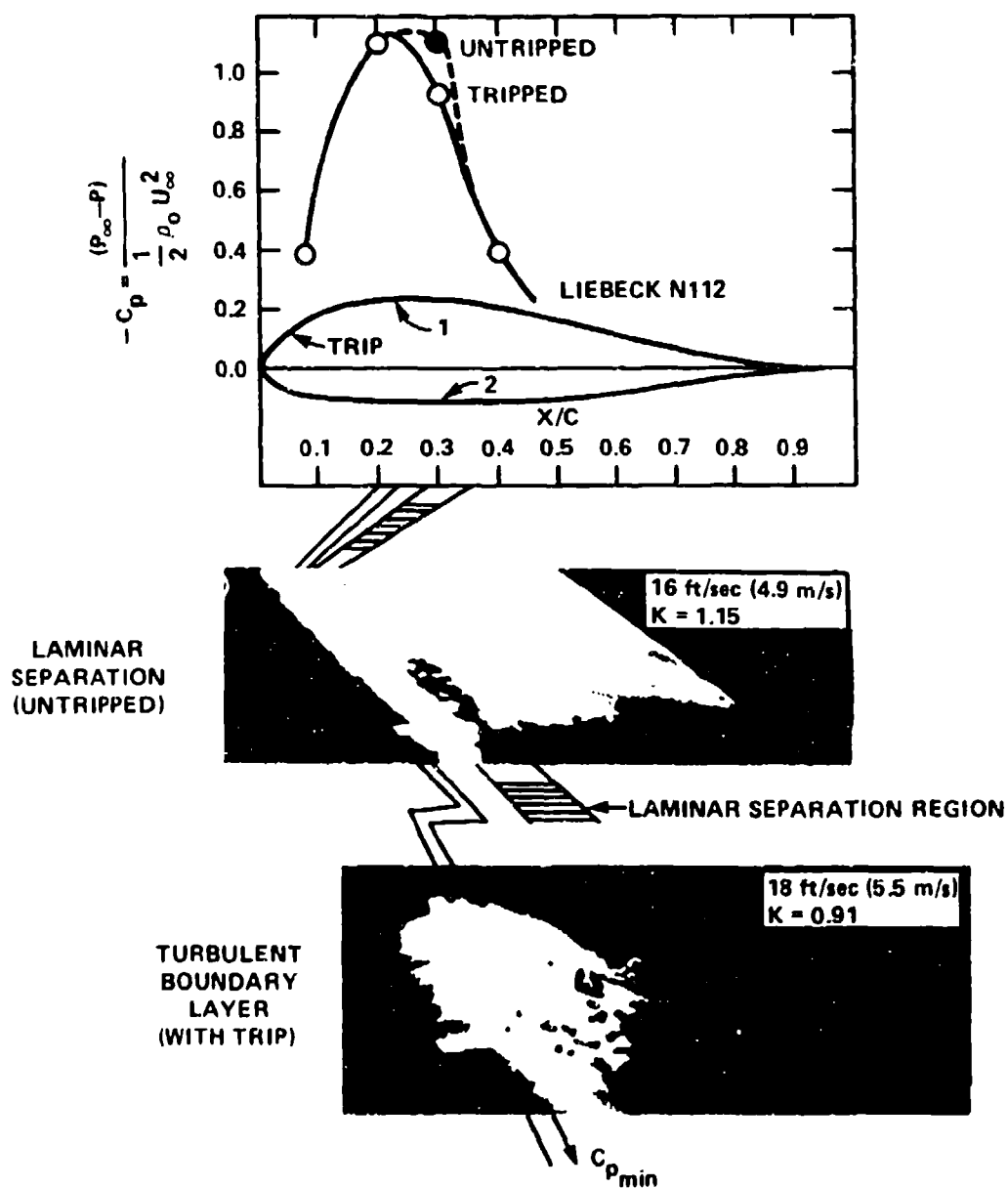


Figure 4.38 - Pressure Distributions and Cavitation Patterns near Inception as Influenced by Viscous Effects

(Photographs were obtained at differing angles to optimize lighting; lines mark coordinates of  $x/c = 0.2$ ,  $C_{p_{min}}$ , and the observed separation zone.<sup>118)</sup>

characteristics that were described in Section 4.3.2.7, although the downstream behavior of the sheet was undoubtedly influenced by the prominent pressure gradient on the downstream part of the foil.

Within the distribution of the traveling bubbles was a sub-group whose behavior was very similar to that illustrated in Figure 4.14. The bubbles grew to a maximum size and then collapsed as spheroids; other bubbles disintegrated. Figure 4.39 shows measured sound pressures from the traveling-bubble cavitation for a variety of indices above and below  $K_1$ . Also shown is a representative spectrum for the sheet cavitation that was obtained for a corresponding value of  $K_1$ . It can be seen in this case that the sheet cavitation is less noisy than traveling bubble cavitation, but it is not yet known how generally this result would apply to other hydrofoil flows.

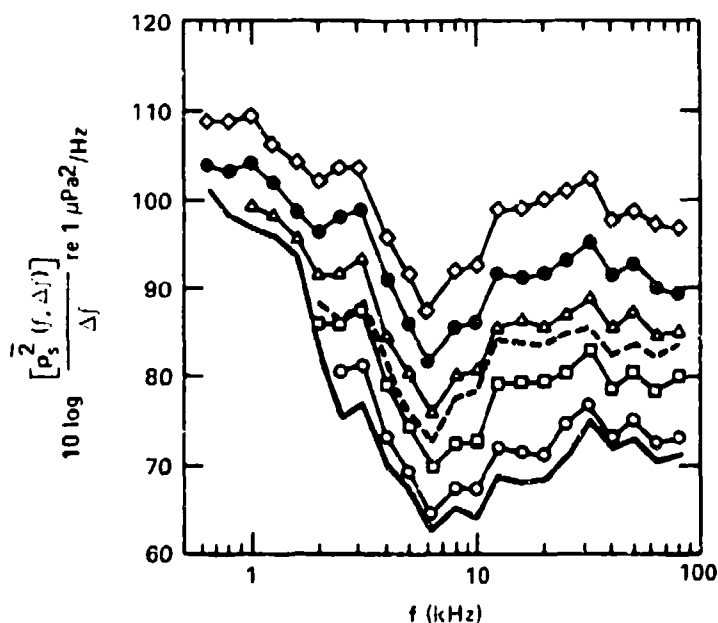


Figure 4.39 - Spectral Densities at 1 Yard of Traveling-Bubble Cavitation Noise for Various Cavitation Indices

(Levels are for a tripped boundary layer at  $U_\infty = 18$  feet per second,

$\alpha = 4$  degrees,  $\sigma_1 = 1.15$  with 5 percent air content at atmos-

pheric pressure.  $\diamond$  (with trip):  $\diamond$ , 0.80;  $\bullet$ , 0.90;  $\triangle$ , 1.00;  $\square$ , 1.10;  $\circ$ , 1.20; —, 1.30,

$\circ$  (without trip): ---, 0.92.<sup>118</sup>)

The noise spectra for the traveling-bubble noise were nondimensionalized according to Equation (4.154), using Equations (4.53) and (4.115) for the maximum size of the bubbles. Strictly speaking, however, this nondimensionalization may be interpreted as a modeling of the actual bubble dynamics only for those spheroidal bubbles that do not disintegrate by splitting. Therefore, we write

$$R_M \sim T \frac{U_\infty}{2^{1/2}} (K_1 - K)^{1/2} \quad (4.157)$$

where  $T$  is the residence time of the bubble in the rarefaction zone. Letting the chordwise length of this zone be  $\ell_r$  ( $\approx 0.2c$  for the experiment of Blake et al.), and the average translation velocity of the bubble be

$$U = U_\infty (1 - \bar{C}_p)^{1/2}$$

where  $\bar{C}_p \approx -0.8$  is the average pressure coefficient in that zone, it is found that

$$R_M = \frac{\ell_c (K_1 - K)^{1/2}}{(1 - \bar{C}_p)^{1/2}} \quad (4.158)$$

so that the dimensionless spectrum function is

$$\begin{aligned} S(r, \omega \ell_c) &= \frac{\overline{p_s^2}(\omega, \ell_c)}{2 \rho_o U_\infty} \cdot \frac{U_\infty / c}{\left( \frac{1}{2} \rho_o U_\infty^2 \right)^2 [K(K_1 - K)]^{1.5}} \times \left[ \frac{r}{c} \right]^2 \\ &\times \left[ 2 \left( \frac{c}{\ell_r} \right)^3 (1 - \bar{C}_p)^{1.5} \right] \end{aligned} \quad (4.159)$$

and

$$\omega \tau_c = 2\pi f \tau_c$$

$$= \frac{\omega c}{U_\infty} \frac{\ell_r}{c} \left[ \frac{K_i - K}{K(1 - \bar{C}_p)} \right]^{1/2} \quad (4.160)$$

where  $c$  is the chord of the hydrofoil. The term in brackets ( $\approx 1811$ ) in Equation (4.159) is a numerical constant for a given pressure distribution as long as  $\ell_r$  is relatively invariant with changes in  $K$ . Bubble sizes that are predicted from Equations (4.157) and (4.158) agree closely with those observed on a Joukowski hydrofoil by Parkin,<sup>116</sup> on the subject hydrofoil by Blake et al.,<sup>117,118</sup> as well as on the body of revolution used by Plesset.<sup>14</sup>

Figure 4.40 shows the dimensionless spectrum levels according to Equations (4.159) and (4.160) compared with the ideal spectrum of Figure 4.33. The measured

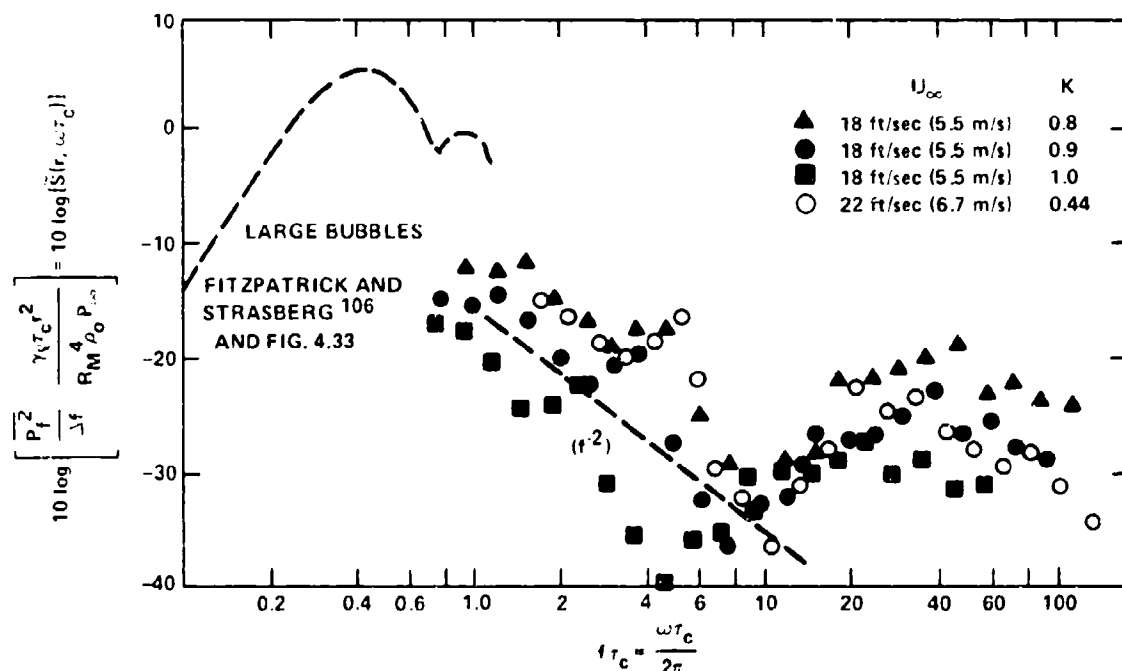


Figure 4.40 - Dimensionless Spectral Densities for Various Conditions of Traveling Bubble Cavitation

(Normalization is based on variables associated with single-bubble cavitation noise.<sup>118</sup>)



spectrum levels extend over a frequency range above that which is dominated by the growth of the large bubbles. For dimensionless frequencies in the range  $3 < \omega \tau_c < 60$  the spectrum levels decrease as  $\omega^{-2}$ , which is in close correspondence with the behavior,  $\omega^{-2.4}$ , shown for dimensionless spectrum of jet cavitation noise in Figure 4.37. It is apparent, therefore, that for  $\omega \tau_c < 60$ , the spectrum levels of noise from traveling bubbles on the hydrofoil and from traveling bubbles in the shear flow of the jet are roughly similar when expressed in terms of estimated bubble radii using characteristic length and time scales for the respective flows. The generality of this result to bubble cavitation in other types of flows remains to be proven. Indeed, as we shall see below, noise levels from sheet cavitation similarly non-dimensionalized are less than those for bubble cavitation.

At frequencies that are greater than  $\omega \tau_c = 60$ , the spectrum in Figure 4.40 has a secondary peak which is of uncertain origin. It is suspected, however,<sup>118</sup> that the motions of microbubbles which result from the disintegration of the larger bubbles cause this noise.

Noise from the sheet cavitation associated with laminar separation, nondimensionalized using the same set of parameters as used for Figure 4.40, i.e., Equations (4.159) and (4.160), is shown in Figure 4.41. In this case, because

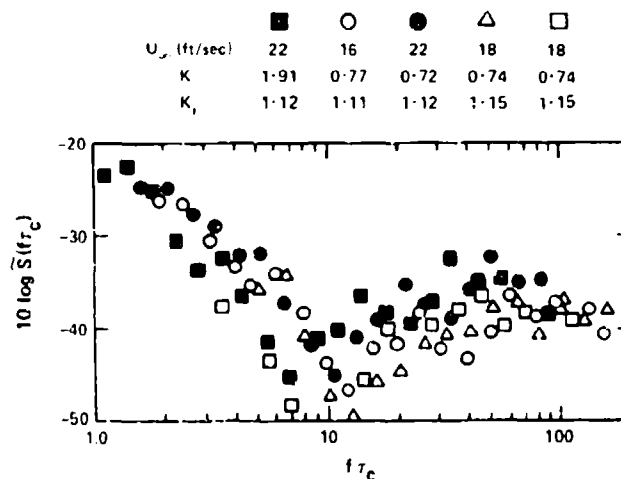


Figure 4.41 - Dimensionless Spectral Densities of Cavitation Noise from the Untripped Hydrofoil Calculated Using Equations (4.159) and (4.160)<sup>118</sup>

spheroidal large traveling bubbles were not produced, the nondimensionalized spectra cannot be interpreted as modeling any particular bubble dynamics, but rather as a form of approximate similitude. (The bracketed term in Equation (4.159) was again taken as equal to 1811 just to make the numerical comparison.) These dimensionless spectra provide a basis for comparing the noise from the two types of cavitation at equivalent pressures and similar values of  $(K_1 - K)$  and they show the greater noise levels for the traveling bubble cavitation in a relative sense compared to this type of sheet cavitation at similar stages of development.

Both representations, Equations (4.155) and (4.159), are functionally equivalent, as can be determined by rearranging the terms in either equation to replace pressure and velocity. For two dynamically similar cavitation flows, Equations (4.155) or (4.159) reduce to the simple form of Equation (4.143), since  $(K)_1 = (K)_2$  and  $(K_1)_1 = (K_1)_2$  when similarity exists between cases 1 and 2. Equations (4.155) and (4.159) are also the same as Equation (4.145) which was derived without recourse to explicit reference to dynamics of single bubbles, modeled as convected through a low pressure region.

Noise from sheet cavitation on side two of the hydrofoil shown in Figure 4.38 was 10 dB quieter than that generated by the sheet cavitation on side one in Figure 4.41. An example of the sheet cavitation on side two is shown in the inset of Figure 4.42 which shows the sound pressure spectra for a similar parameter range as presented in Figure 4.39.

The dimensionless forms used in Figures 4.37, 4.40, and 4.41 provide a format for analyzing other data, as well as perhaps a means of crudely estimating noise from other similar systems. Unfortunately, there is to date little additional acoustical information on which to develop dimensionless noise spectra for other flow types. Most experimenters, being interested mainly in general trends (speed dependence, etc.), do not (or are not able to) carry out the necessary acoustical calibrations with which to deduce absolute values.

So far our discussion of hydrofoil cavitation noise has addressed only direct monopole radiation from cavitation bubbles. Additional radiation from resonant motion of the hydrofoil responding to surface pressures will also be produced. This noise will be dipole like and will depend upon the relative impedances of the water and the hydrofoil. For surfaces which are stiff and lightly damped yet have low

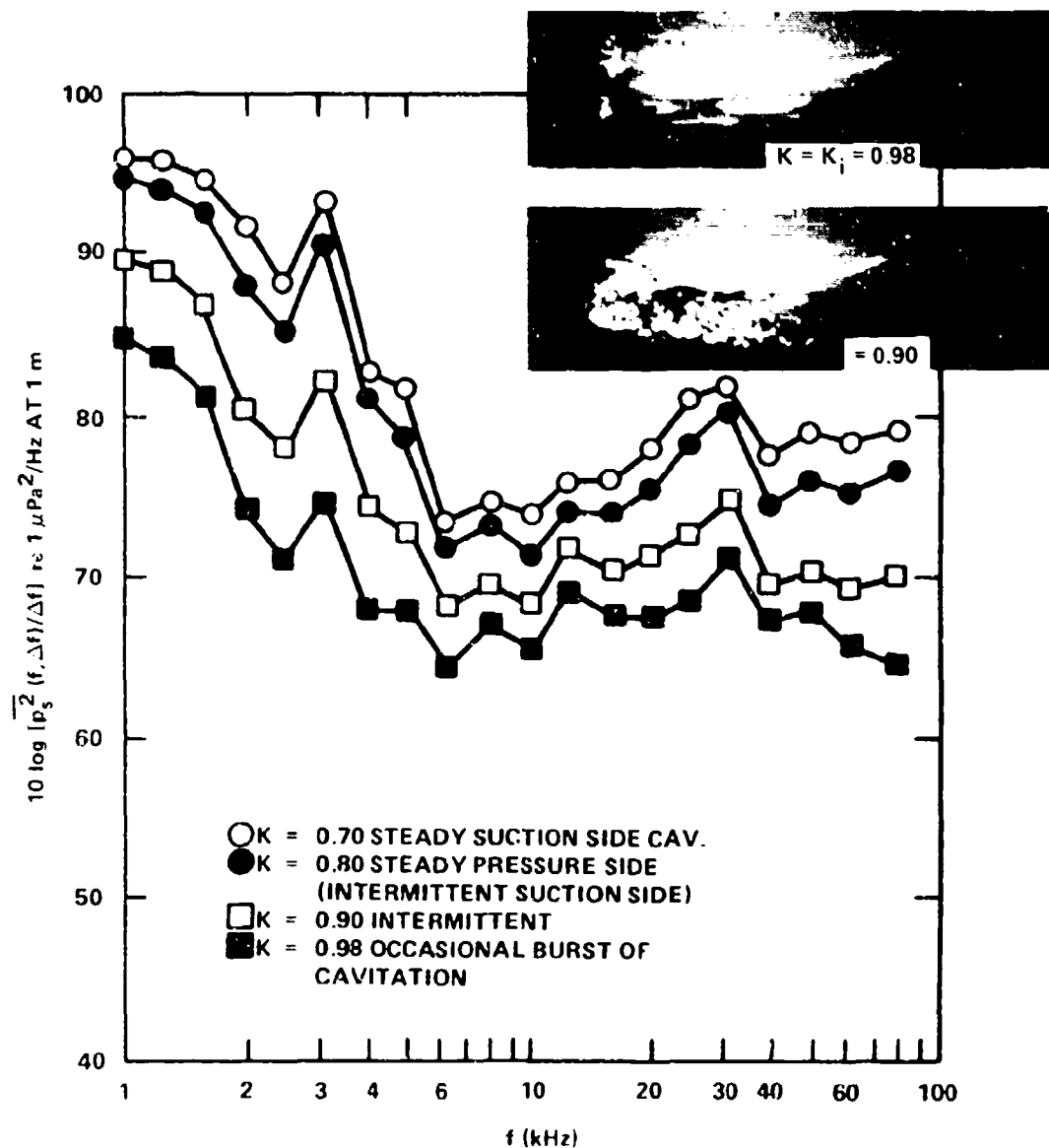


Figure 4.42 - Spectral Densities of Noise from Cavitation on High-Pressure Side of Hydrofoil for  $U = 16$  Feet per Second (4.9 Meters per Second) and  $-2$  Degrees Angle of Attack; 8 Percent Air Content; 64 Fahrenheit (18 Celsius)<sup>117</sup>

mass per unit area, the hydrofoil will doubtlessly act as a sounding board and radiate additional energy. On the other hand, more massive surfaces and surfaces with higher damping may act only as reflectors of sound energy so that the sound power radiated will not be enhanced by any re-radiation from the surface. No systematic work on the subject has been done. In one investigation, Barker<sup>175,176</sup> has observed certain spectral peaks in the noise radiated from his hydrofoil specimens; the frequencies of the peaks changed when both ends of the hydrofoil were fixed compared to when the hydrofoil was a cantilever. Barker deduced that the spectral character was due to a modal radiation from the hydrofoil excited into flexure by the cavitation. Contradictory evidence, on the other hand, has been shown by Blake et al.<sup>117,118</sup> In their experiment, flow-excited acceleration of the hydrofoil was monitored, and then the sound level to be expected from this vibration alone was later deduced by mechanically shaking the hydrofoil in the absence of cavitation. The vibration-induced dipole sound power was then found to be less than one-tenth of the total throughout most of the 1 kHz to 100 kHz frequency range of interest, reaching a fraction of one-half the total power at 40 kHz to 80 kHz. At these frequencies the radiation efficiency (see Chapter 6) of the hydrofoil is roughly unity so that differences in structural radiation will be effected by differences in mass impedance. The average thickness of both Barker's and Blake's hydrofoils was the same, however, Barker's hydrofoil was aluminum (specific gravity . 3) and Blake's was brass (specific gravity 8). The high-frequency sound power from vibration will be in rough proportion to (for nearly structurally-similar hydrofoils)  $\rho_p^2$ ; this implies nearly 9 dB more structural radiation from Barker's aluminum hydrofoil than for the brass hydrofoil. This increased level nearly accounts for the apparently greater structural radiation observed by Barker than by Blake et al. Although this is a plausible explanation for greater modal sound in Barker's experiment, clearly more work is necessary to clear-up the issue.

#### 4.4.4 Propeller Cavitation

4.4.4.1 General Characteristics. A primary application of the principles of the preceding sections is the scaling and diagnosis of model propeller noise measurements. Models of both surface ship and submarine propellers have often been tested in the design stage to evaluate their noise-control characteristics. Notable

important requirements for the use of noise-control in cavitating propellers can be found in positioning thrusters of oceanographic vessels,<sup>172</sup> and in the achievement of greater crew comfort on merchant vessels<sup>172,173-181</sup> and reduction of radiated noise interference to fish finding sonars on fishing vessels.<sup>171,182</sup> The types of cavitation occurring on propeller blades are basically the same as those occurring on hydrofoils, but with the obvious complication that more than one type of cavitation may appear simultaneously as shown in Figure 4.43. Figure 4.43a shows a propeller with the trailing vortices from the blade tips heavily cavitating. Sheet cavitation on the leading edge of the pressure face of the propeller blades is also apparent and extends toward the hub of the propeller.

Noise from cavitation on propellers is further complicated by the fact that the inflow to the propeller, being modified by the boundary layer of the hull, is not symmetric about the axis of the propeller. This nonuniformity induces local changes in the angle of attack of the propeller blade sections as they rotate. Considering the blade as a progression of elemental hydrofoils along the radius of the propeller from the hub to the tip, it is expected that the quality and extent of cavitation will depend upon the nature of the chordwise load distribution and the type of boundary-layer at each elemental blade section. Whatever characteristics of the cavitation may exist in steady, uniform flow into the propeller, nonuniformity in the inflow will impose a time varying change in the overall bubble volume as the local sectional loading and boundary layer development become periodically altered by the attendant oscillating angle of attack. The frequency distribution of radiated sound power will be accordingly modified to contain concentrations of noise about the frequencies of angle-of-attack variations.

4.4.4.2 Noise at Blade Passage Frequency and its Harmonics. An example of this type of behavior is provided by Lovik and Vassenden<sup>172</sup> for the near-field pressures measured on the hull section of an oceanographic research ship just above the propeller. Figure 4.44 shows an illustration of the model test configuration to simulate actual flow into the propeller as well as the pressure level at a ship speed of 12.2 knots for two alternate propeller designs. The diameter of each model propeller was 225 mm, with a scale factor of 10. The measurements of noise from the models were scaled to full-scale using Equation (4.150), which ignores differences between  $(K_i)_m$  and  $(K_i)_{ship}$  and, furthermore, is subject to the caveats

Figure 4.43 - Examples of Types of Cavitation Occurring on Marine Propellers<sup>128</sup>  
 (Photographs courtesy of Netherlands Ship Model Basin)



Figure 4.43a - Bubble-Spot Cavitation

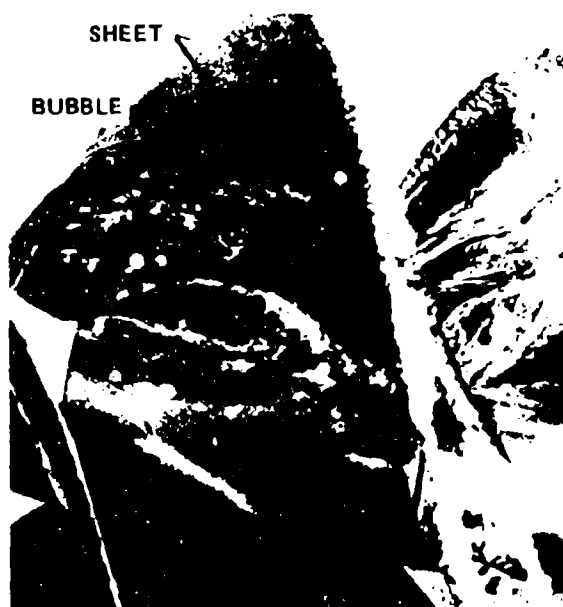


Figure 4.43b - Bubble-Sheet Cavitation

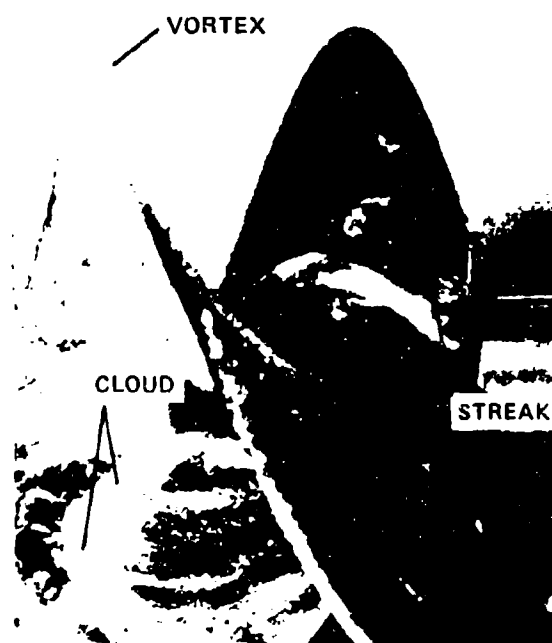


Figure 4.43c - Vortex-Cloud-Streak Cavitation

Figure 4.43 (Continued)

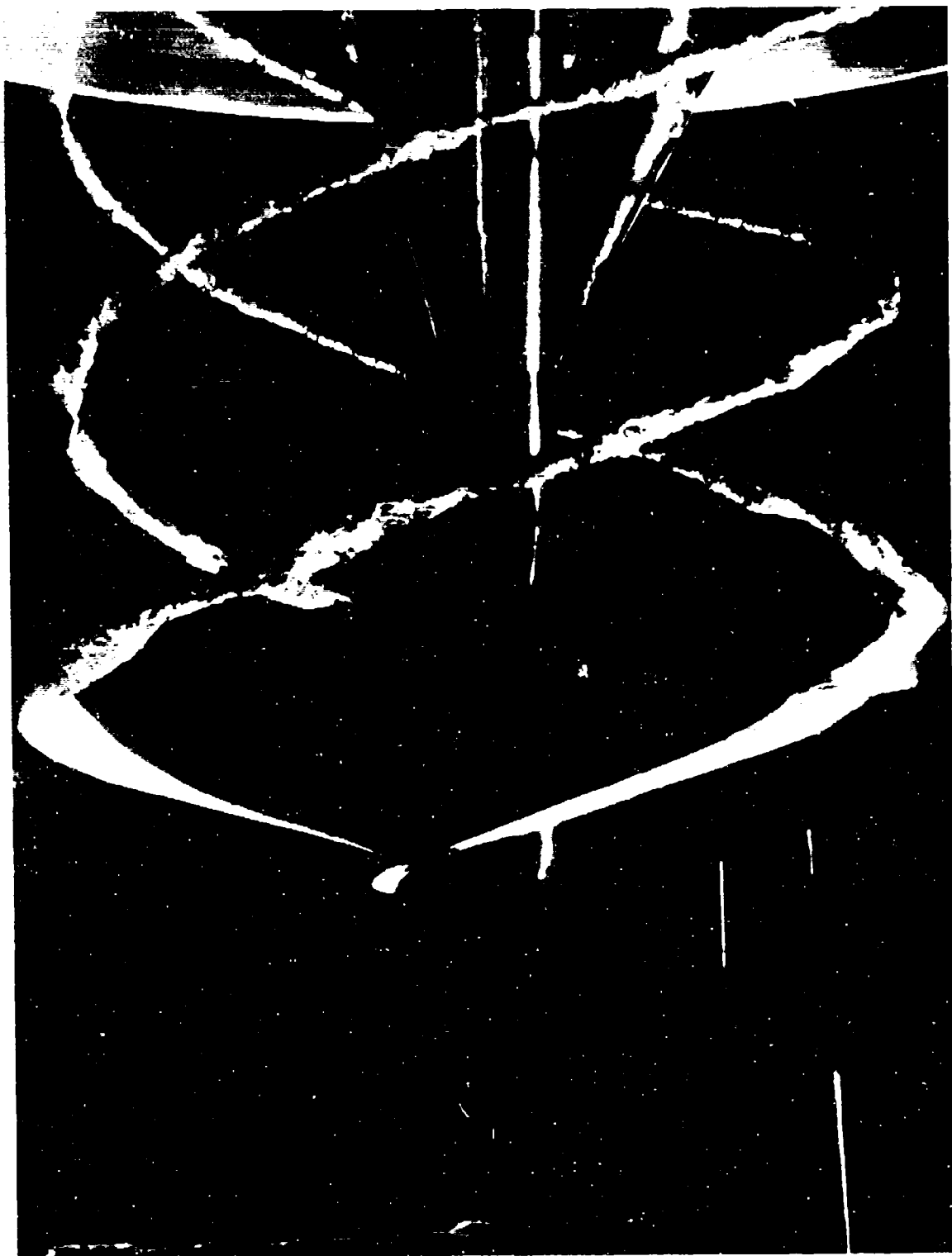


Figure 4.43d - Tip-Vortex Cavitation

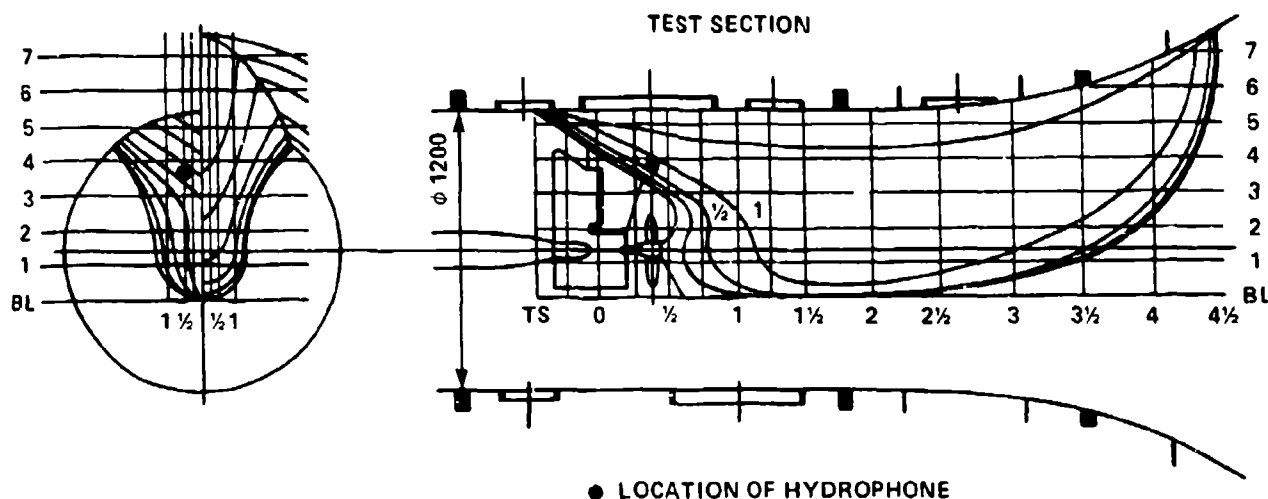


Figure 4.44a - Typical Model Arrangement in Cavitation Tunnel

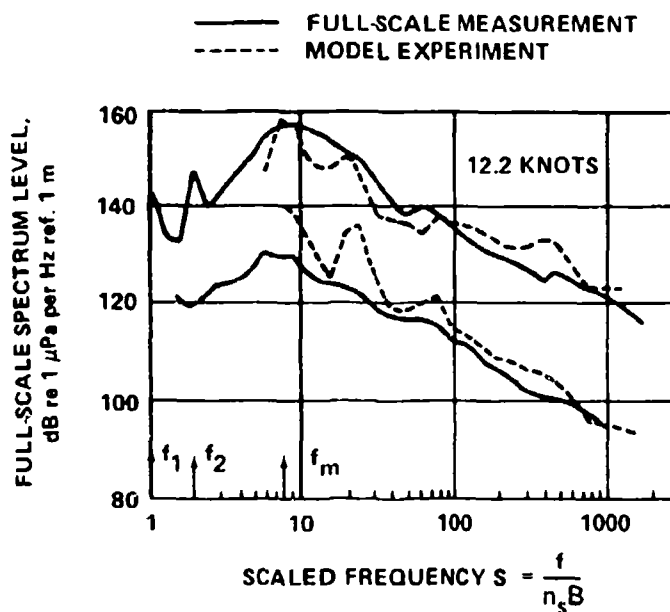


Figure 4.44b - Spectrum Level Scaled to Full Size,<sup>172</sup>  
Upper and Lower Curves Pertain to  
Two Propeller Designs

Figure 4.44 - Cavitation Noise Testing at the Ship Research  
Institute of Norway (From Ref. 172)



mentioned in Section 4.4.2 because it ignores requirements of similarity in compressibility. For comparisons of sound pressure measured in fixed bandwidths  $\Delta f_m$  and  $\Delta f_s$ , Equation (4.150) is rewritten

$$10 \log \left( \frac{\overline{p^2}}{\Delta f} \right)_s = 10 \log \left( \frac{\overline{p^2}}{\Delta f} \right)_m + 10 \log \left\{ \frac{(P_\infty D^3)_s}{(P_\infty D^3)_m} \right\} \quad (4.161)$$

assuming

$$(K_1)_m \approx (K_1)_F$$

at a ship frequency of

$$f_s \approx f_m \left( \frac{D_m}{D_s} \right) \left( \frac{P_\infty s}{P_\infty m} \right)^{1/2} \quad (4.162)$$

The premise of a constant ratio between acoustic and potential energies for valid application of Equation (4.150) cannot be maintained since the model and full-scale measurements of Lovik and Vassenden<sup>172</sup> were made at values of  $P_\infty$  that differed by a factor of two. However, the difference in scaled noise levels by assuming  $\overline{p^2} \propto P_\infty$  rather than  $\overline{p^2} \propto P_\infty^{3/2}$  amounts to approximately only 1.5 dB. To emphasize the effect of nonuniformity in the inflow, the frequency was normalized on the product of the number of blades  $B$  and the shaft rotation rate  $n_s$ . The peaks at  $f/n_s B = 1$  and 2 for the greater magnitude spectrum occur at the blade passage frequency and its harmonic. The peaks at  $f/n_s B = 20$  in the scaled model noise were due to vortex shedding sounds from the wake-simulation screens near the hull model. In the redesign of the propeller, the overall noise levels were markedly reduced and the peaks

at the harmonics of the blade passage frequency were eliminated. Noise at blade passage frequency can be generated because of the periodic changes in local angle of attack as the blades pass through spatial nonuniformities in the inflow. The consequent changes in blade pressure coefficients alter the cavitation.

Such variations in traveling bubble cavitation at the blade passage frequency have been theoretically analyzed by considering harmonic variations in the maximum sizes of traveling bubbles by Pudovkin.<sup>183</sup> These effects have been observed on both bubble and sheet cavitation as deduced from experiments in which the angle of attack variations have been simulated by imparting a pitching motion to hydrofoils. Some of the more recent experiments with oscillating angles of attack are those of Bark and van Berlekom<sup>182</sup> using a cantilever hydrofoil in pitching motion about its mid-chord. They observed pressure pulses that are radiated as the instantaneous angle of attack favors a reduction in the extent of the cavity. Tip vortex cavitation, sheet cavitation, and bubble cavitation were developed on different hydrofoils. The most noisy type was bubble cavitation, with the sheet cavitation 10 dB quieter, while the least noisy was the vortex type, being 20 to 30 dB quieter. A similar experiment of Shen and Peterson<sup>158</sup> disclosed large volumes of bubble clouds shed from the trailing edges of collapsing sheets. Experimental and theoretical attention has been given to the forces induced on the hull by periodic changes in the volumes of sheet cavities.

A review of theoretical and experimental treatments of the time histories of cavity volumes of sheet cavities and the associated induced pressures and hull forces is somewhat outside the scope of the present discussion. Reference material may be found in the recent theoretical paper by Noordzij;<sup>184</sup> extensive experimental observations of time-varying hull pressures and associated cavitation patterns can be found in the papers by Huse<sup>185</sup> and van der Kooij and Jorik.<sup>186</sup> General reviews of the subject have been compiled for the ITTC<sup>187</sup> and more recently by Breslin et al.<sup>217</sup> It is possible, using Equation (4.120), to estimate far-field sound pressures from a known or calculated time history of the cavity volume changes at the blade passage frequency. This calculation is a prerequisite to calculate either radiated sound or hull pressures. Unfortunately, however, it is not possible to make similar calculations which apply to frequencies  $\geq f_m$ , in Figure 4.43, because this noise deals with details of microbubble collapse that are not amenable to calculation.

4.4.4.3 Review of Attempts at Scaling Cavitation Noise. Noise occurring from the disintegration of cavities and other small-scale bubble motions that account for the acoustic energy in the range  $r > f_m$  in Figure 4.44 can only be determined empirically on scaled models. This noise occurs at frequencies that are significantly greater than the fundamental blade passage frequency  $n_s N_b$ . Just as in the case of hydrofoil cavitation noise, bubble-type cavitation is probably more of a noise problem than the sheet or vortex type when both are present in an advanced stage of development. A systematic investigation of this type, as reported by Noordzij et al.,<sup>188</sup> was conducted in supersaturated water ( $\alpha/\alpha_s > 1$ ) seeded with microbubble nuclei upstream of the propeller. Each of three propellers was designed to produce predominantly one type of cavitation in the wake of a transom-stern surface vessel: tip vortex, bubble, and sheet cavitation. Figure 4.45 shows representative spectra measured in

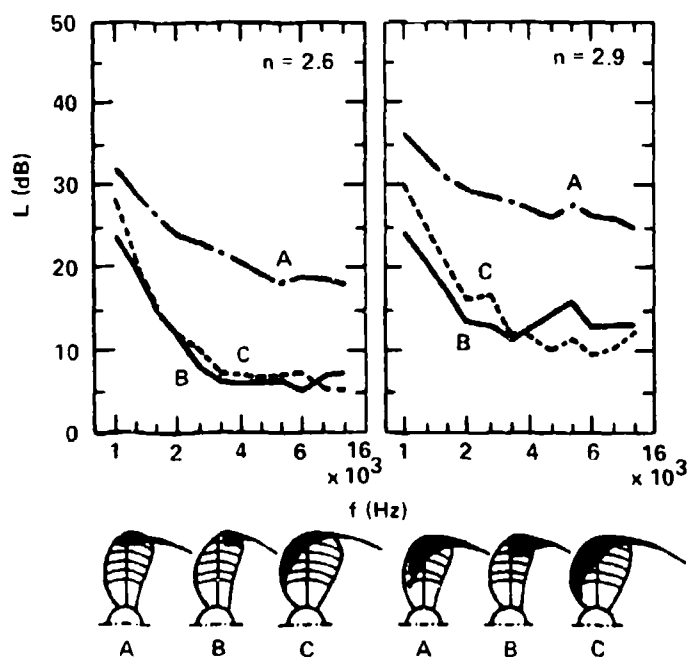


Figure 4.45 - Sound Spectra (1 Hertz Band) for the Propellers A, B, and C at  $n_s = 2.6 \text{ Second}^{-1}$  (Left) and  $n_s = 2.9 \text{ Second}^{-1}$  (Right);  $\alpha/\alpha_s = 4.4$  Seeded by Electrolysis.<sup>188</sup> Sound Level Reference is Arbitrary

the far field directly below the ship model over the range of high frequencies  $70 < f/n_s D < 1300$ . The advanced stage of bubble cavitation apparently generates at least 10 dB greater sound pressure than either of the advanced forms of sheet or tip vortex cavitation that were generated. However, it must be realized that this comparison is subjective since no indication of the inception index was given for each type of cavitation.

Attempts at scaling model noise to full-scale using the hypothesis of equivalent energy ratios, e.g., Equations (4.148) through (4.150) have both overlooked a possible dissimilarity that  $(K_1)_m \neq (K_1)_s$  as well as  $(P_\infty/\rho_o c_o^2)_m \neq (P_\infty/\rho_o c_o^2)_s$ . An example of such usage by Lovik and Vassenden<sup>172</sup> has already been given. This mode of scaling has also been used by Björheden and Aström<sup>173</sup> to predict the noise radiated by a twin-screw ferry, Figure 4.46.

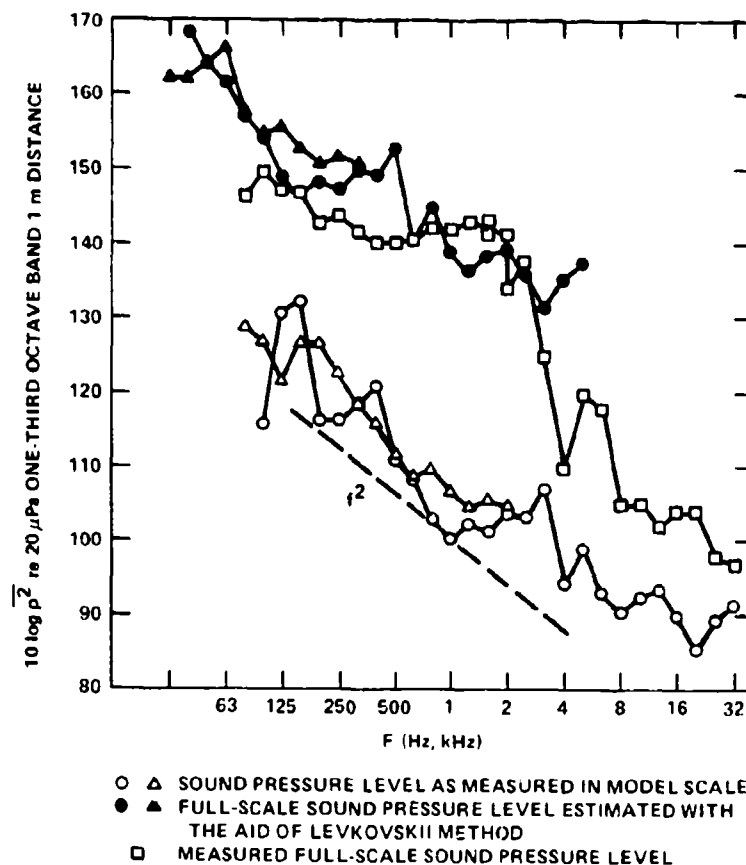


Figure 4.46 - Estimated Full-Scale Sound Pressure Level Compared with Measured Sound Pressure Level for a Twin-Screw Ferry<sup>171</sup>

Strasberg,<sup>167</sup> has recognized that the inception indices of tip vortex cavitation on model and full-scale are not identical, but rather depend on Reynolds number as Equations (4.111) and (4.112). Therefore, he assumed the relation, Equation (4.143) to apply at equal values of  $(K/K_1)$  in order to scale the model noise to full-scale. Figure 4.47 shows overall sound pressure levels,

$$\overline{p^2} = 2 \int_{\omega_1}^{\omega_2} \phi(\omega) d\omega$$

from full-scale and scaled-model measurements according to Equation (4.146)

$$10 \log \overline{p_s^2} = 10 \log \overline{p_m^2} + 20 \log \left[ \frac{(P_\infty)_s}{(P_\infty)_m} \right] \\ + 20 \log \left( \frac{D_s}{D_m} \right) + 20 \log \left( \frac{r_m}{r_s} \right)$$

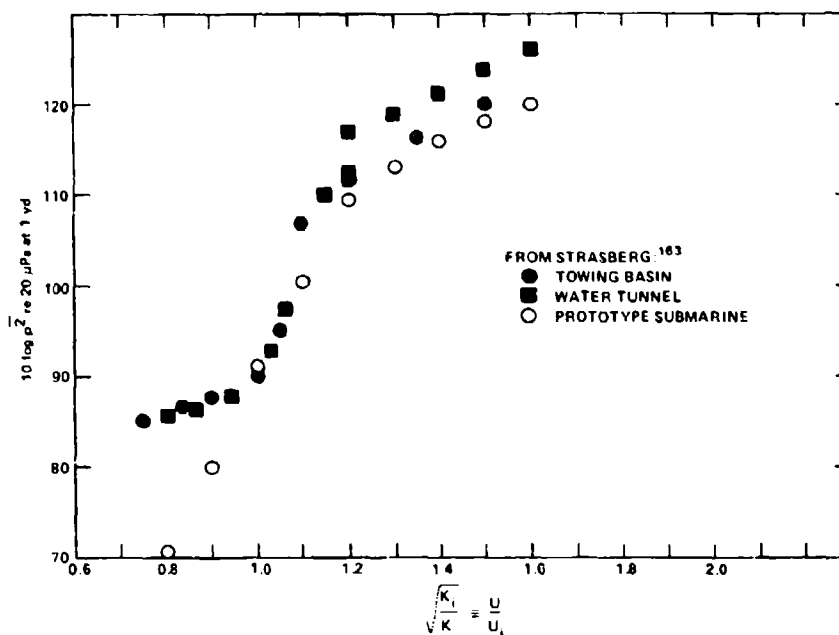


Figure 4.47 - Dependence of Overall Sound Pressure Level on Speed from Cavitating Tip Vortices on World War II Submarine Propeller. Comparison is made with Various Theoretical Functions

for  $\overline{p_s^2}$  and  $\overline{p_m^2}$  in the corresponding ranges,  $\Delta f = (\omega_2 - \omega_1)/2\pi$ ,

$$\left[ (\Delta f) D \left( \frac{\rho_c}{\rho_\omega} \right)^{1/2} \right]_m = \left[ (\Delta f) D \left( \frac{\rho_c}{\rho_\omega} \right)^{1/2} \right]_s$$

and

$$\left( \frac{K}{K_1} \right)_m = \left( \frac{K}{K_1} \right)_s$$

This noise possesses the characteristic frequency dependence of cavitation noise, as shown in Figure 4.48.

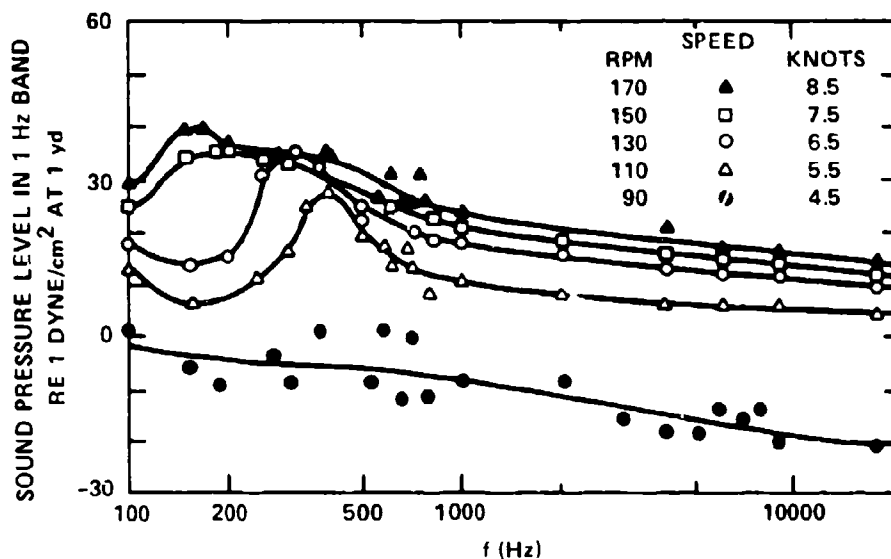


Figure 4.48 - Spectra of Noise; From World War II Submarine Propeller with Tip Vortex Cavitation; All Speeds at 55 Feet Depth<sup>167</sup>

4.4.4.4 Similitude and Speed Dependence for the Cavitation Noise. The similitude arguments of the Section 4.4.2 will now be generalized to case of propeller noise. Two of those relationships, i.e., Equations (4.143) and (4.150), have already been shown, i.e., Figures 4.44, 4.46, and 4.47, to effectively scale sound from propellers. Now a more comprehensive method for both scaling and accounting for the speed dependence of the sound will be given.

The increase of the overall sound pressure level with the rotation speed of a propeller is shown in Figure 4.47 to be pronounced once cavitation begins, but the increase becomes more gradual as the cavitation becomes developed. This abrupt onset of sound as the speed increases from the speed at inception is qualitatively expected from Equations (4.147) or (4.155) which gives the dependence of the sound level on  $K$  and  $K_i$  as  $(K_i - K)$ . This behavior is illustrated in Figure 4.49 (line 1) along with measured sound levels of Lesunovskii and Khokha and other, more elaborate, theories that will be discussed below. As noted on the abscissa of Figure 4.49 the

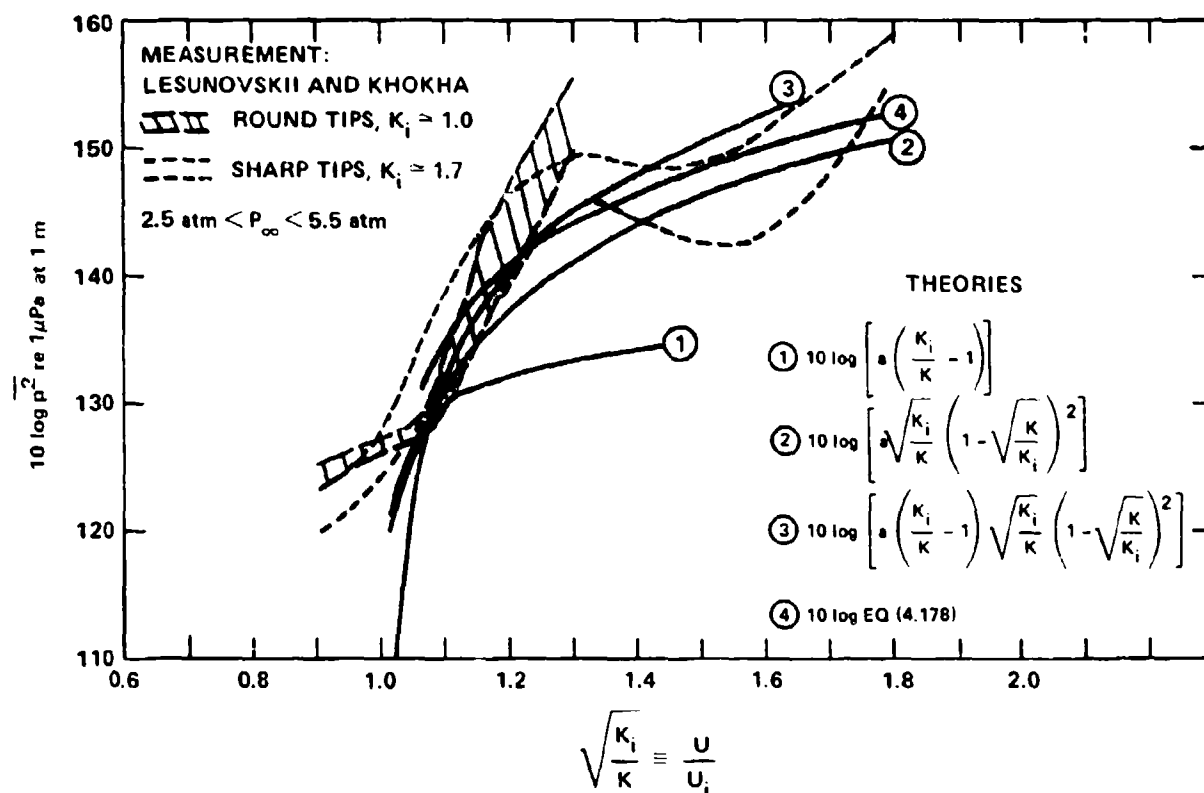


Figure 4.49 - Overall Sound Pressure Level from Cavitating Rotating Blade (with Joukowski Section) as a Function of Cavitation Index

dependence of sound on speed and the cavitation index are related;  $U_i$  is the velocity at the condition of inception. Thus  $U/U_i = (K_i/K)^{1/2}$  at a given static pressure where  $U$  may be either the advance, tip, or angular rotation speed of the propeller.

The sound pressure levels measured by Lesunovskii and Khokha<sup>190</sup> were generated by an unpitched cavitating rotating blade (with a 27 percent thick Joukowski section) in stationary water. It can be seen that the simple dependence of  $K_i - K$  does not account for the observed speed dependence very well, but it does qualitatively predict an initial rapid increase with speed that is followed by a more moderate increase with speed when  $K$  is substantially less than  $K_i$ . The dependence on speed shown in Figure 4.49 is quite similar to that shown in Figure 4.47.

The experimental results of Lesunovskii and Khokha deserve some additional comment. Two rotating vanes differing only in tip detail were used. With sharp tips the noise spectral densities in a range of indices,  $1.26 < (K_i/K)^{1/2} < 1.49$ , showed peaks approximately one-third of an octave wide occurring in the frequency range  $1.0 < f < 4.0$  kHz depending upon  $K/K_i$ . The frequency of the maximum of the peak decreased as  $K$  decreased. This behavior did not occur for the vanes with rounded tips. Otherwise for both rounded and sharpened tips the spectrum of noise from advanced cavitation had the classical frequency dependence. The variation of environmental static pressures in the experiments was partly responsible for the observed spread in the overall sound levels.

Lines (2), (3), and (4) are the result of more comprehensive analyses that will be discussed in Section 4.4.5. The factor  $(1 - \sqrt{K/K_i})^2$  appearing for lines (2) and (3) accounts for the growth of the area of the blade covered by cavitation as  $K$  decreases from  $K_i$ . This dependence was derived originally by Ross and McCormick.<sup>189</sup> As the rotation speed of the propeller increases, the fraction of the span of the blade over which cavitation can occur will increase because the local cavitation index will be reduced below  $K_i$  for radii closer to the hub at greater rotation speeds. Furthermore, at a given blade section, the fraction of the chord over which the local pressure coefficient is less than  $K_i \approx -C_{p_{min}}$ , as illustrated previously in Figures 4.1 and 4.21, will also increase as the rotation speed increases. Thus, the total volume of cavitation, or the total number of cavitation events occurring in a unit time, will continue to increase with speed after inception causing a continued increase in noise after  $K < K_i$  even though  $(K_i - K) = \text{constant} \approx K_i$ .



The factor  $(K_1/K)^{1/2}$  represents the increase of cavitation events in proportion to speed since the rate of encounter of cavitation events by the propeller blade increases with velocity. Other dependences derived in Section 4.4.5 give little additional refinement to the agreement with measurements. It is to be noted that line (2) in Figure 4.49 is similar to a relationship of Ross<sup>5</sup> except for a multiplicative factor  $K_1/K$  which arises from an earlier postulation<sup>189</sup> that the sound intensity is not proportional to  $P_\infty$ , but rather to  $\rho_0 U^2/2$ .

A comprehensive similarity rule for propeller cavitation noise that expresses both the dependence on size and ambient pressure and the dependence on operating condition ( $K$  and  $K_1$ ) can be developed as an extension of the similitude arguments of Section 4.4.2. Under the assumption that each blade of a  $B$  bladed propeller radiates sound independently we can write for the sound pressure

$$\overline{p^2} \propto B P_\infty^2 \left( \frac{D}{r} \right)^2 \cdot f \left( \frac{K}{K_1} \right) \cdot \phi(\omega \tau_c, R) \Delta(\omega \tau)$$

where  $f(K/K_1)$  replaces  $K^{-1/2}$  and  $K_1 = K$  in Equations (4.146) and (4.147) and it may be any of the lines (2), (3), and (4) in Figure 4.49. This function, as discussed above, accounts for both the growth of the cavitation zone with decreasing  $K$  and the increase of cavitation events with velocity. The function  $\phi(\omega \tau_c, R)$  is the normalized frequency spectrum function that is specific to the particular type of propeller. The dimensionless frequency is given by  $\omega \tau_c = 2\pi f D (\rho_0/P_\infty)^{1/2} (K_1 - K)^{1/2}$ . In these relationships,  $P_\infty$  is the static pressure on the shaft axis. The assumption of statistical independence of noise contributions from the blades applies only for frequencies that are substantially greater than the blade passage frequency. Finally, the behavior of the overall sound pressure is given by the coefficients of  $\phi(\Omega, R) \Delta\Omega$  since the integral of  $\phi(\Omega, R)$  over  $\Omega$  is a constant over the speed range for geometrically and dynamically similar propellers.

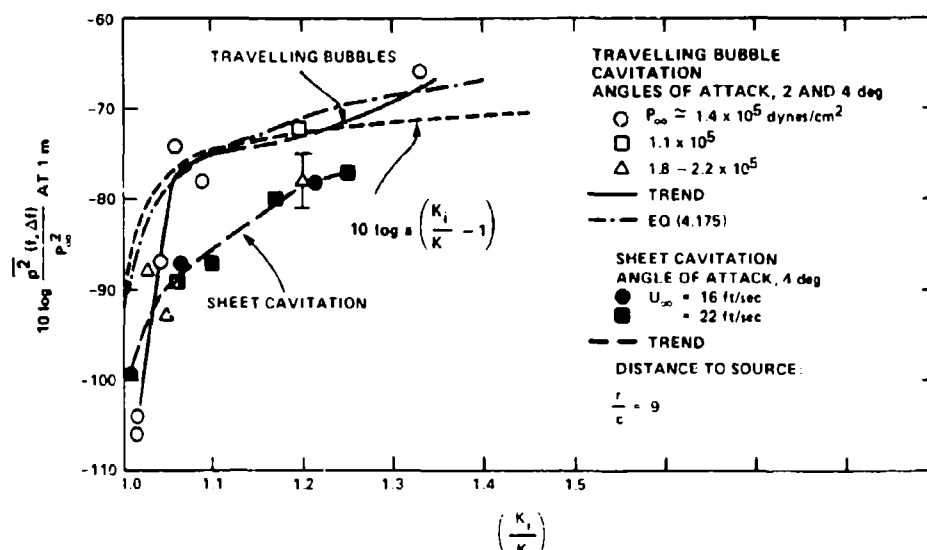


Figure 4.50 - One-Third-Octave Band Levels of Sound Pressure from Two Types of Cavitation on a Hydrofoil. Levels at Dimensionless Frequency  $f c (K_1 - K)^{1/2} / (\rho_0 / P_\infty)^{1/2} = 26$

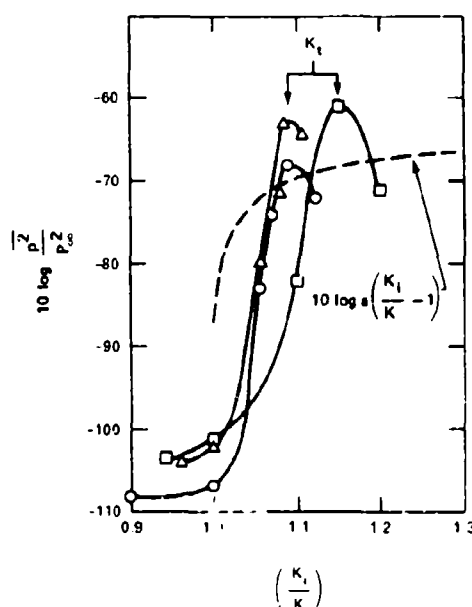


Figure 4.51 - Overall Sound Pressure Level in 1 KiloHertz < f < 25 KiloHertz ( $\sim 2.5 < \omega R_M (\rho_0 / P_\infty)^{1/2} < \sim 80$  at  $K/K_1 \sim 1.08-1.15$ ), for Traveling Bubble Cavitation on a Hydrofoil  $r/c = 16.4$ ,  $4.7 \times 10^5 \leq R_c \leq 9.5 \times 10^5$  (From Clark,  $\gamma = 11.5$  percent,  $C = 7$  Centimeters<sup>177</sup>)

This similarity rule reduces to any of those of the previous section when dealing with geometrically similar model and full scale propellers at the same values of  $P_\infty$  and  $K$  given that the cavitation inception index  $K_1$  is the same in both scales.

The dependence of the noise level on speed for different types of cavitation on stationary hydrofoils deserves some further comment in the sense that departure from the simple  $(K_1 - K)$  can depend on the type of cavitation. In Figure 4.50, the one-third octave band levels, from the work of Blake et al.,<sup>117,118</sup> are nondimensionalized on the static pressure. The dimensionless frequency is held fixed for all values of  $K_1/K$ ;

$$\frac{fC}{\left(\frac{P_\infty}{\rho_0}\right)^{1/2}} (K_1 - K)^{1/2} = 26$$

corresponding to

$$f\tau_0 = 2.9$$

see also Figures 4.43 and 4.44. These band levels were selected because they are included in the frequency range dominated by the collapse of large bubbles. Traveling bubble noise apparently increased roughly as the simple  $(K_1 - K)$  and more rapidly with speed than the sheet cavitation. The speed dependence of traveling bubble noise slackens as the speed continues to further increase. In Figure 4.51, taken from the work of Erdmann et al.,<sup>177</sup> a similarly rapid increase in overall noise level with speed occurs. However, in their experiment the following factors contributed to the prevention of a continued increase in overall noise level as the cavitation progressed. For cavitation indices less than a limiting value  $K_+$ , the cavitation was well developed, and unsteady becoming a fully developed separated cavity at  $K < 0.4 K_1$ . At indices corresponding to more advanced cavitation  $K < K_+$ , an accumulation of free gas bubbles caused attenuation of the noise in the test section. The work of Erdmann et al.,<sup>177</sup> was conducted on a Clark--y, 11.5 percent section whose characteristics have been extensively evaluated by Numachi.<sup>191,192</sup>

Since the dependences on speed of cavitation sound from hydrofoils shows some case-to-case variation one must be prepared to expect similar variations for propellers of different geometries. The behavior with  $K_1/K$  shown in Figure 4.59 must therefore be regarded as illustrative rather than as a well-behaved rule.

#### 4.4.5 Stochastic Models of Bubble Cavitation Noise

A number of statistical theories for cavitation noise have been given, however, ultimately all have the shortcoming that they fail to possess both the observed speed and scale dependence that has been observed or that might be expected on the basis of simple dimensional analysis, as will be made apparent below. All of these theories are based on the collapse of spherical bubbles and ignore the fact that actual propeller cavitation is more complex, having the features illustrated in Figure 4.43.

4.4.5.1 General Descriptions. Noise emanating from cavitation in turbulent boundary layers may be considered as a superposition of temporal pulses. Such behavior has, in fact, led to the use of event-counting as an aid to systematically quantifying the inception of cavitation<sup>82,83,88,117,118,193-195</sup> on various bodies. This behavior has also promoted the development of a number of analytical models of traveling bubble noise as a train of random pulses for which the probability of occurrence has been associated with either the random distribution (assumed Poisson) of bubble nuclei<sup>174,183,196-199</sup> or the assumed-Gaussian statistics of the turbulence itself.<sup>141,200,201</sup> The earliest treatment of the subject is that of Il'ichev,<sup>141</sup> the frequency of cavity formation, in terms of the characteristic length and velocity scales of the flow, and the Gaussian probability that the local pressure in the flow will fall below the necessary critical pressure for nonlinear bubble growth  $P_c$ ; see Section 4.2.3.

The probability that a bubble nucleus will cavitate is determined jointly by the product of the probability that the hydrodynamic pressure will be less than the critical pressure and the (assumed independent) probability that there will be bubble nuclei present with radii large enough. These two factors may be written,

Probability of a cavitation occurrence =

$$\text{Prob} \{p < P_c, R_b > R_c\} = \quad (4.163)$$

(cont.)

$$\int_{R_{cr}}^{\infty} \int_{-\infty}^{P_{cr}} P_N(R_b) P(p, P_{cr}) dR_b dp \quad (4.163)$$

where  $P_N(R_b)$  is the probability density function applicable to the nucleus distribution, and  $P(p, P_{cr})$  is the probability distribution of  $p$  less than some value  $P_{cr}$ . This probability is also equal to the fraction of number of events which favor cavitation to the total number of events, i.e., (see Section 4.2.4.3)

$$\int_0^{\infty} P_N(R_b) dR_b = 1$$

and

$$\int_{-\infty}^{\infty} P(p) dp = 1$$

The probability density  $P(p)$  is assumed to be distributed about a static pressure  $P_s$ .

In the problem considered by Il'ichev, the number of nuclei available at  $p - P_c$  was considered both plentiful and homogeneous so that the probability of cavitation reduced to the probability of finding  $p < P_{cr}$  as illustrated in Figure 4.25. If the probability density function of pressure is assumed to be Gaussian, then

$$P(p) = \left( \frac{1}{\overline{p^2}} \right)^{-1/2} \frac{1}{\sqrt{2\pi}} \exp \left[ - \frac{(p - P_s)^2}{2\overline{p^2}} \right]$$

where  $\overline{p^2}$  is the variance of the pressures (it is also the mean-square fluctuating pressure at a point) and  $P_s$  is the local mean static pressure. We may consider the

probability density to be a function of Reynolds number through variability of  $\overline{p^2}$ . According to Rice<sup>202,203</sup> the frequency of occurrence,  $F$ , that  $p < P_c$  and, therefore, of cavitation in a fluid of high nucleus density, is given by\*

$$F = \frac{1}{2} \left[ \frac{\int_{-\infty}^{\infty} \phi_p(\omega) \omega^2 d\omega}{\int_{-\infty}^{\infty} \phi_p(\omega) d\omega} \right]^{1/2} \exp \left[ -\frac{(P_c - P_g)^2}{2\overline{p^2}} \right] \quad (4.164)$$

where the mean-square pressure fluctuation is

$$\overline{p^2} = \int_{-\infty}^{\infty} \phi_p(\omega) d\omega$$

The term in brackets is the frequency of occurrence of pressure pulses at a fixed point near the body

$$2\pi f_p = \left[ \frac{\overline{\left(\frac{dp}{dt}\right)^2}}{\overline{p^2}} \right]^{1/2}$$

and the exponential function is the fraction of the pressure pulses for which  $p < P_{cr}$ .

4.4.5.2 Models Based on Gaussian Statistics of Turbulence. The nucleus population is still assumed to be dense enough so that only the pressure statistics will influence the cavitation rate. Note, however, that each "event" may involve many cavitating bubbles. The frequency of pressure pulses must be determined a fixed reference frame, i.e., in one not moving with the flow, so that  $(dp/dt)$  must be

---

\*See also the discussion of cavitation inception in free jets, Section 4.3.2.5.

deduced from the time constant of a fixed-axis correlation (Chapter 3) or the auto-spectrum. (Recall that the bubble lifetime is determined by the time constant of the moving-axis correlation.) In the case of bubbles formed in the wake of a bluff body, the formation rate  $f_p$  will be proportional to the ratio

$$f_p \propto \frac{U_\infty}{d} \quad (4.166)$$

where  $U_\infty$  is the mean incidence velocity and  $d$  is the cross-stream dimension of the body. In incompressible flow,  $f_p$  is just the characteristic frequency of the formation of vortices in the wake.

In homogeneous turbulent shear layers,  $f_p$  is determined by the time microscale of turbulent pressure  $\lambda_t$  (see Section 7.2.5 of Chapter 7). This scale will be proportional in a rough approximation to the free-stream speed  $U_\infty$  and the thickness of the boundary layer  $\delta$  so that

$$f_p \sim \left( \frac{U_\infty}{\delta} \right) S \quad (4.167)$$

where  $S$  is an appropriate Strouhal number of the flow.

Turning now to the exponential part of Equation (4.164), we recall that the critical pressure  $P_c$  and the vapor pressure  $P_v$  are nearly indistinguishable for large enough bubble nuclei, so that adding and subtracting the free-stream pressure  $P_\infty$ , Equation (4.164), can be written

$$F = \frac{U_\infty}{L} S \exp \left[ - \frac{1}{2} \frac{(K+C)^2}{\alpha^2} \right] \quad (4.168)$$

where

$$S = \frac{fL}{U_\infty}$$

is a Strouhal number of the flow and

$$\alpha^2 = \frac{\overline{p^2}}{\left(\frac{1}{2} \rho_o U_\infty^2\right)^2}$$

is a Reynolds number-dependent factor relating the mean-square pressure and the square of the free-stream dynamic pressure. Equation (4.168) expresses the occurrences per unit time that the local pressure coefficient will be small enough for cavitation to occur. When  $K = -C_p$ , then  $F = (U_\infty/L) S$  and cavitation will occur every time a vortex is shed. Now, as we discussed in Section 4.3.1.2, the condition for continuous cavitation  $K = K_1$  may not always correspond to  $K_1 = (-C_p)_{\min}$ , but rather to some effective pressure coefficient,  $(-C_p)_{\text{eff}}$ , for example, as given by Equation (4.96); therefore, in Equation (4.168) we can easily replace  $C_p$  by some effective value, e.g.,  $(C_p)_{\text{eff}}$ . No generally acceptable procedure has been developed for this although Il'ichev replaces  $C_p$  by an equation that amounts to Equation (4.96). The number of bubbles cavitating per unit time will then be given by

$$\frac{dN}{dt} = FN_o \quad (4.169)$$

where  $N_o$  is the number of available cavitation nuclei. Equation (4.168) was found by Il'ichev<sup>141</sup> to closely approximate the rate of cavitation events in periodic vortex streets behind a circular cylinder with  $\alpha$  taken as 1.16 and  $S$  as 0.2. In that example the pressure coefficient at the point of vortex formation was taken to be -2 (see also Chapter 5, Figure 5.11) as this is the pressure coefficient at the point of separation on the cylinder.

The significance of Equation (4.168) in terms of reported inception indices for turbulent boundary layers will now be examined. As shown in Section 4.3.2.6 for inception of traveling bubble cavitation in a turbulent boundary layer on a body,  $K_1$  is normally approximated by  $(-C_p)_{\min}$  plus a correction term to account for the effects of turbulence. As the cavitation number is reduced to  $K_1$ , Equation (4.168) shows that the event rate will increase. From Chapter 7 (Figure 7.33) at the wall,



$\alpha_w = 3$  to  $4C_f$ , where  $C_f$  is the local wall shear coefficient, but within the boundary layer Meecham and Tavis<sup>127</sup> have indicated on theoretical grounds that  $\alpha \sim 1.2$  to  $1.4\alpha_w$ , so that we can assume  $\alpha \sim 4.5C_f$ . Furthermore, the appropriate Strouhal number for the pressure fluctuations may be taken as  $S = f\delta/U_\infty \approx 1$ . At the observed inception point,  $K = K_1 = (-C_p)_{\min} + 16C_f$  (see Figure 4.26), the frequency of cavitation events is, accordingly,

$$\frac{F\delta}{U_\infty} \sim 2 \times 10^{-3}$$

Unfortunately, there exist no reported statistics on such event rates, but taking some typical values of  $U_\infty = 50$  ft/sec and  $\delta = 1/20$  ft, the above suggests one cavitation event in every 1.8 seconds. This event interval would certainly be an acceptable one on which to base an observation of incipient cavitation and it suggests that Il'ichev's model should give a generally adequate portrayal of single bubble cavitation events.

**4.4.5.3 Models Based on Bubble Statistics.** To extend the method, the statistical bubble distribution is coupled with the pressure statistics. The number of cavitation events is influenced by the flux of bubbles carried into a zone of cross-sectional area  $\ell_3(\delta_c)$  where  $\ell_3$  is the lateral dimension of a rarefaction zone and  $\delta_c$  is the height above the body in which the static pressure is less than the critical pressure required for cavitation of all bubbles of radius greater than  $R_0$ ; see Figure 4.52. There is also an upper bound radius,  $R^*$ , of available cavitation nuclei in  $(\delta_c)$ . According to Johnson and Hsieh<sup>204</sup> a screening occurs so that smaller bubble trajectories migrate closer to the body than the larger ones. Therefore, some larger bubbles will not cavitate because their trajectories will not occur within the region  $K \leq -C_p$ , as illustrated in Figure 4.52. Following the notation of Section 4.2.4.3, the number of cavitating nuclei per unit volume will be

$$\delta N = \int_{R_0}^{R^*} n(R) dR = N \int_{R_0}^{R^*} P_n(R) dR$$

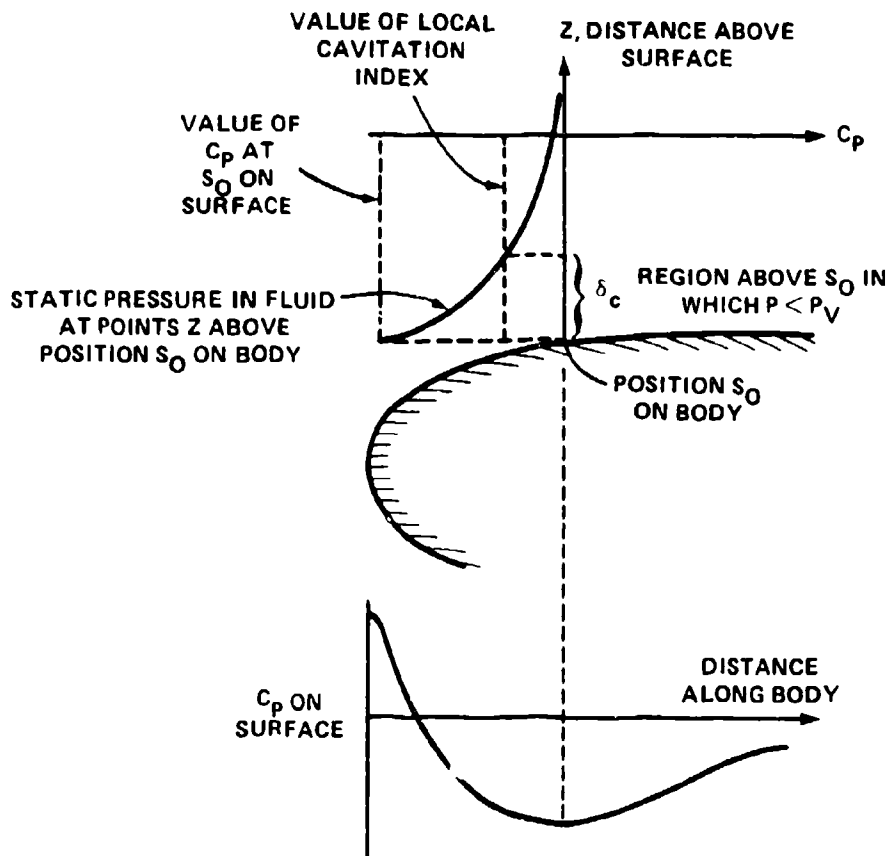


Figure 4.52 - Illustration of the Critical Height,  $\delta_c$ , Above Wall Above which Local Stream Static Pressure Exceeds the Vapor Pressure of Water or the Critical Pressure for Cavitation

where  $n(R)$  is the bubble radius distribution per unit volume (Figures 4.12 and 4.13) and  $N$  is the total number of bubbles per unit volume. In consideration with Equation (4.169), the number of bubbles cavitating per unit time will be

$$\frac{dN}{dt} = F \cdot \delta N \quad (4.170)$$

where  $\delta N$  is the number of available nuclei;  $\delta N$  will be determined later.

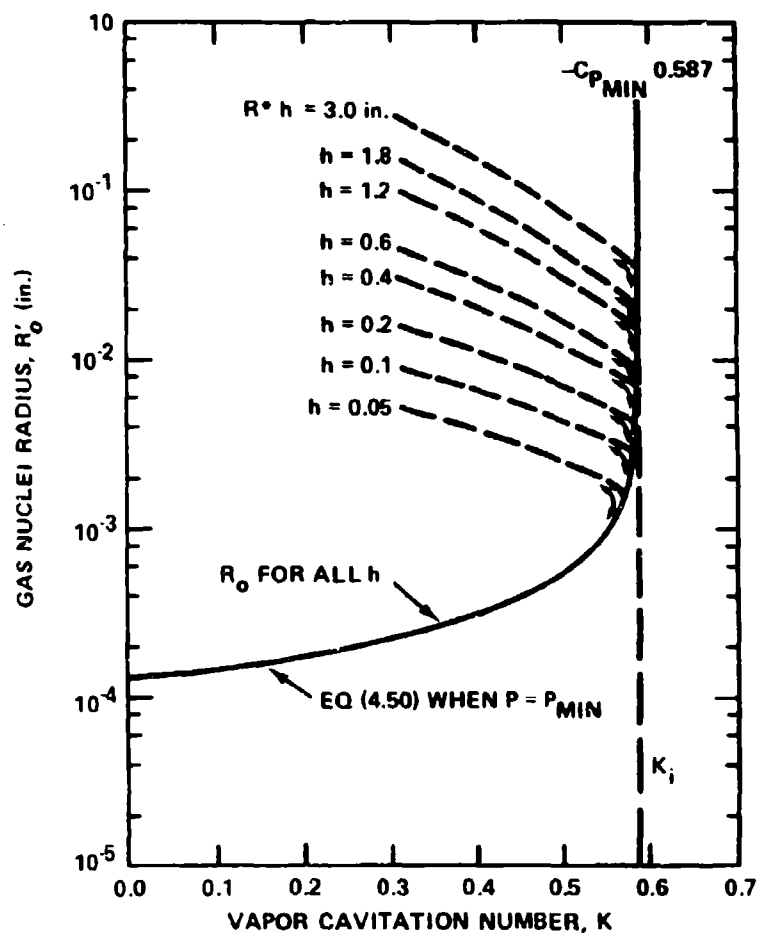


Figure 4.53 - An Example of Upper and Lower Critical Sizes of Gas Nuclei  
as a Function of Vapor Cavitation Number and the Body Size<sup>204</sup>;  
U = 25 Feet per Second. Cavitation will Occur for all  
Bubbles Whose Radii Fall Between  $R_0$  and  $R^*$ ;  
the Upper Limit is Set by Bubble Screening

It is assumed that the static pressure is below the critical pressure so that the statistical nature of bubble cavitation is incorporated wholly in the bubble statistics rather than in the pressure fluctuations. The bubble density is assumed to be small.

The frequency of cavitation events is determined by the number density of the bubbles and the rate of flux of those bubbles into the rarefaction zone, i.e.,

$$\begin{aligned} \frac{dN}{dt} &= (\delta N) \lambda_3(\delta_c) U_\infty \\ &= \lambda_3(\delta_c) U_\infty \int_{R_0}^{R^*} n(R) dR \end{aligned} \quad (4.171)$$

this frequency also represents the number of cavitating bubbles per unit time.

To illustrate the dependence of  $R^*$  on body size and speed, Johnson and Hsieh calculated the trajectories of bubbles of various sizes about a two-dimensional half body of ultimate thickness  $h$  whose shape was defined by

$$x = -y \cot \pi y$$

Figure 4.53 shows both  $R_0$  and  $R^*$  for the body, with the critical pressure evaluated at the point of minimum pressure, the range of radii of unstable bubbles lies between

$$R_{\text{crit}} \leq R \leq R^*$$

Dependence of  $R^*$  on speed is rather weak, but  $R^*$  increases linearly with body dimension. As expected,  $R_{\text{crit}}$  decreases with increasing  $U_\infty^{-2}$ , see Equation (4.98), but is independent of body dimension. Therefore, according to Equation (4.171), the number of cavitation nuclei should depend both on speed and body dimension.

The magnitude of  $\delta_c$  in Equation (4.171) will depend upon the radius of curvature and shape of the body. For an elliptic cylinder transverse to the flow, Levkovskii<sup>199</sup> has shown

$$\frac{\delta_c}{a} = \frac{\ln \left( \frac{K_1}{K} \right)}{1.3 + 0.27 K_1} \quad (K_1 \approx (-C_p)_{\min})$$

where  $a$  is the semimajor axis that is assumed to be parallel to the flow. For a circular cylinder of radius  $a$ ,  $\delta_c$  is given by

$$K = \left( \frac{a}{a + \delta_c} \right)^2 \left[ 2 + \left( \frac{a}{a + \delta_c} \right)^2 \right], \quad K_1 = 3$$

or

$$\frac{\delta_c}{a} = \left( \frac{K_1}{K} \right)^{1/2} - 1$$

These relationships indicate that, in general,  $\delta_c$  is a function of  $K_1$  and  $K$

$$\delta_c \propto a f \left[ \left( \frac{K_1}{K} \right)^{1/2}, K_1 \right]$$

so the frequency of cavitation can be written in the general form

$$\frac{dN}{dt} \propto \ell_3 a U_\infty \int_{R_{crit}}^{R^*} n(R) dR \cdot f \left[ \left( \frac{K_1}{K} \right)^{1/2}, K_1 \right] \quad (4.172)$$

For cavitation (and other bubble noise) that is determined by the bubble statistics in this model, the event-rate will increase with the square of the body size scale (with slight additional increase through  $R^*$ ) and linearly with speed. This behavior contrasts with that determined only by the statistics of the liquid-phase turbulence, Equations (4.168) and (4.169) ignore a possible growth of  $N_0$  with body size and show that the event rate will be inversely proportional to the body size at a given value of  $K_1/K$ . Both analyses show that the event rate will increase linearly with speed.

4.4.5.4 Predictions of Sound Pressure Levels. The above models of event rates have been used to generate functional predictions of cavitation noise. It will be shown below that all existing models of this type have certain inconsistencies with measured sound. To determine the sound power from a train of cavitation pulses, assume

that the bubbles all behave independently, then the mean-square sound pressure will thus depend upon the contributions from individual bubbles

$$\overline{p_a^2} = \sum_i^N \overline{p_i^2}$$

where the summation is over the contributions of  $N$  bubbles. The composite spectral density  $\phi_c(r, \omega)$ , Equation (4.124), for the bubbly mass is related to the average of the individual densities  $\overline{S}(r, \omega)$  by

$$\phi_c(r, \omega) = \frac{dN}{dt} \overline{S_p}(r, \omega) \quad (4.173)$$

where  $dN/dt$  is given alternatively by Equation (4.169), (4.170), or (4.172). In all those cases the rate increases with  $U_\infty$ . Combination of Equations (4.154) and (4.158) gives

$$\overline{S}(r, \omega) = \rho_o P_\infty \frac{\ell_r^4}{r^2} \left( \frac{K_i - K}{2(1 - C_p)} \right)^2 \tilde{S}_p(r, \omega \tau_c) \quad (4.174)$$

where  $\tilde{S}_p(r, \omega \tau_c)$  = a dimensionless spectrum function like that shown in Figure 4.33.

$\ell_r$  = the chordwise extent of the rarefaction zone

$\overline{C_p}$  = the average pressure coefficient in that zone

To find the mean-square pressure in a proportional frequency band,  $\Delta(\omega \tau_c)$ , we combine Equations (4.174), (4.173), (4.171), (4.158), (4.154), and (4.70) to give (as in the cases of Equations (4.155) and (4.159))

$$\begin{aligned} \overline{p_s^2}(\omega, \Delta\omega) &= 2 \int_{\Delta\omega} \phi(\omega, r) d\omega \\ &\approx (\ell_3 \ell_c \ell_r n_o) P_\infty^2 \left( \frac{\ell_r}{r} \right)^2 \left( \frac{K_i - K}{2(1 - C_p)} \right)^{3/2} \left( \frac{2}{K} \right)^{1/2} \gamma_i^{-1} \tilde{S}_p(\omega \tau_c) [2\Delta(\omega \tau_c)] \\ &\sim a \left( \frac{K_i}{K} - 1 \right)^{1/2} \left( 1 - \frac{K}{K_i} \right) \text{ for given } K_i \text{ and } \omega \tau_c \end{aligned} \quad (4.175)$$

where  $n_0$  is the integral of  $n(R)$  in Equation (4.171) and where  $\tilde{S}(\omega\tau_c)$  is the dimensionless spectrum for single-bubble noise; see Figure 4.33. Equation (4.175) is similar to Equation (4.159), however, the nucleus encounter rate has now been included giving rise to an added dependence on velocity. The velocity dependence indicated by Equation (4.175) is shown in Figure 4.50 to be representative of noise from traveling bubble cavitation. When the statistics of the single-phase pressure fluctuations are important, an equation analogous to Equation (4.175), using Equation (4.170), will replace  $L_3 \delta_c \lambda_c n_0$  with an expression of the form (neglecting the exponential in Equation (4.168))

$$L_3 \delta_c \lambda_c n_0 \sim S \frac{\lambda_c}{\delta}$$

where  $\delta$  is a boundary layer thickness (Equation (4.167)). Both approaches, however, give basically the same speed dependence.

A dependence of bubble cavitation noise on the nucleus concentration itself has been demonstrated by Arndt and Keller<sup>80</sup> for cavitation in the wake of a sharp-edged disk. Measurements of noise in controlled oceans of nuclei have demonstrated a linear increase in noise level as the number of events increased when  $K$  decreased below  $K_1$  for a given nucleus distribution. At a fixed value of  $K$ , the dependence of noise on the number of nuclei  $n_0$  was unclear due to conflicting changes in level at low and high frequencies. At frequencies greater than 5 kHz, the noise decreased with the increase in bubble nuclei; a behavior which could be due to high partial pressures of gas in collapsing bubbles or to absorption. An explanation beyond this was not given and more work should be done in the future.

Equation (4.175) suggests that  $\overline{p^2}(\omega, \Delta\omega)$  will increase as length scale  $L$  and as  $L^5/r^2$ , a dependence that is not supported by the scaled measurements of Figures 4.44 and 4.46, in spite of the fact that the associated dependence on speed can be supported. Those same experimental results suggest that the number of bubble nuclei

$$L_3 \delta_c \lambda_c n_0 \sim N_0$$

is independent of length scale because the noise increases simply as  $L^2/r^2$ .

Balter<sup>170</sup> has also noted this discrepancy between the measured noise and the expected scale factor.

A possible dependence of noise on  $K$  in addition to that indicated in Equation (4.175) is included in the value of  $n_o$ , although it, too, leads to an expression that has not been supported by experiment. As indicated in Figure 4.12, the distribution function  $n(R)$  behaves roughly as

$$n(R) \sim R^{-3.5}$$

therefore, the integral in Equation (4.171), yielding  $n_o$ , is of the form

$$n_o \sim \left\{ \left( \frac{1}{R_o} \right)^{2.5} - \left( \frac{1}{R^*} \right)^{2.5} \right\}$$

where, from Equation (4.99)

$$R_o \approx \frac{4S}{P_\infty} \left( \frac{K}{K_1 - K} \right)^{2/3}$$

and from Figure 4.53 (using  $f(K_1 - K)$  to express the indicated dependence on  $K$ )

$$R^* \approx L f(K_1 - K)$$

$$\geq R_o$$

Therefore, for advanced cavitation, when  $K < K_1$ , this first term gives

$$n_o \sim P_\infty^{2.5} \left( \frac{K_1 - K}{K} \right)^{5/3}$$

Although this expression gives an appropriate speed dependence, the additional dependence on pressure  $P_\infty$  is neither borne out by measurement nor has the associated dependence on surface tension been investigated and, it indeed seems unlikely to be



supportable. Therefore, it seems that a fully consistent analytical model for bubble cavitation has not yet been developed. Such a model must indicate an increased noise level with nucleus content and retain the dependence on  $L^2/r^2$  as well as on  $P_\infty^2$  as indicated by experiment. Clearly, a systematic investigation of the dependence of nuclei on noise of different types of cavitation is also needed.

A somewhat similar approach has been used by Ross<sup>5,189</sup> to account for the speed dependence of noise from rotating vanes. Referring to Equation (4.175) and Figure 4.54 we see that the noise is dependent upon the rarefaction dimension  $\ell_r$  which, in

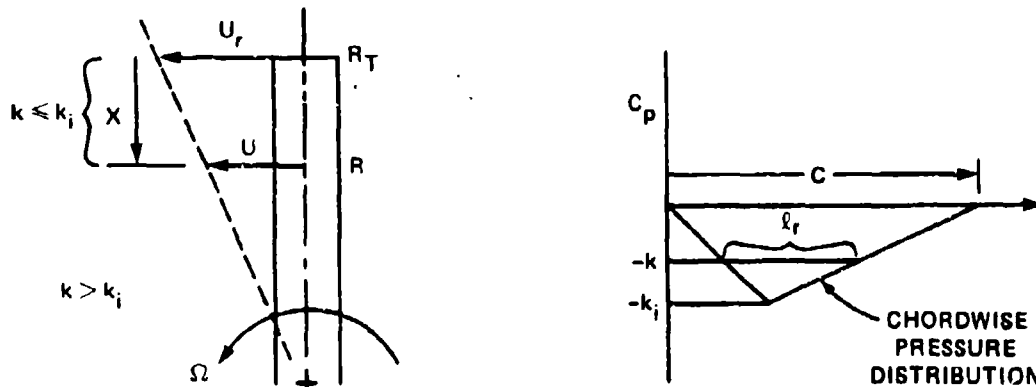


Figure 4.54 - Idealization of Pressure Distribution on a Rotating Vane for the Estimation of the Speed-Dependence of Cavitation Noise

turn, is dependent upon the cavitation number  $K$  relative to  $K_1$ . Ross made the additional step of accounting for the increase in  $\ell_r$  as  $K$  decreases. Also, because the velocity of the vane section increases linearly with distance from the center of rotation  $R$ , cavitation will exist only on the outer portion of the vane defined by

$$\frac{R_T}{R} = \left( \frac{k}{k_T} \right)^{1/2}$$

where  $k_T$  is the cavitation index relative to the tip speed of the vane:

$$k_T = \frac{P_\infty - P_v}{\frac{1}{2} \rho_o (R_T \Omega)^2}$$

where  $R_T \Omega = 2\pi R_T n_s$  is the rotational tip velocity of the blade.

Furthermore, to illustrate the importance of the dependence of  $\ell_r$  on  $K$ , Ross assumed the triangular pressure distribution illustrated in Figure 4.54 for which

$$\frac{\ell_r}{C} = 1 - \frac{k}{k_1}$$

Therefore, the dependence of  $\ell_r$  on radius is

$$\frac{\ell_r}{C} = 1 - \frac{k_T}{k_1} \left[ \frac{R_T}{R} \right]^2$$

$$\frac{\ell_r}{C} = 1 - \frac{K}{K_1} \left[ \frac{R_T}{R} \right]^2, \quad R_T \geq R \geq R_T \left[ \frac{K}{K_1} \right]^{1/2} \quad (4.176)$$

where, now, we have replaced

$$K = k_T \left[ \frac{\Omega R_T}{U_A} \right]^2 = \frac{P_\infty - P_v}{\frac{1}{2} \rho U_A^2}$$

$U_A$  is the advance speed of the vane.\* Ross assumed that the dependence of noise on  $\ell_r$  was only related to an increase in the area of cavitation as  $K$  decreased; the area being given by

$$\begin{aligned} \frac{A_c}{C R_T} &= \int_{(K/K_1)^{1/2}}^1 \left( \frac{\ell_r}{C} \right) d \left( \frac{R}{R_T} \right) \\ &= \left[ 1 - \left( \frac{K}{K_1} \right)^{1/2} \right]^2 \end{aligned}$$

---

\*Actually, here it is assumed that  $\Omega R_T \gg U_A$  so that the resultant velocity of the vane tip is dominated by its rotational velocity. Otherwise it would be more appropriate to write  $[(\Omega R_T)^2 + U_A^2]^{1/2}$  in place of  $\Omega R_T$ .

Furthermore, the number of nuclei was assumed to increase linearly with speed as

$$\frac{U_T}{(U_T)_1} = \frac{U_A}{(U_A)_1} = \frac{\Omega}{\Omega_1} = \left(\frac{K_1}{K}\right)^{1/2}$$

Therefore, instead of the Equation (4.147) or (4.175), we may have for the mean-square sound pressure at scaled frequencies for dynamically-similar vanes ( $\Delta\omega \propto \omega$ )

$$\overline{p^2}(\omega, \Delta\omega) \propto B P_\infty^2 \frac{C R_T}{r^2} (K_1 - K) \left[ 1 - \left(\frac{K}{K_1}\right)^{1/2} \right]^2 \left(\frac{K_1}{K}\right)^{1/2}$$

$$\gamma_{\ell}^{-1} \cdot \tilde{S} \left( \frac{\omega R_T}{\left(\frac{P_\infty}{p_o}\right)^{1/2} (K_1 - K)^{1/2}} \right) \quad (4.177)$$

where B is the number of vanes. This relationship for  $K_1/K$  is similar to one derived by Ross<sup>5</sup> except for the added factor of  $(K_1 - K)$  and a factor  $K_1/K$ . The former factor arises from our earlier postulate involving the bubble dynamics, but it has only a weak influence on the numerical values. The latter factor  $K_1/K$  arises as described on page 379. It amounts to replacing  $p_o$  by  $1/2 \rho_o U^2$  in the relationship preceding Equation (4.148). Figure 4.49 shows that the variation of sound pressure with  $(K_1/K)^{1/2}$ , interpreted as an equivalent speed-dependence, agrees well with measured propeller noise. A major distinguishing feature between Equations (4.175) and (4.177) is only in the assumption that  $dN/dt$  is independent of body dimension in the latter case and dependent on it in the former.

A greater level of complexity is brought on by substituting Equation (4.176) into Equation (4.175) and integrating over  $\ell_3 = R_T (1 - (K_T - K_1)^{1/2})$ . The dependence on  $\ell_c$  is now cubic, leading to a dependence on  $K_1/K_T$  of the form

$$\left(\frac{K_1}{K_T}\right) \left(1 - \frac{K_T}{K_1}\right)^{3/2} \int_{(K_T/K_1)^{1/2}}^1 \left(\frac{\ell_c}{C}\right) d\left(\frac{R}{R_T}\right)$$

$$= \frac{1}{\kappa^2} (1 - \kappa^2)^{3/2} \left\{ (\kappa - 1) (1 + 3\kappa) - 3\kappa(\kappa^3 - 1) + \frac{\kappa}{5} (\kappa^5 - 1) \right\} \quad (4.178)$$

where  $n_o$  has been assumed proportional to  $[(K_T)^{1/2}]^{-1}$ , and where

$$\kappa = \left( \frac{K_T}{K_1} \right)^{1/2}$$

Figure 4.49, line 4, shows that little benefit is to be derived by using either of the forms of Equation (4.177) or (4.178) in preference to Ross' result, but any of these speed dependences will give a better representation to the measurement than the simple  $(K_1 - K)$ .

## 4.5 SOUNDS FROM OTHER BUBBLE MOTIONS

### 4.5.1 Sound Pulses from Formation and Splitting

While the bulk of two-phase flow-noise research has dealt with cavitation noise, there has been some attention given to other types of bubble noise. Perhaps the most comprehensive analysis of the noise of splitting and formation of bubbles has been made by Strasberg.<sup>21,23</sup> For example, the formation of a bubble at a nozzle is illustrated in Figure 4.55; noise is produced at the instant the bubble pinches off from the nozzle. The ensuing sound is a decaying sine function such as the impulse response of a linear harmonic oscillator. Such motion of bubbles is typical when they are formed initially or when they are split. The sound field is given by Equation (4.120), or its analog in frequency space, with the volume fluctuation given by whichever of Equations (4.22) or (4.29) is appropriate. The noise spectrum will, therefore, be centered at a frequency near the average resonance frequency of the bubbles. It remains, therefore, to determine the correct function to describe the time behavior of the excess pressure. Little has been done in this regard although Strasberg<sup>21,23</sup> and Junger and Cole<sup>32</sup> have each given a theory which applies to a different physical conception of the forces acting on the bubble when it is formed.

Strasberg considers the formation of a bubble at a nozzle that forms very slowly so that the pressure differential across the bubble wall remains essentially constant as the bubble grows. When the bubble detaches it undergoes a linear free-decaying

oscillation in its volume mode. This oscillation has initial conditions on both the perturbation volume  $v_o = V - V_o$  and the volume velocity  $\dot{v}_o$ . These two quantities will depend on how the bubble is grown at the nozzle. Before the detachment, as shown in Figure 4.55, as the bubble grows slowly at the nozzle and the ambient

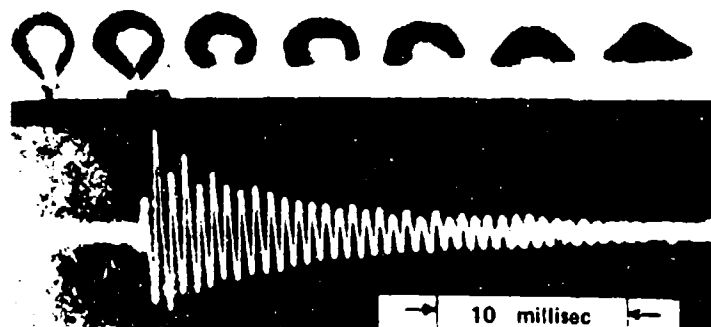


Figure 4.55 - Oscillogram of the Sound Pulse from a Single Gas Bubble in Water, with Four Superimposed Photographs of the Bubble Itself. The Time Each Photograph was taken Corresponds to the Point on the Oscillogram Below the Bubble.

(From Strasberg<sup>21</sup>)

pressure  $P(r,t)$  is constantly equal to  $P_o$ . The liquid pressure at the bubble wall  $P(R,t)$  is determined by the (constant) pressure inside the bubble  $P_g$ , from Equation (4.10), which is greater than  $P_o$  by a time-dependent excess pressure  $p_+(R,t)$  inside that is maintained by the gas supply. Thus,

$$P_g = P_o + \frac{2S}{R} + p_+(R,t) \approx P_o + p_+(R,t)$$

where  $2S/R$  may be neglected for large enough bubbles. Under the influence of this constant pressure, the volume velocity just before the bubble separates is approximately as given by Equation (4.13)

$$\dot{v}_o \approx \left( \frac{2}{3} \frac{P_+}{\rho_o} \right)^{1/2} 4\pi R_o^2 \quad (4.179)$$

where the  $(\dot{v}_o)^2$  term is presumed to dominate the  $\ddot{V}$  term. The initial volume perturbation  $v_o$  is given by the ideal gas law for isothermal motions

$$\frac{dP}{P} = - \frac{dV}{V}$$

therefore,

$$\frac{P_+}{P_o} = \frac{V_o - V}{V_o} = - \frac{V - V_o}{V_o} \quad (4.180)$$

where  $V_o$  is the rest volume of the bubble. For linear bubble motions subject to the initial conditions  $v(t=0) = v_o$  and  $\dot{v}(t=0) = \dot{v}_o$ , but  $p_+(r,0) = p_+(r,t) = 0$ , the transform of Equation (4.22) has the solution

$$V(\omega) = \frac{[(\dot{v}_o)^2 + \omega^2 v_o^2]^{1/2} e^{i\phi}}{2\pi[i(\omega^2 - \omega_o^2) + \eta v_o \omega]} \quad (4.181)$$

where

$$\tan \phi = \frac{-\dot{v}_o}{\omega v_o}$$

with the one-sided time transforms

$$V(\omega) = \frac{1}{2\pi} \int_0^\infty e^{i\omega t} v(t) dt$$

and

$$\frac{1}{2\pi} \int_0^\infty \ddot{v}(t) e^{i\omega t} dt = \dot{v}_o - i \omega v_o - \omega^2 V(\omega)$$

If bubbles are formed at a rate  $n_o$ , then the sound pressure spectrum can be found from the transform of Equation (4.120) with Equations (4.125) and (4.173), with a lifetime  $\tau_\ell = (\eta\omega_o)^{-1}$ . Therefore, the sound spectral density is

$$\phi_{p_{\text{rad}}}(r, \omega) = \frac{n_o}{2\pi} \frac{\rho_o^2 \omega^4}{16\pi^2 r^2} \frac{[(\dot{v}_o)^2 + \omega^2 v_o^2]}{[(\omega^2 - \omega_o^2)^2 + \eta^2 \omega_o^2 \omega^2]} \quad (4.182)$$

and the total mean-square sound pressure is controlled by frequencies  $\omega \approx \omega_o$  so

$$\overline{p_{\text{rad}}^2}(r) = \frac{1}{2} \frac{n_o}{16\pi^2 r^2} \frac{\rho_o^2 \omega_o^2}{\eta \omega_o} \frac{[(\dot{v}_o)^2 + \omega_o^2 v_o^2]}{\eta \omega_o} \quad (4.183)$$

The quantities  $\dot{v}_o$  and  $v_o$  are given, respectively, by Equations (4.179) and (4.180). The excess pressure  $p_+$  for a slowly-growing bubble is that which just overcomes the surface-tension at the interface between the nozzle (of radius  $R_N$ ) and the bubble wall, thus,

$$p_+ = \frac{2S}{R_N} \quad (4.184)$$

Typically  $p_+/P_o < 1$ , therefore, the  $\dot{v}_o \gg \omega_o v_o$  and Equation (4.183) becomes, using Equations (4.20) and (4.27)

$$\overline{p_{\text{rad}}^2}(r) = \frac{\rho_o c_o}{4\pi r^2} Q \frac{\eta r}{\eta} p_+ \quad (4.185)$$

which is equivalent to the relationship derived by Strasberg. In this instance the size of the bubble is determined by the relationship between the force acting to remove the bubble from the nozzle and the tensile force acting to hold it on the nozzle. Ultimately this force relationship will determine both the size of the bubble and its resonance frequency.

Strasberg treats the problem of bubble splitting or coalescence in the same manner, however, the excess pressure is determined by the change in equilibrium surface tension pressures required to maintain the smaller bubbles relative to the larger bubble. If a large bubble splits into two equal values then Strasberg notes that approximately

$$p_+ \sim \left(2^{1/3} - 1\right) \frac{2S}{R} \quad (4.186)$$

where  $R$  is the radius of the large bubble. This pressure is the same whether the bubbles split or coalesce.

The sound pressures emitted when bubbles formed are theoretically greater than sound pressures emitted when bubbles split. As an example, Strasberg<sup>23</sup> notes that the root-mean-square sound pressure from bubbles of 0.3 cm radius emitted from a nozzle of 0.1 cm radius at a rate  $(n(t))$  of  $10 \text{ sec}^{-1}$  in an ocean of atmospheric pressure will have a frequency of 1000 Hz and a magnitude of 132 dB re 1  $\mu$ Pa, with  $n \sim 0.014$ . On the other hand, if each of the 0.3-cm radius bubbles split, then the root-mean-square sound pressure at one meter distance will be 75 dB re 1  $\mu$ Pa centered on a frequency of 1260 Hz.

In the example considered by Junger and Cole,<sup>32</sup> bubbles are formed from a disintegrating gas jet emerging into a liquid. The jet velocity at the orifice is so large that single bubbles do not form. This case might be realized when the Weber number

$$We_g \approx \frac{\rho U^2}{\frac{S}{R_n}} \quad (4.187)$$

is greater than one. Alternatively, Strasberg's example applies when  $We \ll 1$ . In the case of the disintegrating gas jet, the cylindrical jet forms a series of spherical bubbles of radius  $R_b$ ; as seen in Section 4.5.4,  $R_b$  is greater than the nozzle radius ( $R_b \approx 5 R_n$ ). The added mass of the array of spheres  $M_b$  is greater than



that of the cylinder of gas that forms them,  $M_j$ . It is assumed that the kinetic energy of the liquid is preserved during the disintegration. Therefore, the translation velocity  $U_b$  of the bubbles is less than the velocity of the jet  $U_j$ ; actually  $U_b/U_j \approx (R_j/R_b)^{3/2}$  because  $U_b/U_j \sim (M_j/M_b)^{1/2}$ . This reduction in velocity carries with it an increase in the Bernoulli pressure in the gas phase. This increased pressure which is impressed on the newly-formed bubbles is

$$P_+ \sim \frac{1}{2} \rho_g U_j^2 \quad (4.188)$$

if  $R_j/R_b < 1$  so that  $U_b^2 \ll U_j^2$ . This pressure change is assumed to last for a time duration which is equal to  $1/4$  of the natural period of oscillation of the  $n = 2$  oscillation mode of the bubble  $\omega_2^{-1}$ ; see Equation (4.218). In this view of the bubble excitation, the initial conditions on volume velocity and volumetric perturbation ( $\dot{v}_0$  and  $v_0$ ) are assumed to vanish and the only source of excitation is from this change in total head.

Since the duration  $2\pi(4\omega_2)^{-1}$  is much longer than the period of oscillation  $2\pi(\omega_0)^{-1}$  of the new bubbles, the details of the pressure time history are not crucial to the problem. Junger and Cole assume that the pressure has a variation of

$$P(R, t) = p_+ (1 - \cos \omega_2 t) \quad 0 < t < \frac{\pi}{2\omega_2}$$

$$= p_+ \quad t > \frac{\pi}{2\omega_2}$$

The Fourier time transform of this function is

$$P(R, \omega) = p_+ \delta(\omega) + \frac{p_+}{2\pi} \left[ e^{i(\omega+\omega_2)\tau/2} \frac{\sin(\omega+\omega_2)\frac{\tau}{2}}{\omega + \omega_2} + e^{i(\omega-\omega_2)\tau/2} \frac{\sin(\omega-\omega_2)\frac{\tau}{2}}{\omega - \omega_2} \right]$$

in which case, for Equation (4.29) with  $\omega \sim \omega_0 \gg \omega_2$ , this reduces to

$$P(R, \omega) \approx \frac{-p_+}{\pi} \frac{\sin \frac{\omega \tau}{2}}{\omega} e^{i(\omega \tau / 2)}$$

where  $\tau = \pi / 2\omega_2$ . In the above fashion the autospectrum of the sound pressure can be written for a rate  $n$  of bubble formation

$$\phi_{\text{rad}}(r, \omega) = \frac{n}{\pi} \frac{R_b^2 (p_+)^2 \omega^2}{r^2 [(\omega_0^2 - \omega^2)^2 + \eta^2 \omega^2 \omega_0^2]} \text{ for } \omega > \omega_2 \quad (4.189)$$

and the mean square sound pressure is

$$\overline{p_{\text{rad}}^2} = \frac{\rho_0 c_0}{4\pi r^2} Q \frac{\eta_r}{\eta} (p_+) \left( \frac{p_+}{p_\infty} \right) \quad (4.190)$$

where  $Q$  is the volumetric flow rate of gas. In the above, since  $\pi\omega_0/2\omega_2 > 1$ , the effective value of  $\sin^2 \omega\tau/2$  was taken as  $1/2$ .

Equations (4.185) and (4.190) differ in the dependence on the excess pressure stemming in each case from the assumptions on the initial conditions. Junger and Cole ignore effects of surface tension, instead of putting all the source of excitation into the inertial forces associated with the total head of the fluid motion. Accordingly, Equation (4.190) implies a strong dependence of sound pressure on volumetric flow rate, while Equation (4.185) does not. Note that in Equation (4.190)  $p_+$  is proportional to  $Q^2$ , while in Equation (4.183) it is not.

The above analyses have not accounted for any effects of liquid motion, however, they do suggest some general behavior and that some distinctions between high and low Weber-number flows need to be made when interpreting the results. At the low Weber number of Strasberg's problem, the interfacial stresses are governed by surface tension while at high gas Weber numbers the interfacial stresses that drive the bubbles are governed by the inertia of the gas. In both cases, however, the dependence of sound level on speed and volumetric flow rate should be roughly as given by Equation (4.185), i.e.,

$$\overline{p_{\text{rad}}^2} \sim Q U_{\infty}^0 \quad (4.191)$$

i.e., independent of any small enough liquid velocity that either  $\frac{1}{2} \rho_o U_{\infty}^2 \ll 25/R_n$  or  $U_{\infty} \ll U_g$ .

At high enough Weber numbers and with the liquid velocity greater than the gas velocity, then interfacial stresses will be inertial (analogous to the disintegrating jet). When the bubbles enter a region of turbulent motion, Whitfield and Howe have suggested that the turbulent excitation on the bubble of radius  $R$  in a local pressure gradient  $\partial p / \partial x_i$ , will cause the bubble to stretch in the direction of  $x_i$ . Ultimately, when the bubble splits, the excess pressure will be proportional to

$$p_+ \sim a \frac{\partial p}{\partial x_i} \\ \sim a r_o^2 U_{\infty}^2 \frac{\partial p}{\partial x_i}$$

Equation (4.181) suggests that

$$\overline{p_a^2}(r) \sim \frac{\rho_o c_o a^2}{4\pi r^2} Q \frac{n_r}{r_i} \frac{\rho_o U_{\infty}^4}{P_o} \left( \frac{\partial p}{\partial x_i} \right)^2 \quad (4.192)$$

as long as the resonance period is much shorter than the time scale of the hydrodynamic pressure. This expression gives a  $U_{\infty}^4$  velocity dependence.

Finally, as discussed in Section 3.7, sound emitted from turbulent bubbly jets, without bubble splitting or formation, will behave as

$$\overline{p_a^2} \sim U_{\infty}^6 \quad (4.193)$$

#### 4.5.2 Bubbles Excited by a Pressure Field: Speed Dependence

When a bubble is convected past a body or through a nozzle, in steady flow  $U_{\infty}$ , it experiences a transient pressure field. If the spatial dependence of the pressure is given by Equation (4.80), then the fluctuating pressure on the bubble is

$$p(R_b, t) = \frac{1}{2} \rho_o U_\infty^2 C_p (U_c t) \quad (4.194)$$

Also, if the length of this low-pressure zone is  $\ell_r$ , the time scale of the pressure pulse exciting the bubble will be  $\ell_r/U_c$  which will generally be less than the resonance period of the bubble. The convection velocity of the bubble will generally be within 80 percent of  $U_\infty(1-C_p)^{1/2}$ . Because the pressure field induces a transient forced motion at a frequency less than the resonance frequency, Equations (4.18) or (4.36) together with Equation (4.120) give the sound pressure as

$$p_a(r, t) = \frac{-V\rho_o}{4\pi r} \frac{1}{\rho_g c_g^2} \frac{D^2 p(R_b, t)}{Dt^2} \quad (4.195)$$

where

$$\frac{D}{Dt} = \frac{\partial}{\partial t} + U_c \frac{\partial}{\partial x_1}$$

and  $p(r, t)$  is given in Equation (4.184).

Equation (4.195) has been used by both Strasberg<sup>23</sup> and Chalov<sup>205</sup> to calculate sounds radiated by bubbles passing by circular and elliptic cylinders, respectively. Whitfield and Howe<sup>26</sup> and Crighton and Ffowcs-Williams<sup>1</sup> have also derived a relationship similar to Equation (4.195); the relationship of Whitfield and Howe<sup>26</sup> differs from Equation (4.195) in the replacement of the gas compressibility with a composite of compressibilities of the surrounding fluid and of the bubble gas, i.e., they write

$$p_a(r, t) = \frac{V\rho_o}{4\pi r} \left( \frac{1}{\rho_m c_m^2} - \frac{1}{\rho_g c_g^2} \right) \frac{D^2 p(R_b, t)}{Dt^2} \quad (4.196)$$

However, if we deal with mixtures of moderate concentration of gas so that  $\rho_o = \rho_m$  and  $c_o = c_m$ , then  $\rho_m c_m^2 \gg \rho_g c_g^2$  (see Figure 4.5) and the ambient fluid compressibility can be ignored.

To put this noise in the perspective of splitting and bubble formation, we refer again to a calculation of Strasberg.<sup>23</sup> The sound pressure level from a stream of 10 bubbles/sec of radius 1/3 cm convected at a speed of  $U_c \sim U_\infty = 10$  m/sec will be 116 dB re 1  $\mu$ Pa at a frequency band of 1 Hz. The resonance frequency of the bubble is 1000 Hz.

The dependence of this noise on liquid velocity is  $U_\infty^8$  even though the acoustic source is a monopole. This dependence is suggested by Equation (4.195)

$$p_a(r, t) \sim \frac{-v \rho_o}{4\pi r} \frac{1}{\rho_g c_g^2} \cdot U_c^2 \left[ \frac{1}{2} \rho_o U_\infty^2 \right] \frac{\partial^2 C_p}{\partial x_1^2}$$

so that

$$\overline{p_a^2}(r) \sim \frac{v^2}{r^2} \left( \frac{\rho_o}{\rho_g} \right)^2 \left( \frac{U_\infty}{c_g} \right)^4 U_\infty^4 \left( \frac{\partial^2 C_p}{\partial x_1^2} \right)^2 \quad (4.197)$$

which is the same speed-dependence derived by Crighton and Ffowcs Williams; see Chapter 3. This speed dependence is to be contrasted with that which may exist if bubbles split under hydrodynamic turbulent excitation.

If, on the other hand, the hydrodynamic time scale and the bubble resonance period do coincide, but the bubbles still do not split and the gas concentration is very dilute, then Equation (4.22) gives the mean-square sound pressure in a narrow-band at a frequency somewhat greater than the bubble-resonance frequency; a result like Equation (4.192) is obtained:

$$\begin{aligned} \overline{p_a^2}(r) &\sim \left( \frac{R_b}{r} \right)^2 \frac{\phi_p(\omega)\omega}{\eta} \\ &\sim \left( \frac{R_b}{r} \right)^2 \frac{(\rho_o U_\infty^2)^2}{\eta} \left\{ \frac{\phi_p(\omega)\omega}{(\rho_o U_\infty^2)^2} \right\} \end{aligned} \quad (4.198)$$

giving a  $U_\infty^4$  dependence, where  $\phi_p(\omega)$  is the frequency spectrum of the pressure sensed by the bubble; this spectrum is dimensionless in the form shown in brackets. This result would have to be modified if there is a large enough concentration of neighboring bubbles so that there would be significant acoustic transmission loss.

Thus, for bubbles which are excited below their resonances,  $\overline{p_a^2}$  increases as  $U_\infty^8$ , while when the excitation time scale is short enough that the bubbles are excited at their resonance frequencies, then  $\overline{p^2}$  increases as  $U_\infty^4$ .

### 4.5.3 Measurements of Bubble Noise

While analytical investigation of the noise from noncavitating bubble motions has received little attention, measurements of the bubble noise are more scarce. No comprehensive experimental work has been done on noncavitating bubble noise production. It is, therefore, not possible to state unequivocally which of the noise mechanisms outlined in Section 4.5.2 are dominant in practical situations.

Measurements were made by Gavigan et al.<sup>206</sup> of noise from an exhaust of nitrogen bubbles emitted through a multiholed strainer plate set in the tail of a test body of revolution. Figure 4.56 shows an example of their results. The test body was installed in a water tunnel, so that the gas was emitted on the axis of the turbulent wake of the body. The spectral densities of noise in the frequency range  $6.3 < f/1000 < 40$  kHz were found to decrease roughly as  $f^{-1}$  (i.e., one-third octave band levels nearly independent of frequency) which contradicts the premise that noise is due to decaying resonant motion. The levels increased with volumetric flow rate as

$$\overline{p_a^2} \sim Q^{0.5} \text{ to } Q^{0.8}$$

No information was given on the dependence of the noise on speed, however, the noise level was independent of the radius of holes in the strainer plate. This last observation is not surprising since at high values of gas Weber number the bubble size is only weakly dependent on orifice size, see Section 4.5.4.1.

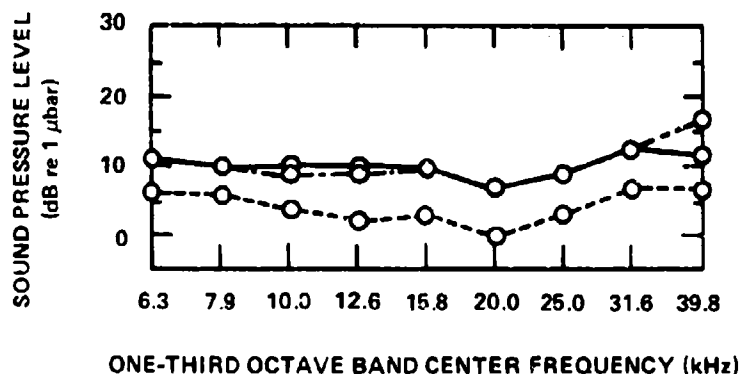


Figure 4.56 - Sound-Pressure Levels in One-Third-Octave Frequency Bands  
 $Q = 41.7$  Cubic Centimeters per Second,  $r_s = 0.025$  Centimeters  
 (Solid Line);  $Q = 41.7$  Cubic Centimeters per Second,  
 $r_s = 0.063$  Centimeters (Dot-Dash); Background  
 Noise, No Gas Flow (Small Dash)

Another investigation, also not comprehensive in the range of variables examined, is that of Blake.<sup>207</sup> Air was emitted from a small hole at the midchord and midspan of a symmetrical hydrofoil at 0 deg angle of attack. The section roughly resembled a NACA 653-018, but modified with an elliptic trailing edge. Air passed from a supply tank through a channel in the hydrofoil to the circular exit orifice. Figure 4.57 shows photographs of four characteristic bubble patterns that were observed. These photographs indicate three types of interactions between the air efflux and the water cross flow that lead to: a regular formation of bubbles (Regime I), a smooth conical air tube enshrouded with laminar flow (Regime IV) which lies either above IVA or on IVB the surface of the hydrofoil, a bubbly jet in the turbulent boundary layer (Regime III) and a transitional range (Regime II), which is dependent on the orifice diameter and in which either a bubble stream that results from a jet break-up or an air cone is formed. The regimes did not otherwise depend on the orifice size used; 0.01 in. and 1/32 in. with choked flow existing in the 0.01 in. orifice at  $Q_o = 8.3 \text{ cm}^3/\text{sec}$ .

Examples of the frequency spectra of sound radiated in the three important formation regimes are shown in Figure 4.58. The notable characteristic of the noise spectra is a general broadening of the noise peak as  $U_\infty$  increases at nearly constant supply flow rate. Possibly this is related to the increased quantity of small bubbles with increasing water velocity. Four additional features of the noise spectral density are to be noted:

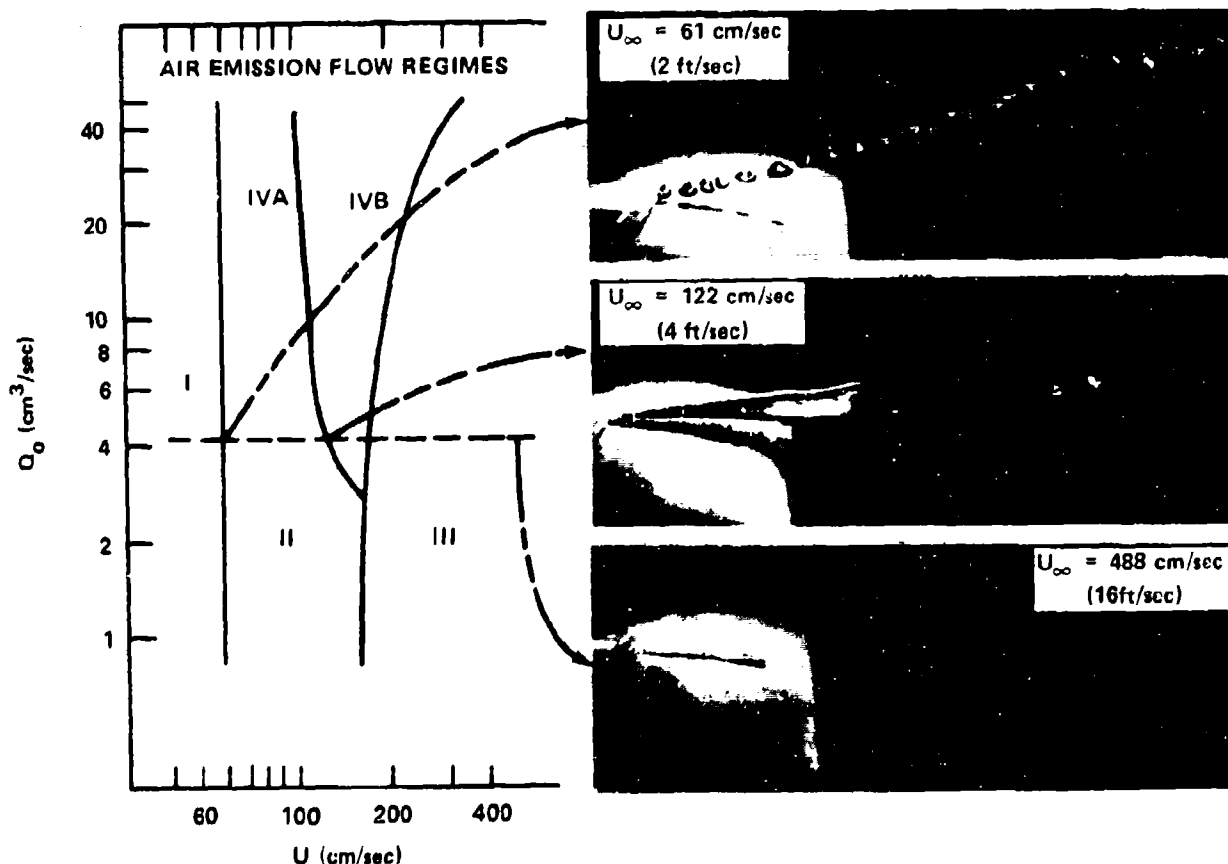


Figure 4.57 -- Regimes of Bubble Formation for an Air Jet Issuing into a Cross-Flow of Water<sup>207</sup> ( $Q_o = Q$  at STP)

1. The one-third-octave levels decrease as  $\sim f^{-1}$  for frequencies greater than the frequency  $f_m$  of maximum intensity.

2. In the region  $f > f_m$  the spectrum level increases as  $\sim Q^{0.5}$ .

3. In the region of  $f > f_m$ , the level was independent of orifice radius for a given  $Q$  and  $U_\infty$  when the radius was decreased from 1/32 in. to 1/100 in. This independence is suggestive that surface tension effects at the opening, as implied by Equation 4.184, do not control the bubble dynamics.

4. In the region  $f > f_m$ , the level increases as  $U_\infty^0$  and  $U_\infty^2$  to  $U_\infty^4$ , depending on the flow regime. Figure 4.59 shows the dependence of noise on both  $Q$  and  $U_\infty$ . The dependence as  $U_\infty^4$  suggests influence of splitting as per Equation (4.192).



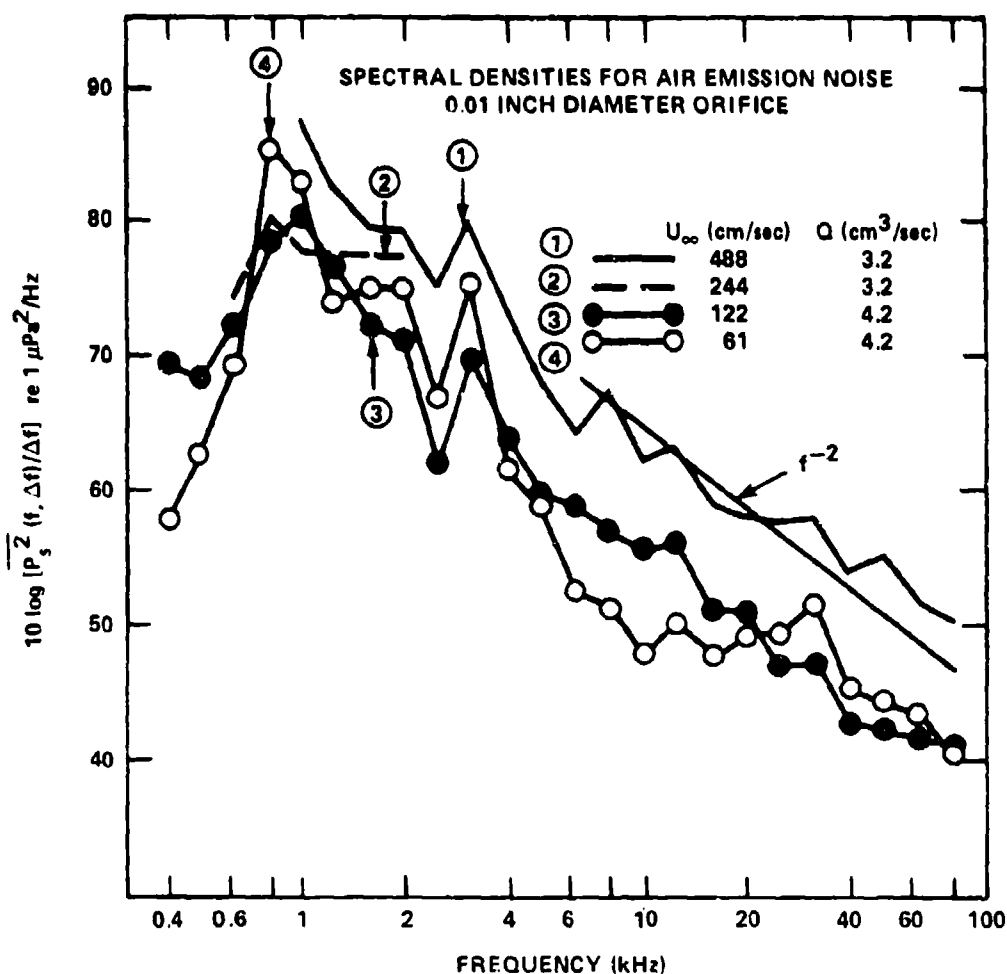


Figure 4.58 - Sound Spectral Densities at 1 Yard for Various Bubble Regimes for which  $Q_0 = 3.3$  Cubic Centimeters per Second, Arrows Denote Frequencies of Bubble Resonance for the Bubble Radii Noted in the Text and Given by Equation (4.216)<sup>207</sup>

The ambiguity in the behavior of the sound pressure with orifice radius  $U_{\infty}$  and  $Q_0$  compared to the theoretical variations given by Equations (4.197), (4.193), especially (4.192), and (4.191) suggest that the sound is possibly controlled by a combination of detachment of bubbles from the orifice and bubble splitting by turbulent flow.

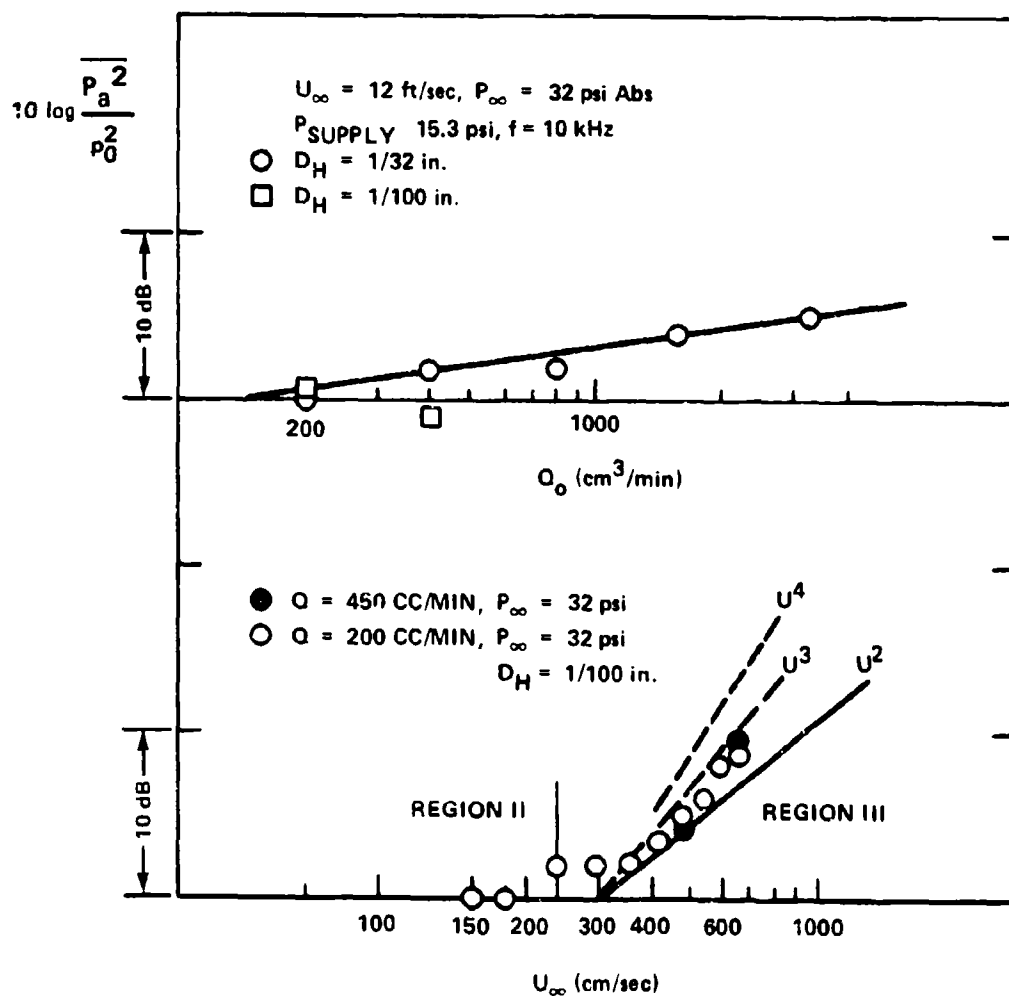


Figure 4.59 - Relative Variations of Air Emission Noise in the 10 KiloHertz One-Third-Octave Band with  $Q_o$ ,  $U_\infty$ <sup>207</sup>

#### 4.5.4 Hydromechanics of Bubble Formation

Less comprehensive work has been conducted to establish general relationships for predicting bubble sizes in various types of flow fields than has been conducted in cavitation, in spite of the large number of researches devoted to the formation of drops and bubbles. Most investigations are empirical with numerical results reduced in terms of certain dimensionless quantities which represent the balances of

forces acting on the interface. Theoretical work has been largely confined to the determination of conditions of interfacial stability between two fluid phases. Brief reviews of the literature dealing with bubble formation can be found in the monograph by Wallis<sup>42</sup> and in a paper by Sevik and Park.<sup>208</sup>

Bubbles are created under the influence of interfacial surface tension forces, buoyant forces, and inertial forces provided by the motions of either the gas or the liquid phases (or both). In stationary liquids,<sup>42,44</sup> the predominant forces acting on bubbles formed at a nozzle or orifice are buoyancy and surface tension at low flow rates of gas. Table 4.2 summarizes the important results of this and the preceding section.

TABLE 4.2  
SIZES AND SOUNDS OF BUBBLES FORMED IN MOVING LIQUIDS

Parameter Range	Flow Condition	Bubble Size	Probable Speed - Dependence of Noise
$0 < We < 1.2$ $\frac{U_i}{U_g} \sim 0[1]$	Rayleigh instability in parallel flow; free jets and wall jets; Figure 4.61	$2.0 < \frac{R_b}{R_j} < 3.0$ $R_b \approx [1.2(Q/U_i)^{1/2}]$ Small bubbles, 30 percent of bubbles may be $< 0.4 R_b$ . Figure 4.62	$\overline{p^2} \sim QU_\infty^4 U_i > U_g$ (Eq. (4.192)) $f_{max} \sim \frac{330}{R_b(m)} \left( \frac{p}{p_{atm}} \right)^{1/2}$
$We > 1.2$ $0 \leq \frac{U_i}{U_g} < 1$ $\frac{We}{F^{2/3}} > 5$	Bubbles generated from a jet which forms at an orifice--not yet observed on wall jets	$2.0 < \frac{R_b}{R_j} \leq 3.75$ Figure 4.60 $\frac{R_b}{R_j} \sim 2 \left[ \frac{We}{F^{2/3}} \right]^{1/3}$	$\overline{p^2} \sim Q^5$ (Eq. (4.190)) No measurements
$We > 1.2$ $\frac{U_i}{U_g} > 1$	Bubbles periodically sheared from orifice not yet observed in practical flows--perhaps upper range of Regime III, Figure 4.57	$\frac{R_b}{R_o} \sim U_i^{-1}$	Unknown
$We = We_g < F^{2/3}$ $0 \leq \frac{U_i}{U_g} \ll U_g$	Bubbles periodically formed at orifice under influence of liquid inertia regime, Figure 4.57	$R_b \approx 0.9 \left[ \frac{Q^2}{g} \right]^{1/5}$	$\overline{p^2} \sim QU_\infty^0$ (Eq. (4.185)) Section 4.5.3 $f_{max} \sim \frac{330}{R_b} \left( \frac{p}{p_{atm}} \right)^{1/2}$
Turbulent liquid $We_t = We_t \sim cr$	Splitting of bubbles by continuous phase with turb length scale, $\lambda$	$2 R_b \sim \lambda \left[ \frac{1.2}{(We_t) cr} \right]^{1/2}$ (Eq. (4.219))	$\overline{p^2} \sim Q^n U_\infty^m$ $0.5 < n < 1$ $m \sim 4$ Section 4.5.3

4.5.4.1 Bubble Formation in Stagnant Liquids. Sevik\* identifies three regimes of bubble formation in stagnant liquids: a quasistatic regime in which bubbles form at a nozzle and break off under the influence of buoyancy; a periodic regime in which bubbles stream, as a string of pearls (see Figure 4.57, Regime I), under the influence of both inside gas pressure causing acceleration of the bubble wall, and surface tension; and jet breakdown at large volumetric flow rates in which the gas emission from the orifice is a cylindrical jet on the interface of which growing waves appear.

4.5.4.1.1 Quasistatic Bubble Formation. The bubble of radius  $R_b$  is connected to the gas supply through a nozzle of radius  $R_n$  ( $\ll R_b$ ). The buoyancy force is given by

$$F_B = \frac{4}{3} \pi R_b^3 (\rho_o - \rho_g) g \quad (4.199)$$

while the tension force holding the bubble to the nozzle is

$$F_T = 2\pi R_n S \quad (4.200)$$

The bubble breaks off when  $F_B > F_T$  so the bubble radius is given by

$$R_b \approx 1.1 \left[ \frac{SR_n}{(\rho_o - \rho_g)g} \right]^{1/3}$$

Rearranging, we find

$$\frac{R_b}{R_n} \approx 1.1 \left[ \frac{Fr^2}{We_g} \right]^{1/3} \quad (4.201)$$

where the Weber number

---

\*Internal DTNSRDC Technical Note, November 1973, "The Formation of Bubbles at an Orifice." This subsection is extracted from the technical note.

$$We_g = \frac{\rho_g U_g^2}{\frac{S}{R_n}} \quad (4.202)$$

is the ratio of gas inertial forces to surface tension forces, and the Froude number  $F_r$

$$F_r = \left[ \frac{\rho_g U_g^2}{(\rho_o - \rho_g) R_n g} \right]^{1/2} \quad (4.203)$$

is the ratio of inertial forces to buoyant forces.

4.5.4.1.2 Periodic Bubble Formation. As the flow rate of gas increases, the volume of bubbles breaking away increases. When the volumetric flow rate of gas is less than<sup>209</sup>  $Q = 30 S R_n$  ( $\text{cm}^3/\text{sec}$ ), the volume of bubble used in Equation (4.199) is modified by

$$V = (V)_{\text{quasi-static}} + T_A Q$$

where  $T_A$  has been deduced from measurements as  $0.052 (R_n)^{1/3}$  sec (where  $R_n$  has dimensions of cm).

At slightly larger gas flow rates, surface tension forces are dominated by the inertial liquid forces associated with added mass of the more-rapidly-growing bubble so that the bubble is "held" in place by the liquid. In this case<sup>206</sup> it is found that

$$\left( \frac{R_b}{R_n} \right)_{\text{periodic}} \sim B (F_g)^{2/5} \quad (4.204)$$

where

$$F_g = \left[ \frac{U_g^2}{R_n g} \right]^{1/2} \quad (4.205)$$

is a "gas" Froude number and

$$1.1 < B < 1.5$$

Rearranging Equation (4.204) we find

$$R_b \approx 0.9 \left[ \frac{Q^2}{g} \right]^{1/5} \quad (4.206)$$

Note that

$$\left( \frac{R_b}{R_n} \right)_{\text{quasi-static}} < \left( \frac{R_b}{R_n} \right)_{\text{periodic}}$$

The bubbles are formed with regularity as illustrated in Regime I of Figure 4.57; the arrow in Figure 4.60 denotes the frequency of noise produced by this formation.

A mechanism for the bubble formation illustrated in Figure 4.57 has been suggested by Silberman<sup>210</sup> and differs from that above because of the liquid cross flow. When the liquid velocity is large enough relative to the gas exit velocity, bubbles will be sheared off as the gas exits the orifice. Then the force balance that exists is between the surface tension and the drag force, so that the bubble radius is approximated by

$$R_b \approx \left[ \frac{32SR_o}{C_D \rho_o U_l^2} \right]^{1/2} = R_o \left[ \frac{32}{C_D} \left( \frac{U_g}{U_l} \right)^2 \frac{\rho_g}{\rho_o} \frac{1}{We_g} \right]^{1/2} \quad (4.207)$$

where  $C_D$  is the drag coefficient of flow around the bubble. Other force balances for bubbles in moving liquids have been examined by van der Walle.<sup>46</sup>

4.5.4.1.3 Bubble Formation at Large Volumetric Flow Rates. Kutadeladze and Styrikovich<sup>211</sup> have found that the flow pattern of periodic bubble formation gives rise to the formation of a cylindrical jet when the average velocity of the jet  $U_g$  satisfies the condition

$$\frac{U_g (\rho_g)^{1/2}}{[gS(\rho_o - \rho_g)]^{1/4}} > 1.25 \left[ \frac{S}{g(\rho_o - \rho_g) R_n^2} \right]$$

which Sevik points out is equivalent to the jet regime existing when

$$\frac{We_g}{(F_r)^{2/3}} > 1.31 \quad (4.208)$$

see Equations (4.202) and (4.203). Figure 4.60 shows the two regimes of bubble

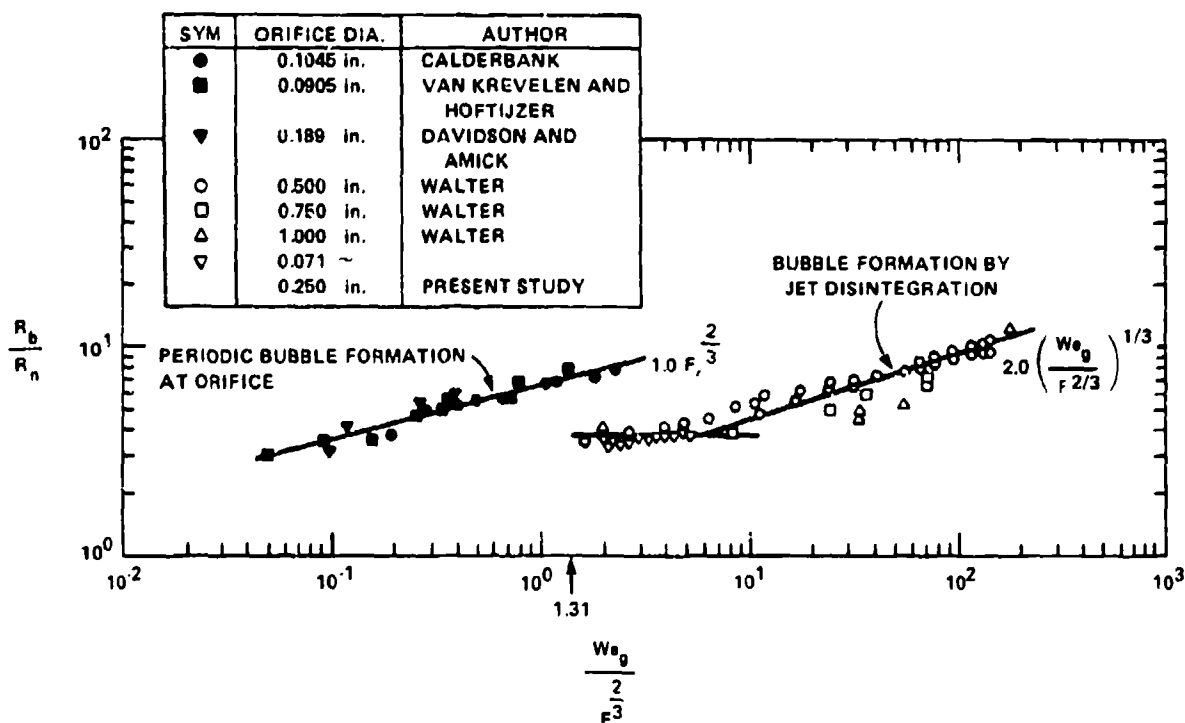


Figure 4.60 - Variation of Bubble Radius with Nozzle Size for an Air Jet Disintegrating in a Coaxial Water Jet for which  $U_g \gg U_l$ , the Jets were Vertical

formation for which either periodic bubbles or a gas jet is formed. At  $We_g/(Fr)^{2/3} = 1.31$  there is a break in the radius dependence. At larger values of this parameter the cylindrical jet undergoes axisymmetric vibration which results in the formation of large bubbles after a wavelength or so downstream of the nozzle exit. The larger bubbles then break up in 3 to 4 water-jet diameters; this location corresponds to the extremity of the potential core.

4.5.4.2 Bubble Formation in Laminar Parallel Moving Liquids. In this case, three regimes of bubble formation have been identified; these depend upon the existence or nonexistence of orderly wave structure on the interface of the cylindrical jet (occurring at magnitudes of liquid-phase and gas-phase velocity that are similar). When the velocities of the separate phases are greatly dissimilar, the bubble formation depends upon which phase has the larger velocity.

The condition of interfacial stability between the liquid and gas phases on either side of cylindrical and planar interfaces has been worked out by Rayleigh<sup>212</sup> and the method has been applied to the stability of a cylindrical gas jet in water by Sevik.\* For a cylinder of radius  $R_j$ , illustrated with the photograph in Figure 4.57, the radius is given by the relationship

$$\frac{R}{R_j} = 1 + \epsilon e^{ik(x-ct)} \quad (4.209)$$

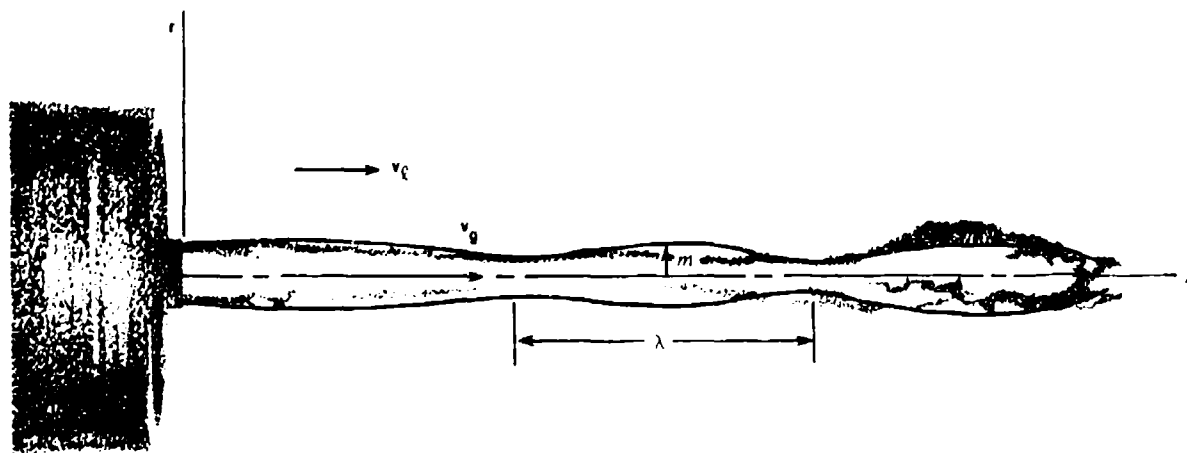


Figure 4.61 - Coordinate System for the Analysis of Interfacial Stability

\*Internal DTNSRDC Technical Note, November 1973, "The Formation of Bubbles at an Orifice." This subsection is extracted from the technical note.



where  $\epsilon \ll 1$  is the amplitude of the traveling-wave undulation. The hydrodynamic pressures inside or outside the cylinder, whose wall is moving at speed  $c$ , are given by Bernoulli's equation; e.g., inside the cylinder

$$\frac{P_g}{\rho_g} + \frac{1}{2} \left( U_g + \frac{\partial \phi_g}{\partial x} \right)^2 + \frac{\partial \phi_g}{\partial t} = \frac{P_{g_o}}{\rho_g} + \frac{1}{2} U_g^2 \quad (4.210)$$

where  $u_g = \nabla \phi_g$  is a velocity fluctuation in the cylinder as a result of the undulation of the walls, and  $P_{g_o}$  and  $U_g$  are quantities in the exit plane. To illustrate, for small disturbances and long wavelengths ( $kR_j \ll 1$ ), the equation of continuity gives

$$(U_g + u_g) - c = (U_g - c) (1 - 2\epsilon e^{ik(x-ct)})$$

so

$$u_g = -2(U_g - c) \epsilon e^{ik(x-ct)} \quad (4.211)$$

Equation (4.211) shows that as the walls contract ( $\epsilon e^{ik(x-ct)} < 0$ ), the velocity perturbation is positive causing a local increase in velocity. By Equation (4.210), this increase in speed causes a decrease in internal pressure  $P_g$ , which favors a further reduction in cross section of the cylinder. As the waves progress in amplitude, the contraction of the cylinder will pinch off. The details of the process are actually more complicated since the time-derivative term, provides a phase lag and, furthermore, Equation (4.210) has a counterpart for the external flow that behaves in an analogous manner. At the interface, the fluid pressure  $p_\ell$  for the liquid side and  $P_g$  for the gas side, are connected by the analog of Equation (4.10),

$$\frac{P_g - P_\ell}{S} = \left[ \frac{1}{R_j} + \left| \frac{\partial^2 R_j}{\partial x^2} \right| \right] \quad (4.212)$$

where the radius of curvature along the axial direction is  $|\partial^2 R / \partial x^2|^{-1}$  for long wave lengths. At the exit plane of the jet

$$\frac{P_{g_o} - P_{l_o}}{S} = \frac{1}{R_j} \quad (4.213)$$

Combination of Equation (4.210) and its analog in the external flow, Equations (4.200) and (4.213) yields a dispersion relationship for the wave speed. The wave speed, which turns out to be mathematically complex, is a function of wave number  $kr_j$ , and a Weber number based on the relative gas and fluid velocities,

$$We = We_g \left( 1 - \frac{U_l}{U_g} \right)^2 \quad (4.214)$$

For values of  $c$  that are positive-imaginary, the waves grow exponentially. A unique relationship between the wave number of the neutrally-stable waves ( $kr_j$ ) and  $We$  can be derived. When  $We < 1.2$ , then  $kr_j$  is less than unity; specifically, the wave number for neutrally stable waves lies between  $0.47 < kr_j < 0.6$  when  $We < 0.2$ . The volume of gas entrained in a wavelength  $2\pi k^{-1}$  is, therefore, approximately

$$V_b = \frac{2\pi R_j}{kr_j} \cdot \pi R_j^2 \approx 13.65 R_j^2 \quad (4.215a)$$

$$= \frac{4}{3} \pi R_b^3$$

This gives

$$R_b \approx 2 R_j \quad (4.215b)$$

with smaller bubbles being formed at larger values of  $We$  accordingly as  $kR_j$  increases with  $We$  increasing as shown in Figure 4.62. Equation (4.215b) has been verified by Taylor<sup>213</sup> and van Krevelen and Hoftijzer.<sup>214</sup>

This mechanism of jet break-up possibly applies to the bubble formation as illustrated in Regimes III and V of Figure 4.57. In these regimes, especially at low to moderate water velocities, the air jet is bent along the hydrofoil before it desintegrates. When  $U_\ell$  is of the same order of magnitude as  $U_g$ ,  $We$  must be less than 1; accordingly Equation (4.215b) should apply. In an arrangement similar to that shown in Figure 4.57, Silberman<sup>210</sup> has quantified the magnitudes of the largest bubbles formed in the break-up of similarly-formed single and multiple jets. The

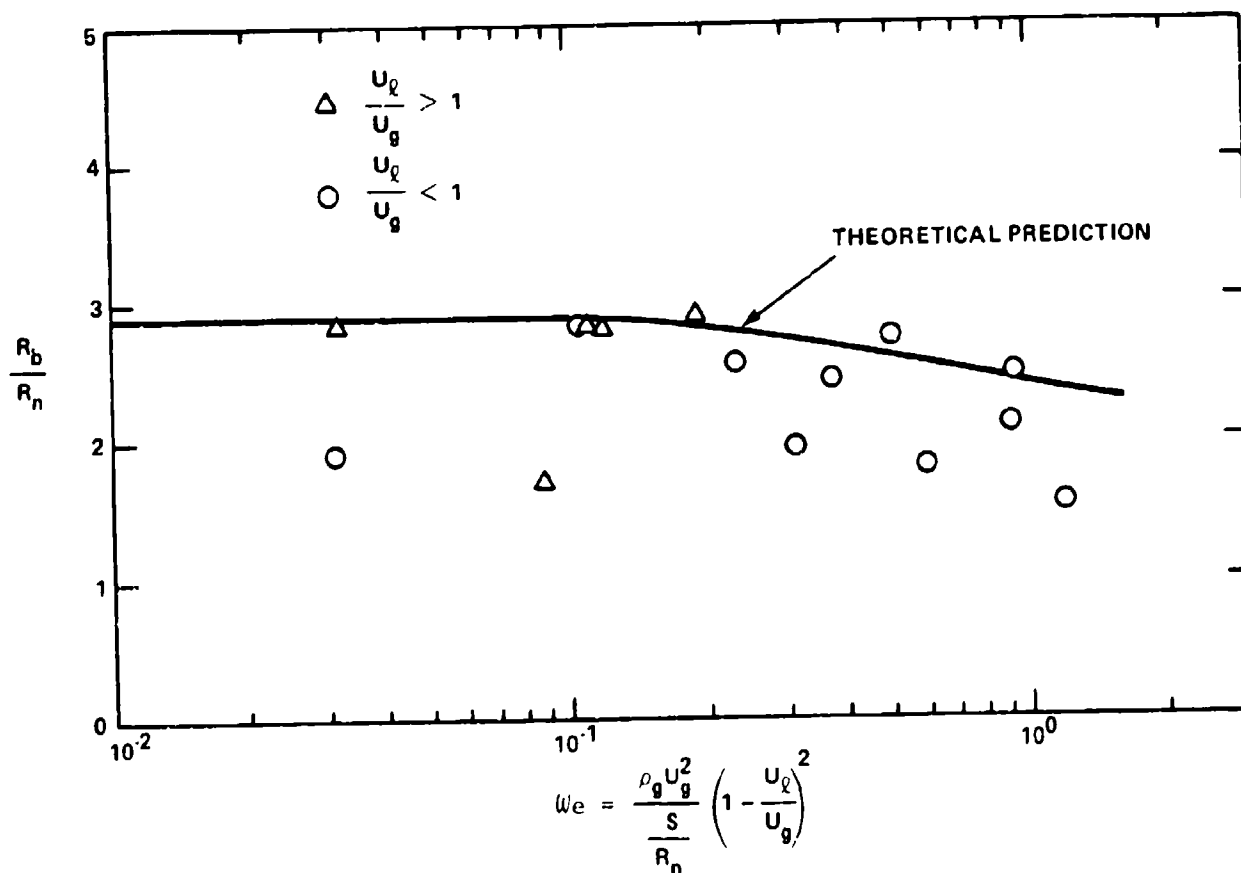


Figure 4.62 - Variation of Bubble Size with Weber Number in Rayleigh Instability Regime

results confirmed that the bubble radius behaved independently of orifice or nozzle size and depended upon flow parameters as

$$R_b \sim 1.2 \left( \frac{Q}{U_\ell} \right)^{1/2} \quad (4.216)$$

This result may be derived using Equation (4.215b) together with the assumption that  $U_g = U_\ell$  so that

$$Q = \pi R_j U_\ell$$

Equation (4.216) holds only approximately because the formation of larger bubbles is accompanied by the formation and splitting of a larger number of satellite bubbles. Silberman found that the volumes of bubbles in the bubble cloud was logarithmically distributed. At large values of  $Q/U_\ell$ , favoring the formation of large bubbles, 70 percent of the bubbles had radii smaller than 0.8 times the value given by Equation (4.216). At small values of  $Q/U_\ell$  (approaching Regime III in Figure 4.57) the distribution widened so that 30 percent of the bubbles had radii smaller than 0.4 times the radius given by Equation (4.216). This broadening of bubble distribution suggests that the frequency spectrum of noise radiated by these bubble clouds will also be broadened as  $Q/U_\ell$  is increased. Furthermore, the noise spectrum should be peaked near a frequency given by a combination of Equations (4.20) and (4.216). In Figure 4.58, these frequencies are indicated with arrows.

Regular bubble formation is not observed for vertical gas jets  $We > 1.2$ , and for  $U_g > U_\ell$ ; i.e., large gas velocities. The flow patterns do, however, roughly resemble those for which there is a transitional range of values of  $We_g/F^{2/3}$  shown in Figure 4.60 and for which the dominant bubble sizes range from

$$2 < \frac{R_b}{R_j} < 3.75$$

On either free or wall jets for which  $We > 1.2$ , but  $U_\ell > U_g$ , i.e., large liquid velocities, the interface is drawn by the drag of the moving liquid. Turbulence in

the surrounding liquid should cause a rippling and contribute to the disintegration of the jet. Nothing is known about this flow regime.

4.5.4.3 Bubble Formation in Turbulent Flow. When bubbles move into a turbulent liquid, the velocity fluctuations surrounding the bubble cause deformations from the spherical shape. For large-enough deformations, the bubbles split into two or more bubbles. Conditions for the formation of  $n$  bubbles have been established in terms of the intensity of turbulence by Sevik and Park,<sup>208</sup> following the work of Hinze.<sup>215</sup> Bubbles will be split when a turbulence Weber number,

$$We_t = \frac{\rho_o \overline{u^2}}{\frac{S}{R_b}} \quad (4.217)$$

where  $\rho_o \overline{u^2}$  is a measure of the turbulent stress acting on the bubble, reaches a critical value, e.g.,  $(We_t)_c$ . For liquid globules splitting in the turbulent flow between coaxially rotating cylinders,  $(We_t)_c \sim 0.5$ , while for air bubbles splitting in the mixing region of a water jet,  $(We_t)_c \sim 1.3$ .

When a bubble vibrates in the second order mode its deformation resembles a dumb-bell shape. In the extreme it splits into two bubbles. Accordingly, the  $n^{th}$  order mode of vibration results in  $n$  smaller bubbles.

The  $n^{th}$  resonance frequency of a spherical bubble has been shown by Lamb<sup>216</sup> to be

$$\begin{aligned} (\omega_n)^2 &= (2\pi f_n)^2 \\ &= \frac{n(n+1)(n-1)(n+2) S}{\{(n+1)\rho_g + n\rho_l\} R_b^3} \\ &\sim \frac{(n+1)(n-1)(n+2) S}{\rho_l R_b^3} \end{aligned} \quad (4.218)$$

when  $\rho_g \ll \rho_l$  (in general,  $\rho_g$  applies to the split phase and  $\rho_l$  to the continuous phase). The frequency of excitation by the turbulence acting on the bubble as it is convected by the liquid is given by Equation (4.103). This frequency arises from the relative motion of the bubble and the mean motion of the liquid. When  $f = f_n$ , the bubble will be excited and may split into  $n$  bubbles. Splitting into two bubbles requires the lowest order vibration;

$$\frac{u^2}{\Lambda}^{1/2} \approx \frac{f_2}{2\pi} \left( \frac{12 S}{\rho_l R_b^3} \right)^{1/2}$$

therefore,

$$(We_t)_{cr} = \frac{12}{\pi^2} \left( \frac{\Lambda}{2R_b} \right)^2 \quad (4.219)$$

Setting  $\Lambda = 2R_b$ , because there is a spectrum of eddy sizes, Sevik and Park find

$$(We_t)_{cr} \sim 1.2 \quad (4.220)$$

which agrees with the experimental value cited above. Analogously, they find for two liquid phases ( $\rho_l \sim \rho_g$ ) that  $(We_t)_c \sim 0.5$  in agreement with Hinze's observation.

The result can be interpreted to indicate that splitting of bubbles into  $n$  segments will occur as a result of a pressure perturbation whenever the turbulence Weber number reaches some critical value whose magnitude will almost certainly depend upon the details of the flow. Also, the result should have some application to the formation of microbubbles in cavitation zones as was discussed in connection with Figures 4.39 to 4.42. For the value of the integral scale  $\Lambda$ , that does not change with liquid velocity, Equation (4.192) indicates that the acoustic intensity of this form of bubble splitting should behave as  $U_\infty^4$ .

## 4.6 APPENDIX A — DERIVATION OF APPROXIMATE SPECTRAL FUNCTIONS

In Section 4.2.5, various time intervals were highlighted to emphasize different aspects of the bubble collapse. These times will have corresponding frequency intervals which determine the spectral form of  $S_p(r, \omega)$ . To isolate each of these events in the life of a bubble, the instantaneous volume will be approximated by a sum of  $N$  functions which combine to approximate the original  $V(t)$

$$v(t) = \sum_{n=0}^N v_n(t) u(t, \Delta\tau_n) \quad (4.A221)$$

where  $v_n(t)$  has the functional form

$$\begin{aligned} v_n(t) &= a_n (t - t_n)^m & t > t_n \\ &= 0 & t < t_n \end{aligned} \quad (4.A222)$$

as illustrated in Figure 4.A63. The unit function  $u(t, \Delta\tau_n)$  is defined so that

$$\begin{aligned} u(t, \Delta\tau_n) &= 1 & t_n < t < t_n + \Delta\tau_n \\ &= 0 & \text{for } t \text{ outside the interval} \end{aligned}$$

Figure 4.A63 illustrates the use of functions which generally describe the maximum volume, collapse, and rebound phases of the bubble that were highlighted in Figures 4.15 and 4.19.

The Fourier transform of the  $n^{\text{th}}$  contribution to Equation (4.A221) gives

$$\begin{aligned} v_n(\omega) &= \frac{1}{2\pi} \int_0^{\infty} v_n(t) u(t, \Delta\tau) e^{i\omega t} dt \\ &= \int_{-\infty}^{\infty} \tilde{v}_n(\Omega) u_n(\omega - \Omega) d\Omega \end{aligned} \quad (4.A223)$$

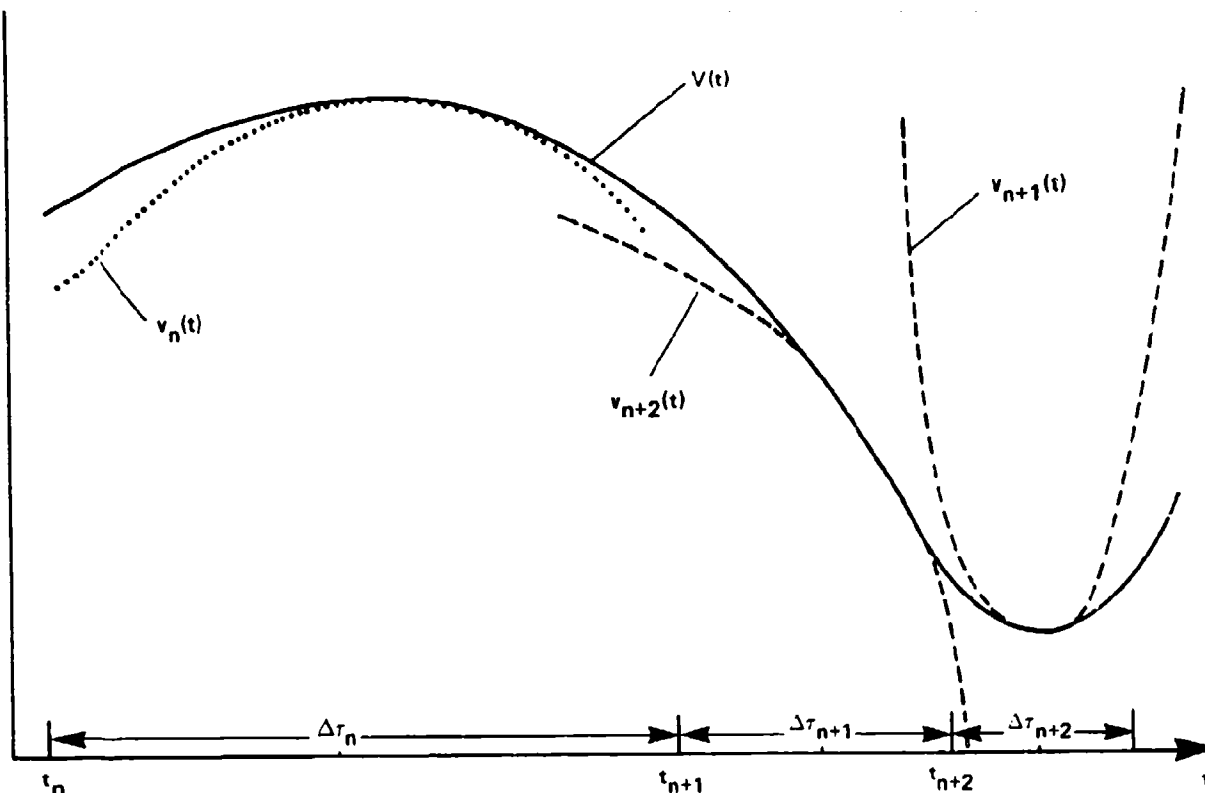


Figure 4.A63 - Use of the Series Approximations of Equation (4.97)

where

$$\tilde{v}_n(\omega) = \frac{1}{2\pi} \int_0^{\infty} e^{i\omega t} v_n(t) dt$$

and

$$\begin{aligned} u_n(\omega) &= \frac{e^{i\omega t_n}}{2\pi} \int_{-(\frac{1}{2})\Delta\tau_n}^{(\frac{1}{2})\Delta\tau_n} e^{i\omega t} dt \\ &= \frac{\Delta\tau_n}{2\omega} \left( \frac{\sin \Delta\tau_n \frac{\omega}{2}}{\Delta\tau_n \frac{\omega}{2}} \right) \cdot e^{i\omega t_n} \end{aligned} \quad (4.A224)$$



The Fourier transform  $\tilde{V}_n(\omega)$  of  $V_n(t)$  is formally convergent for arbitrary noninteger values of  $m$  only in a limit for which  $\omega = \omega + i\delta$ ;  $\delta$  must be positive, but it can be taken arbitrarily small, i.e.,  $\delta \rightarrow 0^+$ . Thus,

$$\tilde{V}_n(\omega) = \frac{a_n \Gamma(m+1)}{2\pi(i\omega)^{m+1}} \quad m > -1 \quad (4.A225)$$

where  $\Gamma(m+1)$  is the gamma function. It has the following approximate values needed for numerical evaluations

$$\Gamma(1+3(0.4)) = \Gamma(2.2) \sim 1 \quad \text{for Equation (4.81)}$$

$$\Gamma(1+3(2)) = \Gamma(7) = 6! = 720 \quad \text{for Equation (4.75)}$$

Therefore, for any interval Equations (4.A223) through (4.A225), give

$$V_n(\omega) \approx e^{i\omega t_n} \int_{-\infty}^{\infty} \frac{a_n \Gamma(m+1)}{2\pi(i\Omega)^{m+1}} \cdot \frac{\Delta\tau_n \sin \Delta\tau_n \frac{(\omega-\Omega)}{2}}{\Delta\tau_n \frac{(\omega-\Omega)}{2}} \cdot d\Omega \quad (4.A226)$$

In the limit as  $\omega\Delta\tau_n > 1$  we make the approximation given by Equation (2.112) that Equation (4.A226) may be formally evaluated in the approximate form

$$|V_n(\omega)| \sim \frac{a_n \Gamma(m+1)}{2\pi(i\omega)^{m+1}} \quad \text{for } \frac{\Delta\tau_n \omega}{2} > 1 \quad (4.A227)$$

Note that although

$$V(\omega) = \sum_n V_n(\omega)$$

as indicated in Section 4.4.1.1 each stage  $V_n(t)$  is responsible for a frequency range  $(\omega_l)_n < \omega < (\omega_u)_n$  for which we approximate the  $n$ th frequency interval

$$V(\omega) = V_n(\omega) \quad (\omega_l)_n < \omega < (\omega_u)_n.$$

#### 4.7 APPENDIX B — PHYSICAL PROPERTIES OF AIR AND WATER

Useful physical properties of air and water, on which all the dimensionless groups in this chapter are based, are given below. Properties for air are given at standard temperature and pressure; 20°C and 1 atm pressure. Properties for water are given at 20°C.

	Air	Water
Density ( $\text{g/cm}^3$ )	0.0012	1.0
Speed of Sound (m/sec)	330	1500
Kinematic Viscosity ( $\text{m}^2/\text{sec}$ )	$14.9 \times 10^{-6}$	$10^{-6}$

##### Air-Water Mixture Equilibrium Constants:

Surface Tension  $S = 73$  dynes/cm

Henry's Law Constant  $H = 7.07 \times 10^{10}$  dynes/cm<sup>2</sup> - mole fraction air in water

(1 atm=14.7 psi= $10^6$  dynes/cm<sup>2</sup>, therefore,  $H=1.04 \times 10^6$  psi/mole fraction; 1 mole air=29g, 1 mole water=18g)

Water Vapor Pressure  $P_v = 24 \times 10^3$  dynes/cm<sup>2</sup>

Diffusivity (Mass)  $D_s = 2.0 \times 10^{-5}$  cm<sup>2</sup>/sec

## 4.8 APPENDIX C — NOMOGRAPHS FOR COMPUTING PROPELLER PARAMETERS

Although parameters for describing the powering performance of propellers will be discussed in Chapter 10 it is useful to introduce the relationship between rotational velocity and forward velocity here. This is done for the purpose of predicting cavitation indices; as shown in Figures 4.47 and 4.49, the sound pressure level in proportional bands may be expressed in the form

$$L_s(f, \Delta f) = A + 20 \log P_\infty - 20 \log \left( \frac{L}{r} \right) + f \left( \frac{K}{K_1} \right)$$

where  $A$  is a factor dependent upon the type of cavitation, where  $K$  is the cavitation index, and where the function  $f(K/K_1)$  is dependent upon the type of cavitation. Most significantly, it appears that  $f(K/K_1)$  varies from line 1 in Figure 4.49, for bubble cavitation on hydrofoils, to any of lines 2 through 4 for cavitation on propellers and other rotating systems. The length parameter  $L$  may be the chord of a lifting surface or a propeller diameter. Therefore, for purposes of scaling or for purposes of estimating conditions for cavitation inception, Figure 4.064 is useful.

The cavitation index may be based on the advance velocity of a propeller  $V_a$  or on the tip velocity of a propeller  $U_t$ , i.e.,

$$K = \frac{P_\infty - P_v}{\frac{1}{2} \rho_o V_a^2}$$

or, as in Section 4.4.5.4,

$$K_t = \frac{P_\infty - P_v}{\frac{1}{2} \rho_o U_t^2}$$

As described in Section 1.4.4  $U_t$  and  $V_a$  are related by the advance coefficient, for either definition  $K$  or  $K_t$ , as long as  $J = \text{constant}$ , the ratio of the cavitation index to its value at inception is also related to a velocity ratio. Thus,

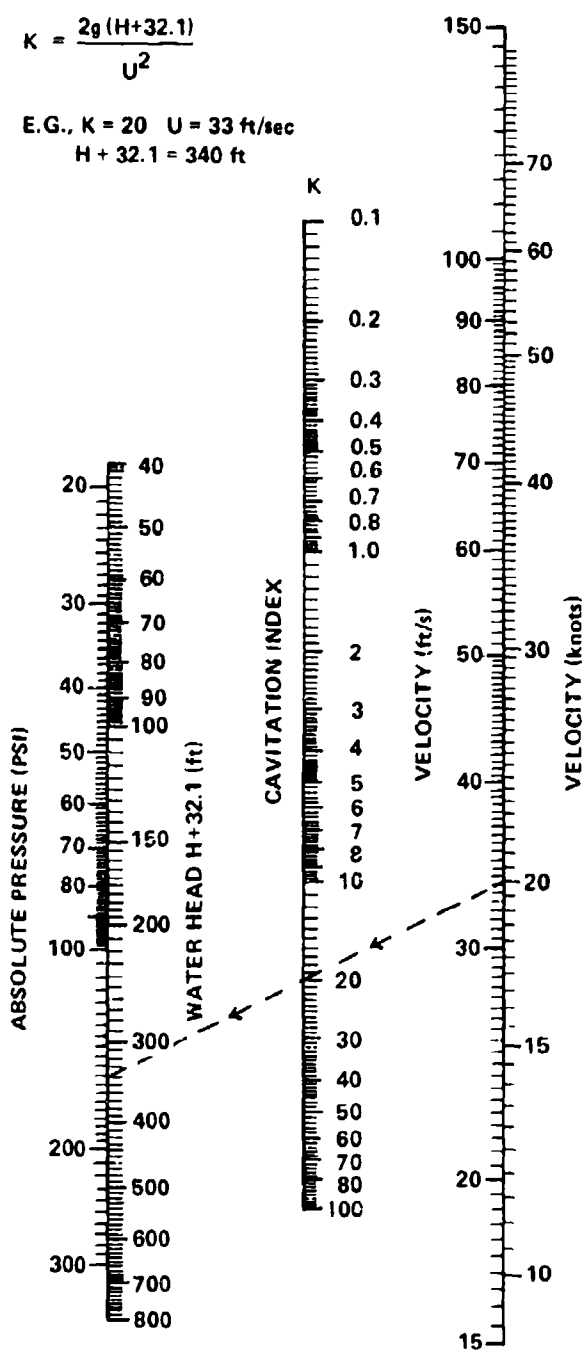


Figure 4C.64 - Nomograph for Computing Cavitation Indices

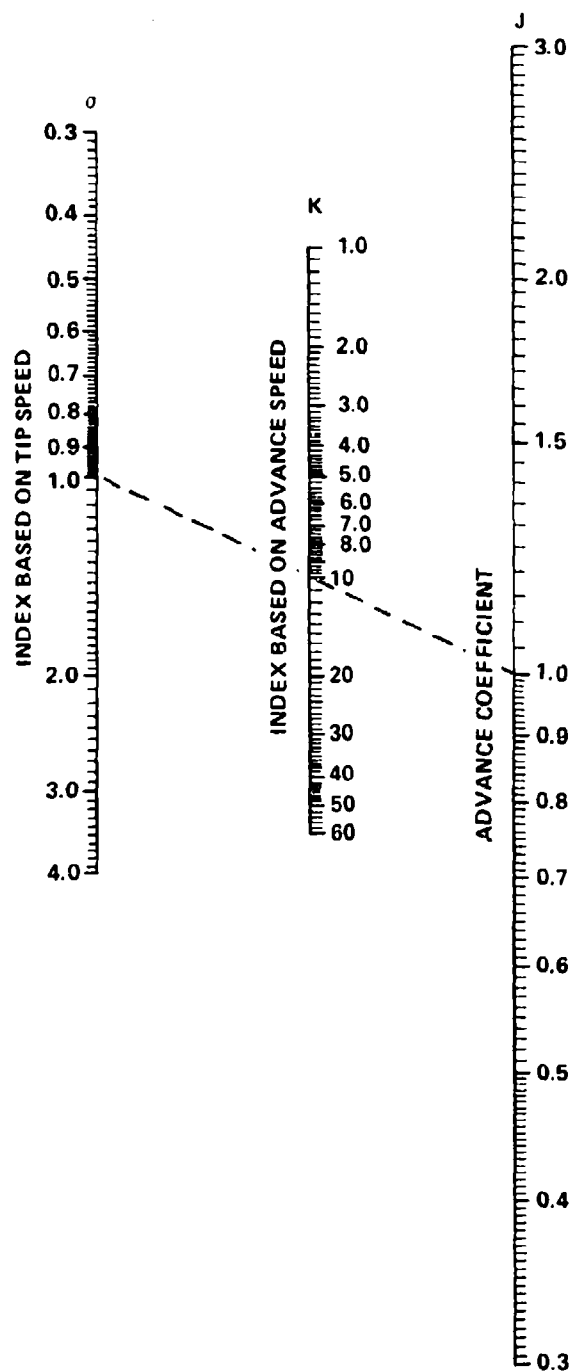


Figure 4C.65 - Nomograph for Transforming Cavitation Index Based on Tip Velocity to Index Based on Advance Speed.

E.g.  $J = 1.0$ ,  $K = 10$ ,  $\sigma = 1.01$ ,

and  $\sigma = (J/\pi)^2 K$

$$\frac{V_a}{(V_a)_1} = \frac{U_t}{U_{t_1}} = \left(\frac{K}{K_1}\right)^{1/2} = \left(\frac{(K_t)_1}{K_t}\right)^{1/2}$$

in all the figures of Section 4.4.4. When the two definitions of cavitation index are related by

$$K_t = K \left(\frac{J}{\pi}\right)^2$$

they become equal when  $J = \pi$ .

Figure 4.C64 shows the relationship between  $V_a$ ,  $J$ , and  $P_\infty - P_v = \rho_0 g (H+32.1)$ . The pressure at the shaft axis of the propeller is taken as the atmospheric pressure at the water surface plus hydrostatic pressure at the depth  $H$  (in feet). This nomograph can be used for propellers of a given  $J$  defined consistently with the velocity entered on the right and it can be used for bodies in simple translation by letting  $J = \pi$ . Figure 1.13 is a nomograph for a computation of propeller tip velocity once given either the ship velocity (in which case the shaft speed-forward speed (revolutions per minute per knot) ratio must be known) or the advance velocity, in which case the consistently-defined  $J$  must be known.

## 4.9 REFERENCES

1. Crighton, D.G. and J.E. Ffowes Williams, "Sound Radiation by Turbulent Two-Phase Flow," J. Fluid Mechanics, Vol. 36, pp. 585-603 (1969).
2. Flynn, H.G., "Physics of Acoustic Cavitation in Liquids," Physical Acoustics, Vol. 1b, W.P. Mason Ed. (1964).
3. Akulichev, V.A., "Calculation of the Cavitation Strength of Real Liquids," Sov. Phys. Acoust., Vol. 11, pp. 15-18 (1965).
4. Knapp, R.T. et al., "Cavitation," McGraw-Hill Book Co. (1970).
5. Ross, D., "Mechanics of Underwater Noise," Permagon Press (1976).
6. Beyer, R.T., "Nonlinear Acoustics," Naval Ship Systems Command (1974).
7. Pernik, A.D., "Problems of Cavitation," Problemy Kavitatsii, Leningrad, IZD-VO Sudostroyeniye (in Russian) (1966).
8. Kuiper, G., "Cavitation Testing of Marine Propellers in the NSMB Depressurized Towing Tank," Proc. Conf. on Cavitation, Inst. of Mech. Eng., Heriot-Watt Univ., Edinburgh, Scotland (1974).
9. DeBruyn, A. and T. Ten Wolde, "Measurement and Prediction of Sound in Board and Outboard of Ships as Generated by Cavitating Propellers," Symposium on High Powered Propulsion of Large Ships, Publication 490, Netherlands Ship Model Basin, Wageningen, The Netherlands (1974).
10. Danel, P. and J. Duport, "The Selection of Length and Head Scales for Cavitation Tests," Trans. ASME, pp. 84-794 (1960).
11. Holl, J.W. and G.F. Wislicenus, "Scale Effects on Cavitation," J. Basic Eng., Vol. 83, pp. 385-398 (1961).
12. Holl, J.W., "Limited Cavitation," ASME Symposium Cavitation State of Knowledge, pp. 26-63 (Jun 1969).
13. Lord Rayleigh, "On the Pressure Developed in a Liquid During the Collapse of a Spherical Cavity," Phil. Mag., Vol. 34, pp. 94-98 (1917).
14. Plesset, M.S., "The Dynamics of Cavitation Bubbles," Trans. ASME J. Appl. Mech., Vol. 16, pp. 277-282 (1949).

15. Neppiras, E.A. and B.E. Noltingk, "Cavitation Produced by Ultrasonics: Theoretical Conditions for the Onset of Cavitation," Proc. Phys. Soc., London, Ser. 64B, pp. 1032-1038 (1951).
16. Neppiras, E.A. and B.E. Noltingk, "Cavitation Produced by Ultrasonics," Proc. Phys. Soc. London, Ser. 63B, pp. 674-685 (1950).
17. Houghton, G., "Theory of Bubble Pulsation and Cavitation," J. Acoust. Soc. Am., Vol. 35, pp. 1387-1393 (1963).
18. Blue, J.E., "Resonance of a Bubble on an Infinite Rigid Boundary," J. Acoust. Soc. Am., Vol. 41, pp. 369-372 (1967).
19. Howkins, S.D., "Measurements of the Resonant Frequency of a Bubble Near a Rigid Boundary," Vol. 37, pp. 504-508 (1965).
20. Shima, A., "The Natural Frequency of a Bubble Oscillating in a Viscous Compressible Liquid," J. Basic Eng. Trans. ASME, pp. 555-562 (Sep 1970).
21. Strasberg, M., "The Pulsating Frequency of Non-Spherical Gas Bubbles in Liquids," J. Acoust. Soc. Am., Vol. 25, pp. 536-537 (1953).
22. Plesset, M.S. and D. Hsieh, "Theory of Gas Bubble Dynamics in Oscillating Pressure Fields," Phys. Fluids, Vol. 3, pp. 882-892 (1960).
23. Strasberg, M., "Gas Bubbles as Sources of Sound in Liquids," J. Acoust. Soc. Am., Vol. 28, pp. 20-26 (1956).
24. Minnaert, M., "On Musical Air Bubbles and the Sounds of Running Water," Phil. Mag., Ser. 7, Vol. 16, pp. 235-248 (1933).
25. Devin, C., Jr., "Survey of Thermal, Radiation, and Viscous Damping of Pulsating Air Bubbles in Water," J. Acoust. Soc. Am., Vol. 31, pp. 1654-1667 (1959).
26. Whitfield, O.J. and M.S. Howe, "The Generation Sound by Two-Phase Nozzle Flows and its Relevance to excess Noise of Jet Engines," J. Fluid Mech., Vol. 75, pp. 553-576 (1976).
27. Carstensen, E.L. and L.L. Foldy, "Propagation of Sound through a Liquid Containing Bubbles," J. Acoust. Soc. Am., Vol. 19, pp. 481-501 (1947).

28. Meyer, E. and E. Skudrzyk, "Über die Akustischen Eigenschaften von Gasblasenschleiern in Wasser," *Acustica*, Vol. 3, pp. 434-440 (1953), translated by G. Devin, "On the Acoustical Properties of Gas Bubble Screens in Water," DTMB Translation 285 (1958).
29. Hsieh, D. and M.S. Plesset, "On the Propagation Sound in a Liquid Containing Gas Bubbles," *Phys. Fluids*, Vol. 4, pp. 970-975 (1961).
30. Fox, F.E. et al., "Phase Velocity and Absorption Measurements in Water Containing Air Bubbles," *J. Acoust. Soc. Am.*, Vol. 27, pp. 534-539 (1955).
31. Silberman, E., "Sound Velocity and Attenuation in Bubbly Mixtures Measured in Standing Wave Tubes," *J. Acoust. Soc. Am.*, Vol. 29, pp. 925-933 (1957).
32. Junger, M.C. and J.E. Cole, "Selected Topics in Acoustics," DTNSRDC Report SAD-398E-1965, Sept 1982. Parts also published as "Bubble Swarm Acoustics: Insertion Loss of a Layer on a Plate," *J. Acoust. Soc. Am.*, Vol. 68, pp. 241-247 (1980).
33. Plesset, M.S., "Bubble Dynamics, Cavitation in Real-Liquids," R. Davies, Ed., Elsevier Pub. Co. (1964).
34. van Wijngaarden, L., "One-Dimensional Flow of Liquids Containing Small Gas Bubbles," *Ann. Rev. Fluid Mech.*, pp. 369-396 (1972).
35. Whitam, G.B., "On the Propagation of Weak Shock Waves," *J. Fluid Mech.*, pp. 290-318 (1956).
36. Benjamin, T.B. and J. E. Feir, "Nonlinear Processes in Long-Crested Wave Trains," *Proc. 6th Symp. Naval Hydrodynamics*, pp. 497-498 (1966).
37. Zwick, S.A., "Behavior of Small Permanent Gas Bubbles in a Liquid, Part I, Isolated Bubbles," *J. Math. and Phys.*, Vol. 37, pp. 246-268 (1958).
38. Zwick, S.A., "Behavior of Small Permanent Gas Bubbles in a Liquid, Part II, Bubble Clouds," *J. Math. and Phys.*, Vol. 37, pp. 339-353 (1959).
39. Zwick, S.A., "Behavior of Small Permanent Gas Bubbles in a Liquid, Part III, A Forced Vibration Problem," *J. Math. and Phys.*, Vol. 37, pp. 354-370 (1959).
40. Isay, W.H. and T. Roestel, "Berechnung der Druck-verteilung and Flügelprofilen in gashaltiger Wasserströmung," *ZAMM*, Vol. 54, pp. 571-588 (1974).



41. Isay, W.K. and T. Roestel, "Die niederfrequent instationäre Druckverteilung an Flügelprofilen in gashaltiger Wasserströmung," Inst. für Schiffbau der U. Hamburg, Report 318 (1975).
42. Wallis, G.B., "One-Dimensional Two-Phase Flow," McGraw-Hill (1969).
43. Solomon, L.P. and M.S. Plesset, "Non-Linear Bubble Oscillations," Int. Shipbuilding Progress, Vol. 14, pp. 98-103 (1967).
44. Blake, F.G., "The Onset of Cavitation in Liquids," Harvard Univ. Acoust. Res. Lab., Tech. Memo 12 (1949).
45. Akulichev, V.A., "The Calculation of the Cavitation Strength of Real Liquids," Sov. Phys. Acoustics, Vol. 11, pp. 15-18 (1965).
46. van der Walle, "F., "On the Growth of Nuclei and the Related Scaling Factors in Cavitation Inception," Proc. 4th Symposium on Naval Hydrodynamics (1962).
47. Strasberg, M., "The Influence of Air-Filled Nuclei on Cavitation Inception," DTMB Report 1078 (Aug 1956).
48. Arndt, R.E.A. and A. Ippen, "Rough Surface Effects on Cavitation Inception," Trans. ASME J. Basic Eng. Vol. 90, pp. 249-261 (1968).
49. Boguslavskii, Y.Y. and V.L. Korets, "Cavitation Threshold and its Frequency Dependence," Sov. Phys. Acoustics, Vol. 12, pp. 364-368 (1967).
50. Guth, W., "Nichtlineare Schwingungen von Luftblasen in Wasser," Acustica, Vol. 6, pp. 532-538 (1956).
51. Epstein, P.S. and M.S. Plesset, "On the Stability of Gas Bubbles in Liquid-Gas Solutions," J. Chem. Phys., Vol. 18, pp. 1505-1509 (1950).
52. Parkin, B.R. and R.N. Kermeeen, "The Roles of Convective Air Diffusion and Liquid Tensile Stresses During Cavitation Inception," Proc. IAHR Symposium on Cavitation and Hydraulic Machinery, Sendai, Japan (1963).
53. van Wijngaarden, L., "On the Growth of Small Cavitation Bubbles by Convective Diffusion," Int. J. of Heat and Mass Transfer, Vol. 10, pp. 127-134 (1967).
54. Hsieh, D. and M.S. Plesset, "Theory of Rectified Diffusion of Mass into Gas Bubbles," J. Acoust. Soc. Am., Vol. 33, pp. 206-215 (1961).

55. Eller, A.I. and H.G. Flynn, "Rectified Diffusion During Non-Linear Pulsations of Cavitation Bubbles," J. Acoust. Soc. Am., Vol. 37, pp. 493-503 (1965).
56. Strasberg, M., "Onset of Ultrasonic Cavitation in Tap Water," J. Acoust. Soc. Am., Vol. 31, pp. 163-176 (1959).
57. Strasberg, M., "Rectified Diffusion: Comments on a Paper of Hsieh and Plesset," J. Acoust. Soc. Am., Vol. 33, p. 161 (1961).
58. Pode, L., "The Deaeration of Water by a Sound Beam," DTMB Report 854 (1953).
59. Eller, A.I., "Growth of Bubbles by Rectified Diffusion," J. Acoust. Soc. Am., Vol. 46, pp. 1246-1250 (1969).
60. Kapustina, O.A. and Y.G. Statnikov, "Influence of Acoustic Microstreaming on the Mass Transfer in A Gas Bubble--Liquid System," Sov. Phys. Acoustics, Vol. 13, pp. 327-329 (1968).
61. Boguslavskii, Y.Y., "Diffusion of a Gas into a Cavitation Void," Sov. Phys. Acoust., Vol. 13, pp. 18-21 (1967).
62. Liebermann, L., "Air Bubbles in Water," J. Appl. Phys., Vol. 28, pp. 205-211 (1957).
63. Crump, S.F., "Determination of Critical Pressures for the Inception of Cavitation in Fresh and Sea Water as Influenced by Air Content of the Water," DTMB Report 575 (1949).
64. Fox, F.E. and K.F. Herzfeld, "Gas Bubbles with Organic Skin as Nuclei," J. Acoust. Soc. Am., Vol. 26, pp. 984-989 (1954).
65. Herzfeld, K.F., "Comments to a paper by M.S. Plesset," 1st Symposium on Naval Hydrodynamics (1956).
66. van der Meulen, J.H.J., "A Holographic Study of Cavitation on Axisymmetric Bodies and the Influence of Polymer Additives," Ph.D. Thesis, Enschede, The Netherlands (1976).
67. Harvey, E.N. et al., "Bubble Formation in Animals I, Physical Factors," J. Cellular and Comparative Physiology, Vol. 24, pp. 1-22 (1944).

68. Harvey, E.N. et al., "Bubble Formation in Animals II, Gas Nuclei and their Distribution in Blood and Tissues," J. Cellular and Comparative Physiology, Vol. 24, pp. 23-24 (1944).
69. Apfel, R.E., "The Role of Impurities in Cavitation-Threshold Determination," J. Acoust. Soc. Am., Vol. 48, pp. 1179-1186 (1970).
70. Yilmaz, E. et al., "Cavitation Inception Thresholds in Water and Nuclei Spectra by Light-Scattering Techniques," J. Acoust. Soc. Am., Vol. 59, pp. 329-338 (1976).
71. Messino, D. et al., "Statistical Approach to Ultrasonic Cavitation," J. Acoust. Soc. Am., Vol. 35, pp. 1575-1583 (1963).
72. Bernd, L.H., "Cavitation, Tensile Strength, and the Surface Films of Gas Nuclei," 6th Symposium on Naval Hydrodynamics (1966).
73. Morgan, W.B., "Air Content and Nuclei Measurement," Report to the Cavitation Committee 13th ITTC, Hamburg, Germany (1972).
74. Medwin, H., "In Situ Acoustic Measurement of Bubble Populations in Coastal Ocean Waters," J. Geophys. Res., Vol. 75, pp. 599-611 (1970).
75. Medwin, H., "In Situ Acoustic Measurements of Microbubbles at Sea," J. Geophys. Res., Vol. 82, pp. 921-976 (1977).
76. Peterson, F.B., "Hydrodynamic Cavitation and Some Considerations of the Influence of Free-Gas Content," 9th Symposium on Naval Hydrodynamics (1972).
77. Peterson, F.B. et al., "Determination of Bubble and Particulate Spectra and Number Density in a Water Tunnel with Three Optical Techniques," 14th ITTC (1975).
78. Gates, E.M. and A.J. Acosta, "Some Effects of Several Free-Stream Factors on Cavitation Inception on Axisymmetric Bodies," 12th Symposium on Naval Hydrodynamics (1978).
79. Keller, A., "The Influence of the Cavitation Nucleus Spectrum on Cavitation Inception Investigated with a Scattered Light Counting Method," J. Basic Eng., pp. 917-925 (Dec 1972).

80. Arndt, R.E.A. and A.P. Keller, "Free Gas Content Effects on Cavitation Inception and Noise in a Free Shear Flow," IAHR Symposium on Two Phase Flow and Cavitation in Power Generation Systems, Grenoble, France (1976).
81. Ill'in, V.P. et al., "Experimental Study of the Content of Cavitation Nuclei in Water," Sov. Phys. Acoust., Vol. 22, pp. 166-184 (1976).
82. Schiebe, F.R., "The Influence of Gas Nuclei Size Distribution on Transient Cavitation Near Inception," St. Anthony Falls Hydraulic Laboratory, Univ. of Minn., Report 107 (1969).
83. Schiebe, F.R. and J.M. Killen, "An Evaluation of Acoustic Techniques for Measuring Gas Bubble Size Distributions in Cavitation Research," St. Anthony Falls Hydraulic Laboratory, Univ. of Minn., Report 120 (1971).
84. Gavrilov, L.R., "Free Gas Content of a Liquid and Acoustical Techniques for its Measurements," Sov. Phys. Acoust., Vol. 15, pp. 285-295 (1970).
85. Dobrokhotoy, S.N. et al., "On the Size Distribution of Stable Bubbles in a Liquid," Sov. Phys. Acoust., Vol. 15, pp. 527-528 (1970).
86. Agrest, E.M. and G.N. Kuznetsov, "Dynamics of the Bubble Size Distribution in Sound Fields," Sov. Phys. Acoust., Vol. 20, pp. 213-216 (1974).
87. Margulis, M.A., "Kinetics of the Number of Cavitation Bubbles in an Ultrasonic Field," Sov. Phys. Acoust., Vol. 22, pp. 145-147 (1976).
88. Brockett, T., "Some Environmental Effects on Headform Cavitation Inception," NSRDC Report 3974 (1972).
89. Besant, W.H., "Hydrostatics and Hydrodynamics," Cambridge Univ. Press (1859).
90. Knapp, R.T. and A. Hollander, "Laboratory Investigations of the Mechanism of Cavitation," Trans. ASME, Vol. 70, pp. 419-435 (1948).
91. Trilling, L., "The Collapse and Rebound of a Gas Bubble," J. Appl. Phys., Vol. 23, pp. 14-17 (1952).
92. Gilmore, F.R., "The Growth or Collapse of a Spherical Bubble in a Viscous Compressible Fluid," Hydromechanics Laboratory, Cal. Inst. Tech, Report 26-4 (1952).

93. Kirkwood, J.G. and H.A. Bethe, "The Pressure Wave Produced by an Underwater Explosion," OSRD Report 588 (1942).
94. Mellen, R.H., "An Experimental Study of the Collapse of a Spherical Cavity in Water," J. Acoust. Soc. Am., Vol. 28, pp. 447-454 (1956).
95. Mellen, R.H., "Spherical Pressure Waves of Finite Amplitude from Collapsing Cavities," U.S. Navy Underwater Sound Laboratory Report 326 (1956).
96. Hunter, C., "On the Collapse of an Empty Cavity in Water," J. Fluid Mech., Vol. 8, pp. 241-263 (1960).
97. Joshman, W.E., "Collapse of a Gas-Filled Spherical Cavity," J. Appl. Mech., Vol. 90, pp. 579-587 (1968).
98. Esipov, I.B. and K.A. Naugol'nykh, "Collapse of a Bubble in a Compressible Liquid," Sov. Phys. Acoust., Vol. 19, pp. 187-188 (1973).
99. Hickling, R. and M.A. Plesset, "Collapse and Rebound of a Spherical Bubble in Water," Phys. Fluids, Vol. 7, pp. 7-14 (1964).
100. Hickling, R., "Some Physical Effects of Cavity Collapse in Liquids," J. Basic Eng., Vol. 88, pp. 229-235 (1966).
101. Ivany, R.D. and F.G. Hammitt, "Cavitation Bubble Collapse in Viscous, Compressible Liquids - Numerical Analysis," J. Basic Engineering, Trans. ASME, Vol. 87, pp. 977-985 (1965).
102. Esipov, I.B. and K.A. Naugol'nykh, "Expansion of a Spherical Cavity in a Liquid," Sov. Phys. Acoust., Vol. 18, pp. 194-197 (1972).
103. Güth, W., "Zur Entstehung der Stosswellen bei der Kavitation," Acustica, Vol. 6, pp. 526-531 (1956).
104. Khoroshev, G.A., "Collapse of Vapor-Air Cavitation Bubbles," Soviet Physics-Acoustics, Vol. 9, pp. 275-279 (1964).
105. Knapp, R.T., "Cavitation Mechanics and its Relation to the Design of Hydraulic Equipment," Proc. Inst. Mech. Eng., London, Ser. 166A, pp. 150-163 (1952).
106. Fitzpatrick, H.M. and M. Strasberg, "Hydrodynamic Sources of Sound," 1st Symp. on Naval Hydrodynamics, Washington, D.C., pp. 241-280 (1956).

107. Fitzpatrick, H., "Cavitation Noise," 2nd Symposium on Naval Hydrodynamics, Washington, D.C., pp. 201-205 (1958).

108. Kuznetsov, G.N. and I.E. Shchekin, "Effect of Viscosity on the Dynamics of a Collapsing Bubble Executing Translational Motion," Sov. Phys. Acoustics, Vol. 19, pp. 463-467 (1974).

109. Levkovskii, Y.L., "Growth and Collapse of a Vapor Bubble in a Viscous Liquid," Sov. Phys. Acoustics, Vol. 20, pp. 168-170 (1974).

110. Avenesov, A.M. and G.N. Kuznetsov, "Dynamics of a Cavity in a Viscous Compressible Medium," Sov. Phys. Acoust., Vol. 20, pp. 399-402 (1975).

111. Harrison, M., "An Experimental Study of Single Bubble Cavitation Noise," DTMB Report 815 (1952).

112. Lauterborn, W., "Kavitation durch Laserlicht," Acustica, Vol. 31, pp. 51-78 (1974).

113. Lauterborn, W., "General and Basic Aspects of Cavitation," Proc. Symp. Finite Amplitude Effects in Fluids, L. Bjorno ed. IPC Science and Technology Press Ltd. (1974).

114. Ivany, R.D. et al., "Cavitation Bubble Collapse Observations in a Venturi," J. Basic Eng., Vol. 88, pp. 649-657 (1966).

115. Ill'in, V.P. and V.P. Morozov, "Experimental Determination of the Ratio of Cavitation Noise Energy to the Initial Bubble Energy," Sov. Phys. Acoust., Vol. 20, pp. 250-252 (1974).

116. Parkin, B.R., "Scale Effects in Cavitating Flow," Hydrodynamics Lab., Cal. Inst. of Technology, Report 21-7 (1951).

117. Blake, W.K. et al., "Effects of Boundary Layer Development on Cavitation Noise and Inception on a Hydrofoil," DTNSRDC Report 76-0051 (1976).

118. Blake, W.K. et al., "Cavitation Noise and Inception as Influenced by Boundary Layer Development on a Hydrofoil," J. Fluid Mech., Vol. 80, pp. 617-640 (1977).

119. Schutler, N.D. and R.B. Messler, "A Photographic Study of the Dynamics and Damage Capabilities of Bubbles Collapsing Near Solid Boundaries," J. Basic Eng., Vol. 87, pp. 511-517 (1965).

120. Ellis, A.T., "On Jets and Shock Waves from Cavitation," 6th Symposium on Naval Hydrodynamics (1966).
121. Kozirev, S.P., "On Cumulative Collapse of Cavitation Cavities," J. Basic Eng. Trans. ASME, Ser. D., Vol. 90, pp. 116-124 (1968).
122. Hammitt, F.G., discussion to "On Cumulative Collapse of Cavitation Cavities," J. Basic Eng. Trans. ASME, Ser. D., Vol. 91, pp. 857-858 (1969).
123. Plesset, M.S. and T.P. Mitchell, "On the Stability of the Spherical Shape of a Vapor Cavity in a Liquid," Hydrodynamics Laboratory, Cal. Inst. of Technology, Report 26-9 (1954).
124. Shima, A. and K. Nakajima, "The Collapse of a Non-Hemispherical Bubble Attached to a Solid Wall," J. Fluid Mech., Vol. 80, pp. 369-391 (1977).
125. Shima, A., "The Behavior of a Spherical Bubble in the Vicinity of a Solid Wall," J. Basic Eng. ASME Trans., Ser. D, Vol. 90, pp. 75-89 (1968).
126. Levkovskii, Y.L., "Collapse of a Spherical Gas-Filled Bubble Near Boundaries," Sov. Phys. Acoust., Vol. 20, pp. 36-38 (1974).
127. Daily, J.W., "Cavitation Characteristics and Infinite Aspect-Ratio Characteristics of a Hydrofoil Section," Trans. ASME, Vol. 71, pp. 269-284 (1949).
128. Lindgren, H. and C.A. Johnson, "Cavitation Inception on Headforms I.T.T.C. Comparative Experiments," Proc. 11th Int'l. Towing Tank Conference, Tokyo, pp. 219-232 (1966).
129. Batchelor, G.K., "Homogeneous Turbulence," Cambridge University Press (1960).
130. Armstrong, R., "Einfluss Der Machzahl Auf Die Kohärente Turbulenzstruktur Eines Runden Freistrahls," Ph.D. Thesis, University of Berlin (1977).
131. Arndt, R.E.A., "Cavitation Inception and Howlt Scales, A Review of the Problem with a Summary of Recent Research," Symposium on High Powered Propulsion of Large Ships, Publication 490 Netherlands Ship Model Basin, Wagenengen, The Netherlands (1974).
132. Meecham, W.C. and M.T. Tavis, "Theoretical Pressure Correlation Functions in Turbulent Boundary Layers," Phys. Fluids, Vol. 23, pp. 1119-1131 (1980).

133. Holl, J.W., "An Effect of Air Content on the Occurrence of Cavitation," J. Basic Eng., Vol. 82, pp. 941-945 (1960).
134. Holl, J.W., "Nuclei and Cavitation," J. Basic Eng., Vol. 92, pp. 681-688 (1970).
135. Holl, J.W. and A.L. Treaster, "Cavitation Hysteresis," J. Basic Eng., Vol. 88, pp. 199-212 (1966).
136. McCormick, B.W., "On Cavitation Produced by a Vortex Trailing from a Lifting Surface," J. Basic Eng., Vol. 84, pp. 369-379 (1962).
137. Noordzij, L., "A Note on the Scaling of Tip Vortex Cavitation Inception," Int. Shipbuilding Prog., Vol. 24, pp. 1-4 (1977).
138. Arndt, R.E.A., "Pressure Fields and Cavitation," IAHR/AIRH Symposium, Vienna, Austria (1974).
139. Billet, M.L., "Cavitation Results for a Secondary Flow Generated Trailing Vortex," Penn. State Univ., Appl. Res. Lab., Tech Memo 76-234 (1976).
140. Billet, M.L., "Secondary-Flow-Related Vortex Cavitation," Penn. State Univ., Ph.D. Thesis (1978).
141. Il'ichev, V.I., "The Frequency of Cavity Formation in Turbulent Boundary Layers and Wakes," Sov. Phys-Doklady, Vol. 6, pp. 118-120 (1961).
142. Young, J.O. and J.W. Holl, "Effects of Cavitation on Periodic Wakes Behind Symmetric Wedges," J. Basic Eng., pp. 163-176 (1966).
143. Kermeen, R.W. et al., "Mechanism of Cavitation Inception and the Related Scale Effects Problems," Trans. ASME, pp. 533-541 (May 1955).
144. Arndt, R.E.A., "Semi-empirical Analysis of Cavitation in the Wake of a Sharp-Edged Disk," J. Fluids Eng. Trans. ASME, Ser. 1, Vol. 98 (1976).
145. Numachi, F. et al., "Cavitation Effect on the Discharge Coefficient of the Sharp-Edged Orifice Plate," Trans. ASME J. Basic Eng., Vol. 82, pp. 1-11 (1960).
146. Jorgensen, D.W., "Noise from Cavitating Submerged Water Jets," J. Acoust. Soc. Am., Vol 33, pp. 1334-1338 (1961).
147. Daily, J. and V.E. Johnson, "Turbulence and Boundary Layer Effects on Cavitation Inception from Gas Nuclei," Trans. ASME, Vol. 78, pp. 1695-1706 (Nov 1956).



148. Arndt, R.E.A. and A.T. Ippen, "Cavitation Near Surfaces of Distributed Roughness," MIT Hydrodynamics Laboratory Report 104 (1967).
149. Oshima, R., "Theory of Scale Effects on Cavitation Inception on Axially Symmetric Bodies," J. Basic Eng., pp. 379-384 (1961).
150. Huang, T.T. and F.B. Peterson, "Influence of Viscous Effects on Model/ Full-Scale Cavitation Scaling," J. Ship Res., Vol. 20, pp. 215-223 (1976).
151. van der Meulen, J.H.J., "Incipient and Desinent Cavitation on Hemispherical Nosed Bodies," Int. Shipbuilding Prog., pp. 21-32 (1972).
152. van der Meulen, J.H.J., "A Holography Study of Boundary Layer and Surface Characteristics on Incipient and Developed Cavitation on Axisymmetric Bodies," 12th Symposium on Naval Hydrodynamics (1978).
153. Peterson, F.B., "Cavitation Originating at Liquid-Solid Interfaces," NSRDC Report 2799 (1968).
154. Peterson, F.B., "Water-Tunnel-High Speed Basin Cavitation Inception Comparisons," 12th ITTC (1969).
155. Gates, E.M., "The Influence of Free-Stream Turbulent, Free-Stream Nuclei Populations, and a Drag-Reducing Polymer on Cavitation Inception on Two Axisymmetric Bodies," Cal. Inst. of Technology, Eng. Report 183-2 (Apr 1977).
156. Arakeri, V.H. and A.J. Acosta, "Viscous Effects in the Inception of Cavitation on Axisymmetric Bodies," J. Fluids Eng. Trans. ASME, Ser. 1, Vol. 95, pp. 519-528 (1973).
157. Huang, T.T. and D.E. Hannan, "Pressure Fluctuations in the Regions of Flow Transition," DTNSRDC Report 4723 (1975).
158. Shen, Y.T. and F.B. Peterson, "Unsteady Cavitation on an Oscillating Foil," 12th Symposium on Naval Hydrodynamics (1978).
159. Arakeri, V.H., "A Note on the Transition Observations on an Axisymmetric Body and Some Related Fluctuating Wall Pressure Measurements," J. Fluids Eng., Vol. 97, pp. 82-87 (1975).
160. Alexander, A.J., "An Investigation of the Relationship between Flow Separation and Cavitation," Proc. Conf. on Cavitation, Inst. of Mech. Eng., Heriot-Watt University, Edinburgh, Scotland (Sep 1974).

161. Casey, M.V., "The Inception of Attached Cavitation from Laminar Separation Bubbles on Hydrofoils," Proc. Conf. on Cavitation, Inst. of Mech. Eng., Heriot-Watt Univ., Edinburgh, Scotland (Sep 1974).
162. Huang, T.T. and N. Santelli, "Cavitation Inception Observation on Two Axisymmetric Headforms," DTNSRDC Report SPD-807-1 (1977).
163. Holl, J.W., "The Inception of Cavitation on Isolated Surface Irregularities," J. Basic Eng., Vol. 82, pp. 169-183 (1960).
164. Bohn, J.C., "The Influence of Surface Irregularities on Cavitation: A collation and Analysis of New and Existing Data with Application to Design Problems," Penn. State Univ., Appl. Res. Lab. Report 72-223 (1972).
165. Arndt, R.E.A. et al., "Limited Cavitation on Surface Irregularities," IAHR/AIRH Symposium, Rome (1972).
166. Mellen, R.H., "Ultrasonic Spectrum of Cavitation Noise in Water," J. Acoust. Soc. Am., Vol. 26, pp. 356-360 (1954).
167. Strasberg, M., "Propeller Cavitation Noise After 35 Years of Study," Proc. ASME Symposium on Noise and Fluids Engineering, Atlanta, Ga. (1977).
168. Khoroshev, G.A., "Application of the Similarity Principle to the Study of Oscillations Excited by Cavitation," Sov. Phys., Vol. 5, pp. 485-492 (1959).
169. Levkovskii, Y.L., "Modeling of Cavitation Noise," Sov. Phys. Acoust., Vol. 13, pp. 337-339 (1968).
170. Baiter, H.J., "Aspects of Cavitation Noise," Proc. Symposium on High Powered Propulsion of Large Ships, Publication 490 Netherlands Ship Model Basin, Wageningen, The Netherlands (1974).
171. Bark, G., "Propeller Cavitation as a Source of Sound," in Swedish, "Propellerkavitation Som Bullerkälla," Report 52, Statens Skeppsprovsningsanstalt, Göteborg, Sweden (1975).
172. Lovik, A. and J. Vassenden, "Measurements of Noise from Cavitating Propellers," Specialist Meeting on Acoustic Cavitation, Dorset (1977).
173. Bjorheden, O. and L. Astrom, "Prediction of Propeller Noise Spectra," Proc. Symposium on Hydrodynamics of Ship and Offshore Propulsion Systems, DetNorski Verites, Oslo, Norway (1977).

174. Levkovskii, Y.L., "Effect of Diffusion on the Sound Radiation from a Cavitation Void," Sov. Phys. Acoust., Vol. 14, pp. 470-473 (1969).
175. Barker, S.J., "Measurements of Radiated Noise in the Caltech High-Speed Water Tunnel, Part II: Radiated Noise from Cavitating Hydrofoils," Graduate Aeronautical Laboratories, CIT (Mar 1975).
176. Barker, S.J., "Measurements of Hydrodynamic Noise from Submerged Hydrofoils," J. Acoust. Soc. Am., Vol. 59, pp. 1095-1103 (1976).
177. Erdmann, et al., "Investigation of the Production of Noise by the Propeller Particularly with Regard to the Combined Acoustic Problem-Work Segments II and III" (1969).
178. Thompson, D.E. and M.L. Billet, "Initial Investigation of Stationary Hydrofoil Cavitation on Cavitation Noise," Tech. Memo TM 77-327, Penn. State Univ. Appl. Res. Lab. (1977).
179. Thompson, D.E. and M.L. Billet, "The Variation of Sheet Type Surface Cavitation Noise with Cavitation Number," Tech. Memo TM 78-203, Penn. State Univ. Appl. Res. Lab (1978).
180. Morozov, V.P., "Theoretical Analysis of the Acoustic Emission from Cavitation Line Vortices," Sov. Phys. Acoust., Vol. 19, pp. 468-471 (1974).
181. Stuurman, A.M., "Fundamental Aspects of the Effect of Propeller Cavitation on the Radiated Noise," Symposium on High Powered Propulsion of Large Ships, Netherlands Ship Model Basin, Wageningen, The Netherlands (1974).
182. Bark, G. and W.B. van Berlekom, "Experimental Investigations of Cavitation Noise," 12th Symposium on Naval Hydrodynamics (Jun 1978).
183. Pudovkin, A.A., "Noise Emission by the Cavitation Zone of a Marine Propeller," Sov. Phys. Acoust., Vol. 22, pp. 151-154 (1976).
184. Noordzij, L., "Pressure Field Induced by a Cavitating Propeller," Int. Ship. Prog., Vol. 23, pp. 1-13 (1976).
185. Huse, E., "Cavitation Induced Hull Pressures, Some Recent Developments of Model Testing Techniques," Symposium on High Powered Propulsion of Large Ships, Netherlands Ship Model Basin, Wageningen, The Netherlands (1974).

186. van der Kooij, J. and A. Jonk, "Propeller-Induced Hydrodynamic Hull Forces on a Great Lakes Bulk Carrier; Results of Model Tests and Full Scale Measurements," Symposium on High Powered Propulsion of Large Ships, Netherlands Ship Model Basin, Wageningen, The Netherlands (1974).

187. Report of the Cavitation Committee, "Review of Research on Cavitation of Importance to the ITTC," 15th ITTC, the Hague, The Netherlands (1978).

188. Noordzij, L. et al., "Radiated Noise of Cavitating Propellers," ASME Symposium on Noise and Fluids Engineering, Atlanta, Ga (1977).

189. Ross, D. and B.W. McCormick, Jr., "A Study of Propeller Blade-Surface Cavitation Noise," Ord. Res. Lab. Report 7958-115, Penn. State Univ. (Oct 1948).

190. Lesunovski, V.P. and Y.V. Khokha, "Characteristics of the Noise Spectrum of Hydrodynamic Cavitation on Rotating Bars in Water," Sov. Phys. Acoust., Vol. 14, pp. 474-478 (1969).

191. Numachi, F., "Transitional Phenomena in Ultrasonic Shock Waves Emitted by Cavitation on Hydrofoils," Trans. ASME, J. Basic Eng., Vol. 81, pp. 153-166 (Jun 1959).

192. Numachi, F. et al., "Effect of Surface Roughness on Cavitation Performance of Hydrofoils I," Trans. ASME, J. Basic Eng., Vol. 87, pp. 495-503 (Jan 1965).

193. Brockett, T., "Cavitation Occurrence Counting-Comparison of Photographic and Recorded Data," ASME Cavitation Forum (1969).

194. Peterson, F.B., "Cavitation on a Head Form Using Occurrence Counting," ASME Cavitation Forum (1969).

195. Schiebe, F.R., "Cavitation Occurrence Counting--A New Technique in Inception Research," ASME Cavitation Forum (1966).

196. Akulichev, V.A. and V.V. Ol'shevskii, "Relationship Between the Statistical Characteristics of Acoustic Cavitation and Cavitation Noise," Sov. Phys. Acoust., Vol. 14, pp. 22-26 (1968).

197. Akulichev, V.A. and V.V. Ol'shevskii, "Statistical Characteristics of Cavitation Phenomena," Sov. Phys. Acoust., Vol. 14, pp. 35-139 (1968).

198. Morozov, V.P., "Cavitation Noise as a Train of Sound Pulses Generated at Random Times," Sov. Phys. Acoust., Vol. 14, pp. 361-365 (1969).
199. Levkovskii, Y.L., "Statistical Characteristics of Bubble Cavitation," Sov. Phys. Acoust., Vol. 19, pp. 135-138 (1973).
200. Il'ichev, V.I. and V.P. Lesunovskii, "On the Noise Spectra Associated with Hydrodynamic Cavitation," Sov. Phys. Acoust., Vol. 9, pp. 25-28 (1963).
201. Lyamshev, L.M., "On the Theory of Hydrodynamic Cavitation Noise," Sov. Phys. Acoust., Vol. 15, pp. 494-498 (1970).
202. Rice, S.O., "Mathematical Analysis of Random Noise," Bell System Tech. J., Vol. 23, pp. 282-332 (1944).
203. Rice, S.O., "Mathematical Analysis of Random Noise," Bell System Tech. J., Vol. 24, pp. 46-156 (1945). Reprinted in "Selected Papers on Noise and Stochastic Processes," N. Wax (ed.) Dover, N.Y. (1954).
204. Johnson, V.E. and T. Hsieh, "The Influence of the Trajectories of Gas Nuclei on Cavitation Inception," Sixth Symposium on Naval Hydrodynamics (1964).
205. Chalov, A.V., "Sound Emission by a Bubble Moving in a Liquid Flow Near an Elliptical Cylinder," Sov. Phys. Acoust., Vol. 20, pp. 370-372 (1975).
206. Gavigan, J.J., E.E. Watson and W.F. King, "Noise Generation by Gas Jets in a Turbulent Wake," J. Acoust. Soc. Am., Vol. 56, pp. 1094-1099 (1974).
207. Blake, W.K., "Noise Generated by Single-Orifice Air Emission from Hydrofoils," DTNSRDC Evaluation Report SAD-148E-1942 (Aug 1976).
208. Sevik, M. and S.H. Park, "The Splitting of Drops and Bubbles by Turbulent Fluid Flow," Trans. ASME J. Fluids Eng., Vol. 95, pp. 53-60 (1973).
209. Siemes, W. and J.F. Kauffman, "Die Periodische Entstehung von Gasblasen an Dusen," Chem. Eng. Sci., Vol. 5, pp. 127-139 (1956).
210. Silberman, E., "Prod. of Bubbles by the Disintegration of Gas Jets in Liquid," Proc. 5th Midwestern Conference of Fluid Mech., Univ. Mich. (Apr 1957).
211. Kutadeladze, S.S. and M.A. Styrikovich, "Hydraulics of Air-Water Systems," Moscow, Wright-Field Trans. F-TS-9814/V (1958).

212. Rayleigh, L., "On the Instability of Jets," Proc. London Math. Soc., Vol. 10, pp. 4-13 (1978).
213. Taylor, E., "Instability of Liquid Jets," Phil. Mag., Vol. 16, pp. 504-518 (1933).
214. van Krevelen, D.W. and P.J. Hoftijzer, "Studies of gas Bubble Formation," Chem. Eng. Prog., Vol. 46, pp. 29-35 (1950).
215. Hinze, J.O., "Fundamentals of the Hydrodynamics Mechanisms of Splitting in Dispersion Process," Am. Inst. Chem. Eng. J., Vol. 1, pp. 289-295 (1955).
216. Lam, H., "Hydrodynamics," Dover Press, N.Y. (1932).

## CHAPTER 5

### GENERATION OF AEOLIAN TONES BY RIGID CYLINDERS

#### 5.1 INTRODUCTION: GENERAL DESCRIPTION OF VORTEX FLOW, LIFT FLUCTUATION, AND SOUND

Possibly one of the most investigated topics of subsonic flow-induced noise generation is that which is concerned with the flow over cylinders. Historically, Strouhal<sup>1\*</sup> and shortly later Rayleigh<sup>2</sup> examined the frequencies of tones which emanated when air flowed past stretched wires. Strouhal noted that the pitch of the whirring sounds, which were generated by air passage transversely to the cylinder axis, were proportional to the velocity  $U_\infty$  divided by the cylinder diameter  $d$ . In his experiments a wire was stretched in a frame and the frame was rotated about an axis perpendicular to its length. Rayleigh's experiments<sup>2,3</sup> were conducted with a wire stretched across a chimney. He found that the frequency of the tone  $f_s$  would diminish as the kinematic viscosity of the air  $\nu$  decreased by heating. This result and that of Strouhal<sup>1</sup> lead to the postulation that a dimensionless frequency depended on Reynolds number,  $dU_\infty/\nu$ , as

$$\frac{f_s d}{U_\infty} = F\left(\frac{dU_\infty}{\nu}\right) \quad (5.1)$$

where  $F(dU_\infty/\nu)$  is an increasing function of its argument. Rayleigh postulated that the generation of the tone was in some way related to a vortex instability and that the cylinder need not vibrate for the tone to be generated. Rayleigh observed that the passage of air caused vibration of the cylinder in a direction perpendicular to the wind direction.

A formal relationship between the frequency of sound radiation and the process of vortex shedding was not made until 1908 when Benard<sup>4</sup> associated the pitch of the note with the formation of the vortex street. He observed photographically the formation of concentrated regions of vorticity in the wake of a circular cylinder. The vortex spacing was seen to be regular. Subsequently, von Karman and Rubach<sup>5</sup> in 1912 (see also Lamb<sup>6</sup>) determined the conditions for the stable existence of parallel rows of vortices of alternate sign. They found that the distance between rows and the distance between vortices in a row must be in the ratio 0.281 in order

---

\*A complete listing of references is given on page 529.

for the vortex street to undergo stable translation. This simple analytical treatment of von Karman is, even today, fundamental to much of the theoretical analysis of vortex induced forces. There is still no fully satisfactory analytical model of the vortex street that contains the refinements necessary to comprehensively describe the generation, translation, and final decay of the vortex streets behind bluff bodies. The analytical model of von Karman has permitted the calculation of the translation velocity of the vortex street as well as steady drag induced on the shedding cylinder by the vortices.<sup>5-7</sup>

In the subsequent years following von Karman's classical analysis, investigations of vortex shedding were generally experimental and devoted largely to establishing the frequencies of vortex generation and drag coefficients over various ranges of Reynolds number.

Investigations which quantified the sound levels generated by the aeolian tone in terms of flow variables began with that of Stowell and Deming<sup>8</sup> in 1936. They developed empirical correlations between the sound radiated and the length diameter, and rotation speed of the rods. They also determined the directionality of the sound as being radiated normal to the direction of flow. Later investigations further determined empirically the dependence of the radiated sound on the size of the cylinder and the speed of flow over the cylinder.

Systematic analytical treatments of the noise problem awaited the attention of Phillips<sup>9</sup> and (apparently nearly simultaneously) Etkin, Korbacher, and Keefe.<sup>10</sup> The analysis given by Phillips demonstrated that the sound intensity depended upon the axial length scale of the force fluctuations which are generated by the vortex shedding. This was the first formal treatment of the stochastic nature of the shedding process. Phillips' result showed clearly how the physical variables, which control the intensity of the aeolian tone could be derived within the framework of the theory of aerodynamic noise.

In this chapter we will examine the noise from flow over the surfaces of acoustically compact, rigid bodies from vortex-surface interactions. The flow-induced noise from circular cylinders which generate periodic wakes will be examined in depth. Formulations will be derived which estimate oscillatory lift coefficients on the wake-forming bodies in terms of the strength and geometries of the shed vortex streets. Measured parameters, including shedding frequency, lift



coefficients, and axial correlation-length scales, will be reviewed. Influences on these parameters of upstream turbulence and cylinder vibration will be considered from an experimental basis. The acoustic problem will be formulated as a straightforward application of the result of Section 2.4.3 and extended to emphasize the importance of the flow variables in controlling the intensity of sound. Measured noise levels will then be examined in connection with the theoretical formulations for both translating and rotating cylindrical bodies. Other forms of vortex-body interaction due to eddies incident on leading edges and to turbulent flow off the trailing edges of airfoils will be examined in Chapter 9. Fluid-body interactions leading to vortex-induced lift enhancement will also be examined in Chapter 9, although some aerodynamic aspects of this important phenomenon will be considered in Section 5.4 of this chapter.

## **5.2 MECHANICS OF VORTEX FORMATION BEHIND CIRCULAR CYLINDERS**

### **5.2.1 General Description of Wake Structure and Vortex Generation**

In the case of viscous flow over circular cylinders, a sequence of flow domains exist which are defined in terms of  $R_d$ , where  $R_d$  is the Reynolds number based on the diameter of the cylinder  $d$  and the inflow velocity  $U_\infty$ . Figure 5.1 shows a series of photographs which were taken by Homann.<sup>11</sup> These pictures of oil films show representative vortex streets whose patterns are sketched in Figure 5.2. For  $R_d = 32$  the flow is stable; the oil film is a single streak downstream of a pair of bound vortices. We note that although the flow is laminar, Stokes flow (ideal viscous flow) ceases to exist at  $R_d$  above unity. Even when the cylinder is vibrated, as if by plucking, as Kovasznay<sup>12</sup> points out, the flow pattern remains stable. At and above Reynolds numbers of 40, Kovasznay reports that sinusoidal disturbances begin to propagate and grow downstream of the cylinder. At  $R_d = 65$  these disturbances change in character forming vortices at some distance behind. Increases in  $R_d$  cause the vortices to be formed closer to the cylinder; the street of regularly-spaced vortices exists with laminar cores over the range of Reynolds numbers from 65 to approximately 400. At higher Reynolds numbers, the regular vortex street persists; however, Roshko<sup>13</sup> has shown that the cores of the vortices become turbulent. The



$R_d = 32$



$R_d = 55$



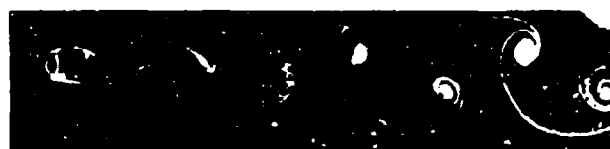
$R_d = 65$



$R_d = 73$



$R_d = 102$



$R_d = 161$



$R_d = 225$



$R_d = 281$

Figure 5.1 -- Flow Around a Circular Cylinder (Homann<sup>11</sup>)

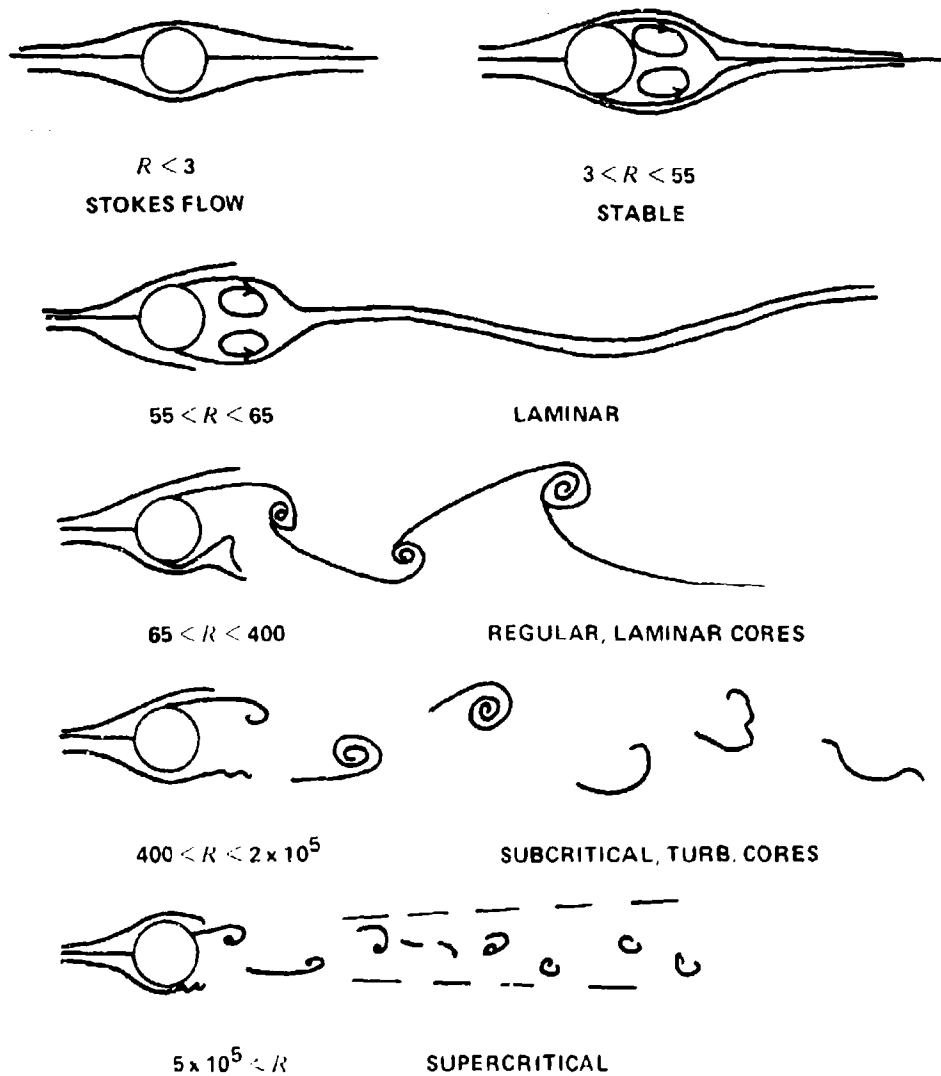


Figure 5.2 - Flow Patterns Around Circular Cylinders in Various Reynolds Number Regimes

process of laminar to turbulent flow transition in the shear layers and vortex cores has been examined in detail by Bloor<sup>14</sup> who has shown that some turbulent motion can actually be observed at Reynolds numbers just above 200. The range of Reynolds numbers over which vortices with turbulent cores are shed periodically extends to approximately  $2 \times 10^5$ . At the upper extreme of this range, irregularity eventually culminates in the complete disintegration of the vortex street. For Reynolds numbers greater than  $5 \times 10^5$  or  $10^6$  the wake is no longer fully periodic. The separation points on the cylinder occur further downstream, as shown in Figure 5.2, because the boundary layers on the surface of the cylinder are actually turbulent. In spite of the general irregularity of the shed wake, however, there are weakly periodic disturbances which persist at slightly higher dimensionless frequencies than those observed at lower Reynolds numbers. Also, due to the occurrence of attached boundary-layer flow over a greater portion of the periphery of the cylinder, the drag coefficient is reduced.

### 5.2.2 Wave-Mechanical Analysis of Vortex Production

The fluid dynamics of the vortex shedding is complex and without a complete and rigorous mathematical description. An example of an experimental and theoretical examination of vortex generation at low values of  $R$  is that of Sato and Kuriki<sup>15</sup> who have calculated the characteristic wave speeds and frequencies of the disturbances which are generated at low Reynolds numbers in the wake of a flat plate. The development of laminar wake disturbances behind plates and cylinders at low Reynolds numbers is quite similar and occurs in the manner described in Chapter 3 for the propagation of disturbances in shear layers. The study of Sato and Kuriki supports this statement. Their experimental work was conducted on a wake generated by laminar flow downstream of a very thin flat plate. The vortex structure, which they photographed using a visualization technique, resembled that shown in Figure 5.2 for  $55 < R_d < 65$ . An analysis of the type performed by Sato and Kuriki consists of a solution of the eigen-functions of the homogeneous Orr-Sommerfeld equation, Equation (3.4a), for a prescribed velocity profile. The analysis applies directly in the case of cylinder wakes to vortex structures which result from the motion of the wake as a whole as depicted especially in the

$R_d < 65$  range. The results are probably only qualitatively applicable for  $100 < R_d < 400$ , and not applicable outside this range.

There are a number of numerical computation schemes for solving Equation (3.4a) that are available in the literature, among them are those of Landahl and Kaplan,<sup>16</sup> Landahl,<sup>17</sup> and Wazzan et al.<sup>18</sup> For the analysis of wakes in this chapter the mean velocity profile is conveniently expressed in the same form used by Sato and Kuriki,<sup>15</sup>

$$\frac{U_o - U(y_2)}{U_o - U_m} = \exp \left[ - \left( \frac{Py_2}{b} \right)^2 \right] \quad (5.2)$$

where  $b$  is a length scale defined as

$$U(b) = \frac{U_o + U_m}{2} \quad (5.3)$$

Velocity profiles of the flow at various distances behind cylinders, measured by Kovasznay,<sup>12</sup> are shown in Figures 5.3 and 5.4 for  $R_d = 56$ . The root-mean-square fluctuating velocities show local maxima; the cross-stream distance between these maxima contracts slightly near  $x/d = 5$  and the disturbances attain an absolute maximum at  $x/d \approx 7$  as shown in Figure 5.5. These results show that a spatial growth of disturbances occurs. Comparison with the measurements of Ballou,<sup>19</sup> which were obtained at higher Reynolds number, shows that this process is much amplified at higher Reynolds number. Equation (5.3) fits Kovasznay's measured velocity profile at  $x/d = 5$  with  $U_m = 0.3 U_o$ ,  $P = 0.69$ , and  $b = 0.8d$ . Substitution of Equation (5.2) into Equation (3.4a) using  $R_b = 0.8 R_d$  permits a numerical solution for the eigen values of Equation (5.1) by the methods of Landahl; References 16 and 17. This results in the computed curve of neutral stability of small disturbances that is shown in Figure 5.6. The cross-hatched portion of the figure shows wave numbers,  $\omega b/c_r$ , of unstable, or growing disturbances for which  $c_1$  is positive. In the unstable range, at  $R_d$  greater than 100 particularly, the linear flow model is only qualitatively correct and on the boundary  $c_1 = 0$  so that the disturbances are neutrally stable. The wave number of  $\omega d/U_o = 0.9$  ( $\omega b/c_r = 1.2$ )

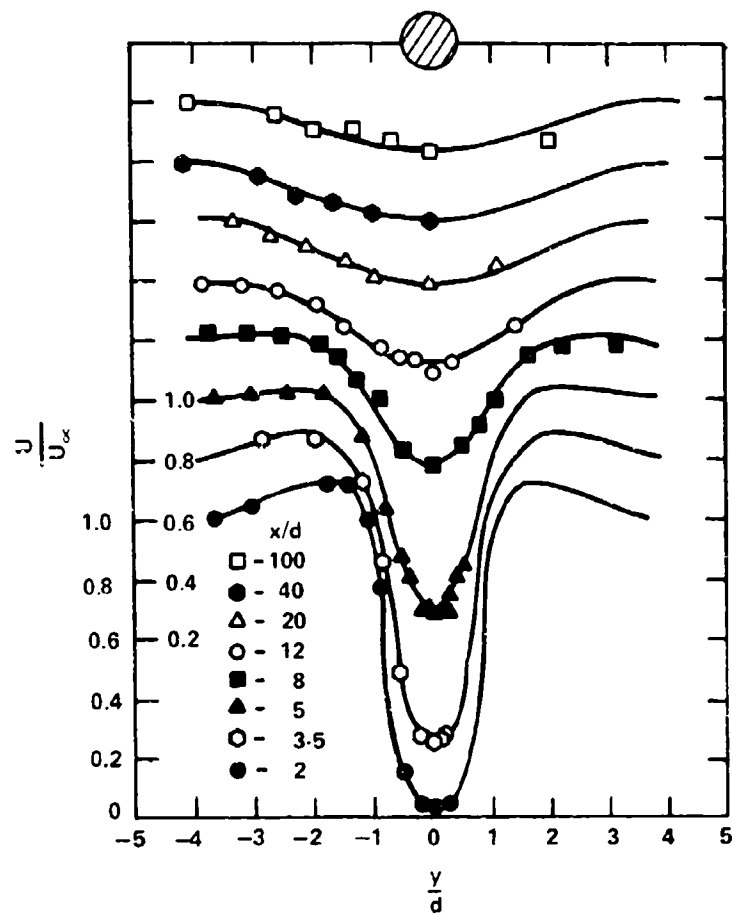


Figure 5.3 - Measurements of Mean Velocities in the Wake of a Cylinder at  $R_d = 56$   
(Kovaszny<sup>12</sup>)

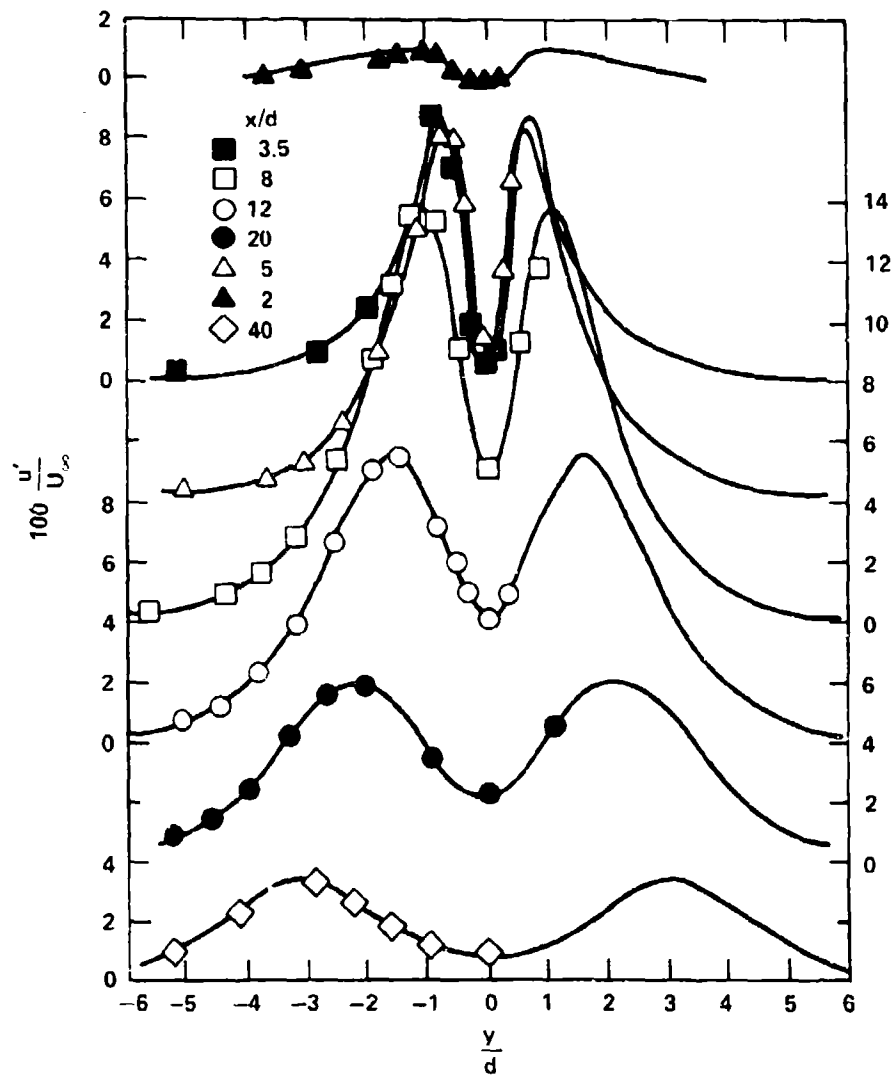


Figure 5.4 - Measurements of Fluctuating Velocity in the Wake of a Circular Cylinder at  $Re_d = 56$   
(Kovaszny<sup>12</sup>)

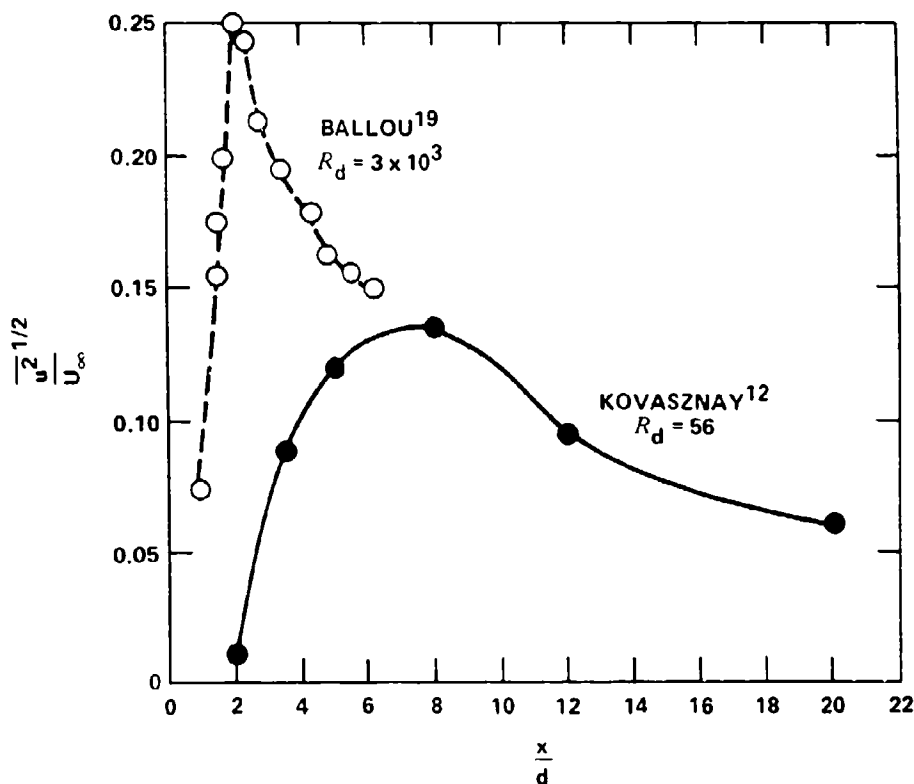


Figure 5.5 - Downstream Growth and Decay of Local Maxima of Root-Mean-Square Fluctuating Velocity in the Wakes of Rigid Circular Cylinders

observed by Kovasznavy at  $R_d = 56$  ( $U_\infty b/\nu=45$ ) is a value which is close to the least-stable wave number calculated using Equation (3.4a) as shown by the point in Figure 5.6. The calculated value of  $c_r$  is  $0.65 U_\infty$  for  $\omega b/U_\infty = 0.75$ . For  $R_d$  greater than 10, all shear layers with mean-velocity-profiles of the form given by Equation (5.4) with  $U_m = 0.3 U_\infty$  are theoretically unstable, although Kovasznavy<sup>12</sup> found instabilities not to occur for  $R_d$  less than 40.

At Reynolds numbers greater than  $2 \times 10^2$  the range of theoretically unstable frequencies, or wave numbers is independent of Reynolds number. Although a broad range of wave numbers is unstable, a discrete frequency of vortex formation occurs. The linearized theory does not predict the occurrence of this discrete frequency, although it does give a frequency of the most unstable disturbance. As an example, Figure 5.7 shows calculated wave speeds and amplification factors of the form used



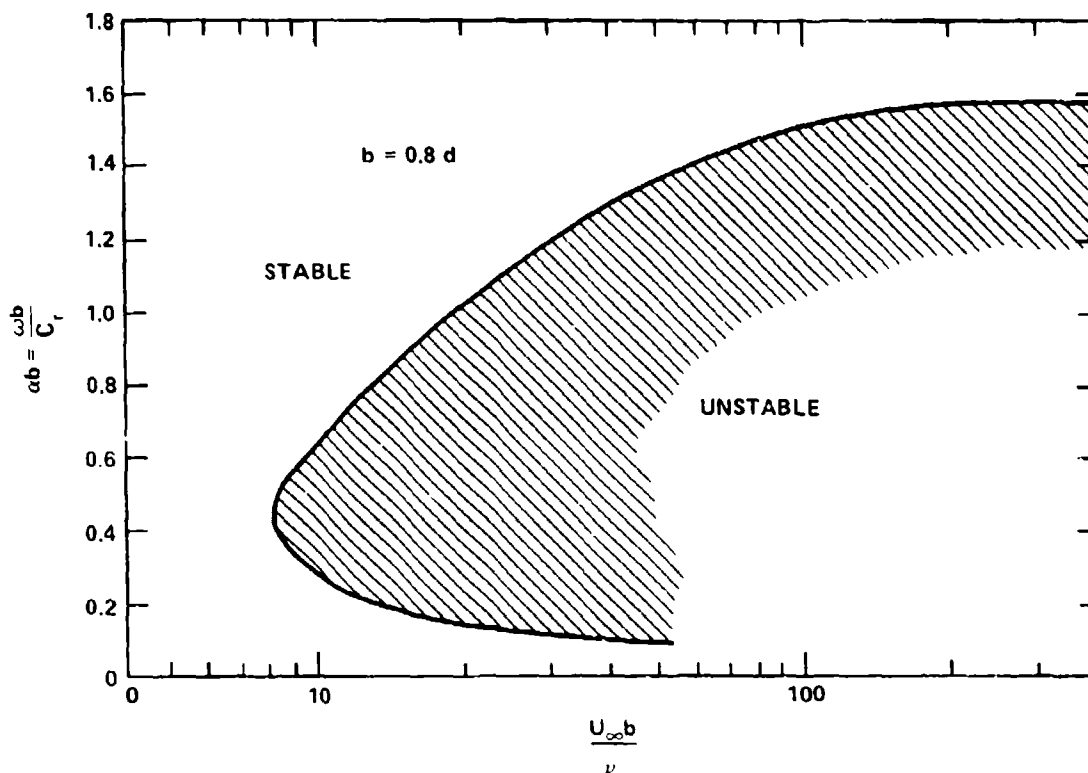


Figure 5.6 - Stability Diagram of a Typical Mean Velocity Profile in the Two-Dimensional Wake of a Blunt Body;  
 $U_m/U_0 \approx 0.31$ ,  $P = 0.69$

in Equation (5.3) and these compare favorably with those which were measured by Sato and Kuriki in a laminar wake for which  $U_m/U_0 = 0.3$ . The calculation shows that the most unstable disturbance occurs at a frequency, or wave number, near  $\omega b/U_0 \approx 0.6$ . Agreement with the measured amplification rates of Sato and Kuriki is rather good. Sato's and Kuriki's amplification rates were measured over a Reynolds-number range from  $U_0 b/\nu = 500$  to 1000 which is equivalent to the range examined by Kovasznay. They were, however, measured in the wake of a flat plate rather than behind a cylinder.

The observed growth rates behind cylinders that are shown in Figure 5.5 for  $R_d = 56$  are greater by a factor of six than the calculated rates in Figure 5.7. A plausible explanation for this discrepancy is that waves in the shear layer are sensitive to extraneous disturbances as well as to increases in Reynolds number. The dramatic influence of Reynolds number on the generation of the vortex street can

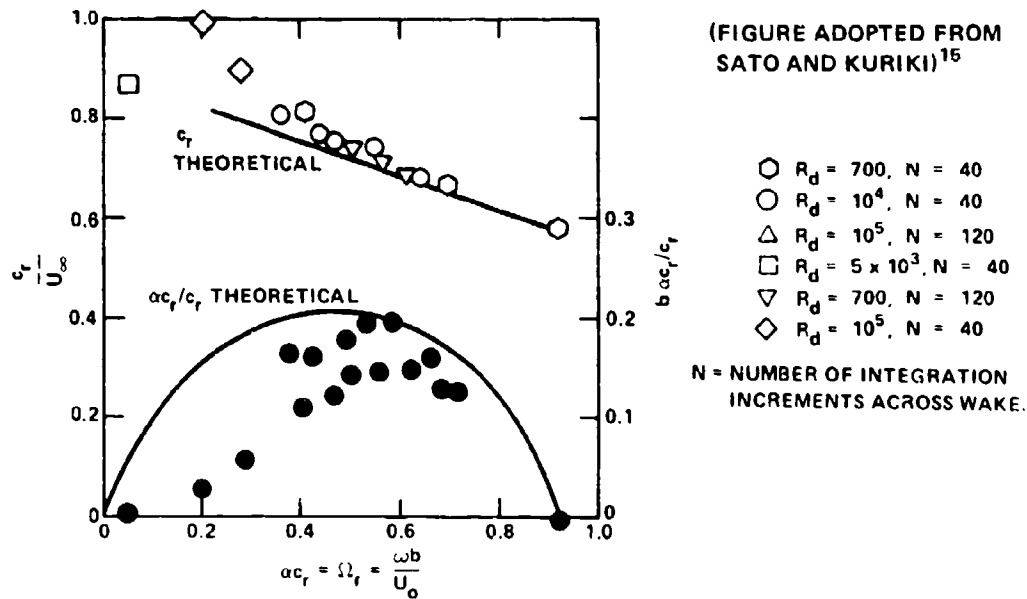


Figure 5.7 - Phase-Speeds and Amplification Factors for the Mean Velocity Profile Used in Figure 5.6. Additional Points were Analytically Determined Using Equation (5.2) and the Landahl-Kaplan<sup>16</sup> Computation Scheme

be further seen in the photographs of Figure 5.1 for  $R_d = 55, 65$ , and  $73$ . It is now known that extraneous disturbances of various types can influence vortex formation at  $R_d$  above  $10^3$ ; these will be discussed next and in various sections later in this chapter.

### 5.2.3 Secondary Disturbances in the Vortex Formation Zone

The observed growth of disturbances shown in Figure 5.5 indicate that Reynolds number is an important variable in determining the growth rates in shear layers. It has recently been shown that this dependence on Reynolds number is strongly related to the transition to turbulence of the flow in the near wake of the cylinder (or at very high Reynolds numbers on the cylinder itself). This transition phenomenon is superimposed on the development of the primary vortex structure and has been shown to modify it. This leads to a flow behavior more complex than discussed above and which has not yet been fully analyzed either experimentally or

theoretically. Roshko,<sup>13</sup> Bloor,<sup>14</sup> and Dale and Holler<sup>20</sup> have provided relatively detailed experimental descriptions of this phenomenon. Earlier, Schiller and Linke<sup>21</sup> had disclosed the importance of near-wake turbulence in determining the behavior of drag coefficients of cylinders with Reynolds number.

At Reynolds numbers less than  $3 \times 10^5$  the laminar boundary layer on the cylinder separates at an angle of approximately 80 degrees from the forward stagnation point. The free shear-layer that is formed in the near wake is unstable with secondary spatially and temporally growing wave-like disturbances which depend on the fluid velocity, the thickness of the shear layer, and the kinematic viscosity of the fluid. The breakdown of these transition waves to turbulence occurs closer to the cylinder than the formation of the primary vortex pattern at Reynolds numbers greater than  $1.3 \times 10^3$ ; it occurs within the cores of the vortices<sup>13,14</sup> after their formation at Reynolds numbers greater than 150 to 300 and less than  $1.3 \times 10^3$ . The frequencies of the transition waves  $f_t$  for  $R_d > 1.3 \times 10^3$  have been shown by Bloor,<sup>14</sup> Dale and Holler,<sup>20</sup> and Roshko<sup>22</sup> to be a large multiple of the fundamental frequency of vortex shedding  $f_s$ , such that

$$\frac{f_t}{f_s} = A \left( \frac{f_s d}{U_\infty} \right)^{-1} \left( \frac{U_\infty d}{\nu} \right)^{1/2} \quad (5.4)$$

where A has an experimental value of approximately  $2 \times 10^{-2}$  to  $3 \times 10^{-2}$ . This behavior of the transition wave frequency  $f_t$  suggests that  $f_t \delta_e / U_\infty$  is nearly a constant, where  $\delta_e$  is the laminar boundary-layer thickness at the point where the flow separates from the cylinder. The breakdown of these disturbances, and the limit of laminar flow, occurs closer to the cylinder as Reynolds number increases above  $1.3 \times 10^3$  as shown by the experimental results of Bloor<sup>14</sup> and Schiller and Linke<sup>21</sup> in Figure 5.8. As noted above, at Reynolds numbers less than  $1.3 \times 10^3$ , the transition waves are not observed before the formation of vortices. Undoubtedly, these secondary waves contribute to an overall reduction in the formation distance of the primary vortex street.

Also shown in Figure 5.8 are the distances behind the cylinder where vortices are formed. The available range of experimental data are sufficient to give a

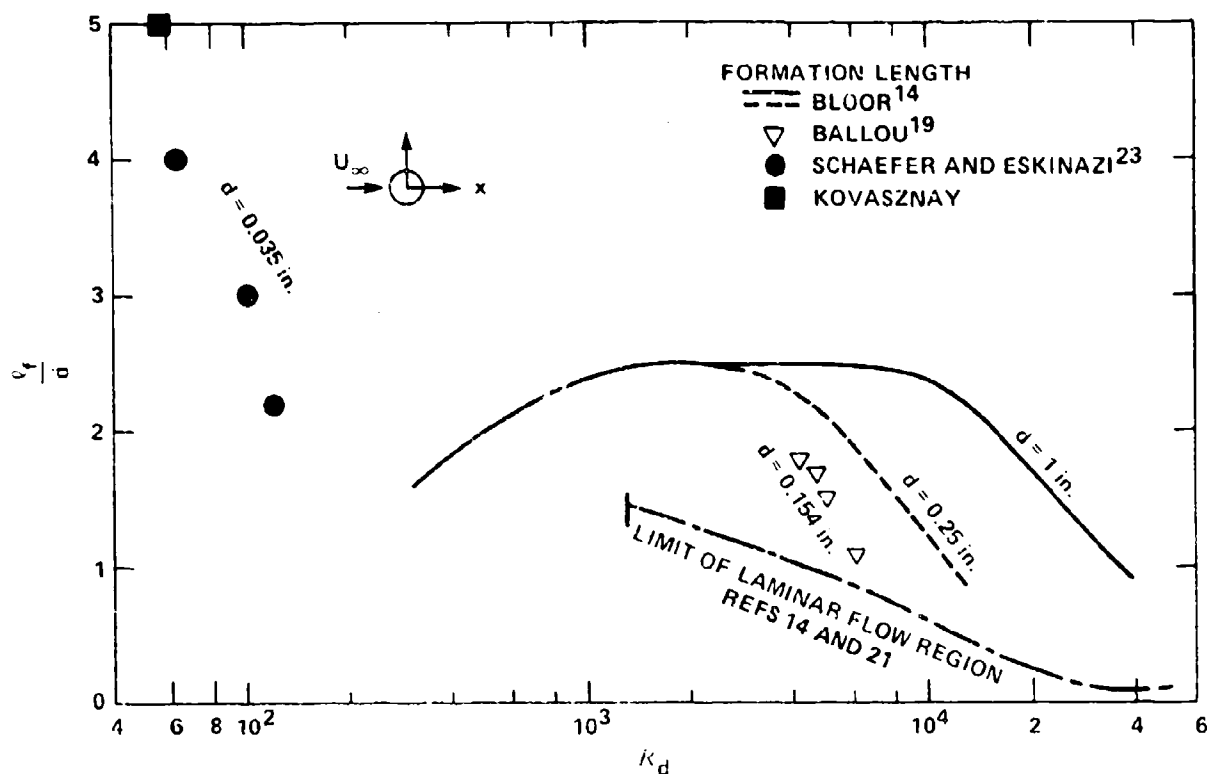


Figure 5.8 - Vortex Formation Lengths Behind Circular Cylinders as a Function of Reynolds Number

fairly complete Reynolds number behavior of the formation length. The length of the formation region can be defined in various alternative ways. The region extends downstream of the shedding cylinder to a point where the width of the wake is a minimum, as discussed by Schaefer and Eskinazi.<sup>23</sup> According to Bloor,<sup>14</sup> the formation region extends downstream of the laminar limit within which the secondary disturbances have become irregular. The end of the formation region is marked by a clearly distinguishable reduction in the amplitude of these secondary disturbances. Bailou<sup>19</sup> interpreted the formation length, alternatively, as extending to the location of the maximum values of fluctuating velocity at  $f_s$  in the wake as shown in Figure 5.5. Measurements have been obtained on a range of cylinders and although the results are shown in dimensionless form, there seems to be a consistent

dependence of  $\lambda_f$  on the diameter of the cylinder. It is notable that an analogous dependence on diameter of the limit on the extent of laminar flow was not observed by Bloor, although the connection between this limit and the formation length is fairly apparent. Both distances decrease with an increase in Reynolds number. At Reynolds numbers greater than 100, the formation length is on the order of 2.5 cylinder diameters or less; as Reynolds number decreases below 100 the distance for formation increases. The increase in formation length at low Reynolds number is also suggested by the photographs in Figure 5.1.

This discussion of the near-wake dynamics and the previous one on vortex development precedes our description of the other elements of the fluid dynamics of the cylinder wake because it is probably fundamental to the behavior of the other wake characteristics. Although it is not well explained by rigorous theory and extensive empirical characterization, there is ample evidence that this secondary transition (a) contributes to the generation of three-dimensional disturbances in the primary vortex street, and (b) is the vehicle through which transverse cylinder motion and upstream turbulence (Gerrard<sup>24</sup>) can influence vortex formation (see also Reference 20). The three-dimensional nature of the vortex street, the formation length, and the vortex strength are the dominant wake characteristics which control the sound radiation as will be discussed subsequently.

## 5.3 MEASURED FLOW-INDUCED FORCES AND THEIR FREQUENCIES

### 5.3.1 Mean Drag and Vortex Shedding Frequencies

The time-averaged drag on a circular cylinder is strongly dependent upon Reynolds number because, as the characteristics of the formation of vortices change, so too will the rate of fluid momentum that is transferred to the wake. Also, as vortices are formed, time-dependent forces are generated on the cylinder which balance the rate of change of momentum associated with the circulation of each vortex. The force system and its relationship to a vortex pattern is diagrammed in Figure 5.9. The illustrations of Figures 5.1 and 5.2 show a regular vortex system to exist; we have truncated the street in Figure 5.9 to only three vortices. For the time being we will restrict our attention to the average drag force  $F_x$  designated in the figure. A drag coefficient  $C_D$  is defined as

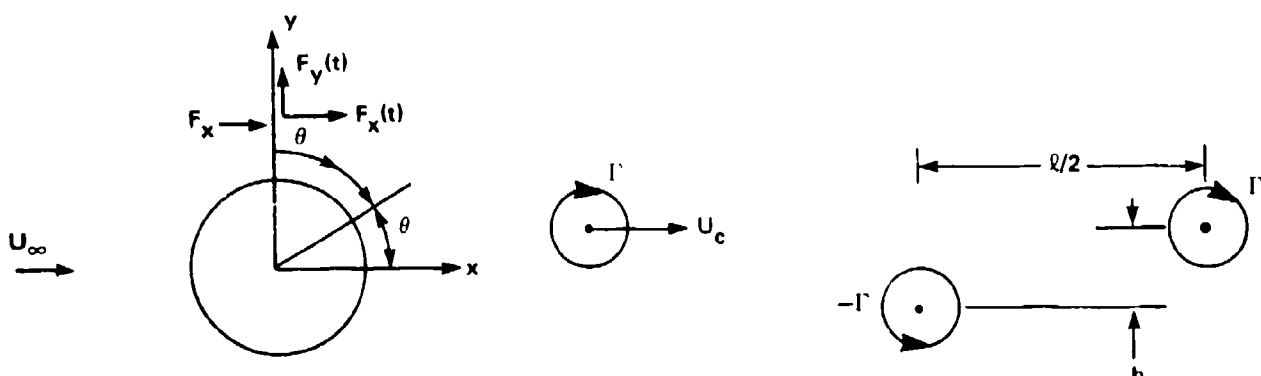


Figure 5.9 - Vortex Street and Force System on a Shedding Cylinder

$$\overline{C_D} = \frac{F_x}{\frac{1}{2} \rho_o U_\infty^2 d L} \quad (5.5)$$

where  $L$  is the length of the cylinder and  $d$  is its diameter. Figure 5.10 shows the dependence of  $C_D$  on  $R_d$  as published by Roshko.<sup>25</sup> The characteristic vortex-shedding regimes of Figure 5.2 are also indicated in the figure.\* For  $R_d$  less than 20, the drag coefficient is largely controlled by viscous friction. The two transition regions which are indicated pertain to the development of turbulence in the wake. In the range of Reynolds numbers 150 to 300, turbulent vortex cores exist; in the range from  $2 \times 10^5$  to  $5 \times 10^5$  the boundary layers on the upper and lower arcs of the periphery of the cylinder become turbulent. These turbulent boundary layers separate at an angle of approximately 120 deg along the periphery from the forward stagnation point. The influence of this viscous effect is seen in the pressure distributions shown in Figure 5.11. The local pressure  $P(\theta)$  on the surface of the cylinder is presented as a coefficient

$$C_p = \frac{P(\theta) - P_\infty}{\frac{1}{2} \rho_o U_\infty^2} \quad (5.6)$$

\*The curve in Figure 5.10 is constructed from a number of experimental results. Schlichting<sup>26</sup> cites many of these as does Chen.<sup>27</sup>

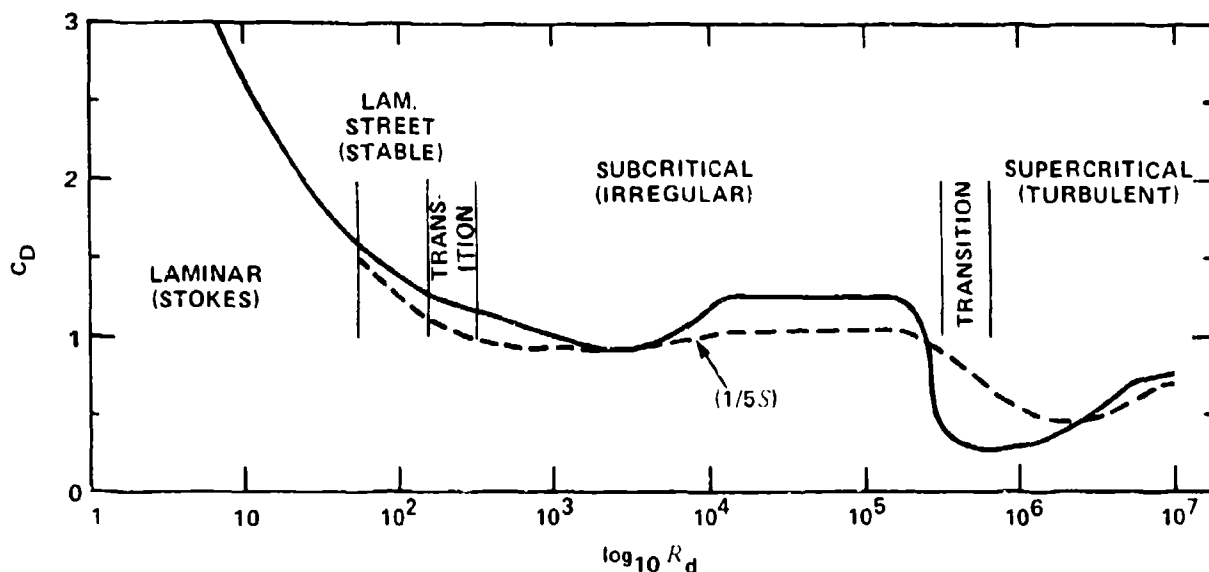


Figure 5.10 - Drag Coefficient of Circular Cylinder (Roshko<sup>25</sup>)

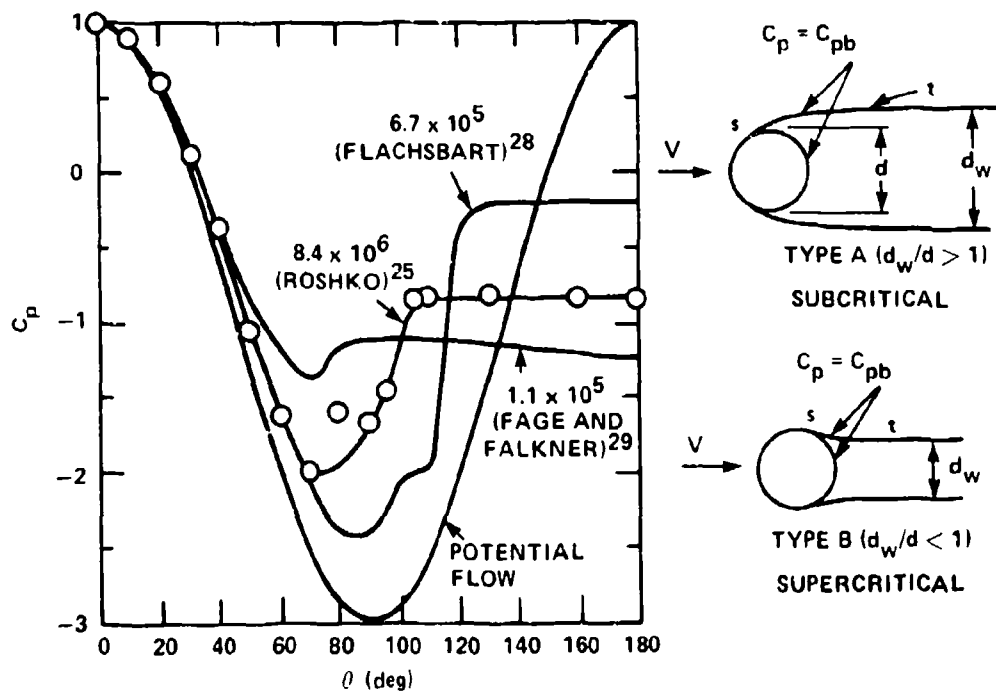


Figure 5.11 - Pressure Distributions on Cylinders in the Subcritical-to-Supercritical Flow Ranges (Roshko<sup>25</sup>)

In the subcritical range,  $R_d < 2 \times 10^5$ , the pressure coefficients reflect the separation occurring over a larger sector of the cylinder than it does in the supercritical range. In the latter range the pressure coefficient in the separated zone, called the base pressure coefficient  $C_{p_b}$ , increases and the wake contracts. This results in the observed reduction in  $C_D$ . In the supercritical region the width of the wake  $d_w$  reduces in size to less than a cylinder diameter, but as  $P_d$  continues to increase the streamlines expand again. This expansion is reflected in Roshko's pressure distribution for  $R_d = 8.6 \times 10^6$  and causes an increase in the drag coefficients.

In the range of  $10^4 < R_d < 3 \times 10^5$  the drag coefficient is particularly constant, probably owing to the nearly invariant wake characteristics in this range. It is also the upper extreme of the range over which laminar to turbulence transition has occurred in the formation zone of the wake. For  $R_d$  greater than  $8 \times 10^3$ , Bloor<sup>14</sup> has shown that this transition occurs abruptly in the shear layer within a distance less than one-half cylinder diameter from the separation point (see Figure 5.8). Before the formation of a vortex, these transition waves fully breakdown to turbulence. This abrupt breakdown in the shear layer is in contrast to that which occurs in the Reynolds number range  $1.3 \times 10^3$  to  $8 \times 10^3$  for which the breakdown occurs more gradually and is preceded by the clearly-distinguished transition waves. Thus, we see that the behavior of the drag coefficient is paralleled by the occurrence of the secondary disturbances. The drag is, therefore, governed by the mechanics of wake vortex development. As we shall soon see, it is also related to the frequency of vortex shedding. Roughness on the surface of the cylinder has been observed<sup>30</sup> to decrease the base pressure coefficient and increase the steady drag at Reynolds numbers near  $3 \times 10^5$  when the boundary layers are turbulent. The boundary layer separation points move forward when the cylinder is roughened.

The vortex shedding frequency can be measured by placing a hot wire anemometer probe into the cylinder wake and measuring the frequency of the velocity disturbances that are sensed. The probe must be on one side or the other of the axis of the wake. The fluctuations in velocity are associated with the individual vortices, as shown in Figure 5.9. The vortices move with a velocity  $U_c$  and vortices with the same circulation direction have a streamwise separation distance  $\lambda$ . Two rows of



vortices exist, each with vortices of a common circulation direction. Thus, a fixed probe on one side of the wake will sense an undulating velocity of frequency

$$f_s = \frac{U}{\ell}$$

because as vortices of alternating sign pass by the probe, the direction of the velocity disturbance will alternate. If the probe were to be placed on the axis of the wake, it would sense alternating velocities of a frequency  $2f_s$ . The frequency of vortex passage, or of vortex production, is typically expressed in the dimensionless form

$$S = \frac{f_s d}{U_\infty} = \frac{U}{U_\infty} \frac{d}{\ell}$$

This dimensionless frequency is called the Strouhal number in honor of the earliest investigator of the phenomenon. Another method of measurement consists of determining the frequency of fluctuations of the oscillating lift on the shedding cylinder. This force component is  $F_y(t)$  in Figure 5.9.

Strouhal numbers in the range of Reynolds numbers from  $10^1$  to  $10^4$  are shown in Figure 5.12 which is reproduced from Roshko's original report. It shows Kovasznay's as well as Roshko's<sup>13</sup> measurements on a variety of cylinder diameters. Background turbulence levels in the wind tunnels reported by the two investigators were between 0.03 and 0.18 percent. It is interesting to recall now Rayleigh's<sup>2,3</sup> postulation that  $S$  is an increasing function of  $R_d$ , and to see that it applies in Figure 5.12 from  $R_d = 40$  (Kovasznay's<sup>12</sup> lower limit of vortex function) until  $R_d = 10^3$ . Except for the Reynolds number range 140 to 300 the Strouhal number depends smoothly on  $R_d$ . In this short range (Roshko's transition range) Roshko<sup>13</sup> reports irregularities and bursting of the fluctuating velocities in the wake. At lower  $R_d$ , velocity fluctuations are sinusoidal, as well as above this range. However, although the vortices are shed uniformly and coherently along the entire axis of the cylinder up to  $R_d = 150$ , as shown visually by Hama,<sup>31</sup> three-dimensionality begins to develop in the wake at  $R_d$  between 150 and 300. At  $R_d$  greater than 300, Hama's photographs show

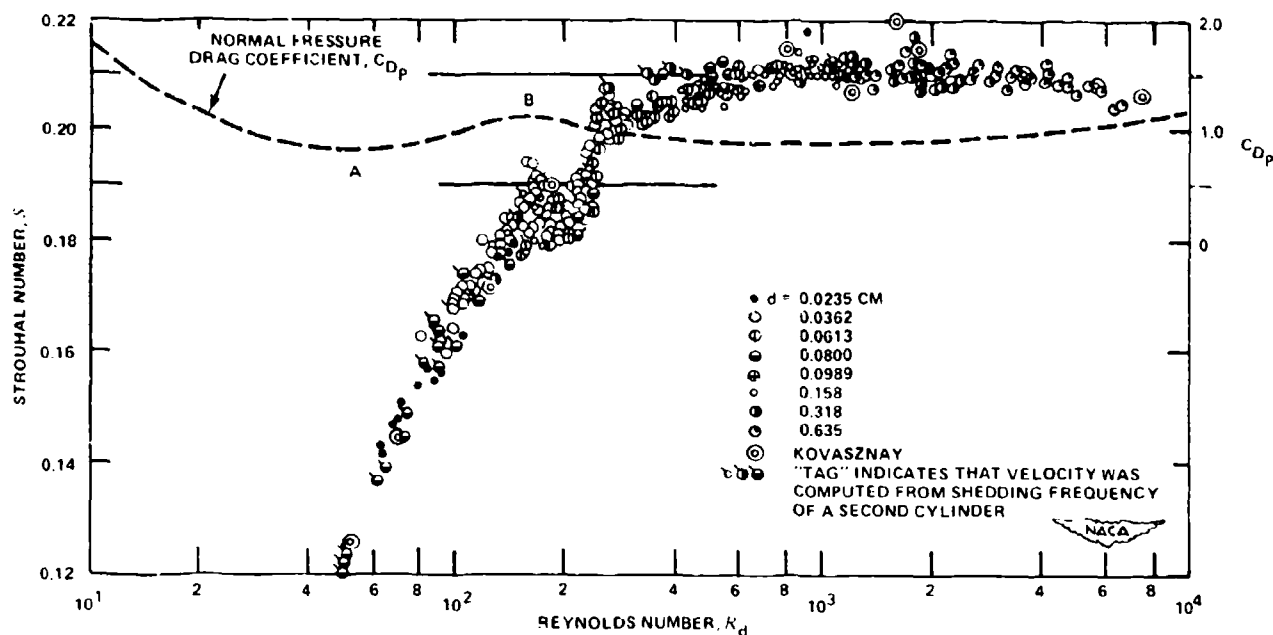


Figure 5.12 - Strouhal Numbers for Vortex Shedding Behind Circular Cylinders--Low Reynolds Numbers (Roshko<sup>13</sup>)

that a spatial periodicity occurs in the filaments of shed vortices. As the vortices are convected downstream, the vortex street becomes turbulent. The range of  $R_d$  between  $4 \times 10^2$  and  $1.3 \times 10^3$  we have already noted corresponds to that<sup>14</sup> in which laminar-to-turbulent transition occurs just prior to vortex formation. At Reynolds numbers above  $1.3 \times 10^3$ , corresponding to the shrinking region of observed transition waves, the Strouhal number is nearly constant.

Measured values of Strouhal number at higher values of Reynolds number are shown in Figure 5.13. These values have been obtained by measuring frequencies of fluctuations in lift or wake velocity. The collection of points reflects the degree of repeatability in the values of  $S$  throughout the Reynolds number range up to the "transition" range\* shown in the figure. For Reynolds numbers greater than  $5 \times 10^5$ , the irregularity in the cylinder wake is reflected in the wider range of

\*This and other names used in this text which are given to the various regions of vortex shedding are due to Roshko. However, other names have been given by other authors. To avoid confusion, names will be used here sparingly and always with reference to a figure.

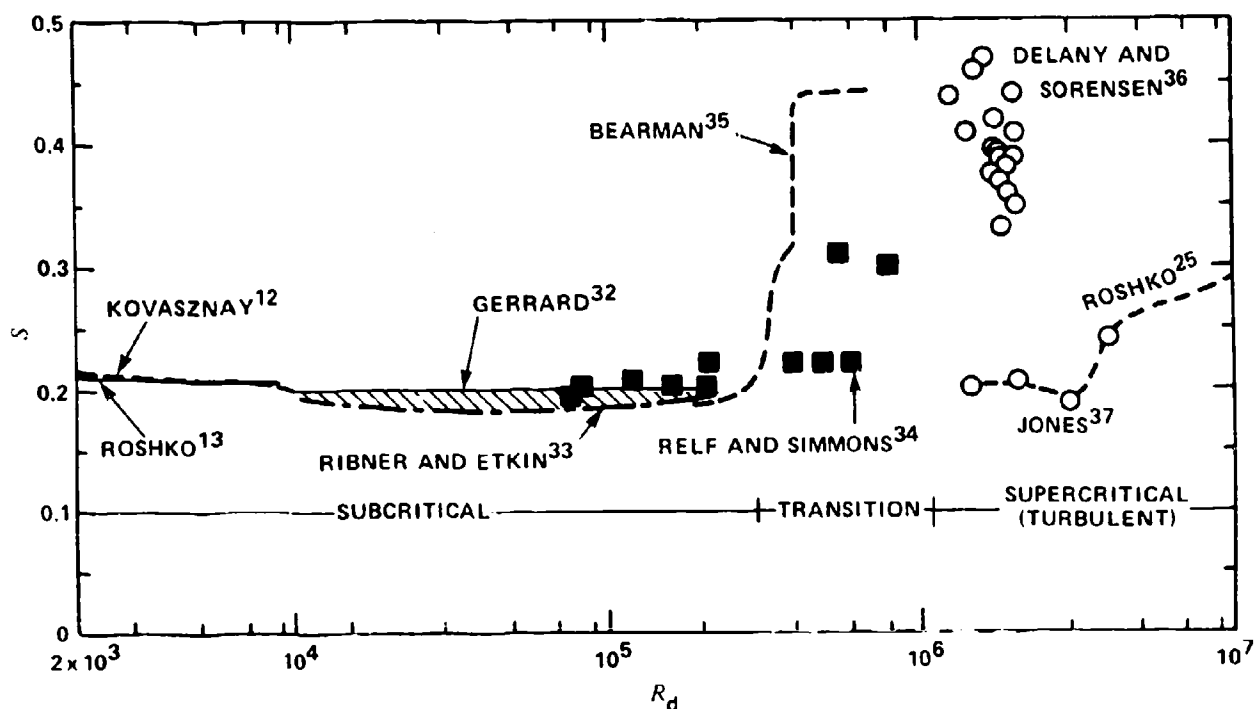


Figure 5.13 - Strouhal Numbers at High Reynolds Numbers

reported values of Strouhal number that have been reported. The particularly large values of  $S$  that have been reported by Delany and Sorensen<sup>36</sup> and Bearman<sup>35</sup> relative to those of Jones<sup>37</sup> and of Roshko<sup>38</sup> appear to be out of line with other values. The reason for this is not understood, however, all investigators of this range of Reynolds number have reported difficulty in establishing a predominant frequency. Jones,<sup>31</sup> for example, quotes a range of Strouhal frequencies for the lift fluctuations of from  $2.5 \times 10^{-2}$  to  $2.1 \times 10^{-1}$  at any given Reynolds number in the range of from  $1 \times 10^6$  through  $5 \times 10^6$ . At higher Reynolds numbers in the range  $5 \times 10^6$  to  $2 \times 10^7$  the lift fluctuations are more periodic, with a predominant Strouhal frequency of 0.3. Bearman<sup>35</sup> used flow visualization to disclose the existence of two laminar separation bubbles, indicating the formation of two separate vortices above and below the stagnation point as illustrated in Figure 5.4 for the supercritical range.

The existence of higher Strouhal numbers at high Reynolds number has been linked with the contraction of the wake that is illustrated in Figure 5.11. The streams are assumed to be parallel downstream of location  $t$ ; separation occurs at location  $s$ . Roshko<sup>38</sup> has postulated that the frequency of vortex shedding is dependent upon the (theoretically-calculated) separation of the free stream lines of the shear layers  $d_w$  and the velocity of the free stream lines  $U_s$ . Now,

$$U_s = U_\infty (1 - C_{p_b})^{1/2}$$

where  $C_{p_b}$  is the base pressure coefficient. Thus, Roshko's<sup>38</sup> definition of Strouhal number is

$$S^* = \frac{f_s d_w}{U_s}$$

This number has the value  $S^* \approx 0.16$  for circular cylinders, 90 deg wedges, and flat plates set normal to the flow. It is nearly constant over the range of  $U_s d_w / \nu$  from  $1 \times 10^4$  to  $4.4 \times 10^4$ . The point is that the increase in Strouhal number for  $R_d$  in the supercritical region of Figure 5.13, as reported by Roshko, is in direct proportion to the product

$$S = S^* \left( \frac{d}{d_w} \right) (1 - C_{p_b})^{1/2}$$

The variations in observed values of  $S$  are accompanied by corresponding variations in the mean drag coefficient. High values of  $S$  are associated with relatively low values of  $C_D$ . As will be seen in Section 5.5, von Karman's<sup>5</sup> formula for the drag on a bluff body shedding a vortex street is (since  $h/\ell = 0.281$ )

$$C_D = \frac{h}{d} \left[ 5.65 \frac{U_\infty - U_c}{U_\infty} - 2.25 \left( \frac{U_\infty - U_v}{U_\infty} \right)^2 \right]$$

where  $h$  is the vortex row spacing shown in Figure 5.9. For the case that the vortex velocity  $U_c$  is a constant percentage of  $U_\infty$  over the Reynolds number range, the drag coefficient is proportional to  $h/d$ . Now, further assuming that the vortex street spacing is proportional to the shear layer spacing  $d_w$ , and that  $S^*$  is constant, we find the result

$$C_D = k S^{-1}$$

where  $k$  is constant over the range of Reynolds number. Arbitrarily selecting  $k = 1/5$  we use Strouhal numbers in Figures 5.12 and 5.13 to construct the dotted line shown in Figure 5.10. This comparison, first shown by Roshko,<sup>38</sup> supports the speculated correspondence and it further shows the intimacy between cylinder drag and the details which govern the vortex generation.

The interdependence of the mean drag coefficient and the geometry of the vortex street has been further clarified by Bearman.<sup>39</sup> He used Kronauer's<sup>40</sup> stability criterion which states that the vortex spacing ratio  $h/\ell$  is determined by a requirement that the drag induced by the wake is a minimum. It will be shown in Section 5.5 (Equation (5.37)) that the drag coefficient of the vortex street for an arbitrary spacing ratio is

$$C_D = \frac{4}{\pi} \frac{\ell}{d} \left( \frac{U_v}{U_\infty} \right)^2 \left[ \coth^2 \frac{\pi h}{\ell} + \left( \frac{U_\infty}{U_v} - 2 \right) \frac{\pi h}{\ell} \coth \frac{\pi h}{\ell} \right]$$

Kronauer's criterion states that the spacing ratio, for a given vortex speed  $U_v$  relative to the free stream velocity, i.e.,  $U_v = U_\infty - U_c$ , is determined by

$$\left[ \frac{\partial C_D}{\partial \left( \frac{h}{\ell} \right)} \right]_{U_v = \text{constant}} = 0$$

Bearman has shown that this condition predicts spacing ratios which depend upon the vortex velocity as shown in Figure 5.14. Using measured values of  $U_v/U_\infty$  and of

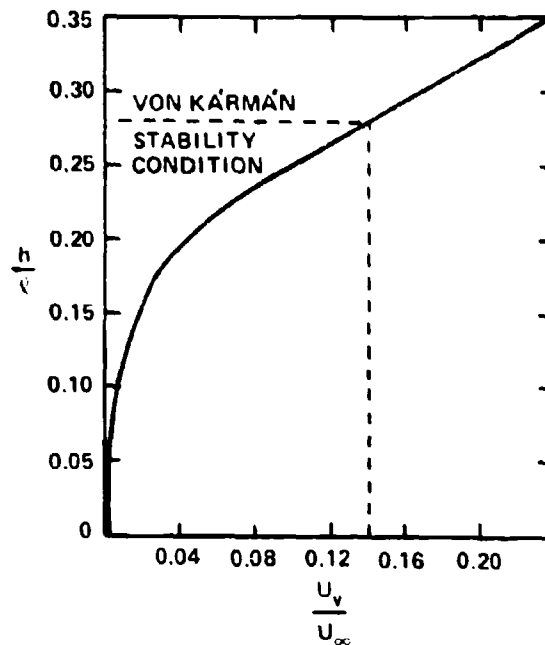


Figure 5.14 - Vortex Spacing Ratio as a Function of Vortex Velocity for the Kronauer Minimum-Drag Requirement

the streamwise vortex spacing  $\lambda$  for a variety of vortex wakes\* Bearman was, thus, able to determine the transverse spacing  $h$ . Then he defined a Strouhal number analogous to Roshko's,<sup>38</sup> which is

$$S^{**} = \frac{f_s h}{U_s}$$

For values of  $U_s/U_\infty$  between 1.1 and 1.47 (which represents a range of base pressure coefficients of from -0.21 to -1.1) this Strouhal number is a constant, equal to 0.18; see also Chapter 9. The significance of this number is that it applies to a wide variety of bluff-body cross-section shapes: circular, elliptical, ogival, prismatic, and flat-plate. Also, both Roshko's and Bearman's definition of Strouhal number are entirely compatible and the assertion that  $h/d_w$  is a constant is apparently borne out by available experiment.

\*These wakes were varied and controlled by bleeding fluid and by inserting splitter plates at the base of the cylinder; see also the end of Section 5.4.

### 5.3.2 Oscillatory Lift and Drag on Circular Cylinders

Our consideration, later in this chapter, of the acoustic radiation from vortex-shedding cylinders will require a knowledge of the oscillatory forces,  $F_x(t)$  and  $F_y(t)$  on the cylinder. As each vortex is shed from the cylinder it generates a lift force which changes direction as vortices are produced in each shear layer. This force may be written

$$F_y(t) = \tilde{F}_y e^{-i\omega_s t}$$

where  $\omega_s = 2\pi f_s$  is the shedding frequency. The drag fluctuation is generated as a result of oscillations in the base pressure coefficient. Since the base pressure responds to disturbances which are spatially symmetric about the wake axis, and since these disturbances are generated twice as each vortex pair is produced, the frequency of the drag fluctuations will be  $2f_s$ , and

$$F_x(t) = \tilde{F}_x e^{-i2\omega_s t}$$

The vortex shedding is essentially nonuniform along the axis of the cylinder for  $R_d > 150$ . Thus, our consideration of the fluctuating forces must be founded on a statistical basis. The pressure distribution on the cylinder we, therefore, write in a general form as

$$p(\theta, z, t) = \left[ p_L(\omega_s) \cos \theta e^{-i\omega_s t} + p_b(2\omega_s) \sin \theta e^{-i2\omega_s t} \right] \cdot e^{i[\phi(z, t)]} \quad (5.7)$$

Here  $\theta$  is measured from the y axis as shown in Figure 5.9. The expression shows that the circumferential variation of the pressure fluctuations which yield lift is maximum at  $\theta = 0$  deg and minimum at  $\theta = 90$  deg. The fluctuating base pressure is given by  $p_b$  because the pressure component at  $2\omega_s$  has a maximum amplitude there. The phase function  $e^{i[\phi(z, t)]}$  expresses the axial variation in vortex structure

which occurs for  $R_d > 150$ . We assume that both the fluctuating lift and drag have similar axial correlation characteristics. Although the pressure amplitude can be a deterministic function of location, the phase function has been observed to be a stochastic variable at most Reynolds numbers.

The total force on the cylinder is

$$\vec{F}(t) = (F_x(t), F_y(t)) = \int_0^{2\pi} \int_0^L p(\theta, z, t) \vec{n}(\theta) \frac{d}{2} dz \quad (5.8)$$

where  $\vec{n}(\theta) = (\sin \theta, \cos \theta)$  is the normal to the surface of the cylinder and  $L$  is its length. Substitution of Equation (5.7) into Equation (5.8) gives an expression for the dimensionless forces:

$$\frac{F_y(t)}{\frac{1}{2} \rho_o U_\infty^2 dL} = \frac{1}{2} \left( \frac{p_L(\omega_s)}{\frac{1}{2} \rho_o U_\infty^2} \right) \cdot \frac{1}{L} \int_0^L e^{i\phi(z,t)} e^{-i\omega_s t} dz \quad (5.9a)$$

and

$$\frac{F_x(t)}{\frac{1}{2} \rho_o U_\infty^2 dL} = \frac{1}{2} \left( \frac{p_b(2\omega_s)}{\frac{1}{2} \rho_o U_\infty^2} \right) \cdot \frac{1}{L} \int_0^L e^{i\phi(z,t)} e^{-2i\omega_s t} dz \quad (5.9b)$$

The time-mean-square oscillatory lift coefficient is defined as

$$\overline{C_L^2} = \left( \frac{1}{2} \rho_o U_\infty^2 dL \right)^{-2} \overline{F_y^2(t)} \quad (5.10a)$$

and the drag coefficient is

$$\overline{C_D^2} = \left( \frac{1}{2} \rho_o U_\infty^2 dL \right)^{-2} \overline{[F_x^2(t)]} \quad (5.10b)$$



where the bar denotes a time average. Looking ahead to an interpretation of experimental data, we note that if the unsteady forces are temporally harmonic, the mean-square is just  $(1/2) \bar{F}^2$ . This situation is expected at Reynolds numbers less than  $3 \times 10^5$  where the shedding frequency is well-defined. At higher values of  $R_d$  where the vortex-shedding covers a more distributed frequency range the mean-square must be taken in its strictest meaning. This discussion is pertinent because various investigators have measured the fluctuating lift by determining either peak values or temporal mean-square values. Later, the measurements will be compared.

Another difficulty in interpreting lift coefficient measurements lies in the unknown function  $\phi(z,t)$ . As Hama's<sup>31</sup> photographs have shown, the vortices are two-dimensional, i.e.,  $\phi(z,t) = 0$ , only for  $R_d < 140$ . At greater values of  $R_d$ , three-dimensionality occurs. Thus, if we let  $\ell_z$  describe a typical axial length scale over which  $\phi(z,t)$  is constant, it is important that the shedding cylinder on which the lift is measured have a length less than  $\ell_z$ . Of course, if the lift is deduced from a pressure distribution, as in the case of Gerrard,<sup>32</sup> the lift coefficient is closely related to a pressure coefficient,  $p(1/2\rho U_\infty^2)^{-1}$ , as is seen by comparing Equations (5.9) and (5.10).

Values of the root-mean-square oscillatory lift coefficients measured by various investigators are summarized by the points and solid lines in Figure 5.15.

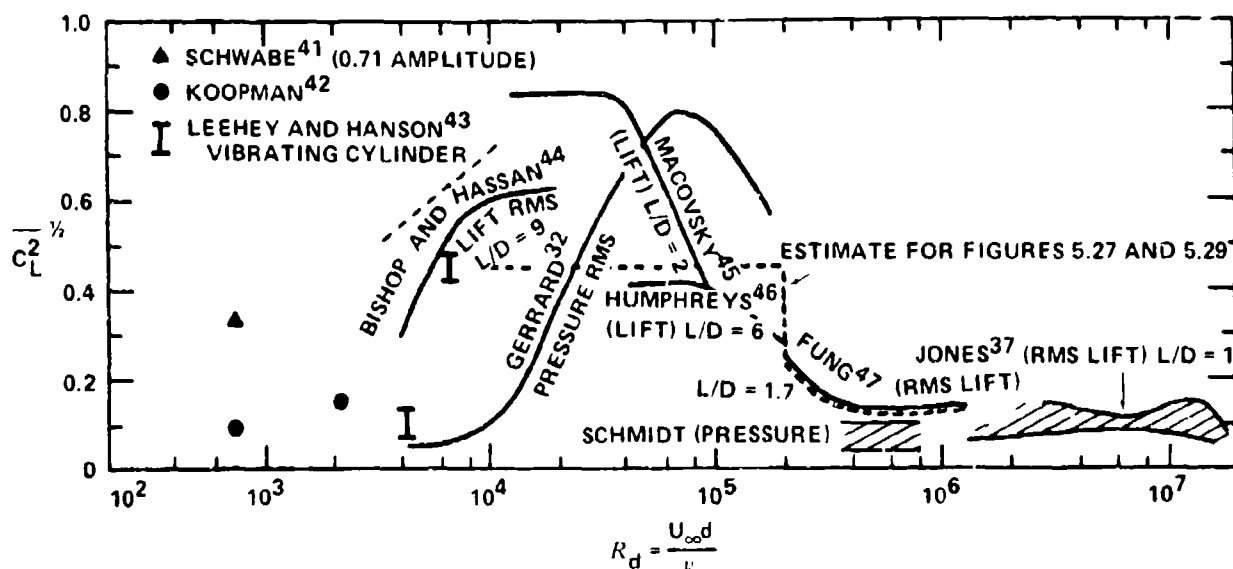


Figure 5.15 - Summary of Measured Values of Root-Mean-Square Oscillatory Lift Coefficients on Circular Cylinders

(Representative values, which will be used later are shown as dotted lines.) Of the group, only Gerrard,<sup>32</sup> McGregor,<sup>48</sup> Koopmann,<sup>42</sup> and Schmidt<sup>49</sup> determined fluctuating lift by the integration of a measured fluctuating pressure distribution. Their measurements confirm our representation for the circumferential variation of pressure used in Equation (5.7). McGregor obtained the value of 0.42 for the lift coefficient in the range of  $R_d$  from  $4 \times 10^4$  to  $1.2 \times 10^5$  and this agrees well with Humphrey's value. The values shown here attributed to Humphrey<sup>46</sup> and Macovsky<sup>45</sup> have been deduced from their measured values of lift amplitude by assuming periodic lift fluctuations. Their published oscillographs (time histories) of lift fluctuations show that this is a reasonably accurate interpretation of the data. In Humphrey's case there was some irregular modulation, of long time scale, of an otherwise periodic lift signal, thus, his quoted values of average amplitude were used to estimate a root-mean-square lift. Because  $R_d = 2 \times 10^5$  marks the upper limit of observed periodicity, this approximation could not be applied to Humphrey's data in the range  $2 \times 10^5$  to  $6 \times 10^5$ . Maximum values of lift coefficient decreased in this range of Reynolds number from 0.8 to 0.35 roughly matching the peak values obtained by Fung. Root-mean-square values reported by Fung<sup>47</sup> and by Jones<sup>37</sup> appear to agree closely. Schmidt's<sup>49</sup> measurements were obtained in the same facility as Fung's, but he noted that the lift coefficients were reduced if the cylinder was well-polished. Bishop and Hassan<sup>44</sup> have provided direct measurements of root-mean-square lift while the coefficients attributed to Macovsky were determined from his quoted maximum lift levels. The single point attributed to Koopman is the lowest value of Reynolds number for which oscillatory lift data are available; it was obtained by integrating a pressure distribution. Finally, the measurements of Leehey and Hanson<sup>43</sup> were obtained by an indirect method.\* The vertical bars denote the upper and lower limits of lift coefficient that were reported. Unfortunately, a

---

\*These measurements were accomplished during an experiment involving wind-induced cylinder vibration and Aeolian tones. They first determined the level of wind-induced vibration at a particular vortex-shedding frequency. They then excited the cylinder electromagnetically in still air at the same frequency that it was wind-excited. This was accomplished by passing an alternating current through the steel wire around which had been placed a system of permanent magnets. By measuring the current through the wire and magnetic field strength they determined the force generated on the wire and this was proportional to the cylinder vibration level which they measured at the same time. From this they deduced the aerodynamic lift on the wire at any given point in the experiment.

certain level of cylinder vibration accompanied the measurement, and this is known to influence the lift (see Section 4 of this chapter).

In spite of the wide range of reported lift coefficients shown in Figure 5.15 there appears to be a general trend toward maximum values in a range of Reynolds numbers near  $4 \times 10^4$ . At either extreme of this region the coefficients appear to be somewhat smaller in value. The three most plausible reasons for disagreement among investigators are:

1. Environmental influences, such as upstream turbulence and cylinder motion can modify the lift (see Section 5.4 of this chapter).
2. Spatial averaging of local pressure along the axis of the cylinder can reduce the apparent lift as suggested by Equation (5.9).
3. These measurements, being dynamical in nature, are subject to a degree of experimental inaccuracy. Scatter in individually-reported data is for example,  $\pm 12$  percent in the case of Bishop and Hassan,<sup>\*</sup> 30 percent for the pressures reported by Gerrard, and 25 percent for Macovsky's measurements. The range of values shown in Figure 5.15 is not too far out of line with the scatter.

Measured fluctuating drag coefficients are less numerous than lift coefficients. Figure 5.16 shows measurements of Fung,<sup>47</sup> Schmidt,<sup>49</sup> van Nunen,<sup>50</sup> McGregor,<sup>48</sup> and Gerrard<sup>32</sup> which are substantially in agreement. The maximum appears to be at Reynolds numbers near  $4 \times 10^4$ . The drag fluctuations are approximately one-tenth of the lift coefficients.

### 5.3.3 Representations of Axial Phase-Uniformity: Correlation Lengths

Even though the vortex-induced fluctuating pressures may be locally of the same amplitude along the cylinder axis, the phase of the pressure may vary stochastically as  $\phi(z,t)$  in Equation (5.7). Various attempts have been made to quantify the axial phase variations. Most of these measurements have been made using flow visualization. Phillips,<sup>9</sup> Macovsky,<sup>45</sup> and Hama<sup>31</sup> examined the patterns of dye injected into the wake of cylinders, and Macovsky<sup>45</sup> also observed the three-dimensional patterns of wool tufts attached to cylinders. Roshko<sup>13</sup> estimated the length scales of the vortices by observing the behaviors of Lissajous patterns between two hot-wire anemometer probes in a wake as the probes were moved away from

---

\*Errors are the limits of the spread in observed values expressed as percentages of the centroid of the population of data.

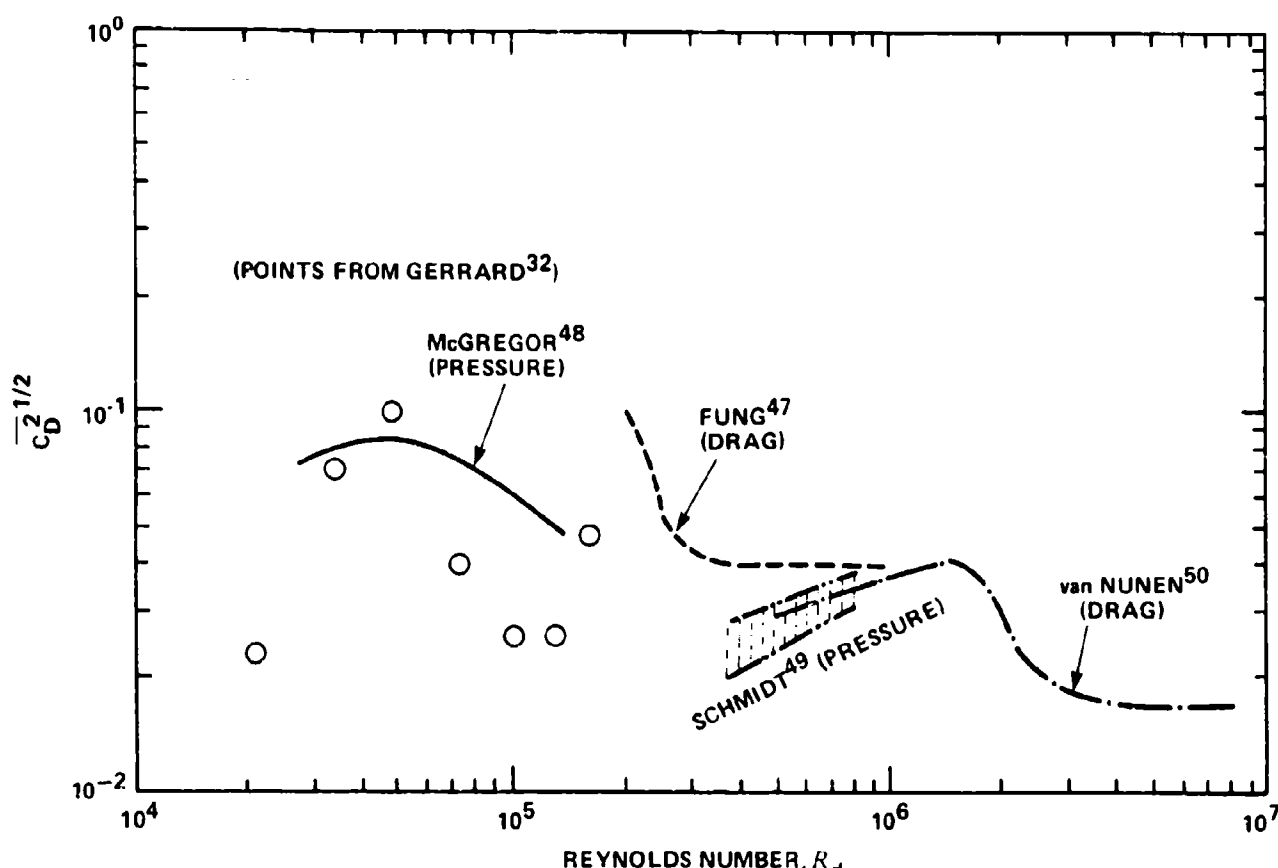


Figure 5.16 - Summary of Fluctuating Drag Coefficients on Circular Cylinders

one another along the axis of the cylinder. Gerrard<sup>51</sup> does not cite the details of any measurements, but he states that the correlation length is on the order of three diameters for  $R_d$  less than  $2 \times 10^5$ . Correlation measurements, in the strict sense, have been made between axially-separated sensors by Prendergast<sup>52</sup> (pressure fluctuations), ElBaroudi<sup>53</sup> (velocity fluctuations near the separation point), Ballou<sup>19</sup> (velocity fluctuations in the wake), Leehey and Hanson<sup>43</sup> (velocity fluctuations in the wake), and Schmidt<sup>49</sup> (local lift fluctuations).

The two-point correlation yields the form of the function  $\phi(z,t)$  that is employed in Equation (5.7). Considering that the pressure is measured at two locations which are separated axially, the time-averaged product of the pressures is written

$$\overline{p(\theta, z_1, t) p(\theta, z_2, t)} = \frac{1}{T} \int_0^T p(\theta, z_1, t) p(\theta, z_2, t) dt$$

This is just the correlation which can be expressed in an approximate form in terms of Equation (5.7) as

$$\begin{aligned} \overline{p(\theta, z_1, t) p(\theta, z_2, t)} &= \frac{1}{2} [p_L(\omega_s) \sin^2 \theta + p_b^2(2\omega_s) \cos^2 \theta] \\ &\times \operatorname{Re} \left\{ \overline{\exp i[\phi_1(z_1) - \phi_2(z_2)]} \right\} \end{aligned} \quad (5.11)$$

The averaging time  $T$  must be longer than both the characteristic shedding period  $2\pi/\omega_s$  and the period of oscillation of the phase function  $\phi(z, t)$ . Also, for Equation (5.11) to be valid, the period of variation of the phase function must also be longer than  $2\pi/\omega_s$ . The bars over the phase functions denote the replacement of the time average of the exponential by an exponential of the average phase difference. In effect if  $\omega_s \gg \partial\phi/\partial t$  this assumption could be considered to be equivalent to the use of a conditional average of time larger than  $2\pi/\omega_s$ , yet less than  $2\pi (\partial\phi/\partial t)^{-1}$ . The function  $\phi(x, t)$  could also be assumed to be of the form

$$\phi(z, t) = +kz + i\alpha z \quad (5.12)$$

This gives rise to a phase of the form  $i(\omega_s t - kz) - \alpha z$  which describes a travelling wave of speed  $\omega_s/k$ . Actually, the vortex filaments have been observed to "peel off" the cylinder, propagating from one end to the other of the cylinder so that once formed the axis of the vortex is not quite parallel to the axis of the cylinder. With a phase of Equation (5.12) the time-averaged phase function is simply

$$\operatorname{Re} \left\{ \overline{\exp i[\phi_1(z_1) - \phi_2(z_2)]} \right\} = e^{-\alpha(z_1 - z_2)} e^{+ik(z_1 - z_2)} \quad (5.13)$$

which is a decaying harmonic function of the argument  $\alpha(z_1 - z_2)$ .

The correlation coefficient is defined as

$$R_{pp}(z_1, z_2) = \frac{\overline{p(\theta, z_1, t) p(\theta, z_2, t)}}{\left[ \overline{p^2(\theta, z_1, t)} \overline{p^2(\theta, z_2, t)} \right]^{1/2}} \quad (5.14)$$

where the  $\overline{p^2(\theta, z, t)}$  are the mean-square pressures measured at any location along the axis. From Equation (5.7), we have

$$\overline{p^2(\theta, z_1)} = \frac{1}{2} [p_L^2(\omega_s) \sin^2 \theta + p_b^2(2\omega_s) \cos^2 \theta] \quad (5.15)$$

Combining Equations (5.11), (5.13), (5.14), and (5.15) gives

$$R_{pp}(z_1, z_2) = e^{-\alpha |z_1 - z_2|} \cos k(z_1 - z_2) \quad (5.16)$$

This form of the correlation coefficient is typical of those which are often measured in fluid mechanics. It is also an analytical form which is frequently used in theoretical modeling. The correlation length we will define as Equation (3.82a)

$$2\Lambda_3 = \int_{-\infty}^{\infty} R_{pp}(\xi) d\xi \quad (5.17)$$

so that

$$2\Lambda_3 = \frac{2\alpha}{k^2 + \alpha^2} \quad (5.18)$$

therefore, if  $k \ll \alpha$ ,  $\Lambda_3 = \alpha^{-1}$ .

The above analysis is pertinent to the axial correlations of wake velocity as well as to lift correlations. Figure 5.17 shows examples of correlation functions

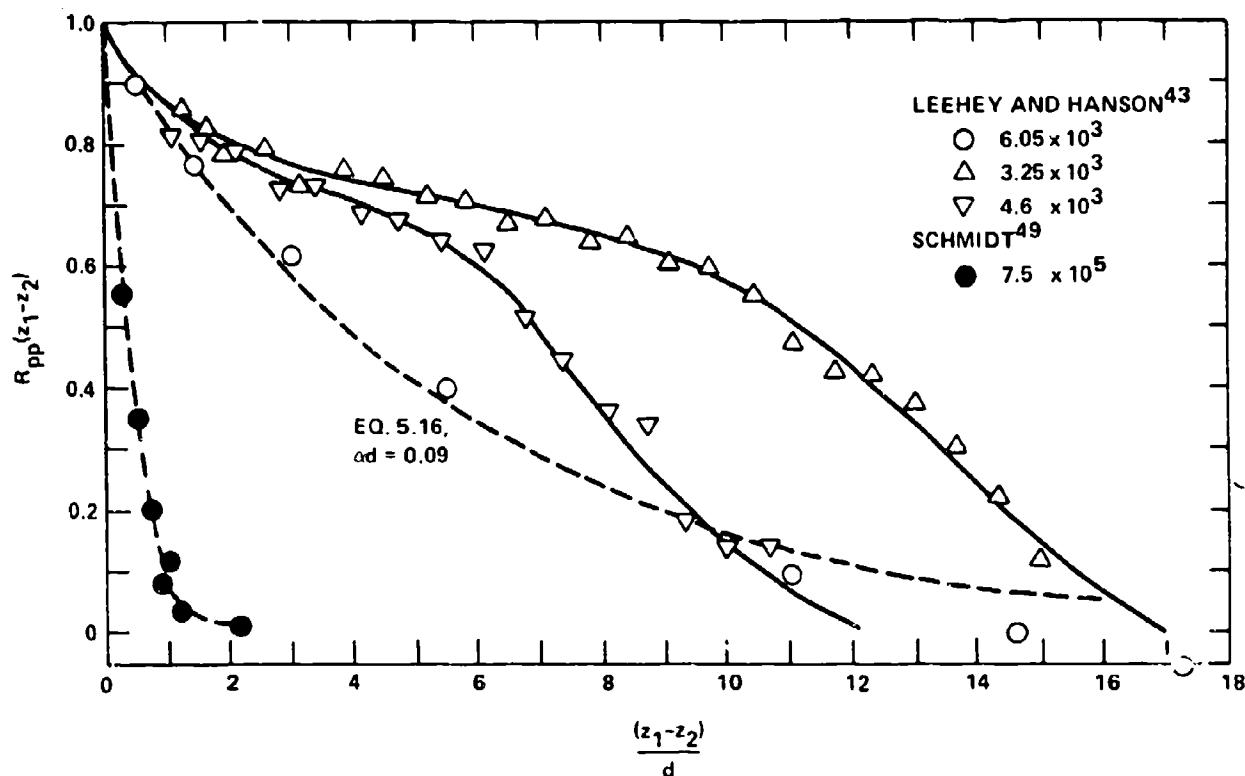


Figure 5.17 - Axial Covariance Functions for Fluctuating Lift on Circular Cylinders

at various Reynolds numbers from  $3.3 \times 10^3$  to  $7.5 \times 10^5$ . Note that at the lower end of the range of  $R_d$  the function is unlike the representation given in Equation (5.16), but at the upper end the equation matches the measured functions. Figure 5.18 shows values of  $2\Lambda_3/d$  which have been reported by the various investigators. Perhaps the most striking aspect of Figure 5.18 is that it is difficult to draw a general conclusion about the correlation length, although for  $R_d < 140$  all investigators are unanimous in reporting large correlation lengths. Hama's photographs show that vortices are correlated along the entire length of the cylinder when  $R_d = 117$ , i.e.,  $2\Lambda_3/d \approx 96$ . With the exception of the correlation lengths measured by Leehey and Hanson, most investigators cite  $\Lambda_3 \approx d$  to  $6d$  for  $R_d < 2 \times 10^5$ . It

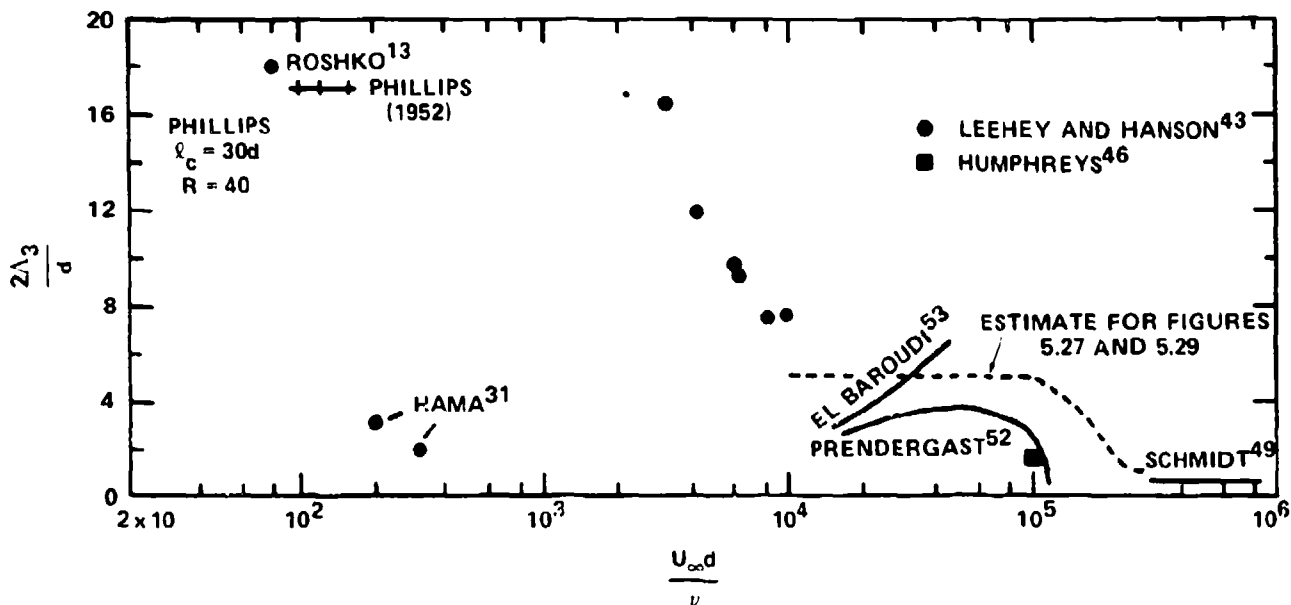


Figure 5.18 - Summary of Measured Values of Lift Correlation Lengths on Circular Cylinders

is tempting to explain the larger  $\Delta_3$  of Leehey and Hanson as being caused by cylinder vibration, however, they suggest that the uniform decrease of  $\Delta_3$  with increasing  $R_d$  is evidence to the contrary.

#### 5.4 ENVIRONMENTAL INFLUENCES ON VORTEX SHEDDING

As suggested in the last section, measured values of lift fluctuations can be influenced by cylinder motion, surface roughness, and upstream turbulence. There are few self-consistent investigations which quantify these effects. Gerrard<sup>24</sup> has made a systematic investigation of the effects of upstream turbulence in the range of  $R_d$  from  $8 \times 10^2$  to  $4 \times 10^4$ . He measured the intensity of the velocity fluctuations in the cylinder boundary layer just downstream of separation, at  $x = 0$ ; see Figure 5.10. This velocity increases with  $R_d$  in a fashion similar to the fluctuating lift coefficient. Figure 5.19 shows this behavior for two levels of upstream turbulence, 0.02 and 1 percent of the free-stream velocity. There is a consistent increase of a factor of 3 to 4 in the fluctuating velocity,  $u_s$ , for Reynolds numbers greater than  $10^3$  and this increase is caused by the increase in inflow turbulence. The similar variation of  $u_s$  and  $C_\ell$  with  $R_d$  suggested to Gerrard that



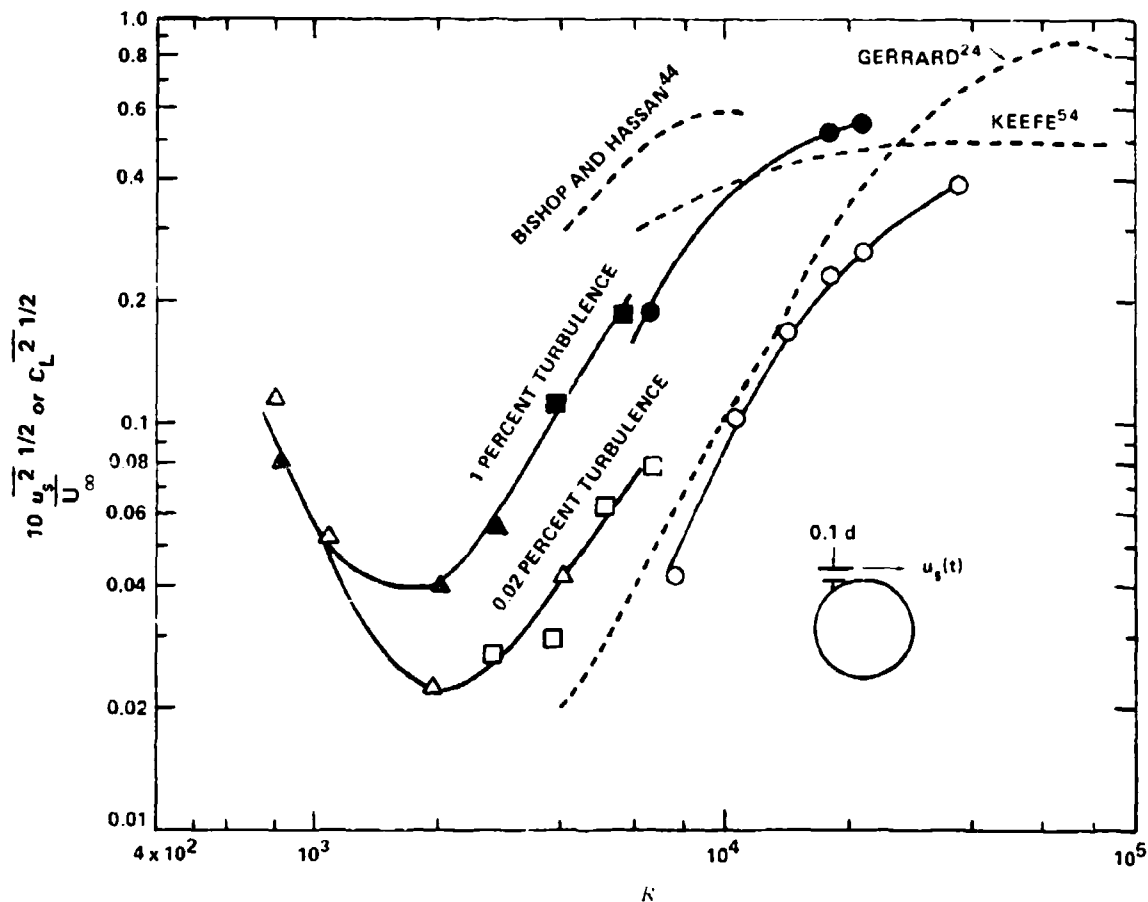


Figure 5.19 - Variation of Life Coefficient (dashed lines) and of "Shedding Velocity" (solid lines), with Upstream Turbulence Intensity (Gerrard<sup>24</sup>)

these two flow variables were related and that environmental influences on one variable reflected similar influences on the other. Furthermore, Gerrard<sup>55</sup> has argued that high free-stream turbulence slightly increases both the vortex strength and the vortex shedding frequency. He has also speculated that the variation in formation length for cylinders of different diameters measured by Bloor,<sup>14</sup> shown in Figure 5.8, is attributable to a higher level of incident turbulence for the smaller diameter cylinder. This may not be entirely correct, because the measurements by

Ballou,<sup>19</sup> also shown in Figure 5.8, were obtained with a free-stream turbulence level of 0.04 percent of the mean velocity.<sup>19,43</sup> This level of turbulence is comparable to or less than that encountered in Bloor's measurements. Gerrard<sup>55</sup> contends that an increase in lift of a factor of four, suggested by the increase in  $u_s$ , cannot be explained by the possible reduction in formation length and increase in vortex strength that he has speculated as due to incident turbulence. It would appear that the question of the cause of increased lift by upstream disturbances can only be fully answered by an experimental investigation in which all the pertinent dependent variables: lift, formation length, vortex strength (see also Reference 56), and shedding frequency are measured as functions of both Reynolds number and upstream turbulence. A formal connection between  $u_s$  and fluctuating lift should also be established.

As well as effects of incident free-stream turbulence, Gerrard<sup>24</sup> has determined that the streamwise velocity fluctuation at separation, which he called the shedding velocity  $u_s$ , can be increased by acoustic excitation. At a Reynolds number of  $6.9 \times 10^3$ , Gerrard found that sound with a root-mean-square velocity of 0.01 percent of the free-stream velocity could increase  $u_s$  by a factor of 2.5. The effect is frequency-dependent and this increase in  $u_s$  was observed at an excitation frequency equal to the transition wave frequency of secondary disturbances.<sup>14</sup>

Motion of the shedding cylinder, transverse to the direction of flow, has been observed by Jones<sup>37</sup> to increase the root-mean-square lift at high Reynolds numbers. Figure 5.20 shows one set of his results. Not only the lift amplitude, but also its phase relative to the cylinder displacement are important as will be discussed as a nonlinear interaction in Chapter 9. The effect is undoubtedly dependent upon Reynolds number. Some other isolated measurements of fluctuating lift coefficients have been published with observed values of cylinder displacement. Those data are also shown in Figure 5.20. An increase of the lift coefficient with the peak-to-peak displacement of the cylinder appears to be uniform. It is also more pronounced in the  $R_d$  range between  $2 \times 10^3$  and  $4.5 \times 10^4$ .\*

It is not possible at this time to quantitatively relate the increase in lift coefficient to cylinder vibration other than in a completely empirical sense. An experimental relationship between the rate of vorticity generation and transverse

---

\*Note that Koopmann<sup>42</sup> measured fluctuating pressure and that Leehey and Hanson<sup>43</sup> determined an increase fluctuating lift without a corresponding increase in  $\ell_c$ .

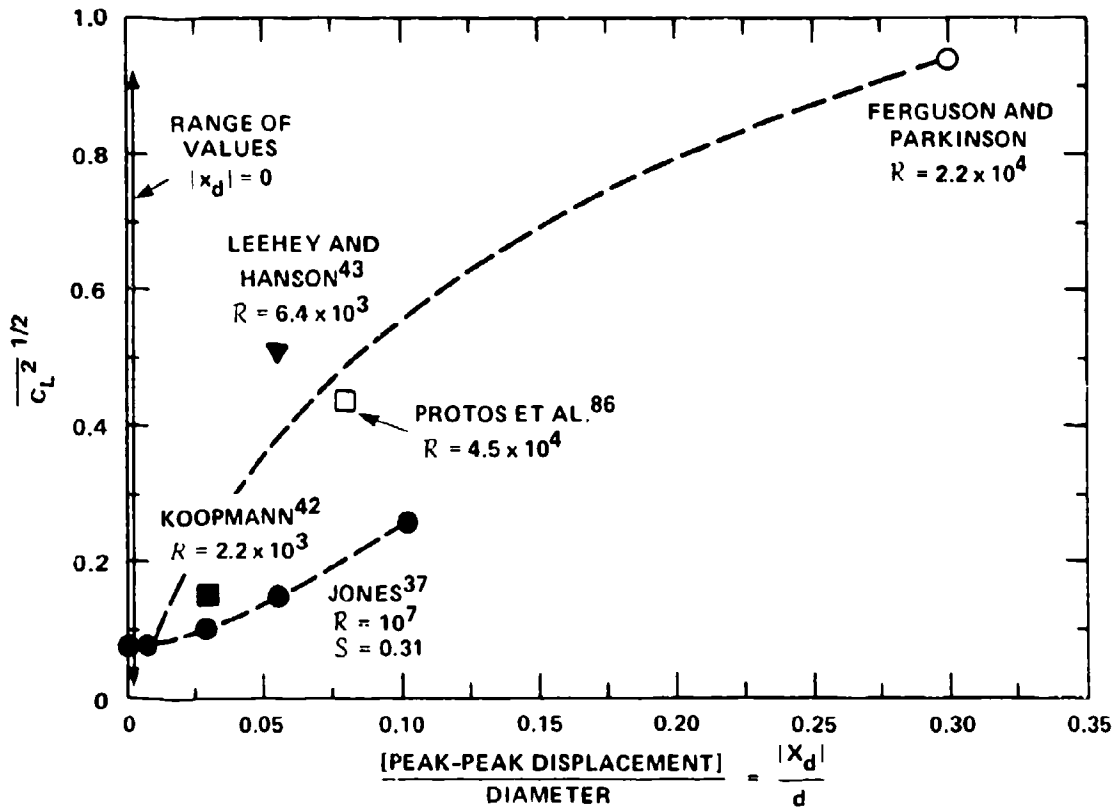


Figure 5.20 - Dependence of Root-Mean-Square Lift Coefficient on Cylinder Displacement

displacement has been shown by Griffin and Ramberg<sup>57</sup> at a Reynolds number of 144. Using a forced vibration frequency equal to the vortex-shedding frequency and an amplitude of motion equal to one-half the diameter they determined that the rate of vortex generation increased by a factor of 1.65 over the rate for no motion. This implies that the vortex strength is increased by transverse motion. Transverse motion also organizes the vortex shedding along the axis of the cylinder, shown visually by Koopmann<sup>58</sup> at  $R_d = 200$ , as well as changing the vortex spacing in the vortex street.<sup>57</sup> These aspects will be further discussed in Section 5.5. The effect of cylinder motion goes far beyond influencing the magnitude of oscillating lift. The entrainment of the wake disturbances by the motion of the cylinder brings about both a phase and amplitude relationship between the cylinder motion and the wake induced lift as will be discussed in Section 9.6.2.

Another influence on vortex-shedding can be effected by splitter plates. Figure 5.21, by Gerrard,<sup>55</sup> shows a diagram of a cylinder with a splitter plate and the variation of Strouhal number as the length of the splitter plate was changed. The splitter plate interferes with the cross-wake interaction of the shear layers. The reduction in Strouhal number for a plate length equal to the cylinder diameter implies that a spreading in the wake width occurs and that the drag coefficient

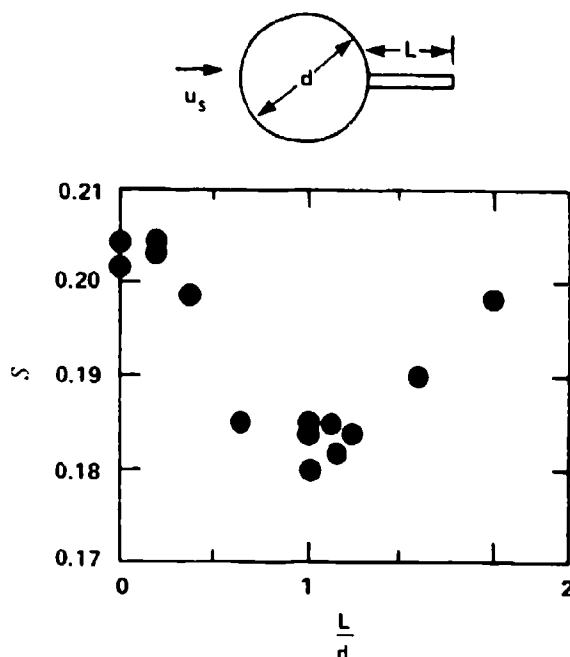


Figure 5.21 - Variation of  $S$  with Length of Splitter Plate;<sup>55</sup>  
 $d = 1 \text{ in.}, R_d = 2 \times 10^4$

increases; see Section 5.3.1. The results are essentially in agreement with those of Apelt, West and Szweczyk.<sup>59,60</sup> Because a point in the wake, one diameter downstream from the cylinder, coincides with a formation length of  $1.5d$ , as shown in Figure 5.8, the splitter plate interference is conjectured to have caused a downstream shift in formation. This downstream shift may also cause a reduction in the strengths of shed vortices. In earlier studies, Roshko<sup>38</sup> found similar effects of splitter plates on Strouhal numbers in the same range of Reynolds number, and in Reference 25 he found that a splitter plate, with  $L/d = 2.65$ , annihilated vortex shedding at  $R_d > 3 \times 10^6$ . The influence of splitter plates on vortex shedding from airfoils will be discussed in Section 9.3.

## 5.5 ESTIMATIONS OF WAKE-INDUCED FORCES IN TWO-DIMENSIONAL FLOW

A very simple, yet analytically powerful, representation of the vortex street as a two-dimensional array of line vortices which trail behind a two-dimensional bluff shedding body is illustrated in Figure 5.22. We will use these diagrams to illustrate the estimation of the oscillating forces as well as to discuss some stability characteristics of the wake. The modeling of the two-dimensional vortex street wake in this manner was originally proposed by von Karman and Rubach<sup>5</sup> and in its original form, the von Karman vortex street, is shown in Figure 5.22a. This consisted of two parallel and infinite rows of vortices which are separated a distance

Figure 5.22 - Vortex Street at Time  $t_0$  Showing the Vortex Spacing and the Control Volume Boundaries

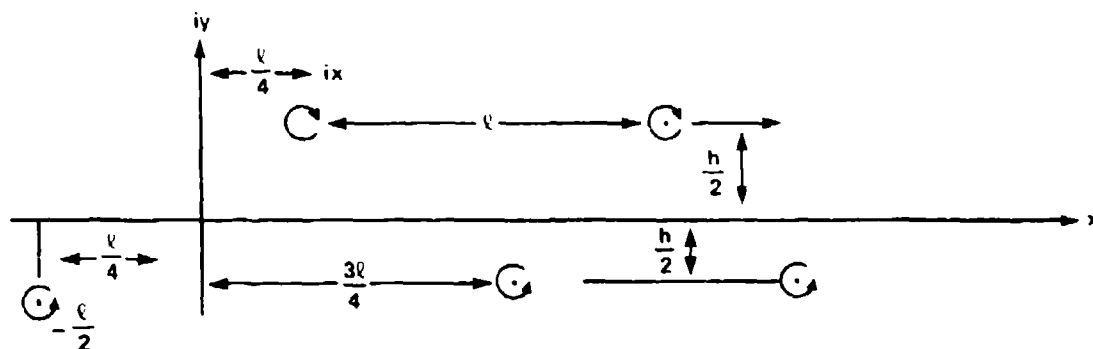


Figure 5.22a - Idealized Infinite Vortex Street of von Karman

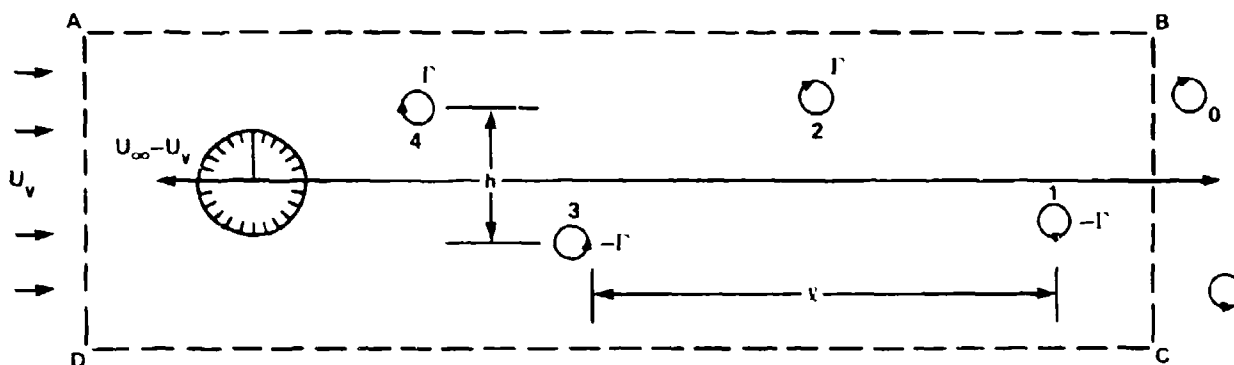


Figure 5.22b - Semi-Infinite Street Behind the Blunt Body, at Time  $t$ , Showing Geometric Parameters

Figure 5.22 (Continued)

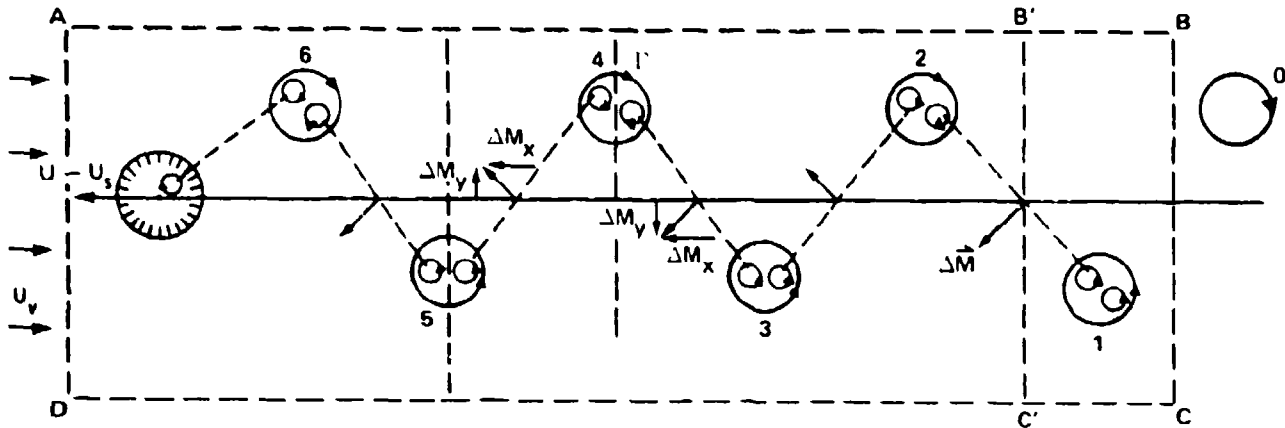


Figure 5.22c - Semi-Infinite Street Behind the Blunt Body, at Time  $t_0 + Dt/2$ , Showing Vector Decompositions of Moments of Circulation

h apart. In each row, the vortices of like sign are separated a distance  $\ell$  apart and those in the upper and lower rows have opposite sign with the vortices alternating in position. In analytically modeling the two-dimensional wake-induced forces, the von Karman vortex street is truncated as a pair of semi-infinite sheets behind the shedding body as shown in Figure 5.22b. In the present context it is assumed that all the time-varying momentum is transferred to the cylinder with no viscous losses.

Complex variables will be used to analyze this two-dimensional problem. The method applied here is essentially that of Sallet<sup>61-62</sup> which is an extension of von Karman's analysis,<sup>5,63</sup> although Ruedy<sup>64</sup> and Chen<sup>65</sup> have presented similar analyses. The complex velocity potential for the finite vortex street, shown in Figure 5.22a,\* is

$$\psi(z) = i \frac{\Gamma}{2\pi} \ln \left[ \frac{\sin \left( \frac{\pi}{\ell} (z - z_0) \right)}{\sin \left( \frac{\pi}{\ell} (z + z_0) \right)} \right] \quad (5.19)$$

\*The analysis of the infinite vortex street is classical, treatments in such books as written by Milne-Thompson,<sup>63</sup> Lamb,<sup>66</sup> and Wille<sup>67</sup> provide excellent reviews of some of the physical aspects of the vortex street stability and configuration.

where

$$z_0 = \frac{\ell}{4} + i \frac{h}{2}$$

and

$$z = x + iy$$

It is assumed that this potential will correctly yield the vortex-induced velocity for the semi-infinite street depicted in Figure 5.22b. The complex velocity of the street is

$$\begin{aligned} \frac{d\Psi(z)}{dz} &= u - iv \\ &= i \frac{\Gamma}{2\ell} \left[ \cot \frac{\pi}{\ell} (z - z_0) - \cot \frac{\pi}{\ell} (z + z_0) \right] \end{aligned} \quad (5.20)$$

The first term in the brackets is the field velocity which is induced by the upper vortex row and the second term is the velocity induced by the lower row at  $y = h/2$ . The velocity induced on vortices in the lower row, i.e., at  $y = x - ih/2$ , by the upper vortex street is

$$U_v(x) = \frac{\Gamma i}{2\ell} \cot \frac{\pi}{\ell} \left( x - \frac{\ell}{4} - ih \right)$$

or at the locations of the centers of the vortices,

$$U_v \left( \frac{n\ell}{2} - \frac{ih}{2} \right) = \frac{\Gamma i}{2\ell} \cot \left( \frac{n\pi}{2} - \frac{ih\pi}{\ell} \right) \quad n = 1, 3, \dots$$

or

$$U_v = \frac{-\Gamma}{2\ell} \tanh \left( \frac{h\pi}{\ell} \right) \quad (5.21)$$

for all vortices in this row. The row is, therefore, seen to translate with this velocity to the left. Similarly, the lower row induces a translation of the same velocity in the upper row so that the whole vortex system translates along the  $x$  axis to the left at  $U_v$ . In a typical physical situation, the vortex street which formed behind a cylinder moving at a velocity  $U_\infty$  is convected at the speed  $U_\infty - U_v$  relative to the fixed frame. Thus, Figure 5.22b shows a control volume ABCD that is fixed with the moving vortices so that a mean flow  $U_v$  enters the control volume on the left. The control volume encloses the shedding body and an arbitrarily large even number of vortices; here we use four vortices. As time increases from  $t_0$  the body moves to the left within the control volume and vortices are produced in its wake. In one complete shedding cycle, a pair of vortices is formed in a time  $\Delta t$ . Figure 5.22c shows the system one-half cycle later after the formation of vortex 5.

The stability of the row, as considered by von Karman and Rubach,<sup>5</sup> and quoted in many texts (e.g., References 63 and 66), determines that there is a fixed relationship between  $h$  and  $\ell$  which is

$$h = 0.281 \ell \quad (5.22)$$

In a later development, however, Birkhoff<sup>68</sup> points out that as the vortex street moves downstream, the momentum of the system, which is proportional to the moment of vorticity  $\Gamma h$ , must remain constant. This requires that  $h$  increase as the circulation  $\Gamma$  of each vortex diminishes under the action of viscosity in the far wake and gives rise to the spreading of the wake which can be observed in Homann's photographs, Figure 5.1, and which has been measured, e.g., Frimberger<sup>69</sup> and Schaefer and Eskinazi.<sup>23</sup> Furthermore, the pair spacing  $\ell$  tends to remain constant so that von Karman's relationship is only approximate. Also Bearman's<sup>39</sup> results, and Figure 5.14 show that the spacing ratio is dependent upon the vortex velocity. However, it is still often analytically convenient to use von Karman's constant because it represents a constant value which roughly agrees with measurements.

A momentum balance for the control volume<sup>62,63</sup> will account for the forces per unit length on the cylinder which are induced by the formation of vortices, i.e., in vector form



$$\bar{F} = \frac{\partial \bar{M}}{\partial t} + \bar{M}_f - \oint p d\bar{c} \quad (5.23)$$

where  $\bar{M}_f$  = net rate of momentum flow from the control volume  
 $p$  = the pressure on the control surface (and the integral is around the circuit ABCD in Figure 5.22)  
 $d\bar{M}/dt$  = the rate of increase of momentum by the formation of vortices in the control volume  
 $\bar{F}$  = the complex force per unit length on the cylinder

The pressure on the control surface is, by Bernoulli's equation, given by

$$p - \frac{1}{2} \rho_o [u^2 + v^2] - \frac{\partial \phi}{\partial t} = C_n \quad (5.24)$$

where  $C_n$  is everywhere a constant and  $\phi$  is the flow potential which is the real part of the function  $\Psi$ . The momentum flux per unit cylinder length that occurs across each surface is, in complex notation,

$$\begin{aligned} \bar{M}_{AB} &= \rho_o \int_A^B u v dx + i \rho_o \int_A^B v^2 dx \\ \bar{M}_{BC} &= -\rho_o \int_B^C u^2 dy - i \rho_o \int_B^C u v dy \\ \bar{M}_{CD} &= \rho_o \int_C^D u v dx + i \rho_o \int_C^D v^2 dx \\ \bar{M}_{DA} &= -\rho_o \int_D^A u^2 dy - i \rho_o \int_D^A u v dy \end{aligned} \quad (5.25)$$

Using the coordinate variable  $z = x + iy$ , substitution of Equations (5.24) and (5.25) into Equation (5.23) gives the two-dimensional force per unit length, now written as a complex variable, as

$$F_x - iF_y = +i \frac{\rho_o}{2} \oint \left( \frac{d\Psi}{dz} \right)^2 dz + i\rho_o \frac{\partial}{\partial t} \oint \phi dz^* + \frac{\partial}{\partial t} (M_x - iM_y) \quad (5.26)$$

where  $z^* = x - iy$ . Milne-Thompson<sup>63</sup> shows that  $\partial\Psi/\partial z = 0$  on surfaces AB, CD, and AD since they are selected far enough from the vortex-shedding body. Then

$$\oint \left( \frac{\partial\Psi}{\partial z} \right)^2 dz = \int_{x_o - i\infty}^{x_o + i\infty} \left( \frac{d\Psi}{dz} \right)^2 dz = \frac{\Gamma^2}{\pi\ell} \left[ 1 + \left( \frac{\pi}{2} - i \frac{\pi h}{\ell} \right) \tanh \frac{\pi h}{\ell} \right] \quad (5.27a)$$

for the line BC lying between vortices 0 and 1 as shown in Figure 5.22b. If BC (or  $x_o$ ) were to lie between vortices 1 and 2, for example on B'C', we would find that

$$\oint \left( \frac{\partial\Psi}{\partial z} \right)^2 dz = \frac{\Gamma^2}{\pi\ell} \left[ 1 - \left( \frac{\pi}{2} + i \frac{\pi h}{\ell} \right) \tanh \frac{\pi h}{\ell} \right] \quad (5.27b)$$

This dependence of the integral on the location of the control surface will be further discussed shortly.

The rate of momentum increase to the control volume can be examined by reference to Figure 5.22c. Following Sallet's<sup>61,62</sup> development, we have decomposed individual vortices into two components, each with circulation  $\Gamma/2$ . The moment-arms of these decomposed vortices are illustrated by the dotted lines on the figure. The incremental momentum of each vortex pair generated in time intervals  $\Delta t$ , e.g., positions 2 and 3, is given by<sup>63</sup>

$$\Delta(M_x + iM_y) = \frac{-\rho_o \Gamma}{2} r_v \left[ \frac{h}{r_v} - i \frac{\ell}{2r_v} \right] \quad (5.28a)$$

where  $r_v$  (the distance between the vortices) =  $(1/2) (\ell^2 + 4h^2)^{1/2}$ . The momentum of the pair at positions 2 and 1 is<sup>63</sup>

$$\Delta(M_x + iM_y) = \frac{-\rho_o \Gamma}{2} r_v \left[ \frac{h}{r_v} + i \frac{\ell}{2r_v} \right] \quad (5.28b)$$

Originally, at  $t = t_o$ , as shown in Figure 5.22b, the control volume contained an even number of vortices. Now, the addition of pairs of vortices, into the control volume occurs at time intervals  $\Delta t$  where

$$\Delta t = \frac{\ell}{(U_\infty - U_s)}$$

is one-half the shedding period. In the instance between Figures 5.22b and 5.22c, vortex 5 was added so that the total circulation was decreased by an amount  $-\Gamma$ .

Using Equation (5.26) to consider the lift component of the forces  $F_y$ , we obtain

$$F_y = \frac{+\rho_o \Gamma^2}{4\ell} \tanh \frac{\pi h}{\ell} + \frac{\partial M_y}{\partial t}$$

since  $\partial\phi/\partial t = 0$  on surfaces AB and CD as long as they are far from the wake, for BC lying midway between vortices 1 and 2. In the time interval  $\Delta t/2$  leading to the creation of vortex 5, the incremental change in momentum is one-half that of a complete vortex pair or

$$\Delta M_y = \frac{+\rho_o \Gamma \ell}{8}$$

so that, for the time interval  $\Delta t/2$

$$\frac{\partial M_y}{\partial t} \approx \frac{\Delta M_y}{\Delta t} = \frac{+\rho_o \Gamma}{4} (U_\infty - U_v)$$

and, therefore,

$$F_y = \frac{+\rho_o \Gamma^2}{4\ell} \tanh \frac{\pi h}{\ell} + \frac{\rho_o \Gamma}{4} (U_\infty - U_v) \quad (5.29a)$$

Alternatively, if the control volume were to be drawn with B'C' between vortices 1 and 2 then the creation of a vortex 6 would increase the momentum by  $\Delta M_y = -\rho_o \Gamma \ell / 8$ , so that now

$$\frac{\partial M_y}{\partial t} \approx \frac{\Delta M_y}{\Delta t} = -\frac{\rho_o \Gamma}{4} (U_\infty - U_v)$$

Then, by using Equations (5.26) and (5.27b), we have

$$F_y = -\frac{\rho_o \Gamma^2}{4\ell} \tanh \frac{\pi h}{\ell} - \frac{\rho_o \Gamma}{4} (U_\infty - U_v) \quad (5.29b)$$

Equations (5.29a) and (5.29b) represent the extremes of lift forces  $F_y$  which occur at the time intervals  $\Delta t/2$  during the formation of vortices so that the amplitude is just the magnitude of one of these extremes. Using Equation (5.21) we obtain the amplitude of the fluctuating force per unit length in the form

$$|F_y| = \frac{\rho_o \Gamma}{4} (U_\infty - 3U_v) \quad (5.30)$$

The rate of momentum increase  $M_x$  is not temporally oscillatory according to this theory so that, from Equation (5.28),

$$\frac{\partial M_x}{\partial t} \approx \frac{-\rho_o \Gamma h}{2} \left[ \frac{U_\infty - U_v}{\ell} \right] \quad (5.31)$$

Combining Equations (5.26), (5.27), and (5.31) we obtain the magnitude of the average drag force per unit length as

$$\overline{F}_x = + \rho_o \Gamma \frac{h}{\ell} (U_\infty - 2U_v) + \rho_o \frac{\Gamma^2}{2\pi\ell} \quad (5.32)$$

Amplitudes of lift and drag coefficients, defined by Equation (5.10), can now be expressed as

$$C_L = \frac{\Gamma}{2U_\infty d} \left[ 1 - \frac{3U_v}{U_\infty} \right] \quad (5.33)$$

$$\overline{C}_D = \frac{2\Gamma}{U_\infty d} \frac{h}{\ell} \left( 1 - \frac{2U_v}{U_\infty} \right) + \frac{\Gamma}{\pi U_\infty d} \frac{\Gamma}{U_\infty \ell} \quad (5.34)$$

The dimensionless frequency of vortex shedding,  $f_s = 1/\Delta t$ , is written

$$S = \frac{f_s d}{U_\infty} = \frac{d}{\ell} \left( 1 - \frac{U_v}{U_\infty} \right) \quad (5.35)$$

Now, by substitution of Equations (5.21) and (5.35) into Equations (5.33) and (5.34), we obtain

$$C_L = \left( 1 - \frac{\ell}{d} \right) \left( 3 \frac{\ell}{d} - 2 \right) \frac{\ell}{d} \coth \left( \frac{\pi h}{\ell} \right) \quad (5.36)$$

$$\overline{C}_D = \frac{4\ell}{\pi d} \left( \frac{U_v}{U_\infty} \right)^2 \left[ \coth \frac{\pi h}{\ell} + \frac{\pi h}{\ell} \left( \frac{U_\infty}{U_v} - 2 \right) \right] \quad (5.37)$$

The parameter  $\ell/d$  has been deduced from measurements of  $U_\infty - U_v$  by a number of authors.\* One of the most classical and complete experimental surveys of wake

\*Equation (5.37) yields the relationships used in Section 5.3.1; von Karman's formula for  $\overline{C}_D$  is obtained by letting  $h/\ell = 0.281$ , or  $\coth \pi h/\ell = (2)^{1/2}$ .

structural parameters is that of Fage and Johanson.<sup>70,71</sup> Figure 5.23a shows the experimentally determined values of  $\ell/d$  with  $R_d$  as summarized by Chen.<sup>27</sup> These values of  $\ell/d$  as well as values of  $S$  in Figures 5.12 and 5.13, are used to calculate the root-mean-square lift coefficient as  $C_L(2)^{-1/2}$  using Equation (5.36) and assuming time-harmonic forces. Figure 5.23b shows the result using the wake properties in Table 5.1. An alternative calculation can be carried out by using Equation (5.33) and empirical values of  $l/U_\infty d$ . The calculated root-mean-square lift coefficients are of the correct order of magnitude, but they do not precisely agree with the high values of  $C_L^{21/2}$  that have been reported by Gerrard<sup>32</sup> and by Macovsky.<sup>45</sup> In assessing the validity of Equations (5.33) and (5.36), it is well to note that wake

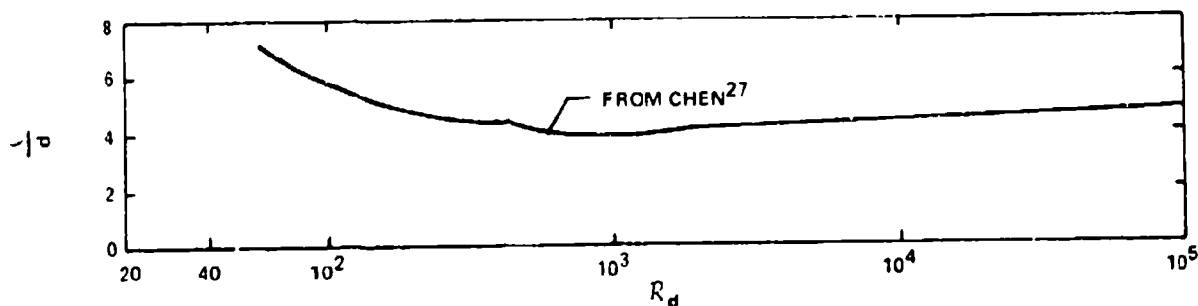


Figure 5.23a - Vortex Spacing

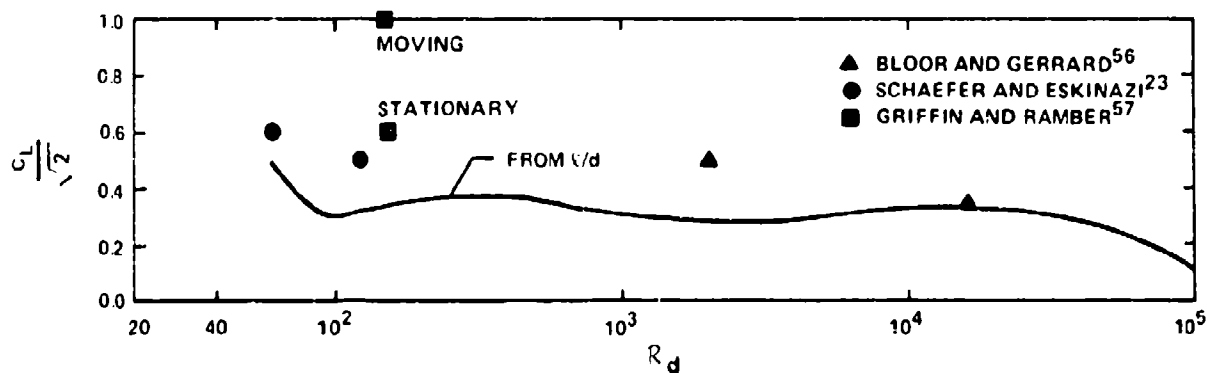


Figure 5.23b - Oscillating Lift

Figure 5.23 - Streamwise Vortex Spacing  $\ell$  and Root-Mean-Square Oscillating Lift Coefficients (Calculated)

TABLE 5.1  
VORTEX STRENGTHS AND VELOCITIES

$R_d$	$\frac{\Gamma}{U_\infty d}$	$\frac{U_v}{U_\infty}$	Author
60	2.44	0.1	Schaeffer and Eskinazi <sup>23</sup>
120	2	0.1	Schaeffer and Eskinazi <sup>23</sup>
144	2.5	0.1 est	Griffin and Ramberg <sup>56</sup>
2,000	1.7	0.14	Bloor and Gerrard <sup>55</sup>
16,000	1.46	0.18	Bloor and Gerrard <sup>55</sup>
144	4.2	0.1 est	Griffin and Ramberg <sup>56</sup> (Vibrating Cylinder)

properties  $\ell/d$ ,  $\Gamma/U_\infty d$ , and  $U_v/U_\infty$  vary with distance downstream of the cylinder. Furthermore, Equation (5.36) is sensitive to small uncertainties in  $\ell/d$ , which is numerically near 0.9. Also, Equation (5.33) is sensitive to values of  $\Gamma/U_\infty d$  which must be derived from velocity measurements; the wake using appropriate modeling of vortices of finite core radius. Thus, vortex strengths are not known to great precision. Finally, measured wake parameters and lift coefficients have not been determined together in an experiment.

The effect of transverse cylinder motion is shown in Figure 5.23 at  $R_d = 144$ . Griffin and Ramberg<sup>57</sup> measured greater vortex strengths with a peak-to-peak cylinder displacement of  $0.3d$  than with no motion. This increase in circulation, shown in Table 5.1, is responsible for the calculated increase in the lift coefficient. Other aspects of the interaction of the vortex-induced lift and motion of the shedding body will be treated in a special section of Chapter 7.

There has been another attempt at calculating the frequency and magnitude of fluctuating lift as reported by Gerrard.<sup>72</sup> This is a direct calculation of the potential field which results from the dynamical behavior of parallel shear layers. Each shear layer is modeled as a sheet of elemental vortices which are free to move under interaction with each other and with the mean flow past the cylinder. The motions of the shear layers generate a resultant set of large-sized vortices or concentrations of vorticity in the wake of the cylinder. The geometry of the vortex street and the dynamical characteristics of the calculated lift coefficients are in

reasonably good agreement with measurement. A similar model of the vortex street generation had been used earlier by Abernathy and Kronauer.<sup>73</sup> Their calculations disclosed that the shear-layer exhibited a "mode-like" behavior in which concentrations of vorticity would occur in groups of 6, 4, and 2. The individual circulation of each cloud, however, increased dramatically as the number of clouds decreased to two per wavelength. They calculated a vortex spacing ratio  $h/\ell = 0.28$  for this case. They also point out that the number of vortex clouds, or concentrations, times the spacing ratio  $h/\ell$  is roughly constant.

## 5.6 FORMULATION OF THE ACOUSTIC PROBLEM FOR COMPACT SURFACES

### 5.6.1 General Equations

For the purposes of this chapter, we consider an acoustically compact surface to be that which has its diameter much smaller than the observation distance from the body and the wavelength of sound. To broaden our base of discussion somewhat, we consider compact surfaces also take those of noncircular cross section which have acoustically-small thicknesses and chords. It will soon be apparent that this important class of surfaces has the special property that the radiated sound power bears a simple relationship to the statistics of alternating forces exerted by wakes on the bodies. This is why an exhaustive treatment of the oscillating loadings has been given in the previous sections.

As a practical matter, we start with the integral relationship for the radiated pressure that is due to Curle,<sup>74</sup> and that was derived in Chapter 2. There we found the linear-acoustic radiated pressure disturbance,  $p_a(\bar{x}, t)$  at a point  $\bar{x}$  is (using Equation (2.73) but disregarding the viscous stress  $\tau'_{ij}$ )

$$\begin{aligned}
 p_a(\bar{x}, t) = & \frac{1}{4\pi} \frac{\partial^2}{\partial x_i \partial x_j} \int_V \frac{T'_{ij}(\bar{y}, t - \frac{r}{c_o})}{r} dV(\bar{y}) \\
 & - \frac{1}{4\pi} \int_S \frac{1}{r} \frac{\partial}{\partial t} [\rho U_n] dS(\bar{y}) \\
 & + \frac{1}{4\pi} \frac{\partial}{\partial x_i} \int_S \frac{n_j}{r} [\rho u_i u_j + p_{ij}] dS(\bar{y})
 \end{aligned} \tag{5.38}$$



The terms of this equation are illustrated\* in Figure 5.24a. The Reynolds stress fluctuation, which we write as

$$T'_{ij}(\bar{y}, t) = \rho u_i u_j - \rho_o \overline{u_i u_j}$$

as we did in connection with Equation (3.58) where  $u_i$  and  $u_j$  are fluid velocity disturbances, are restricted to the wake region. The velocity of the cylinder is  $u_n$ , the stress in a direction normal to its surface tensor  $p_{ij}$  reduces to the normal pressure  $p \delta_{ij}$ , if shear or viscous stresses near the surface are neglected. All integrands are evaluated at the retarded time

$$t_r = t - \frac{r}{c_o}$$

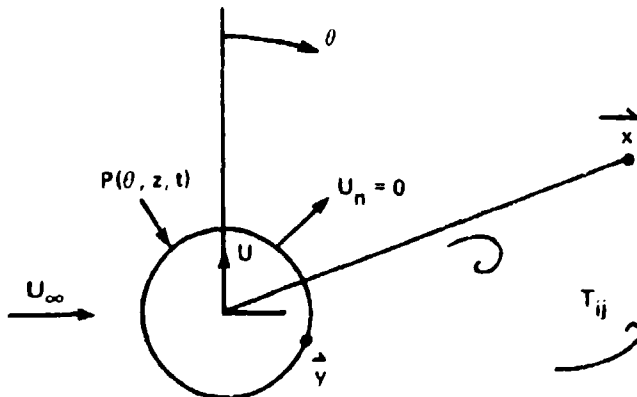


Figure 5.24a - Cross-Section Geometry of a Cylinder in a Cross Flow

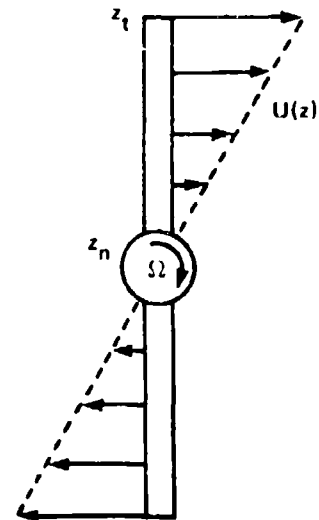


Figure 5.24b - Geometry of the Rotating Cylinder

Figure 5.24 - Diagrams of the Acoustic Fields of the Flow-Excited Cylinders

\*For purposes of illustration the circular cylinder is examined, but generalization is simple.

where  $r = |\vec{x} - \vec{y}|$ . Assumption of a no-slip boundary condition on the cylinder yields

$$u_i u_j = u^2 \delta_{ij} \quad i, j = 1, 2$$

where  $u$  is the resultant surface velocity of the surface. The terms  $n_i$  and  $n_j$  are direction cosines of the outward normal to the surface.

Because we are considering compact surfaces, the derivatives outside the integrals may be used to transform the integrands. For all derivatives of this type we have (as in Section 2.3.3)

$$\begin{aligned} \frac{\partial}{\partial x_i} \int_V \frac{A\left(\vec{y}, t - \frac{r}{c_0}\right)}{r} d\vec{y} \\ = - \int_V \left[ \frac{1}{r} \frac{\partial}{\partial t} A\left(\vec{y}, t - \frac{r}{c_0}\right) \right] \frac{1}{c_0} \frac{x_i}{r} d\vec{y} - \int_V \frac{A\left(\vec{y}, t - \frac{r}{c_0}\right)}{r} \frac{x_i}{r^2} d\vec{y} \end{aligned}$$

If the extent of the body and the volume encompassing fluctuating Reynolds stresses are small compared to  $r$ , then the second term is  $O[1/r]$  compared to the first term. Thus, we write the dominant terms of Equation (5.38) as

$$\begin{aligned} p_a(\vec{x}, t) \approx \frac{1}{4\pi c_0^2} \frac{x_i x_j}{r^3} \int_V \frac{\partial^2}{\partial t^2} \tau_{ij} \left( \vec{y}, t - \frac{r}{c_0} \right) d\vec{y} \\ - \frac{1}{4\pi r} \int_S \frac{\partial}{\partial t} [\rho u_n] dS(\vec{y}) - \frac{1}{4\pi c_0} \frac{x_i}{r^2} \int_S n_i \frac{\partial}{\partial t} [\rho u^2 + p] dS(\vec{y}) \end{aligned} \quad (5.39)$$

This result is identical to that which was derived by Phillips<sup>9</sup> and it applies to both stationary and moving cylinders. The connection between the radiated sound, the unsteady lift on the cylinder, and the wake vortex development has been made in a general way by Equations (2.99) through (2.101), and Figure 3.4.

### 5.6.2 Importance of Quadrupole Radiation

The first term in Equation (5.39) is the quadrupole source radiation, while the other terms are dipole terms. To appreciate the significance of the dipole terms relative to the quadrupole we consider the specific surface pressure field on the cylinder in Figure 5.24 which is responsible for fluctuating lift forces acting normal to the direction of flow. These forces are expressed in Equation (5.7) as

$$p(\theta, z, t) = p_L(\omega_s) \cos \theta e^{-i[\omega_s t - \phi(z, t)]} \quad (5.40)$$

Any motion which is induced in the cylinder as a result of this pressure distribution will be perpendicular to the stream, so that the normal component of velocity of the cylinder surface is

$$u_n(\theta, z, t) = U(z) \cos \theta e^{-i\omega_s t} \quad (5.41)$$

where  $U(z)$  is the velocity (perpendicular to the flow direction) of the center of the cylinder. The acceleration associated with this velocity causes a directly proportional fluid reaction pressure which also has the directivity  $\cos \theta$ . Thus, both of these integrands have the same circumferential directivity which is identically zero in the direction of flow and which has its maximum absolute value in the cross-stream direction.

We will now consider the rough orders of magnitude of the quadrupole and dipole terms before establishing specific analytical forms. To simplify our evaluation we will consider the stationary cylinder. The maximum fluctuating velocity in the cylinder wake is, for example,  $u$ , so that the quadrupole contribution can be written in an approximate form as

$$p_q \sim \frac{\rho_o}{c_o^2 r} \int \omega_s^2 u u \, d\vec{y}$$

$$\sim \frac{\rho_o}{c_o^2 r} \omega_s^2 u^2 d \cdot m d \Lambda_3$$

where  $r$  is the distance to the observation point. We have considered the coherent vortices in the wake to radiate coherently over an axial length segment  $\Lambda_3$  and to extend a distance downstream of the cylinder equal to  $md$ , where  $m$  is a large number. The upper bound of the volume within which vortices are correlated we write as  $d \cdot md \cdot \Lambda_3$  since the width of the wake is  $d$  and the effective axial length is  $\Lambda_3$ . Now, the dipole term behaves as

$$p_d \sim \frac{1}{c_o r} \omega_s p_f \pi d \Lambda_3$$

where  $p_f$  is the fluid pressure and, using Equation (5.10a), is given by

$$p_f \sim \frac{1}{2} \rho_o U_\infty^2 C_L$$

Using Equation (5.33), we find the lift coefficient to depend upon the velocity fluctuations of the convecting vortex as

$$C_L \sim \frac{\Gamma}{2U_\infty d} \sim \frac{\pi u d}{2U_\infty d}$$

since  $\pi u d$  is a measure of the vortex strength. Combining these expressions, we have the ratio of acoustic pressures radiated by the quadrupole to that by the dipole:

$$\frac{p_q}{p_d} \sim \frac{\frac{m}{r} \frac{\omega_s^2}{c_o^2} d^2 \rho_o u^2}{\frac{\pi}{2r} \frac{\omega_s}{c_o} \rho_o U_\infty u} = \frac{2m}{\pi} \frac{U}{c_o} 2\pi S \frac{u}{U_\infty} \quad (5.42)$$

Now, because  $2\pi S \sim 1$ , the ratio of quadrupole strength to dipole strength increases with the Mach number of the mean flow and the intensity of the wake. The downstream

extent of the coherent wake has been shown by Roshko<sup>13</sup> to decay to less than 40 percent of its maximum in a downstream distance  $10d$  for  $R_d$  between 500 and 4,000. The distance is most likely smaller than this at higher Reynolds numbers. The intensity in the wake is on the order of  $u/U_\infty \approx 0.2$ , as indicated in Figure 5.4 and in measurements at greater  $R_d$ . Thus, for these instances of practical importance Equation (5.42) assumes the order of magnitude

$$\frac{p_q}{p_d} \sim M$$

where  $M$  is the Mach number  $U_\infty/c_o$ . Thus, for the low mean Mach-number flows that are the topic of this chapter, the quadrupole radiation is not a significant contributor to the total flow-induced radiation. In the remainder of our discussions the quadrupole term will be ignored.

### 5.6.3 Radiation from a Rigid Cylinder in a Cross-Flow

A closed-form expression for the radiation from the rigid cylinder in a cross-flow will now be derived. By neglecting cylinder motions,\* we find that Equation (5.39) takes on the simple form

$$p_a(\vec{x}, t) = -\frac{1}{4\pi c_o} \frac{x_1}{r^2} \int_0^{2\pi} \int_{-L/2}^{L/2} n_1 \frac{\partial p\left(\theta, z, t - \frac{r}{c_o}\right)}{\partial t} \frac{d}{2} d\theta dz \quad (5.43)$$

The force per unit length exerted by the flow on the cylinder is given by

$$F_1(z, t) = \int_0^{2\pi} n_1 p(\theta, z, t) \frac{d}{2} d\theta \quad (5.44)$$

so that Equation (5.43) can be rewritten

---

\*The radiation which results from the transverse motion of the cylinder will be discussed in Chapter 9.

$$p_a(\bar{x}, t) = - \frac{1}{4\pi c_o} \frac{x_1}{r^2} \int_{-L/2}^{L/2} \frac{\partial}{\partial t} \left[ F_1 \left( z, t + \frac{r}{c_o} \right) \right] dz \quad (5.45)$$

This relationship is identical to Equation (2.77). The radiated sound pressure in any direction is, thus, seen to be proportional to the time rate of change of the total force on the cylinder in that direction. Thus, there is sound radiated normal to the flow direction by the lift fluctuations as well as in the flow direction by the drag fluctuations although these forces are only one-tenth the lift forces. Note that the radiation is also independent of the shape of the body. Expressions for the forces which permit a consideration of the axial nonuniformity of phase are derived from Equations (5.7) and (5.8) or (5.44). The forces per unit length are of the form

$$F_1(z, t) = \tilde{F}_1(\omega) \exp[i\phi(z, t)] e^{-i\omega t} \quad (5.46)$$

where  $\phi(z, t)$  is the axial phase function and  $\omega$  is the radian frequency. The amplitude of the force per unit length at a location on the cylinder is  $\tilde{F}_1(\omega)$ , which for a given value of  $U_\infty$  is, in general, a function of frequency. When the vortex shedding is discrete, the lift and drag components are concentrated at the frequencies  $\omega_s$  and  $2\omega_s$ , respectively.

The time-averaged radiated sound intensity  $I(\bar{x})$  is found using Equation (2.15); by substitution of Equation (5.45)

$$I(\bar{x}) = \frac{1}{16\pi^2} \frac{\omega^2}{\rho_o c_o^3} \frac{x_1 x_1}{r^4} \int_{-L/2}^{L/2} dz_1 \int_{-L/2}^{L/2} dz_2 \times \frac{1}{T} \int_0^T \left[ F_1 \left( z_1, t + \frac{r}{c_o} \right) F_1^* \left( z_2, t + \frac{r}{c_o} \right) \right] dt \quad (5.47)$$

where  $\omega$  is  $\omega_s$  or  $2\omega_s$  depending upon whether periodic lift or drag fluctuations are considered. In determining this equation we have assumed that  $\omega \gg \partial\phi(z,t)/\partial t$  as we did in Section 5.3. Now, incorporating Equation (5.46) into Equation (5.47), we find

$$I(\bar{x}) = \frac{\omega^2}{16\pi^2 \rho_o c_o^3} \frac{x_1 x_1}{r^4} |\bar{F}_1(\omega)|^2 \int_{-L/2}^{L/2} \int_{-L/2}^{L/2} R_{pp}(z_1 - z_2) dz_1 dz_2 \quad (5.48)$$

where we have assumed that the characteristics of the correlation function are those which were developed in Equations (5.11) through (5.16). The integral in Equation (5.48) can be evaluated in terms of the correlation length as

$$\begin{aligned} \int_{-L/2}^{L/2} \int_{-L/2}^{L/2} R_{pp}(z_1 - z_2) dz_1 dz_2 &= \int_{-L}^L dr \int_{-L/2+r}^{L/2} dz_2 R_{pp}(r) \\ &= 2[L\Lambda_3 - \gamma_c \Lambda_3] \end{aligned}$$

where  $\Lambda_3$  is the correlation length as defined by Equation (5.17) and

$$\gamma_c = \frac{1}{\Lambda_3} \int_0^\infty r R_{pp}(r) dr$$

is the centroid of the correlation function. The centroid of the correlation function is on the order of  $2/3 \Lambda_3$  as indicated in Reference 47. Therefore, under these simplifications, Equation (5.48) reduces to

$$I(\bar{x}) = \frac{\rho_o}{16c_o^3} \frac{\cos^2 \theta}{r^2} \bar{C}_L^2 U_\infty^6 S^2 2\Lambda_3(L - \gamma_c) \quad (5.49)$$

for the sound intensity radiated by sinusoidal lift fluctuations; for sound radiated by drag fluctuations we replace  $C_L^2$  by  $C_D^2$ ,  $\omega_s$  by  $2\omega_s$ , and  $\cos \theta$  by  $\sin \theta$ . In the range of Reynolds number for which the vortex shedding is irregular,  $|\tilde{F}_1(\omega)|^2$  is continuous over a frequency range and Equation (5.49) must be modified. For these broadband fluid forces,  $|\tilde{F}_1(\omega)|^2$  describes a force spectrum which can be written as a spectral density  $\phi_{pp}(\omega)$ , i.e.,

$$|\tilde{F}_1(\omega)|^2 = \phi_{pp}(\omega) \cdot \left[ \frac{1}{2} \rho_o U_\infty^2 \right]^2 d^2 \quad (5.50)$$

by generalizing Equation (5.9). The  $\phi_{pp}(\omega)$  is a dimensionless surface pressure spectral density which would be measured locally by a pressure transducer on the cylinder. Equation (5.50) expresses the dimensional spectral density of the circumferentially-integrated pressure, which is equivalent to the lift per unit length. Our fluctuating lift coefficient is related to this pressure spectrum by

$$\overline{C_L^2} = \int_{-\infty}^{\infty} \phi_{pp}(\omega) d\omega \quad (5.51)$$

this relationship can be deduced by comparing Equations (5.50) and (5.10). Similar relationships can be determined for the drag spectrum in terms of a pressure distribution which is maximum at  $\theta = 90$  and  $270$  deg.

Use of these relationships gives Equation (5.48) in the form

$$\begin{aligned} I(\bar{x}) = & \frac{\cos^2 \theta}{16\pi^2 \rho_o c_o r^2} \left( \frac{U_\infty}{c_o} \right)^2 \left( \frac{1}{2} \rho_o U_\infty^2 \right) \int_{-\infty}^{\infty} \left( \frac{\omega d}{U_\infty} \right)^2 \phi_{pp}(\omega) d\omega \\ & \times \int_{-L}^L (L-r) R_{pp}(r) dr \end{aligned} \quad (5.52)$$



These variations, Equations (5.49) and (5.52), in the expressions for the radiated sound intensity can be used to estimate sound levels from the known properties of the flow-induced forces over rather extensive ranges of Reynolds number.

#### 5.6.4 Review of Measured Acoustic Intensities

Measurements of sound levels from cylinders in a cross flow have been conducted in recent times by Holle,<sup>75</sup> Gerrard,<sup>76</sup> Phillips,<sup>9</sup> Leehey and Hanson,<sup>43</sup> Koopmann,<sup>42</sup> Etkin et al.,<sup>10</sup> and Guedel.<sup>77</sup> To facilitate comparisons with theory we follow Phillips' example and rewrite Equation (5.49) in the form

$$\frac{\overline{p}_a^2}{\rho_o^2} \frac{c_o^2}{c_L^2} = U_\infty^6 \left[ \frac{S^2 L d}{r^2} \right] \frac{\cos^2 \theta}{16} \frac{\overline{C}_L^2}{d} \frac{2\Lambda_3}{d} \left( 1 - \frac{\gamma_c}{L} \right) \quad (5.53)$$

which clearly exposes the sound pressure level as a function of the lift coefficient and the axial correlation length. Figure 5.24 shows the measurements of Phillips, Holle, and Gerrard, as presented by Phillips in the form of a linear function of  $U_\infty [S L d / r^2]$ . The measurements were conducted at  $\theta = 90$  deg and, collectively, over a wide range of Reynolds numbers. The slopes of the lines in Figure 5.25 are given by

$$M = \left[ \frac{1}{16} \frac{\overline{C}_L^2}{d} \frac{\Lambda_3}{d} \left( 1 - \frac{\gamma_c}{L} \right) \right]^{1/6}$$

In the Reynolds number range between  $10^3$  and  $10^4$  a typical value of the lift coefficient is 0.3 (Figure 5.15), and of the correlation length is  $10d$  (Figure 5.16). This gives  $M = 0.6$  which agrees favorably with the slope of the line through the data of Holle and Gerrard.

This correspondence between the measured sound pressure and the calculations which use the parameters of Figures 5.14 and 5.17 are approximate. Inconsistencies in the measurements are minimized by taking the 1/6-th root of the pertinent parameters  $\overline{C}_L^2$  and  $\Lambda_3/d$ . A precise verification of Curle's equation and of the integrated result, Equations (5.49) or (5.53), awaited the nearly simultaneous

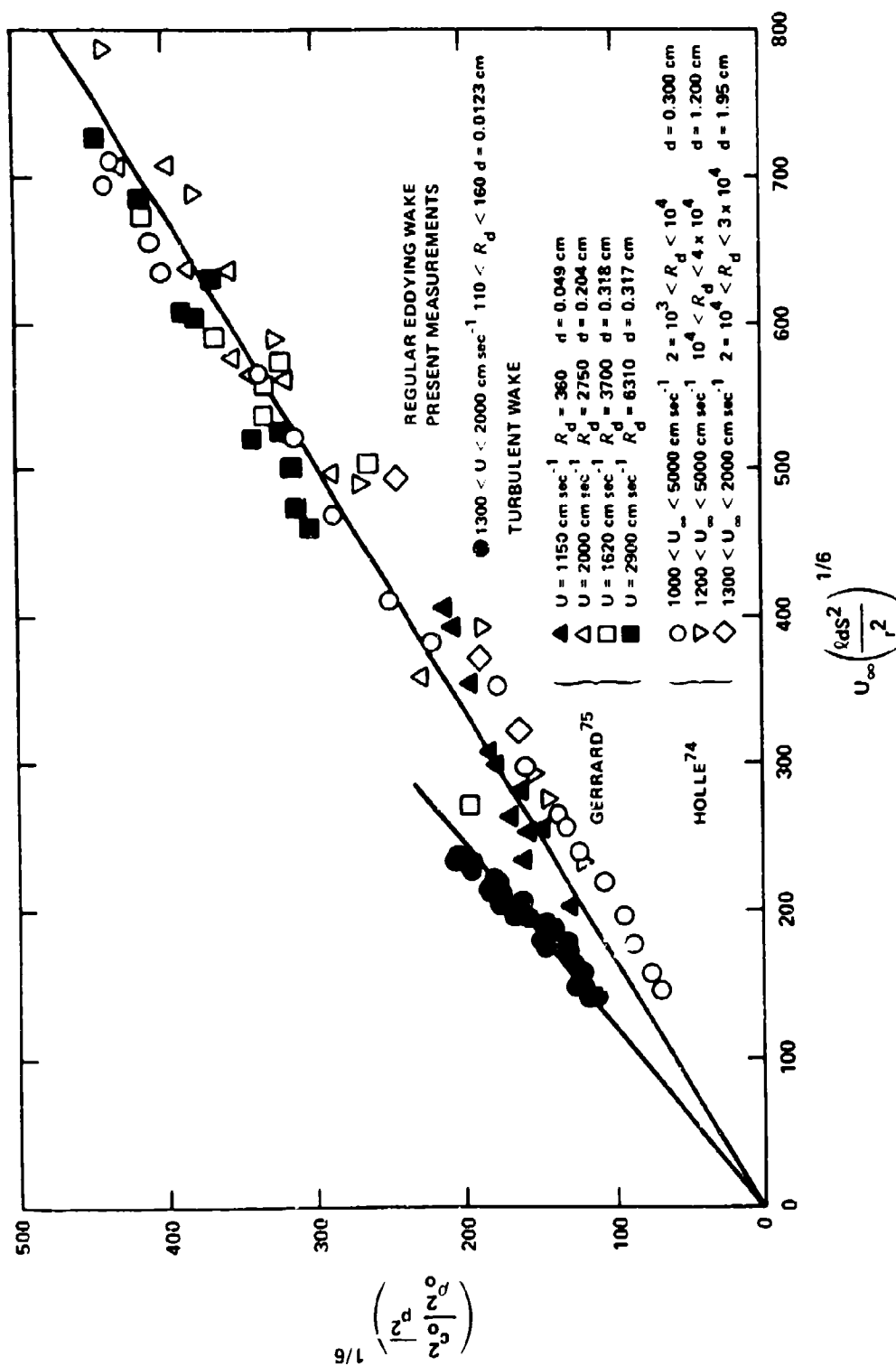


Figure 5.25 - Far-Field Sound Pressure Levels for Aeolian Tones Shown as a Function of Wind Speed (Gerrard<sup>75</sup>)

attentions of Leehey and Hanson<sup>43</sup> and of Koopmann.<sup>42</sup> In both cases, simultaneous measurements of the fluctuating lift coefficient and of the correlation length provided a critical comparison of experiment and theory. Table 5.2 shows the ratios of calculated-to-measured sound intensities for the investigations. In all cases, the flow induced peak-to-peak cylinder displacement  $2X_d$  was not zero so that the measured values of  $C_L^2$  may have been influenced by this effect.\* The agreement in this table, however, clearly shows that calculations of sound levels may be made quite reliably given accurate measurements of the cylinder forcing parameters.

TABLE 5.2  
COMPARISON OF MEASURED AND CALCULATED SOUND INTENSITIES

$R_d$	$\frac{2X_d}{d}$	$\frac{1}{C_L^2}$	$\frac{2\Lambda_3}{d}$	$10 \log \frac{I_{calc}}{I_{meas}}$	Author
2100	0.03	0.15	$4(=L/d)$	3	Koopmann <sup>42</sup>
4000	*	0.04	15	1	Leehey and Hanson <sup>43</sup>
4090	*	0.03	13	0	Leehey and Hanson <sup>43</sup>
4140	*	0.08	12.5	1	Leehey and Hanson <sup>43</sup>
6050	*	0.42	9.7	2	Leehey and Hanson <sup>43</sup>
6260	*	0.43	9.2	2	Leehey and Hanson <sup>43</sup>
6450	0.056	0.51	8.5	3	Leehey and Hanson <sup>43</sup>
*Indicates that cylinder displacements were not measured.					

We now consider the speed-dependence of the mean-square radiated sound pressure by noting that Equation (5.53) shows a  $U_\infty^6$  increase for a given cylinder diameter  $d$ . This dependence is borne out by the collection of experimental results in Figure 5.25. However, in specific instances, for example, a specific cylinder over a considerable speed range, this dependence on speed may not be observed. An example is shown in Figure 5.26 where the measured sound level increases with a substantially greater speed dependence than  $U_\infty^6$ . The change in the dependence shown in the figure occurs at a speed for which the vortex shedding frequency coincides with a resonance frequency of vibration of the cylinder. This change reflects the change in the oscillatory lift coefficient as the speed increases.

\*Recall that it is the contention of Leehey and Hanson that cylinder motion did not influence the correlation length in their measurements.

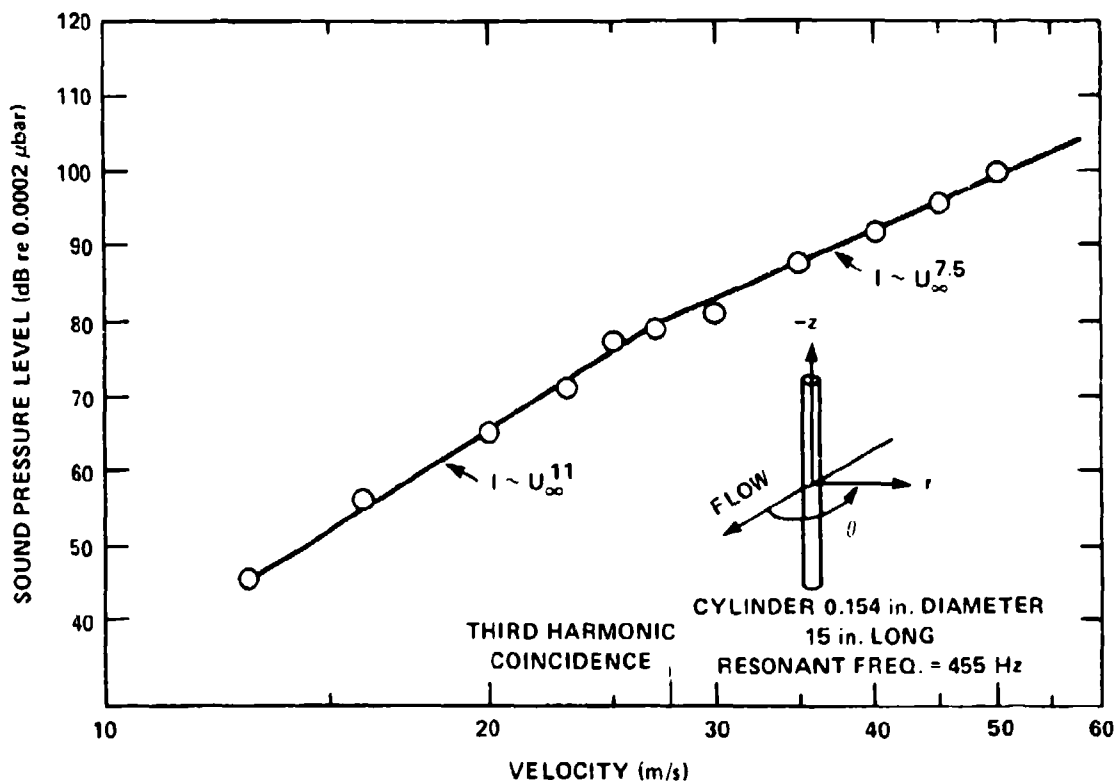


Figure 5.26 - Sound Intensity at Shedding Frequency Measured at  $r = 12$  Inches and  $\theta = 90$  Degrees (Leehey and Hanson<sup>43</sup>)

In spite of this apparent complication in a simplified interpretation of the relationship, Equations (5.48) and (5.49) are very powerful for making simple acoustic estimates. Equation (5.48) states that the radiated sound intensity from any acoustically-compact rigid body is directly proportional to the time derivative of the mean-square fluctuating force so that

$$I(\bar{x}) = \frac{1}{16\pi^2 \rho_o c_o^3} \frac{\cos^2 \theta}{r^2} \left[ \frac{\partial F(t)}{\partial t} \right]^2 \quad (5.54)$$

where  $\theta$  is measured from the direction of the fluctuating force vector. Thus, in a practical situation in which the radiating surface is small, the acoustic intensity

could be estimated by calculating the magnitude of the mean-square fluctuating force, and the overall sound pressure has the dependence on speed as given by Equation (5.53).

The radiation from a circular cylinder whose axis is set at an angle to the flow direction has been measured experimentally by Guedel. Let  $\phi$  be the angle between the flow direction and the normal to the axis of the cylinder in the flow-cylinder plane so that the velocity component normal to the cylinder is  $U_\infty \cos \phi$ . Assuming that the root-mean-square periodic forces are proportional to  $[U_\infty \cos \phi]^2$  and that the vortex shedding frequency is proportional to  $U_\infty \cos \phi$ , Equation (5.53) shows that

$$\bar{p}_a^2 \sim U_\infty^6 (\cos \phi)^6$$

Guedel's experiments substantially support this result, yielding an exponent which varies from 5.34 to 6.

Measurements of shedding frequencies by Smith et al.,<sup>78</sup> and Ramberg<sup>79</sup> have verified that  $f_s d = S U_\infty \cos \phi$  increases slightly with yaw angle  $\phi$ . The increase is approximately 15 percent with  $\phi = 30$  deg and 25 percent with  $\phi = 60$  deg. The implication of this can be seen by referring to Equation (5.33). Given that the Strouhal number based on  $U_\infty \cos \phi$  is constant, an increase in  $C_L$  based on  $U_\infty \cos \phi$  would imply an increase in  $l'/U_\infty d \cos \phi$  and, therefore, an increase in the fluctuating lift coefficient. Guedel's results, however, indicate that the product  $\overline{C_L^2} \Lambda_3$  decreases with  $\cos \phi$  since the dependence of sound intensity is less than  $(\cos \phi)^6$ . This discrepancy can be interpreted as indicating a loss in axial coherence as  $\phi$  is increased. Indication of a decrease in  $\Lambda_3$  with increased yaw angle have been shown by Smith et al.<sup>78</sup> The recent results of Ramberg<sup>79</sup> show that the wake thickness at the end of the formation zone is independent of yaw ( $\phi < 50$  deg) and that the formation length is only weakly influenced by yaw. The base pressure coefficient, defined with the velocity  $U_\infty \cos \phi$ , is generally less than the coefficient at zero yaw angle by a factor as large as 1.2 at  $\phi \sim 50$  deg. For yaw angles greater than 50 deg, Ramberg finds, for cylinders without end plates, that the character of shedding changes from one in which the vortices are nearly parallel to the cylinder, to one in which they peel off from the tip and are aligned with the flow direction.

Vortex induced vibrations of yawed cylinders due both to oscillating lift fluctuations and oscillating drag fluctuations have been studied by King<sup>80</sup> (see also Chapter 9).

## 5.7 RADIATION FROM ROTATING RODS

We turn now to an examination of the acoustic intensity from cylinders rotating transversely to their axes. Such cylinders represent the most rudimentary treatment of vortex shedding sounds of propellers. Figure 5.24b shows the spin axis to be perpendicular to the axis of the cylinder with the angular velocity of spin denoted by  $\Omega$ . The local tangential mean velocity is

$$U(z) = \Omega z \quad (5.55)$$

and at the tip of the cylinder

$$U(z_T) = \Omega z_T = U_T$$

where  $z$  is the radial coordinate measured from the spin axis. We assume that if there is a mean advance velocity parallel to the spin axis it is uniform and negligible compared to the tangential velocity at  $z = z_t/2$ , where  $z_t$  is the tip coordinate, or the radius of spin. The rod extends from a hub of radius  $z_h$ .

The analysis consists of writing Equation (5.43) in a slightly more general form to account for the fact that the fundamental frequency of shedding and the magnitude fluctuating forces increase outward along the cylinder. The linear increase in shedding frequency with distance from the hub is given by

$$\omega_s d = 2\pi U(z) \text{ for } z_h < z < z_t \quad (5.56)$$

We are essentially assuming that the vortices are shed from the cylinder continuously along its length although experiments by Maul and Young<sup>81</sup> suggest that this assumption is not strictly correct; the vortices are shed in a stepwise fashion along the length with lengths of individual patterns on the order of  $4d$  at  $R_d = 2.85 \times 10^4$ . Also, since the shedding frequency varies along the rod, we must maintain the general interpretation of the oscillating force spectrum that is given in Equation

(5.50). Now, combining Equations (5.47) (with  $\omega$  moved inside the integral), Equations (5.50) and (5.56), we obtain the total far-field acoustic intensity as\*

$$I(\bar{x}) = \frac{1}{16\pi^2 \rho_o c_o^3} \frac{\cos^2 \beta}{r^2} \int_{-\infty}^{\infty} d\omega \int_{z_h}^{z_t} dz_1 \int_{z_h}^{z_t} dz_2 \left[ \frac{1}{2} \rho_o U^2(z) \right]^2 d^2 \times \omega^2 R_{pp}(z_1 - z_2) \phi_{pp}(\omega) \quad (5.57)$$

where  $\beta$  is the polar angle measured from the axis of rotation. The continuous spectral density function  $\phi_{pp}(\omega)$  is strongly peaked near  $\omega = \omega_s$ ; we will assume that it can be expressed in terms of a universal function with a dimensionless frequency as its argument. Thus,

$$\phi_{pp}(\omega) = \frac{d}{U} \phi_{pp}\left(\frac{\omega d}{U}\right) \quad (5.58)$$

In order to conveniently substitute Equation (5.58) into Equation (5.57) we must further assume that the correlation length is small relative to the distance  $z_t - z_h$  and that the shedding frequency is constant over the correlation length. Under this further assumption we now obtain the frequency spectral density of acoustic intensity as

$$I(\bar{x}, \omega) = \frac{\cos^2 \beta}{16\pi^2 \rho_o c_o^3 r^2} \omega^2 \int_{z_h}^{z_t} \left[ \frac{1}{2} \rho_o U^2(z) \right]^2 d^2 2\Lambda_3 \times \frac{d}{U(z)} \phi_{pp}\left[\frac{\omega d}{U(z)}\right] dz \quad (5.59)$$

---

\*Here we will neglect the effect of rotation on the retarded time; when a rotating source is a tone the rotation causes the generation of harmonics of the tone frequency at multiples of  $\Omega$ . The effect disappears as  $\beta \rightarrow 0$  and for broadband sources at all values of  $\beta$ . These harmonics will be discussed in Chapter 9.

The total acoustic intensity is given by an integral over frequency,

$$I(\bar{x}) = \int_{-\infty}^{\infty} I(\bar{x}, \omega) d\omega$$

In deriving Equation (5.59), it was assumed for simplification that the centroid of the correlation is negligible. If also  $\Lambda_3$  is independent of  $z$ , we rewrite the intensity spectrum in terms of the rotational tip speed  $U_T$  as

$$I(\bar{x}, \omega) = \frac{\cos^2 \beta d^2}{16\pi^2 r^2 \rho_o c_o} \left( \frac{U_T}{c_o} \right)^2 \left( \frac{\omega d}{U_T} \right)^2 \frac{2\Lambda_3}{d} \frac{2L}{d} \\ \times \left[ \frac{1}{2} \rho_o U_T^2 \right]^2 \frac{d}{U_T} \int_{z_h/L}^{z_t/L} \left[ \frac{U(z)}{U_T} \right]^4 \frac{U_T}{U(z)} \phi_{PP} \left( \frac{\omega d}{U(z)} \frac{dz}{L} \right) \quad (5.60)$$

where  $L = (z_t - z_h)$  is one-half of the total length of the rotating cylinder. Equation (5.60) clearly shows how the acoustic intensity depends upon both the Mach number and the dynamic pressure based on tip speed as well as on a dimensionless frequency based on tip speed. The integral signifies the summing of the local oscillating pressures along the cylinder; the magnitude of the mean-square pressure increases with  $U^4(z)$  while the time-scale of the vortex shedding decreases as  $[U(z)]^{-1}$ . The integral is a net oscillating pressure spectrum which has been made dimensionless on the cylinder diameter and the rotational tip speed. This net spectral density has the form

$$\Gamma \left( \frac{\omega d}{U_T} \right) = \int_0^1 \left[ \frac{z}{L} \right]^3 \phi_{PP} \left[ \left( \frac{\omega d}{U_T} \right) \left( \frac{L}{z} \right) \right] d \left[ \frac{z}{L} \right] \quad (5.61)$$

if  $z_h \ll z_t$  so that since  $L = z_t$  then  $U(z_n) \approx 0$  and  $U(L) = U_r$ .



The spectral density of the radiated sound pressure from the rotating rod is distributed over frequency even if the vortex shedding at a point on the radius of the rod is locally a pure sinusoid. This can be seen more clearly by considering a simple analytical example of a locally periodic spectrum at each value of  $z$  given by

$$\phi_{pp} \left[ \frac{\omega d}{U} \right] = \frac{\overline{C_L^2}}{2} \left[ \delta \left( \frac{\omega d}{U(z)} - 2\pi \right) + \delta \left( \frac{\omega d}{U(z)} + 2\pi \right) \right]$$

for  $-\infty < \omega < \infty$ . The pressure fluctuations at a radial point  $z$  on the rod occur at discrete frequencies given by

$$\frac{\omega d}{U(z)} = \pm 2\pi S$$

The sound spectral density for the rotating system is obtained by substitution into Equation (5.61) as

$$\begin{aligned} \frac{\Gamma \left( \frac{\omega d}{U_T} \right)}{\overline{C_L^2}} &= \frac{1}{2} \left| \frac{\omega d}{2\pi U_T S} \right|^4 \frac{1}{2\pi S} \quad \text{for } \left| \frac{\omega d}{2\pi U_T S} \right| \leq 1 \\ &= 0 \quad \text{for } \left| \frac{\omega d}{2\pi U_T S} \right| > 1 \end{aligned} \quad (5.62)$$

so that the acoustic intensity spectrum is

$$\begin{aligned} I(\bar{x}, \omega) &= \frac{\cos^2 \beta}{16\pi^2 r^2 \rho_o c_o} d^2 (M_T)^2 (2\pi S)^2 \frac{2\Lambda_3}{d} \frac{2L}{d} q_T^2 \overline{C_L^2} \\ &\times \frac{d}{U_T} \left( \frac{\omega d / U_T}{2\pi} \right)^2 \times \left\{ \begin{array}{ll} \frac{1}{2} \frac{1}{2\pi S} \left| \frac{\omega d}{2\pi U_T S} \right|^4 & \text{for } \frac{\omega d}{U_T} < 2\pi S \\ 0 & \text{for } \frac{\omega d}{U_T} > 2\pi S \end{array} \right\} \end{aligned} \quad (5.63)$$

and the total intensity of the sound is determined by integration to be

$$I(\bar{x}) = \frac{\cos^2 \beta d^2}{28r^2 \rho_o c_o} M_T^2 S^2 \frac{2\Lambda_3}{d} \frac{2L}{d} q_T^2 \overline{C_L^2} \quad (5.64)$$

where  $M_T = U_T/c_o$  and  $q_T = 1/2 (\rho_o U_T^2)$ . These relationships will be compared to measured sound levels.

The validation of these relationships is provided by experiments conducted by Yudin,<sup>82</sup> Stowell and Deming,<sup>83</sup> Scheiman et al.,<sup>84</sup> and previously unpublished results of the author. In the 1930 to 1950 time-span, most quantitative measurements of radiated dipole sound from cylinders were obtained on rotating cylinders. This was the only practical means of achieving high Reynolds number flow without high background acoustic levels. Stowell and Deming's results, for example, demonstrate that the radiated intensity behaves as

$$I(x) \propto \cos^2 \beta \frac{U_T^6 L}{r^2}$$

Examples of measured autospectral densities of the radiated sound intensity are shown in Figure 5.27. Reynolds numbers  $R_T$ , based on the diameter of the cylinder

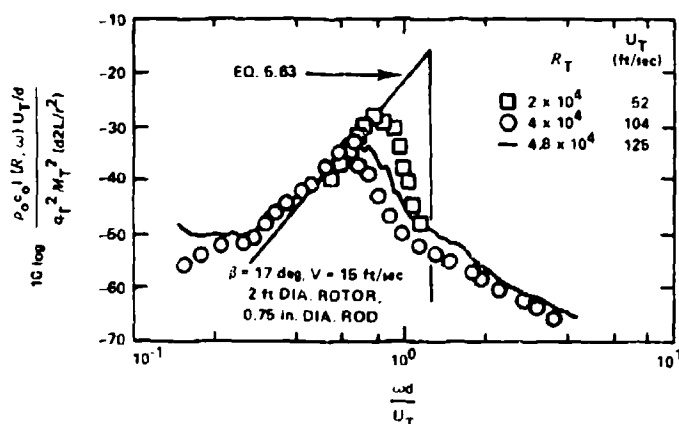
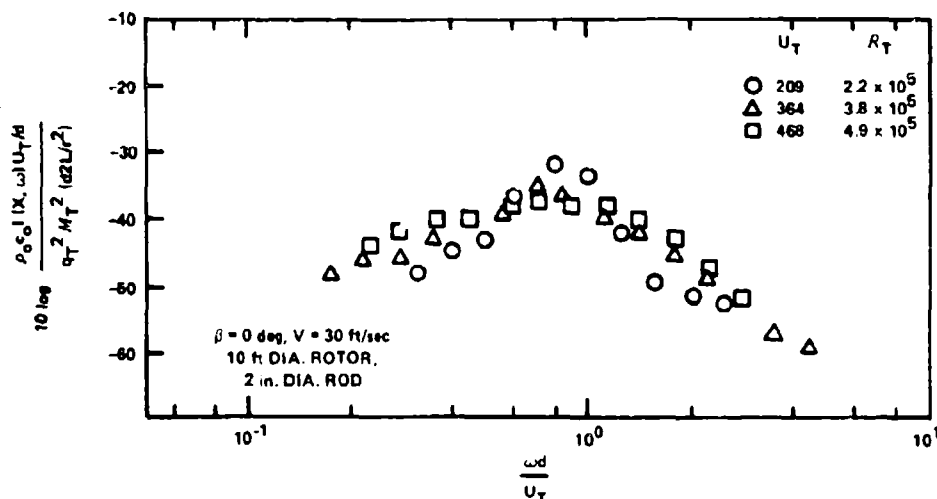


Figure 5.27a - Spectral Density of Noise from Rotating Rod  
(Author's Measurements,  $L/d = 16$ )

Figure 5.27 (Continued)

Figure 5.27b - Spectral Density of Noise from Rotating Rod  
(Scheiman et al.,<sup>84</sup>  $L/d = 30$ )

and the tip speed, range from  $2 \times 10^4$  to  $4.9 \times 10^5$ . The measurements were obtained on rods of length  $2L$  which were spun about their centers either out of doors or in an anechoic room.\* That cylinder vibration did not influence the measurements is indicated by the absence of resonance effects in the measured spectral densities. For Reference 84 and the present case, the sound levels were found to be insensitive to a superimposed axial mean velocity with magnitudes at least as large as  $1/10 (U_T)$ . The measured spectral densities are shown to be dimensionless functions of  $q_T$  and  $M_T$  which are more peaked at the lower values of  $R_T$ . Comparison with Equation (5.63), with  $C_L^{-1/2} = 0.45$ ,  $S = 0.2$ , and  $2\Lambda_3 = 5d$ , is shown in Figure 5.27a. Theoretically, if the vortex shedding is temporally sinusoidal along the entire radius of rotation of the cylinder, a spectral peak will occur at  $\omega d/U_T = 2\pi S = 1.26$  with sound absent at higher frequencies. The measured spectral density at  $R_T = 2 \times 10^4$  increases as  $(\omega d/U_T)^6$ , and then rapidly decreases for  $\omega d/U_T > 1.0$  in rough agreement with the simple theory. The disagreement for  $\omega d/U_T \approx 1$  is probably due to a spectral broadening of the local vortex shedding such as has been observed by Maul and Young for a bluff body in a shear flow. As Reynolds number increases,

\*The measurements by the author were obtained at the David W. Taylor Naval Ship Research and Development Center Anechoic Flow Facility.

the spectral densities of the intensities broaden in a systematic fashion until at  $R_T = 4.9 \times 10^5$  the spectrum has a greatly suppressed peak.

Various directivity measurements are shown in Figure 5.28; they generally support the  $\cos \beta$  dependence. The discrepancy at  $\beta = 30$  deg is unexplained particularly in light of the observations of Gerrard<sup>76</sup> and Guedel<sup>77</sup> on a stationary rigid cylinder which confirm the basic cosine directivity.

Total radiated intensities for a variety of experimental cases are shown as a function of tip speed Mach number in Figure 5.29. The measured intensities are in close agreement with values which were calculated using Equation (5.64) and the measured parameters in Figures 5.13, 5.15, and 5.18 at the appropriate values of  $R_T$ . Estimated values of the measured  $C_L^2$ <sup>-1/2</sup> and  $2\Lambda_3$  are shown in the respective figures. An average value of a given parameter was selected for a range of Reynolds number between  $1/2 R_T$  and  $R_T$  for each estimate. Although the precise values of the shedding parameters are perhaps somewhat questionable, the trends of computed and measured intensities, shown in Figure 5.29, demonstrate an important point.

The speed dependence of the radiated sound is  $U_T^6$  for a limited range of  $M_T$  that is bounded by  $R_T < 4$  to  $10 \times 10^4$ . For higher values of Mach (and Reynolds) numbers, the speed dependence falls off becoming more like  $U_T^4$ . This change in speed dependence is matched by the calculated intensities. The calculations show that the reduction in both the fluctuating lift coefficient and the axial correlation length at high Reynolds numbers can account for this observed change in speed dependence.<sup>105</sup> This result amplifies the statement made in the last section regarding Gerrard's observed  $U_\infty^5$  speed dependence.

In certain practical situations, the speed dependence of a particular sound source does not always uniquely describe the physical nature of the source. As seen in these instances, the nature of the noise mechanism is identical in each case. The observed  $U^4$ ,  $U^5$ , and  $U^6$  speed dependences are the result of the shedding process itself being strongly Reynolds-number dependent over a large range.

## 5.8 OTHER TOPICS IN VORTEX-INDUCED NOISE

The problems of acoustic radiation from, and the forced vibration of, cylinders of noncircular cross section are rather specialized to specific instances. Also, extensions of the acoustics and vibration problem to multiple tube banks has been

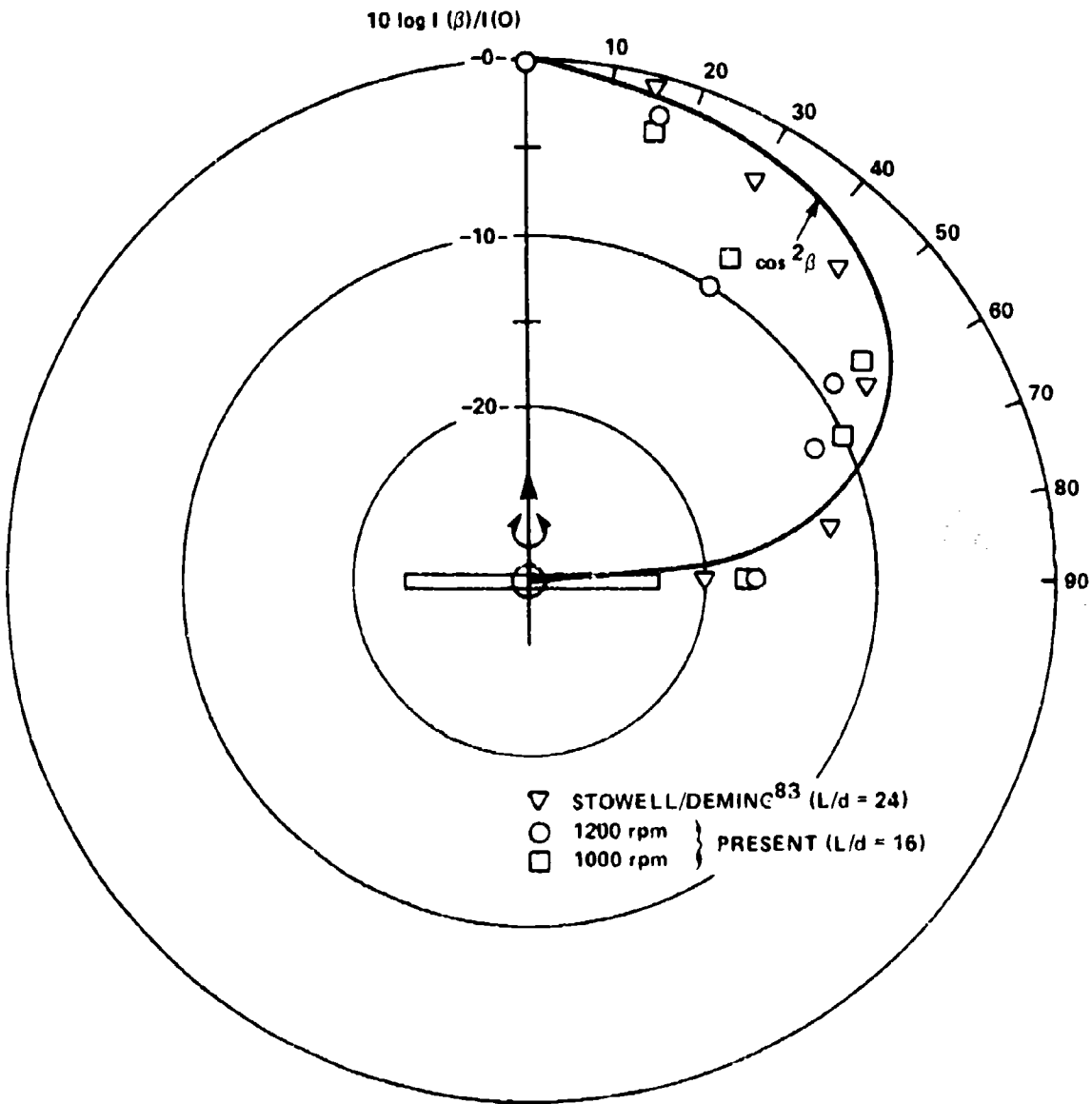


Figure 5.28 - Noise from Rotating Rods: Directivity Patterns

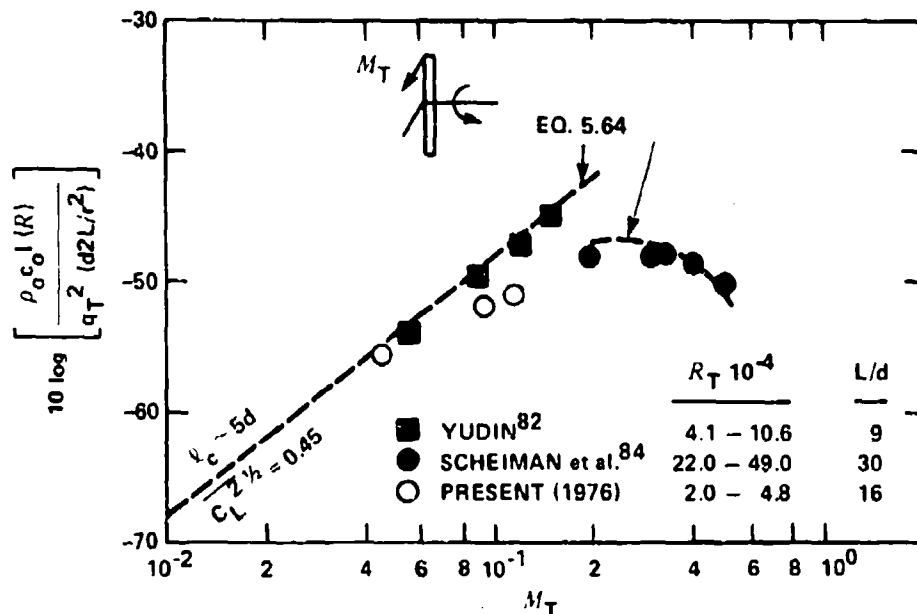









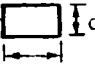
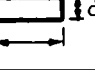
Figure 5.29 - Variation of Sound Intensity Level with Tip Mach Number

given by some investigators. In those cases for which data are nonexistent, the fundamental formulations of the previous sections can be used to provide estimates of force coefficients. When vortex structures are known, the estimated and measured magnitudes and correlation lengths of lift can be used to predict acoustic intensities for these, more complex, instances.

### 5.8.1 Cylinders with Noncircular Cross Sections

There has been a surprisingly large number of measurement programs in recent years that have yielded data useful for acoustic estimations. The measurements often have had application to the prediction of wind-induced fluctuating forces on architectural structures. Generally, the measurements are limited in scope so that wide ranges of Reynolds number or large numbers of unsteady parameters have not been reported. Table 5.3 summarizes a number of useful results on some important shapes. In all cases, with the obvious exception of shape d, sharp corners existed on the shapes. The oscillatory lift coefficient, when it was determined as the result of a direct force measurement, has been made dimensionless on the thickness  $d$  and the total span of lift measurement  $L$ . In all cases, the highest reported value of the lift coefficient occurred when the flat side of the sharp-edged cylinder faced the wind.

TABLE 5.3  
LIFT COEFFICIENTS ON CYLINDERS

Shape	$R_d$	$\frac{1}{C_L^2}$	$2\hat{h}_3/d$	S	Source
a → 	$10^4 - 3 \times 10^4$	0.054	-	-	Integrated pressure <sup>85</sup>
b → 	$4.5 \times 10^4$	0.054	-	0.23	Measured lift <sup>86</sup> (L/d=6)
c → 	$4.5 \times 10^4$	0.52	-	0.14	Measured lift <sup>86</sup> (L/d=6)
d → 	$4.5 \times 10^4$	0.28	-	0.21	Measured lift <sup>86</sup> (L/d=6)
e → 	$3 \times 10^4 - 11 \times 10^4$		2.5		Integrated pressure <sup>87</sup>
f → 	$10^4$	0.7 to 1.3	3 to 6	0.12	Integrated pressure <sup>88</sup>
g → 	$3.3 - 13 \times 10^4$	1.0	-	0.125	Measured lift <sup>89</sup> (L/d=4.65)
h → 	$3.3 - 13 \times 10^4$	0.35	0	0.083	Measured lift <sup>89</sup> (L/d=4.65)
i → 	$3.3 - 13 \times 10^4$	0.05	-	0.118	Measured lift <sup>89</sup> (L/d=7.8)

According to Vickery,<sup>88</sup> the magnitude and the correlation length of the lift are reduced by free-stream turbulence; both values are shown in Table 5.3. The periodicity of the lift is also reduced. Bearman and Trueman<sup>90</sup> show separation to occur at the forward sharp edge of the square cross-section which causes a strong wake vortex field that is strongly correlated along the span. In case h the separated shear layers still do not reattach<sup>89</sup> before the trailing edge, but in case i they reattach before clearing the downstream trailing edge. In this case the lift coefficient is small, perhaps due to the formation of a weaker, more irregular wake than in the other cases.

Steady drag coefficients and vortex shedding frequencies have been obtained on a variety of shapes by Delany and Sorensen.<sup>36</sup> The largest values of drag were observed on shapes with sharp corners such as c, e, f, and g in Table 5.3. Drag coefficients of approximately  $\bar{C}_D = 2$  were measured in the nominal Reynolds number range  $10^4$  to  $10^6$ . Rounding the corners, to the extent that the radius of curvature

was 0.25 to 0.3 of the length  $d$ , resulted in values of  $\overline{C_D}$  and  $S$  which were similar to those observed on cylinders of circular cross section. In the absence of measurements of fluctuating lift coefficients, we can only surmise that oscillating lift on the noncircular cylinders reduces and becomes comparable to those measured on circular cylinders as the edges are somewhat rounded. Rockwell<sup>91</sup> has found that oscillating pressures on square cylinders depend upon the angle of incidence to the flat facing side  $\alpha$ . The pressures increase somewhat as  $\alpha$  reaches 4 to 6 deg, but drop to less than 0.1 of the value at  $\alpha = 0$  when  $\alpha > 10$  deg.

Strouhal numbers and vortex spacings have been measured in the wakes of elliptic cylinders of Modi and Dikshit.<sup>92</sup> Elliptical cross sections of various eccentricities  $e$  were used;  $e = \left[1 - b^2/a^2\right]^{1/2}$  where  $a$  and  $b$  are the major and minor axes, respectively,  $e = 0$  for circular cylinders, and  $e = 1$  for a flat plate. The cylinders were oriented with their major axes aligned with the direction of flow. Strouhal numbers defined as  $S_h = fh/U_\infty$ , where  $h$  is the projected height in the direction normal to the flow, ranged from 0.20 to 0.22 for angles of attack 0 deg through 90 deg and eccentricities  $e = 0.8, 0.6$ , and  $0.44$ . The Reynolds number  $U_\infty a/\nu$  was 68,000. Unsteady lifts, or vortex strengths, were not measured, but the steady drag coefficient based on  $h$  was reported to increase with angle of attack. At zero angle of attack,  $C_D$  was on the order of 0.67 to 0.8 for the values of eccentricity cited above. Longitudinal vortex spacing in the far wake was found to be approximately  $5h$ . Finally, the vortex convection velocity  $(U_\infty - U_v)/U_\infty$ , was found to be, approximately, 0.9 for  $e = 0.92$  and 0.95 for  $e = 0.44$ . With these parameters, the equations in Section 5.5 can be used to make order-of-magnitude estimates for the oscillating lift coefficient.

### 5.8.2 Unsteadiness in Tube Bundles

This topic is of specific importance in diagnosing vibration and noise in some heat exchanger applications. However, the fluidic interactions of parallel-oriented vortex-shedding bodies in close proximity are of sufficient general importance that we will briefly discuss some aspects of the sources of unsteadiness in tube-banks. Other, very much related, vortex-shedding phenomena are known to control the edge tone and the jet tone; these are discussed in Chapter 3.



Flow across two parallel cylinders which are displaced a distance  $G$  perpendicular to the flow direction causes unsteadiness with a range of frequencies. Figure 5.30 shows the frequencies which have been observed by Spivack<sup>93</sup> in the range of  $R_d$  from  $10^4$  to  $10^5$ . As the gap thickness between the cylinder surfaces increases from zero the Strouhal number, based on the single cylinder diameter, increases from approximately 0.1. This is because the vortex-shedding, which occurs on the outer surfaces of the cylinders when the gap is closed, is determined by twice the cylinder diameter. As the gap opening increases, the velocity of flow through the gap increases. For  $G/d > 0.5$ , disturbances of two frequencies were sensed throughout the region of flow surrounding the cylinders.\* The source of the higher-frequency disturbances is believed by Spivack to be related to jet instabilities associated with gap flow. Unfortunately, his measurements of mean velocity were not conducted near enough to the gap to disclose the existence of a jet-like mean velocity profile which would have generated these disturbances. As the gap width was increased to a

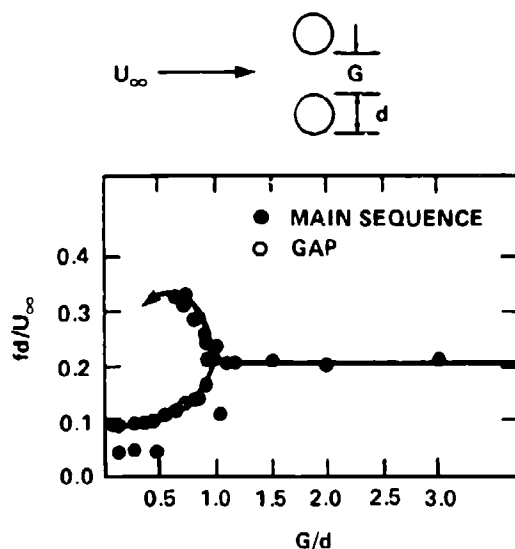


Figure 5.30 - Strouhal Number as a Function of Separation of Two Cylinders (for Air Speeds from 20 to 140 Feet per Second with 11/8-Inch Diameter Cylinders)  
(Spivack<sup>93</sup>)

\*These higher frequency disturbances were not restricted to locations immediately behind and on the centerline of each cylinder, but rather they existed at locations both above and below the cylinder pair.

critical value,  $G/d = 1$ , the disturbances attained a single frequency because the vortex shedding occurred independently on each cylinder.

Measurements of unsteady forces on this geometry are not available, however, it is likely that lift fluctuations will occur at both frequencies because both of the disturbances were easily detected throughout the flow field.

When the tubes are grouped into bundles, the tube interactions are more complex and dependent upon the cylinders in adjacent rows being staggered or in-line. The work of Chen<sup>94-96</sup> has provided unsteady lift coefficients and Strouhal numbers useful for the purpose of making predictions. Figure 5.31 shows the general arrangements of in-line and staggered tube groupings. The pertinent parameters are the dimensionless transverse  $T/d$  and longitudinal  $L/d$  tube spacings. For either arrangement, the wakes of forward cylinders impinge on those downstream influencing the shedding from those cylinders. Measured spectral densities of velocity fluctuations in the tube banks have disclosed disturbances of increasing degrees of periodicity as the tube spacings increase.<sup>96</sup> At small tube spacings, such that the clearance magnitudes are less than the diameters of the cylinders, the fluid velocity disturbances can be broadband,<sup>97</sup> other than tonal. Figure 5.32 shows the Strouhal numbers, defined as  $S = f_s d/U_\infty$ , as obtained by Chen<sup>94</sup> from measurements of the frequencies of flow-induced vibration in tube bundles with both the in-line staggered arrangements. The increase in the Strouhal number with a reduction in  $L/d$  for a constant value of  $T/d$  near two can be explained by postulating<sup>96</sup> that the length scale which is pertinent to the fluid disturbances is proportional to  $L$  rather than to  $d$ . This is because  $L$  determines the intertube gap distance. Thus, as  $L/d$  decreases, a Strouhal number  $f_s L/U_\infty$ , where  $U_\infty$  is the mean velocity into the tube bank, will be roughly a function of  $T/d$ .

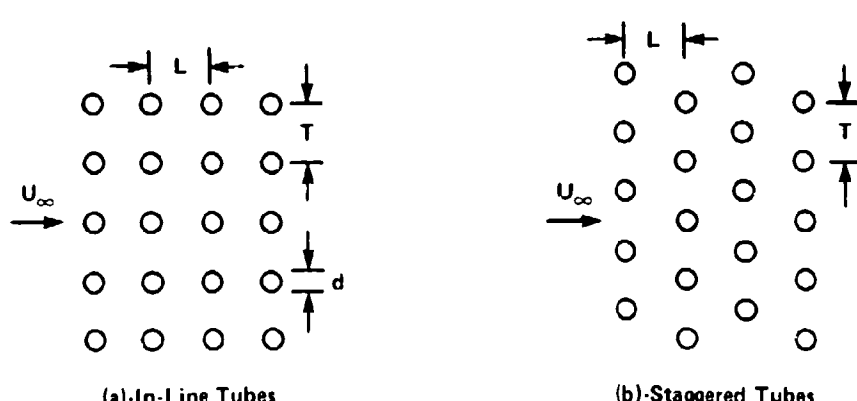


Figure 5.31 - Arrangements of Tube Bundles

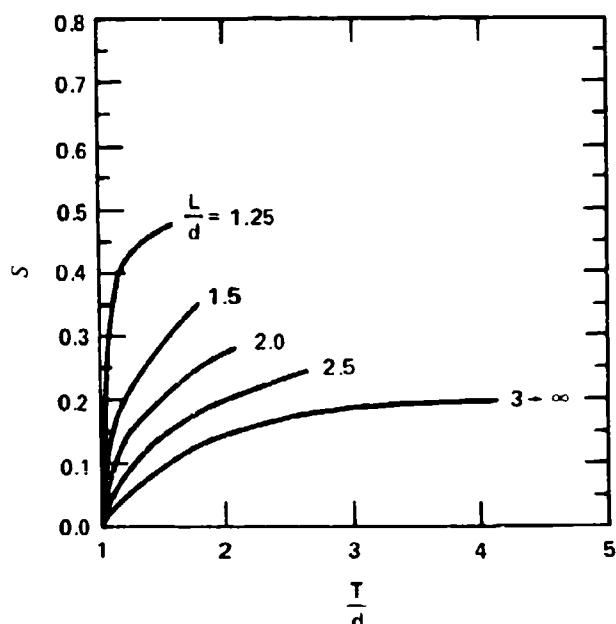


Figure 5.32a - In-Line

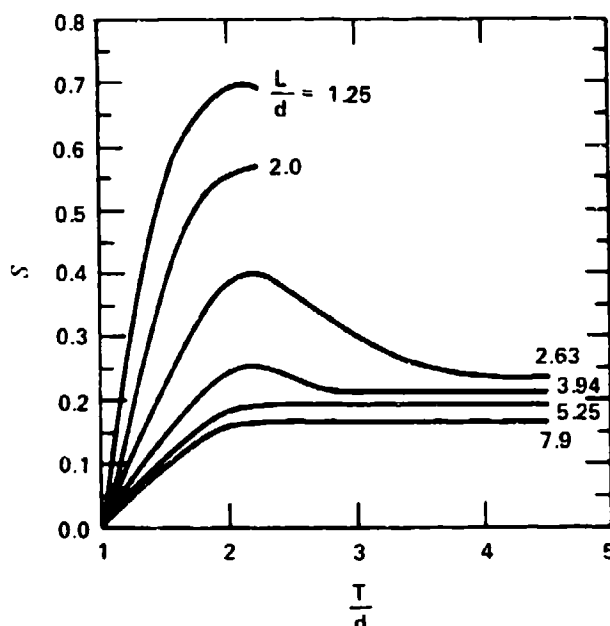


Figure 5.32b - Staggered

Figure 5.32 - Strouhal Numbers for Tube-Bundles as Functions of Tube Spacing Parameters (Chen<sup>94</sup>)

The amplitudes of unsteady forces on tubes have been deduced from the measured values of vortex-induced tube vibration by Chen.<sup>96</sup> His results, which are summarized in Figure 5.33, show higher amplitudes of lift coefficients in staggered tube alignments. For  $L/d$  greater than 3.0 (a gap distance  $G/d \geq 2$ ) the lift coefficients increase with  $T/d$  in a regular fashion. Chen's values attained 0.5 to 0.9 for  $R_d$  between  $1 \times 10^3$  and  $4 \times 10^4$  depending upon the geometry of the bundle. In this Reynolds number range, as we have already shown in Sections 5.3 and 5.4 and Figures 5.15 and 5.19, the lift fluctuations on single cylinders are particularly sensitive to environmental disturbances. In his method of measuring the lift fluctuations, Chen<sup>94</sup> necessarily recorded levels of transverse vibration whose peak-to-peak displacements were on the order of  $0.5d$ . Motion of this magnitude is certainly capable of causing an augmentation of fluctuating lift as indicated by Figure 5.20. Also, as Leehey and Hanson<sup>43</sup> have shown, lift augmentation can occur without substantial increases in correlation length and without the attendant "lock-in" which often occurs



(Chen<sup>94</sup>)

**Fig. 10a—continued**

●



Combinations of forces on tubes both in the flow direction (drag) and perpendicular to the flow cause a whirling motion of the tube when those forces attain the appropriate relative phase and magnitude with respect to each other and to the motion of the tube. A condition of self-excitation has been derived by Blevins<sup>98-100</sup> which states that the critical velocity through the tube bundle is given by

$$\frac{U_{cr}}{f_r d} = \left[ \frac{2(2\pi)^{1/2}}{(C_x K_y)^{1/4}} \right] \left( \frac{\pi m r_l}{\rho_o d^2} \right)^{1/2}$$

where  $m$  = mass per unit length of the tube

$U$  = average velocity in the tube gaps

$f_r$  = mechanical resonance frequency of the tubes with loss factor  $\eta$

The first term in brackets contains a dimensionless force coefficient  $C_x$ ;  $K_y$  a stiffness coefficient for forces aligned with the flow direction. For  $T/d < 1.7$  the formula  $C_x K_y \approx [2(d/T) - 1] (d/T)^4$  agrees well enough with measurements to give  $\pm 20\%$  error in estimating the bracketed term. Forces  $F_x$  arise from changes of tube drag due to variations in flow between adjacent cylinders as they vibrate. The entire term in square brackets is called the whirling parameter, and is a function of transverse spacing  $T/d$  as shown in Figure 5.34. When the velocity exceeds  $U_{cr}$ , the self-excitation occurs. The source of excitation, as postulated by Blevins, has to do with motion transverse to the flow causing stream-wise forces induced by changes in gap clearance as the tubes vibrate. Modulation of the gap clearance alters the through-flow and, therefore, the drag on the tubes. The problem is most severe when  $T/d$  lies between 1 and 2 so that modulation of the gap clearance is most severe. Although the theory has some proponents, it is apparently not without question.<sup>101,102</sup>

### 5.8.3 Methods of Reducing Vortex-Induced Forces

We will end this chapter by considering methods of reducing the total forces on cylinders, because these reductions will necessarily reduce the noise and vibration of cylinders.

Reducing the axial correlation length reduces directly the total mean-square force. This has been accomplished by Scruton<sup>103</sup> and Weaver<sup>104</sup> who installed a

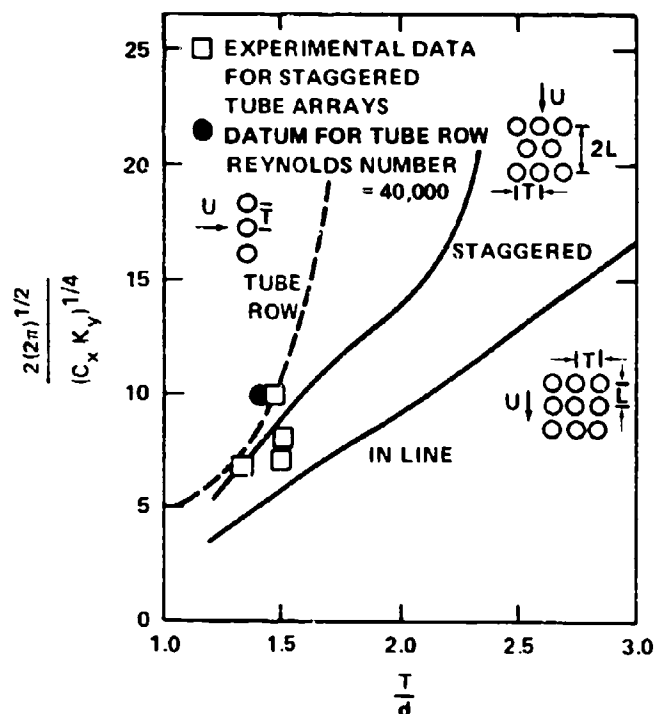


Figure 5.34 - Whirling Parameters for Tube Arrays (Blevins<sup>99</sup>)

helical strake consisting of a smaller-diameter cylinder wrapped around the larger cylinder in a helical pattern. Sharp-edged strakes are more effective than those with cylindrical cross section. Strakes of height  $0.1d$  and pitch  $5d$  to  $10d$  have been found to be effective in completely reducing vibrations.

Axial taper of the cylinder is also effective since it allows for a variation of vortex shedding frequencies. Because the correlation length of vortices is on the order of  $5d$  to  $8d$ , the taper should be sufficient to change the vortex shedding frequency by at least 30 percent in distances of  $5d$ . This is equivalent to a 6 percent taper.

Splitter plates, discussed in Section 5.4, are known to modify the shedding frequency. Although measurements of fluctuating forces are not available, we can speculate that splitter-plate lengths greater than  $3d$  should reduce fluctuating forces. This reasoning is based on the fact that formation lengths extend as far as  $2d$  downstream of the base of the cylinder, as shown in Figure 5.8. The splitter plate will interfere with wake formation, delaying it while allowing viscous

dissipation to reduce the rate of introduction of circulation into the wake. Also, shear-layer reattachment may occur on opposite sides of the splitter plates perhaps prohibiting the formation of the vortex street altogether. Splitter plates will be further discussed in Chapter 9.

Since free-stream turbulence apparently increases alternating lift forces (see Section 5.4 and Figure 5.19) in the Reynolds number range  $10^3$  through  $10^5$ , reductions of upstream turbulence may reduce alternating forces. Accordingly, it is expected that slightly rough cylinders and tubes will generate larger lift coefficients than will smooth ones. Schmidt<sup>49</sup> has observed reductions of nearly 1/4 in  $C_L^2$  with smoothing of the surface of the cylinder. His data, shown in Figure 5.14, were obtained with polished surfaces. The effect could be more pronounced at lower Reynolds numbers. Alternatively, we would expect large-size roughness to cause decorrelation of the vortex structure. Prismatic forms located at the separation position could be expected to generate trailing vortices which decorrelate the vortex street. Unfortunately, such shapes would also cause cavitation in liquid applications. Finally, we note that Vickery<sup>88</sup> has found that increases in upstream turbulence result in decreases in lift coefficients on prismatic forms.

A particularly useful method of reducing vortex shedding is to install fairings to reduce "bluntness." These, then, are classed as airfoil (or hydrofoil) shapes which will be discussed in Chapter 9.

## 5.9 REFERENCES

1. Strouhal, V., "Über eine besondere Art der Tonerregung," Ann. Phys. und Chemie, Neue Folge, Vol. 5, Heft 10, pp. 216-251 (Oct 1878).
2. Lord, Rayleigh, "Acoustical Observations," Phil. Mag., Ser. 5, Vol. 7, No. 42, pp. 149-162 (Mar 1879).
3. Lord, Rayleigh, "The Theory of Sound," Vol. 11, Dover Publications (1945).
4. Bénard, H., "Formation de Centres de Giration à l'arrière d'un Obstacle en mouvement," Comp. rend. Acad. Sci. (Paris), Vol. 147, pp. 839-842 (9 Nov 1908).
5. von Karman, T. and H. Rubach, "Über den Mechanismus des Flüssigkeits- und Luftwiderstandes," Phys. Zeitschr, Vol. 13, Heft 2, pp. 49-59 (15 Jan 1912).
6. Lamb, H., "Hydrodynamics," Dover Publications (1945).
7. Goldstein, S., "Modern Developments in Fluid Dynamics," Vol. 11, Dover Publications (1965).
8. Stowell, E.Z. and A.F. Deming, "Vortex Noise from Rotating Cylindrical Rods," J. Acoust. Soc. Am., Vol. 7, pp. 190-198 (1936).
9. Phillips, O.M., "The Intensity of Aeolian Tones," J. Fluid Mech., Vol. 1, Part 6, pp. 607-624 (1956).
10. Etkin, E.T. et al., "Acoustic Radiation from a Stationary Cylinder in a Fluid Stream (Aeolian Tones)," J. Acoust. Soc. Am., Vol. 29, No. 1, pp. 30-36 (1957).
11. Homann, F., "Einfluss grosser Zähigkeit bei Strömung um Zylinder," Forschung Ing. Wes., Vol. 7, pp. 1-10 (1936).
12. Kovasznay, L.S.G., "Hot-Wire Investigation of the Wake Behind Circular Cylinders at Low Reynolds Numbers," Proc. Roy. Soc. London, Ser. A198, pp. 174-190 (1949).
13. Roshko, A., "On the Development of Turbulent Wakes from Vortex Streets," NACA Tech. Note 2913 (Mar 1953).
14. Bloor, S.M., "The Transition to Turbulence in the Wake of a Circular Cylinder," J. Fluid Mech., Vol. 19, pp. 290-304 (1964).



15. Sato, H. and K. Kuriki, "The Mechanism of Transition in the Wake of a Thin Flat Plate Placed Parallel to a Uniform Flow," J. Fluid Mech., Vol. 11, pp. 321-352 (1961).
16. Landahl, M.T. and R.E. Kaplan, "Effect of Compliant Walls on Boundary Layer Stability and Transition," AGARDograph 97, Part 1, p. 360 (1965).
17. Landahl, M.T., "A Time-Shared Program for the Stability for Parallel Flows Over Rigid or Flexible Surfaces," M.I.T., ASRL 116-4 (1965).
18. Wazzan, A. et al., "Stability of Laminar Boundary Layers at Separation," Phys. Fluids, Vol. 10, pp. 2540-2545 (1967).
19. Ballou, C.L., "Investigation of the Wake Behind a Cylinder at Coincidence of a Natural Frequency of Vibration of the Cylinder and the Vortex Shedding Frequency," M.I.T. Acoustics and Vibrations Laboratory Report 76028-2 (19 May 1967).
20. Dale, J.R. and R.A. Holler, "Secondary Vortex Generation in the Near Wake of Circular Cylinders," J. Hydronautics, Vol. 4, pp. 10-15 (1969).
21. Schiller, L. and W. Linke, "Pressure and Frictional Resistance of a Cylinder at Reynolds Numbers 5,000 to 40,000," NACA TM 715 (Jul 1933).
22. Roshko, A., "Transition in Incompressible Near-Wakes," The Physics of Fluids, Vol. 10, pp. 5181-5183 (1967).
23. Schaefer, J.W. and S. Eskinazi, "An Analysis of the Vortex Street Generated in a Viscous Fluid," J. Fluid Mech., Vol. 6, pp. 241-260 (1959).
24. Gerrard, J.H., "A Disturbance-Sensitive Reynolds Number Range of the Flow Past a Circular Cylinder," J. Fluid Mech., Vol. 22, pp. 187-196 (1965).
25. Roshko, A., "Experiments on the Flow Past a Circular Cylinder at Very High Reynolds Number," J. Fluid Mech., Vol. 10, pp. 345-356 (1961).
26. Schlichting, H., "Boundary Layer Theory," McGraw-Hill, Seventh ed. (1979).
27. Chen, Y.N., "Fluctuating Lift Forces of the Karman Vortex Streets on Single Circular Cylinders and in Tube Bundles, Part 1 - The Vortex Street Geometry of the Single Circular Cylinder," ASME J. of Eng. For. Ind., pp. 603-612 (May 1972).
28. Flachsbart, O., From an article by H. Mutfrey 1932. Handb. Experimental physik, Vol. 4, Part 2 (Leipzig).

29. Fage, A. and V.M. Falkner, "The Flow Around a Circular Cylinder," Aero. Res. Council., London, Rep. and Mem. 369 (1931).
30. Guven, O. et al., "A Model for High-Reynolds Number Flow Past Rough-Walled Circular Cylinders," Trans. ASME J. Fluids Eng., Vol. 99, pp. 486-494 (1977).
31. Hama, F.R., "Three-Dimensional Vortex Pattern Behind a Circular Cylinder," J. Aero. Sci., Vol. 24, pp. 156-158 (1957).
32. Gerrard, J.H., "An Experimental Investigation of the Oscillating Lift and Drag of a Circular Cylinder Shedding Turbulent Vortices," J. Fluid Mech., Vol. 11, pp. 244-256 (1961).
33. Ribner, H.S. and B. Etkin, "Noise Research in Canada," Proc. 1st Int. Congr. Aero. Sci., Madrid, published by Pergamon Press, London (1959).
34. Relf, E.F. and L.F.G. Simmons, "The Frequency of Eddies Generated by the Motion of Circular Cylinders through a Fluid," Aero. Res. Council., London, Rep. and Mem. 917 (1924).
35. Bearman, P.W., "Vortex Shedding from a Circular Cylinder in the Critical Reynolds Number Regime," J. Fluid Mech., Vol. 37, pp. 577-585 (1969).
36. Delany, N.K. and N.E. Sorensen, "Low-Speed Drag of Cylinders of Various Shapes," NACA Tech. Note 3038 (Nov 1953).
37. Jones, G.W., "Unsteady Lift Forces Generated by Vortex Shedding About Large Stationary, and Oscillating Cylinder at High Reynolds Number," ASME Symposium on Unsteady Flow Paper 68-FE-36 (1968).
38. Roshko, A., "On the Drag and Shedding Frequency of Two-Dimensional Bluff Bodies," NACA TN 3169 (1954).
39. Bearman, P.W., "On Vortex Street Wakes," J. Fluid Mech., Vol. 28, pp. 625-641 (1967).
40. Kronauer, R.E., "Predicting Eddy Frequency in Separated Wakes," Paper presented at the IUTAM Symposium on Concentrated Vortex Motions in Fluids, University of Michigan, Ann Arbor, Michigan (6-11 Jul 1964).
41. Schwabe, M., "Über Druckermittlung in der nichtstationären ebenen Strömung," Ingenieur - Archiv, Vol. 6, pp. 34-50 (1935).

42. Koopmann, G.H., "Wind Induced Vibrations and Their Associated Sound Fields," Ph.D. Dissertation, Cath. Univ. America, Washington, D.C. (1969).
43. Leehey, P. and C.E. Hanson, "Aeolian Tones Associated with Resonant Vibration," J. Sound Vib., Vol. 13, pp. 465-483 (1971).
44. Bishop, R.E.D. and A.Y. Hassan, "The Lift and Drag Forces on a Circular Cylinder in a Flowing Fluid," Proc. Roy. Soc., Ser. A277, pp. 32-50 (1964).
45. Macovsky, M.S., "Vortex-Induced Vibration Studies," DTMB Report 1190 (Jul 1958).
46. Humphrey, J.S., "On a Circular Cylinder in a Steady Wind at Transition Reynolds Numbers," J. Fluid Mech., Vol. 9, pp. 603-612 (1960).
47. Fung, Y.C., "Fluctuating Lift and Drag Acting on a Cylinder in a Flow at Supercritical Reynolds Numbers," J. Aero. Sci., Vol. 27, pp. 801-814 (1960).
48. McGregor, D.M., "An Experimental Investigation of the Oscillating Pressures on a Circular Cylinder in a Fluid Stream," Univ. Toronto Inst. Aerophys., Tech. Note 14 (1957).
49. Schmidt, L.V., "Measurement of Fluctuating Air Loads on a Circular Cylinder," J. Aircraft, Vol. 2, pp. 49-55 (Jan-Feb 1965).
50. van Nunen, J.W.G., "Steady and Unsteady Pressure and Force Measurements on a Circular Cylinder in a Cross Flow at High Reynolds Numbers," Paper H5, Symposium on Flow-Induced Structural Vibrations, Karlsruhe, Germany (14-16 Aug 1972).
51. Gerrard, J.H., "The Calculation of the Fluctuating Lift on a Circular Cylinder and its Application to the Determination of Aeolian Tone Intensity," AGARD Report 463 (1963).
52. Prendergast, V., "Measurement of Two-Point Correlations of the Surface Pressure on a Circular Cylinder," Univ. of Toronto, UTIA Tech. Note 23 (Jul 1958).
53. ElBaroudi, M.Y., "Measurement of Two-Point Correlations of Velocity Near a Circular Cylinder Shedding a Karman Vortex Street," Univ. of Toronto, UTIA Tech. Note 31 (Jan 1960).
54. Keefe, R.T., "An Investigation of the Fluctuating Forces Acting on a Stationary Circular Cylinder in a Subsonic Stream and of the Associated Sound Field," Univ. of Toronto, UTIA Report 76 (1961).

55. Gerrard, J.H., "The Mechanics of the Formation Region of Vortices Behind Bluff Bodies," J. Fluid Mech., Vol. 25, pp. 401-413 (1966).
56. Bloor, M.S. and J.H. Gerrard, "Measurements on Turbulent Vortices in a Cylinder Wake," Proc. Roy. Soc. London, Ser. A294, pp. 319-342 (1966).
57. Griffin, O.M. and S. Ramberg, "The Vortex-Street Wakes of Vibrating Cylinders," J. Fluid Mech., Vol. 66, pp. 553-576 (1974).
58. Koopmann, G.H., "The Vortex Wakes of Vibrating Cylinders at Low Reynolds Numbers," J. Fluid Mech., Vol. 28, pp. 501-512 (1967).
59. Apelt, C.J. et al., "The Effects of Wake Splitter on the Flow Past a Circular Cylinder on the Range  $104 < R < 5 \times 10^4$ ," J. Fluid Mech., Vol. 61, pp. 187-198 (1973).
60. Apelt, C.J. and G.S. West, "The Effects of Wake Splitter Plates on Bluff Body Flow in the Range  $104 < R < 5 \times 10^4$ , Part 2," J. Fluid Mech., Vol 71, pp. 145-161 (1975).
61. Sallet, D.W., "The Lift Force Due to von Karman's Vortex Wake," J. Hydronautics, Vol. 7, pp. 161-165 (1973).
62. Sallet, D.W., "On the Prediction of Flutter Forces," IUTAM Symposium on Flow-Induced Structural Vibrations, Karlsruhe, Germany, Paper B-3 (14-16 Aug 1972).
63. Milne-Thompson, L.M., "Theoretical Hydrodynamics," fourth ed., The Macmillan Co., N.Y. (1960).
64. Ruedy, R., "Vibration of Power Lines in a Steady Wind," Canadian J. of Res., Vol. 13, pp. 82-98 (1935).
65. Chen, Y.N., "Fluctuating Lift Forces of the Karman Vortex Streets on Single Circular Cylinders and in Tube Bundles, Part II, Lift Forces of Single Cylinders," ASME J. of Eng. for Ind., pp. 613-622 (May 1972).
66. Lamb, H., "Hydrodynamics," Dover Publications, N.Y. (1945).
67. Wille, R., "Karman Vortex Streets," Adv. Appl. Mech., Vol. 6, pp. 273-287 (1960).
68. Birkhoff, G., "Formation of Vortex Streets," J. Applied Physics, Vol. 24, pp. 98-103 (1953).

69. Frimberger, R., "Experimentelle Untersuchungen an Kármánschen Wirbelstrassen," Zeitschrift Flugwissenschaft, Vol. 5, pp. 355-359 (1957).
70. Fage, A. and F.C. Johansen, "On the Flow of Air Behind an Inclined Flat Plate of Infinite Span," Proc. Roy. Soc. London, Ser A116, pp. 170-197 (1927).
71. Fage, A. and F.C. Johansen, "The Structure of Vortex Streets," Aeronautical Research Committee, Reports and Memoranda 1143, Vol. 1, Aerodynamics, pp. 124-128 (1928).
72. Gerrard, J.H., "Numerical Computation of the Magnitude and Frequency of the Lift on a Circular Cylinder," Proc. Roy. Soc. London, Ser A118, Vol. 261, pp. 137-162 (1967).
73. Abernathy, F.H. and R.E. Kronauer, "The Formation of Vortex Streets," J. Fluid Mech., Vol. 13, pp. 1-20 (1962).
74. Curle, N., "The Influence of Solid Boundaries Upon Aerodynamic Sound," Proc. Roy. Soc. London, Ser A231, pp. 505-514 (1955).
75. Holle, W., "Frequenz-und Schallstärkemessungen an Hiebtönen," Akustische Zeitschrift, Vol. 3, pp. 321-331 (1938).
76. Gerrard, J.H., "Measurements of the Sound from Circular Cylinders in an Air Stream," Proc. Phys. Soc. London, Ser B68, pp. 453-461 (1955).
77. Guedel, G.A., "Aeolian Tones Produced by Flexible Cables in a Flow Stream," U.S. Marine Engineering Laboratory Report 116/67 (1967).
78. Smith, R.A. et al., "Experiments on the Flow About a Yawed Circular Cylinder," Catholic University of America, Institute of Ocean Sciences and Engineering Report 70-7 (Dec 1970); also J. Basic Eng., pp. 771-776 (Dec 1972).
79. Ramberg, S.E., "The Influence of Yaw Angle Upon the Vortex Wakes of Stationary and Vibrating Cylinders," Ph.D. Thesis, Catholic Univ. of Am. (1978).
80. King, R., "Vortex Excitation of Yawed Circular Cylinders," Trans. ASME J. Fluids Eng., Vol. 99, pp. 495-502 (1977).
81. Maul, D.J. and R.A. Young, "Vortex Shedding from Bluff Bodies in a Shear Flow," J. Fluid Mech., Vol. 60, pp. 401-409 (1973).

82. Yudin, E.Y., "On the Vortex Sound from Rotating Rods," Zhurnal Tekhnicheskoi Fiziki, Vol. 14, No. 9, p. 561 (1944); Translated as NACA TM 1136 (1947).
83. Stowell, E.Z. and A.F. Deming, "Vortex Noise from Rotating Cylindrical Rods," J. Acoust. Soc. Am., Vol. 7, pp. 190-198 (1936).
84. Scheiman, J. et al., "Acoustical Measurements of the Vortex Noise for a Rotating Blade Operating with and without its Shed Wake Blown Downstream," NASA Technical Note TN D-6364 (Aug 1971).
85. Twiggs-Molecey, C.F.M. and W.D. Baines, "Measurements of Unsteady Pressure Distributions Due to Vortex-Induced Vibration of a Cylinder of Triangular Section," IUTAM Symposium on Flow-Induced Structural Vibrations, Karlsruhe, Germany, Paper E-1 (14-16 Aug 1972).
86. Protos, A. et al., "Hydroelastic Forces on Bluff Cylinders," ASME J. Basic Eng. Paper 68-FE-12 (1968).
87. Wilkinson, R.H. et al., "On the Correlation of Dynamic Pressures on the Surface of a Prismatic Bluff Body," IUTAM Symposium on Flow-Induced Structural Vibration, Karlsruhe, Germany, Paper E-4 (14-16 Aug 1972).
88. Vickery, B.J., "Fluctuating Lift and Drag on a Long Cylinder of Square Cross Section in a Smooth and Turbulent Stream," J. Fluid Mech., Vol. 23, p. 481 (1966).
89. Nakamura, Y. and T. Mizota, "Unsteady Lifts and Wakes of Oscillating Rectangular Prisms," ASCE J. Eng. Mech. Div., Vol. 101, No. EM-6, pp. 855-871 (Dec 1975).
90. Bearman, P.W. and D.M. Trueman, "An Investigation of the Flow Around Rectangular Cylinders," The Aeronautical Quarterly, Vol. 23, pp. 229-237 (1972).
91. Rockwell, D.O., "Organized Fluctuations Due to Flow Past a Square Cross Section Cylinder," ASME J. Fluids Eng., Vol. 99, pp. 511-516 (1977).
92. Modi, V.J. and A.K. Dikshit, "Near Wakes of Elliptic Cylinders in Subcritical Flow," AIAA Journal, Vol. 13, pp. 490-496 (1975).

93. Spivack, H.M., "Vortex Frequency and Flow Pattern on the Wake of Two Parallel Cylinders at Varied Spacing Normal to an Air Stream," J. Aero. Sci., pp. 289-301 (Jun 1946).
94. Chen, Y.N., "Flow-Induced Vibration and Noise in Tube-Bank Heat Exchangers Due to von Karman Streets," Trans. ASME, Ser. B, Vol. 90, pp. 134-146 (Feb 1968).
95. Chen, S.S., "Dynamics of Heat Exchanger Tube Banks," J. Fluids Eng. Trans. of ASME, Vol. 99, pp. 462-468 (1977).
96. Chen, Y.N., "Fluctuating Lift Forces of the Karman Vortex Streets on Single Circular Cylinders and in Tube Bundles Part 3 - Lift Forces in Tube Bundles," ASME J. Eng. Ind., Vol. 94, pp. 623-628 (May 1972).
97. Owens, P.R., "Buffeting Excitation of Boiler Tube Vibrations," J. Mech. Eng. Sci., London, Vol. 7, pp. 431-438 (1965).
98. Blevins, R.D., "Fluid Elastic Whirling of a Tube Row," J. Pressure Vessel Technology, Trans. ASME., Ser. J., Vol. 96, pp. 263-267 (1974).
99. Blevins, R.D., "Fluid Elastic Whirling of Tube Rows and Tube Arrays," Trans. ASME J. Fluids Eng., Vol. 99, pp. 457-461 (1977).
100. Blevins, R.D., "Flow-Induced Vibration," Van Nostrand Reinhold, N.Y. (1977).
101. Savkar, S.D., "A Note on the Phase Relationships Involved in the Whirling Instability in Tube Arrays," Trans. ASME J. Fluids Eng., Vol. 99, pp. 727-31 (1977).
102. Savkar, S.D., "A Brief Review of Flow Induced Vibrations of Tube Arrays in Cross-Flow," Trans. ASME J. Fluids Eng., Vol. 99, pp. 517-519 (1977).
103. Scruton, C., "On the Wind-Excited Oscillations of Stacks, Towers, and Masts," Paper 16 International Conference on the Wind Effects on Buildings and Structures, National Physical Laboratory, Middlesex, England (Jun 1963).
104. Weaver, W., "Wind-Induced Vibrations in Antenna Members," J. Eng. Mech. Div., Proc. ASCE, pp. 141-165 (Feb 1961).
105. Bazhenova, L.A., "Characteristics of Vortex Noise Radiated By Rotating Blades," Sov. Phys. Acoust. Vol. 23, pp. 295-297 (1977).

## CHAPTER 6

# STOCHASTIC THEORY OF FLOW-INDUCED VIBRATION AND NOISE

### 6.1 INTRODUCTION

Flow-induced noise from an interaction of a structure and its bounding fluid is related to both the forces of interaction and the vibration of the surface. We have already seen in Chapter 5 that the Aeolian tone intensity is proportional to the mean square force exerted on the fluid by the cylinder. In more complicated fluid-structure interactions the structure is most certainly excited to motion and this motion causes additional sound. In general, it is possible for these two contributions to be equal in magnitude to each other, in which case, they may constructively or destructively interfere, thus, causing a modification of the total sound power radiated. Often, however, in many practical situations one of these contributions will dominate. The determination of which component is dominant may be ascertained, of course, by separate evaluations of the respective powers. A commonly encountered situation is that of boundary-layer induced noise. If the surface is flat and rigid and if the boundary layer is also homogeneous in the plane of the surface, then the direct radiation from the boundary layer is, by Powell's reflection principle, Chapter 2, quadrupole. If the bounding surface is allowed to vibrate in flexure, but not so much as to alter the boundary layer, additional noise will be generated by the vibration of the surface. In many practical occurrences this noise will generally overwhelm the direct quadrupole noise from the boundary layer itself. In another example (Chapter 9), when a lifting surface encounters a gust, the reaction force between the body and the fluid radiates sound. However, given a finite structural impedance, the lifting surface will vibrate and radiate additional sound.

In this chapter general relationships, which describe flow-induced vibration and structural radiation will be derived. These relationships will be fundamental to many of the discussions in the remainder of this monograph. Therefore, it is necessary to express a response variable, e.g., the normal surface vibration velocity  $\vec{n} \cdot \vec{u}$  in Equation (2.73), to an interaction variable, e.g., fluid surface pressure. We define a blocked surface pressure as that which is generated by the fluid on the surface, but with the surface rigid. We will assume, in this chapter that whatever surface motion occurs, it does not influence the fluid dynamics. This assumption is essential to keep the analysis straightforward and it is physically valid for most fluid-structure interactions except those involving vortex shedding



and hydrofoil singing discussed in Chapters 9 and 10. Furthermore, we will assume that the response of the structure is linear, i.e., the response velocity is linearly proportional to the driving force. The structure, unless it is highly damped (we will define "highly" in due course), will be assumed to respond in its "normal" modes of vibration. Therefore, given a known description of the blocked fluid characteristics on the surface, we ask the question: what surface motion will result, and what acoustic radiation will this motion induce?

Because the subject of fluid-structure interaction is complex and many-faceted, it is expedient, at this point to interface with several well-known texts. The analysis that will be presented in this chapter is to be considered somewhat introductory and only the results that are necessary to interface with these references will be developed. The problems of structural acoustics can be approached in varying levels of approximation. The response of each structural mode is formally written down as a blocked force coefficient divided by the impedance of the mode (see Lin,<sup>1\*</sup> Crandall,<sup>2,3</sup> Cremer, Heckl, and Ungar,<sup>4</sup> and Skudrzyk<sup>5</sup>) then the total response of the structure is found by a summation of the responses of the individual modes. In this chapter the impedance of a mode we are interested in is defined as the ratio of a complex force applied normal to the surface divided by the normal response velocity; i.e., in the notation of Section 2.4,  $z = \vec{n} \cdot \vec{F} / \vec{n} \cdot \vec{u} = \ell_i F_i / \ell_i u_i$ . Reference 1 extensively examines the statistical formulations for both stationary and nonstationary random driving fields as well as linear and nonlinear vibrating systems; References 2 and 3 are collections of contributions by experts and include discussions of vibration caused by jet noise and turbulent boundary layer pressures. Reference 4 emphasizes the statistical description of structural vibration (including the use of damping treatments) for both local and distributed force excitation, Reference 5 emphasizes more the single mode-character of vibrating systems. Once the vibration velocity is known, the acoustic radiation can be determined either for each mode,<sup>6</sup> or for the overall response using an average radiation coefficient.<sup>7,8</sup> Basically, the far-field acoustic power is equal to the response vibration velocity times a radiation impedance. Junger and Feit<sup>6</sup> present the general methods of calculating the radiated fields for known vibration distributions on plates and shells. Although these are deterministic analytical problems, the methods can be used to derive the radiation impedance for use in statistical analyses. Maidanik<sup>7,8</sup> provides

---

\*A complete listing of references is given on page 619.

radiation impedances for individual modes of essentially flat rectangular panel members but he also shows how to determine average impedances which are averaged over a multiplicity of modes. Lyon,<sup>9</sup> and Lyon and Maidanik<sup>10</sup> show how to avoid considering the responses of individual modes by using energy balances. Here the kinetic energy of response is assumed to be shared equally by all modes of vibration in the structure and the power dissipated by the damping in excited modes is equal to input power from the fluid excitation. Because the dissipated power is proportional to the time and space-averaged mean square vibration velocity, the average vibration level of complex structures can be estimated once the input power is known. Radiated power is proportional to the product of the mean-square vibration velocity and the average radiation impedance of the modes. This approach, known as statistical energy analysis (or SEA), is successful for highly complex structures for which many modes are excited by the flow. Analysis of individual modes of structures is necessary when considering narrow enough frequency bands, so that only a few modes are concerned.

## 6.2 RESPONSE OF SINGLE-DEGREE-OF-FREEDOM SYSTEMS TO TEMPORALLY RANDOM EXCITATION

Consider the motion of a spring-mass system that is illustrated in Figure 6.1. The mass  $M$  is excited to a displacement  $x(t)$  by a force  $f(t)$ . The force on the

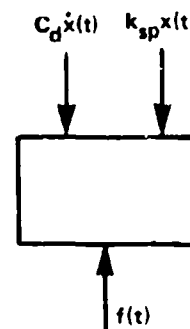
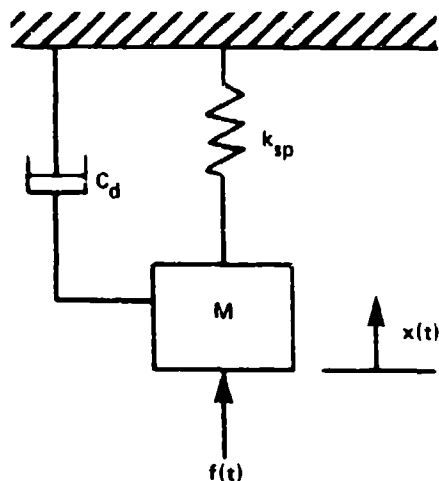


Figure 6.1a - Mass-Spring System

Figure 6.1b - Free-Body Diagram

Figure 6.1 - Illustration of a Single Degree-of-Freedom Linear Oscillator

mass by the spring is opposite  $f(t)$  and equals  $k_{sp} x(t)$ , where  $k_{sp}$  is the spring constant. The damping is assumed to be linear and viscous so that the damping force of the "dash pot" is  $C_d(dx(t)/dt)$ . The force balance on the mass, which leads to its acceleration,  $d^2x(t)/dt^2$ , is

$$\frac{M d^2 x(t)}{dt^2} = f(t) - k_{sp} x(t) - C_d \frac{dx(t)}{dt}$$

thus,

$$M\ddot{x}(t) + C_d \dot{x}(t) + k_{sp} x(t) = F(t) \quad (6.1)$$

where the dot denotes the time differentiation.

Because the force is random in time, we formally introduce the Fourier transform pair

$$X(\omega) = \frac{1}{2\pi} \int_{-\infty}^{\infty} x(t) e^{i\omega t} dt \quad (6.2)$$

and

$$x(t) = \int_{-\infty}^{\infty} X(\omega) e^{-i\omega t} d\omega$$

in order to consider the steady-state vibration. (If we were interested in transient motion, we would necessarily have to introduce initial conditions and then use the Laplace transform. Here we assume that the motion has lasted a number of cycles so that transients have diminished.) Substitution of Equation (6.2) into (6.1) leads to

$$[-M\omega^2 - iC_d\omega + k_{sp}] X(\omega) = F(\omega) \quad (6.3)$$

or

$$\frac{-i\omega X(\omega)}{F(\omega)} = \frac{+i\omega}{M(\omega_o^2 - \omega^2 - i\eta\omega_o\omega)} \quad (6.4)$$

where

$$\omega_o = \left( \frac{k_{sp}}{M} \right)^{1/2} \quad (6.5)$$

is the resonance frequency. The loss factor is defined as

$$\eta\omega_o = \frac{C_d}{M} \quad (6.6)$$

The Fourier transform of the velocity of the mass is  $-i\omega X(\omega)$ ; the ratio of the velocity to the force is the admittance (the reciprocal of the impedance) of the spring-mass system. When  $\eta \ll 1$  and the frequency of the force coincides with the resonance frequency, the velocity is largest.

The spectral densities of the force and velocity are simply related. Using the definitions of the generalized Fourier transform and the autospectral density developed in Equations (2.104), (2.124a), or (3.39), the relationship between the force and velocity spectra is

$$\frac{\phi_{vv}(\omega)}{\phi_F(\omega)} = \frac{\omega^2}{M^2 \left[ (\omega_o^2 - \omega^2)^2 + \eta^2 \omega_o^2 \omega^2 \right]} \quad (6.7)$$

where  $\phi_{vv}(\omega) = \omega^2 \phi_{xx}(\omega)$ . The mean-square velocity is found by integrating over all frequencies:

$$\overline{v^2} = \int_{-\infty}^{\infty} \phi_{vv}(\omega) d\omega \quad (6.8)$$

The maximum response occurs when  $\omega = \pm \omega_0$  and it is controlled by damping, i.e., for frequencies slightly above and below  $\omega_0$  (for  $\pm\omega = \omega_0 \pm \omega_0 \eta/2$ ),  $\phi_{vv}(\omega) = 1/2 \phi_{vv}(\omega_0) = 1/2 M^2 \eta^2$  as illustrated in Figure 6.2. Figure 6.2 illustrates this behavior of Equation 6.7, but in a dimensionless form that also represents the acceleration response of the mass. At low frequencies,  $\omega \ll \omega_0$ , the acceleration response is proportional to  $\omega^4$ ; because  $\phi_{aa}(\omega)$ , the acceleration spectrum, is equal to  $\omega^2 \phi_{vv}(\omega) = \omega^4 \phi_{xx}(\omega)$ ,

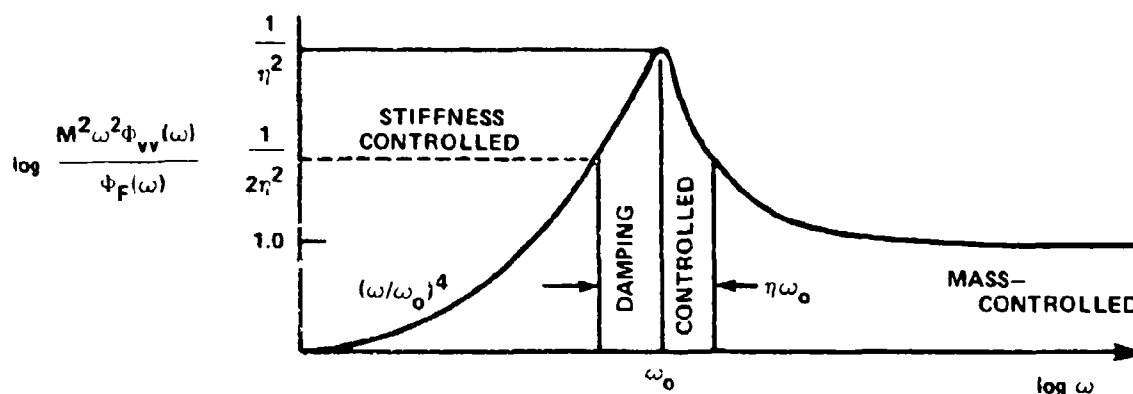


Figure 6.2 - The Magnitude Squared of the Admittance of a Simple Harmonic Oscillator Consisting of Mass, Linear Spring, and Viscous Damping

and because  $\phi_{xx}(\omega) = k_{sp}^{-2} \phi_{FF}(\omega)$  when  $M \phi_{aa}(\omega) \ll k_{sp}^2 \phi_{xx}(\omega)$  (i.e.,  $M \ddot{x} \ll k_{sp} x$ ) this response is stiffness-controlled. On the other hand, when  $M \phi_{aa} \gg k_{sp}^2 \phi_{xx}(\omega)$ , i.e.,  $\omega \gg \omega_0$ , the response is determined by the inertia of the mass. In the vicinity of the resonance, the response is sensitive to the damping in the system as represented by the loss factor  $\eta$ . The quality factor of the system  $Q$  is

$$Q = \frac{1}{\eta} \quad (6.9)$$

and it is a measure of the ratio of resonant vibration to the mass-controlled vibration of the system; while the fraction of critical damping is defined

$$\frac{c_d}{c_o} = \frac{1}{2\eta} \quad (6.10)$$

The critical damping is that required to just prevent oscillatory motion. For light damping,  $\eta \ll 1$  (typically,  $\eta$  lies between  $10^{-3}$  and  $10^{-2}$  unless special lossy treatments are applied to the structure) the acceleration response to a broadband force is dominated by the peak in the frequency range  $\omega_o - \omega_o \eta/2 < \omega < \omega_o + \omega_o \eta/2$ . The mean-square response is found by integrating over all frequencies as in Equation (6.8); thus,

$$\begin{aligned} \overline{V^2} &= 2 \frac{\omega_o^2 \phi_F(\omega_o)}{M^2 \eta^2 \omega_o^4} \left( \frac{\pi}{2} \right) \eta \omega_o \\ \overline{V^2} &= \frac{\pi \phi_F(\omega_o)}{M^2 \eta \omega_o} \end{aligned} \quad (6.11)$$

The first factor of two arises from the double peaks at  $\omega = \pm \omega_o$  and the effective bandwidth of the resonance is  $(\pi/2) \eta \omega_o$ , thus, we require that the bandwidth of the force  $(\delta\omega)_F$  satisfies

$$(\delta\omega)_F \gg \frac{1}{2} \pi \eta \omega_o \quad (6.12)$$

It is instructive to note that the time-average power dissipated  $P_D$  in the system in a time  $T \gg 1/\omega_o$  is just equal to the power applied to the mass  $P_{in}$ , i.e.,

$$P_{in} = \frac{1}{T} \int_{-T/2}^{T/2} f(t) \dot{x}(t) dt = \overline{f(t) V(t)} \quad (6.13)$$

or

$$P_D = P_{in} \quad (6.14)$$

For the single mode of vibration that we have here, the dissipated power

$$P_D = c_d \overline{v^2}$$

which is rewritten in term of the mass and loss factor

$$P_D = M \eta \omega_0 \overline{v^2} \quad (6.15)$$

These relationships can be seen by multiplying Equation (6.1) by  $\dot{x}(t)$  and integrating. Since the motion is simple harmonic, i.e.

$$x(t) = A \cos \omega_0 t + B \sin \omega_0 t \quad (6.16)$$

we have  $\overline{x(t)\dot{x}(t)} = \overline{\ddot{x}(t)x(t)} = 0$ . Using Equation (6.6) to eliminate the damping coefficient  $c$  and combining Equations (6.14) and (6.15) we have a simple expression for the steady state mean-square velocity

$$\overline{v^2} = \frac{P_{in}}{M \eta \omega_0} \quad (6.17)$$

With the initial conditions  $x(t=0) = x_0$  and  $\dot{x}(t=0) = 0$  the resulting vibration will have the decaying sinusoid

$$x(t) = x_0 \exp(-\eta \omega_0 t/2) \cos \omega t$$

for light damping,  $\eta \ll 1$ .

Now, we see that if we know either the average input power, or the spectrum of the oscillating force we can find the mean-square response. However, although Equations (6.11) and (6.17) differ in functional form, neither has a clear advantage if the calculation of mean-square response to a flat excitation spectrum of a single degree of freedom system is desired. They simply differ in the descriptor used for the excitation variable. Statistical energy analysis which is a generalization of Equation (6.17) is a direct and useful tool for estimating mean square response of complex systems of many degrees of freedom; the development of this method is offered

by Lyon<sup>9,11</sup> and Lyon and Maidanik,<sup>10</sup> with further discussions by Smith and Lyon,<sup>12</sup> Fahy,<sup>13</sup> and Maidanik.<sup>14</sup> Equation (6.17) is just the simplest of many more-general relationships. Note that in developing Equation (6.17), we assumed that  $\Phi_f(\omega)$  is flat compared to the impedance function; this is the only limitation to using the relationship for the simple oscillator.

We will now consider the simple vibrating plate excited by the stochastic force field to see the extent to which these notions apply. We shall see, in fact, that Equation (6.17) will apply to this case as well.

## 6.3 GENERAL FEATURES OF STRUCTURES DRIVEN BY RANDOMLY-DISTRIBUTED PRESSURE FIELDS

### 6.3.1 Modal Velocities and Excitation Functions

The method of normal modal analysis used in this subsection has been developed and used in a number of references, among them are References 15 through 27; a text on the method is that of Lin.<sup>1</sup> A motion variable for the vibrating surface is expanded in its normal modes; each mode describes a condition of resonance. The vibration of the surface is, therefore, regarded as a summation of the contributions of the complete set of these modes. The equation of motion\* for the flexural displacement directed normal to the surface  $\xi = \xi(\vec{y}, t)$  is

$$m_s \ddot{\xi} + C \dot{\xi} + L(\xi) = -p(\vec{y}, t) \quad (6.18)$$

where  $m_s$  = mass per unit area of the surface

$C$  = viscous damping coefficient

$p(\vec{y}, t)$  = fluctuating load per unit area which is assumed to be distributed over the surface of the structure

The function  $L(\xi)$  is a linear differential operator specific to the type of structure.<sup>28,29</sup>

$$\begin{aligned} L(\xi) &= -T_e \nabla^2 \xi && \text{membrane of uniform tension per unit length, } T_e \\ &= D_s \nabla^4 \xi && \text{thin plate of uniform stiffness, } D_s \end{aligned}$$

where

$$\nabla^4 \xi = \frac{\partial^4 \xi}{\partial y_1^4} + 2 \frac{\partial^4 \xi}{\partial y_1^2 \partial y_2^2} + \frac{\partial^4 \xi}{\partial y_2^4}$$

\*The sign conventions must be respected:  $\xi$  is positive in the up direction, but  $p$  is directed downward; therefore the minus sign is used.



$$L(\xi) = T_e \frac{\partial^2 \xi}{\partial y_1^2} \quad \text{string of uniform tension per unit length, } T_e$$

$$= D_s \frac{\partial^4 \xi}{\partial y_1^4} \quad \text{beam of uniform stiffness, } D_s \text{ the "Bernoulli-Euler" beam.}$$

The bending stiffness for flat plates is

$$D_s = Eh^3/12(1-\nu_p^2) \quad (6.19)$$

and for beams it is

$$D_s = Eh^3/12$$

where  $E$  = Young's modulus

$h$  = thickness of the plate or beam

$\nu_p$  = Poisson's ratio

The radius of gyration

$$\kappa = \frac{h}{12^{1/2}} \quad (6.20)$$

is also used. For structures with boundaries, the flexural displacement may be expanded in terms of its normal modes  $\psi_n(\vec{y})$

$$\xi = \sum_{n=1}^{\infty} A_n \psi_n(\vec{y}) g_n(t) \quad (6.21)$$

where the subscript  $n$  is used here to simply order the progression of modes.\* If the  $L(\xi)$  operator is fourth-order

$$L(\psi_n(\vec{y})) = D_s k_n^4 \psi_n(\vec{y}) \quad (6.22)$$

---

\*For two-dimensional structures, the double index  $(m,n)$  would replace the single index for  $m$  order along  $y_1$  and  $n$  order along  $y_3$ . For a one-dimensional system, a string, or a beam, the single order  $n$  would be retained.

while the second order operators give

$$L(\psi_n(\vec{y})) = T_e k_n^2 \psi_n(\vec{y}) \quad (6.23)$$

The parameter  $k_n$  is the wave number of the spatial distribution of  $\xi$ ; it is determined by the boundary conditions applied to the surface; an example will be given in Section 6.4. The functions  $\psi_n(\vec{y})$  are the eigenfunctions of the operator; they are the normal modes of the structural vibration and they also depend upon the geometry of the structure and its boundary conditions. The coordinate  $\vec{y}$  is in the plane of the structure and the displacement  $\xi$  is normal to that plane. The eigenfunction  $\psi_n(\vec{y})$  we will make dimensionless (although there is no universal opinion in this regard) and normalized according to

$$\iint_A \psi_n(\vec{y}) \psi_m(\vec{y}) d^2\vec{y} = A_p \delta_{mn} \quad (6.24)$$

where  $\delta_{mn} = 1$  when  $m = n$  and  $\delta_{mn} = 0$  when  $m \neq n$  if the modes are uncoupled. Solutions of  $L(\xi)$  are not necessarily uncoupled, but in many cases the solutions may be expanded into a series of orthogonal functions which represent the mode shapes of fundamental modes that would exist if the structure were in a vacuum, i.e., without fluid loading. Examples:  $\psi_m(\vec{y})$  will be given in Section 6.4.

The displacement, as presented in Equation (6.23) also includes an amplitude function  $a_n$  and a time function  $g_n(t)$ . The time behavior may well be stochastic and representable as a generalized Fourier transform as used in Section 6.2. Equation (6.21) is similar to Equation (6.1) except that the structural dynamics provide the stiffness (or potential energy). This stiffness is dependent upon not only the properties  $D_s$  and  $T_e$ , but also upon the wavelength of vibration and the geometry of the structure. For example, through the harmonic operator  $\nabla^2 \xi$ , some modes of a curved structure will have a greater stiffness than modes of a flat structure.

The load per unit area is applied normal to the plane of the structure; it may consist of a superposition of locally applied forces, random (in space and time) pressure fields, and fluid back reaction to the motion  $\xi$ . The fluid back reaction

included in  $p(\vec{y}, t)$  can be viscous (damping), inertial (added mass), and acoustic radiation (appearing as a damping because it represents energy irradiated from the plate). In more complicated situations in which multiple structures enclose a fluid, the fluid reaction on each structure is dependent upon the motions of adjacent structures in which cases the whole fluid-structure system becomes coupled, see, e.g., Strawderman,<sup>30</sup> Obermeyer,<sup>31</sup> Arnold,<sup>32</sup> and especially White and Powell<sup>21</sup> for general treatments. Only the single structure and the unbounded acoustic medium will be considered in this chapter. The nature of the fluid back reaction will be discussed in Section 6.6.

In the case of an excited plate or beam, we substitute Equations (6.21) and (6.22) into Equation (6.18) to obtain

$$\sum_n [m_s \ddot{g}_n(t) + C_d \dot{g}_n(t) + k_n^4 D_s g_n(t)] a_n \psi_n(\vec{y}) = -p(\vec{y}, t)$$

where  $C_d$  is a damping coefficient and the wave number  $k_n$  and eigenfunction  $\psi_n(\vec{y})$  are determined by the boundary conditions. Multiplying both sides of the equation by  $\psi_n(\vec{y})$  and integrating over the panel area we obtain

$$\begin{aligned} [m_s \ddot{g}_n(t) + C_d \dot{g}_n(t) + k_n^4 D_s g_n(t)] a_n &= \frac{-1}{A_p} \iint_{A_p} p(\vec{y}, t) \psi_n(\vec{y}) d^2 y \\ &= -P_n(t) \end{aligned} \quad (6.25)$$

and similarly for second order operators for which  $k_n^2 T_e$  replaces  $k_n^4 D_s$ . Now, Equation (6.25) is in the form of Equation (6.1), where  $a_n g_n(t)$  is the modal displacement and  $p_n(t) \cdot A_p$  is the modal force. Thus motion of the uniform structure can be thought of as comprised of a set of motions and oscillators, all of which respond simultaneously and independently if the modes are uncoupled.

If the motion is free,  $p_n(t) = 0$ , and undamped,  $\eta = 0$ , then Equation (6.25) reduces to

$$\ddot{g}_n(t) + \frac{k_n^2 \eta}{m_s} g_n(t) = 0$$

and  $g_n(t)$  has the form

$$g_n(t) = e^{-i\omega_n t}$$

where  $\omega_n$  satisfies

$$\omega_n^2 = k_n^4 \frac{D_s}{m_s} \quad (6.26)$$

and is the resonance frequency of the  $n^{\text{th}}$  mode of vibration. Similarly, for the second order operator of springs and membranes,  $k_n^2 T_e$  replaces  $k_n^4 D_s$ . In the above there will be a set of  $\omega_n$  corresponding to each  $k_n$  allowed by the boundary conditions on the structure.

### 6.3.2 Vibration of Effectively Infinite Surfaces; The Infinite Plate

A wave-mechanical interpretation of the motion can be seen clearly in the case of free-bending waves on an infinite plate. The displacement is of the form

$$\xi = e^{i(\vec{k} \cdot \vec{y} - \omega t)}$$

which represents waves traveling on the plate in the direction  $\vec{k}/|\vec{k}|$  as illustrated in Figure 6.3. Substituting this function into Equation (6.18) we find

$$(-m_s \omega^2 - iC_d \omega + D_s k^4) e^{i(\vec{k} \cdot \vec{y} - \omega t)} = 0$$

for the free traveling waves which exist very far from the source of wave excitation. For the case of light damping we can neglect the term  $iC_d \omega$  leaving the criterion that the wave number of the waves is related to the frequency by

$$k^4 = k_p^4 = \omega^2 \frac{m_s}{D_s} \quad (6.27)$$

The phase speed of the bending waves is defined as

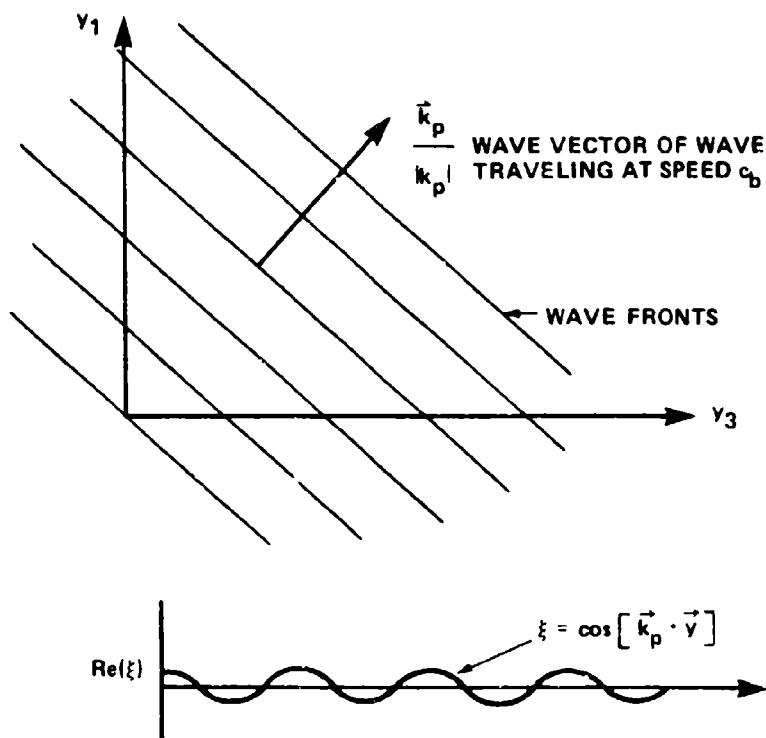


Figure 6.3 - Amplitude of Straight-Crested Bending Waves on a Flat Plate  
The Function that is Illustrated,  $\text{Re}(\xi)$ , Represents the Physically Realizable Amplitude

$$c_b = \frac{\omega}{k} = k_p \left( \frac{D_s}{m_s} \right)^{1/2} \quad (6.28)$$

which leaves

$$\xi \sim \exp \left\{ i |k_p| \left[ \frac{\vec{k}_p \cdot \vec{y}}{|k_p|} - c_b t \right] \right\}$$

The term in brackets defines the phase fronts of the traveling waves.

The magnitude of the wave vector  $|k_p|$  is related to the wavelength by

$$|k_p| = \frac{2\pi}{\lambda_b}$$

and Equation (6.28) shows that the shorter bending waves travel faster than the longer bending waves. Figure 6.4 illustrates the behavior of  $c_b$  with  $k_p$ . For membranes and strings, the operator  $L(\xi)$  is second order which gives rise to a  $k_p^2$  rather than a  $k_p^4$  in Equation (6.27). Thus for membranes, the phase speed is

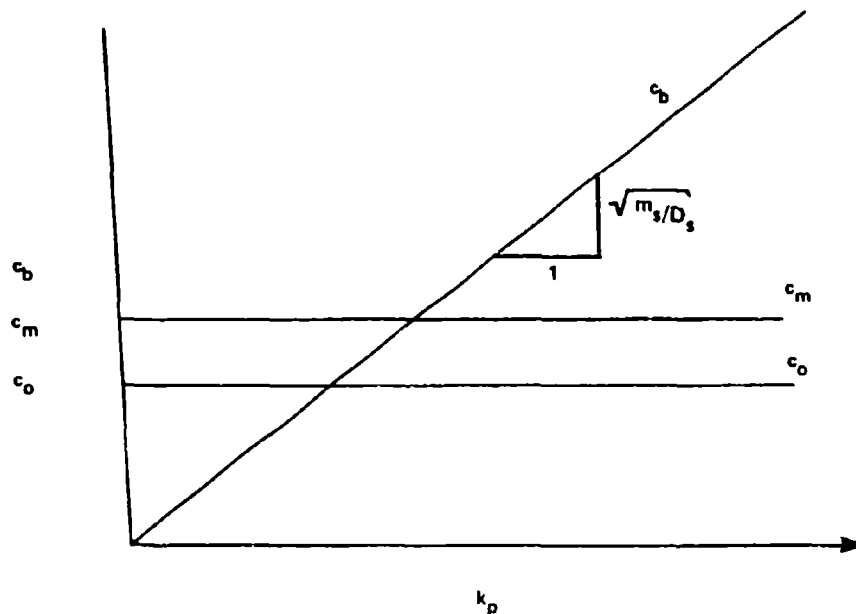


Figure 6.4 - Phase Speeds as a Function of Wave Number for Bending Waves on Plates  $c_b$ , Membranes  $c_m$ , and Acoustic (Dilational) Waves  $c_o$ .

$$c_m = \left( \frac{T_B}{m_s} \right)^{1/2} \quad (6.29)$$

which is independent of wave number. Membrane waves are similar to dilational acoustic waves in this respect.

Another facet to be noted from Equations (6.28) and (6.29) is that when the structure is stiffened by increasing  $D_s$  or stretched to increase  $T_e$ , the bending wave speeds are increased. We shall see in Section 6.5 that the wave number dependence of flexural waves of plates (these are called dispersive waves) complicates the acoustic radiation phenomenon, because as frequency is increased, the bending waves travel faster with speeds which may exceed the speed of sound in the adjacent fluid.

The motion of finite panels is a superposition of free-bending waves. Depending upon the shape of the panel and the manner in which its boundaries are constrained, the superimposed waves will reinforce or interfere. Thus, only at preferred frequencies will there be a large group of waves reinforced with a discrete value of  $k_p = k_n$ . At some other frequencies these waves will interfere. The frequencies of reinforcement are  $\omega_n$  and they are related to the values of  $k_n$  by Equation (6.28). The functions  $\psi_n(\vec{y})$  describe the spatial variation of amplitude for the reinforcing wave systems and they are also called mode shapes of the vibrating plate.

### 6.3.3 Random Excitation of Single Mode Oscillators

Analysis for each mode of the finite plate proceeds along lines similar to those in Section 6.2. It is convenient, however, to deal with the velocity of the mode. Analogously to the derivation of Equations (6.4) and (6.10) we introduce the flexural velocity analog to Equation (6.23)

$$V(\vec{y}, t) = \int_{-\infty}^{\infty} V(\omega, \vec{y}) e^{-i\omega t} d\omega \quad (6.30)$$

and

$$V(\omega, \vec{y}) = \sum_n V_n(\omega) \psi_n(\vec{y}) \quad (6.31)$$

The autospectral density of the velocity can be described in terms of the autospectral density of surface pressure and impedance of the surface following the methods leading to Equation (6.10). From Equation (6.31) the velocity spectral density is just a summation over the  $n$  modes. Assuming that the modes are uncoupled and described by an orthogonal set of  $\psi_n(\vec{y})$  (see Equation (6.24)) we have

$$\begin{aligned} \phi_{VV}(\omega) &= \sum_n 2\pi \frac{|V_n(\omega)|^2}{T} \\ &= \sum_n \phi_n(\omega) \end{aligned} \quad (6.32)$$

For the  $n^{\text{th}}$  mode of a vibrating structure, Equation (6.25) gives

$$V_n(\omega) = \frac{+i\omega P_n(\omega)}{-m_s \omega^2 - i m_s \eta_s \omega + \omega_n^2 m_s} \quad (6.33)$$

where  $\eta_s$  is the mode-dependent structural loss factor that replaces  $C_d/\omega_n$  and where  $P_n(\omega)$  is the Fourier transform of the  $P_n(t)$  of Equation (6.25). The spectral density of the mode  $n$  of the panel velocity is, using Equation (2.124),

$$\phi_n(\omega) = \frac{\omega^2 \phi_{p_n}(\omega)}{m_s^2 \left\{ (\omega_n^2 - \omega^2)^2 + \eta_s^2 \omega_n^2 \omega^2 \right\}} \quad (6.34)$$

This relationship is general, as long as there is negligible modal coupling. If there is a case of fluid loading that is not negligible, it may still be used to approximate the response,  $m_s$  should be increased by the added mass and  $\eta_s$  should be increased by the radiation loss factor  $\eta_r$ , so that it is replaced by a total loss factor

$$\eta_T = \eta_s + \eta_r \quad (6.35)$$

see Section 6.6.2. The simple approximation afforded by Equation (6.34) does not apply in cases of heavy fluid loading if such loading strongly couples the invacuo modes; see Section 6.5.2.

The function  $\phi_{p_n}(\omega)$  is the autospectral density of the modal pressure  $P_n(t)$  that was introduced in Equation (6.25). Physically, it expresses the degree with which the excitation field couples to the structure. As shown by the integral that defines  $P_n(t)$ , this coupling is spatial, i.e., it depends upon the spatial phase of the driving force relative to the spatial phase of the vibration mode. A simple example would be for  $p(y,t) = g(t) \sin 2k_n y_1$  and  $\psi_n(y) = \sin k_n y_1$ , then  $P_n(t)$  would be identically zero. The modal pressure for this mode would be greatest when  $p(y_1,t) = g(t) \sin k_n y_1$  because the spatial phases would exactly coincide. It is necessary to express the autospectrum of the modal pressure in terms of the



statistics of the surface pressure induced on the plate by the flow. Defining the autocorrelation

$$\tilde{R}_{p_n p_n}(\tau) = \langle p_n(t+\tau) p_n(t) \rangle \quad (6.36)$$

and using the definition of  $p_n(t)$  given in Equation (6.25), we have

$$\tilde{R}_{p_n p_n}(\tau) = \frac{1}{A_p^2} \iint_{A_p} \cdot \iint_{A_p} \overline{p^2} \tilde{R}_{pp}(\vec{y}_1 - \vec{y}_2, \tau) \psi_n(\vec{y}_1) \psi_n(\vec{y}_2) d\vec{y}_2 d\vec{y}_1 \quad (6.37)$$

The wave-number-frequency spectrum of the surface pressure is related to its correlation function by

$$\overline{p^2} \tilde{R}_{pp}(\vec{r}, \tau) = \int_{-\infty}^{\infty} \int_{-\infty}^{\infty} e^{+i(\vec{k}\vec{r} - \omega\tau)} \phi_p(\vec{k}, \omega) d\vec{k} d\omega \quad (6.38)$$

in the case of the correlation being spatially homogeneous in the sense of Equations (2.129) or (3.45). Modal shape functions are also defined

$$s_n(\vec{k}) = \iint_{A_p} e^{-i\vec{k} \cdot \vec{y}} \psi_n(\vec{y}) d\vec{y} \quad (6.39)$$

Substitution of Equations (6.38) and (6.39) into Equation (6.37) leaves the auto-spectrum of the modal pressure as a generalization of Equation (2.133)

$$\phi_{p_n}(\omega) = \frac{1}{A_p^2} \int_{-\infty}^{\infty} \int_{-\infty}^{\infty} \phi_p(\vec{k}, \omega) |s_n(\vec{k})|^2 d\vec{k} \quad (6.40a)$$

where the normalization condition, Equation (6.24), is

$$\int_{-\infty}^{\infty} \int |S_n(\vec{k})|^2 d\vec{k} = (2\pi)^2 A_p \quad (6.40b)$$

Equations (6.37) and (6.40a) represent generalizations of Parseval's theorem.

Equations (6.34), (6.38), and (6.40a) provide the cardinal results of this section and these results may be further used to derive general input functions. As long as the mode shape function  $\psi_n(\vec{y})$  and the statistical properties of the excitation are known, the velocity spectrum of the mode can be calculated using Equation (6.34). The mean-square velocity of mode  $n$  at frequency  $\omega_n$  can be determined from Equations (6.14), (6.24) and (6.31) as

$$\overline{v_n^2} = \frac{1}{T} \int_{-T/2}^{T/2} dt \frac{1}{A_p} \iint_{A_p} v_n^2(\omega_n, \vec{y}) |\psi_n(\vec{y})|^2 d^2y$$

so that

$$\overline{v_n^2} = \frac{\pi A_p^2 \phi_{p_n}(\omega_n)}{M^2 \eta_{s_n} \omega_n} \quad (6.41)$$

where  $M = m_{s_p} A_p$ . The velocity is also related to the time-average input power to the mode  $(P_{in})_n$ , by Equation (6.17), rewritten here to apply to a single mode

$$\overline{v_n^2} = \frac{(P_{in})_n}{M \eta_{s_n} \omega_n} \quad (6.42)$$

and the restriction of a flat spectrum  $\phi_{p_n}(\omega)$  must be maintained.

By equating Equations (6.41) and (6.42) we obtain an explicit relationship for the time-average input power into the mode in terms of the statistics of the exciting pressure field, i.e.,

$$(P_{in})_n = \frac{\pi A_p^2 \phi_{p_n}(\omega_n)}{M} \quad (6.43)$$

The function  $\pi A_p^2 \phi_{p_n}(\omega)$  is the spectral density of the mean-square modal force applied to the  $n^{th}$  mode, and it is flat over the frequency band  $\Delta\omega = \eta_{s_n} \omega_n$ .

In comparing Equations (6.41) through (6.43) we see that the average kinetic energy of mode  $MV_n^2$  is determined by the resonant motion in the frequency band  $\eta_s \omega_n$ , and that the power into the mode depends upon the spectrum level of the modal force  $A_p^2 \Phi_p(\omega)$  and the mass of the structure.

### 6.3.4 Response Estimates for Structures of Many Modes

In some practical circumstances the response parameter of interest involves large groups of modes of a structure rather than the response of a single mode. This interest would come from a need for a broadband rather than a narrowband description. Prior to actually estimating broad band response of a structure we must first find a descriptor of the number of structural modes resonant in a frequency band. Recall from Equation (6.26) that the uncoupled modes of a structure (either one- or two-dimensional, membrane or plate) will resonate at specific frequencies  $\omega_n$  which are uniquely determined by a discrete set of one- or two-dimensional wave numbers  $k_n$ . These wave numbers are roughly determined by the number of flexural wavelengths that will "fit" within the boundary of the structure. Furthermore, the mode-shape of the vibration will be dependent upon both the geometry of the boundary and the structural constraint that it applies to the boundary, i.e., clamping, pinning, etc. We will be considering the influence of boundary conditions on the shape functions  $S_n(\vec{k})$  in the next section. To illustrate the method of ordering and numbering modes, we will examine the invacuo modal patterns of a simply supported rectangular panel in Figure 6.5. The order of a mode of vibration on a rectangular panel is given by the number of half-wavelengths that can "fit" within its boundaries. In the two diagrams shown, the 1,3 mode has 1 half-wave in the 1-direction and 3 half-waves in the 3-direction. The fundamental would have a half-wave in each direction, and the wave number ordering involves two indices so that  $k_{mn}$  replaces  $k_n$  in our discussion. The wave numbers for this 1,3 mode are  $k_1 = 2\pi/\lambda_1 = \pi/L_1$  and  $k_3 = (2\pi/(2L_3/3)) = 3\pi/L_3$ . Letting  $m$  be the mode order in the 1-direction and  $n$  be the mode order in the 3-direction we have

$$\begin{aligned} k_{mn}^2 &= k_m^2 + k_n^2 \\ &= \left( \frac{m\pi}{L_1} \right)^2 + \left( \frac{n\pi}{L_3} \right)^2 \end{aligned} \quad (6.44)$$

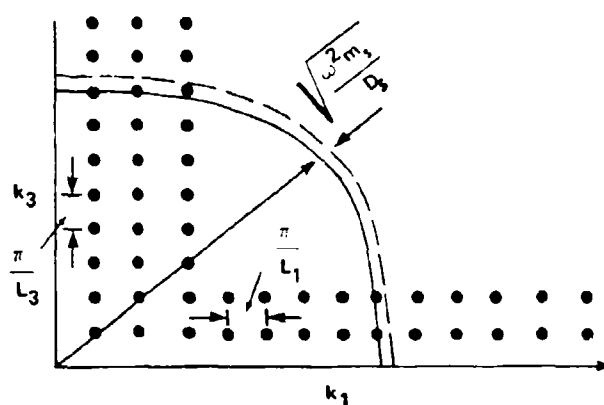


Figure 6.5a - Wave Number Lattice for a Simply Supported Rectangular Plate

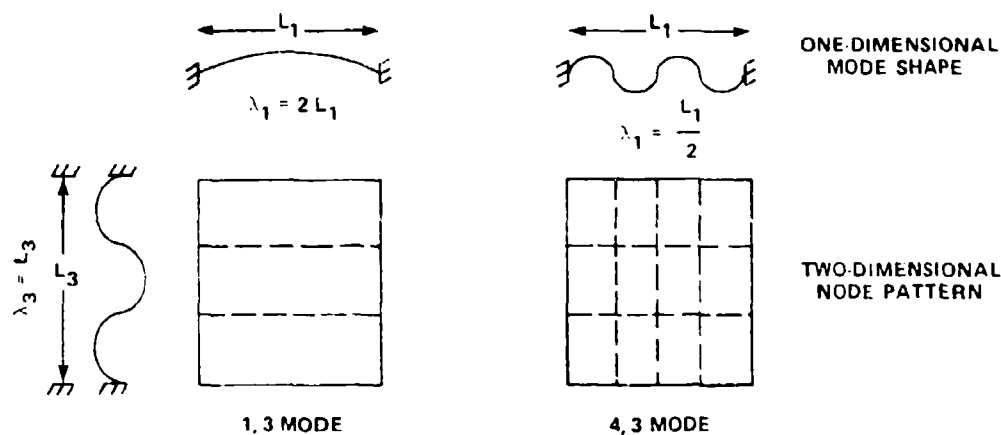


Figure 6.5b - Modal Patterns and Mode Shapes in the 1- and 3-Directions

Figure 6.5 - Mode Orders of Structural Vibration of Rectangular Panels which are Simply Supported

for a resultant wave number of the  $(m,n)$  mode. That the  $k_m$  and  $k_n$  combine quadratically for a rectangular panel can be seen by reference to the form of  $L(\xi)$  in Equation (6.22). If the flexural displacement of the panel or membrane is given by

$$\xi = \psi_m(y_1) \psi_n(y_3)$$

where  $\psi_m(y_1)$  and  $\psi_n(y_3)$  are harmonic functions in  $k_m y_1$  and  $k_n y_3$ , then for membranes, the Laplacian of  $\xi$  becomes

$$\begin{aligned} \nabla^2 \xi &= k_m^2 \psi_m(y_1) \psi_n(y_3) + k_n^2 \psi_m(y_1) \psi_n(y_3) \\ &= (k_m^2 + k_n^2) \psi_m(y_1) \psi_n(y_3) \end{aligned}$$

because  $\partial \xi / \partial y_1 = \psi'_m(y_1) \psi_n(y_3) = k_m \psi_m(y_1) \psi_n(y_3)$ . For panels, the biharmonic operator applies and we have

$$\nabla^4 \xi = \frac{\partial^4 \xi}{\partial y_1^4} + 2 \frac{\partial^2 \xi}{\partial y_1^2} \frac{\partial^2 \xi}{\partial y_3^2} + \frac{\partial^4 \xi}{\partial y_3^4}$$

therefore,  $\nabla^4 \xi = (k_m^2 + k_n^2)^2 \psi_m(y_1) \psi_n(y_3)$ . Alternative representations are given by Leissa<sup>33</sup> for certain other boundary geometries.

Still considering the vibrations of a rectangular structure, we note that a combination of Equations (6.28) and (6.44), with indices  $m, n$  replacing the single index  $n$ , will give the resonance frequency  $\omega_{mn}$  for the  $m, n$  mode of the plate. The available resonance wave numbers will appear as a lattice as shown in Figure 6.5a and the resonant mode at frequency  $\omega = \omega_{mn}$  is that value of  $m$  and  $n$  for which Equation (6.28) is satisfied. If we consider a band of frequencies  $\Delta\omega$ , that is large enough to contain at most one mode, then there will also be as many available modes included as illustrated in the annular sector. First consider the number of resonances included in the quarter circle of radius  $k = k_p$  which is the wave number of free-banding waves on an infinite plate with the same properties as the finite plate. This wave number is

$$k_p = \left( \frac{\omega_m^2 s}{D} \right)^{1/2} \quad (6.45)$$

and the total number of modes accumulated in the range  $0 < k < k_p$  is<sup>4,12</sup>

$$N = \frac{\frac{\pi}{4} k_p^2}{\frac{\pi}{L_1} \cdot \frac{\pi}{L_3}} = \frac{k_p^2 L_1 L_3}{4\pi}$$

because the area of the quarter circle is  $\pi k_p^2/4$  and the area defined by each of the interstices in the lattice is  $\pi/L_1 \cdot \pi/L_3$ . Resonance conditions exist whenever  $k_p = k_{mn}$ . The average increase in the number of modes per unit increase in wave number is, therefore,

$$n(k_p) = \frac{dN}{dk_p} = \frac{k_p L_1 L_3}{2\pi} \quad (6.46a)$$

and, accordingly, the increase in the number of modes per unit increase in frequency is

$$n(\omega) = \frac{dN}{dk_p} \cdot \frac{dk_p}{d\omega} = \frac{n(k_p)}{c_g}$$

$$n(\omega) = \frac{L_1 L_3}{4\pi} \left( \frac{m_s}{D_s} \right)^{1/2}$$

where  $c_g$  is the group velocity of the waves,

$$c_g = 2k \left( \frac{D_s}{m_s} \right)^{1/2}$$

Because the longitudinal wave speed in a plate is

$$c_L = \left[ \frac{E}{\rho_p (1-\nu^2)} \right]^{1/2} = \left( \frac{D_s}{m_s \kappa^2} \right)^{1/2} \quad (6.46b)$$

we can write the mode density as

$$n(\omega) = \frac{A_p}{4\pi k C_g} \quad (6.47)$$

where  $A_p = L_1 L_3$  is the area of the plate.

Equation (6.47) shows that the modal density of a plate is independent of frequency. Also, the plate area has been introduced instead of the length and width. Equation (6.47) applies generally for the higher modes of all single plates. For membranes, Equation (6.46) still applies

$$n(k_p) = \frac{k_p A_p}{2\pi} \quad (6.46c)$$

but, because

$$k_p = \omega \left( \frac{m}{T_e} \right)^{1/2} = \frac{\omega}{C_m}$$

the frequency modal density increases with frequency as

$$n(\omega) = \frac{A_p \omega}{2\pi C_m^2} \quad (6.48)$$

In like manner, the wave-number modal density for a beam of length  $L$  is

$$n(k_p) = \frac{L}{\pi}$$

and

$$n(\omega) = \frac{n(k_p)}{C_g} = \frac{L}{2\pi (\omega k C_g)^{1/2}} \quad (6.49)$$

which shows that the frequency mode density decreases as frequency increases. For a long narrow structure one would expect  $n(\omega)$  to follow Equation (6.49) for frequencies above the fundamental resonance frequency and below the first lateral mode for which  $k_p L_3 < \pi$ . For both,  $k_p L_3 > \pi$  and  $k_p L_1 > \pi$ , Equation (6.49) applies. Figure 6.6 illustrates this dependence of the mode density on the width  $k_p L_3$  of a rectangular panel for which  $L_1 > L_3$  for all modes  $k_p L_1 > \pi$ .

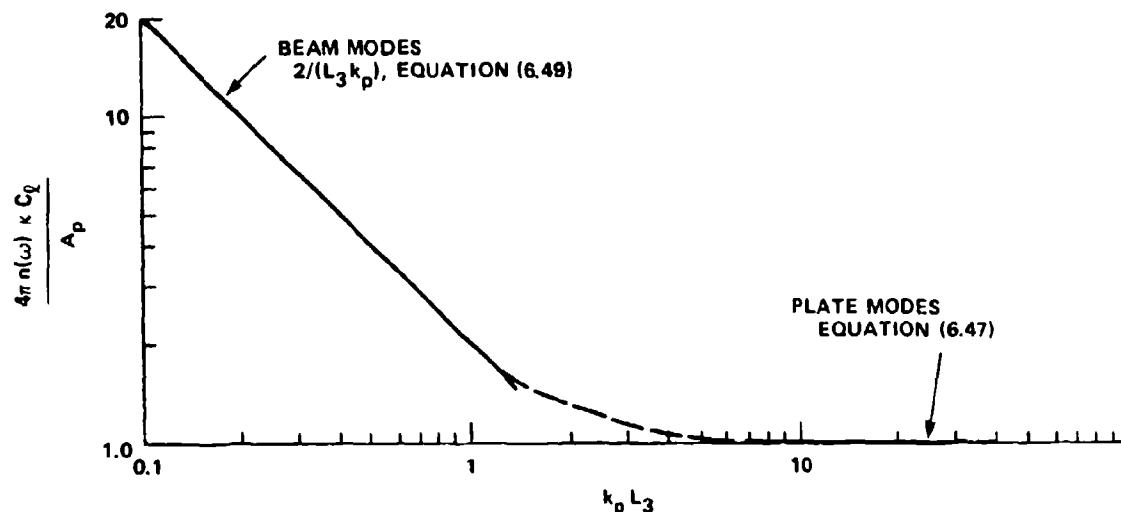


Figure 6.6 - Modal Density for Rectangular Plate for which  $k_p L_1 > \pi$  and  $L_3 < L_1$ . Note Regions of Plate-Like and Beam-Like Vibration.

Equations (6.47) and (6.49) are independent of the nature of the constraint applied to the panel or beam (clamped, free, etc.) for modes that have more than 1-half-wave between boundaries. Thus, we need not be concerned with the details of constraint at this point, but only with the one- or two-dimensionality of the structure and whether the bending waves are nondispersive with  $C_g$  as a constant, or dispersive with  $C_g$  dependent upon wave number.

Thus, we are now in a position to illustrate the methods of estimating the flow-induced response of structures in frequency bands for which\*

$$n(\omega_f) \Delta\omega_f > 1$$

\*In order to distinguish between resonance frequencies  $\omega_n$  and the frequency bands over which they may be observed, we shall temporarily invoke the filter band  $\Delta\omega_f$  centered on  $\omega_f$  to avoid confusion.



As indicated by Equations (6.31) and (6.32), the flexural velocity spectral density on a two-dimensional structure is a summation over all modes of the modal velocity spectra  $\phi_{mn}(\omega)$ . It has been assumed that the modes are uncoupled. As illustrated in Figure 6.2 and shown in Equation (6.34), the  $\phi_{mn}(\omega)$  for each mode is sharply peaked about all frequencies for which  $\omega = \pm \omega_n$ . Thus, where we consider the mean-square velocity in the broad frequency band of a filter  $\Delta\omega$ , centered on  $\omega_f$ ,  $\Delta\omega_f$  must be large enough that  $\Delta\omega_f \gg \pi(\eta_T \omega_n)/2$  and  $n(\omega_f) \Delta\omega_f \gg 1$ . The total mean-square velocity in the  $\Delta\omega_f$  is just the summation of all  $\omega_n$  lying in  $\omega_f \pm \Delta\omega_f$ . The frequency interval between modes must be small enough that the set of resonances resembles a continuum. Using Equation (6.32)

$$\begin{aligned} \overline{v^2}(\omega_f, \Delta\omega) &= 2 \int_{\omega_f - \Delta\omega_f/2}^{\omega_f + \Delta\omega_f/2} \phi_{vv}(\omega) d\omega \\ &= 2 \sum_{mn} \int_{\omega_f - \Delta\omega_f/2}^{\omega_f + \Delta\omega_f/2} \phi_{mn}(\omega) d\omega \\ &= \sum_{\substack{\text{all modes} \\ \text{in } \Delta\omega}} \overline{v_{mn}^2} \end{aligned}$$

where  $\omega_f$  is the center frequency of the filter band and  $\overline{v_{mn}^2}$  is given by Equation (6.41). We already specified that the modal force spectrum,  $\phi_{p_{mn}}(\omega)$  must be roughly constant over the resonance frequency band  $(\pi/2)\eta_T \omega_{mn}$ , but now if we also require that it is flat over the entire filter bandwidth of interest  $\Delta\omega_f$ , then we can approximate the summation by an integration over all  $\omega_n$  lying in  $\Delta\omega_f$  because  $n(\omega_f) \Delta\omega_f \gg 1$ . Thus,

$$\overline{v^2}(\omega_f, \Delta\omega_f) \approx \int_{\omega_f - \Delta\omega_f/2}^{\omega_f + \Delta\omega_f/2} \overline{v_{mn}^2}(\omega) n(\omega) d\omega \quad (6.50)$$

(cont.)

$$\approx \overline{V_{mn}^2}(\omega_f) n(\omega_f) \Delta\omega_f \quad (6.50)$$

where  $\overline{V_{mn}^2}(\omega_f)$  is again given by Equation (6.41), but it now represents the typical mean-square modal velocity generalized as a continuous function of frequency. If the structure is a plate of area  $A_p$ , then Equations (6.41), (6.47), and (6.50) give the mean-square (time- and area-averaged) panel velocity as

$$\overline{V^2}(\omega_f, \Delta\omega_f) = \frac{\pi \phi_{p_{mn}}(\omega_f)}{m_s^2 \eta_T} \frac{A_p}{4\pi c \ell} \frac{\Delta\omega_f}{\omega_f} \quad (6.51)$$

The time-average power per unit area that is supplied to the plate by the flow is

$$P_{in} = \frac{1}{A_p} \sum_{\substack{\text{modes in} \\ \Delta\omega}} (P_{in})_n$$

For a large enough bandwidth to include more than one mode this may be approximated as

$$= \frac{1}{A_p} \int_{\omega_f - \Delta\omega_f/2}^{\omega_f + \Delta\omega_f/2} P_{in}(\omega) n(\omega) d\omega$$

From Equation (6.41), we find the power spectral density\* per unit area to be

$\pi_{in}(\omega) = P_{in}(\omega)/2\Delta\omega$  and  $-\infty < \omega < \infty$ ,

$$\pi_{in}(\omega) = \frac{\pi \phi_{p_{mn}}(\omega)}{2m_s} \cdot n(\omega)$$

---

\*Reverting now to the standard frequency notation.

$$= \frac{\pi \phi_{p_{mn}}(\omega)}{2m_s} \frac{A_p}{4\pi c_\ell} \quad (6.52a)$$

with the total input power given by

$$\pi_{in} = \int_{-\infty}^{\infty} \pi_{in}(\omega) d\omega$$

The input impedance per unit area of an infinite plate is equal to the average (over all modes) resistance of an infinite plate,<sup>4,9,12</sup>

$$R_\infty = 8m_s c_\ell$$

therefore, the input power spectral density per unit area can be rewritten

$$\pi_{in}(\omega) = \frac{\phi_{p_{mn}}(\omega) A_p}{R_\infty} \quad (6.52b)$$

where  $\phi_{p_{mn}}(\omega)$  is given by Equation (6.40).

The relationships just derived, Equations (6.50), (6.51), and (6.52), are subject to rigid restrictions. It must be established before these are valid that  $\overline{v_{mn}^2}(\omega)$  is indeed nearly independent of the mode order. This, in turn, requires that the modal damping is roughly constant for all modes in the frequency band. If one mode is very lightly damped its response will overwhelm the vibration of others in the band and it must, therefore, be considered separately. A less obvious but often more important restriction to the use of these approximations is that the auto-spectrum of the modal pressure,  $\phi_{p_{mn}}(\omega)$  of Equation (6.40), is the same for all modes in the band. Such may not be true if, for example, the wave number spectrum of the excitation pressure is very large for only a restricted range of wave number. Then, only certain modes in the frequency band will be selectively excited. This

situation can arise when boundary layers excite structures. It is also likely to arise when vortex-induced pressures excite the trailing edges of hydrofoils. Another restriction can occur when acoustic radiation from the structure is ultimately estimated. As we shall see in Section 6.5, certain classes of modes more effectively radiate sound than others. Generally such a modal averaging as undertaken above is not appropriate when a self-excited acoustic or hydrodynamic feedback is involved. The input power, Equation (6.52b), is related to the mode-ensemble mean-square velocity  $\overline{v^2}(\omega, \Delta\omega)$ , Equation (6.50), by a relationship analogous to Equation (6.50).

$$\overline{v^2}(\omega, \Delta\omega) = \frac{P_{in}}{M \eta_{T\omega}} \quad (6.52c)$$

The mean-square velocity is dependent upon the boundary conditions of the plate by influencing the details of the shape function  $S_{mn}(\vec{k})$ , as we shall see in the next section.

## 6.4 MODAL SHAPE FUNCTIONS FOR SIMPLE STRUCTURES

The input power and the mean-square flow-induced velocity depend upon the nature of the modal shape function  $S_{mn}(\vec{k})$  which appears in Equation (6.40). Equation (6.39) gives this function as a spatial transform of the mode shape function  $\Psi_{mn}(\vec{y})$ . For more general boundary conditions and geometries, other than clamped, simple, and free boundaries, closed-form expressions for either  $\Psi_{mn}(\vec{y})$  or  $S_{mn}(\vec{k})$  need to be derived for each case.

The simplest and most straightforward boundary condition for which to write  $\Psi_{mn}(\vec{y})$  is the simply supported rectangular plate. In this case the displacement and curvature of the plate vanish because it is considered to be held in place with pins that do not exert moments on the edges. The mode shape function (for  $y_1, y_3=0$  the center of the plate) satisfying Equations (6.22), (6.24), and, (6.25) is<sup>33</sup>

$$\Psi_{mn}(\vec{y}) = 2 \cos(k_m y_1) \cdot \cos(k_n y_3) \quad |y_1| < \frac{L_1}{2} \quad (6.53a)$$

$$|y_3| < \frac{L_3}{2}$$

where the cosine function is used for odd-order modes and the sine function for even-order modes, as illustrated by the sketches of mode lines in Figure 6.5b. For odd-order modes which have an odd number of half-waves along a dimension e.g.,  $\cos k_m L_1 / 2 = 0$

$$\frac{k_m L_1}{2} = \left(m + \frac{1}{2}\right) \pi, m = 0, 1, 2, 3, 4, \dots \quad (6.53b)$$

and similarly for  $k_n L_3$ . For even-order modes having an even number of half waves,  $\sin k_m L_1 / 2 = 0$

$$\frac{k_m L_1}{2} = m\pi, m = 1, 2, 3, 4, \dots \quad (6.53c)$$

and similarly for  $k_n L_3$ . Note the use of the double index  $(m, n)$  in the subscript of  $\Psi_{mn}(\vec{y})$ , this denotes the two-dimensional nature of the function. The related modal shape function<sup>12,24,27</sup> for the simply-supported membrane or plate is

$$S_{mn}(\vec{k}) = 2A_p \frac{\sin\left(\frac{1}{2} k_1 L_1\right)}{\cos\left(\frac{1}{2} k_1 L_1\right)} \cdot \frac{\sin\left(\frac{1}{2} k_3 L_3\right)}{\cos\left(\frac{1}{2} k_3 L_3\right)} \quad (6.54a)$$

$$\frac{1}{2} (k_m L_1) \left(1 - \left(\frac{k_1}{k_m}\right)^2\right) \quad \frac{1}{2} (k_n L_3) \left(1 - \left(\frac{k_3}{k_n}\right)^2\right)$$

which separates into the two functions

$$S_{mn}(\vec{k}) = S_m(k_1) S_n(k_3) \quad (6.54b)$$

A direct consequence of the normalizing Equation (6.26) is that the integral of  $|S_{mn}(\vec{k})|^2$  over all  $\vec{k}$  is

$$\frac{1}{(2\pi)^2} \int_{-\infty}^{\infty} \int_{-\infty}^{\infty} |S_{mn}(\vec{k})|^2 d\vec{k} = \iint |\Psi_{mn}(\vec{y})|^2 d\vec{y}$$

Therefore, the analog to Equation (6.40b) for the normalization is

$$\int_{-\infty}^{\infty} \int |S_{mn}(\vec{k})|^2 d\vec{k} = (2\pi)^2 A_p \quad (6.55)$$

regardless of either the shapes of the panel or of its dynamic boundary conditions.

The function  $S_{mn}(k)$  is peaked about  $k_1 = k_m$  and  $k_3 = k_n$ , which defines its main acceptance region. We consider the separate functions  $S_m(k_1)$  for the even-order mode which can be written in the alternative forms

$$\begin{aligned} \frac{2S_m(k_1)}{L_1} &= \frac{4(2)^{1/2} k_m \sin\left(\frac{1}{2} k_1 L_1\right)}{L_1 (k_m^2 - k_1^2)} \\ &= \frac{2(2)^{1/2} \sin\left(\frac{1}{2} k_m L_1 \cdot \frac{k_1}{k_m}\right)}{\left(\frac{k_m L_1}{2}\right) \left(1 - \left(\frac{k_1}{k_m}\right)^2\right)} \end{aligned}$$

and similarly for the cosine-dependent function. Figure 6.7 shows  $2S_m(k_1)/L_1$  as a function of  $k_1/k_m$ . By virtue of the boundary condition of vanishing displacement at  $y_1 = \pm L_1/2$ ,  $k_m L_1/2 = m$  for the even-ordered mode. The maximum occurs when  $k_1 = k_m$ , so,

$$\left| \frac{2S_m(k_m)}{L_1} \right|^2 = 2 \quad (6.56)$$

and the wave number bandwidth of this main acceptance region is

$$\begin{aligned} \frac{\Delta k_1}{k_m} &= \frac{2}{m} \text{ or} \\ \Delta k_1 &= \frac{4\pi}{L_1} \end{aligned} \quad (6.57)$$

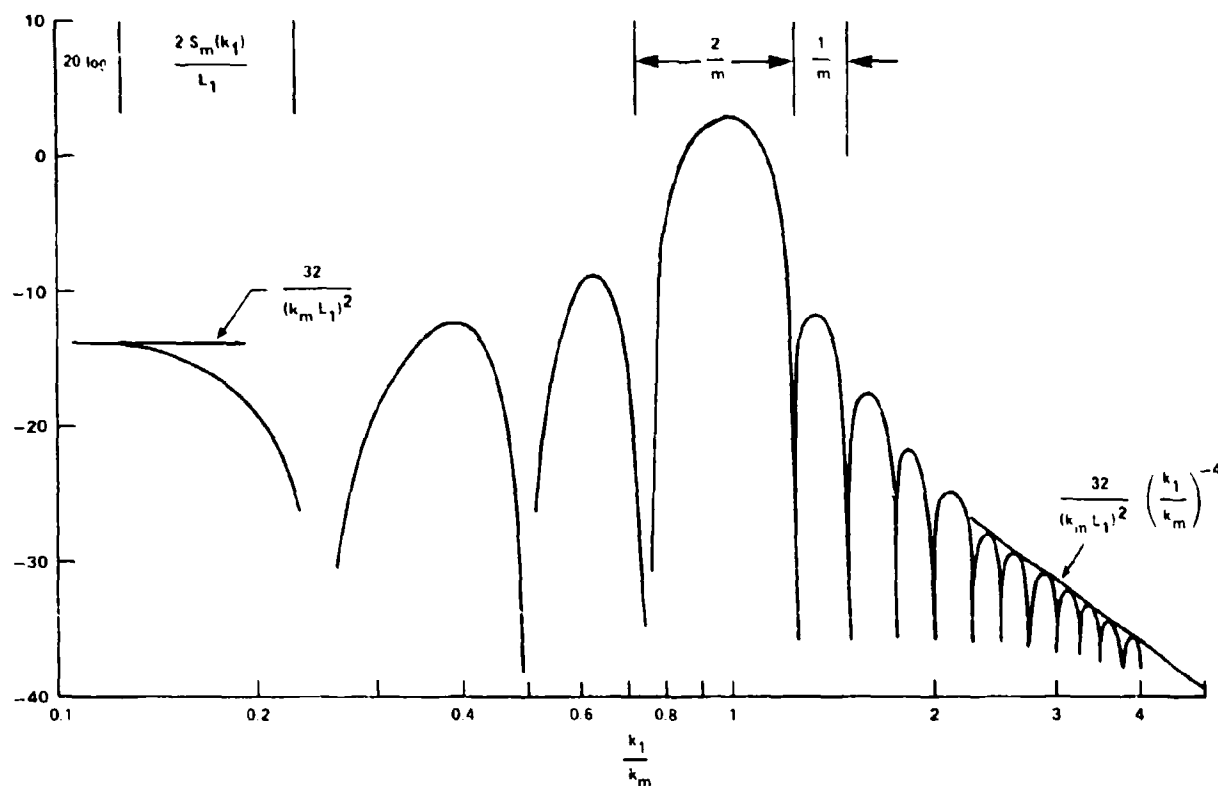


Figure 6.7 - Modal Shape Function for One-dimensional Even-Order Mode Shape  
Shown Here for  $(k_m L_1)/2 = m\pi = 4\pi$ ; Simply-Supported Panel

In the limit of  $k_1 \ll k_m$

$$\left| \frac{2S_m(k_1)}{L_1} \right|^2 \approx \frac{32}{(k_m L_1)^2} \sin^2 \left( \frac{k_1 L_1}{2} \right) \quad (6.58)$$

and when  $k_1 \gg k_m$

$$\left| \frac{2S_m(k_1)}{L} \right|^2 \approx \frac{32}{(k_m L_1)^2} \left( \frac{k_m}{k_1} \right)^4 \sin^2 \left( \frac{1}{2} k_1 L_1 \right) \quad (6.59)$$

The only difference between the even- and odd-ordered modes lies in the appearance of the sine or cosine function in the transfer, and accordingly, in the behavior as  $k_1$  approaches zero;  $S_m(k_1)$  and  $S_n(k_3)$  for even-order modes vanish in the limits of zero wave number. Otherwise, the approximate relationships of Equations (6.56) through (6.59) apply.

The shape function for a clamped-clamped beam of length  $L$  has been given by Aupperle and Lambert<sup>34</sup> and Martin<sup>35</sup>

$$\left| \frac{2S_m(k_1)}{L} \right|^2 \approx \frac{32}{1 - (k_m L)^{-1}} \left[ \frac{(k_m L)^2}{(k_m L)^2 + (k_1 L)^2} \right]^2 \cdot \left[ \frac{\sin(k_m - k_1) \frac{L}{2}}{(k_m - k_1) L} + \frac{\sin(k_m + k_1) \frac{L}{2}}{(k_m + k_1) L} \right]^2 \quad (6.60)$$

where  $k_m L = (m+1/2)\pi$  for  $m > 3$ . The value  $|(2S_m(k_m))/L|^2 = 2$  just as it is for simply-supported beams. However, the limiting values are

$$\left| \frac{2S_m(k_1)}{L} \right|^2 \approx \frac{64}{(k_m L)^2} \left( \frac{k_m}{k_1} \right)^6 \sin^2 \left( \frac{k_1 L}{2} \right) \text{ for } k_1 \gg k_m \quad (6.61)$$

and

$$\left| \frac{2S_m(k_1)}{L} \right|^2 \approx \frac{64}{(k_m L)^2} \sin^2 \frac{k_1 L}{2} \text{ for } k_1 \ll k_m \quad (6.62)$$



The shape function-squared for the clamped-clamped boundary condition at low wave numbers is, thus, a factor of two greater than for the simply supported boundary condition, but it is functionally similar.

The effect of the boundary condition on  $S_m(k_1)$  for  $k_1 \gg k_m$  can be more generally considered by noting that for  $k_1/k_m > 1$ , integration by parts of Equation (6.39) with

$$\psi_{mn}(\vec{y}) = \psi_m(y_1) \psi_n(y_3)$$

yields, e.g.,<sup>36</sup>

$$\lim_{k_1/k_m \gg 1} \frac{2S_m(k_1)}{L_1} = \sum_{j=0}^{N-1} (i)^{j-1} \left( \frac{k_1 L_1}{2} \right)^{-j-1} \left[ e^{+i \frac{k_1 L_1}{2}} \psi_m^{(j)}(1) - e^{-i \frac{k_1 L_1}{2}} \psi_m^{(j)}(-1) \right] + 0 \left[ \frac{k_1 L_1}{2} \right] \quad (6.63)$$

where

$$\psi_m^{(j)}(1) = \left( \frac{L_1}{2} \right)^j \frac{\partial^j \psi_m \left( \frac{L_1}{2} \right)}{\partial y_2^j}$$

and similarly for  $S_n(k_3)$ . Chase<sup>37</sup> has derived similar expressions to Equation (6.63) for both circular axisymmetric surfaces and rectangular surfaces. The boundary conditions determine the values of the edge derivatives,  $\psi_m^{(j)}(\pm L_1/2)$ ,  $i = 1, 3$ . Thus we have the following possibilities:

1.  $\psi_m(\pm L_1/2) = 0$  for zero displacement at the edges.
2.  $\frac{\partial \psi_m(\pm L_1/2)}{\partial y_1} = 0$  for zero slope for a clamped boundary condition requiring a nonvanishing moment.

$$3. \frac{\partial^2 \psi_m(+L_1/2)}{\partial y_1^2} = 0 \text{ for zero curvature for a simple (pinned) boundary}$$

requiring a vanishing moment.

The symmetry of mode order about the center of the panel determines the combination of the terms in the brackets. One needs only to consider the lowest-order nonzero derivative in evaluating Equation (6.63). For substitution into Equation (6.60) we find for  $\psi_m(y_1)$  harmonic in  $k_m y_1$  that

$$\psi_m^{(j)}(1) \propto \left( \frac{k_m L_1}{2} \right)^j \quad \text{for } k_1 \gg k_m$$

which makes

$$\left| \frac{2S_m(k_1)}{L_1} \right| \approx \frac{2}{k_1 L_1} \left( \frac{k_m}{k_1} \right)^j \quad \text{for } k_1 \gg k_m \quad (6.64)$$

where  $j$  is the lowest-order nonvanishing derivative boundary condition. For a clamped plate,  $j = 2$ ; for a simple support,  $j = 1$ ; and for a free motion (or nearly free allowing some displacement) at the edge,  $j = 0$ .

## 6.5 ESSENTIAL FEATURES OF STRUCTURAL RADIATION

### 6.5.1 Analysis of a Simply Supported Panel

The mathematical problem of determining the sound that is radiated by a body with a known velocity normal to its surface, is a deterministic one. The prescription of the velocity of the fluid normal to and on the surface is identified as a Neumann boundary value problem; the complexity of the solution of the acoustic wave equation depends upon the geometry of the body as well as upon the variation of the velocity over the surface. General methods of solution for flat, baffled surfaces, and spherical and cylindrical shells have been described by Junger and Feit.<sup>6</sup>

It is outside the scope of this book to discuss, in any extensive detail, the problem of structural radiation. To provide for a straightforward application of other published accounts it is instructive to outline here, as an example, the

solution of the problem of radiation from a rectangular baffled plate. Figure 6.8 illustrates the geometry, of the panel that lies in the  $y_2 = 0$  plane with coordinates  $\pm L_1/2, \pm L_3/2$ . The field point at which the sound pressure is to be evaluated is  $\vec{y}' = y_1', y_2', y_3'$ . The velocity of the panel normal to the  $y_2 = 0$  plane is

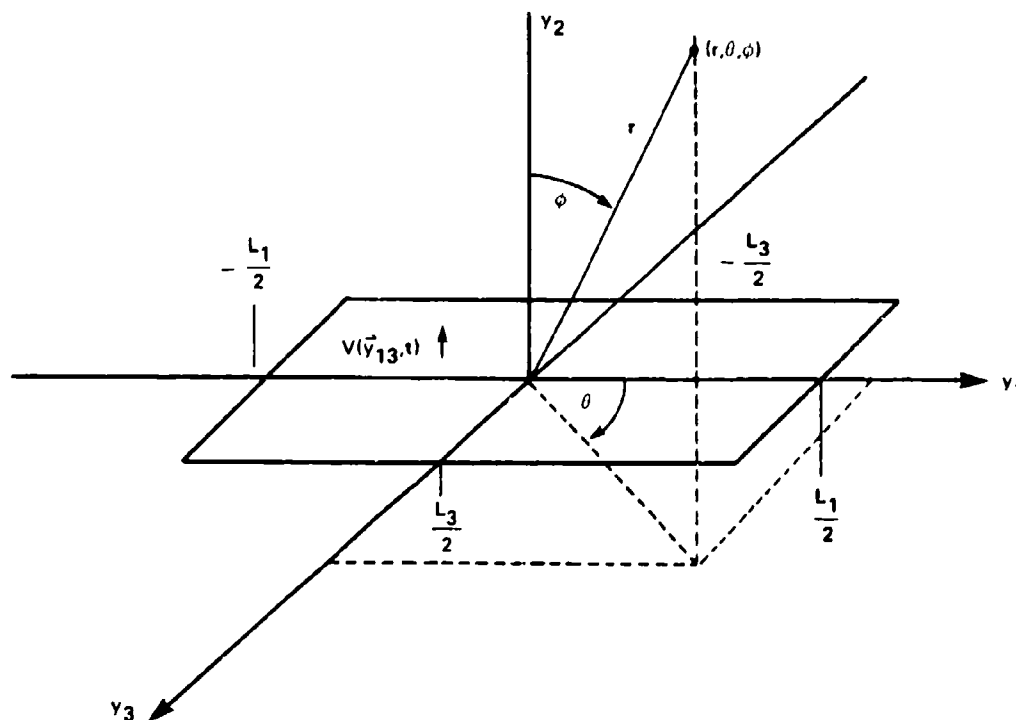


Figure 6.8 - Coordinates of the Rectangular Plate and the Contiguous Medium

$V_2(\vec{y}, t)$  within the region belonging to  $|y_1| < L_1/2$  and  $|y_3| < L_3/2$ . Outside this region the velocity is identically zero, i.e., it is baffled. This velocity field can be described in terms of its temporal Fourier transform  $V_2(\omega, \vec{y})$ , Equation (6.30) and it is a superposition of the normal modes of the surface  $\Psi_{mn}(\vec{y})$ , as in Equation (6.31). The equation for the acoustic pressure in the fluid  $p_a(\vec{y}, t)$  is Equation (2.5), repeated here:

$$\nabla^2 p_a - \frac{1}{c_o^2} \frac{\partial^2 p_a}{\partial t^2} = 0 \quad (6.65)$$

In as much as  $v(\vec{x}, t)$  is a stochastic function of time, it is convenient to use the Fourier transform of the acoustic pressure

$$p_a(y_2, \vec{k}, \omega) = \frac{1}{(2\pi)^2} \int_{-\infty}^{\infty} \int \int e^{-i\vec{k} \cdot \vec{y} + i\omega t} p_a(y_1, y_2, y_3, t) dy_1 dy_3 dt \quad (6.66)$$

so that Equation (6.65) becomes

$$\frac{\partial^2 p_a(y_2, \vec{k}, \omega)}{\partial y_2^2} + (k_o^2 - k^2) p_a = 0 \quad (6.67)$$

which has a solution

$$\begin{aligned} p_a(y_2, \vec{k}, \omega) &= A \exp \left[ -iy_2(k_o^2 - k^2)^{1/2} \right] \text{ for } y_2 < 0 \\ &= A \exp \left[ +iy_2(k_o^2 - k^2)^{1/2} \right] \text{ for } y_2 > 0 \end{aligned} \quad (6.68)$$

where  $k^2 = k_1^2 + k_3^2$  and we use the convention

$$(-1)^{1/2} = i \quad \text{for } y_2 > 0 \quad (6.69)$$

$$(-1)^{1/2} = -i \quad \text{for } y_2 < 0$$

The linearized boundary condition (for which the convection term  $(\vec{v} \cdot \vec{\nabla}) \cdot \vec{v}$  in Equation (2.4) is ignored) is

$$\frac{\partial v_2}{\partial t} = -\frac{1}{\rho_o} \frac{\partial p_a}{\partial y_2} \quad (6.70)$$

so now we can relate the field acoustic pressure to the panel velocity. To do this we write the Fourier transform of the velocity  $V(\vec{k}, \omega)$  given by Equations (6.30), (6.31), and (6.39). Thus,

$$V(\vec{k}, \omega) = \frac{1}{(2\pi)^3} \int_{-\infty}^{\infty} \int \int v_2(\vec{y}, t) e^{-i(\vec{k} \cdot \vec{y} - \omega t)} dy_1 dy_2 dt \quad (6.71)$$

$$V(\vec{k}, \omega) = \frac{1}{(2\pi)^2} \sum_{mn} v_{mn}(\omega) S_{mn}(\vec{k})$$

Note that the double sum over  $m$  and  $n$  replaces the simple sum over  $n$ , and that  $V(\vec{k}, \omega)$  is subject to the requirement that  $V(\vec{y}, t)$  vanishes on the baffle. Equation (6.70) becomes

$$-i\omega V(\vec{k}, \omega) = -\frac{1}{\rho_0} \frac{\partial p_a(y_2, \vec{k}, \omega)}{\partial y_2} \quad \text{for } y_2 > 0 \quad (6.72)$$

Combining Equations (6.68), (6.71), and (6.72), we find the Fourier transform of the pressure to be a summation of influences of all modes,

$$p_a(y_2, \vec{k}, \omega) = \sum_{mn} \frac{1}{(2\pi)^2} \rho_0 c_0 \frac{v_{mn}(\omega) S_{mn}(\vec{k})}{\left[1 - \frac{k^2}{k_0^2}\right]^{1/2}} e^{+iy_2(k_0^2 - k^2)^{1/2}} \quad (6.73)$$

The acoustic pressure  $p_a(\vec{y}, t)$  is the inverse Fourier transform of the wave number transform. The function  $p_a(\vec{y}, \omega)$  is

$$p_a(\vec{y}, \omega) = \sum_{mn} \frac{1}{(2\pi)} \rho_0 \omega v_{mn}(\omega) \int_{-\infty}^{\infty} \int \frac{S_{mn}(\vec{k}) e^{+i \left[ (k_1 y_1 + k_3 y_3) + (k_0^2 - k_1^2 - k_3^2)^{1/2} y_2 \right]}}{(k_0^2 - k_1^2 - k_3^2)^{1/2}} dk_1 dk_3 \quad (6.74)$$

This function is the same as derived by Junger and Feit<sup>6</sup> who evaluate the integral approximately using the method of the stationary phase.<sup>36</sup> The result is most profitably written in spherical coordinates, Figure 6.8, as

$$\begin{aligned}y_2 &= r \cos \phi \\y_1 &= r \sin \phi \cos \theta \\y_3 &= r \sin \phi \sin \theta\end{aligned}$$

The dominant part of the integral occurs when the phase of the exponent has a vanishing rate of change with  $k_1$  or  $k_3$ . Junger and Feit<sup>6</sup> show that this pair of wave number components is

$$\begin{aligned}\overline{k_1^2} + \overline{k_3^2} &= k_o^2 \sin^2 \phi \\ \overline{k_1} &= k_o \sin \phi \cos \theta \\ \overline{k_3} &= k_o \sin \phi \sin \theta\end{aligned}\tag{6.75}$$

these wave numbers are the trace wave numbers of the acoustic wave front projected on the surface of the panel. The approximate integral is<sup>6</sup>

$$p_a(R, \theta, \phi, \omega) \approx \sum_{mn} \frac{-i}{(2\pi)} \rho_o \omega V_{mn}(\omega) S_{mn}(\overline{k_1}, \overline{k_3}) \frac{e^{+ik_o r}}{r}\tag{6.76}$$

which is valid only when  $k_o r \gg 1$ .

The sound pressure in the far field will be the linear superposition of pressures from all uncoupled modes which are resonant at the frequency. The directivity of the sound from each mode is associated with the coincidence of trace wave numbers  $\overline{k_1}$  and  $\overline{k_3}$  with mode wave numbers  $k_m$  and  $k_n$ , respectively. There will be distinct points in space  $(\theta, \phi)$  at which each mode radiates most effectively; these points occur because of the local reinforcement of sound waves at  $(R, \theta, \phi)$  radiated outward to that point from the mosaic of half-waves which compose the mode of the plate. The individual waves will be most in phase when  $k_m$  and  $k_n$  coincide with the trace

wave numbers  $\overline{k_1}$  and  $\overline{k_3}$ , respectively. We will discuss this coincidence further in Section 6.5.3. The coordinates of maximum sound intensity will be determined by maxima of  $S_{mn}(\overline{k_1}, \overline{k_3})$ .

Equation (6.76) applies to the far field pressure of a baffled rectangular panel of any modal character. All that is required is a specification of  $S_{mn}(\vec{k})$  for that panel. For flat panels that are not rectangular,<sup>6</sup> the pressure is functionally similar to Equation (6.76), but there are differences in numerical coefficients and in the detailed forms of  $S_{mn}(\vec{k})$ . Similar expressions can be derived for curved surfaces.<sup>6</sup> The presence of the modal acceptance function  $S_{mn}(\vec{k})$  in the integrand is common to all cases. The differences lie in the replacement of the harmonic function

$$e^{i(k_o^2 - k^2)^{1/2} y_2} \frac{1}{(k_o^2 - k^2)^{1/2}}$$

which is characteristic of the planar radiator, with functions that are appropriate to other coordinate systems, spherical, cylindrical, etc.

## 6.5.2 Fluid Impedance of a Simply Supported Panel

In our solution of Equation (6.21) no specifications were placed on the components of the pressure  $P(\vec{y}, t)$ . It must now be recognized that, in general,  $P(\vec{y}, t)$  includes a number of contributions. The first is a pressure, e.g.,  $p_{bl}(\vec{y}, t)$ , which is the primary driving pressure caused by hydrodynamic flow. This will be discussed in subsequent chapters. The fluid adjacent to the panel offers reaction pressures to the panel motion. Most often these are acoustic and inertial and they are governed by equations of the form just described. In specialized cases fluid viscous damping and hydrodynamic damping (see Chapter 9 and References 38 and 39).

We will now restrict attention only to the impedance offered by the acoustic reaction pressure and separate it from the primary driving pressure so that in Equation (6.2) we replace the single pressure by

$$p(\vec{y}, t) = -p_a(\vec{y}, t) + p_{bl}(\vec{y}, t) \quad (6.77)$$

and we are ultimately\* interested in the vibration  $v(\vec{y}, t)$  and sound  $p_a(\vec{y}, t)$  induced by the hydrodynamic pressure field  $p_{b1}(\vec{y}, t)$ . We still assume that the flow is unaffected by the panel motion. Furthermore, we will assume that  $p_a(\vec{y}, t)$  acts on both sides of the plate and that

$$\lim_{y_2 \rightarrow 0+} p_a(\vec{y}, t) = -\lim_{y_2 \rightarrow 0-} p_a(\vec{y}, t)$$

The modal acoustic pressure, following Equation (6.25), is

$$p_{a \text{ mn}}(y_2, \omega) = \frac{1}{2\pi} \int_{-\infty}^{\infty} \int_{A_p} p_a(y_1, y_2, y_3, t) \psi_{mn}(\vec{y}_{13}) e^{+i\omega t} d\vec{y}_{13} dt$$

$$p_{a \text{ mn}}(y_2, \omega) = \int_{A_p} p_a(\vec{y}, \omega) \psi_{mn}(\vec{y}_{13}) d\vec{y}_{13}$$

Because

$$p_a(\vec{y}, \omega) = \int_{-\infty}^{\infty} e^{+i\vec{k} \cdot \vec{y}_{13}} p_a(y_2, \vec{k}, \omega) d\vec{k}$$

substitution gives

$$p_{a \text{ mn}}(y_2, \omega) = \int_{-\infty}^{\infty} \int p_a(y_2, \vec{k}, \omega) S_{mn}^*(\vec{k}) d\vec{k} \quad (6.78)$$

---

\*Here, again, we must respect the sign convention:  $\xi$  is positive upwards, and  $p(\vec{y}, t)$  is directed downwards. However, the reaction pressure will be opposite the excitation pressure, therefore, we have used the minus sign.



for the modal acoustic pressure in terms of the acceptance function. Now, combining Equations (6.73) and (6.74) gives the required expression

$$p_{a_{mn}}(y_2, \omega) = \frac{1}{(2\pi)^2} \rho_o c_o \sum_{op} v_{op}(\omega) \cdot \int_{-\infty}^{\infty} \int_{-\infty}^{\infty} \frac{S_{mn}^*(\vec{k}) S_{op}(\vec{k})}{\left[1 - \left(\frac{k}{k_o}\right)^2\right]^{1/2}} e^{+iy_2 (k_o^2 - k^2)^{1/2}} d\vec{k}$$

The fluid reaction pressure  $p_a(y_2 \rightarrow 0^+, \omega)$  on the upper side of the panel (with an equal, but opposite value on the bottom side) involves the integral of the combination of  $S_{mn}^*(k) S_{op}(k)$  for all indices  $o, p$ . Because the integral is not identically zero for  $mn$  different than  $op$ , it is clear that the  $m, n$  mode is influenced by the motion of the  $o, p$  mode; i.e., the modes are coupled by the reaction of the fluid. This fluid-modal-coupling in unbounded fluids has been discussed in these terms by Davies;<sup>40-42</sup> coupling by enclosed fluids has been discussed by White and Powell,<sup>21</sup> Obermeier,<sup>31</sup> and Arnold,<sup>32</sup> and inertial coupling of modes in cantilever plates by Blake and Muga.<sup>38</sup> If the fluid is light enough we can ignore the coupling of modes; for flat plates the coupling by acoustic radiation appears to be much exceeded by inertial coupling at low frequencies. The equation for the modal pressure on the surface of the plate becomes

$$p_{a_{mn}}(y_2 \rightarrow 0, \omega) = \left\{ \frac{1}{(2\pi)^2} \rho_o c_o \int_{-\infty}^{\infty} \int_{-\infty}^{\infty} \frac{|S_{mn}(\vec{k})|^2}{\left[1 - \left(\frac{k}{k_o}\right)^2\right]^{1/2}} d\vec{k} \right\} v_{mn}(\omega) \quad (6.79)$$

The dominant contribution in the integral will come from wave numbers near  $k_1 = k_m$  and  $k_3 = k_n$ . This is because these are the large acceptance regions of  $S_{mn}(k)$ , see Figure 6.7. Physically, the fluid and structure can most effectively transfer energy when the length scales of motion are well matched. If both  $k_m$  and  $k_n$  are less than  $k_o$  the integral is primarily real, meaning that the fluid reaction appears as a pure resistance because power is radiated away from the plate. However, if

either  $k_m$  or  $k_n$  is larger than  $k_o$ , then  $k_{mn} = k$  is larger and the radical in the denominator provides an imaginary or inertial term that decays as  $\exp \left[ -\left( k_m^2 - k_o^2 \right)^{1/2} y_2 \right]$  with increasing ( $y_2 > 0$ ) distance from the plate. The modal reaction pressure on the plate can, therefore, be written in the convenient form of an impedance

$$A_{p_a} (0, \omega) = A_p (r_{mn} - i\omega m_{mn}) V_{mn}(\omega) \quad (6.80)$$

$$= A_p [\rho_o c_o \sigma_{mn} - i\omega m_{mn}] V_{mn}(\omega)$$

if we ignore modal coupling in Equation (6.75). If such coupling exists then the  $r_{mn}$  and  $m_{mn}$  are really parts of an impedance matrix with the maximum values on the diagonal  $m, n = o, p$ . The terms  $r_{mn}$  is the radiation resistance per unit area<sup>7</sup> (given by the real part of the integral) and  $m_{mn}$  is the added mass or accession to inertia<sup>6</sup> per unit area (given by the imaginary part of the integral). The radiation resistance has been further reduced

$$r_{mn} = \rho_o c_o \sigma_{mn} \quad (6.81)$$

where the dimensionless coefficient  $\sigma_{mn}$  is called the radiation efficiency of the mode.

### 6.5.3 Radiated Acoustic Power

The time-average radiated acoustic power radiated to one side of the plate is defined as

$$P_{rad} = \lim_{T \rightarrow \infty} \frac{1}{T} \int_{-T/2}^{T/2} \iint_A p_a(\vec{y}, t) V(\vec{y}_{13}, t) dt d\vec{y}_{13}$$

By substitution of the inverse transform of Equation (6.66), the pressure on  $y_2 \rightarrow 0$ , and the representations of the velocity given Equations (6.30), (6.31), and (6.71) we find the average radiated power is the real part of the integral

$$P_{\text{rad}} = \sum_{mn} \int_{-\infty}^{\infty} \int_{-\infty}^{\infty} d\vec{k} \int_{-\infty}^{\infty} d\omega \int_{-\infty}^{\infty} d\omega' V_{mn}^*(\omega) S_{mn}^*(\vec{k}) p_a(y_2 \rightarrow 0, \vec{k}, \omega)$$

$$\lim_{T \rightarrow \infty} \frac{\sin(\omega - \omega') \frac{T}{2}}{(\omega - \omega') \frac{T}{2}}$$

or, making use of the formal limit

$$\lim_{T \rightarrow \infty} \frac{\sin(\omega - \omega') \frac{T}{2}}{(\omega - \omega') \frac{T}{2}} = \frac{2\pi}{T} \delta(\omega - \omega')$$

it is the real part of

$$P_{\text{rad}} = \sum_{mn} \int_{-\infty}^{\infty} \int_{-\infty}^{\infty} d\vec{k} \int_{-\infty}^{\infty} d\omega \lim_{T \rightarrow \infty} \frac{2\pi}{T} \left[ p_a(y_2 \rightarrow 0, \vec{k}, \omega) V_{mn}^*(\omega) \right] S_{mn}^*(\vec{k})$$

Using Equation (6.73) for the wave number transform of the pressure we have a formal expression for the radiated power,

$$P_{\text{rad}} = \frac{1}{(2\pi)^2} \rho_o c_o \sum_{mn} \sum_{op} \int_{k < k_o} \int_{-\infty}^{\infty} d\vec{k} \int_{-\infty}^{\infty} d\omega \frac{\lim_{T \rightarrow \infty} \left[ \left( \frac{2\pi}{T} \right) V_{mn}(\omega) V_{op}^*(\omega) \right] S_{mn}(\vec{k}) S_{op}^*(\vec{k})}{\left[ 1 - \left( \frac{k^2}{k_o^2} \right) \right]^{1/2}}$$

As before, we can ignore the cross coupling and make use of the autospectral density of the velocity, Equation (6.32) in order to simplify the relationship. Furthermore, because  $P_{\text{rad}}$  is the integral over all frequencies and the sum of all modal contributions of the power spectral density  $\Pi_{\text{rad}}(\omega)$ , then we have the final result that

$$\Pi_{mn}^{\text{rad}}(\omega) = \rho_o c_o \frac{1}{(2\pi)^2} \int_{k < k_o} \int \frac{|S_{mn}(\vec{k})|^2}{\left[1 - \left(\frac{k^2}{k_o^2}\right)\right]^{1/2}} \Phi_{mn}(\omega) d\vec{k}$$

or

$$\Pi_{mn}^{\text{rad}}(\omega) = \rho_o c_o A_p \sigma_{mn} \Phi_{mn}(\omega) \quad (6.82)$$

is the radiated sound power spectral density of the mn mode where

$$\sigma_{mn} = \frac{1}{A_p (2\pi)^2} \int_{k < k_o} \int \frac{|S_{mn}(\vec{k})|^2}{\left[1 - \left(\frac{k^2}{k_o^2}\right)\right]^{1/2}} d\vec{k} \quad (6.83)$$

is the modal radiation efficiency. This factor has already appeared in Equations (6.79) and (6.80). The flow-induced vibration velocity spectrum for the m,n mode is given by Equation (6.34).

The radiation efficiencies of baffled flat plates has been determined by Maidanik,<sup>7,8</sup> Davies,<sup>24</sup> and Wallace<sup>43,44</sup> for various ratios of length to width. Radiating modes have been classified by Maidanik<sup>7</sup> into surface, edge, and corner modes depending upon the relationships between  $k_o$ ,  $k_m$ , and  $k_n$ . We have already seen the importance of these relationships in determining the directivity of sound in Equation (6.76). Figure 6.9 illustrates the edge and corner mode classifications that arise from these relationships. First we recall our discussion of multipoles as illustrated in Figure 2.2. There it was said that for two sources that are separated a distance d the sound pressure increased as  $k_o d = 2\pi d/\lambda_o$  until  $k_o d \gtrsim 1$ , in which case the two sources radiated without interaction. Similarly, in the case of a radiating surface, we have already said that the modal pattern represents a mosaic of alternately-phased pistons which are spaced  $\lambda_m/2 = \pi/k_m$ . If  $\lambda_m/\lambda_o < 1$  the fluid can pass from one piston to the other before they can oscillate through one

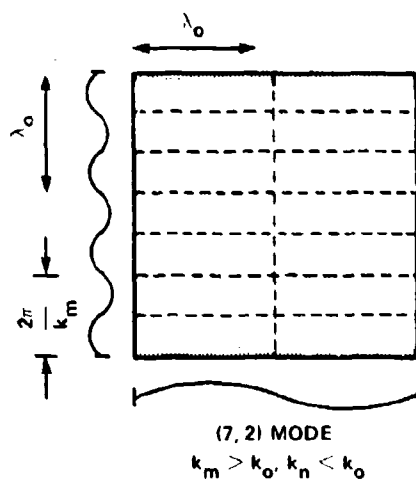


Figure 6.9a - Edge Mode

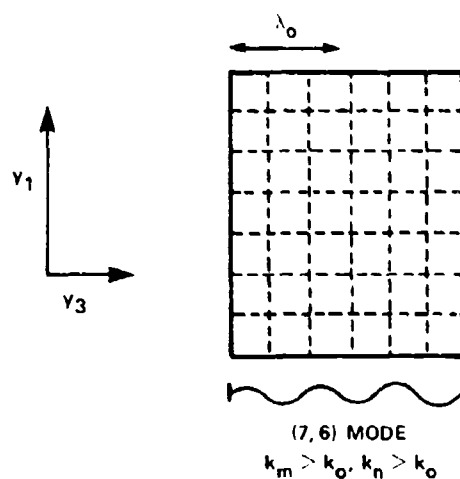


Figure 6.9b - Corner Mode

Figure 6.9 - "Edge" and "Corner" Mode Radiation for a Simply-Supported Rectangular Panel. Shaded Areas Indicate Uncancelled Regions of Volume Velocity.

cycle because the characteristic wave speed in the fluid  $c_o$  is faster than the wave speed of the piston motion,  $2\pi\omega/\lambda_m$ . Therefore, the pistons effectively cancel each other. Maidanik argues that this cancellation occurs everywhere between adjacent pistons except at the baffled edge of the pistons at each end of the array. If  $\lambda_m/\lambda_o > 1$ , then the adjacent pistons can radiate more independently because they cannot interfere. In the illustrated case of an edge mode there is cancellation along  $y_1$ , but not along  $y_3$ . In the case of a corner mode, there is cancellation along both coordinate directions, and, in the case of surface modes, we have  $k_o > k_m$  and  $k_o > k_n$  so there is no cancellation. In Figure 6.4 we see that for wave numbers above a threshold  $k_p = c_o (m_s/D_s)^{1/2}$  the phase speeds of waves on a given plate will be supersonic. This is because of the frequency-dependent character of the phase speed. The frequency at which the in-vacuo bending wave speed equals the acoustic wave speed is called the acoustic coincidence frequency

$$f_c = \frac{c_o^2}{2\pi} \left( \frac{D_s}{m_s} \right)^{-1/2}$$

For membranes, on the other hand, dependency on the phase speed will be either subsonic or supersonic at all frequencies, because of the nondispersive nature of the phase speed.

The mode classifications are illustrated in the wave number plane in Figure 6.10. The locii of edge modes lie along the  $k_m$  and  $k_n$  coordinate axes. When both  $k_m$  and  $k_n$  are less than  $k_o$  all modes are well-radiating surface modes and they radiate analogously to the infinite plate on which the bending wave speeds exceed the speed of sound, i.e.,  $k_p < k_o$  or  $C_p > C_o$ . The evaluation of the integral in Equation (6.79) is controlled by the location of modes in the wave number plane. Figure 6.10 illustrates the critical regions of  $k_m, k_n$  that will be evaluated below.

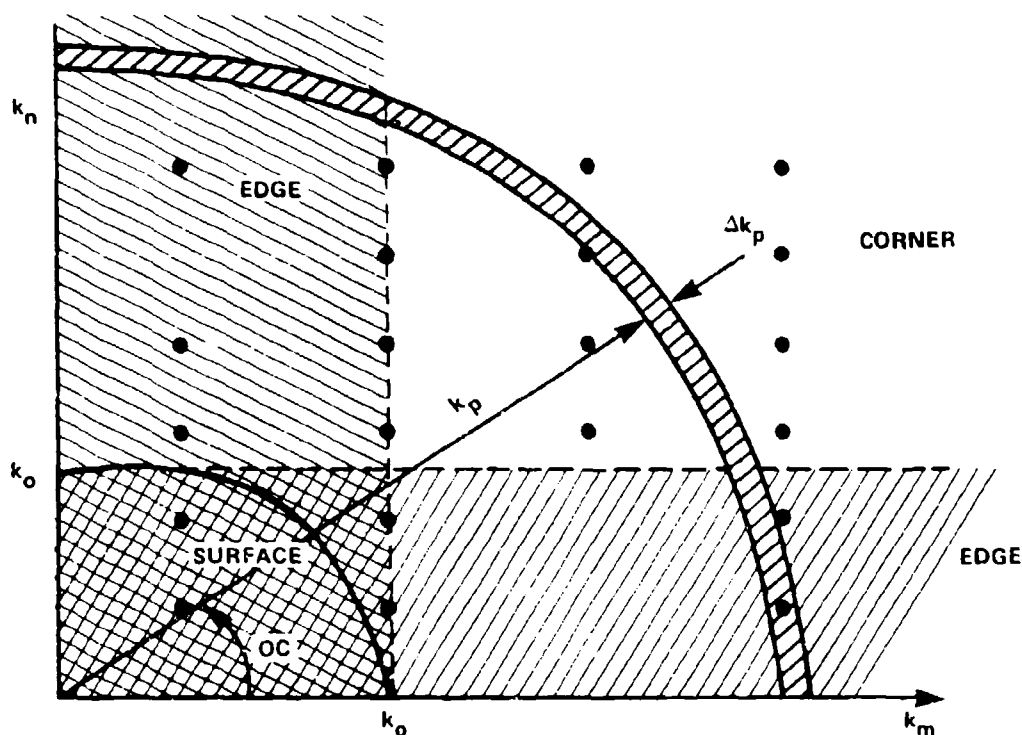


Figure 6.10 - Radiation Classification for Rectangular Plates  
Shown in the Wave Number Plane

### 6.5.4 Radiation Efficiencies of Simple Structures

For corner modes  $k_m > k_o$  and  $k_n > k_o$  then

$$k_{mn} = (k_m^2 + k_n^2)^{1/2} > k_o$$

lies outside the region of integration in Equation (6.83) and the radiation efficiency is controlled by the low wave number tail of the acceptance functions (see Figure 6.7 and Equations 6.53 and (6.54)). Thus,

$$\sigma_{mn} \approx \frac{1}{A_p (2\pi)^2} \cdot \left(\frac{4}{k_m^2}\right) \left(\frac{4}{k_n^2}\right) 2\pi k_o \int_0^{k_o} \frac{k dk}{(k_o^2 - k^2)^{1/2}} \quad (6.84)$$

$$\approx \frac{32}{A_p (2\pi)^2} \frac{k_o^2}{k_m^2 k_n^2} \quad \begin{array}{l} \text{for } k_m > k_o \\ \text{and } k_n > k_o \end{array}$$

$$\sigma_{00} \approx \frac{8}{\pi} k_o^2 A_p \quad \text{for lowest order modes, } m=n=0, k_o \sqrt{A_p} \ll 1$$

For edge modes, e.g.,  $k_n < k_o$  and  $k_m > k_o$ , a general approximation is

$$\sigma_{n,n} \approx \frac{2k_o}{A_p (2\pi)^2} \left(\frac{4}{k_m^2}\right) \cdot \int_{-\infty}^{\infty} |S_n(k_3)| dk_3 \cdot \int_0^{k_o^2 - k_n^2} \frac{dk_1}{(k_o^2 - k_3^2 - k_1^2)^{1/2}} \quad (6.85a)$$

$$\approx \frac{2\pi}{A_p k_m^2} \frac{k_o L_3}{\pi} \quad \begin{array}{l} \text{for } k_n < k_o \\ \text{and } k_m > k_o \end{array}$$

Nearer to coincidence a more exact relationship is

$$\sigma_{mn} = \frac{2\pi}{A_p k_m^2} \left( \frac{k_o L}{\pi} \right) \frac{1 + \left\{ \frac{(k_{mn}^2 - k_o^2)}{k_m^2} \right\}}{\left[ \frac{(k_{mn}^2 - k_o^2)}{k_m^2} \right]^{3/2}} \quad (6.85b)$$

Finally, at frequencies above the acoustic coincidence frequency we have acoustic surface modes, and, using Equation (6.55) because  $k_o \gg k_{mn}$

$$\sigma_{mn} \approx 1.0 \quad \text{for } k_o \gg k_{mn} \quad (6.86)$$

These modes radiate well because each half-wave of the vibration behaves like a baffled piston whose dimension exceeds an acoustic wave length.

These formulas have been derived as examples. More exact formulas will be found in References 7, 8, and 24. Figure 6.11 shows radiation efficiencies derived by Davies for the cases  $k_{mn} > 2k_o$ ,  $k_o L_1 > \pi$ , and  $k_m > 2k_o$ . One can clearly see the dependence of  $\sigma_{mn}$  upon mode order. For clamped panels  $\sigma_{mn}$  should be increased by 6 dB for corner modes and by 3 dB for edge modes because of the difference between the low wave number acceptance functions.

Radiation efficiencies of unbaffled plates and beams have been derived by Blake.<sup>45,46</sup> For an unbaffled plate which is  $k_o L_1 > \pi$ ,  $k_o L_3 > \pi$  and for which  $k_n/k_o < 1$ ,  $k_m/k_o > 1$ , it is found<sup>45</sup>

$$\sigma_{mn} \approx \frac{1}{8} \left( \frac{2\pi}{k_m^2 A_p} \frac{k_o L_3}{\pi} \right) \left( \frac{k_o}{k_n} \right) \quad (6.87a)$$

closer to coincidence  $k_o \rightarrow k_m$

$$\sigma_{mn} \approx \frac{(2)^{1/2} + 1}{16\pi} \frac{2\pi}{k_m^2 A_p} \frac{k_o L_3}{\pi} \left( \frac{k_o}{k_m} \right) \left[ \frac{-\epsilon_n \left( 1 - \frac{k_o}{k_m} \right)}{1 - \left( \frac{k_o}{k_m} \right)^{1/2}} \right] \quad (6.87b)$$



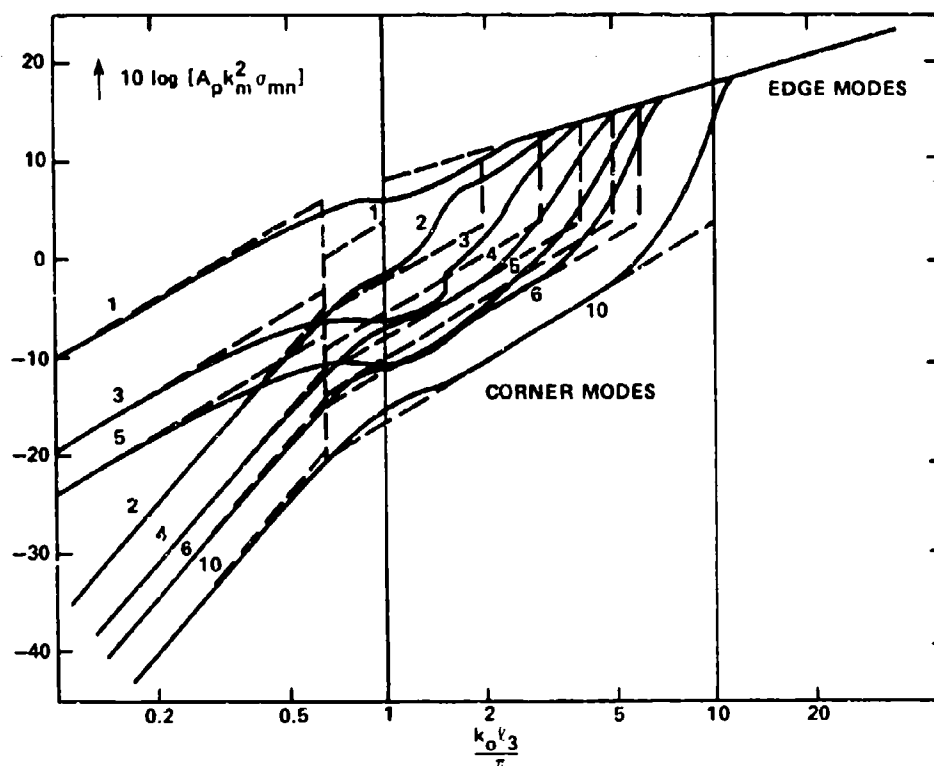


Figure 6.11 - Values of the Radiation Efficiency  $\sigma_{mn}$  for Large Odd  $m$  and Various  $n$ ;  $m = k_1 L_1 / \pi$ ,  $n = k_3 L_3 / \pi$ ,  $k_m > 2k_o$ ,  $k_p > 2k_o$ . Panel is Rectangular in a Rigid Baffle.

(From Ref. 24)

The unbaffling introduces an additional  $(k_o/k_m)$ -dependence. Measured radiation efficiencies of an unbaffled steel panel measuring  $0.6 \text{ m} \times 0.4 \text{ m} \times 0.0127 \text{ m}$  in water are compared to theoretical expressions for baffled and unbaffled plates in Figure 6.12. Note that  $k_m \approx k_p$  in the vicinity of coincidence where there is little difference between the measured points and those calculated by either the baffled or unbaffled theory. Although a peak in  $\sigma_{mn}$  does not occur near  $k_o/k_{mn}$ , a value greater than unity was reported there.

The radiation efficiency for an unbaffled beam for which  $k_o L_3 < 1$ ,  $k_o L_1 > 1$ , and  $k_o/k_n \ll 1$  is<sup>46</sup>

$$\sigma_n \approx \frac{\pi^2}{192} (k_o w)^2 \frac{w}{\pi L} \left( \frac{k_o}{k_n} \right)^2 \quad (6.88a)$$

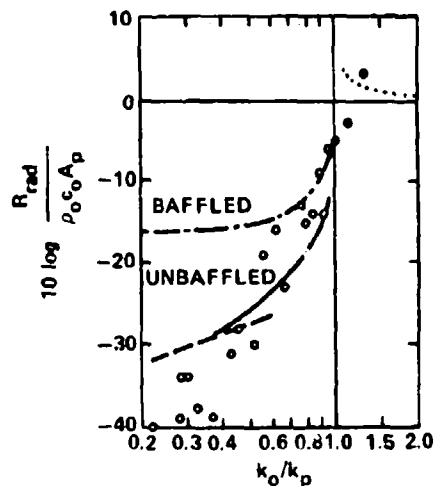


Figure 6.12 - Measured and Theoretical Radiation Resistances of the Unbauffed 1.33 Feet by 2 Feet by 1/2-Inch Steel Plate in Water

(The points are from o 50 Hertz analysis and • 1/3-octave band levels. The curves are ---, Equation (6.87a); —, Equation (6.87b); -.-, Equations (6.85) and ....; Equations (6.90).)

which, when compared to the baffled case,<sup>10</sup>

$$\sigma_n \approx \frac{w}{\pi L} \left( \frac{k_o}{k_n} \right)^2 \quad (6.88b)$$

shows additional  $(k_o w)^2$ -dependence due to baffling. Other radiation efficiencies of cylindrical shells are given by Junger and Feit<sup>6</sup> and Manning and Maidanik.<sup>47</sup> Radiation from prolate spheroids has been calculated by Chertock.<sup>48,49</sup>

### 6.5.5 Relationships for Estimating Total Acoustic Power

In Section 6.3 relationships were derived for estimating the mean-square flexural velocity averaged over the structure in terms of the input power accepted from the flow. Equivalently, the mean-square velocity of the structure could have been derived from knowledge of the modal excitation force. Either way, the response of both simple and complex structures can be estimated. In like manner, the

power in a frequency band  $\Delta\omega$  radiated from the structure with a high mode density can be estimated as<sup>7</sup>

$$P_r(\omega_f, \Delta\omega_f) = 2 \int_{\omega_f - \Delta\omega_f/2}^{\omega_f + \Delta\omega_f/2} \sum_{\substack{mn \\ \text{in } \Delta\omega}} \rho_o c_o A_p \sigma_{mn} \psi_{mn}(\omega) d\omega$$

$$\approx \rho_o c_o A_p \overline{\sigma(\omega_f)} \overline{V_{mn}^2(\omega_f)} n(\omega_f) \Delta\omega_f \quad (6.89a)$$

$$\approx \rho_o c_o A_p \overline{\sigma(\omega_f)} \overline{v^2} \quad (6.89b)$$

as long as there are many modes in the band,  $n(\omega_f) \Delta\omega_f \gg 1$ , and  $\Delta\omega_f$  is larger than the band of resonance.\* The mean-square modal velocity  $\overline{v_{mn}^2}(\omega_f)$  is the average over modes so that

$$\overline{v^2} = \overline{v_{mn}^2}(\omega_f) n(\omega_f) \Delta\omega_f$$

is the total reverberant velocity in the bandwidth. Furthermore, it is assumed that the mean-square velocity of edge modes is the same as for corner modes so that we can integrate the radiation efficiency over all regions in the wave number domains illustrated in Figure 6.10. The mean-square velocity  $\overline{v^2}$  is taken as the physically measurable motion as would be deduced from a set of accelerometer measurements. It is also that which can be estimated from Equation (6.51).

The average radiation efficiency of a simply-supported rectangular panel has been determined by Maidanik<sup>7,8</sup> and by Davies.<sup>24</sup> This quantity is

$$\bar{\sigma} = \frac{1}{N} \left[ 2 \int_0^\alpha \sigma_{mn} \text{edge} n(k) k dk d\alpha + \int_\alpha^{\pi/2-\alpha} \sigma_{mn} \text{corner} n(k) k dk d\alpha \right]$$

\*Note that in the above, the functions  $\phi_{mn}(\omega)$  and  $\bar{\sigma}(\omega)$  are all symmetric for  $+\omega$ . The total power in the band is, therefore, twice that given by the integral.

where  $n(k)$  is the wave number mode density, Equation (6.45), and  $N$  is the total number of modes, i.e.,  $k_{mn}$ , included in the annular wave number region

$$(\Delta k)^2 = \frac{\pi}{4} k_p \Delta k_p$$

where

$$\Delta k_p = \frac{1}{2} \Delta \omega (\omega k c_\ell)^{-1/2}$$

The angle  $\alpha_e$  is the arc through the edge mode region  $\sin \alpha_e = k_o/k_p$  as can be deduced in Figure 6.10. Using the approximate relationships of Section 6.5.4 we find, for edge and corner modes combined,

$$\bar{\sigma} \approx \frac{32 k_o}{2\pi A_p k_p^3} + \frac{2}{\pi} \left( \frac{k_o}{k_p} \right)^2 \frac{2(L_1+L_3)}{k_p A_p} \quad (6.90a)$$

for  $k_o/k_p < 1$  and either or both  $k_o L_1 > 2$  and  $k_o L_3 > 2$ . Maidanik<sup>7,8</sup> has provided this and additional formulas, e.g.,

above acoustic coincidence:  $\bar{\sigma} \approx \left( 1 - \left( \frac{k_p}{k_o} \right)^2 \right)^{-1/2}$  for  $k_p < k_o$  (6.90b)

at acoustic coincidence:  $\bar{\sigma} \approx (2)^{1/2} \left( (k_m L_1)^{1/2} + (k_n L_3)^{1/2} \right)$  for  $k_p = k_o$  (6.90c)

and for acoustic corner modes:

$$\bar{\sigma} \approx \frac{16}{\pi^3} \frac{L_1+L_3}{A_p k_o} \left( \frac{k_o}{k_p} \right)^2 \quad \text{for } k_o L_1 \text{ and } k_o L_3 \ll 2 \quad (6.90d)$$

while Davies<sup>24</sup> obtains, for still lower wave number corner modes,

$$\bar{\sigma} = \frac{32}{\pi^3} \frac{L_1 + L_3}{A_p k_o} \left( \frac{k_o}{k_p} \right)^3 \quad \text{for } k_o L_1 \text{ and } k_o L_3 \ll 3\pi \quad (6.90e)$$

Equation (6.90a) shows the important result that adding rib stiffeners to a panel will increase the radiation efficiency of the panel. This increase is brought about by increasing the total perimeter  $2(L_1 + L_3)$  of the edges while keeping the total radiating area constant. The second term of Equation (6.90a) is controlled by the edge modes and it is the magnitude of this term that is increased by ribbing.

Maidanik<sup>7</sup> has experimentally verified these equations using the arrangement illustrated in Figure 6.13. A reverberant vibration was generated in the ribbed aluminum test panel by a mechanical shaker; radiated sound power was measured in an acoustically reverberant chamber while the mean square velocity  $\bar{V}^2$  was determined on

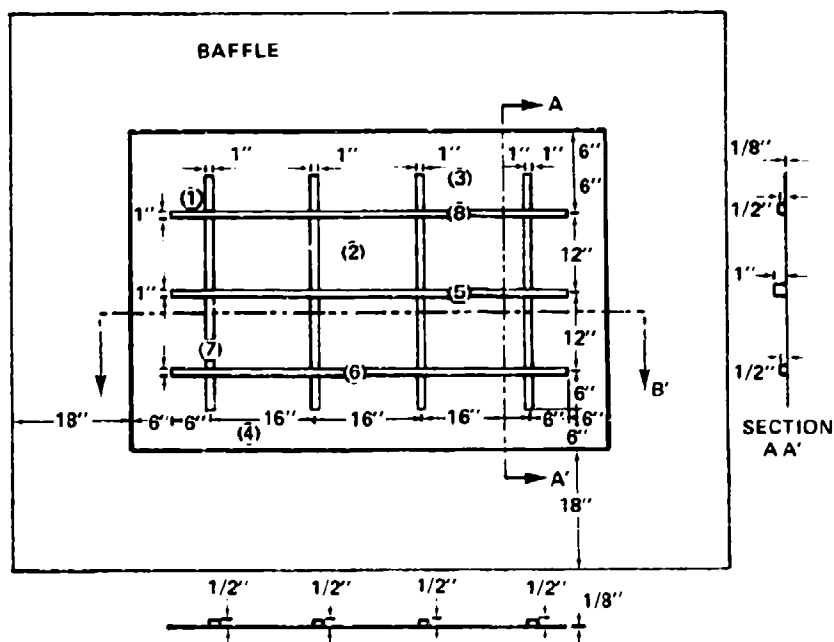


Figure 6.13 - Aluminum Test Panel, Steel Ribs, and Wooden Panel.  
Circled Numbers Indicate Accelerometer Positions;  
Shaker at Position 4  
(From Ref. 7)

the panel. The radiation efficiency was determined using Equation (6.89). Figure 6.14 shows the measured values of  $\bar{\sigma}$  with and without the baffle in place. Generally the vibration level of the ribs was from 6 to 15 dB lower than that of the panels. The radiation efficiencies as determined from the mechanically driven panel are in close agreement with the theory. Also shown are  $\bar{\sigma}$  for the unbauffed panel without ribs. These values are notably even less than those of the ribbed panel without a baffle. This is because adjacent subpanels provide baffling to their neighbors. For frequencies less than 250 Hz there are a number of limitations to the experiment including the fact that rib and plate vibration levels were comparable. Other points included in Figure 6.14 were determined by exciting the panel with a reverberant acoustic field and measuring the response. The agreement of these points with those measured by direct shaking shows that the individual panels inside the ribs were acoustically independent of each other and responded to the sound field essentially as described in Section 6.3.

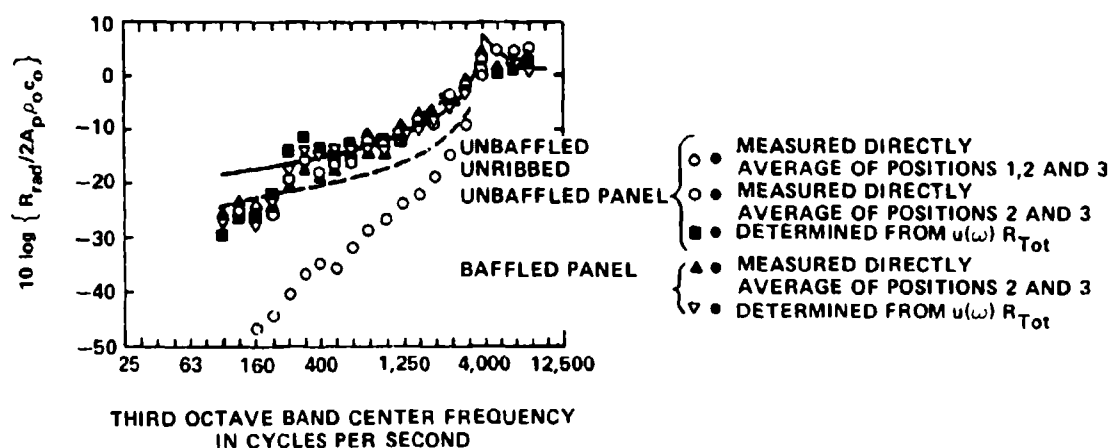


Figure 6.14 - Normalized Radiation Resistance of Test Panel in Figure 6.13  
(From Ref. 7)

(—Theoretical curve for the ribbed test panel from  
Equation (6.90). ---Theoretical curve for the unribbed  
baffled test panel from Equation (6.90.)

Another example of a radiation efficiency measurement is provided by Manning and Maidanik<sup>47</sup> for a cylindrical shell. The geometry of the shell is shown in Figure 6.15. The flanges were removable so that the effects of adding rib stiffeners could be determined. The ends were baffled with plywood boards. Measured radiation efficiencies are shown in Figure 6.16. The ring frequency  $f_r$  is

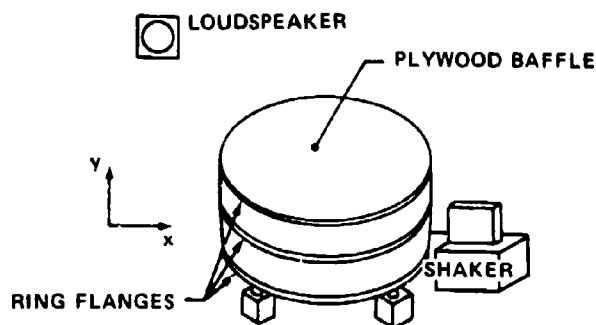


Figure 6.15 - Test Cylinder. Diameter  $d = 36$  Inches, Length  $l = 24$  Inch Thickness,  $h = 1/8$  Inch, Flanges  $1/2 \times 1$  Inch Area  $A = 19$  Feet Squared. From Reference 47.

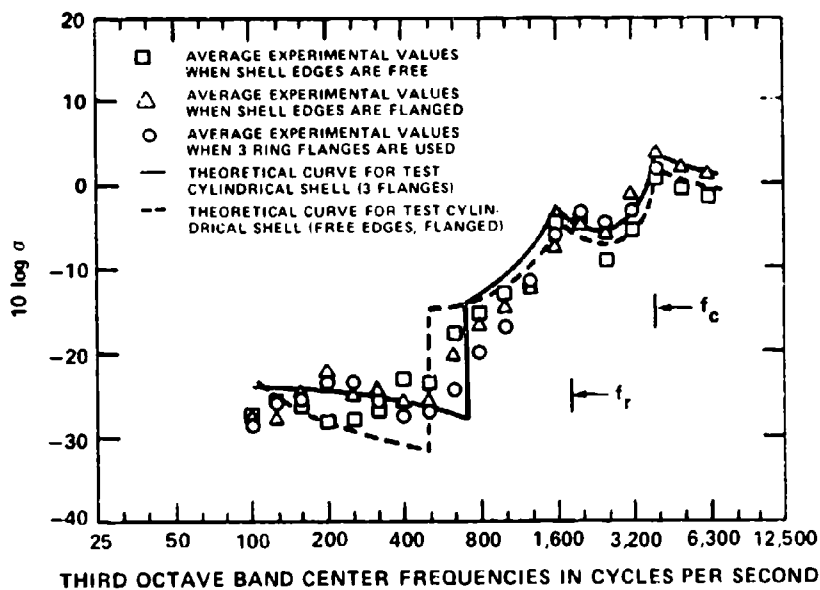


Figure 6.16 - Average Values of the Measured Radiation Efficiency for Three Different Boundary Conditions. From Reference 47

$$f_r = \frac{c_\ell}{2\pi a}$$

where  $a$  is the radius of the cylinder;  $f_c$  is the acoustic coincidence frequency of the cylinder. The modes that radiate most efficiently are those which form circumferential strips at the ends of the cylinder. These modes are such that there is little acoustic cancellation around the circumference. Theoretical estimates are based on applying the appropriate of Equations (6.90) for the classes of modes that were calculated for the cylinder.

The approach to be used in roughly estimating structural radiation and response is to first determine the excitation spectrum  $\Phi_p(\vec{k}, \omega)$  that is included in Equation (6.40a). The autospectrum of the modal pressure  $\Phi_{p_{mn}}(\omega)$  can then be approximated using the limiting functions for  $|S_{mn}(\vec{k})|^2$  shown in Section 6.4. The input power, Equation (6.52) or the mean-square velocity, Equation (6.51), then can be estimated. The radiated sound power can be estimated from Equation (6.87) using the approximate relationships for the radiation efficiency  $\bar{\sigma}$ . Illustrations of these procedures will be given in Sections 6.7 and 6.8. In succeeding chapters some estimates will be compared to measured flow excited vibration and sound for simply defined situations. Another and perhaps more potent use of the equations is their use in scaling one known circumstance to another. Often it is desired to conduct an experiment on a prototype and extrapolate the results to another size. These relationships provide guidelines for planning and conducting the experiments. It is hoped that the examples of acoustic measurements shown exemplify the character of precision to be expected in other similar experiments of the future.

### 6.5.6 Added Masses of Simple Structures

The added mass per unit area on one side of the panel can be determined from the integral in Equation (6.79) for  $k > k_o$ . In the case of low frequencies for which  $k_{mn} > k_o$ , the integral gives the mass per unit area as

$$\begin{aligned} m_{mn} &= \frac{\rho_o}{k_{mn}} & k_{mn} > k_o \\ &= 0 & k_{mn} < k_o \end{aligned} \quad (6.91a)$$



This function is fairly universal, applying both baffled<sup>6,40</sup> and unbaffled<sup>45</sup> plates. In the case of beams, the added mass per unit area is<sup>46</sup> for  $k_m > k_o$

$$m_m = \frac{\pi \rho_o L}{4} \quad \text{for } k_m L_3 < 1 \quad (6.91b)$$

and

$$m_m = \frac{\pi \rho_o L_3}{2} \frac{1}{1 + (k_o L_3)^{-1}} \quad \text{for } k_m L_3 > 1$$

where  $L_3$  is the width of the beam. Similarly, for vibrating circular cylinders<sup>6</sup> of radius  $a$ , the mass per unit area is

$$\begin{aligned} m_m &\approx \rho_o a & \text{for } k_m > k_o \\ &\approx 0 & \text{for } k_m < k_o \end{aligned} \quad (6.92)$$

## 6.6 RADIATION FROM STRUCTURES IN HEAVY FLUIDS

### 6.6.1 Radiation from Essentially Infinite Point-Driven Plates

Until this point, the chapter has been concerned with resonant response of structures with boundaries. When damping is large enough for real structures, waves generated in the structure by a localized force are dissipated before they reach the boundary. As a rule, this occurs when  $\eta k_p L > 1$ . Without reflections at the boundary of the surface, the multiple reflections necessary for resonant modal vibration cannot occur and the surface is effectively infinite. Accordingly, we examine the radiation from locally-applied forces on effectively infinite planar structures.

Although this topic is treated elsewhere<sup>6,50-53</sup> it is instructive to quote some results here. For the geometry illustrated in Figure 6.17, the acoustic far field pressure far enough from the plate that  $k_o r \gg 1$  is<sup>50-52</sup>

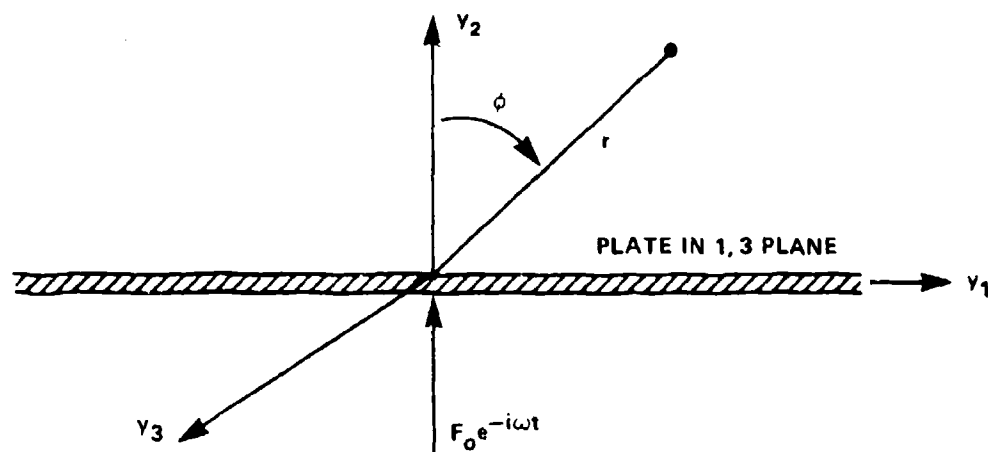


Figure 6.17 - Coordinate System for the Field of a Point-Driven Infinite Plate

$$p(r, \theta, t) = -\frac{ik_o \beta F_o}{2\pi} f(\phi) \frac{e^{i(k_o r - \phi)}}{r} \quad (6.93)$$

where

$$f(\theta) = \frac{\cos \phi}{\cos \phi + \beta} \quad (6.94)$$

and

$$\beta = \frac{\rho_o c_o}{m_s \omega} \quad (6.95)$$

Equation (6.93) applies when the area over which the force extends is smaller than the bending wavelength which, in turn, is smaller than the acoustic wavelength, i.e., the frequency of excitation must be low enough that  $\kappa_p > k_o$ . When the fluid loading is large,  $\beta \gg 1$ , then

$$p(r, \theta, t) = \frac{-ik_o F_o \cos \phi}{2\pi} \frac{e^{-i(k_o r - \omega t)}}{r} \quad (6.96)$$

This expression should be compared to Equation (2.63b) for the dipole radiation from a point force in an unbounded fluid. We see that when the fluid loading is large, a point force applied to the panel radiates twice the sound pressure that it would in free space, but still with a  $\cos \phi$  directivity.

Now if fluid loading is small,  $\beta \ll 1$ , then the pressure is omnidirectional (except near  $\phi=0$  and  $\phi=\pi$ )

$$p(r, \phi, t) = \frac{k_o \beta F_o}{2\pi r} e^{-i(k_o r - \omega t)} \quad (6.97)$$

but reduced by the factor  $\beta$ . This source has monopole-like directivity in contrast to the dipole-like directivity that occurs with fluid loading.

Figure 6.18 illustrates these relationships for cases of an oscillating force of one newton magnitude applied to various materials and thicknesses. The ordinate is  $20 \log |p(r, \phi, t)|$  for  $R = 1$  meter, and on the axis of the force,  $\theta = 0$ .

## 6.6.2 Elements of Fluid Loading Without Modal Coupling

Although fluid loading may, in general, be expected to couple modes as a first approximation, such coupling is frequently neglected. An example of when such coupling can be ignored was given in Section 6.5.2 when it was shown for flat rectangular panels what cross terms may be ignored. Therefore, fluid loading is often approximated as an added mass and damping to the modes which are assumed to have the same in-vacuo mode shapes  $\psi_{mn}(\vec{y})$ .

The fluid loading factor  $\beta$  defined in Equation (6.95) has a general importance in hydroacoustics, especially, that should be emphasized; even for finite plates the value of  $\beta$  determines the relative importance of fluid loading. To see this, we rewrite Equation (6.25) incorporating Equations (6.30) and (6.31) and including the decomposition of pressures:

$$[-m_s \omega^2 + i m_s r_{s, mn} \omega + \omega_{mn}^2 m_s] V_{mn}(\omega) = + i \omega \left[ p_{b, mn}(\omega) - p_{a, mn}(\omega) \right] \quad (6.98)$$

where  $p_{b, mn}(\omega)$  is the modal excitation pressure, but  $p_{a, mn}(\omega)$  is the fluid loading

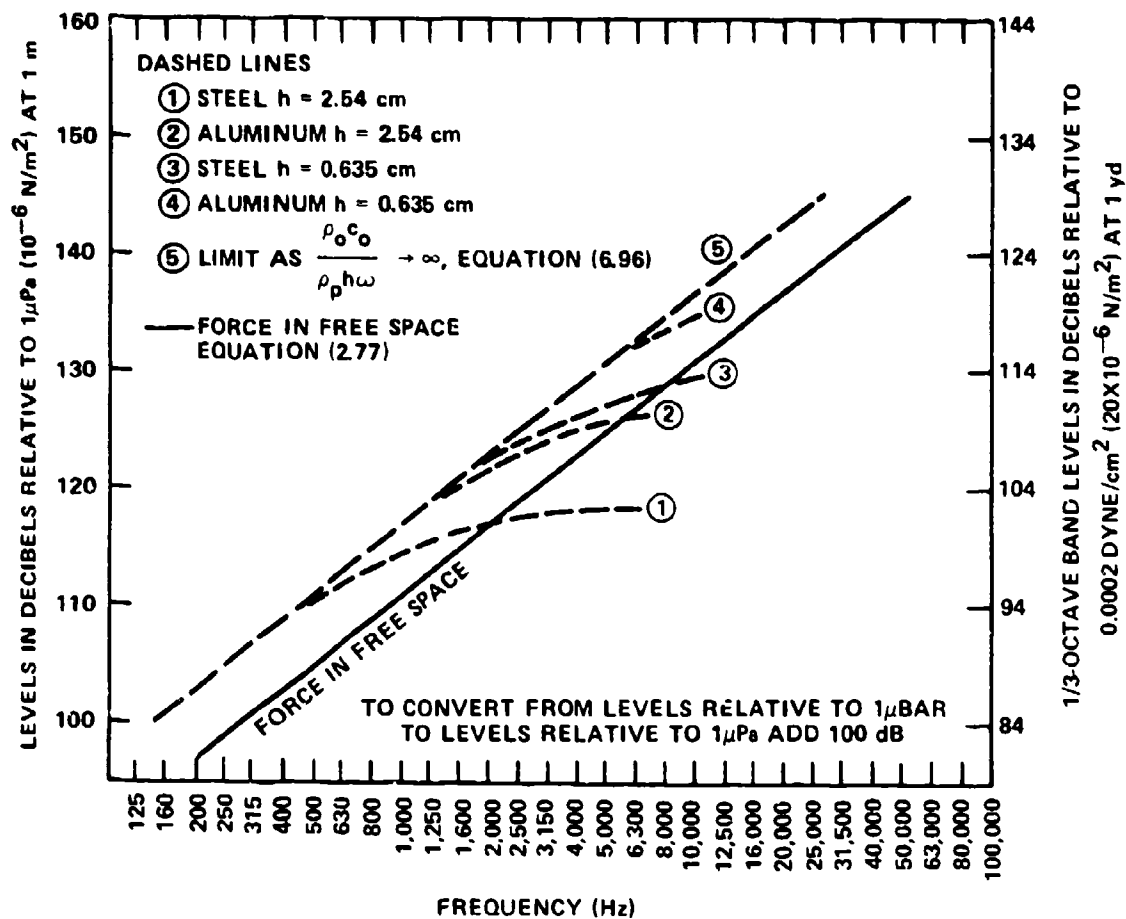


Figure 6.18 - Radiated Sound Pressure Level at 1 Meter on the Axis of a 1 Newton Point Force Applied to Water in Free Space and Applied to Infinite Plates of Various Area Densities

pressure given in terms of the inertia and fluid loading coefficients, Equation (6.76). Introducing these coefficients we have a modified form of Equation (6.33):

$$[(-m_{s_{mn}} - m_{mn})\omega^2 - i\omega(m_{s_{mn}}\eta_{s_{mn}} + \rho_o c_o \sigma_{mn}) + \omega_{mn}^2 m_{s_{mn}}] V_{mn}(\omega) = +i\omega p_b(\omega) \quad (6.99)$$

$mn$

$\omega_{mn}$  is the in-vacuo resonance frequency of the plate. Under the influence of fluid loading we have a new resonance condition

$$\omega_{mn}^2 \underset{\text{F.L.}}{\approx} \omega_{mn}^2 \underset{\text{VAC}}{\left( \frac{m_s}{m_s + m_{mn}} \right)} \quad (6.100a)$$

with a new effective bending wave speed of

$$c_{b_F} = c_{b_{VAC}} \left( \frac{m_s}{m_s + m_{mn}} \right)^{1/4} \quad (6.100b)$$

and an effective, or total, loss factor  $\eta_T$  which is defined as

$$\eta_T = \left[ \eta_s + \frac{\rho_o c_o \sigma_{mn}}{m_s \omega_{mn}} \right] \left[ \frac{m_s}{m_s + m_{mn}} \right] \quad (6.101)$$

$$= \eta_s + \beta \sigma_{mn} = \eta_s + \eta_{rad}$$

The factor  $\eta_r$  is the radiation loss factor of the structure. Thus, the magnitude of the fluid loading factor determines the level of radiation damping to a structure. In the previous equations of Section 6.3, if fluid loading is to be accounted for,  $\eta_s$  should be replaced by  $\eta_T$ . The methods for doing this will be illustrated in the following examples.

Finally, we note that the ratio of the modal input power to the modal acoustic radiated power is, by Equations (6.42), (6.82), and (6.99),

$$\frac{(P_{rad})(\omega)_{mn}}{(P_{in})(\omega)_{mn}} = \frac{\rho_o c_o A_p \sigma_{mn} \sqrt{v_{mn}^2} n(\omega) \Delta\omega}{m_s A_p \eta_T \omega_{mn} \sqrt{v_{mn}^2} n(\omega) \Delta\omega} \quad (6.102)$$

$$= \frac{\rho_o c_o \sigma_{mn}}{m_s \omega_{mn} \eta_T} = \frac{(\eta_{rad})_{mn}}{(\eta_{rad} + \eta_s)_{mn}}$$

If the assumption of equal modal energies applies for all modes in a band and if the modal excitation force is the same for all the modes, then<sup>9</sup> Equation (6.102) applies for average power levels of all modes in large frequency bands, i.e.,

$$\frac{P_{\text{rad}}(\omega)\Delta\omega}{P_{\text{in}}(\omega)\Delta\omega} = \frac{\bar{\eta}_{\text{rad}}}{\bar{\eta}_{\text{rad}} + \bar{\eta}_{\text{s}}} \quad (6.103)$$

where the bars denote average values. Structures may be considered to be lightly radiation loaded when  $\bar{\eta}_{\text{rad}} \ll \bar{\eta}_{\text{s}}$ . Only in these cases do increases in structural damping result in commensurate reductions in radiated sound power. In the alternative case of  $\bar{\eta}_{\text{rad}} > \bar{\eta}_{\text{s}}$ , structural damping is ineffective and all power into the structure is radiated as sound.

## 6.7 EXAMPLE I: RADIATION FROM A RECTANGULAR PANEL DRIVEN BY A TONAL LOCAL FORCE

Examples of the use of the relationships that have been derived in the previous sections will be worked out. The sound that is radiated at large distances from a steel rectangular panel driven at its center with a temporally periodic (tonal) point force will be calculated. The situation is as shown in Figure 6.19. A tonal force of magnitude  $F$  is applied to the center of the rectangular panel of a structure which forms the interface between unbounded air and water regions. The water phase is unbounded and occupies the region  $y_2 > 0$ . As a practical aspect, the panel may be a structural member which is uncoupled from its surroundings just enough to be considered a separate member of a structural aggregate. It is assumed that the panel is simply supported. Because the excitation is a pure tone, energy methods which involve power sums and modal averages are useless. Instead, the following factors must be determined:

1. The mode order
2. Acoustic classification of the mode order
3. Response amplitude of the panel
4. The location in space of the maximum for field pressure
5. The magnitude of the far field pressure

The particulars of the problem are:

Magnitude of the force,  $F = 1$  N amplitude

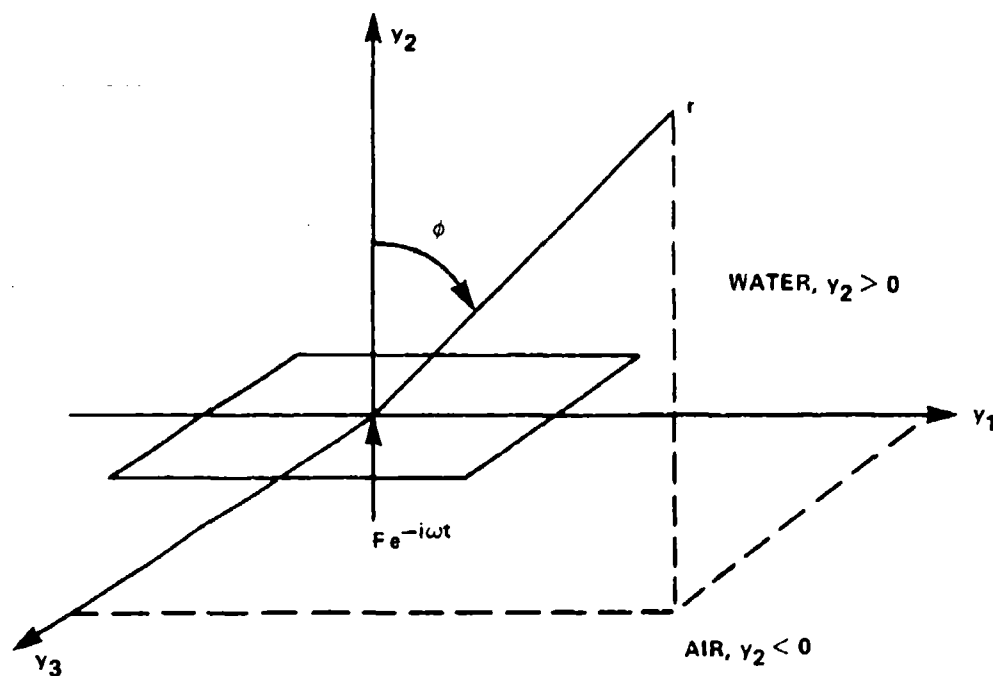


Figure 6.19 - Geometry of a Point-Driven Rectangular Plate Set in a Rigid Baffle which Separates Air and Water Regions

Length,  $L_1 = 1.5$  meter

Width,  $L_3 = 0.6$  meter

Thickness,  $h = 0.0254$  meter (1 inch)

Structural loss factor,  $\eta_s = 0.01$

Frequency of excitation,  $f = 4180$  Hz

Speed of sound in water,  $C_o = 1480$  m/s

Longitudinal wave speed in steel,  $C_k = 5300$  m/s

### 6.7.1 Determination of Mode Order

We must determine which mode, or modes are resonant at 4180 Hz with water loading on one side. The added mass is

$$\frac{m_{mn}}{m_s} = \frac{\rho_o}{\rho_p k_{mn} h} = \frac{\rho_o}{\rho_p k_p h}$$

To a first approximation we use the in-vacuo value of wave number:

$$(C_b)_{VAC} = (\omega C_\ell)^{1/2}$$

$$= \left[ 6.28 \times 4180 \times \frac{0.0254}{(12)^{1/2}} \times 530 \right]^{1/2}$$

$$(C_b)_{VAC} = 1010.1 \text{ m/s}$$

Thus, the modes in the panel are subsonic,

$$k_b = \frac{\omega}{C_b} = \frac{2\pi f}{C_b} = 26 \text{ m}^{-1}$$

Therefore

$$\frac{m_{mn}}{m_s} = 7.7 \times 26 \times 0.0254$$

$$= 0.20$$

The added mass is 20 percent of the steel mass. The bending wave speed is adjusted to

$$C_b = 1010 \left( \frac{1}{1.2} \right)^{1/4}$$

$$C_b = 966 \text{ m/s}$$

and, therefore,

$$k_b = 27 \text{ m}^{-1}$$



It is convenient to normalize the wave number on  $(A_p)^{1/2} = 0.95 \text{ m}$ , thus,

$$\frac{k_b (A_p)^{1/2}}{2\pi} = 4.1$$

The resonant modes of the panel are defined as

$$\begin{aligned} \frac{k_{mn} (A_p)^{1/2}}{2\pi} &= \frac{1}{2\pi} (k_m^2 A_p + k_n^2 A_p)^{1/2} \\ &= \left[ \gamma_m^2 \frac{L_3}{L_1} + \gamma_n^2 \frac{L_1}{L_3} \right]^{1/2} \end{aligned}$$

where  $\gamma_m$  is either  $m$  or  $(m+1/2)$  as defined by Equation (6.53). Figure 6.20 is a diagram of the dimensionless wave numbers  $k_m (A_p)^{1/2}$  and  $k_n (A_p)^{1/2}$ . The intersection of  $k_p$  with the  $k_{mn}$ , which determines the resonance lattice, defines the resonant mode. This occurs for  $(m,n) = (2,2)$  and  $(m,n) = (5,1)$ . The former modes are not resonantly excited because  $\psi_{2,2}$  is zero at the center of the panel. Thus, only the  $(5,1)$  mode is important to this problem. To a first order of approximation this is true, but for insurance one should ideally examine other modes that lie very near the  $k_p$ -arc.

### 6.7.2 Acoustic Classification of Mode Order

At 4180 Hz the acoustic wave number is

$$\begin{aligned} k_o &= \frac{2\pi f}{C_o} \\ &= \frac{6.28 \times 4180}{1480} = 17.74 \text{ m}^{-1} \end{aligned}$$

and

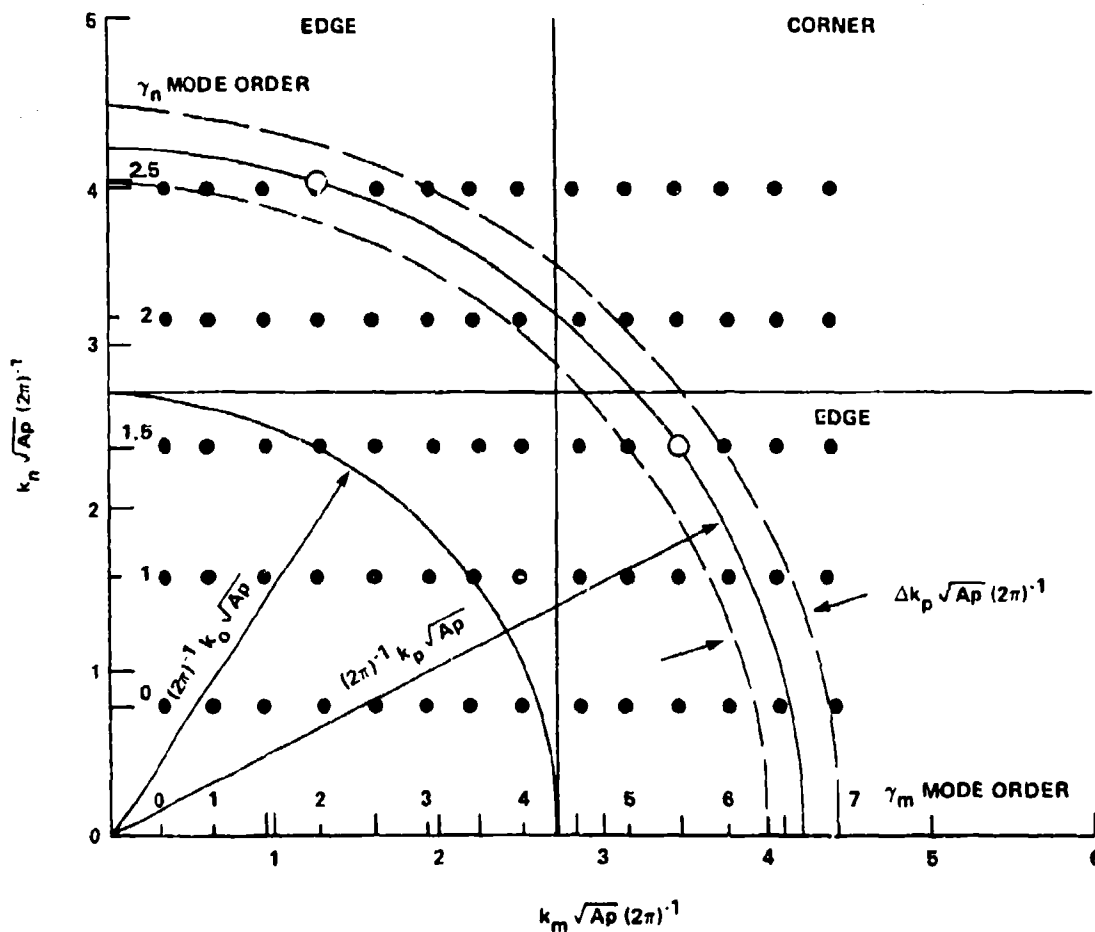


Figure 6.20 - Wave Number Locus for  $1.5 \times 0.6 \times 0.0254$  Meter Panel at  $f = 4180$  Hertz; Half-Integer Modes are those with Maximum Admittance at the Center of the Panel. The Wave Number Band  $\Delta k_p$  is Commensurate with a One-Third-Octave Analysis Band.

$$\frac{k_o (A_p)^{1/2}}{2\pi} = 2.68$$

The arc  $k_o (A_p)^{1/2} / 2\pi$  is also drawn in Figure 6.20 showing that the (5,1) mode is an edge mode. Thus,

$$k_m > k_o \text{ and } k_n < k_o$$

### 6.7.3 Response Amplitude of the Panel

Equation (6.33), which must be used for a pure tone, gives

$$|v_{mn}(\omega)| = \frac{\omega p_{mn}(\omega)}{(m_s + m_{mn})(\omega_{mn}^2 - \omega^2 - i\eta_T \omega_{mn} \omega)}$$

where  $\omega_{mn}$  is the resonance frequency of the mode. The modal pressure is

$$\begin{aligned} p_{mn}(\omega) &= \frac{1}{A_p} \iint p(\vec{y}, \omega) \psi_{mn}(\vec{y}) d\vec{y} \\ &= \frac{1}{A_p} \iint F \delta(\vec{y} - \vec{y}_o) \psi_{mn}(\vec{y}) d\vec{y} \\ &= \frac{F}{A_p} \psi(\vec{y}_o) \\ &= \frac{2F}{A_p} \end{aligned}$$

by Equation (6.53b). Therefore, we have the modal acceleration

$$\omega |v_{mn}(\omega)| = \frac{2F}{M} \frac{1}{\left| \left( \frac{\omega_{mn}}{\omega} \right)^2 - 1 - i\eta_T \frac{\omega_{mn}}{\omega} \right|}$$

for the response where

$$M = (m_s + m_{mn}) A_p$$

### 6.7.4 Location in Space of the Maximum Sound Pressure Level

For the edge modes we have  $k_m > k_o$  and  $k_n < k_o$ , so, by Equation (6.53),

$$S_{5,1}(\bar{k}_1, \bar{k}_3) = 2 \frac{2 \cos\left(\frac{1}{2} \bar{k}_1 L_1\right)}{k_m} \cdot \frac{2k_n \cos\left(\frac{1}{2} \bar{k}_3 L_3\right)}{(k_n^2 - \bar{k}_3^2)}$$

where  $\bar{k}_1$  and  $\bar{k}_3$  are given by Equation (6.75). The amplitude of the sound pressure in Equation (6.76):

$$|p_a(R, \theta, \phi, \omega)| \approx (2\pi)^{-1} \frac{\rho_o \omega}{r} v_{5,1}(\omega) S_{5,1}(\bar{k}_1, \bar{k}_3)$$

where  $S_{5,1}$  is maximum at the angles defined by

$$\bar{k}_3 = k_n = k_o \sin \theta_o \sin \phi_o$$

Therefore, by Equation (6.75),

$$k_o^2 \sin^2 \phi_o = \bar{k}_1^2 + k_n^2$$

so if  $\bar{k}_1 = 0$ , insuring that  $\cos(k_1 L_1/2) = 1$ ,

$$\sin \phi_o = \frac{k_n}{k_o}$$

and this makes

$$\sin \theta_o = 1$$

$$\theta_o = + \frac{\pi}{2}$$

because water occupies only the upper half plane. The maximum sound pressure will occur in the  $y_2, y_3$  plane at angles with the  $y_2$ -axis of

$$\phi_o = + \sin^{-1} \left[ \frac{2.38}{2.7} \right]$$

$$= + 62 \text{ deg}$$

The magnitude of the cosine function is, by L'Hôspital's rule,

$$\lim_{\substack{\rightarrow \\ k_3 \rightarrow k_m}} \frac{\cos \left( \frac{1}{2} k_3 L_3 \right)}{k_n^2 - k_3^2} (-1)^n \frac{L_3}{4k_n} \quad \text{for } n = 0, 1, 2, \dots$$

so that

$$S_{5,1}(k_1, k_3) = 2 \cdot \frac{2}{k_m} \cdot \frac{2L_3}{4}$$

### 6.7.5 Magnitude of the Far Field Pressure

We find now that

$$|p_{a,1}(\omega)| \approx (2\omega)^{-1} \cdot \frac{\rho_o}{r} \cdot \omega |v_{5,1}(\omega)| \cdot \frac{2L_3}{k_m}$$

$$\approx \frac{L_1 L_3}{\pi^2 r} \frac{\rho_o \omega |v_{5,1}(\omega)|}{2\gamma_5}$$

or

$$|p_{a,1}(\omega)| \approx \frac{4}{\pi \gamma_5} \left( \frac{m_s}{m_s + m_{mn}} \right) \left( \frac{k_o F \beta}{4 \pi r} \right) \frac{1}{\left| 1 - \left( \frac{\omega_{res}}{\omega} \right)^2 + i \eta_T \frac{\omega_{res}}{\omega} \right|}$$

where  $\gamma_5 = 5.5$ . The first term in brackets is the ratio of the dry-to-wetted mass. The second term is one-half the sound pressure that would be radiated into the space above the plate if the plate was infinite and lightly loaded, Equation (6.97). It is also  $\beta$  times the pressure that would be radiated by a point in free space. The third term shows the resonance effect.

The total loss factor includes both radiation and structural damping by Equation (6.101). Thus, because the radiation is edge-mode, we have, by Equation (6.85) or Figure 6.11 and the parameters of the problem (letting  $L = A_p^{1/2}$ ),

$$\begin{aligned}\sigma_{mn} &= \frac{2}{\left[ k_m (A_p)^{1/2} \right]^2} k_o (A_p)^{1/2} \frac{L_3}{(A_p)^{1/2}} \\ &= \frac{2}{(6.28 \times 3.5)^2} (6.28 \times 2.68) \left( \frac{0.6}{0.95} \right) \\ &= 44 \times 10^{-3}\end{aligned}$$

The fluid loading factor is

$$\begin{aligned}\beta &= \frac{\rho_o c_o}{\rho_p h \omega} \\ &= \frac{1480}{7.7(0.0254)(6.28)(4180)} \\ &= 0.29\end{aligned}$$

Therefore, by Equation (6.101)

$$\begin{aligned}\eta_T &= 0.01 + (0.29)(0.044) \left[ \frac{1}{1.2} \right] \\ &= 0.018\end{aligned}$$

The radiation damping accounts for half of the total damping of the panel.

The radiated sound pressure level at the resonance is

$$20 \log \left( \frac{p_a}{p_{\text{ref}}} \right) = 20 \log \frac{4}{\pi \gamma_5} + 20 \log \frac{m_s}{m_s + m_{mn}} + 20 \log \beta$$

$$- 20 \log \eta_T + 20 \log \frac{k_o F}{4\pi r P_o}$$

where the final term is then the free space sound pressure level (Equation (2.77)) given in Figure 6.18 and  $p_{\text{ref}}$  is  $10^{-6} \text{ N/m}^2$ . At 4000 Hz

$$20 \log \frac{k_o F}{4\pi r P_o} = 122$$

Therefore,

$$20 \log \left( \frac{p_a}{p_{\text{ref}}} \right) = -13 + (-2) + (-11) - (-35) + 122$$

$$= 131 \text{ re } 10^{-6} \text{ N/m}^2$$

is the sound pressure level at 62 deg off the centerline of the plate in the  $y_2, y_3$  plane referred to a distance from the center of 1 meter. Of course, the actual sound pressure level at a 1 meter distance is not 131 dB because, at this distance, the field point is not in the far field of the plate. The 1 meter reference for far field sound pressures is just a universally recognized convenient distance at which to specify the far-field sound pressure. At other distances  $r'$  the sound pressure level would be adjusted by

$$20 \log \frac{p_a(r')}{p_{\text{ref}}} = 131 + 20 \log \left[ \frac{1 \text{ meter}}{r'} \right]$$

The sound pressure level at the field point  $(r, \phi, \theta) = (1 \text{ m}, 62 \text{ deg}, 90 \text{ deg})$  is shown in Figure 6.21 for a 1 N force. In showing the resonance curve the calculation is envisioned that the frequency of excitation varies through the resonance

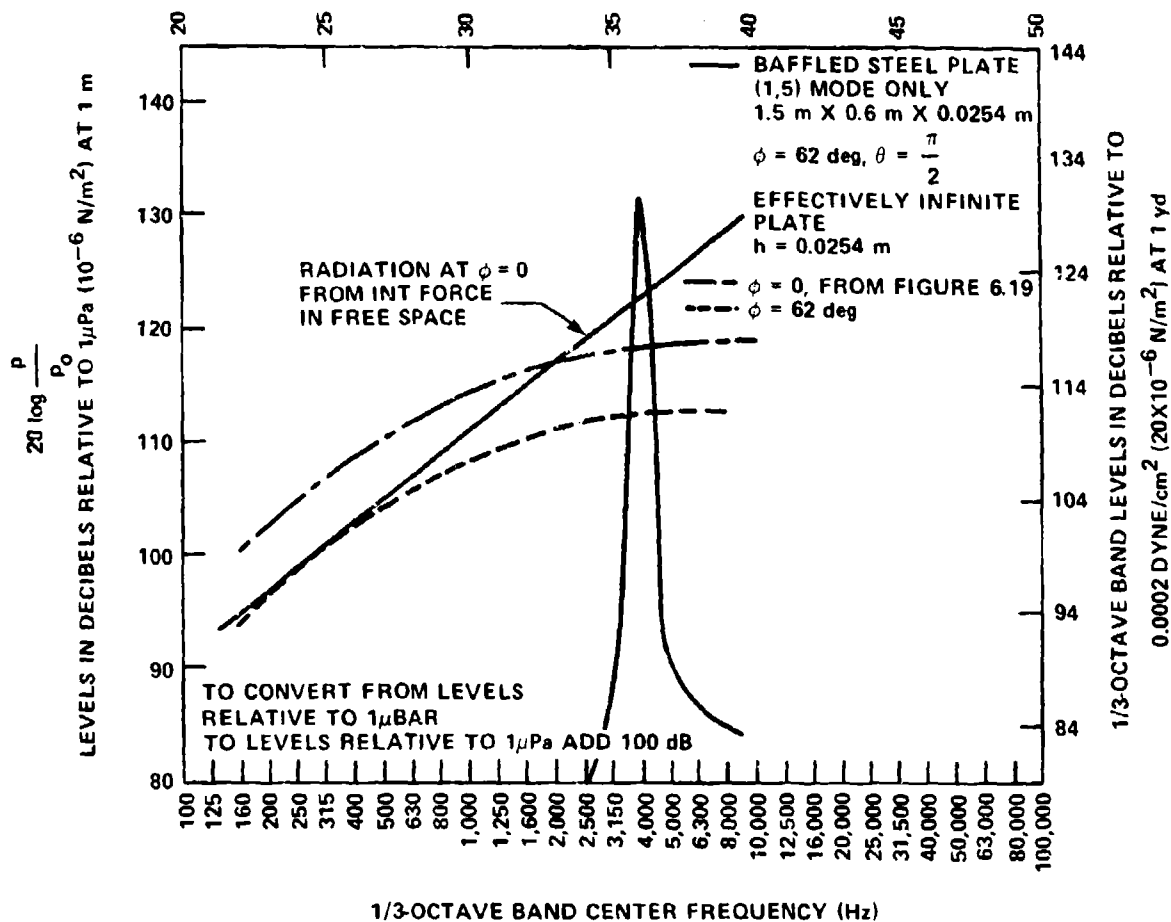


Figure 6.21 - Radiated Sound Pressure at 1 Meter from a Point Force of 1 Newton Driving the Center of a Rectangular Steel Panel. The Field Point ( $R, \phi, \theta$ ) = (1 Meter, 62 Degrees, 90 Degrees) is the Point of Maximum Sound Level)

frequency,  $\omega_{\text{res}} = 2\pi f_{\text{res}}$ . Thus, for this mode, a sharp peak in the noise level occurs. Also shown are two calculations for radiation from a very large (effectively infinite) plate of the same thickness. The directivity of this sound is symmetric, a torus, about the axis of the force. The upper curve applies to the sound pressure on the axis while the lower curve applies to the sound pressure at 62 deg off the axis. This curve is to be compared to the sound pressure level of the rectangular panel. Even though the panel is finite the vibration that is structurally "near-field" or within a distance of  $1/2$ -flexural wavelength from the



drive point, radiates sound just as if the panel was infinite in extent. These sound pressures are presented by the "infinite plate" levels in Figure 6.21. Thus, when the mode is driven off resonance, the sound that is radiated is given by the "infinite plate" levels. Of course, in reality, the sound from other modes of the panel could overwhelm the drive point radiation. If the panel could be suitably damped, for example, with a total loss factor of  $\eta_T = 0.2$ , the resonance mode radiation would be dominated by the radiation from the drive point.

## 6.8 EXAMPLE II: RADIATION FROM A RECTANGULAR PANEL DRIVEN BY A BROADBAND FORCE

The example just considered will be extended to apply to the panel that is point driven with a broadband force spectrum that has a magnitude of 1 N root-mean-square in each adjacent one-third-octave band. This one-third-octave spectrum extends from 500 Hz through 25,000 Hz. The sound pressure level,  $\langle p_a^2 \rangle$  far from the panel, averaged over the surface of a hemisphere of radius  $r$ , is related to the power by (see Equation (2.11c))

$$P_{\text{rad}} = \frac{\langle p^2 \rangle}{\rho_o c_o} 2\pi r^2$$

The power is also related to the mean square velocity of the panel  $\langle v^2 \rangle$  by Equation (6.89b)

$$P_{\text{rad}} = \rho_o c_o A_p \overline{\langle v^2 \rangle}$$

The cross correlation of the pressure on the panel is

$$\begin{aligned} R_{pp}(\vec{r}) &= \frac{1}{A_p} \int p(\vec{y}, t) p(\vec{y} + \vec{r}, t) d\vec{y} dt \\ &= \frac{F^2}{A_p} \delta(\vec{r}) \end{aligned}$$

Therefore, the wave number spectrum  $\Phi_p(k, \omega) d\omega$  can be written

$$\begin{aligned} \int_{-\infty}^{\infty} \Phi_p(\omega, \vec{k}) d\omega &= \frac{i}{(2\pi)^2} \iint e^{+i\vec{k} \cdot \vec{r}} R_{pp}(\vec{r}) d\vec{r} \\ &= \frac{\overline{F^2}}{A_p (2\pi)^2} \\ &= \frac{1}{A_p (2\pi)^2} \int_{-\infty}^{\infty} \Phi_F(\omega) d\omega \end{aligned}$$

where  $\Phi_F(\omega)$  is the frequency autospectral density of the applied force. Note that the wave number spectrum is white, i.e., it is independent of wave number. When applied to the center of the panel, the force excites all modes that are resonant in the frequency band of the force. The modal pressure spectrum is, by Equation (6.40a),

$$\begin{aligned} \Phi_{p_n}(\omega) &= \frac{1}{A_p^2} \iint \left[ \frac{1}{(2\pi)^2} \frac{\Phi_F}{A_p}(\omega) \right] |S_n(\vec{k})|^2 d\vec{k} \\ &= \frac{1}{A_p^2} \left[ \frac{1}{(2\pi)^2} \frac{\Phi_F}{A_p}(\omega) \right] [(2\pi)^2 A_p] \\ \Phi_{p_n}(\omega) &= \frac{\Phi_F(\omega)}{A_p^2} \end{aligned}$$

The mean-square modal velocity for resonant modes is, by Equation (6.41),

$$\overline{v_n^2} = \frac{\pi}{(m_s + m_{mn})} \frac{\Phi_F(\omega)}{\eta_T \omega A_p^2}$$

and the mean-square velocity of all resonant modes in the frequency band  $\Delta\omega$  is, by Equation (6.50),

$$\overline{v^2} = \frac{1}{4} \frac{\pi \phi_F(\omega) n(\omega) \Delta\omega}{(m_s + m_{mn})^2 \eta_T \omega_A^2 p}$$

where the factor  $1/4$  accounts for the fact that only  $1/4$  of the total number of modes have high admittance at the center of the plate.

The lowest resonance frequency of the panel is for the  $m = n = 0$  mode, that is, following Equation 6.53

$$\left( \frac{\omega_{00}}{\kappa C_\ell} \right)^{1/2} = k_{00} = \left[ \left( \frac{\pi}{L_1} \right)^2 + \left( \frac{\pi}{L_2} \right)^2 \right]^{1/2}$$

where

$$C_\ell = (C_\ell)_{\text{VAC}} \left( \frac{m_s}{m_s + m_{mn}} \right)^{-1/4}$$

and

$$\frac{m_{mn}}{m_s} = \frac{\rho_o}{\rho_p k_{00} h} = 0.88$$

for  $f < f_{00}$ . Accordingly,

$$f_{00} = 161 \text{ Hz}$$

At frequencies less than  $f_{00}$  we assume that the motion of the plate is the stiffness controlled first mode. Equation (6.34) gives

$$\overline{v_{00}^2} = \frac{\omega^2}{(m_s + m_m)^2 \omega_{00}^4} \cdot \left(\frac{2}{A_p}\right)^2 2\phi_F(\omega) \Delta\omega$$

and we will use  $\sigma_{00}$  of Equation (6.84) instead of  $\overline{\sigma}$ .

The total sound pressure from resonant modes is  $\Delta\omega$  and is now

$$\overline{p^2}(\omega, \Delta\omega) = \frac{\pi}{8} \left( \frac{k_o^2 \overline{F^2}(\omega, \Delta\omega)}{16\pi^2 r^2} \right) \beta \left( \frac{c_o}{c_b} \right) \frac{\eta_r}{\eta_T} \left( \frac{m_s}{m_s + m_{mn}} \right)^2$$

where

$$c_b = c_{bVAC} \left( \frac{m_s}{m_s + m_m} \right)^{1/4}$$

and where

$$\overline{F^2}(\omega, \Delta\omega) = 2 \phi_F(\omega) \Delta\omega$$

is applied at the center of the panel. For a one-third-octave band

$$\Delta\omega = 0.235 \omega$$

where  $\omega$  is the center frequency of the filter band. The mean-square sound pressure from nonresonant motion at frequencies less than  $\omega_{00}$  is

$$\overline{p^2}(\omega, \Delta\omega) = \left( \frac{\rho_o}{\rho_p} \right)^2 \frac{16}{\pi^6} \frac{\overline{F^2}(\omega, \Delta\omega)}{r^2 h^2} \left( \frac{\omega}{\omega_{00}} \right)^4 \left( \frac{m_s}{m_s + m_{mn}} \right)^2$$

or

$$\overline{p}^2(\omega, \Delta\omega) = \left(\frac{4}{\pi}\right)^4 \left(\frac{\rho_o c_o}{\rho_p h \omega_{11}}\right)^2 \left(\frac{k_o^2 F^2(\omega, \Delta\omega)}{16\pi^2 r^2}\right) \left(\frac{\omega}{\omega_{00}}\right)^2 \left(\frac{m_s}{m_s + m_{mn}}\right)^2$$

The above equations show the pressure radiated from the finite plate as a function of that radiated by a force on an infinite plate in free-space times pertinent structural-acoustic factors and the mass ratio. This type of grouping of terms will be characteristic of future analyses in this book.

Before proceeding with calculations, we must verify that the number of modes in the frequency band is much greater than one. From Equation (6.47) the density of modes of all orders will be

$$n(\omega) = \frac{A_p}{4\pi k C_\ell} = \frac{A_p \omega}{4\pi C_b^2}$$

therefore, at  $f = 4180$  Hz

$$\begin{aligned} n(\omega) \Delta\omega &= \frac{(0.95) [6.28 \times 4180]}{(4 \times 3.14) (966)^2} \cdot [(0.235) (0.28) (4180)] \\ &= 13 \text{ modes} \end{aligned}$$

while at  $f = 400$  Hz, the number of modes is only slightly greater than unity. The density of modes with a high admittance at the center of the plate is only  $1/4$  the total mode density,  $1/4 n(\omega)$ . Therefore, we can expect at least one excited mode per band only at frequencies greater than about 1 kHz. Between  $f = f_{11} = 160$  Hz and 1000 Hz the actual sound pressure will vary depending upon whether or not a particular band contains a resonance.

Figure 6.22 shows the radiation efficiency  $\bar{\sigma}$  and the function  $k_p/k_o$  for the parameters of the example. Equations (6.84) and (6.90) were used where appropriate. The cross-hatched regions express the uncertainties of Equations (6.90d) and (6.90e).

At  $f = 4180$  Hz we calculate  $n_T$  by Equation (6.101), Figure 6.22, and  $\beta = 0.09$

$$\begin{aligned} n_T &= [(0.01) + (0.29)(0.071)] \left(\frac{1}{1.2}\right) \\ &= 0.025 \end{aligned}$$

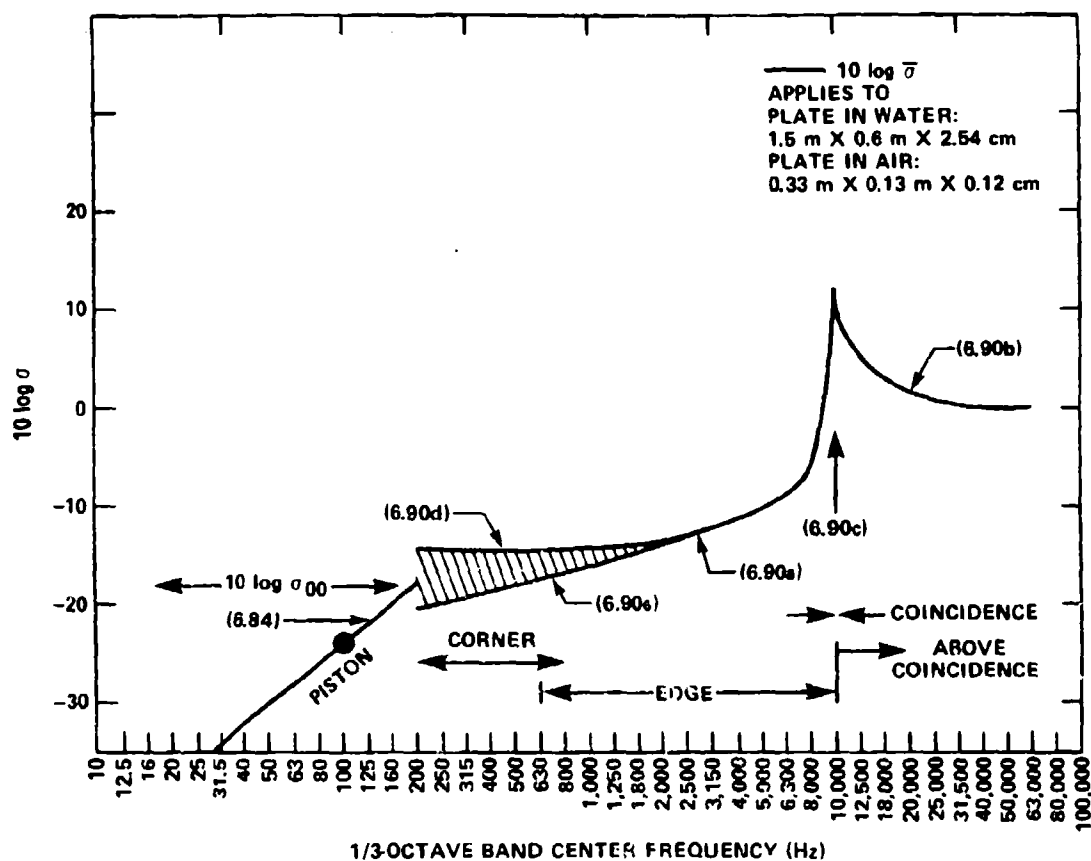


Figure 6.22 - Radiation Efficiencies of Acoustically Equivalent Baffled Steel Plates in Air or in Water Media

Here the radiation damping contributes heavily to the cumulative damping of the modes. Table 6.8.1 shows the ratio  $\eta_r/\eta_T$  for various frequencies including the coincidence frequency,  $f_c = 10,000$  Hz. Note that radiation loss factors are defined as

$$\eta_r = \bar{\sigma} \beta \left( \frac{m_s}{m_s + m_{mn}} \right)$$

TABLE 6.8.1 - COMPARISON OF RADIATION LOSS FACTORS AND TOTAL LOSS FACTORS OF  
A  $1.5 \times 0.6 \times 0.025$  METER PLATE WATER LOADED ON ONE SIDE,  $\eta_s = 0.01$

Frequency Hz	$\bar{\sigma}_r$	$\eta_r$	$10 \log \eta_r / (\eta_r + \eta_s)$
500	0.03	0.04	-2.5
1,000	0.04	0.035	-2
3,000	0.06	0.02	-2
10,000	15	1.5	0
20,000	1	0.10	0

The radiation loss factor at 10,000 Hz indicates that the coincident modes may be critically damped; critically-damped modes have  $\eta_{cr} = 2$ . One could argue, therefore, that radiation loading would probably be important for these modes. The average frequency interval between modes is the reciprocal of the mode density, i.e.,  $\Delta(\omega) = (\eta(\omega))^{-1} = 470 \text{ rad/sec/mode}$ ,  $\Delta(f) = 75 \text{ Hz/mode}$ . For the parameters of this example, the resonant modes at frequencies less than 4 kHz will be uncoupled by radiation damping because, on the average, the band widths of the resonances will be less than the mode spacing of 75 Hz. At greater frequencies the resonance band widths increase due largely to radiation loss, and at 10,000 Hz in particular, all the resonant modes would probably be coupled by radiation damping. The estimate mode without regard to these effects may overestimate the radiation at a given frequency. The root-mean-square force  $F^2$  in all frequency bands is  $1 \text{ N}$ , so that we again use radiation from the free-space force in Figure 6.18 to calculate the panel radiation. Thus, for  $f = 4180 \text{ Hz}$ ,

$$\begin{aligned}
 10 \log \frac{\langle p^2 \rangle}{p_{ref}^2} &= 10 \log \frac{k_o^2 \bar{F}^2(\omega, \Delta\omega)}{16\pi^2 r^2 p_{ref}^2} + 10 \log \frac{\pi}{8} + 10 \log \beta \left( \frac{c_o}{c_b} \right)^2 \\
 &+ 10 \log \frac{\eta_r}{\eta_T} + 10 \log \frac{m_s}{m_s + m_{mn}} \\
 &= 122 -4 + (-1) + [-5 -1 -11 + 16] - 11 \\
 &= 115
 \end{aligned}$$

Figure 6.23 shows the equivalent spatial average sound pressure at 1 m. Note that the expected peak at the coincidence frequencies is removed by radiation damping. At frequencies less than  $f_{00}$  the sound pressure level increases as  $f^4$  due to the fact that it is proportional to the volumetric acceleration of the fluid associated with the displacement of the 0,0 mode of the panel. This example has limited practical significance because the required effects of baffling at low frequencies would be difficult to realize in a physical situation.

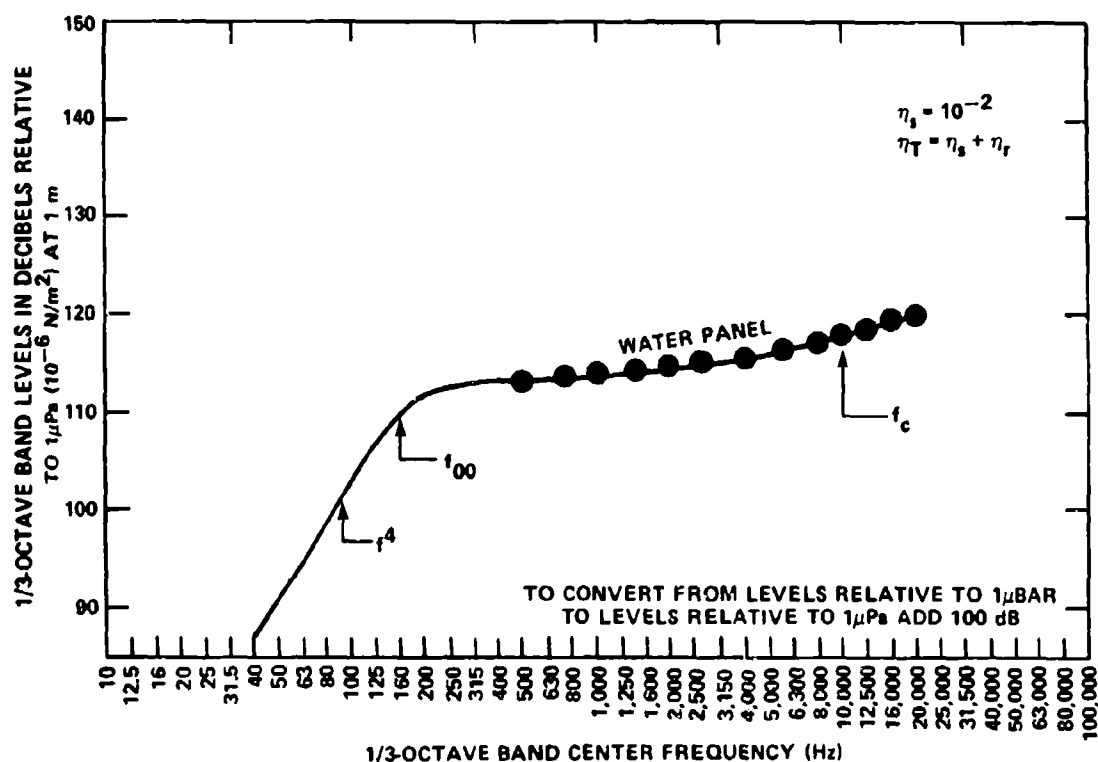


Figure 6.23 - Sound Pressure Levels in One-Third-Octave Bands for 1.5 Meter  $\times$  0.6 Meter  $\times$  2.54 Centimeter Baffled Steel Panel in Water, Driven with 1 Newton Force Spectrum Levels in Each Band, Radiation Efficiencies in Figure 6.22 Apply to the Panel



The effects of radiation damping will not be as apparent in aeroacoustic structures as they are in water-loaded structures. To see this, we rework the example for an acoustically equivalent steel panel in air. To do this, we maintain the plate thickness so that  $(c_o/C_b)$  is the same in air and in water and that  $L_1/h$  and  $L_2/h$  are the same. Such a panel has the dimensions  $0.33 \text{ M} \times 0.13 \text{ M} \times 0.1 \text{ cm}$  with the radiation efficiencies shown in Figure 6.22 applying. Figure 6.24 shows the sound pressure to be expected from such a baffled panel. Note the peak at the coincidence frequency as well as the  $f^4$  behavior at  $f < f_{00}$ . Due to light mass loading, now  $f_{00} \approx 190 \text{ Hz}$ .

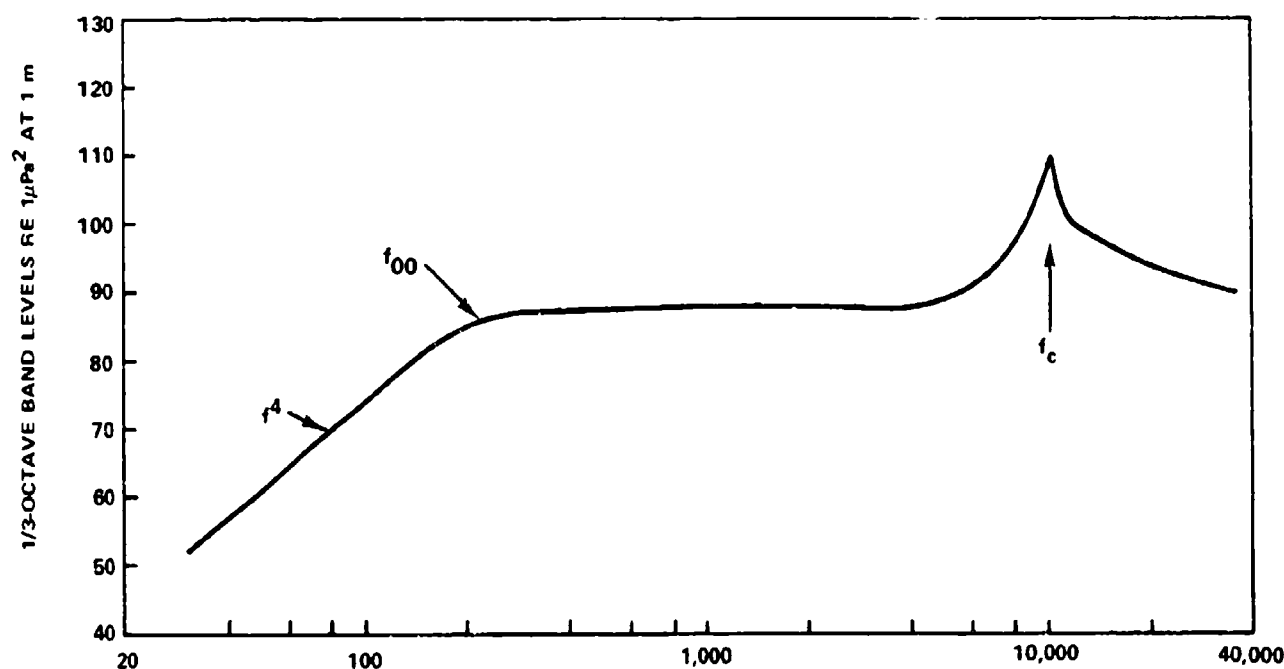


Figure 6.24 - Sound Pressure Levels in One-Third-Octave Bands for Rectangular Steel Plate Simply Supported in a Rigid Baffle Plate in Air.

Dimensions:  $0.33 \text{ Meter} \times 0.13 \text{ Meter} \times 0.12 \text{ Centimeter}$ ;

Structural Damping:  $\eta_s = 10^{-2}$ .

## 6.9 REFERENCES

1. Lin, Y.K., "Probabilistic Theory of Structural Dynamics," McGraw Hill (1967).
2. Crandall, S.H., ed., "Random Vibration," Vol. I, M.I.T. Press (1958).
3. Crandall, S.H., ed., "Random Vibration," Vol. II, M.I.T. Press (1963).
4. Cremer, L. et al., "Structure-Borne Sound," Springer-Verlag (1973).
5. Skudrzyk, E., "Simple and Complex Vibratory Systems," The Pennsylvania State University Press (1968).
6. Junger, M.C. and D. Feit, "Sound, Structures, and Their Interaction," M.I.T. Press (1972).
7. Maidanik, G., "Response of Ribbed Panels to Reverberant Acoustic Fields," J. Acoust. Soc. Am., Vol. 34, pp. 809-826 (1962).
8. Maidanik, G., "Erratum Response of Ribbed Panels to Reverberant Acoustic Fields," J. Acoust. Soc. Am., Vol. 57, p. 1552 (1975).
9. Lyon, R.H., "Statistical Energy Analysis of Dynamical Systems: Theory and Applications," M.I.T. Press (1975).
10. Lyon, R.H. and G. Maidanik, "Power Flow between Linearly Coupled Oscillators," J. Acoust. Soc. Am., Vol. 34, pp. 623-639 (1962).
11. Lyon, R.H., "What Good is Statistical Energy Analyses Anyway," Shock and Vibration Digest, Vol. 2, pp. 1-9 (Jun 1970).
12. Smith, P.W., Jr. and R.H. Lyon, "Sound and Structural Vibration," NASA Contractor Report CR-160 (1965).
13. Fahy, F.J., "Statistical Energy Analyses - A Critical Review," Shock and Vibration Digest, Vol. 6, pp. 1-20 (Jul 1974).
14. Maidanik, G., "Some Elements in Statistical Energy Analysis," J. Sound and Vibration, Vol. 52, pp. 171-191 (1977).
15. Lyon, R.H., "Response of Strings to Random Noise Fields," J. Acoust. Soc. Am., Vol. 28, pp. 391-398 (1956).

16. Kraichnan, R.H., "Noise Transmission from Boundary Layer Pressure Fluctuations," J. Acoust. Soc. Am., Vol. 29, pp. 65-80 (1956).
17. Powell, A., "On the Fatigue Failure of Structures due to Vibrations Excited by Random Pressure Fields," J. Acoust. Soc. Am., Vol. 30, pp. 1130-1135 (1958).
18. Dyer, I., "Response of Plates to a Decaying and Convecting Random Pressure Field," J. Acoust. Soc. Am., Vol. 31, pp. 922-928 (1959).
19. Maidanik, G. and R.H. Lyon, "Response of Strings to Moving Noise Fields," J. Acoust. Soc. Am., Vol. 33, pp. 1606-1609 (1961).
20. Smith, P.W., "Response and Radiation of Structural Modes Excited by Sound," J. Acoust. Soc. Am., Vol. 34, pp. 640-647 (1962).
21. White, P.H. and A. Powell, "Transmission of Random Sound and Vibration through a Rectangular Double Wall," J. Acoust. Soc. Am., Vol. 40, pp. 821-832 (1966).
22. Lyon, R.H., "Boundary Layer Noise Response Simulation with a Sound Field," Acoustical Fatigue in Aerospace Structures, Chapter 10, Syracuse Univ. Press, N.Y. (1965).
23. White, P.H., "Transduction of Boundary Layer Noise by a Rectangular Panel," J. Acoust. Soc. Am., Vol. 40, pp. 1354-1362.
24. Davies, H.C., "Sound from Turbulent-Boundary-Layer Excited Panels," J. Acoust. Soc. Am., Vol. 49, pp. 878-889 (1971).
25. Jameson, P.W., "Measurement of Low Wave Number Component of Turbulent Boundary Layer Pressure Spectral Density," Symposium on Turbulence in Liquids, Rolla, Mo. (1975).
26. Leehey, P., "Trends in Boundary Layer Noise Research," Aerodynamic Noise, Proc. AFOSR-UTIAS Symposium, Toronto, Canada (May 1968).
27. Chandiramani, K.L., "Vibration Response of Fluid-Loaded Structures to Low-Speed Flow-Noise," J. Acoust. Soc. Am., Vol. 61, pp. 1460-1470 (1977).
28. Timoshenko, S. and S. Woinowsky-Krieger, "Theory of Plates and Shells," McGraw-Hill (1959).

29. Kinsler, L.E. and A.R. Frey, "Fundamentals of Acoustics," John Wiley and Sons (1962).
30. Strawderman, W.A., "The Acoustic Field in a Closed Space Behind a Rectangular Simply Supported Plate Excited by Boundary Layer Turbulence," U.S. Navy Underwater Sound Laboratory Report 827 (1967).
31. Obermeier, F., "On the Response of Elastic Plates Backed by Enclosed Cavities to Turbulent Flow Excitations," M.I.T. Acoustics and Vibration Laboratory Report 70208-6 (1971).
32. Arnold, R., "Vibration of a Cavity Backed Panel," M.I.T. Acoustics and Vibration Laboratory Report 70208-7 (1971).
33. Leissa, A.W., "Vibration of Plates," NASA Report SP-160 (1969).
34. Aupperle, F.A. and R.F. Lambert, "On the Utilization of a Flexible Beam as a Spatial Filter," J. Sound Vibration, Vol. 24, pp. 259-267 (1972).
35. Martin, N.C., "Wave Number Filtering by Mechanical Structures," Mass. Inst. Tech., Ph.D. Thesis (1976).
36. Copson, E.T., "Asymptotic Expansions," Cambridge University Press (1965).
37. Chase, D.M., "Turbulent Boundary Layer Pressure Fluctuations and Wave Number Filtering by Non-Uniform Spatial Averaging," J. Acoust. Soc. Am., Vol. 46, pp. 1350-1365 (1969).
38. Blake, W.K. and L.J. Maga, "On the Flow-Excited Vibrations of Cantilever Struts in Water. I Flow-Induced Damping and Vibration," J. Acoust. Soc. Am., Vol. 57, pp. 610-625 (1975).
39. Blake, W.K. and L.J. Maga, "On the Flow-Excited Vibrations of Cantilever Struts in Water. II. Surface Pressure Fluctuations and Analytical Predictions," J. Acoust. Soc. Am., Vol. 57, pp. 1448-1464 (1975).
40. Davies, H.G., "Low Frequency Random Excitation of Water-Loaded Rectangular Plates," J. Sound Vibration, Vol. 15, pp. 107-126 (1971).
41. Davies, H.G., "Excitation of Fluid-Loaded Rectangular Plates and Membranes by Turbulent Boundary Layer Flow," presented at the American Society of Mechanical Engineers Winter Annual Meeting, Paper 70-WA/DE-15 (Dec 1970).

42. Davies, H.G., "Acoustic Radiation by Fluid Loaded Rectangular Plates," M.I.T. Acoustics and Vibration Laboratory Report 71476-1 (1969).
43. Wallace, C.E., "Radiation Resistance of a Baffled Beam," J. Acoust. Soc. Am., Vol. 51, pp. 936-945 (1972).
44. Wallace, C.E., "Radiation Resistance of a Rectangular Panel," J. Acoust. Soc. Am., Vol. 51, pp. 946-952 (1972).
45. Blake, W.K., "The Acoustic Radiation from Unbaffled Strips with Application to a Class of Radiating Panels," J. Sound Vibration, Vol. 39, pp. 77-103 (1975).
46. Blake, W.K., "The Radiation of Free-Free Beams in Air and Water," J. Sound Vibration, Vol. 33, pp. 427-450 (1974).
47. Manning, J.E. and G. Maidanik, "Radiation Properties of Cylindrical Shells," J. Acoust. Soc. Am., Vol. 36, pp. 1691-1698 (1964).
48. Chertock, G., "Sound Radiation from Prolate Spheroids," J. Acoust. Soc. Am., Vol. 33, pp. 871-880 (1961).
49. Chertock, G., "Sound Radiation from Vibrating Surfaces," J. Acoust. Soc. Am., Vol. 36, pp. 1305-1313 (1964).
50. Maidanik, G. and E.M. Kerwin, "The Influence of Fluid Loading in the Radiation from Infinite Plates Below the Critical Frequency," Bolt Beranek and Newman Report 1320 (1965).
51. Maidanik, G., "The Influence of Fluid Loading on the Radiation from Orthotropic Plates," J. Sound Vibration, Vol. 3, pp. 288-299 (1966).
52. Feit, D., "Pressure Radiated by a Point-Excited Elastic Plate," J. Acoust. Soc. Am., Vol. 40, pp. 1489-1494 (1966).
53. Ross, D., "Mechanics of Underwater Noise," Pergamon Press (1976).

## INDEX

- Acoustic coincidence frequency, 582
- Acoustic compactness, 497
  - and lifting surface noise, 908
- Acoustic impedance, specific, 39
- Acoustic intensity, 17, 39
  - Aeolian tone, 504
  - far field, definition, 38
  - jet noise, 166
  - rotating rod, 514
- Acoustic power, 40
  - and input power, 599
  - dipole, 49
  - effect of reflecting surface on, 48
  - free jet, 169
  - monopole, 48
  - rectangular plate, 579-581
- Acoustic radiation:
  - point force on infinite plate, 594-597
  - rectangular panel:
    - example, 604-609
    - formulation, 571-575
- Acoustic radiation damping, 598
- Acoustic radiation efficiency, 8
  - baffled beam, 587
  - definition, 8, 581
  - measurements, 587, 590-593
  - modal average, 588-590
  - mode classifications of
    - rectangular plate, 583, 602
  - numerical example, 615
  - unbaffled beam, 586
  - unbaffled plates, 585
- Acoustic radiation efficiency,
  - rectangular plate:
    - corner mode, 584
    - edge mode, 584
    - surface mode, 585
- Acoustic radiation loss factor, 247, 553, 615
- Acoustic radiation resistance, 579
  - (see also acoustic radiation efficiency)
- Actuator disc, propeller, 1112
- Added mass, 593
  - and fluid loading, 597-598
- Adiabatic, 35, 55
  - expansions, 36, 240
  - oscillations, 245
- Advance coefficient, 428, 1113
  - nomographs, 33, 429
- Aeolian tone, 89, 449, 507
  - intensity of, 504-507
  - (see also vortex shedding, cylinder, airfoil)
- Aerodynamic Influence Functions
  - (see lift, fluctuating on airfoils)
- Air, physical properties of, 427
- Airfoils, summary of noise source (table), 903-904
- Array, as a spatial filter, 760
- Average:
  - in space, 154, 555
  - in time, 17, 153, 543
  - over resonant modes, 562-563
- Axial flow fan noise:
  - basic equation for blade rate tones, 1131
  - broadband related to loading, 1152-1159
  - ducted rotor, basic equation, 1199
  - general equation for, 1124-1128
  - Gutin Sound, 1142
  - laminar flow tones, 1145
  - table of rotor parameters, 1154
  - thickness noise, 1159
  - turbulence induced, 1190
- Barotropic fluid, definition, 35
- Beam, mode density, 560
- Beam, radiation efficiency, 587
- Bending waves, phase speed of, 549
- Bernoulli's equation, 82, 233
- Bernoulli-Euler equation, 546
- Bessel's functions, 1128
- Blade element analysis:
  - turbulent inflow, 1181-1185
- Blade rate forces:
  - acoustic radiation from, 1136-1147
  - blade element analysis, 1130-1136
    - (see also lift, fluctuating on airfoils)
  - induced by turbulence, 1186
    - example, 1192
    - limiting equations, 1189-1190
  - influence of expanded area ratio, 1180
  - measurement example, 1141
- Blade rate noise:
  - from compact rotor, 1141
  - general behavior, 1100-1103
  - general equations, 1131, 1138
- Blade row:
  - acoustic blade interactions, 1176
  - and unsteady lifting and surface theory, 1177
  - aerodynamic blade interactions, 1174
  - as spatial filter, 1100-1101, 1187
  - basic equation of interaction tones, 1164
  - harmonic analysis of wake defects, 1161
  - Kemp-Sears theory, 1161, 1166-1168
  - thrust coefficient, influence of blade interaction, 1120
  - viscous and potential interactions, 1167

- Blade slap, 1169-1172
- Blade stresses, 1123
- Blade thickness noise, 1159
- Blade turbulence interaction, 1103
- Blade vortex interactions, 1097, 1169-1173  
(see also Blade slap)
- Boundary layers:
  - equilibrium, 624
  - self-preserving, 624, 629
- Bubbles, collapse of cavitation, 283
  - adiabatic gas law, 292
  - and presence of walls, 301
  - collapse time, 285
  - details of final stage, illustration, 293
  - effect of internal pressure on, 291  
(see also diffusion and vaporous cavitation)
  - effects of viscosity, 300
  - empty bubbles, 294
  - illustrations, 286-287
  - limiting functions, 295-299
  - limiting velocities of bubble wall, 288, 297
  - minimum radius, 291-292
  - non-spherical bubbles, 300
  - Rayleigh's equation, 383-385
- Bubbles, formation of, 413-423
  - and noise, 413  
(see also bubbles, linear oscillations)
  - by diffusion, 267-272
  - in turbulence, 312-316, 422-423
  - jet break-up, 417-421
  - jet break-up in cross flow, 408-411
  - periodic, 409, 414
  - sizes and sounds (table), 412
  - splitting, 422
- Bubbles, linear oscillations, 244-258
  - amplification factors, 266
  - damping, 243-247
  - noises emitted from, 397-412
    - observed, 407-411
    - sound pulse illustration, 398
    - speed dependence, 404, 406, 411, 412
  - resonance frequency, 243, 245
  - simple harmonic motion, 243-248
- Bubbles, non-linear motion, 259ff
  - critical pressure, 260-262
  - critical pressure illustration, 262
  - critical radius, 261
  - limiting radius, 265
  - onset of, 259
  - radius time curve illustration, 259
  - radius time dependence in turbulent layer, 326
  - radius time formula, 264

- Bubble distribution:
  - definition of, 250
  - in mixtures, 252  
(see also nucleus distribution)
- Bubble dynamics, basic equation of, 238-242
- Bubble equation, linearization, 243
- Bubble rebounds, 287, 335
- Bubbly mixture:
  - sound propagation, 248-259
  - speed of sound, 251
  - transmission in, 251
- Cascade (see Blade row)
- Cavitation:
  - and nucleus distribution, 381-383, 386-390
  - and turbulence structure, 386
  - behind disk, 321
  - behind orifice plate, 321
  - bubble screening, 387-388
  - event rates, 384-390
  - free jet, 322
  - in periodic vortex street, 320
  - mass of gas diffused during, 271
  - propeller noise, bubble model, 394-397
  - propellers, 365  
(see also propeller cavitation)
  - separating laminar boundary layers, 327
  - tip vortex, 319, 368
    - photograph, 368
  - turbulent boundary layer, 324
- Cavitation, bubble:
  - photographs on hydrofoil, 358
  - photographs on propeller, 367
- Cavitation inception:
  - bubble equation, 306-310
  - critical pressures for, 260, 308
  - diffusion influences, 268
  - disk, sharp edged, 321
  - hydrofoil, 303, 312
  - influence of dissolved gas, 272, 310
  - in turbulent boundary layer, 324
  - isolated roughness, 331-333
  - orifice plates, 321
  - scale effects, 302-306, 327-331
  - separated laminar boundary layer, 327-330
  - thresholds for gaseous type equation, 311, 315
  - turbulent jets, 322
  - vortex cavitation, 316
  - vortex streets, 320
- Cavitation index, 17, 234, 302-333
  - nomograph, 429

- Cavitation noise:
  - alternative length and time scales, 346, 348-350, 370
  - dependence on hydrostatic pressure, 347-352, 370
  - free jet observation, 353
  - hydrofoil cavitation observation, 357-365
  - hydrofoil noise from, 357
  - rotating blade, 376
    - (see also propeller cavitation)
  - rotating rod, 345
  - rules of similitude, 344-352
    - with shock formation, 350-352
    - with unequal cavitation indices, 348-349
  - single bubbles:
    - and liquid compressibility (shocks), 341
    - and liquid compressibility (shocks)
      - effect on spectrum, 343
    - and stages in bubble history, 338
    - ideal spectrum function, 337-341
    - time trace, 335
  - stochastic models:
    - and statistics of turbulence, 383
    - and bubble statistics, 386
    - prediction and scaling rules, 374-380, 390-397
- Cavitation noise modeling:
  - and hydrofoil cavitation, 360-361, 378-379
  - and jet cavitation, 354-355
  - propeller cavitation, 394-397
  - stochastic theories of, 381-397
- Cavitation nuclei,
  - (see Nucleus distribution)
- Cavitation number,
  - (see Cavitation index)
- Cavitation sheet, 367
  - photograph on hydrofoil, 364
- Cavitation thresholds, 272
  - (see also nucleus distribution, critical pressure)
  - acoustic methods of measurement, 281
    - (see also bubbly mixture, transmission of sound in)
  - event counting, 281
  - influence of gas content, 272
  - measurements, 273, 274
  - stabilized cavitation nuclei, 275
- Cavitation types:
  - photograph on headform, 305
  - photograph on propeller, 367, 368
- Cavity resonance, 125
- Cavity tones, 129, 130
  - sound radiation from, 133
  - Strouhal number illustration, 130
- Circulation, definition, 84
- Circulation of Vortex Streets, 320, 988, 992
- Clamped beam, 565
- Coincidence frequency:
  - acoustic, 582
  - hydrodynamic, 842-844
- Coaxial nozzle, vortex shedding, 1011
- Compressor noise:
  - overview of sources, 1097-1100
- Continuity equation, 34, 52, 82
- Convection velocity of turbulence, 177, 665
- Corner (acoustic) mode, 583
- Correlation area, 189, 669, 868
  - definition, 669
- Correlation functions:
  - and statistical probability, 153
  - and Taylor's hypothesis, 183
  - centroid, 504
  - Fourier transform of, 155-160
  - illustrations of, 216, 480, 656, 658, 738, 999, 1059
  - inequalities, 659
  - separable representations of, 182, 184
- Correlation length, 64, 180, 672
  - relationship to wave number spectrum, 180
- Correlation volume, 189
- Covariance (see also correlation functions)
  - spatial, 64
- Critical pressures, 234
  - cavitation inception, 260-262
  - crevices in hydrophobic particles, 276
- Cross spectral density:
  - determination from filtered signals, 213
  - measurement, 208
  - physical interpretation of, 208-209
  - spatial, 155, 158
- Curle of vector, 82
- Curle's equation, 69, 497
- Cut-off, (cut-on) frequency, 1169, 1200
- Cylinder:
  - drag coefficients of, 464
  - pressure distribution, 464
- Cylinders, noncircular cross section, 519
- Cylindrical coordinate system, 41
- Damping:
  - acoustic radiation, 598
  - bubbles, 244-246
  - control of hydroelastic vibrations, 1055-1056
  - hydrodynamic, 1044
  - in presence of vortex shedding, 1050
  - in simple harmonic oscillator, 542, 533
  - vibration decay, 544
  - viscous, 1046
  - with fluid loading, 599



- Decibel, 18
- Delta function, 99
  - as Fourier transform of exponential, 99, 156
- Diffusion of Gas:
  - and gaseous cavitation, 267
  - and vaporous cavitation, 270
  - coefficient, 269
  - convective, 268-270
  - critical pressure for, 262
  - rectified, 270
- Diffusivity, (diffusion coefficient), 269, 427
- Dipole, 2, 44, 69, 91
  - directivity, 48, 518, 917
  - enhancement to jet noise, 1011, 1034
  - force, 46, 73-74
  - heaving sphere, 71-73
  - near a half-plane, 914
  - sound in free space, 44, 914
  - sound in two phase flow, 203-204
- Directivity patterns:
  - compact dipole, 48
  - edge noise, 916-917
  - jet noise, 167
  - point force on infinite plate, 595-596
  - propeller noise, 1144
  - quadrupole, 50
  - rotating rod noise, 518
- Displacement thickness, 642
- Distortion harmonics
  - (see also axial flow fan)
  - general description, 953, 1101
  - formulation of unsteady loads, 1132-1135
  - rotor-stator interaction, 1162-1165
- Divergence operator, 35
- Divergence theorem (see Gauss' theorem)
- Drag coefficient, cylinders:
  - definition, 462
  - fluctuating, 472, 477
  - oscillatory, 473
- Duct acoustics, 1193-1196
- Eddy (see vortex)
- Edge (acoustic) mode, 582-583
- Edge tone, 140, 143-148
  - effective dipole force, 148
  - Strouhal number, illustration, 146
- Efficiency, Propeller, 1121
- Eigenfunctions, 547
  - in Plesset theory, 269
  - in process, 154
- Error Function, 985
- Euler's equation, 52
  - (see also momentum equation)
- Expanded area ratio, 1117
- Fan (see axial flow fan)
- Feedback:
  - in self excited flows, 144
  - vortex shedding
    - cylinder wakes, 484, 1056, 1057
    - trailing edge flow, 1057-1062
- Filter:
  - electronic, 18
  - one-third octave, 22
- Flexural waves, 549-551
  - matching with acoustic waves, 578
  - matching with hydrodynamic waves, 851
- Flow induced vibrations:
  - by convected pressure fields, 834-844
  - cavitation induced, 363-365
  - hydroacoustic mode classification, 858
  - mode classifications, 851
  - noise control principles, 861-868
- Fluctuations, stochastic, 97
- Fluid loading, 553, 566-579, 1097
- Force dipole, 73-74
- Fourier transform, 24, 92, 98, 158-160
  - relationships, 155-160
  - spatial, 102
- Free surface boundary, 48
- Frequency, 19
- Frequency filter function, 211
- Friction velocity, 628
- Froude number, 17, 237, 414
- Gaseous cavitation, 231, 267-272
- Gauss' theorem, 62, 68
- Gradient operator, 35
- Green function:
  - free space, 93
  - half-plane, 912
  - opening in rigid wall, 133
  - rigid plane, 95
  - separable, 102
  - sources in ducts, 1195-1196
- Gutin sound, 1142
  - in duct, 1201
- Half-plane (see trailing edge)
- Helicopter rotor noise, 1153, 1172
  - (see also blade vortex interactions)

- Helmholtz integral equation, 92
  - trailing edge noise, 919
- Helmholtz (cavity) resonance, 132, 135
- Henry's law, 268, 427
- Hole tones, 139, 143
- Hydrodynamic coincidence, 834-840
  - frequency, 837, 839, 842, 844
- Hydrodynamic instability, 118-121, 135-149
  - amplification by sound, 142-144
  - amplification by vibration, 1057-1060
  - free shear layer, 121, 963
  - in wake of airfoil, 963-969
  - in wake of cylinder, 457-459
- Hydrophobic particles, 275
- Impedance, definition, 538
- Impedance:
  - acoustic, 39
  - infinite plate to point force, 564
- Inlet flow distortion (see Distortion Harmonics)
- Intensity (see acoustic intensity)
- Intermittency, 795
- Isothermal motion, 240
- Jets, turbulent:
  - noise, 61
    - axisymmetric disturbances, 196
    - enhancement by proximate edge, 1034
    - formal analysis, 160-166, 189
    - frequency dependence, 169, 192
    - measurements, 166-170
    - subsonic noise, 160-170
  - turbulent velocity:
    - covariances, 177
    - cross spectral densities in, 187
    - dimensional analysis, 192-195
    - integral scales, 180
    - turbulence levels, 174, 179
    - vortex structures, 141
    - wave number spectrum, 182
  - two-phase, 197-207
    - bubble noise from, 206-207
    - dipole sound from, 201, 203
    - monopole sound from, 203
- Jet laminar, 118, 121-122, 135-149
- Jet stability, 135-149
- Jet tones, Strouhal number illustration, 139
- Karman vortex street, 486, 906
- Kirchhoff's equation, 56-60
- Kutta condition, steady flow, 929
  - importance in analysis of trailing edge noise, 1016
- Laminar boundary layer, 118, 121, 327, 790, 971, 1007-1010, 1145-1149
- Laplacian operator, definition, 37
- Law of the wake, 636
- Law of the wall, 633
- Leading edge noise (see Lift, fluctuating on airfoils)
- Lift, fluctuating on airfoils:
  - aerodynamic influence functions, 933, 939-942
  - differential pressures due to, 935, 943-946, 952
  - due to gusts, 932, 939-942
  - due to upstream wakes, 951-954
  - due to vortex shedding, 1001
  - sound radiation in turbulence, 946-950
  - surface pressures due to, 943-945
- Lift, fluctuating on cylinders:
  - correlation function for, 479
  - correlation length, definition, 479
  - measurement illustration, 474
  - sound radiation from, 502-508
  - theory versus measurement, 495
  - two-dimensional vortex model, 486-495
- Lifting surface theory, 1177
- Lighthill's equation, 52, 60
  - free-space form, 62
- Loss factor, definition, 541
  - (see also damping)
- Mach number, 5, 14, 31
- Matched asymptotic expansion, 109
- Mean square, 18, 152
- Membrane waves, 551
- Micropascal, 18
- Microscale, turbulence, 180
- Modal density, 559, 615
- Modal force (see modal pressure)
- Modal Pressure:
  - definitions for random excitation, 548, 554
  - from turbulent boundary layer, 840
  - from point force, 604, 606, 611
  - random excitation of single mode, 554
  - vibration of hydrofoils, 1039
- Modal shape functions:
  - asymptotic forms of, 570
  - cantilever plates, 1042
  - ducts, 1195-1196
  - even-order mode shape, 568
  - for simple structures, 565-571
  - normalization, 566
  - simply-supported membrane, 566
  - simply-supported plates, 565
- Mode count:
  - hydrodynamically coincident modes, 852
- Momentum equation, 34, 82

- Momentum integral equation, 642
- Momentum thickness, 642
- Monopole, 2, 4?
  - and cavitation, 334
  - sound in inhomogeneous discharge, 203
- Moving axis correlation, 185, 660, 1184
- Newmann boundary condition, 95
- Nomographs:
  - advance coefficients, 33
  - bubble resonance frequencies, 245
  - cavitation indices, 429
  - decibel addition chart, 24
  - dynamic pressure, 31
  - hydrodynamic coincidence frequencies, 844
  - radiation efficiencies of plates, 615
  - tip velocities of propellers, 33
  - vibration and noise control, 863
- Nozzles, 135-137
- Nucleation, cavitation, 275
  - wetting, 275-277
- Nucleus distribution:
  - illustration, 279, 280
  - measurement of, 278
    - event counting, 281
    - acoustic absorption, 281
    - optical methods, 283
- Orifices, 149
- Orifice tones, 141
  - Strouhal numbers, illustration, 142
- Orr-Sommerfeld equation, 120
  - (see also hydrodynamic instability)
- Orthogonal functions, 547
- Pascal, 18
- Peclet number, 270
- Pipe flow, 783
- Pitch, 1186
- Pitch angle, 1115
- Plane boundary, sound from turbulence near, 76-79
- Powell's reflection theorem, 74-79
- Powell's theory of vortex sound, 80-90
- Power dissipated, 543
- Power, input:
  - simple harmonic oscillator, 544
- Power:
  - and modal pressure, 563
  - input to flexural waves, 555, 563-565
  - net of many modes, 563, 565
- Power spectral density (see spectral density)
- Pressure, acoustic, 18, 35-39
- Pressure, dynamic, 27, 30
- Pressure release boundary (see free-surface boundary)
- Propeller cavitation, 365-376
  - blade analyses, 390-397
  - blade passage frequency, 366
  - noise, 369, 372
  - noise, dependence on speed, 374-378
  - noise scaling, 370, 373, 375
  - photographs, 367-368
  - tip vortex, illustration, 368
  - velocity dependence, 376
- Propeller diagram, 1115
- Propeller noise control tradeoff example, 1124
- Propeller singing, 1158-1159
- Propulsive efficiency, 1112
- Quadrupole, sound, 2, 49-51, 61
  - importance to Aeolian tone, 500-502
  - lateral, 49
  - longitudinal, 49
  - Reynolds stresses as sources of, 66
  - sources, 49-51
  - jet noise, 66, 167
- Quality factor, 542
  - (see also damping)
- Radiation:
  - condition, 51-52, 94
  - loss factor (see acoustic radiation loss factor)
  - resistance (see acoustic radiation efficiency)
- Radius of gyration, plate, 546
- Random variable:
  - homogeneous, 153-159
  - spatially homogeneous, 103, 153
  - temporally homogeneous, 153
- Random vibration:
  - (see also power, input and modal pressure)
  - multi-mode oscillators, 556-564
  - simple harmonic oscillator, 541
  - two-dimensional structures, formulation, 552-565
- Rectangular plate:
  - flexural modes, 556
  - mode density, 559
- Reduced wave equation, 92
- Retarded time, 61
- Reynolds number, 13, 235, 236
- Reynolds stress, 54, 55
  - fluctuating, 63
  - near a half plane, 919
- Ring frequency, cylinder, 593

- Ring tone, 143-144
- Rotating cylinder, geometry, 498
- Rotating rods:
  - directivity patterns, 518
  - measured, 515-518
  - radiation, 511-517
  - spectral density of noise from, 516
- Rotor-Stator Interactions (see distortion harmonics)
- Rough surfaces:
  - cavitation inception, 331
  - turbulent boundary layer, 637-641, 647, 654, 679, 727, 734, 742-744, 770-772, 804
- Sears function, 931
- Self-sustained tone, 144, 1046-1056  
(see also Feedback)
- Shape factor, 642
- Shape functions, modal, 554
- Shear Layer, examples, 117
  - and jet tones, 122, 142-148
  - and sound radiation, 124
  - behind cylinders, 457-458
  - instability at trailing edges, 962-963
  - linear stability analysis, 118-123
  - shear noise, 172
- Similitude, 12
  - of turbomachines, 1111
- Simple harmonic oscillator:
  - linear response formula, 541
  - mass controlled motion, 542
  - power relationships, 543
  - resonance frequency, 541
  - stiffness controlled motion, 542
- Singing, hydrofoil (see vortex shedding hydrofoil)
- Solubility of air in water, 268, 427
- Solidity of rotors blading, 1119
- Sommerfeld's radiation condition, 51
- Sound, dipole:
  - from compact body, 509
  - from compact force, 503
  - from rigid cylinder, 504  
(see also vortex shedding, cylinder)
- Sound pressure level, definition, 16
  - combination, 23
  - overall, 20
- Sound pressure spectrum, 18
- Source levels, superposition, 70-71
- Spectral density, 21, 25
  - cross, 100-101
  - dimensionless, 24
  - frequency, 155-160
- Spectral density, (continued)
  - intensity, 217
  - measurement, 20, 213
  - power, 4, 217
  - pressure, 4, 100, 217
  - wave number, 105, 155-160
- Speed of sound, 36
- Sphere:
  - heaving, 71-73, 107
  - volume source, 42
- Spherical coordinates, 41
- Spinning modes, 1140, 1200-1201
  - condition for propagation in ducts, 1200
- Stability (see hydrodynamic instability)
- Stagger angle, 1162, 1176, 1186
- Stationary phase, method of, 574-575
- Statistical energy analysis, 539, 544
- Stiffness, bending of plate, 546
- Stokes' theorem, 85
- Stress tensor, 96
  - Lighthill's, 53
  - Stokes', 53, 82
- Strip theory, 939
- Strouhal number, 466-468
  - definition, 127
  - lifting surfaces, 969-978
  - table, 974
  - vortex shedding cylinder, illustration, 467-468
- Surface, acoustic influence on sound generation, 67, 74-80, 915-917
- Surface tension, 238, 427
- Taylor's hypothesis, 174
- Tensile strength of water, 231  
(see also cavitation thresholds)
- Third-octave-band spectrum, 21, 218
- Thrust coefficient, propeller, 1112, 1114
- Time average, 17
- Torque coefficient, 1114
- Total loss factor, 247, 553  
(see also damping)
- Trailing edge noise:
  - (see also vortex shedding, airfoils)
  - aeroacoustic scattering theory, 1012-1018
  - and surface pressures, 1018
  - axial flow fans, 1148-1152
  - blown flaps and impinging jets, 1027-1033
  - compared to boundary layer noise, 889, 891, 1016
  - compactness arguments, 908-917
  - dipole near half plane, 909-915
  - evanescent wave theories of, 1023

- Trailing edge noise: (continued)
- from flexible surfaces, 1035
  - from wedges, 1036
  - from turbulent flow past edge, 918-924
  - general scaling relationship, 923, 1022
  - influence of yaw, 923
  - measurements, 1031, 1032, 1034
  - measurements on propeller fan, 1151
  - relationship to surface pressures, 1018-1023
- Transition to turbulence:
- body of revolution, 790
  - condition for in boundary layer, 787-790
  - intermittency, 795
- Tube bundles, 521
- fluctuating lift, 525
  - Strouhal numbers, 524
  - vibration in, 525
  - whirling parameters, 526
- Turbulence:
- correlation functions, 158
  - expectation, 151
  - mean square, 152
  - probability, 151
  - sound from free, dimensional analysis, 61-66
  - variance, 152
  - wave number spectrum and Fourier transform, 156
  - in axial flow fan inlet, 1181-1193
  - interaction with airfoil, 904-907, 936-943
- Turbulence microscale, 670
- Turbulent boundary layer:
- axisymmetric on cylinders, 807
  - body of revolution, 790-795
  - bursting events, 680
  - convection velocities, turbulence, 665
  - law of the wake, 636
  - law of the wall, 633
    - on circular cylinders, 809
  - logarithmic region, 636, 637
  - on NACA 0012 airfoil, 962
  - on NACA 63-009 airfoil, 964
  - parameter estimation formula, 645
  - Reynolds stresses, 654, 673-675
  - roughness height, 638
  - streamwise vortex, structures in, 675
  - surface roughness, table, 647
  - turbulence intensities, 649-653
  - turbulence spectra, 661-663
  - turbulence statistics, 655
  - von Karman constant, 637
  - with pressure gradients, 800
  - with pressure gradients, wall pressures in, 801-805
  - wall shear coefficient, 631
  - in transitional flow, 793-795
- Turbulent boundary layer, induced vibrations:
- Dyer's criteria for spatially homogeneous excitation, 838-840, 856
  - hydrodynamic coincidence, 842
    - of hydrofoils, 1039-1040
  - measurements, 847-848
  - modal pressure, 841, 843
  - mode classifications, 845
  - multi-modal estimates, 849
  - parametric dependences, 864-865
  - sound from, 856-861
  - speed dependence, 855
- Turbulent boundary layers, sound radiation from: (see also trailing edge noise)
- boundary layers on flexible surfaces, 878
  - comparisons with other mechanisms, 889, 891
  - dipole sound, 871-873
  - efforts at measuring, 873
  - formulas for, 878, 880, 883, 885
- Turbulent boundary layer, wall pressure:
- and quadrupole sound, 885
  - at low wave number, measurements, 863
  - at sonic wave numbers, measurements, 766
  - at sonic wave numbers theory, 878
  - attenuation by elastomer layers, 783
  - circular cylinders, 810
  - covariances on trailing edges, 998-1000
  - convection velocities, 744
  - influences of surface impedance, 878-881
  - influences of viscous absorption, 881
  - in transitional flow, 797
  - measured frequency spectrum, 731-735
  - on trailing edges, 993-998
  - outer-inner variable scaling, 734
  - rough walls, 770
  - separated flow, 806
  - space-time statistics, 737
  - spatial resolution, 772, 777
  - theoretical frequency spectrum, 709
- Unsteady airfoil theory, 926-931  
(see also lift, fluctuating on airfoils)
- Viscosity, kinematic of water, 427
- Viscous sublayer, 633
- Vortex, 1, 80, 81
- sound 87-89, 124, 497-508
  - sound from half plane, 1004
- Vortex formation lengths, 461, 962
- Vortex shedding, airfoils (see also Vortex shedding, cylinders, hydrofoils)
- acoustic radiation formula, 1007
  - blunt edges, 1011

- Vortex shedding, airfoils, (continued)
  - and turbulent flow structures, 967-970
  - at blunt trailing edge, 961-962, 966-969
  - at sharp trailing edge, 959-960, 971
  - effects of edge vibration, 1058-1060
  - fluctuating forces, 1001
  - frequency of, 971-978, 974 (table)
  - laminar flow tones, 1007
  - relationship to other sources, 903-905
  - rotating blade with laminar flow, 1145
  - suppression with splitter plates, 964
  - tonal pressures due to, 985-987, 990, 992, 1008, 1010-1011
  - wake strengths, 992
- Vortex shedding, cylinder:
  - acoustic intensity, 505-511
  - acoustic intensity, effect of yaw, 510
  - and Orr-Sommerfeld's equation, 453-459
  - effects of cylinder vibration on, 483, 509, 1057-1058
  - effects of free stream turbulence on, 483
  - effect of splitter plates on, 485
  - fluctuating velocities in wake, 456
  - formation zone, 459-462
  - frequency of, 465, 467-469
  - mean velocity in wake, 455
  - photograph, 451
  - vibration control, 526-528, 1056
  - vibration modeling, 1066
- Vortex shedding, hydrofoils:
  - (see also vortex shedding, airfoils, cylinders)
  - analytical modeling techniques, 1042, 1061-1067
  - control by hysteretic damping, 1051-1056
  - vibration, 1037-1041, 1046-1049
  - wake-vibration coupling, 1057-1061
- Vortex shedding frequency, 466
- Vortex sheet, 118, 121
- Vortex spacing ratio, 471
- Vorticity vector, 82
- Wall shear stress, 631
- Wall pressure fluctuations (see turbulent boundary layer, wall pressure)
- Water, physical properties, 427
- Wave equation, 37
- Wave number:
  - acoustic, 43
  - free flexural waves, 549
  - lattice, 557
  - mode density, 559-560
  - on resonant rectangular plate, 566
  - trace, 164, 575
- Wave speed, longitudinal, 559
- Wave vector filter:
  - analogy to rotor response, 1101-1104, 1182, 1186-1190
  - as measurement tool, 760
  - formulae, 755
- Weber No., 17, 413
- Wedge, scattering, 1036
- Wiener-Hopf technique, 912
- Young's modulus, 546

**END**

**FILMED**

**4-85**

**DTIC**